

UCLA

UCLA Electronic Theses and Dissertations

Title

Investigating the role of select receptors in radiation-induced cellular plasticity events in glioblastoma

Permalink

<https://escholarship.org/uc/item/0zw8m139>

Author

IOANNIDIS, ANGELIKI DIOTIMA

Publication Date

2024

Peer reviewed|Thesis/dissertation

UNIVERSITY OF CALIFORNIA

Los Angeles

Investigating the role of select receptors in radiation-induced
cellular plasticity events in glioblastoma

A dissertation submitted in partial satisfaction of the requirements for the degree of
Doctor of Philosophy in Molecular Toxicology

by

Angeliki Diotima Ioannidis

2024

© Copyright by
Angeliki Diotima Ioannidis
2024

ABSTRACT OF THE DISSERTATION

Investigating the role of select receptors in radiation-induced
cellular plasticity events in glioblastoma

by

Angeliki Diotima Ioannidis

Doctor of Philosophy in Molecular Toxicology

University of California, Los Angeles, 2024

Professor Frank Pajonk, Chair

All living matter is under constant environmental stress that jeopardizes the genomic integrity of individual cells and the functional integrity of tissues in higher organisms. At the level of non-post-mitotic tissues, stem cells constantly divide to give rise to all lineages of differentiated cells. Once thought to be unidirectional, cellular differentiation can now be reversed and overexpression of developmental transcription factors can turn somatic cells into induced pluripotent stem cells by means of reprogramming. This process is critically dependent on optimal co-stimulation of the innate immune response through activation of pattern recognition receptors (PRRs) by pathogen and/or damage associated molecular patterns (PAMPs/DAMPs). Ionizing radiation (IR) being an extreme form of genotoxic stress, can lead to the release of DAMPs. Our lab has identified that radiation induces the formation of cancer stem cells from non-cancer stem cells, a process termed IR-induced phenotype conversion. Cellular plasticity, an umbrella term encompassing reprogramming and radiation-induced phenotypic conversion

events, allows cells to effectively respond to triggers that would otherwise compromise them. The underlying mechanisms driving these processes are incompletely understood but PAMPs and DAMPs are readily involved and employ common pathways downstream of their respective receptors. Glioblastoma (GBM) is a highly aggressive, malignant primary brain tumor for which cancer stem cells play a critical role in therapy resistance, recurrence and overall disease progression. This in combination with the radiation-induced cellular plasticity response could further exacerbate patient outcome if unaccounted for. Thus, to better understand the underlying mechanisms driving IR-induced cellular plasticity events, cancer stem cell maintenance/self-renewal (SFAs, ELDA) and *de novo* stem cell induction (reprogramming assays) were studied using patient-derived glioblastoma cells. Several Toll-like receptors (TLRs) as well as components of the free cytosolic DNA sensing machinery, the cGAS/STING pathway, were evaluated. Our main study findings were as follows: 1) stem cell maintenance following irradiation is mediated through cGAS-independent STING signaling, with potential crosstalk with TLR4 and TLR9 and 2) *de novo* stem cell induction following irradiation implicates TLR3 signaling and potentially other receptors and processes affected by chloroquine. Collectively, these point to a direct link between innate immune signaling and IR-induced cellular plasticity events.

The dissertation of Angeliki Diotima Ioannidis is approved.

Patrick Allard

Oliver Hankinson

Harley I. Kornblum

Frank Pajonk, Committee Chair

University of California, Los Angeles

2024

TABLE OF CONTENTS

| | |
|--|----------|
| ABSTRACT..... | ii |
| COMMITTEE PAGE | iv |
| TABLE OF CONTENTS | v |
| LIST OF FIGURES | vii |
| LIST OF TABLES | viii |
| LIST OF SUPPLEMENTARY FIGURES | viii |
| LIST OF SUPPLEMENTARY TABLES | ix |
| ACKNOWLEDGMENTS | xi |
| PREFACE | xvi |
| VITA | xvii |
| | |
| CHAPTER 1. Introduction | 1 |
| 1.1 Glioblastoma..... | 2 |
| 1.2 Radiation therapy: ionizing radiation overview | 6 |
| 1.3 Innate immunity: pattern recognition receptors (PRRs) and their ligands..... | 7 |
| 1.3.1 TLRs | 9 |
| 1.3.1.1 TLR structural features & downstream signaling | 9 |
| 1.3.1.2 TLRs in cancer | 10 |
| 1.3.2 RLRs | 12 |
| 1.3.2.1 RLR structural features & ligand recognition..... | 12 |
| 1.3.3 Receptor crosstalk..... | 13 |
| 1.4 cGAS/STING | 15 |
| 1.4.1 cGAS/STING structural features & signaling | 15 |
| 1.4.2 Functions of STING | 16 |
| 1.4.3 cGAS nuclear localization | 18 |
| 1.4.4 cGAS/STING in cancer..... | 19 |
| 1.5 Reprogramming | 22 |
| 1.5.1 History overview & important studies..... | 22 |
| 1.5.2 Role of innate immunity in reprogramming..... | 25 |
| 1.6 Cellular plasticity..... | 30 |

| | | |
|---|--|------------|
| 1.6.1 | Overview..... | 30 |
| 1.6.2 | Hallmarks of cancer..... | 31 |
| 1.6.3 | Epigenetic regulation of cellular plasticity..... | 33 |
| 1.6.4 | SWI/SNF chromatin remodeling complex..... | 35 |
| SUMMARY OF CHAPTERS | | 37 |
| CHAPTER 2. Radiation-induced cellular plasticity | | 39 |
| 2.1 | Materials & Methods | 40 |
| 2.2 | Results | 49 |
| 2.3 | Discussion | 77 |
| 2.4 | Future Directions | 91 |
| CHAPTER 3. Lab publications & Contributions | | 99 |
| 3.1 | Lab publications/papers | 100 |
| 3.1.1 | <i>Prevention of radiation-induced phenotypic conversion of non-stem glioma cells to glioma stem/initiating cells (GSCs/GICs)</i> | <i>100</i> |
| 3.1.2 | <i>Implications of drug treatments on normal tissue following irradiation</i> | <i>193</i> |
| 3.1.3 | <i>Leveraging radiation-induced multipotency to drive surviving GBM cells towards a mitotically incompetent, neuron-like state</i> | <i>247</i> |
| 3.1.4 | <i>Pro-inflammatory signaling in mammary gland development and carcinogenesis..</i> | <i>299</i> |
| 3.2 | Summaries & Contributions | 313 |
| Supplementary Figures | | 329 |
| Supplementary Tables | | 333 |
| REFERENCES | | 362 |

LIST OF FIGURES:

Figure 1 (page 50): Heatmap representation of differentially expressed damage associated molecular pattern (DAMP) and pattern recognition receptor (PRR) genes from an RNA sequencing analysis performed in HK-374 monolayer cells, 48h post 4 Gy irradiation.

Figure 2 (page 51): **RT-PCR** validation heatmap representing differentially expressed damage associated molecular pattern (DAMP) and pattern recognition receptor (PRR) genes previously identified from RNA sequencing analysis performed in HK-374 monolayer cells, 48h post 4 Gy irradiation.

Figure 3 (page 53): **Sphere forming assay** for TLR3 and TLR4 inhibitors in HK-374 glioma spheres.

Figure 4 (page 54): **Sphere forming assay** for endosomal TLR inhibitor, chloroquine (CQ) in HK-374 glioma spheres.

Figure 5 (page 55): **Sphere forming assay** for TLR9 inhibitor in HK-374 glioma spheres.

Figure 6 (page 57): **Sphere forming capacity** as determined from extreme limiting dilution assays (ELDAs) for HK-374 and HK-308 glioma sphere samples treated with TLR9 inhibitor (1x).

Figure 7 (page 58): **Stem cell frequency** as determined by ELDA analysis in HK-374 and HK-308 glioma spheres treated with TLR9 inhibitor (1x).

Figure 8 (page 59): Principles of reprogramming assay.

Figure 9 (page 60): **Reprogramming** assay in HK-374 monolayer cells treated with TLR3, TLR4 inhibitors and CQ to determine their respective effects on the generation of stem-like cells from non-stem cells.

Figure 10 (page 62): Relative expression of Yamanaka factors (YFs), in HK-374 monolayers (ZsGreen negative sorted cells) irradiated with 4 Gy and treated with TLR3/TLR4 inhibitors.

Figure 11 (page 63): **RT-PCR** for evaluating the expression levels of human cGAS/STING in HK-374 and HK-308 glioma cell lines (adherent monolayer cells).

Figure 12 (page 64): **Sphere forming capacity** for HK-374 glioma spheres treated (1x) with hcGASi (G140) as determined by ELDA.

Figure 13 (page 65): **Sphere forming capacity** for HK-374, HK-157 and HK-308 glioma spheres treated (1x) with human STINGi (H-151) as determined by ELDAs.

Figure 14 (page 66): **Stem cell frequency** as determined by ELDA analysis in HK-374, HK-157 and HK-308 glioma spheres treated with STINGi (H-151) (1x).

Figure 15 (page 68): Pathway analysis of DEGs identified from RNAseq comparing irradiation (4 Gy) vs control (0 Gy) in HK-374 monolayer samples 48h post irradiation.

Figure 16 (page 70): Pathway analysis of DEGs identified from RNAseq comparing IR + STINGi (4 Gy + 1uM H151) vs irradiation (4 Gy) in HK-374 monolayer samples 48h post irradiation.

Figure 17 (page 73): Heatmap representation of differentially expressed genes corresponding to chromatin remodeling complex components (log2 fold changes) as determined from RNAseq analysis in HK-374 monolayer cells 48h post 4 Gy irradiation (QTP dataset).

Figure 18 (page 74): **RT-PCR** analysis showing the relative expression of chromatin remodeling complex components, SMARCA1 and SMARCD3, in HK-374 monolayers (ZsGreen negative sorted cells) irradiated with 4 Gy and treated with TLR3, TLR4 inhibitors and CQ. RT-PCR analysis performed 48h post irradiation.

Figure 19 (page 76): **RT-PCR** analysis showing the relative expression of chromatin remodeling complex components, SMARCA1 and SMARCD3, in HK-374 monolayers (ZsGreen negative sorted cells) irradiated with 4 Gy and treated with TLR9 inhibitor.

Figure 20 (page 92): Graphical representation of research questions presently explored and useful future avenues to consider for better understanding how radiation-induced cellular plasticity events come about.

LIST OF TABLES:

Table 1 (page 42). List of inhibitors used and their specific characteristics.

Table 2 (page 67). Differentially expressed genes (DEGs) as determined by DESeq2 analysis using FDR: 0.1 and min. fold change: 2, based on iDEP software.

Table 3 (page 69). Pathway analysis of DEGs identified from RNAseq comparing irradiation (4 Gy) vs control (0 Gy) in HK-374 monolayer samples 48h post irradiation.

Table 4 (page 71). Pathway analysis of DEGs identified from RNAseq comparing IR + STINGi (4 Gy + 1uM H151) vs irradiation (4 Gy) in HK-374 monolayer samples 48h post irradiation.

Table 5 (page 97). Predicting blood-brain-barrier (BBB) permeability of select inhibitors.

LIST OF SUPPLEMENTARY FIGURES:

Supplementary Figure 1 (page 329): **Sphere forming capacity** as determined from extreme limiting dilution assays (ELDAs) for HK-374 and HK-345 glioma sphere samples treated (4x) with TLR4 inhibitor.

Supplementary Figure 2 (page 330): **Sphere forming capacity** as determined from extreme limiting dilution assays (ELDAs) for HK-345 glioma sphere samples treated with TLR9 inhibitor (1x).

Supplementary Figure 3 (page 331): **Stem cell frequency** as determined by ELDA analysis in HK-345 glioma spheres treated with TLR9 inhibitor (1x).

Supplementary Figure 4 (page 332): [Stem cell frequency](#) as determined by ELDA analysis in HK-374 and HK-345 glioma spheres treated with TLR9 (1x) and TLR4 inhibitors (4x treatment).

LIST OF SUPPLEMENTARY TABLES:

Supplementary Table 1 (page 333). Primer sequences (Integrated DNA Technologies) used for RT-PCR validation experiments represented in Figure 2.

Supplementary Table 2 (page 334). Two-way ANOVA analysis results of multiple comparisons for data represented in Figure 3.

Supplementary Table 3 (page 335). Two-way ANOVA analysis results of multiple comparisons for data represented in Figure 4.

Supplementary Table 4 (page 336). Two-way ANOVA analysis results of multiple comparisons for data represented in Figure 5.

Supplementary Table 5 (page 337). Two-way ANOVA analysis results of multiple comparisons for HK-374 glioma sphere data represented in Figure 6.

Supplementary Table 6 (page 338). Two-way ANOVA analysis results of multiple comparisons for HK-308 glioma sphere data represented in Figure 6.

Supplementary Table 7 (page 339). Two-way ANOVA analysis results of multiple comparisons for HK-374 glioma sphere data represented in Figure 7.

Supplementary Table 8 (page 340). Two-way ANOVA analysis results of multiple comparisons for HK-308 glioma sphere data represented in Figure 7.

Supplementary Table 9 (page 341). One-way ANOVA analysis results of multiple comparisons for data represented in Figure 9.

Supplementary Table 10 (page 346). Primer sequences (Integrated DNA Technologies) used for RT-PCR validation experiments represented in Figure 10.

Supplementary Table 11 (page 347). Two-way ANOVA analysis results of multiple comparisons for HK-374 data represented in Figure 10.

Supplementary Table 12 (page 349). Primer sequences used for evaluating the expression levels of human cGAS/STING, as shown in Figure 11.

Supplementary Table 13 (page 350). Two-way ANOVA analysis results of multiple comparisons for data represented in Figure 12.

Supplementary Table 14 (page 351). Two-way ANOVA analysis results of multiple comparisons for HK-374 glioma sphere data represented in Figure 13.

Supplementary Table 15 (page 352). Two-way ANOVA analysis results of multiple comparisons for HK-157 glioma sphere data represented in Figure 13.

Supplementary Table 16 (page 353). Two-way ANOVA analysis results of multiple comparisons for HK-308 glioma sphere data represented in Figure 13.

Supplementary Table 17 (page 354). Two-way ANOVA analysis results of multiple comparisons for HK-374 glioma sphere data represented in Figure 14.

Supplementary Table 18 (page 355). Two-way ANOVA analysis results of multiple comparisons for HK-157 glioma sphere data represented in Figure 14.

Supplementary Table 19 (page 356). Two-way ANOVA analysis results of multiple comparisons for HK-308 glioma sphere data represented in Figure 14.

Supplementary Table 20 (page 357). Primer sequences (Integrated DNA Technologies) used for evaluating the expression levels of SMARCA1 and SMARCD3.

Supplementary Table 21 (page 358). One-way ANOVA analysis results for SMARCA1 data represented in Figure 18.

Supplementary Table 22 (page 359). One-way ANOVA analysis results for SMARCD3 data represented in Figure 18.

Supplementary Table 23 (page 360). One-way ANOVA analysis results for SMARCA1 data represented in Figure 19.

Supplementary Table 24 (page 361). One-way ANOVA analysis results for SMARCD3 data represented in Figure 19.

ACKNOWLEDGMENTS

When I first joined UCLA back in 2018, I embarked upon my PhD journey having somewhat of a vague idea regarding my future scientific endeavors. I knew I enjoyed science and was curious to explore new areas of scientific research I had not previously considered. I was confident that UCLA, and the MolTox IDP specifically, would give me the flexibility to explore different research environments, in the hopes of finding my niche. The multidisciplinary culture fostered at the university- and program- level was undoubtedly a key contributing factor here. And here comes my small confession: while my initial goal was to get as diverse an exposure as possible through my rotations, I was somewhat certain (or so I thought!) that I would not be joining a cancer lab. Here I am though, 5 years in the making, about to graduate from a Radiation Oncology lab! At the time, the great uncertainty and complexity of cancer research seemed *VERY* overwhelming, well beyond what I would have considered being an enjoyable challenging scientific exploration. However, while the complexity of this field still reigns strong, my experience at the Pajonk lab, even as early as the first few weeks into my rotation, quickly made me reconsider my original viewpoint. I mainly attribute this to my fellow lab members who have all strived to create a supportive, collaborative and scientifically stimulating environment. The guidance, mentorship and willingness to help each other out were defining factors in making me appreciate, but most importantly enjoy being a member of this research lab! Dr. Pajonk's guidance and mentorship instilled in me the notion that there is beauty in the unknown. Having the freedom to explore different avenues of scientific research to address important questions becomes so much more manageable and enjoyable when there is no agenda to be fulfilled. I am grateful for this opportunity and use this experience as a guiding lesson for moments when I find myself feeling scared of the "unknown".

I would like to thank Dr. Pajonk for his kind support, guidance, patience and understanding throughout this journey. It has definitely had its ups and downs (more downs than I would like to admit to), but Dr. Pajonk and the Pajonk lab members, past and present, have all been there supporting and cheering me on, even in moments when I found myself lost in my overthinking little world. I would like to specifically thank Dr. Ling He for her invaluable mentorship, guidance, support, encouragement and friendship. Ling and I started in the lab around the same time. Despite her having to navigate through this new environment and establish her bearings as a new lab member, she was, and always has been, willing and eager to help me (and everyone else) and I am forever grateful to her. I remember bombarding her with questions when I first started my rotation (the pattern clearly continued over the years as well). Instead of being annoyed by that she always took the time to help me and quite literally enlighten me with her knowledge, expertise and masterful experimental skillset. Ling, I am extremely thankful to have met you and have the opportunity to learn from you and work with you. You are an amazing person, and your hard work, dedication and perseverance are attributes I greatly admire and look up to. You are truly a role model and thank you for putting up with me all these years! Working alongside you has been an absolute pleasure and definitely one of the highlights of my experience as a graduate student. Thank you, thank you, thank you!

Past and present members of the Pajonk lab have also been instrumental in my journey and I thank each and every one of you for your good nature and support. A quick shoutout to my current, lovely lab mates: Anjelica, I have immensely enjoyed getting to see you flourish as a post doc in our lab and discussing, bouncing off scientific ideas and generally interacting with you. You are so inquisitive and hardworking and I really admire your dedication and strong work ethic. Thank you for being such a good lab mate and friend. Carter, your ability to handle all things lab is admirable to say the least! Thank you for keeping everything running smoothly and for always being so positive and cheerful (and occasionally sarcastic – which has been very

much appreciated and enjoyed)! Linda, you too have grown immensely since joining the lab and your perseverance through it all has been inspiring. Thank you for interacting with me and for our discussions about life and lab.

I need to also extend a special thank you to Purva, one of our absolutely stellar past undergrads in the lab (now a soon to be amazing med school student!) whom I had the great pleasure of working alongside and occasionally offering my few words of wisdom to about experimental procedures and lab fun. Your determination, willingness to undertake new tasks, highly inquisitive nature, strong character and good natured personality have all been attributes I highly admire and look up to. Working with you in the lab was one of the most enjoyable moments of my grad school journey. Besides seeing a very enthusiastic and passionate student undertaking experiments with such determination, I also got a friend in the process. Over the past year, I have gotten to interact with you a lot more outside of lab and I am forever grateful for our conversations and your true compassion and understanding. Thank you so much for being you!

Of course, I cannot forget my fellow grad student/lab mate-by-space-association, now post doc extraordinaire, Dr. Graham Read (I am sorry, I had to say Dr. at least once!) who has helped me immensely in navigating the lovely rollercoaster of grad school. Be it the small doodles left at my desk (along with the occasional yummy treats!), the adventuring, randomly bumping into each other in lab during the weekend, talking about experiments and even your patience, support, compassion and willingness to listen to (and honestly put up with) all my grad school meltdowns and associated life struggles, truly speak to how caring of an individual you are. I am very appreciative that I got to share the lab space with you over the past few years and end up with such a good friend. Thank you for your support and understanding (and for making me

appreciate tea a bit more haha – it's a good switch from my coffee obsession). Thank you for being you and for believing in me even at my lowest moments. I really appreciate all of it!

I need to also extend a big thank you and express my deepest gratitude to my committee members, Drs. Allard, Hankinson and Kornblum, for their patience, support, encouragement and understanding through it all. I greatly appreciate your time and thoughtfulness, without which I would not have been able to reach this defining moment in my graduate studies. Thank you all!

Next, I want to thank my family and friends for supporting me in making this academic journey a reality. Specifically, to my mom and dad, thank you for taking care of me, loving me and showing me what it means to be a hardworking scientist. I am grateful to have been raised by you and for having been given all these opportunities in my life. Thank you! To my grandma, Aggela, I absolutely adore you and I am so so grateful to have you as my grandma. You are a true role model and your strong character and perseverance through life's adversities serve as a daily reminder that I too should push through and strive to accomplish my goals. Thank you for always loving me and for understanding me. Thank you for being a blunt critic of my reality and grounding me when I found myself overthinking. While at the time I might have seen this as a bit harsh, I know that you only say things because you truly love and care about me and want the best for me, so thank you for being you! I appreciate you, admire you, and love you!

Lastly, this might be an odd one, but it has been a crucial part of my reality as a grad student. I want to sincerely thank the KREC and Wooden community for giving me the opportunity to have an outlet for coping with grad school. Thank you all for maintaining such a positive and welcoming environment, and for making sure the facilities were running smoothly. I am convinced that had it not been for these resources and the people working there, I would not be where I am today. Having the gym has been instrumental for my mental health as it provided me

with a safe space to work on my goals (gym and otherwise), all while providing me with a much needed distraction from the endless joys of grad school. Funny enough, growing up I would more often than not find myself going to lab (where my parents worked) after school and extracurriculars. As such, I had rightfully earned the title of a “lab rat” since I would occasionally sneak around the offices and interact with the post docs and med students there. I think going through grad school I might have accumulated additional data to support my “lab rat” title (we can discuss statistics later if you want), all while acquiring a new rodent classification, that of a “gym rat”! Granted there is a lot more work that needs to be done on that front, but it’s a title in progress! Hopefully, as I progress into my future endeavors (academic and otherwise) I get to further support these titles and maybe who knows, add some new ones to the mix. I have been considering getting a pet for the longest time (side note: if you are a grad student reading this and considering getting a pet, the answer is YES!), so maybe next up in line is “rat mom”? Who knows! 😊

Once again, thank you all for your unwavering support and encouragement through it all! I greatly appreciate and value each and every one of you! To anyone I might have missed here, I sincerely apologize, but I hope I have expressed my gratitude in person. If not, please track me down!

PREFACE

Chapter 3.1 includes versions of the following publications/pre-prints:

Section 3.1.1 - Prevention of radiation-induced phenotypic conversion of non-stem glioma cells to glioma stem/initiating cells (GSCs/GICs)

Bhat, Kruttika, et al. "Dopamine receptor antagonists, radiation, and cholesterol biosynthesis in mouse models of glioblastoma." *JNCI: Journal of the National Cancer Institute* 113.8 (2021): 1094-1104.

He, Ling, et al. "Effects of the DRD2/3 antagonist ONC201 and radiation in glioblastoma." *Radiotherapy and Oncology* 161 (2021): 140-147.

He, Ling, et al. "Activation of the mevalonate pathway in response to anti-cancer treatments drives glioblastoma recurrences through activation of Rac-1." *bioRxiv* (2023).

A version of this work has been provisionally accepted in *Cancer Research Communications* (as of 5/20/2024).

Section 3.1.2 - Implications of drug treatments on normal tissue following irradiation

Bhat, Kruttika, et al. "1-[4-Nitrophenyl] sulfonyl]-4-phenylpiperazine treatment after brain irradiation preserves cognitive function in mice." *Neuro-oncology* 22.10 (2020): 1484-1494.

He, Ling, et al. "Effects of Dopamine Receptor Antagonists and Radiation on Mouse Neural Stem/Progenitor Cells." *bioRxiv* (2023): 2023-01.

A version of this work has been submitted for review.

Section 3.1.3 – Leveraging radiation-induced multipotency to drive surviving GBM cells towards a mitotically incompetent, neuron-like state

He, Ling, et al. "Radiation-Induced Cellular Plasticity: A Strategy for Combatting Glioblastoma." *bioRxiv* (2024): 2024-05.

A version of this work has been submitted for review.

Section 3.1.4 - Pro-inflammatory signaling in mammary gland development and carcinogenesis

He, Ling, et al. "Tumor necrosis factor receptor signaling modulates carcinogenesis in a mouse model of breast cancer." *Neoplasia* 23.2 (2021): 197-209.

VITA

EDUCATION

- University of California, Los Angeles** 2018-2024 (expected)
Ph.D. Candidate, Molecular Toxicology
- University of California, Davis** 2016-2018
M.S. Forensic Science, Criminalistics & DNA dual track
- University of California, Davis** 2012-2016
B.S. with Honors, Environmental Toxicology (Forensic Science emphasis; French minor)

RESEARCH EXPERIENCE

- University of California, Los Angeles** 2019-present
Graduate Student Researcher
Department of Radiation Oncology; Advisor: Frank Pajonk, M.D., Ph.D.
- University of California, Davis** 2017-2018
Graduate Student Researcher (Master's student)
Department of Environmental Toxicology; Advisor: Robert H. Rice, Ph.D.
- University of California, Davis** 2015-2016
Undergraduate Student Intern
Department of Environmental Toxicology; Advisor: Andrew Whitehead, Ph.D.

AWARDS

- Summer Mentored Research Fellowship (\$3000; UCLA Academic Planning and Budget) 2021
- California Association of Toxicologists - Robert Cravey Memorial Grant Award (\$500) 2016
- University of California, Davis**
Dean's Honors List for the College of Agricultural and Environmental Sciences W2015, F2013
Dean's Honors List for the College of Biological Sciences S2013, F2012

PUBLICATIONS

- He, L., Azizad, D., Bhat, K., **Ioannidis, A.**, Hoffman, C. J., Arambula, E., . . . Pajonk, F. (2024). Radiation-Induced Cellular Plasticity: A Strategy for Combatting Glioblastoma. *bioRxiv*.

He, L., **Ioannidis, A.**, Arambula, E., Hoffman, C. J., Joshi, P., Kathiravan, A., ... & Pajonk, F. (2023). Activation of the mevalonate pathway in response to anti-cancer treatments drives glioblastoma recurrences through activation of Rac-1. *bioRxiv*.

He, L., Bhat, K., **Ioannidis, A.**, & Pajonk, F. (2023). Effects of Dopamine Receptor Antagonists and Radiation on Mouse Neural Stem/Progenitor Cells. *bioRxiv*, 2023-01.

Ioannidis, A. D., Khan, S. G., Tamura, D., DiGiovanna, J. J., Rizza, E., Kraemer, K. H., & Rice, R. H. (2022). Trichothiodystrophy hair shafts display distinct ultrastructural features. *Experimental Dermatology*, 31(8), 1270-1275.

He, L., Bhat, K., **Ioannidis, A.**, Zhang, L., Nguyen, N. T., Allen, J. E., ... & Pajonk, F. (2021). Effects of the DRD2/3 antagonist ONC201 and radiation in glioblastoma. *Radiotherapy and Oncology*, 161, 140-147.

Bhat, K., Saki, M., Cheng, F., He, L., Zhang, L., **Ioannidis, A.**, ... & Pajonk, F. (2021). Dopamine receptor antagonists, radiation, and cholesterol biosynthesis in mouse models of glioblastoma. *JNCI: Journal of the National Cancer Institute*, 113(8), 1094-1104.

He, L., Bhat, K., Duhacheck-Muggy, S., **Ioannidis, A.**, Zhang, L., Nguyen, N. T., ... & Pajonk, F. (2021). Tumor necrosis factor receptor signaling modulates carcinogenesis in a mouse model of breast cancer. *Neoplasia*, 23(2), 197-209.

Bhat, K., Medina, P., He, L., Zhang, L., Saki, M., **Ioannidis, A.**, ... & Pajonk, F. (2020). 1-[(4-Nitrophenyl) sulfonyl]-4-phenylpiperazine treatment after brain irradiation preserves cognitive function in mice. *Neuro-oncology*, 22(10), 1484-1494.

Janiaud, P., Axfors, C., Van't Hooft, J., Saccilotto, R., Agarwal, A., Appenzeller-Herzog, C., ... & Hemkens, L. G. (2020). The worldwide clinical trial research response to the COVID-19 pandemic-the first 100 days. *F1000Research*, 9.

CHAPTER 1: Introduction

1.1 Glioblastoma

Gliomas, tumors arising from glial or precursor cells within the central nervous system (CNS), account for almost 24% of all primary brain and other CNS tumors (malignant and non-malignant), and make up over ⅔ of these malignancies (S. Li et al., 2023; Ostrom et al., 2023).

Depending on tumor aggressiveness, reflected by how abnormal the cells making up these tumors are, gliomas can be either localized or diffuse, with diffuse tumors corresponding to higher tumor grades, indicative of their more aggressive phenotype (McKinnon, Nandhabalan, Murray, & Plaha, 2021). According to the most recent (5th edition) World Health Organization (WHO) Classification of Tumors of the CNS, gliomas can be classified into: adult-type diffuse gliomas, pediatric-type diffuse gliomas (subdivided into low- and high-grade), and circumscribed astrocytic gliomas (D. N. Louis et al., 2021). Given the complexity of these tumors, classification beyond histopathological features is also required. Therefore, molecular parameters such as isocitrate dehydrogenase (IDH) mutation status and presence or absence of 1p/19q codeletion are just some of the features evaluated (Dietrich, 2024). Presence of IDH mutation (either IDH1 or IDH2, the latter of which is less common) is generally associated with better patient prognosis (D. N. Louis, Schiff, & Batchelor, 2024). Overall, from the combination of histopathological and molecular parameters discussed, diffuse gliomas can be regarded as IDH-wildtype or IDH-mutant tumors falling into one of the following classifications: i) glioblastoma (GBM), IDH-wildtype, ii) astrocytoma, IDH-mutant, grade 4, iii) astrocytoma, IDH-mutant, grade 3 and iv) oligodendroglioma, IDH-mutant and 1p/19q-codeletion, grade 3 tumors (Dietrich, 2024; D. N. Louis et al., 2021). Glioblastomas account for the vast majority of gliomas, making up over 50% these tumors (Ostrom et al., 2023).

More specifically, glioblastoma is a highly aggressive, grade 4 primary brain cancer arising from glial cells, non-neuronal cells found in the peripheral and central nervous system (D. Louis, Schiff, D., Batchelor, T.). While these tumors can develop anywhere within the CNS, the frontal

and temporal lobes are predominantly affected (Larjavaara et al., 2007). The frontal lobes are associated with functions such as decision-making, short-term memory and movement, while processing of information pertaining to smell, taste and sound, as well as functions relating to memory storage are regulated by the temporal lobes (Mayo_Clinic). As such, impairment in one or more of these functions is a typical feature of GBM patients' clinical presentation.

Glioblastomas account for 14.2% of all primary brain tumors and 50.9% of all primary malignant brain tumors (Ostrom et al., 2023). Their incidence in the general population is 3-5 per 100,000 individuals, with majority of cases presenting in adults >65 years of age, even though children and younger adults can also be affected. Males also seem to have a higher (x1.6) incidence of developing this type of cancer (Ostrom et al., 2018). Risk factors for GBM include certain heritable syndromes such as neurofibromatosis and Li-Fraumeni syndrome as well as prior exposure to ionizing radiation, either during therapy, particularly in early childhood, or in cases of radiation exposure such as in atomic bomb survivors (Ostrom et al., 2014). The 5-year relative survival rate following diagnosis for malignant brain and other CNS tumors is 35.7% (Ostrom et al., 2023). As evidenced however by the extremely aggressive and heterogeneous nature of GBM, its profile is dismal with survival rates being as low as 5-10% (Batchelor). Median survival after diagnosis is only 14-16 months, with disease progression being almost inevitable (McKinnon et al., 2021).

The current standard of care for GBM involves initial maximal surgical tumor resection with great care being taken to preserve normal neurological functions. Following surgery, the general therapeutic course involves combination treatment of temozolomide (TMZ), a chemotherapeutic agent, for 6 weeks ($75\text{mg}/\text{m}^2/\text{day}$) along with fractionated irradiation (60 Gy total dose, given in 30 fractions of 2 Gy each, during that 6 week period; 1 Gy = 1 Joule/kg, SI unit for radiation dose), followed by additional maintenance TMZ cycles ($150\text{-}200\text{mg}/\text{m}^2/\text{day}$ for the first 5 days of a 28-day cycle, for a total of 6 cycles) (EPA; Fernandes et al., 2017). While the proposed

treatment scheme represents the currently acceptable gold standard for the management of GBM, it only marginally prolongs patient survival to 12-18 months (Batchelor; Cheray et al., 2017). Factors contributing to limited treatment success include the inherent heterogeneity and highly infiltrative nature of GBMs which render complete surgical resection of these tumors almost impossible. Additionally, the presence of cancer stem cells (CSC) within the tumors provides an added layer of complexity to the management of this disease, as these cells are generally chemo- and radiotherapy-resistant. As such, they can continue growing to recapitulate the tumor anew, contributing to tumor recurrence (Cheray et al., 2017). Given the disappointingly low median survival rates and limited success currently available therapies have had in prolonging patient survival, this highlights the need for studying these tumors to gain a better understand of the underlying mechanisms driving their highly aggressive nature.

Heterogeneity of GBMs can be seen both at the level of general tumor organization, specifically as that relates to molecular characteristics of the tumor, as well as at the cellular level.

Regarding the former, through an analysis of The Cancer Genome Atlas (TCGA) network data on somatic mutations, DNA copy number variations and gene expression profiles of GBM samples, Verhaak and colleagues were able to establish four distinct GBM subtypes, namely: classical, mesenchymal, neural and proneural, each characterized by specific molecular and gene expression profiles. Identification of these subtypes has important implications for choice of therapy and disease prognosis, establishing a level of inter-tumoral heterogeneity for glioblastoma (Verhaak et al., 2010). Use of bulk transcriptomic data can at times skew our interpretations of what gene signatures are tumor specific rather than the result of a mixture of tumor and normal cells from the surrounding tumor microenvironment. As such, in later studies by Wang et al. it was established that the previously identified neural subtype actually corresponded to non-tumor cells found within the GBM microenvironment. Classical, mesenchymal and proneural subtypes distinctly associated with tumor cells (Q. Wang et al.,

2017). Thereafter, advances in single-cell sequencing technologies have highlighted how bulk transcriptomic profiles are actually even more elaborate. In single-cell RNAseq studies, Patel and colleagues found that different TCGA subtypes may coexist within the same GBM, with some cells having an intermediary transcriptomic profile (Patel et al., 2014). While the bulk tumor is categorized based on the most abundant phenotypic state present, this added layer of intra-tumoral heterogeneity implicating phenotypic plasticity further highlights the complexity of GBMs (Nefitel et al., 2019).

At level of cellular organization, the highly heterogeneous nature of GBM can be viewed in terms of two leading theories. On the one hand, the stochastic/clonal evolution model postulates that all tumor cells have the same genetic mutations and can become heterogeneous depending on the presence of distinct intrinsic and/or extrinsic factors. On the other hand, the hierarchical/cancer stem cell model suggests that cancer cells are different and only a subset of them, namely cancer stem cells (CSCs), have tumorigenic potential (Cheray et al., 2017). As of recent, another theory has gained traction, namely that of a plastic/complex model, which likely more closely recapitulates the tumor complexity and heterogeneity. In this system, genetic and epigenetic changes may differentially affect cells within a single tumor, giving rise to more or less differentiated progeny. These in turn can contribute to tumor formation and growth to different extents (Laks, Visnyei, & Kornblum, 2010). Markers such as Sox2, Oct4, Nanog, CD133 and ABCG2 exist and can be used as proxies for identifying CSCs. However, given that otherwise normal cells may also express some of these markers, solely relying on them for the characterization of CSCs quickly becomes problematic (Cheray et al., 2017). As such, combination of marker identification along with functional assays for determining stem cell characteristics is more likely to be of value.

1.2 Radiation therapy: ionizing radiation overview

Cancer is a complex, heterogeneous and highly diverse disease, attributes which complicate the choice of treatment modalities that could be universally applied. This often means that very distinct, specific therapeutic modules need to be put forth in order to address the different cancer types. However, despite this inherent complexity, radiation therapy (RT) is considered a gold standard of care for most cases. The underlying principle governing the use of RT is its ability to kill cancer cells by damaging their DNA, either directly or indirectly. Direct effects result from ionizing radiation (IR) interacting with essential functional molecules of the cells, primarily DNA. This leads to changes in the structure of the affected biomolecules, ultimately impairing their functional integrity. Other cellular proteins, lipids and organelles (e.g. mitochondria, ER and Golgi apparatus) may also be affected during this process. Examples of direct IR effects on DNA include: base changes, DNA-DNA cross links, ss- or dsDNA breaks, or complex damage which is defined as the combination of two or more of the above mentioned effects. Indirect effects, which make up the majority of IR-induced effects, are the result of radiation interacting with water molecules within the cell. Through water radiolysis, highly reactive oxygen species (ROS) are generated. These in turn can cause extensive cellular damage (Baatout Sarah, 2023). Once sufficient DNA damage has accumulated, cells are unable to repair effectively and as a result stop growing, die and are eventually eliminated from the body. While normal cells can also be affected by radiation, the notion that this cell population can more readily and effectively respond to DNA damage and repair faster than the targeted cancer cells, generally means that there is an advantage to employing RT for the purposes of curtailing the cancer (Mayo_Clinic; NCI). Given this mechanism of action, it comes as no surprise then that following exposure to radiation, nucleic acids and other damaged molecules accumulate in the cytosol of the affected cells. The presence of nucleic acids outside of their expected localization engages DNA sensors present in the cytosol and in doing so triggers downstream inflammatory signaling

cascades. Similarly, damaged molecules can also bind to specific cellular receptors to activate diverse pathways (Jesenko et al., 2020).

1.3 Innate immunity: pattern recognition receptors (PRRs) and their ligands

The immune system is widely regarded as the combination of innate and adaptive immune responses following exposure to pathogens. Adaptive immunity refers to the recognition of specific sites, antigens, by highly specialized cells of the immune system, specifically B and T cells. On the contrary, the innate immune system is responsible for orchestrating more generalized responses to host insults and is considered pathogen/damage specific instead (Tan, Ho, Leung, & Ding, 2014). This is the body's first line of defense. More specifically, for innate immunity, host invading pathogens/microorganisms release pathogen associated molecular patterns (PAMPs) which get recognized by specific pattern recognition receptors (PRRs) (Takeuchi & Akira, 2010). While these receptors are primarily found on immune cells, they can also be present in non-immune cells, such as fibroblasts, epithelial and endothelial cells, as well as cancer cells (Takeuchi & Akira, 2010; Yamaga, Aziz, Murao, Brenner, & Wang, 2024; Zeuner et al., 2016). Upon receptor-ligand binding, diverse downstream signaling cascades get activated to allow cells to mount inflammatory responses targeting the invading pathogen (Gong, Liu, Jiang, & Zhou, 2020).

During cellular stress, depending on the extent and type of stressor present, damage associated molecular patterns (DAMPs) can also get actively released from damaged/stressed cells, or be passively secreted from dying cells (Rubartelli & Lotze, 2007; Yamaga et al., 2024). Active release of DAMPs involves processes such as exocytosis of these molecules by means of lysosomes or exosomes, while passive release can be achieved through various programmed (apoptosis, necroptosis, pyroptosis, ferroptosis) and non-programmed (necrosis) cell death mechanisms (Amarante-Mendes et al., 2018; Yamaga et al., 2024). Ionizing radiation (IR) being

an extreme form of genotoxic stress can lead to the release of DAMPs (Feldman, Rotter-Maskowitz, & Okun, 2015; Gong et al., 2020; Hernandez, Huebener, & Schwabe, 2016; Krombach et al., 2019; Mavragani et al., 2016; McKelvey, Hudson, Back, Eade, & Diakos, 2018). Some such examples include high mobility group box 1 (HMGB1), histones, heat shock proteins (HSPs), extracellular ATP, nucleic acids (DNA - nuclear and mitochondrial, RNA), micronuclei, nucleotides, chemokines and uric acid (Baatout Sarah, 2023; Yamaga et al., 2024). While these molecules have physiological functions within the cell under homeostatic conditions, they acquire additional roles when released into the extracellular space. They become “danger signals” that mediate their effects through binding to many of the same PRRs engaged by PAMPs (Venereau, Ceriotti, & Bianchi, 2015). In doing so, similarly to what would be seen during host immune responses, downstream inflammatory signaling cascades get activated which in turn allow cells to deal with the damage/stress injury (Feldman et al., 2015; Gong et al., 2020). Additionally, receptors beyond PRRs can also recognize DAMPs. Some of these include the receptor for advanced glycation end products (RAGE), triggering receptors expressed on myeloid cells (TREM2s), G-protein coupled receptors (GPCRs) as well as ion channels (Gong et al., 2020). This type of immune response occurring in the absence of microorganisms (and their PAMPs) is referred to as sterile inflammation and was proposed as a “danger” theory by Polly Matzinger back in 1994, adding to the complexity of cellular immune responses (Gong et al., 2020; Rosin & Okusa, 2011).

Most common examples of PRRs include: 1) Toll-like receptors (TLRs; can recognize all classes of pathogens - most well understood system), 2) retinoic acid-inducible gene (RIG)-1-like receptors (RLRs; involved mainly in the recognition of RNA viruses), 3) nucleotide oligomerization domain (NOD)-like receptors (NLRs) and 4) C-type lectin receptors (CLRs; primarily implicated in fungal infections) (Tan et al., 2014). While TLRs and CLRs are both membrane-bound (either plasma or endosomal membranes), NLRs, RLRs are cytoplasmic

(Gong et al., 2020). The following sections will provide more details regarding select PRRs, specifically TLRs and RLRs, since both have been shown to play important roles in cellular plasticity responses, the focus of the present dissertation.

1.3.1 TLRs

1.3.1.1 TLR structural features & downstream signaling

TLRs are type 1 transmembrane proteins characterized by an extracellular leucine-rich domain, transmembrane helix and cytoplasmic tail containing a conserved toll/interleukin-1 receptor (TIR) domain (Gao, Xiong, Li, & Yang, 2017). There are currently 10 human (TLR1-10) and 12 mouse (TLR1-9, TLR11-13) TLRs known (Gong et al., 2020). Depending on the ligands they recognize, these receptors can be localized on plasma (TLR1-2, TLR4-6, TLR10) or endo-lysosomal membranes (TLR3, TLR7, TLR8 and TLR9) (El-Zayat, Sibaii, & Mannaa, 2019; Gong et al., 2020). More specifically, cell membrane bound receptors recognize conserved motifs from extracellular pathogens such as bacteria, fungi and protozoa, whereas intracellular TLRs are primarily involved with the detection of single- or double-stranded nucleic acids (Sameer & Nissar, 2021; Takeuchi & Akira, 2010). Endo-lysosomal localization of these latter receptors allows them to effectively respond to non-self DAMPs, all while providing some level of protection against the recognition of self-nucleic acids (Gong et al., 2020). Ligand detection through the leucine-rich domains (Takeda, Kaisho, & Akira, 2003) promotes TLR dimerization, mainly resulting in receptor homodimers, with heterodimers encountered being in the form of TLR2 with TLR1, TLR6 and TLR10, or TLR4 with TLR6 (El-Zayat et al., 2019; Sameer & Nissar, 2021). Once activated by PAMPs/DAMPs, TLRs recruit different adaptor molecules, namely myeloid differentiation primary-response protein 88 (MyD88), TIR domain-containing adaptor protein (TIRAP or MAL), TIR domain-containing adaptor protein inducing interferon (IFN)- β (TRIF) or TRIF-related adaptor molecule (TRAM), and in doing so trigger downstream signaling cascades that activate transcription factors such as nuclear factor kappa beta (NF κ B), activator

protein 1 (AP-1) and interferon regulatory factors 3 and 7 (IRF3, IRF7). This subsequently leads to the promotion of inflammatory responses characterized by the production of inflammatory cytokines and chemokines (Gong et al., 2020; Kawai & Akira, 2005; Lannoy, Cote-Biron, Asselin, & Rivard, 2023).

TLRs are generally regarded as signaling through MyD88-dependent or -independent means. TLR4 is the only TLR capable of both types of signaling, while TLR3 is exclusive at mediating its effects in a MyD88-independent, TRIF-dependent manner (Kawai & Akira, 2005). MyD88-dependent pathways lead to TBK1-dependent activation of NFκB and AP-1 by means of MyD88/IRAK1/IRAK4/TRAF6 complex. MyD88-independent signaling activates NFκB and IRF3/7 signaling instead through TRIF recruitment, with TRAF6/RIP and TBK1-IKKε/IKKi complexes working downstream of TLRs for each signaling pathway respectively (*TBK1: TANK-binding kinase 1, IRAK1/4: interleukin-1 receptor associated kinase 1/4, TRAF6: tumor necrosis factor receptor associated factor 6, RIP: receptor interacting protein, IKK: I-kappa beta kinase*) (Yeh, Huang, Chen, Huang, & Chuang, 2016). However, despite this generalized view regarding MyD88, recent findings suggest that TIRAP and TRAM are also needed for responses mounted by most TLRs, adding to downstream signaling diversity (Lannoy et al., 2023).

1.3.1.2 TLRs in cancer

PRRs such as TLRs have been implicated in many cancers, and depending on the tumor microenvironment, the ligand binding them, the cell expressing the TLR in question, as well as the adaptor molecule recruited, downstream signaling cascades with either pro- or anti-tumor effects may become activated. As such, TLR signaling diversity becomes readily apparent (Alvarado et al., 2017; X. Chen et al., 2019; El-Zayat et al., 2019; Ferrandez, Gutierrez, Segundo, & Fernandez-Luna, 2018; Herrmann et al., 2014; J. Hu et al., 2018; F. Wang et al., 2015; Zang et al., 2020; Zeuner et al., 2016). For instance, TLR2 was found to promote glioma

stem cell invasion (F. Wang et al., 2015) and activation of TLR2/TLR4 by HMGB1 released from dying cells following irradiation was able to regulate stemness in pancreatic cancer (X. Chen et al., 2019). TLR3 activation in breast cancer cells was associated with enhanced cancer cell stemness through activation of β -catenin and NF κ B pathways. This coincided with increased expression of stemness-related genes (e.g. Oct3/4, Sox2 and Nanog) (Jia et al., 2015; Yeh et al., 2016). TLR4 has been shown to be constitutively expressed in most cells of the CNS, including neural stem cells, and play important roles in nervous system development, including the differentiation and proliferation of neuronal precursors (Zeuner et al., 2016). In the context of glioblastoma, glioma stem cells showed downregulated TLR4 expression which promoted their stemness (Alvarado et al., 2017), while in U251 glioma cells, activation of TLR4 reversed differentiation and led to upregulation of stem cell markers (J. Hu et al., 2018). Increased TLR4 expression was found to promote stem-like characteristics as well as the invasive and migratory capabilities of hepatocellular carcinoma cells (W. T. Liu et al., 2015; Yeh et al., 2016). Similarly, cytokine-mediated activation of TLR4 in breast cancer cells was shown to promote their stemness (C. H. Wang et al., 2018). Thereafter, biased signaling through TLR4 can lead to preferential activation of NF κ B or IRF3 downstream signaling pathways, differentially affecting glioma cells. While high induction of NF κ B signaling (and low IRF3 stimulation) was shown to promote glioma cell proliferation, low NF κ B activity coupled with moderate IRF3 activation inhibited the migratory potential of these cells (Zeuner et al., 2016). There is evidence for TLR4 signaling dysregulation in many malignancies. This contributes to tumorigenesis by promoting immune evasion, cancer cell survival, metastatic potential and resistance to therapies through activation of its downstream signaling cascades (Kashani, Zandi, Pourbagheri-Sigaroodi, Bashash, & Ghaffari, 2021). These are just some examples of the complexity of TLR signaling, highlighting the importance of better understanding context-specific functions. Thereafter, TLR9 signaling in androgen-independent prostate cancer was associated with self-renewal capacity and proliferation of these cells (Moreira et al., 2015; Yeh et al., 2016). Expression of this same

receptor was shown to be elevated in glioma stem-like cells and contribute to their growth (Herrmann et al., 2014; Zang et al., 2020). The diverse implications of the TLR system become evident from the plethora of PAMPs/DAMPs that can be recognized, the downstream adaptor molecules engaged, the signaling cascades activated and the potential cross-talk with other receptors. Thus, better understanding how these receptors operate under different conditions is of great interest.

1.3.2 RLRs

1.3.2.1 RLR structural features & ligand recognition

RLRs comprise of RIG-I, melanoma differentiation-associated protein 5 (MDA5) and laboratory of genetics and physiology 2 (LGP2) receptors and are primarily found in the cytosol. RIG-I receptor localization in the nucleus has also been reported. Collectively they are involved in the sensing and detection of RNA molecules possessing specific features that render them distinguishable from host RNAs. More specifically, RIG-I recognizes short RNA molecules that have di- or tri-phosphate (p) groups on their 5' ends, are in double stranded form (i.e. dsRNA), have uncapped 5' pp(p) ends and no ribose 2'-O-methylation (Gong et al., 2020; Rehwinkel & Gack, 2020). The existence of a cap structure at 5' ppp ends of eukaryotic mRNAs renders these molecules less favorable for RIG-I recognition and binding, thus providing a protection against the recognition of self RNAs. In cases where these 5' caps are absent, RNA-binding proteins can shield self RNAs so as to prevent their detection by RLRs and the induction of autoimmunity. Long dsRNA molecules of >300bp are recognized by MDA5. Reactivity to self RNAs in this case is limited as typically these do not have such long stretches of dsRNA (Gong et al., 2020).

Regarding general structural features, all three RLRs possess a central helicase domain with ATPase activity and a carboxy-terminal domain (CTD), both of which are involved in RNA

binding. The former determines the rate of RLR-RNA dissociation resulting from ATP-hydrolysis. RIG-I and MDA5 also have two terminal caspase activation and recruitment domains (CARDs) at their N terminus. These domains are essential for allowing association with CARD of the downstream adaptor molecule mitochondrial antiviral-signaling protein (MAVS). Since LGP2 lacks these domains, it does not have independent signal-transducing activity, but instead is involved in regulating the activities of the other two RLRs (Rehwinkel & Gack, 2020). Similarly to what is seen with TLR signaling, ligand recognition leads to receptor oligomerization and activation. Engagement of adaptor protein MAVS promotes the activation of downstream signaling cascades, ultimately leading to the activation of IRF3/7 and NFκB signaling pathways and the induction of interferons and inflammatory cytokines in a TBK1 and IκB kinase (IKK)-dependent manner (Gong et al., 2020; Rehwinkel & Gack, 2020).

1.3.3 Receptor crosstalk

Given the variety of DAMPs and their respective sensors, it comes as no surprise that receptor crosstalk exists. This feature allows cells to mount more orchestrated inflammatory responses (Tan et al., 2014). For instance, recognition of the same DAMP by multiple receptors (either in parallel or in a successive manner) allows for synergistic downstream action. Activation of multiple signaling pathways in turn promotes diverse responses to take effect. HMGB1 is a DAMP that can activate TLR2/4 as well as RAGE and TREM1. In doing so, it can lead to the induction of proinflammatory cytokines, all while also promoting processes such as migration, proliferation and differentiation (Gong et al., 2020). Another common example is the recognition of DNA by cytoplasmic DNA sensors cyclic GMP-AMP synthase (cGAS) and absence in melanoma 2 (AIM2). Activation of each of these receptors can lead to unique responses which could help enhance the overall inflammatory response mounted by the cell in question (Gong et al., 2020; Harding et al., 2017; B. Hu et al., 2016).

Thereafter, it is also possible to have interaction between different DAMPs ultimately resulting in the initiation of an augmented immune response. This is seen in the case of HMGB1 binding to endogenous DNA and as a result enhancing DNA-induced TLR9 activation (Gong et al., 2020; Tian et al., 2007). Synergistic responses can also arise from the downstream signaling cascades activated. More specifically, activation of DAMP-sensing receptors can lead to the production of proinflammatory molecules which in turn can further stimulate DAMP release and receptor expression, allowing thus for a more amplified inflammatory response to take place (Gong et al., 2020). Besides this synergistic effect, negative receptor crosstalk is also possible. These intricate receptor-receptor interactions are dependent upon the cell type and insult in question (Tan et al., 2014).

Additionally, receptor crosstalk required for establishing an effective response against pathogens/damage might also require sequential stimulation of receptors. For instance, in the case of herpes simplex virus, initial TLR2 activation followed by intracellular TLR9 recognition of viral DNA has to happen within the same cell to achieve an effective response. If the receptor activation order were to be reversed and/or the effects were not to happen within the same cell, this response would be abrogated (Tan et al., 2014). Overall, while this crosstalk is essential for allowing cells and organisms to respond effectively to insults, the existence of appropriate control mechanisms preventing receptor overactivation is also essential. Such control is achieved by means of post-translational modifications, recruitment of inhibitory molecules, receptor trafficking, as well as degradation processes for receptors and their respective adaptor molecules (Cao, 2016; Gong et al., 2020; Rehwinkel & Gack, 2020; Tan et al., 2014).

1.4 cGAS/STING

1.4.1 cGAS/STING structural features & signaling

Cyclic GMP-AMP synthase (cGAS) is a member of the nucleotidyl transferase enzyme family primarily involved in the recognition of free cytosolic DNA. While it is mainly found in the cytosol, it is not free-floating and instead associates through its N-terminal domain with the inner leaflet of the plasma membrane (Hopfner & Hornung, 2020; Kumar, Bauer, & Stewart, 2023). This proximity of cGAS to the cellular membrane allows it to readily mount a response to PAMPs/DAMPs entering the cell (Kumar et al., 2023). There is also growing evidence pointing to cGAS nuclear localization (Hopfner & Hornung, 2020).

Unlike the RNA receptors previously discussed (RLRs) which are able to distinguish between self and non-self RNA due to the presence of structural features unique to viral RNAs (Rehwinkel & Gack, 2020), cGAS recognizes and binds to DNA in a length-dependent manner, rather than sequence- and/or structure-dependent means. Given this specificity, it follows that cGAS can also recognize self-DNA molecules released into the extracellular space following cellular damage (Hopfner & Hornung, 2020; Song, Villagomes, Zhao, & Zhu, 2022). Regarding ligand-length requirements, cGAS' enzymatic activity is promoted by ligands longer than 36bp, with long ssDNAs being able to weakly stimulate cGAS and small dsDNA fragments (15-35bp in length) inhibiting cGAS' catalytic activity and promoting autophagy instead (Kumar et al., 2023). Some examples of common cGAS ligands include: cytosolic DNA (of nuclear or mitochondrial origin, single or double stranded), micronuclei, DNA-RNA hybrids (this being a less optimal agonist) and extracellular chromatin (Hopfner & Hornung, 2020).

In its inactive form, cGAS is composed of a two-lobed catalytic domain and a long N-terminal domain. Upon recognition of DNA, cGAS undergoes a conformational change leading to dimer assembly, whereby each cGAS promoter coming together has a DNA ligand bound to it,

sandwiching the DNA molecules between the two promoters. This dimerization is required for cGAS activation and its subsequent catalytic activity used to produce secondary molecule cyclic GMP-AMP (cGAMP). cGAMP in turn functions as a messenger for the downstream sensor stimulator of interferon genes (STING). STING is a dimeric transmembrane protein residing in the endoplasmic reticulum (ER). Upon binding cGAMP, STING gets activated and undergoes a conformational change which facilitates STING dimer association with TBK1 and subsequent lateral oligomerization of STING dimers. STING oligomers then translocate to the Golgi by means of ER-Golgi intermediate compartment (ERGIC), an organelle specialized in the trafficking between these two cellular compartments. Palmitoylation of cysteine residues near STING's transmembrane domain 3 is essential for STING clustering at the Golgi and its downstream signaling activity. A sequence of phosphorylation events orchestrated by TBK1 autophosphorylation and subsequent STING and interferon regulatory factor 3 (IRF3) phosphorylation, leads to IRF3 transcription factor (TF) dimerization and its nuclear translocation. In the nucleus, this TF enables the production of type I interferons (IFN-I) and expression of interferon-stimulated genes (ISGs) which in turn lead to induction of defense mechanisms (Hong, Mei, Guo, Zhu, & Wang, 2022; Hopfner & Hornung, 2020). Of note, compared to other receptors involved in the sensing of cytosolic dsDNA (e.g. TLR7 and TLR9), activation of the cGAS/STING signaling axis leads to the production of more IFN type I (Kumar et al., 2023). As such, differential receptor engagement and/or crosstalk between PRRs and cGAS/STING could have important implications for host responses.

1.4.2 Functions of STING

Beyond this well characterized function of STING, this sensor has also been implicated in the activation of NF κ B and MAPK signaling pathways, cGAS-independent signaling, as well as the regulation of autophagy and lysosomal degradation processes. More specifically, for NF κ B signaling, there is lack of consensus as to how STING mediates its effects, with reports

suggesting both TBK1-dependent and -independent means (Hopfner & Hornung, 2020; Kumar et al., 2023). While STING is traditionally regarded as a sensor acting downstream of DNA-dependent cGAS activation, there is evidence for STING acting independent of cGAS and cGAMP. Etoposide treatment was found to induce cGAS-independent, STING-dependent activation of NFκB signaling, involving TRAF6 (Dunphy et al., 2018; Hopfner & Hornung, 2020). Non-canonical STING activation has also been shown to play an important role in the sensing of RNA viruses. While these are primarily sensed by RLRs, fusion of cationic liposomes or enveloped RNA viruses with the plasma membrane has been associated with the stimulation of type I interferon expression. This response is STING-dependent, but cGAS-independent. Arginine168 of STING, a highly conserved residue located adjacent to STING's dimerization surface – region critical for STING's activation and downstream signaling – was found to be implicated in the stimulation of IFN expression by liposomes, but not cGAMP (Holm et al., 2016; Vashi & Bakhoun, 2021).

Thereafter, in terms of autophagy, STING located at the ERGIC can function as a base for autophagosome formation and in doing so indirectly provide protection against invading pathogens (Hopfner & Hornung, 2020) This is a primordial function of STING that developed before its IFN signaling capability. STING-mediated autophagy is TBK1- and IFN signaling-independent (Gui et al., 2019). Lastly, once STING has exerted its downstream signaling effects, it gets trafficked to lysosomes for degradation. Alternatively, the presence of STING in lysosomes can lead to lytic cell death (LCD). Accumulation of STING molecules within lysosomes can lead to permeabilization of the lysosomal membranes, release of lysosomal enzymes and subsequent cell death (Gaidt et al., 2017; Gonugunta et al., 2017; Hopfner & Hornung, 2020). As such, these reports highlight the diverse roles and functions of STING in cellular responses.

1.4.3 cGAS nuclear localization

Within the nucleus, cGAS has physiological, non-catalytic functions which include: 1) regulation of DNA replication, 2) inhibition of DNA repair and 3) initiation of innate immune responses. More specifically, in the case of DNA replication, as the dsDNA gets unwound by DNA helicases, specialized proteins and enzymes bind to the strands. This forms a replication fork that moves along to replicate the DNA strand (Dewar & Walter, 2017; Pan et al., 2023). By binding to chromatin, cGAS controls the replication fork's movement, regulating thus DNA replication. This is a STING-independent process (C. Chen & Xu, 2023; Hopfner & Hornung, 2020; Pan et al., 2023). In the case of DNA repair, formation of dsDNA breaks can lead to cGAS nuclear translocation. Through interaction with PARP1, cGAS prevents the formation of PARP1-TIMELESS complexes required for homologous recombination (HR), inhibiting the process as a result (H. Liu et al., 2018; Pan et al., 2023). cGAS can also interfere with HR by compressing the DNA template, preventing thus the invasion of RAD51 on that strand, a crucial step during HR DNA repair (Cui et al., 2020; Pan et al., 2023). cGAS has also been shown to promote irreversible cell cycle arrest through inhibition of mitotic non-homologous end joining (NHEJ) (Pan et al., 2023). Lastly, probably the most relevant function of cGAs for the purposes of the present project is cGAS' involvement in orchestrating innate immune responses. This is primarily achieved through sensing of viral DNA and inducing downstream type I interferon (IFN- α) inflammatory responses, which also further act to inhibit viral DNA replication (Pan et al., 2023; Wu et al., 2022).

The nuclear localization of this sensor raises some concerns regarding the potential for cGAS to respond to self-DNA and thus lead to adverse consequences for the host (Hopfner & Hornung, 2020; Pan et al., 2023). However, this is likely prevented by post-translational modifications (PTMs), compartmentalization of self-DNA in the nucleus and mitochondria, away from sequestered cGAS, as well as mounting evidence pointing to the requirement for

oligomerization and/or more complex organization of cGAS molecules (e.g. in liquid-like phase-separated condensates) for their activation. The combination of these features thus precludes self-reactivity (Z. Hong et al., 2022; Hopfner & Hornung, 2020; Pan et al., 2023; Song et al., 2022; Volkman, Cambier, Gray, & Stetson, 2019). Recent work has pointed to the involvement of barrier-to-autointegration factor 1 (BAF), a chromatin binding protein modulating nuclear membrane reformation post mitosis. BAF was shown to dynamically displace cGAS and outcompete it for DNA binding. In the case of nuclear membrane rupture and DNA release, BAF plays a crucial regulatory role in restricting cGAS activation by self-DNA, preventing cGAS-DNA assembly required for cGAS' catalytic activity (Guey et al., 2020).

Thereafter, an explanation for why cGAS sequestration on chromatin renders it inactive, while binding of extracellular chromatin fragments and micronuclei activates it can be attributed to structural features of the respective chromatin conformations. Research suggests that micronuclei show distinct features of heterochromatin (silenced genomic regions) and accumulation of gamma-H2AX marks, a proxy for dsDNA breaks. The combination of these characteristics points to DNA damage potentially being associated with these cGAS ligands. This feature distinguishes them from the intact chromatin onto which cGAS would normally be sequestered, thus allowing for the differential functionality of cGAS in each case (Dou et al., 2017; Harding et al., 2017; Hopfner & Hornung, 2020).

1.4.4 cGAS/STING in cancer

Of interest, there exist cancer-specific differences in how the cGAS/STING signaling pathway functions that need to be taken into consideration when determining appropriate treatment modalities (Kumar et al., 2023). For example, it has been shown that STING is epigenetically silenced in many tumors, suggesting a potential tumor suppressor function for this sensor. With dysregulated/epigenetically silenced STING, cancer cells are able to promote their growth

instead. Methylation of histone H3 lysine 4 (H3K4me3) residues, commonly found at transcription start sites and correlating with active transcription, have been implicated in this process (Kooistra & Helin, 2012). Specifically, histone H3K4 demethylases, KDM5B and KDM5C, have been shown to suppress STING in breast and colon cancer cells. Using inhibitors targeting these demethylases and/or promoting the activity of H3K4 methyltransferases allow for STING activation, IFN secretion and induction of ISGs (Konno et al., 2018; Kumar et al., 2023; Zheng et al., 2023). In the context of glioblastoma, suppression of STING signaling in both normal brain and glioma cells, but not tumor-associated immune cells and stroma, is the result of epigenetic silencing resulting from hypermethylation of CpG site cd16983159 in the STING promoter. cd16983159 methylation suppresses STING mRNA expression. Normal fetal and adult brains show signs of this hypermethylation suggesting the presence of a STING-silent environment conserved during brain development and tumorigenesis, rather than being the result of gliomagenesis. Treatment with decitabine (DNA methyltransferase inhibitor, DNMTi) led to DNMT1 suppression, decreased methylation at this specific CpG site and increased STING mRNA and protein expression. In doing so, cells that were previously non-responsive to STING agonist could activate innate immune and INF genes (Low et al., 2022). Murine GBM models (e.g. GL261) are generally responsive to STING agonists and have intact cGAS/STING signaling. As such, care should be taken when translating cGAS/STING animal study findings to humans (Kumar et al., 2023).

Research by Jesenko et al. evaluating the response to radiation in tumor cells (murine melanoma) identified that within as early as 24h post irradiation, treated cells accumulate DNA in their cytosol in the form of dsDNA and/or micronuclei (MN), leading to the upregulation of distinct DNA sensing pathways. These included: DexD/H-box helicases family DExD/H-Box Helicase 60 (DDX60), DNA-dependent activator of interferon regulatory factors (DAI) and p204, which is the mouse ortholog for human interferon gamma inducible protein 16 (IFI16). STING,

which ties together many of the upregulated DNA sensing pathways identified, was shown to translocate to peri-nuclear structures as early as 24h post IR, with most significant translocation being observed by 48h. This was associated with NFκB, IRF3 and IRF7 translocation to the nucleus (Jesenko et al., 2020). From the upregulated DNA sensors identified, it is of interest to point out that STING is implicated in both DAI and IFI16 signaling, leading to the induction of NFκB and IRF3 pathways, important for reprogramming. Additionally, DDX60 can function as an upstream component in RIG-1 signaling, which provides a link between DNA sensing following irradiation and a signaling receptor that has been shown to be involved in effective reprogramming of cells. (Cooke, 2019; Cooke & Lai, 2023; Dunphy et al., 2018; Jesenko et al., 2020; Lee et al., 2012; Shu Meng, Chanda, & Cooke, 2016; Sayed et al., 2017). While this study highlighted the importance of these radiation upregulated DNA sensing pathways, it is possible that other signaling components not upregulated, might also play a role here. This was for instance seen in the case of STING. While it did show changes in its cellular localization upon radiation, suggesting its activation, it was not readily upregulated at the mRNA level (Jesenko et al., 2020). Therefore, already existing cytosolic sensors might very well be involved in mediating radiation-induced effects. The complexity of DNA sensing systems becomes even more apparent by considering receptor crosstalk previously discussed.

Lastly, similarly to what was seen with TLRs, cGAS/STING signaling can also have differential downstream effects. Activation of this pathway has been shown to improve survival of chromosomally unstable breast cancer cells in an IL-6-dependent manner (C. Hong et al., 2022), and promote the self-renewal of TET2-mutated hematopoietic stem/progenitor cells (Xie et al., 2023). At the same time, activation of cGAS/STING has also been associated with anti-tumor effects. This is further complicated by the interaction of these sensors with other partners and/or adaptor molecules. As such, the role of this signaling pathway, either in its canonical or

non-canonical form, is complex and can have diverse downstream effects depending on the specific context in question (Vashi & Bakhoun, 2021).

1.5 Reprogramming

1.5.1 History overview & important studies

Once thought to be unidirectional, differentiation can now be reversed (Takahashi & Yamanaka, 2016). Experiments carried out by Sir John Gurdon in the early 1960s, were among the first to demonstrate cellular reprogramming by means of somatic cell nuclear transfer (SCNT), whereby the introduction of a somatic cell nucleus into an enucleated egg was able to produce an embryo genetically identical to the nucleus-donating somatic cell (Gurdon, 1962; Gurdon, Elsdale, & Fischberg, 1958; Takahashi & Yamanaka, 2016). Around the same time, embryonic stem cells (ESCs), cells derived from the inner cell mass of the blastocyst, were first established and were shown to be pluripotent, meaning able to give rise to all cells in our body, and able to sustain indefinite growth (Evans & Kaufman, 1981; Martin, 1981; Takahashi & Yamanaka, 2016). By the end of the 20th century, evidence of cellular reprogramming was further substantiated by cell fusion experiments, most prominent of which was the fusion of ESCs or pluripotent cells (PSCs) with somatic cells, successfully reprogramming the latter towards pluripotency (Cowan, Atienza, Melton, & Eggan, 2005; Tada, Takahama, Abe, Nakatsuji, & Tada, 2001; Takahashi & Yamanaka, 2016). Subsequently, there came studies showing ectopic expression of individual transcription factors in mouse fibroblasts being able to convert cells to a specific lineage. One of the first such examples was the introduction of myoblast determination protein (MYOD) into mouse fibroblasts leading to the formation of myoblasts (Davis, Weintraub, & Lassar, 1987; Takahashi & Yamanaka, 2016). Collectively these experiments brought about the notion that there exist certain factors capable of reprogramming somatic cells, changing thus their once regarded terminal fate.

In the early 2000s, Yamanaka and colleagues started laying the foundations for what would become one of the greatest breakthroughs in biology: the discovery of induced pluripotent stem cells (iPSCs), granting Drs. Gurdon and Yamanaka a joint Nobel Prize in Physiology or Medicine in 2012. Through initial evaluation of mouse ESCs, the Yamanaka group investigated genes deemed important for pluripotency, self-renewal capacity, and proliferative capacity of these cells. Among these were Nanog, Klf4 and Myc, with Oct3/4 and Sox2 included based on knowledge of the role these two transcription factors play in pluripotency. In total, 24 candidate genes were identified from this initial search. Through a series of retroviral transduction experiments using mouse embryonic fibroblasts (MEFs), they were able to show that Oct3/4, Sox2, Klf4 and Myc were the four core factors, commonly referred to as OSKM (or Yamanaka factors; YFs in subsequent sections of this dissertation) able to induce reprogramming of MEFs and adult fibroblasts to mouse ESC-like cells, termed mouse iPSCs. These cells resembled ESCs' morphology, growth capabilities and gene expression profiles. Subcutaneous injection of these cells in nude mice resulted in tumors containing cells from all three germ layers, further supporting the pluripotent state of these cells (Takahashi & Yamanaka, 2006, 2016). In follow-up studies using human fibroblasts, they were able to once more show that these factors were sufficient for inducing human iPSCs from adult human dermal fibroblasts (Takahashi et al., 2007; Takahashi & Yamanaka, 2016). Similarly to what was previously shown with the mouse-derived counterparts, human iPSCs resembled human ESCs in terms of their morphology, proliferative abilities and gene expression profiles. Of interest, while human and mouse ESCs depend on the same core transcriptional network for pluripotency, they differ in their requirements for extrinsic factors and stimuli that allow them to maintain this pluripotency (e.g. differential requirements for growth factors and signaling pathways) (Takahashi et al., 2007).

In the context of Yamanaka factor-generated iPSCs, reprogramming can be viewed as a two-stage process. At first, these core factors bind to genomic loci associated with somatic genes to

suppress them, all while engaging with pluripotency-associated gene-loci which are otherwise epigenetically silenced in somatic cells. Once this initial phase is achieved, YFs can induce the expression of pluripotency-associated genes and lead to iPSCs. Studies evaluating the combination and potential interchangeability of the core factors identified by Yamanaka, showed that while Sox2 could be replaced with Sox1 and Sox3, Klf4 with either Klf2 or Klf5, and all Myc members were able to support reprogramming, Oct3/4 was indispensable (J. Jiang et al., 2008; Nakagawa et al., 2008; Nakagawa, Takizawa, Narita, Ichisaka, & Yamanaka, 2010; Takahashi & Yamanaka, 2016). Inclusion of other factors relating to pluripotency-associated genes, cell cycle-regulating genes, epigenetic modifiers (promoting pluripotency gene expression and/or suppressing somatic genes) along the YFs was able to enhance reprogramming efficiency (Takahashi & Yamanaka, 2016).

Despite the great promise and implications for health and disease stemming from the discovery of iPSCs, the original methods used had some notable limitations. These were the low reprogramming efficiency and the potential for retroviral vector integration into the host's genome. On the one hand, inefficient reprogramming could be attributed to i) the need for a tightly regulated range for the YFs, both in terms of timing of delivery as well as appropriate stoichiometry and expression levels, ii) the requirement for a reprogramming-permissive environment (e.g. need for additional chromosomal alterations facilitating this process), iii) the potential requirement for retroviral integration into specific loci, and to a lesser extent iv) the possibility of YFs transforming only progenitor and/or tissue stem cells, which by default make up a small proportion of the cell population. Nevertheless, this latter notion was disproved from experiments carried out using bone marrow stroma (i.e. tissue expected to be enriched in stem cells), also showing low reprogramming efficiency (Takahashi et al., 2007; Takahashi & Yamanaka, 2006).

On the other hand, retroviral integration into the host genome could have crucial implications by silencing or dysregulating the function of important genes, and potentially even leading to tumor formation. To overcome this challenge, throughout the years, groups have developed integration-free methods including episomal vectors, synthetic mRNAs and Sendai viruses (Takahashi & Yamanaka, 2016). To this end, Cooke and colleagues tested the use of cell permeable peptides (CPPs) as a safer, more efficient alternative for delivering the core reprogramming factors. CPPs are fusion proteins composed of a reprogramming factor, linker and cell transduction domain (Yang et al., 2009). While these proteins can rapidly translocate to the nucleus to transduce cells and regulate the transcription of target genes, CPPs alone were unable to reprogram human fibroblasts to iPSCs. Careful examination of the gene expression profiles comparing CPPs and retroviral vectors previously used by Yamanaka and colleagues, identified differences in temporal gene expression profiles of pluripotency genes, with the former yielding delayed and rather low expression levels. As such, it was postulated that maybe some feature of the viral vector used in the original studies was influencing reprogramming. Through a series of intricate experiments testing the effects of CPPs alone or in combination with retroviral vectors encoding non-integrating green fluorescent protein (GFP), the Cooke group was able to show that co-administration of CPPs with retrovirus encoding GFP could recapitulate the effects of YF retroviral particles, substantiating the role of these viral constructs in reprogramming.

1.5.2 Role of innate immunity in reprogramming

Knowing that viral particles are recognized by the innate immune system by means of PRRs, Cooke and colleagues investigated the role of innate immune receptors. TLR3 activation by the retroviral constructs was found to be an essential step for efficient induction of pluripotency genes and subsequent reprogramming. This was particularly important as it indicated that the retroviral vectors used by Yamanaka to reprogram cells were not simply vehicles for delivering the core YFs, but had much more important roles in activating innate immune signaling

responses essential for effective reprogramming. Next, they showed that TLR3 activation was able to induce changes in epigenetic modifiers such as histone acetyltransferases (HATs), histone deacetylases (HDACs) and histone methyltransferases (HMTs) to create an epigenetically favorable, permissive environment for reprogramming to occur (Lee et al., 2012).

Having observed these epigenetic changes, specifically in terms of HATs, in an attempt to gain better mechanistic insight, they investigated the role of NFκB. The rationale behind looking at this transcription factor was its involvement downstream of the TLR3 signaling pathway, as well as its positive gene regulation of CREB-binding protein (CBP) and p300, proteins known to possess HAT domains and be readily involved in the maintenance of open chromatin states (Lee et al., 2012; Q. Li & Verma, 2002). In this context, the role of IRF3, another TLR3 downstream signaling pathway was also evaluated. Activation of both pathways downstream of TLR3 was found to be essential for efficient reprogramming, and was shown to be associated with changes in H3K4 (permissive) and H3K27 (repressive) trimethylation status at promoter regions of Oct4 and Sox2, favoring an open chromatin conformation. Of note, this work also showed the requirement for optimal TLR3 activation (i.e. appropriate levels that are neither too high nor too low), pointing out the need for tight regulation of this system. All in all, the importance of TLR3 activation in enhancing the yield and efficiency of iPSCs could be attributed to its ability to regulate epigenetic modifiers, which in turn promoted histone modifications favoring an open chromatin state at the promoter regions of Oct4 and Sox2. This function of TLR3 does not preclude the need for the YFs, since these are likely required to direct the epigenetic modifiers to the correct genomic regions. As such, the combination of the above findings highlights a role for innate immune signaling in reprogramming (Lee et al., 2012).

As discussed earlier, PRRs beyond TLR3 are able to recognize viral RNA and activate many of the same downstream signaling pathways (e.g. NFκB, IRF3), raising the possibility some of

them might be involved in reprogramming. Observations from TLR3 knockdown studies showing only partial inhibition of reprogramming prompted the Cooke group to investigate the contributing role of RLRs. These receptors recognize viral RNA and their activation engages IRF3, IRF7 and NFκB downstream signaling cascades to induce type I interferon (IFN-I) and IFN-inducible genes (ISGs) (Kato et al., 2005). Knocking down interferon beta promoter stimulator 1 (IPS1), the common adaptor protein downstream of all RLRs (Kawai et al., 2005), resulted in fewer and smaller iPSC colonies, which however were pluripotent. This was to suggest that RLR signaling is likely implicated in iPSCs' generation rather than their maintenance. Double knockdown of TLR3 and RLR pathways compromised effective nuclear reprogramming in a synergistic manner. However, co-administration of TLR3 and RLR agonists in this setting also showed attenuated expression of pluripotency genes, highlighting once more the importance for optimal innate immune system activation for efficient reprogramming. In line with the partially compromised reprogramming seen in TLR3 KD studies, administration of RLR agonist was not able to completely rescue TLR3 KD effects, suggesting that combined action of the two pathways is required for effective reprogramming to occur. Overall, this and previous work demonstrated anew that the viral vectors used by Yamanaka had functions well beyond just being delivery vessels for the reprogramming factors. They activated innate immune receptors (TLR3 and RLRs), which in turn induced global changes in epigenetic modifiers favoring an open chromatin state. This was achieved in a NFκB- and IRF3-dependent manner (Sayed et al., 2017). Subsequent work looking at transdifferentiation of human fibroblasts to endothelial cells identified the need for PRR activation in establishing an epigenetically favorable environment during this cellular transformation (Sayed et al., 2015). This once more highlighted the diverse implications of innate immune signaling. In their unpublished work, Cooke and colleagues have also identified TLR4 and RIG-1 receptors as playing a role in providing cells with the required cellular plasticity for reprogramming (Shu Meng et al., 2016).

Additionally, beyond the PRRs and downstream signaling cascades identified, a role for other factors/processes such as inducible nitric oxide synthase (iNOS), reactive oxygen and nitrogen species (ROS/RNS), S-nitrosylation, and autophagy in supporting reprogramming was also identified. More specifically, iNOS expression was found to be induced at the early stages of transdifferentiation where it was shown to translocate to the nucleus. There, it engaged Ring1A, a component of the polycomb repressive complex 1 (PRC1), causing its S-nitrosylation. This in turn resulted in the release of PRC1 complex from chromatin, promoting as a result the establishment of an open chromatin state. These iNOS effects were also accompanied by changes in histone marks favoring an open chromatin conformation (Cooke, 2019; Sayed et al., 2015). iNOS expression induced downstream of NFκB leads to the release of high amounts of nitric oxide (NO), a RNS, at the early stages of reprogramming (Chanda et al., 2019). NO in turn can S-nitrosylate proteins, changing their function (Cooke, 2019). The nucleosome remodeling and deacetylase (NuRD) complex is a chromatin remodeling complex composed of two core subunits associated with histone deacetylases 1 and 2 (HDAC1, HDAC2), as well as other components like metastasis-associated genes 1, 2 and 3 (MTA1/2/3) (Lai & Wade, 2011). S-nitrosylation of MTA3, was found to promote pluripotency and reprogramming by disrupting the association of MTA3 and HDAC2. This in turn impaired NuRD's deacetylase activity which would otherwise pose a barrier to reprogramming (Chanda et al., 2019).

Thereafter, ROS are known downstream targets of innate immunity and their expression can trigger the release of additional DAMPs from cells (G. Y. Chen & Nunez, 2010; S. Meng, Chanda, Thandavarayan, & Cooke, 2017). Cooke and colleagues found that the early stages of reprogramming are characterized by a spike in ROS signaling, essential for effective reprogramming. Upregulation of antioxidant enzymes at later stages acts to reduce ROS, highlighting the importance of optimal ROS levels and kinetics for efficient reprogramming (Cooke, 2019; S. Meng et al., 2017; Zhou, Meng, Li, Ghebre, & Cooke, 2016).

Lastly, the highly coordinated fashion through which epigenetic and subsequent transcriptomic profile changes occur during the initial phase of reprogramming, prompted researchers to investigate whether there exists a link between epigenetic modifications and processes involved in the synthesis and degradation of proteins. The induction of autophagy was found to be essential at the initial stages of reprogramming. This is achieved through transient downregulation of the mammalian target of rapamycin (mTOR) mediated by Sox2 recruitment of NuRD to the mTOR promoter. mTOR activation is known to inhibit autophagy. At later stages of reprogramming, mTOR activity is restored, once more highlighting the importance of temporal and optimal signaling in the reprogramming process (S. Wang et al., 2013). The combination of these findings point to the existence of a “Goldilocks zone” for innate immune signaling during reprogramming. This optimal zone is defined both in terms of the magnitude of signaling activation, as well as temporal considerations (Cooke, 2019).

Given that PAMPs and DAMPs engage many of the same receptors investigated above it was hypothesized that similar processes might also be at play during cellular damage responses. The term “transflammation” was coined to describe the epigenetic plasticity induced through the activation of innate immune signaling cascades in non-immune cells. This process provides cells with the appropriate phenotypic fluidity to respond to stressors (Cooke, 2019; Shu Meng et al., 2016; S. Meng et al., 2017; Sayed et al., 2017). For the purposes of the present dissertation, this idea was investigated in the context of ionizing radiation (IR). IR being an extreme form of genotoxic stress, can lead to the release of many of the same DAMPs found during cellular stress/damage responses (Feldman et al., 2015; Gong et al., 2020; Hernandez et al., 2016; Krombach et al., 2019; Mavragani et al., 2016; McKelvey et al., 2018). Research from our lab has shown that radiation induces phenotypic conversion of non-stem cancer cells to cancer stem-like cells (K. Bhat, Saki, et al., 2020; Lagadec, Vlashi, Della Donna, Dekmezian, & Pajonk,

2012). This cellular plasticity response coincided with the re-expression of YFs, namely Sox2, Oct4, Klf4, c-Myc and their downstream target Nanog, and was the result of radiation-induced acquisition of an open chromatin state in the promoter regions of Oct4, Sox2 and Nanog, peaking at 48h post 4 Gy. These findings are important as they highlight radiation-induced epigenetic remodeling, a process that has been deemed critical for effective reprogramming to occur (Cooke, 2019; Lee et al., 2012; Shu Meng et al., 2016; S. Meng et al., 2017; Sayed et al., 2017). The underlying mechanisms that drive this radiation-induced response are incompletely understood, but we know that PAMPs and DAMPs engage many of the same receptors and employ common downstream pathways. The combination of findings presented supports the notion that activation of innate immunity is likely involved here, and warrants the topic of the present dissertation.

1.6 Cellular plasticity

1.6.1 Overview

Throughout evolutionary times, organisms have developed diverse mechanisms for dealing with exposure to constant environmental stressors, most prominent of which is the ability to rapidly and effectively mount responses against infection and processes which would otherwise compromise their functional and genomic integrity. Depending on the cellular compartment being affected, specialized cells known as stem cells, which have the ability to self-renew, proliferate and give rise to more differentiated cells following exposure to specific cues can replenish the cells damaged/affected by the stressor at hand (Jessen, Mirsky, & Arthur-Farraj, 2015). While differentiation has long been perceived as a final stage in cellular development, it has become increasingly apparent that rather than being a fixed, terminal state, in the presence of the right combination of intrinsic and extrinsic factors, differentiated cells can show remarkable plasticity. The ability of cells to drastically change their phenotypes to respond to stress is termed cellular plasticity (Jessen et al., 2015). This is an umbrella term encompassing

both phenotypic changes as well as reprogramming; rapid change in cell identity, primarily arising from induction of specific transcription factors (H. Wang, Yang, Liu, & Qian, 2021). Given the significance of this function, it is not surprising that this phenomenon is conserved across species (Fulda, Gorman, Hori, & Samali, 2010). Understanding how organisms harness this process in response to specific cues, can give important insights regarding the management of diseases and challenging conditions.

1.6.2 Hallmarks of cancer

The importance of cellular plasticity and reprogramming becomes even more apparent from their inclusion in the most recent compilation of cancer hallmarks. The Hallmarks of Cancer, a conceptual toolkit originally proposed by Dr. Hanahan in 2000, subsequently updated in 2011, and most recently revised in 2022, aims to describe a set of common characteristics and functional capabilities normal cells acquire as they transition to form malignant tumors. These otherwise normal cellular functions with important roles in sustaining homeostasis, tissue repair and regeneration become corrupted and dysregulated to benefit the progression of malignancy. Characteristic hallmarks include the maintenance of proliferative growth and replication, evasion of immune detection and destruction, as well as the ability of malignant cells to hijack normal cellular functions to their advantage (Hanahan, 2022). Examples of the latter include accessing and/or establishing vasculature for nutrient and growth support, undergoing metabolic shifts to best support the cancer's increased bioenergetic demands, establishing a favorable tumor microenvironment, facilitating cell signaling, and promoting metastasis (Liberti & Locasale, 2016). Acquiring these characteristics allows cells to progress in pathogenesis, overcome anti-cancer defense mechanisms present and further compromise normal cellular physiology.

While identification of these key features for malignancy initiation and maintenance provides us with important insight in the vast complexity of tumors, the underlying molecular processes

governing these events remain largely unexplored, limiting thus our ability to develop more targeted/specific approaches for tackling this challenging disease. Therefore, in the most recent review, additional emerging hallmarks and enabling characteristics were included as a means of shedding more light on the underlying drivers of tumor pathogenesis, with cellular plasticity and epigenetic reprogramming being among the most prominent. On the one hand, cellular plasticity, which under physiological conditions allows normal cells to maintain their homeostasis and support tissue repair and regeneration, has recently been identified as an emerging hallmark of cancer. In the context of tumorigenesis, cellular plasticity can be seen as one of three conditions: i) dedifferentiation, ii) blocked differentiation or iii) transdifferentiation. Dedifferentiation refers to the process by which differentiated cells may revert back to a progenitor-like state, allowing them to continue growing and proliferating. In a similar fashion, blocked differentiation means that cells evade terminal differentiation, generally viewed as a non-proliferative state, and instead maintain their progenitor-like state which allows them to proliferate further, supporting the growing tumor. Circumvented differentiation, whereby progenitor/stem-like cells assume a quiescent phenotype and exit the cell cycle with the potential of regaining their proliferative potential upon exposure to specific cues/cellular pressures, is also closely related to blocked differentiation as it is a means of once more disrupting the otherwise normal differentiation of cells. In the case of transdifferentiation, cells originally destined to become one type, switch to a completely different one, acquiring features not previously present in their normal cell of origin. This diversification enables cancer cells to escape lineage-specific therapies, allowing them once more to continue growing and proliferating (Hanahan, 2022).

On the other hand, according to Hanahan, enabling characteristics are traits emerging during tumorigenesis that allow cells to acquire the aforementioned hallmarks, hinting thus at the underlying cellular and molecular drivers. Hanahan describes non-mutational epigenetic

reprogramming as an enabling characteristic. While genomic instability and mutations in genes important for chromatin organization and architecture are widely accepted as cancer hallmarks, non-mutational changes, or else gene expression changes resulting from epigenetic modifications, are gaining traction as enablers of cancer hallmarks. It is postulated that conditions in the tumor microenvironment, for instance hypoxia, can affect the activity of specific enzymes responsible for conferring epigenetic modifications, ultimately leading to epigenetic reprogramming. This in turn can facilitate the acquisition of more favorable growth/maintenance conditions for cancer cells (Hanahan, 2022).

1.6.3 Epigenetic regulation of cellular plasticity

Epigenetics, a term first coined by Conrad H. Waddington in the early 1940s, describes changes in phenotype that occur without changes in genotype. These can be transient and reversible, or more stable and get passed onto the next generations, thus sharing the heritable nature of genomic alterations (Weinhold, 2006; Q. Zhang & Cao, 2019). Epigenetic changes are typically characterized by the addition or removal of side chains to either DNA bases or histones, ultimately affecting gene expression and regulation (Figueroa). Common mechanisms of epigenetic regulation include: DNA modifications (e.g. DNA methylation at CpG islands) and histone post-translational modifications (PMTs) (e.g. methylation, acetylation, phosphorylation and ubiquitination of histone marks). DNA modifications can affect the accessibility of chromatin-bound DNA to transcriptional machinery, leading to the activation or repression of certain genomic regions and their associated genes. In a similar manner, histone PTMs function as a “code” coordinating cell- and tissue-specific gene expression through changes in chromatin architecture, or else how tightly DNA is wrapped around histone proteins. As a result, depending on the modification in question, certain DNA regions may become more or less accessible to transcription factors, once more affecting the activity/expression of genes in these regions. Other forms of epigenetic regulation include nucleosome remodeling and non-coding RNAs

(ncRNAs), most prominent of which are long non-coding RNAs (lncRNAs) and microRNAs (miRNAs) (Figueroa; Q. Zhang & Cao, 2019).

Proper chromatin architecture is crucial for ensuring the normal function of cells and organisms thus, it becomes readily apparent how dysregulation of such processes can have important implications in health and disease. In principle, segments of DNA are tightly wrapped around a core histone octamer to form the nucleosome, the fundamental subunit of chromatin (Roberts & Orkin, 2004). At any given moment, genes might have to be activated or repressed. This comes about through a highly coordinated process characterized by chromatin remodeling through the action of histone modifying enzymes as well as ATP-dependent chromatin remodeling complexes. While histone-modifying enzymes recognize and mark histone tails with different residues (e.g. by depositing acetyl-, methyl-, phospho-, ubiquitin- groups onto them), ATP-dependent chromatin remodeling complexes recognize these marks and by hydrolyzing ATP, unwrap, mobilize, exchange or displace nucleosomes, facilitating thus the recruitment of the required transcriptional machinery to the particular DNA segment of interest (Tang, Nogales, & Ciferri, 2010). More specifically, chromatin remodelers are multiprotein complexes that despite each having specialized functions, all carry a subunit with a conserved ATPase domain (Phillips & Shaw, 2008). Based on the specific characteristics of this ATPase domain, eukaryotic chromatin remodelers are divided into four major families, namely: SWItch/Sucrose Non-Fermentable (SWI/SNF), Imitation SWItch (ISWI), Chromodomain Helicase DNA-binding (CHD) and INOsitol requiring 80 (INO80) family. The SWI/SNF family of chromatin remodelers encompasses the SWI/SNF and RSC complexes and is involved in transcription initiation through a process involving the sliding and ejection of nucleosomes. ISWI remodelers which include Isw1a, Isw1b and Isw2 complexes, along with the CHD family are implicated in nucleosome assembly and spacing, as well as transcriptional regulation, and the INO80 family which includes INO80 and SWR1 remodelers plays a role in nucleosome editing through the

deposition of histone variants (Morgan, LeGresley, & Fischer, 2020; Reyes, Marcum, & He, 2021). Mechanistically, binding of the ATPase domain onto genomic DNA within the nucleosome leads to DNA extrusion from the histone octamer surface and subsequent translocation of the nucleosome along the DNA. As such, DNA segments previously inaccessible due to being coiled around the histone core become exposed to regulatory factors that can in turn control gene expression. Proteins and domains beyond the ATPase subunit making up the chromatin remodeling complexes are also readily involved in this process as they bind to histones and DNA, thus selecting the nucleosome to undergo remodeling (Phillips & Shaw, 2008).

1.6.4 SWI/SNF chromatin remodeling complex

In studies carried out by Cooke and colleagues, epigenetic remodeling was identified as a crucial component for effective reprogramming to occur. While the specific epigenetic machinery at play was not identified, their findings suggested that the appropriate, permissive epigenetic landscape has to first be established in order for phenotypic conversion of non-stem cells to stem-like cells to occur (Chanda et al., 2019; Cooke, 2019; Cooke & Lai, 2023; Lee et al., 2012; Shu Meng et al., 2016; S. Meng et al., 2017; Sayed et al., 2017; Sayed et al., 2015; Zhou et al., 2016). The SWI/SNF chromatin remodeling complex has been implicated in cancer development (Roberts & Orkin, 2004), somatic cell reprogramming and stem cell maintenance (Ganguly, Sims, Cai, Fan, & Pfeffer, 2018; L. He, Liu, & Tang, 2012; Hiramatsu et al., 2017). Based on subunit composition, localization within the genome, and function, mammalian SWI/SNF chromatin remodeling complexes are categorized into three classes namely: i) BRG1/BRM-associated factor (BAF), ii) polybromo-associated BAF (pBAF) and non-canonical BAF (ncBAF or else GBAF). All are composed of a base core including a BAF155/BAF170 dimer (SMARCC1/2 gene names respectively) and one subunit of BAF60A/B/C (SMARCD1/2/3), along with other complex-specific subunits. Catalytic subunit BRG1

(SMARCA4) or BRM (SMARCA2) conferring ATPase activity binds to this core complex and recruits additional accessory subunits to complete the SWI/SNF complexes (Navickas, Giles, Brettingham-Moore, & Taberlay, 2023). This highlights the vast compositional and functional diversity available. Radiation-induced cellular plasticity is likely associated with the recruitment of epigenetic machinery acting to establish a permissive environment for this phenotypic change to occur. From our RNA sequencing analyses, components of the SWI/SNF complex were found to be upregulated following irradiation. As such, their potential role in mediating radiation-induced cellular plasticity events in our glioblastoma models was investigated further.

SUMMARY OF CHAPTERS

Given the important implications of radiation-induced phenotypic conversion of non-cancer stem cells to cancer stem cells for tumor recurrence and therapy resistance, understanding how these processes come about is of paramount importance. Prompted by research highlighting the important role PAMP/PRR interactions play in cellular plasticity events, and knowing that IR leads to the release of DAMPs which engage many of the same receptors as PAMPs, we hypothesize that DAMPs released following ionizing radiation genotoxic stress lead to the activation of evolutionarily conserved signaling cascades that result in the promotion of cellular plasticity and multipotency. For the purposes of addressing this question, select receptors were evaluated to gain insights regarding the underlying mechanisms driving IR-induced cellular plasticity. More specifically, the effects of receptor inhibition on stemness of patient-derived glioblastoma cell lines were studied by means of sphere formation assays (SFAs) and extreme limiting dilution assays (ELDAs) for addressing implications on stem cell maintenance/self-renewal capacity. Reprogramming assays (cancer stem cell induction assays) were used for determining effects of such interventions on *de novo* stem cell induction. RNA sequencing and RT-PCR experiments were performed to further validate our findings.

Chapter 2 will discuss the main findings of the present dissertation project (**2.2 Results**), followed by an interpretation (**2.3 Discussion**) and suggestions for future experiments needed to validate our results and elucidate the signaling pathways and epigenetic processes implicated (**2.4 Future Directions**). **Chapter 3** will present research papers (published and/or currently under review) from the lab (**3.1 Lab publications/papers**), followed by a brief study rationale and summary of my direct contributions to each (**3.2 Summaries & Contributions**). These papers can be divided into four main categories addressing the following questions: i) prevention of radiation-induced phenotypic conversion of non-stem cancer cells to cancer stem/initiating cells in the context of glioblastoma, ii) evaluation of the effects of drugs (radiation

mitigators or compounds that prevent radiation-induced phenotypic conversion) on neural stem/progenitor cells, iii) leveraging radiation-induced multipotency to drive surviving GBM cells towards a mitotically incompetent, neuron-like state, and iv) pro-inflammatory signaling in mammary gland development and carcinogenesis. While my own research project aimed to identify the mechanism(s) by which radiation leads to cellular plasticity, thus more closely relating to i and iii described above, its exploration of inflammatory signaling pathways as potential mediators of this effect can be viewed as a common, unifying feature with all categories.

CHAPTER 2: Radiation-induced cellular plasticity

2.1 MATERIALS & METHODS

Cell culture

Cell lines used (HK-374/345/308/157) were a kind gift from Dr. Kornblum. Characteristics of these glioblastoma lines can be found in Laks et al. (Laks et al., 2016).

i. Monolayers/adherent cells

Cells were grown in D10 media composed of DMEM media (Gibco, Cat# 11995-065) supplemented with 10% fetal bovine serum (Seradigm, lot# 048B16) and 1% pen/strep (Gibco, Cat# 15140-122) solution, and grown in a humidified 37°C incubator with 5% CO₂. During passaging, 0.25% Trypsin-EDTA (1x) (Gibco, Cat# 25200-056) was used to detach the cells.

ii. Glioma spheres (denoted as NS within text)

Cells were grown under similar incubation conditions as listed above, in DMEM/F-12 (1:1) (Gibco, Cat# 11320-033) media supplemented with 1% pen/strep, 20ng/ml fibroblast growth factor (bFGF, Sigma), 20ng/ml epidermal growth factor (EGF, Sigma), 1 bottle of SM1 neuronal supplement containing vitamin A (StemCell Technologies, Cat# 05711) and heparin. The combination of all these reagents corresponds to GBM complete media. GBM 10x which is used for treating the spheres in between passaging, is formulated by combining 50ml of incomplete media (contains all the components described above except for bFGF and EGF), supplemented with the volumes of bFGF and EGF that would be normally used for preparing complete media. For sphere cell passaging, TrypLE™ Express (Gibco, Cat# 12604-013) was used.

All cell lines were routinely tested for mycoplasma using mycoplasma specific PCR testing and/or MycoAlert (Lonza). Cell line identity was confirmed by DNA fingerprinting (Laragen, Culver City, CA).

Inhibitor drug preparations

Information regarding the manufacturers and catalog numbers of the inhibitor drugs used can be found in **Table 1**. Specifically, all drugs, with the exception of TLR4i which came as a premade 10mM stock solution in DMSO, were purchased in powder form. 10mM stocks of these powders were prepared by dissolving them in DMSO (TLR3i, CQ, cGASi and STINGi) or HyClone Water (TLR9i). Solutions were subsequently stored at -80°C until further use. Concentrations of interest were achieved by diluting stock solutions in appropriate media. Control treated cells were supplemented with either DMSO or HyClone Water, depending on which one was used for preparing the drugs used, at a concentration matching the highest treatment dose used for the experiment in question.

Table 1. List of inhibitors used and their specific characteristics.

| Target | Inhibitor name | Abbreviations within text | Manufacturer | Cat # | Function |
|------------------------|------------------------------|---------------------------|-------------------|-----------|--|
| TLR3 | TLR3/dsRNA complex inhibitor | TLR3i | Calbiochem® | 614310 | Directly and competitively inhibit dsRNA binding to TLR3 |
| TLR4 | TAK 242 | TLR4i | Calbiochem® | 614316 | Disrupts TLR4 interaction with downstream adaptor molecules TIRAP and TRAM (affecting both NFκB and IFN signaling) |
| TLR9 | E6446 dihydrochloride | TLR9i | Selleck Chemicals | S6719 | Specific TLR9 inhibitor shown to disrupt CpG oligonucleotide induced NFκB signaling |
| cGAS | Human cGAS inhibitor | cGASi, hcGASi, G140 | InvivoGen | inh-g140 | Targets the cGAS catalytic pocket, preventing the synthesis of downstream messenger 2', 3'-cGAMP |
| STING | H-151 | STINGi, H151 | MCE | HY-112693 | Decreases TBK1 phosphorylation and suppresses STING palmitoylation (required for STING activation of type I interferon response) |
| MyD88 & endosomal TLRs | Chloroquine diphosphate salt | CQ | Sigma-Aldrich | C6628 | Inhibition of endosomal TLRs and MyD88 signaling by decreasing IRAK4 and IRF7 molecules and inhibiting IFNα synthesis; cGAS/STING, RIG-1 signaling and autophagy have also been shown to be affected by CQ (Al-Bari, 2017) |

Irradiation

Cells were irradiated at room temperature using an experimental X-ray irradiator (Gulmay Medical Inc. Atlanta, GA) at a dose rate of 5.519 Gy/min for the time required to apply the dose of interest. The X-ray beam was operated at 300kV and hardened using a 4mm Be, 3mm Al and 1.5mm Cu filter, and calibrated using NIST-traceable dosimetry. Controls were sham irradiated.

Sphere formation assay (SFA)/ *In-vitro* limiting dilution assay – determining self-renewal capacity of existing cancer stem cells (CSCs)

For determining self-renewal capacity of cells *in vitro*, glioblastoma spheres were seeded at clonal densities under serum-free conditions using GBM complete media. The cells were plated in non-tissue culture treated 96 well plates using a serial dilution. Specifically, starting cell densities for the serial dilution were as follows: 512 cells/well for 0 and 2 Gy, 1024 cells/well for 4 Gy and 2048 cells/well for 8 Gy. After overnight incubation at 37°C, cells were treated and irradiated with 0, 2, 4 or 8 Gy 1h later using an X-ray irradiator. Treatments were prepared by mixing the required volumes of drug stocks with GBM 10x solution. Cells were grown for 7-10 days, with 10ul/well of GBM 10x (supplement of growth factors) being added every other day. Upon formation of visibly distinct spheres, spheres in each well were counted and recorded using a conventional microscope. Typically, 4 treatments were included in each plate, resulting in an effective 20 wells/treatment condition. The number of spheres formed at each condition was adjusted for the number of cells plated per well and reported as a linear range average. This was subsequently normalized against the equivalent value for the non-irradiated control (DMSO or HyClone Water). The resulting data was plotted to determine the effect of the different treatment interventions on the sphere forming capacity (SFC) of the cells.

Extreme Limiting Dilution Assay (ELDA) - *evaluating self-renewal capacity of existing CSCs and changes in CSC frequencies*

Similar to the procedure described above for SFAs, glioma spheres were seeded at clonal densities under serum-free conditions in non-tissue culture treated 96 well plates using a serial dilution across the entire plate, i.e. either 40 or 80 wells/treatment condition for counting, depending on whether 2 or 1 treatment conditions were included in each plate respectively. Cells were treated, irradiated, supplemented, grown and counted as previously described for SFAs. SFC was determined the same way as for SFAs. For stem cell frequency calculations, open-access ELDA software (Y. Hu & Smyth, 2009) from the Walter+Eliza Hall Bioinformatics Institute of Medical Research was used. Reported values were given in the form of a range (including lower, estimate and upper limits) as the reciprocal of stem cell frequency. Estimates were used for converting data into percent stem cell frequencies and results were plotted.

Reprogramming assay (cancer stem cell induction assay) – *determining phenotypic conversion of non-CSCs to CSCs*

HK-374 ZsGreen-cODC expressing cells were grown in T125 flasks, trypsinized using 0.25% Trypsin-EDTA (1x) (Gibco, Cat# 25200-056), centrifuged at 250rcf at room temperature for 3min, the supernatant was discarded, and the remaining pellets were resuspended in D10 media and placed in appropriately labeled 5ml Falcon round bottom polystyrene test tubes containing a cell strainer cap (Corning, Cat# 352235) and placed on ice. The single cell suspensions were subsequently sorted using a BD FACSAria™ III sorter (BD Biosciences, Franklin Lakes, NJ), and ZsGreen negative cells were collected. Non-ZsGreen transfected HK-374 cells were used as a control for flow cytometry gating and for determining the population of interest to be collected. Sorted cells were centrifuged, supernatant was removed, and pellets were resuspended in fresh D10 media. Upon determining cell density of the sorted sample using a Countess 3 automated cell counter (Invitrogen), cells were plated (~27k cells/well) in 6-

well tissue culture treated plates containing D10 media (3ml). Cells were allowed to grow overnight in a humidified incubator with 5% CO₂ at 37°C. The following day, media was removed from the wells and cells were supplemented with fresh media containing the required drug treatments (duplicates or triplicates of each). Control wells were treated with the same solution used for dissolving the drugs of interest (i.e. DMSO for TLR3/4, and cGAS/STING inhibitors and HyClone Water for TLR9 inhibitor) at a volume matching what was used for the highest drug concentration tested. One hour post treatment plates were irradiated with 0 or 4 Gy and subsequently placed back in the humidified incubator for 5 days. On day 5 post irradiation, cells were harvested using 0.25% Trypsin-EDTA (1x) (Gibco, Cat# 25200-056), centrifuged down, pellets were resuspended in fresh D10 media (200ul), collected in appropriately labeled 5ml Falcon round bottom polystyrene test tubes containing a cell strainer cap (Corning, Cat# 352235) and placed on ice. Samples were then analyzed by means of flow cytometry using a LSRFortessa™ Cell Analyzer (BD Biosciences, Franklin Lakes, NJ) for measuring green fluorescence through the Alexa Fluor 488 detector. Forward scatter and side scatter were both used in A mode and data collected was initially in logarithmic scale, but subsequent experiments were switched to reflect a linear range. The distinction between the two was not an issue in our samples since we were dealing with a population of cells with similar characteristics, unlike what is seen for instance in blood samples having different cellular components. Non-ZsGreen transfected HK-374 cells were used as a background control for setting the required gates for our analysis. Data collected was analyzed using FlowJo software (BD Biosciences). Fold increase in ZsGreen positive cells was determined by normalizing the reported % of ZsGreen positive cells in each sample to the average % ZsGreen positive cells reported for the 0 Gy control treated wells.

RNA isolation & Quantitative Reverse Transcription-PCR (qRT-PCR)

Total RNA was isolated using TRIzol Reagent (Invitrogen). cDNA synthesis was carried out using SuperScript Reverse Transcription IV (Invitrogen). Quantitative PCR was performed using a QuantStudio™ Real-Time PCR System (Applied Biosystems, Carlsbad, CA, USA) using PowerUp™SYBR™ Green Master Mix (Applied Biosystems). C_t for each gene was determined after normalization to GAPDH or PPIA, and $\Delta\Delta C_t$ was calculated relative to the designated reference sample. Gene expression values were then reported as fold changes ($2^{-\Delta\Delta C_t}$) as described by the manufacturer of the kit (Applied Biosystems). All PCR primers were synthesized by Invitrogen with GAPDH and/or PPIA being used as housekeeping genes. More specifically, for RNA isolation of adherent cells, media was removed from plates/cell culture dishes containing cells, wells/dishes were washed using sterile DPBS (Corning), solution was discarded and excess liquid was further pipetted out before the addition of 1ml of TRIzol Reagent per well/dish. Plates/dishes were gently moved around to ensure TRIzol would cover the entire surface area. After 5min cells in TRIzol were collected in appropriately labeled tubes. TRIzol cell samples were either processed directly for RNA isolation or stored at -80°C for future use. In the case of sphere cultures, media containing spheres was collected, centrifuged at 250rcf for 3min, supernatant was discarded, pelleted spheres were washed in 1ml of sterile DPBS and transferred into appropriately labeled 1.5ml eppendorf tubes. These were in turn centrifuged at 12,000g for 3min, at which point supernatant was removed once more and 500ul of TRIzol Reagent was added directly onto the pelleted spheres. Using a piston, spheres in TRIzol were minced and once this process was completed another 500ul of TRIzol Reagent was added to each tube. Further processing was the same as for adherent cell samples. To the tubes containing TRIzol sample 200ul of chloroform was added, tubes were briefly vortexed and set on ice for 5min, time after which they were centrifuged at 12,000g, 4°C for 10min. The supernatant was carefully collected in new appropriately labeled tubes and 500-600ul of isopropanol was added. Samples were then briefly vortexed and centrifuged as described

above. The supernatant was once more removed, making sure to leave the pellet formed as dry as possible, and 1ml of 70% ethanol was added into each tube. The tubes were inverted several times in order to ensure the pellet was sufficiently dislodged and washed. Subsequently, samples were once more centrifuged using the same settings as those described above. After centrifugation, supernatants were completely removed and pellets were left to dry on the bench. Once dried, they were resuspended in HyClone Water and their RNA concentration and purity were determined by means of NanoDrop (ThermoFisher Scientific). For cDNA synthesis, sample mixtures were prepared using 2ug of RNA. For quantitative PCR analysis, 5ul of HyClone Water, 4ul of cDNA sample, 1ul primer mixture (containing both forward and reverse primers) along with 10ul of PowerUp™SYBR™ Green Master Mix (Applied Biosystems) were added in each corresponding well of a PCR compatible 96 well plate.

RNA sequencing (RNAseq) analysis for STINGi data using iDEP

Raw data counts obtained from RNA sequencing of total RNA isolated from HK-374 monolayer cells 48h post irradiation (treatment groups used: 0Gy_DMSO, 4Gy_DMSO and 4Gy_H151 1uM) done by Novogene (Sacramento, CA) were input directly into iDEP (Ge, Son, & Yao, 2018), an open access web application used for performing differential gene expression and pathway analyses. Software versions 0.96, 1.13 and 2.0 were used for subsequent analyses depending on domain availability. Data was originally pre-processed using the following parameters: minimum counts per million (CPM) of 0.5, in 1 library and with a transformation of $\log_2(\text{CPM}+4)$ used for clustering and principal component analysis (PCA) to ensure sample quality. DESeq2 was used for identifying differentially expressed genes (DEGs) with the following parameters: false discovery rate (FDR) cutoff of 0.1 and minimum fold change of 2. Pathway enrichment analysis was done using the hallmarks.MSigDB dataset.

Data representations and statistical analyses

With the exception of figures/tables obtained from iDEP, all other graphical representations and statistical analyses were performed using GraphPad Prism version 9. Unless otherwise specified, data was represented as mean +/- standard error mean (SEM) of at least 3 biological replicates. Statistical significance for one- and two-way ANOVA multiple comparisons testing was determined as follows: 0.1234 (ns), 0.00332 (*), 0.0021 (**), 0.0002 (***) and <0.0001 (****).

2.2 RESULTS

Identifying differentially expressed DAMPs/PRRs from RNAseq datasets

In order to investigate the “danger sensing theory” in the context of radiation, we first studied gene expression changes following radiation pertaining to damage associated molecular patterns (DAMPs) and their respective pattern recognition receptors (PRRs). This was of particular interest given the recent evidence by Cooke and colleagues highlighting the involvement of select PRRs in the process of reprogramming (Cooke, 2019; Cooke & Lai, 2023; Lee et al., 2012; Shu Meng et al., 2016; S. Meng et al., 2017; Sayed et al., 2017). Using a curated list from Roh et al. (Roh & Sohn, 2018; Takeuchi & Akira, 2010) representing such DAMP-PRR interactions, we initially searched for these genes in an RNA sequencing dataset of HK-374 cells, 48h post irradiation, time point at which we had previously shown maximal open chromatin in the promoter region of developmental transcription factors (K. Bhat, Saki, et al., 2020). The unirradiated (0 Gy DMSO) and irradiation control (IR, 4 Gy DMSO) datasets of differentially expressed genes were searched against the lists provided by Roh et al. and the log₂ fold changes of the identified DAMPs and PRRs were plotted in the form of a heatmap (**Figure 1**). DAMPs such as several histone clusters, syndecans (SDCs), glypicans (GPCs), interleukin 33 (IL33), interleukin 1 alpha (IL1 α), versican (VCAN), calreticulin (CALR), heat shock proteins and amyloid beta precursor proteins were all upregulated in the irradiated group. Similarly, PRRs such as TLR4, interleukin 1 receptor (IL1R), absent in melanoma 2 (AIM2), formyl peptide receptors (FPRs), and components associated with nod-like receptor (NLR) formation were also shown to be upregulated following irradiation.

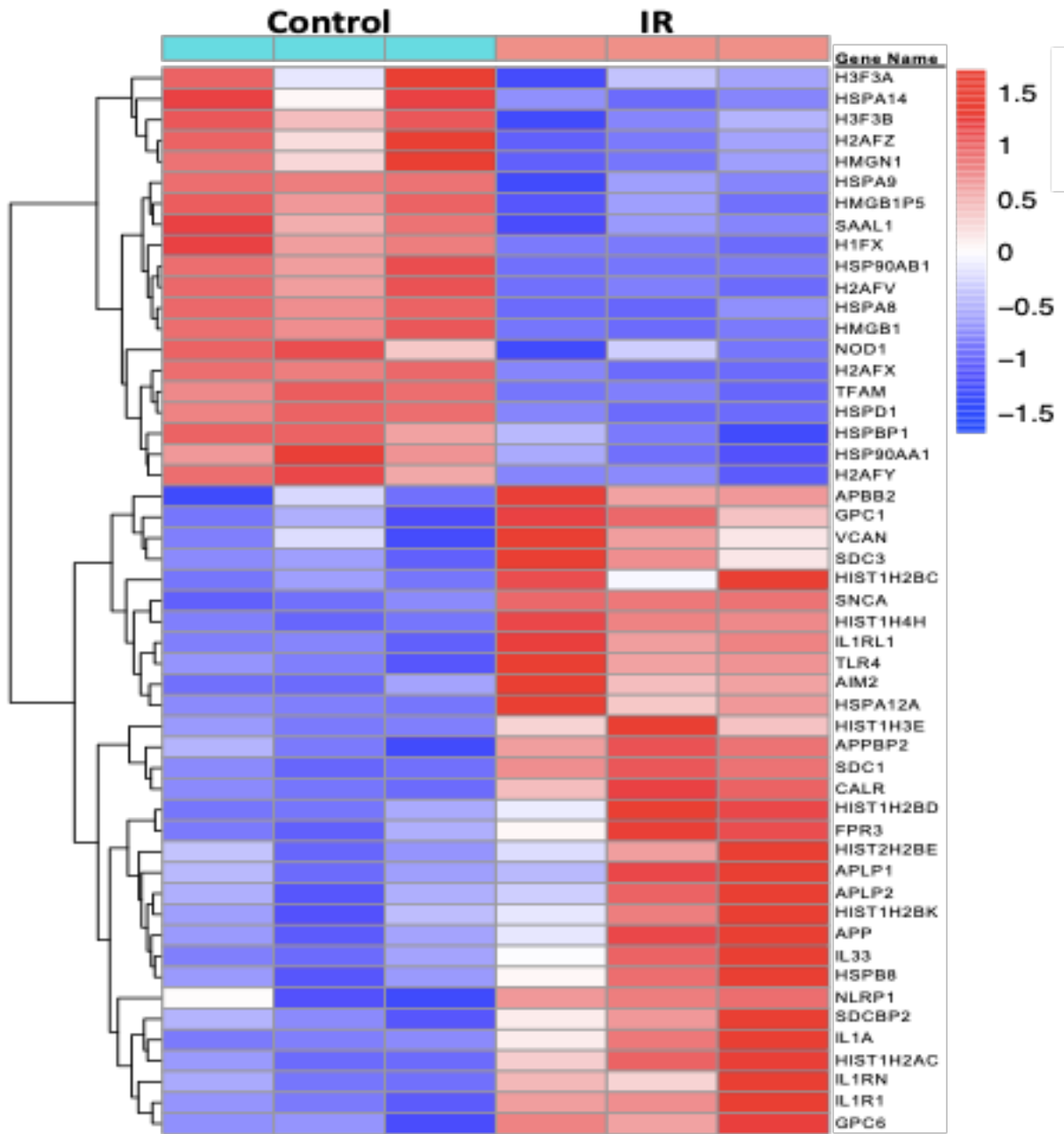


Figure 1: Heatmap representation of differentially expressed damage associated molecular pattern (DAMP) and pattern recognition receptor (PRR) genes from an RNA sequencing analysis performed in HK-374 monolayer cells, 48h post 4 Gy irradiation. Data plotted as log₂ fold changes. Control refers to unirradiated samples (0 Gy) and IR (irradiation) to 4 Gy.

Many of the same DAMPs/PRRs were shown to be upregulated in the irradiated groups of other RNAseq datasets explored (data not shown here). To validate some of the top upregulated genes identified in the irradiated group, RT-PCR experiments were done using HK-374 monolayer cells (**Figure 2**). While the RT-PCR results did not fully recapitulate the heatmap findings, it was still possible to validate some of the DAMPs/PRRs. Specific primer sequences used for these experiments can be found in **Supplementary Table 1**.

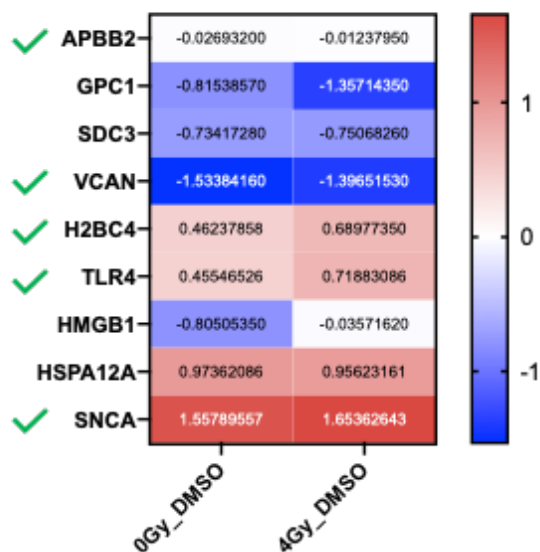


Figure 2: RT-PCR validation heatmap representing differentially expressed damage associated molecular pattern (DAMP) and pattern recognition receptor (PRR) genes previously identified from RNA sequencing analysis performed in HK-374 monolayer cells, 48h post 4 Gy irradiation. N=2 biologically independent repeats. 0Gy_DMSO refers to unirradiated control, while 4Gy_DMSO is the irradiation condition.

Exploring the role of different TLRs in radiation-induced cellular plasticity: stem cell self-renewal capacity/stemness maintenance

Having identified TLR4 as a PRR upregulated by radiation and knowing of TLR3 involvement in reprogramming as reported by Cooke and colleagues (Lee et al., 2012), the next step was to investigate the potential role these two receptors play in mediating radiation-induced phenotype conversion. Using an inhibitor approach (**Table 1**) we evaluated the involvement of TLR3 and

TLR4 in the self-renewal capacity of GBM cells using sphere formation assays (SFAs), their impact on cellular plasticity using reprogramming assays, and their effect on the number of GBM stem cells in extreme limiting dilution assays (ELDAs). Inhibitors for these two receptors were chosen in an attempt to distinguish whether radiation-induced reprogramming signals through a MyD88-dependent or -independent pathway. While TLR3 signaling is exclusively MyD88-independent, TLR4 has the potential for both MyD88-dependent and -independent signaling (Kashani et al., 2021). In parallel, chloroquine (CQ) was also used in similar assays, at first as a MyD88 inhibitor, but was ultimately found to have broader effects. There is evidence for CQ inhibiting signaling of endocytic TLRs, namely TLR3/7/8/9 (Al-Bari, 2017; Yasuda et al., 2008), RIG-1, cGAS/STING, as well as processes such as autophagy (Gies et al., 2020). Initially, sphere forming assays were performed to determine how use of select inhibitors would influence the ability of glioma stem like cells to form more stem cells (i.e. evaluate the sphere forming capacity of these cells under the different experimental conditions). More specifically, cells were treated with TLR3 and TLR4 inhibitors (TLR3i, TLR4i) for five consecutive days starting one day after plating (**Figure 3**), while CQ was administered once, 24 hours after plating (**Figure 4**). Radiation was delivered as a single dose of 4 or 8 Gy and control cells were sham irradiated. This treatment paradigm was followed (and used in all subsequent assays with TLR3/4i) because both TLR3i and TLR4i had only minimal effects when given as a single treatment, likely due to the short half-life of these drugs. Controls were treated with the solvent DMSO, which is known to exhibit some radioprotective effects (Chapman, Reuvers, Borsa, & Greenstock, 1973).

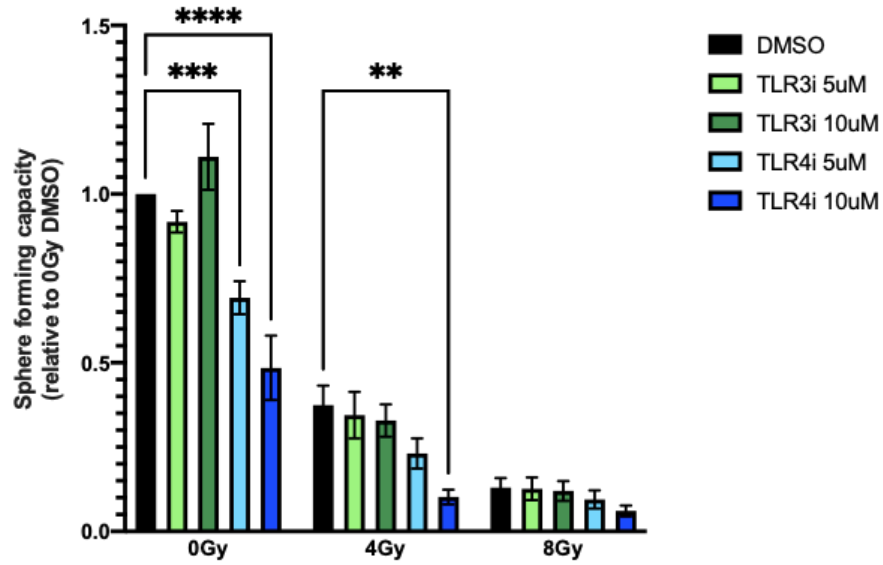


Figure 3: Sphere forming assay for TLR3 and TLR4 inhibitors in HK-374 glioma spheres. 4x treatment was used for both inhibitors (i.e. initial treatment prior to irradiation, followed by an additional 4 days of treatment) to account for potential limitations from inhibitors' half-lives. N=5 biologically independent repeats, data represented as mean +/- SEM. Two-way ANOVA analysis where 0.1234 (ns), 0.0332 (*), 0.0021(**), 0.0002 (***), <0.0001 (****).

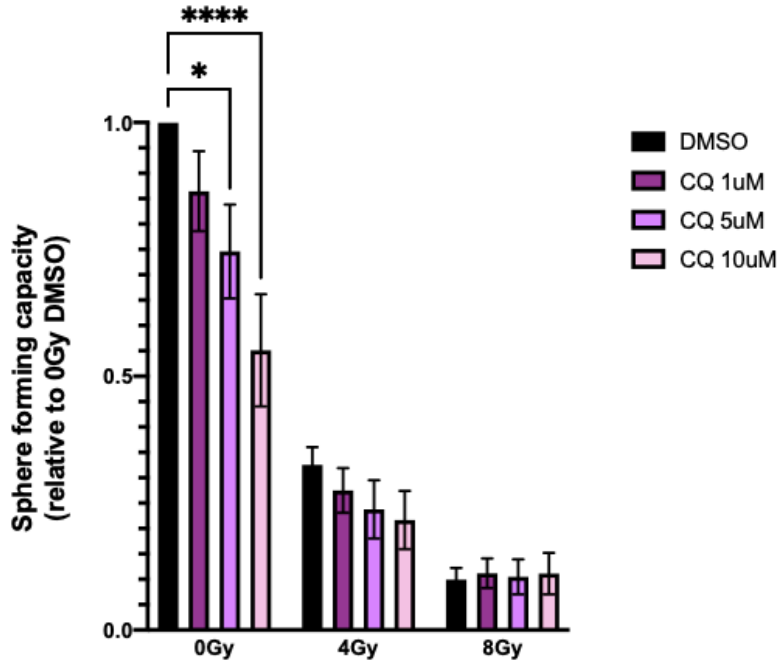


Figure 4: Sphere forming assay for endosomal TLR inhibitor, chloroquine (CQ) in HK-374 glioma spheres. One time treatment used. N=4 biologically independent repeats, data represented as mean +/- SEM. Two-way ANOVA analysis where 0.1234 (ns), 0.0332 (*), 0.0021(**), 0.0002 (***), <0.0001 (****).

For control treated samples, sphere formation decreased by more than 50% following a single dose of 4 Gy and by almost 80% after a single dose of 8 Gy (**Figures 3, 4**). Treatment with TLR3i alone or in combination with radiation did not lead to a statistically significant decrease in the sphere forming capacity of the cells relative to controls. Treatment with TLR4i alone led to a dose-dependent decrease in sphere forming capacity compared to unirradiated control cells (two-way ANOVA; adjusted *p*-values of 0.0003 and <0.0001 for 0 Gy + TLR4i 5uM and 10uM respectively). This effect was also seen in combination with radiation (two-way ANOVA; adjusted *p*-value of 0.0014 for 4 Gy DMSO vs 4 Gy + TLR4i at 10uM) (**Figure 3**). Treatment with CQ alone led to a dose-dependent loss of self-renewal capacity relative to the unirradiated control (two-way ANOVA; adjusted *p*-values of 0.011 and <0.0001 for 0Gy + CQ 5uM and 10uM respectively). When combined with 4 Gy, CQ showed a trend for a dose-dependent reduction in sphere

formation, but these effects did not reach statistical significance (**Figure 4**). A complete list of the numerical results is provided in **Supplementary Tables 2, 3**.

The findings above suggest that signaling through TLR4, but not TLR3, is involved in the maintenance of the self-renewal capacity of pre-existing stem cells. Because CQ showed a trend for decreasing sphere formation while inhibition of TLR3 had no effect, we next tested if endocytic TLRs (Yasuda et al., 2008), other than TLR3, might be involved in mediating the effects of radiation on cellular plasticity. We shifted our attention to TLR9 because of evidence in the literature highlighting the important role TLR9 has in glioma stem cell maintenance and growth (Herrmann et al., 2014). For the purposes of TLR9 inhibitor (TLR9i) experiments, control cells were treated with Hyclone Water, the solvent for TLR9i (**Table 1**).

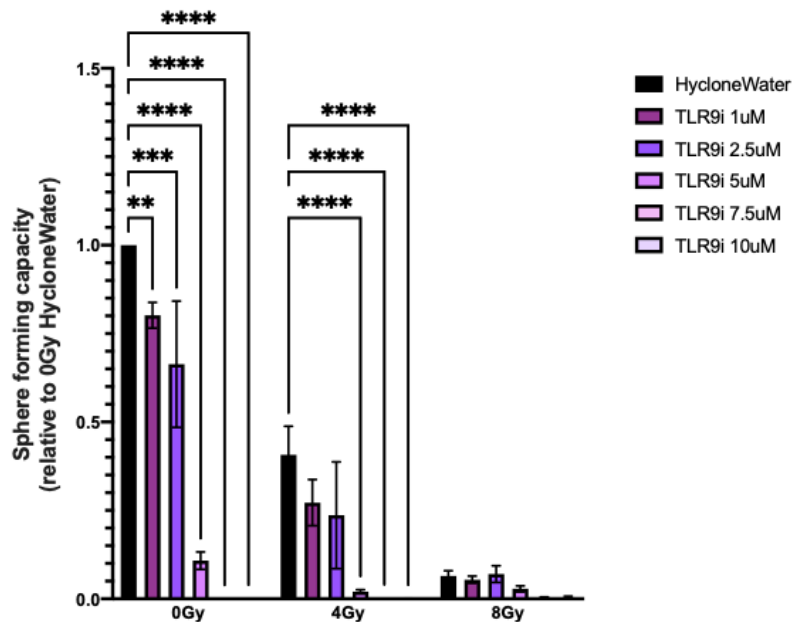


Figure 5: Sphere forming assay for TLR9 inhibitor in HK-374 glioma spheres. N=2 biologically independent repeats for TLR9i 2.5, 7.5 and 10uM, N=5 for HycloneWater (control) and N=6 for TLR9i 1 and 5uM. Data represented as mean +/- SEM. Two-way ANOVA analysis where 0.1234 (ns), 0.00332 (*), 0.0021 (**), 0.0002 (***) and <0.0001 (****).

From SFAs on HK-374 glioma sphere samples (**Figure 5**) using TLR9i it was determined that combination of 4 Gy with TLR9i at the three highest concentrations tested was able to statistically significantly decrease (adjusted p -value <0.0001) the sphere forming capacity of HK-374 glioma spheres relative to the 4 Gy control samples (4 Gy HycloneWater). A comprehensive list of the numerical results is provided in **Supplementary Table 4**. These data support the important role that TLR9 has been shown to play in glioma stem cell maintenance and suggest that similarly to TLR4, this receptor might also be playing a role in mediating the effects of radiation on the self-renewal capacity of pre-existing stem cells. At 8 Gy the number of countable spheres was low, in the single digits, which made detecting drug effects with statistical significance impossible. However, the results at 8 Gy have been included here for completeness.

Next, having evidence suggesting that TLR4 and TLR9 are involved in stem cell maintenance following irradiation, we wanted to test these inhibitors using a more rigorous approach, namely an extreme limiting dilution assay (ELDA). ELDA's are more robust assays compared to the standard SFAs because their results do not depend on the number of spheres counted in each well; they instead provide a binary yes/no response and allow for calculation of an additional important piece of data, the stem cell frequency (Y. Hu & Smyth, 2009). As such, using this assay it is possible to gain insight into not only the effects of select drugs on the stem cell self-renewal capacity but also on stem cell frequency changes. As a proof of principle, we started off by testing the effects of TLR4 inhibition in two glioma sphere lines, HK-374 and HK-345, in order to see if our previous SFA results could be recapitulated (**Supplementary Figure 1**). Once we determined that a similar effect could also be seen in ELDA's using TLR4i, meaning a dose dependent decrease in the sphere forming capacity relative to the control conditions, we next tested TLR9i in this assay using different glioma sphere lines, HK-374/157/345 cells. This was done to validate our original observations (**Figure 5**), and gain insight as to whether different glioma sphere lines respond differently to TLR9 inhibition (**Figure 6, Supplementary Figure 2**).

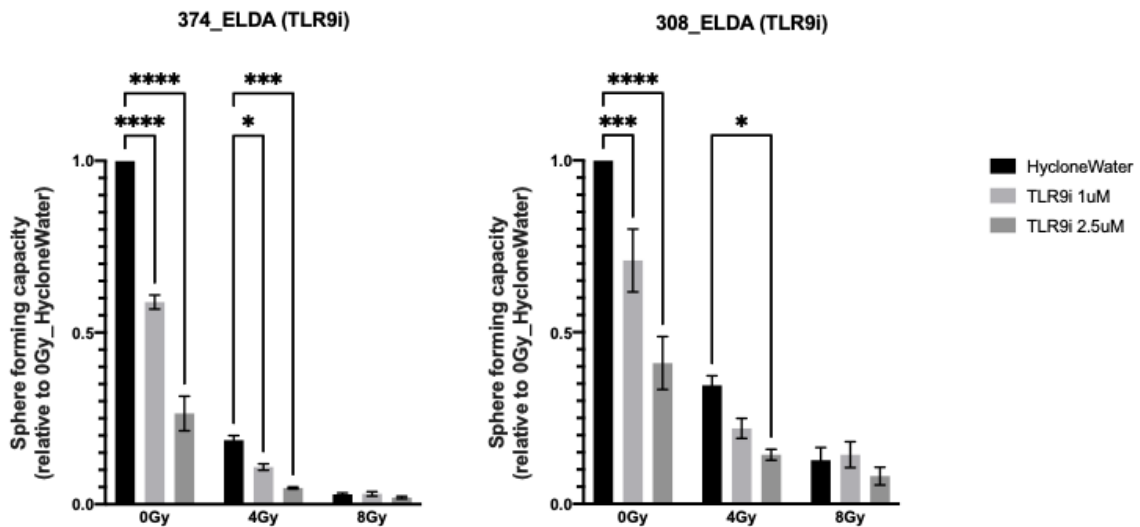


Figure 6: Sphere forming capacity as determined from extreme limiting dilution assays (ELDAs) for HK-374 and HK-308 glioma sphere samples treated with TLR9 inhibitor (1x). N=3 biologically independent repeats for each cell line. Mean +/- SEM data representation. Two-way ANOVA analysis where 0.1234 (ns), 0.00332 (*), 0.0021 (**), 0.0002 (***) and <0.0001 (****). HycloneWater = control.

A statistically significant, dose-dependent decrease in sphere forming capacity was also seen here for the glioma cell lines tested. Specifically, for 4 Gy TLR9i (2.5uM), adjusted p-values from a two-way ANOVA multiple comparisons analysis relative to the irradiated control (4 Gy HycloneWater) were 0.0001 and 0.0127 for HK-374 and HK-308 glioma spheres respectively. Detailed numerical results are provided in **Supplementary Tables 5, 6**. Consistent with the loss of self-renewal capacity, TLR9i treatment decreased the stem cell frequency in a dose dependent manner (**Figure 7, Supplementary Figure 3**). This was statistically significant for HK-374 cells (adjusted p-value for 4 Gy HycloneWater vs 4 Gy TLR9i (2.5uM) was 0.038) but not for the other line tested (**Supplementary Tables 7, 8**).

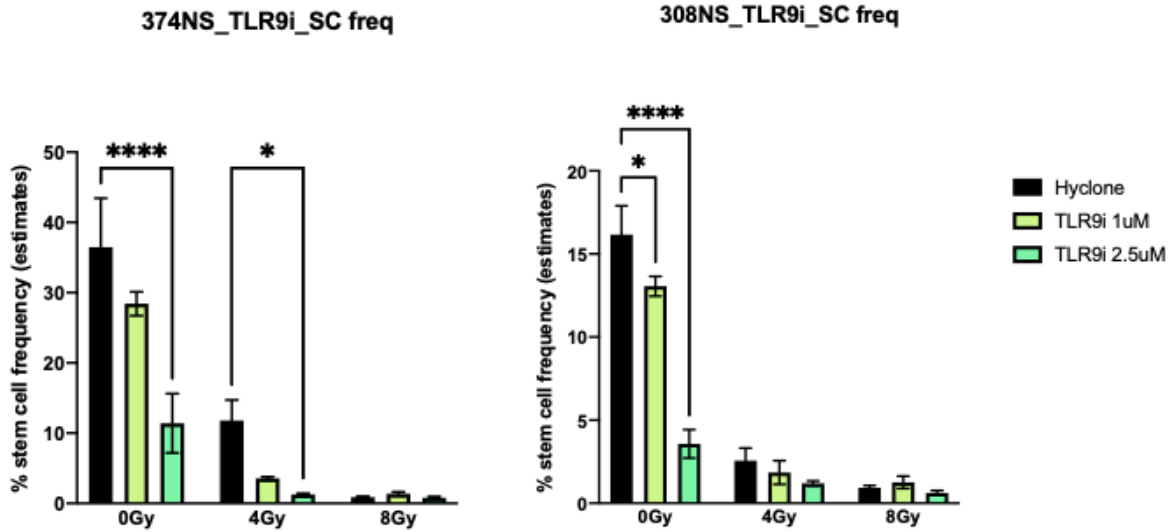


Figure 7: Stem cell frequency as determined by ELDA analysis in HK-374 and HK-308 glioma spheres treated with TLR9 inhibitor (1x). N=3 for biologically independent repeats for each cell line, with data represented as mean +/- SEM. Two-way ANOVA analysis where 0.1234 (ns), 0.00332 (*), 0.0021 (**), 0.0002 (***) and <0.0001 (****).

Evaluating stem cell frequency changes in HK-374 and HK-345 glioma sphere samples treated with TLR4i showed no trend regarding this parameter (**Supplementary Figure 4**) in either line. Overall, the ELDA results recapitulated our previous findings from SFAs testing TLR4i and TLR9i and provided the additional information that TLR9i also affects stem cell frequency of different glioma sphere lines in a dose-dependent manner. Given that spheres encompass heterogeneous populations of cells (stem cells, progenitor cells and differentiated cells) (Pastrana, Silva-Vargas, & Doetsch, 2011), studying this parameter is of value as it allows for evaluation of how different interventions might be specifically affecting the stem cell like population. While additional repeats would be required to validate TLR4i data, the fact that both TLR4i and TLR9i affect stem cell self-renewal, but only one of them seems to be affecting the frequency of these cells suggests that signaling through these receptors could be differentially affecting cells following irradiation.

Exploring the role of different TLRs in radiation-induced cellular plasticity: induction of stemness

While SFAs and ELDAAs can be informative regarding the effect different treatment interventions have on stem cell maintenance, we next wanted to shift our attention towards another aspect of radiation-induced cellular plasticity, and specifically look at the induction of stemness. To do so, we used reprogramming assays (cancer stem cell induction assays) to evaluate the formation of new stem cells from non-stem cell populations following irradiation. **Figure 8** represents a simplified version of the viral construct used to transfect the HK-374 glioblastoma monolayer cells.

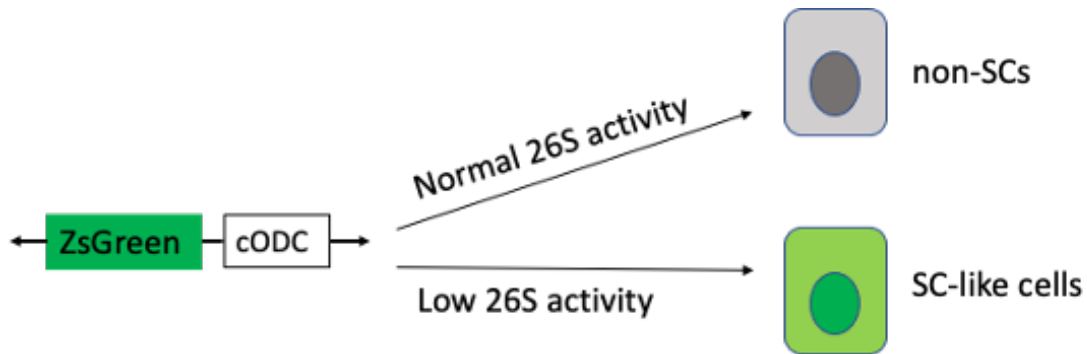


Figure 8: Principles of reprogramming assay. Glioblastoma lines transfected with viral vector (here shown as a simplified construct) to stably express ZsGreen reporter protein fused to the carboxyl-terminal degnon of ornithine decarboxylase (cODC). This allows for sorting of stem and non-stem like cells based on their 26S proteasome activities.

More specifically, this vector allows for stable expression of the ZsGreen reporter protein which is fused to the carboxyl-terminal degnon of ornithine decarboxylase (cODC). cODC is an amino acid sequence that is recognized by the 26S proteasome and leads to the immediate destruction of the associated fused protein. As a result, cells transfected with this vector and having normal 26S proteasome activity show no fluorescence, while cells with low proteasome activity are able to accumulate the ZsGreen protein and fluoresce. Previous research in the lab (Vlashi et al., 2009) has shown that glioma stem cells have low 26S proteasome activity. Therefore, using this

construct it is possible to distinguish between the two populations, stem and non-stem like cells, and make inferences about the effect of different interventions, in this case treatment of cells with select inhibitors, on these populations (**Figure 9**).

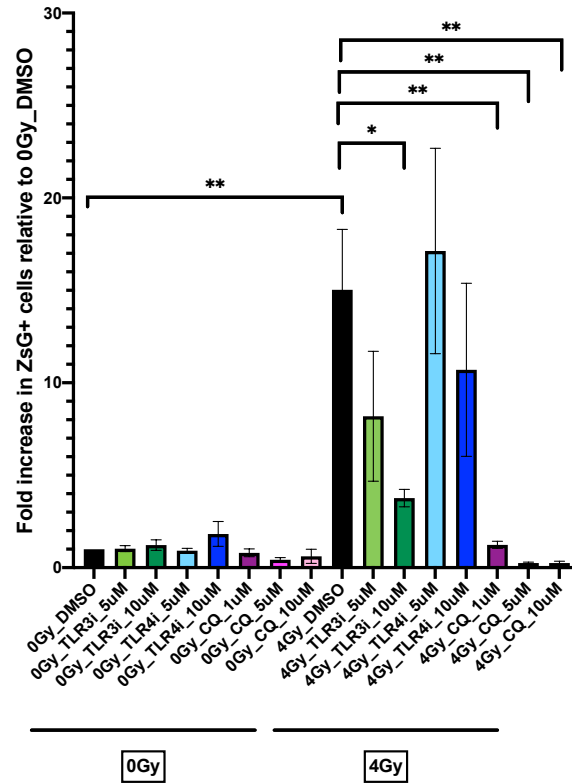


Figure 9: Reprogramming assay in HK-374 monolayer cells treated with TLR3, TLR4 inhibitors and CQ to determine their respective effects on the generation of stem-like cells from non-stem cells. 4x treatment scheme was used for TLR3/4 inhibitors, while 1x treatment for CQ. N=4 biologically independent repeats for all conditions. Data represented as mean +/- SEM. One-way ANOVA testing 0.1234 (ns), 0.0332 (*), 0.0021(**), 0.0002 (***) , <0.0001 (****).

Starting with a sorted population of only ZsGreen-negative cells, meaning putative non-stem cells, and subjecting these to the various interventions, we reached the following conclusions. By plotting the fold increase in the ZsGreen positive population relative to the 0 Gy DMSO control condition, we initially observed the effect of radiation on a population that has been cleared of pre-existing stem cells. This was evidenced by the statistically significant increase in ZsGreen-positive cells irradiated with 4 Gy DMSO relative to the sham irradiated control (adjusted p-value

of 0.0036). This observation confirmed our previous findings of *de novo* induction of stem cells through irradiation (K. Bhat, Saki, et al., 2020; Lagadec et al., 2012; Vlashi et al., 2009). Next, we tested if TLR3i, TLR4i or CQ would prevent radiation-induced plasticity seen following exposure to 4 Gy. Treatment with TLR3i (10uM) led a statistically significant decrease (adjusted p-value 0.0474) in the ZsGreen-positive population induced by 4 Gy irradiation. Likewise, CQ in combination with radiation, at all concentrations used, also reduced induction of ZsGreen-positive cells seen after 4 Gy (adjusted p-values: 0.0046 for 4 Gy + CQ 1 uM and 0.0017 for 4 Gy + CQ at 5 or 10 uM). Combination treatment of TLR4i with radiation was not significantly different from the irradiated control. These results suggest that radiation-induced phenotype conversion of non-stem glioma cells into glioma stem-like cells is likely dependent on TLR3, but not TLR4. The complete numerical results are presented in **Supplementary Table 9**.

The findings above indicate involvement of TLR3, TLR4, and TLR9 in stemness and radiation-induced cellular plasticity. We next tested if treatment of sorted non-stem glioma cells with TLR3 and TLR4 inhibitors in combination with radiation would lead to changes in the expression levels of Yamanaka factors (YFs). This question was of particular interest given previous research in the lab showing radiation-induced phenotype conversion in both breast cancer (Lagadec et al., 2012) and glioblastoma models (K. Bhat, Saki, et al., 2020) coinciding with re-expression of YFs, namely Sox2, Oct4, Klf4, c-Myc and their downstream target Nanog. This re-expression of developmental transcription factors resulted from radiation-induced acquisition of an open chromatin state in the promoter regions of Oct4, Sox2 and Nanog, peaking at 48h post 4 Gy. These findings were important as they highlighted radiation-induced epigenetic remodeling, a process that has been deemed critical for effective reprogramming to occur (Cooke, 2019; Cooke & Lai, 2023; Lee et al., 2012; Shu Meng et al., 2016; S. Meng et al., 2017; Sayed et al., 2017). For our experiments, changes in YFs and Nanog gene expression levels in sorted non-stem glioma cells were assessed by RT-PCR, 48h after irradiation with 4 Gy and treatment with TLR3i

or TLR4i. Specific primer sequences used can be found in **Supplementary Table 10**. Control cells were treated with solvent and were sham irradiated (**Figure 10**).

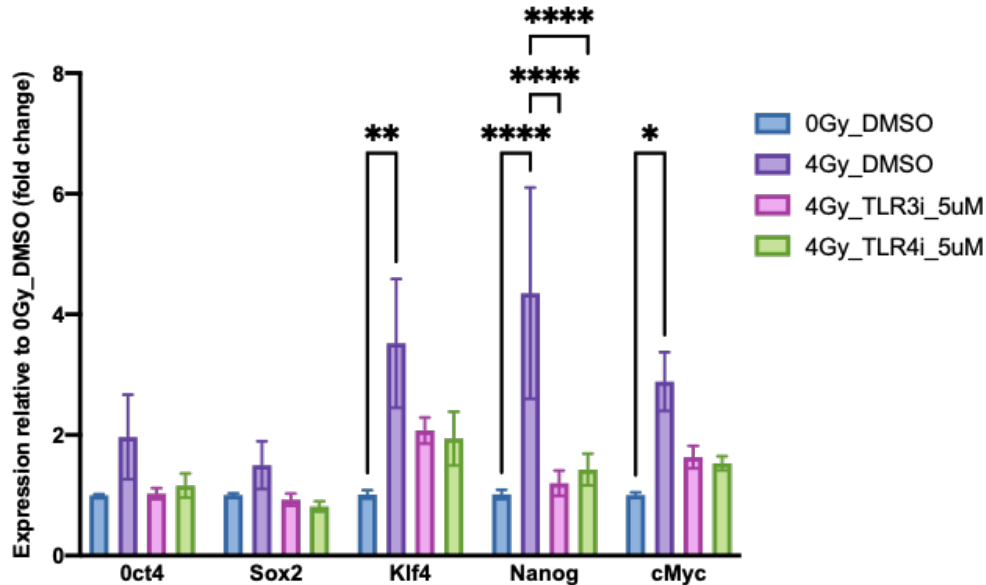


Figure 10: Relative expression of Yamanaka factors (YFs), in HK-374 monolayers (ZsGreen negative sorted cells) irradiated with 4 Gy and treated with TLR3/TLR4 inhibitors. N=2 biologically independent repeats for 0/4Gy_DMSO and N=3 for 4Gy_TLR3/4i_5uM conditions. Data represented as mean +/- SEM. Two-way ANOVA analysis where 0.1234 (ns), 0.00332 (*), 0.0021 (**), 0.0002 (***) and <0.0001 (****).

Following irradiation with 4 Gy we observed increases in the expression of all YFs and Nanog that reached statistical significance for Klf4, Nanog and c-Myc (adjusted p-values: 0.0024, <0.0001 and 0.0372 respectively), confirming data previously reported (K. Bhat, Saki, et al., 2020; Lagadec et al., 2012). The addition of TLR3i or TLR4i prevented or attenuated the effect of radiation on the expression of YFs and Nanog. The complete two-way ANOVA analysis results can be found in **Supplementary Table 11**. The present findings further suggested that TLR3 and/or TLR4 might be implicated in the process of radiation-induced phenotype conversion.

Evaluating the role of cGAS/STING signaling in radiation-induced cellular plasticity

Previously, TLR3 and RLRs, were shown to contribute to reprogramming (Lee et al., 2012; Sayed et al., 2017) and our data presented above suggests potential further involvement of TLR4 and TLR9 in mediating cellular plasticity events, specifically following irradiation. Next, we tested if one of the main signaling pathways involved in the sensing of free cytosolic DNA, the cGAS/STING pathway (Hopfner & Hornung, 2020), could be playing a role here. The rationale behind studying this specific pathway arose from the fact that exposure to radiation is known to lead to DNA breaks, and that these fragments in the form of free dsDNA can be considered DAMPs (Baatout Sarah, 2023). As such, it follows that as a free cytosolic DNA sensor, cGAS/STING might be engaged here. Before testing this hypothesis further, we initially established that cell lines to be used expressed cGAS/STING (**Figure 11**) since there is evidence in the literature suggesting a dysregulated expression of STING in human glioma cells (Berger et al., 2022; Low et al., 2022; Zheng et al., 2023).

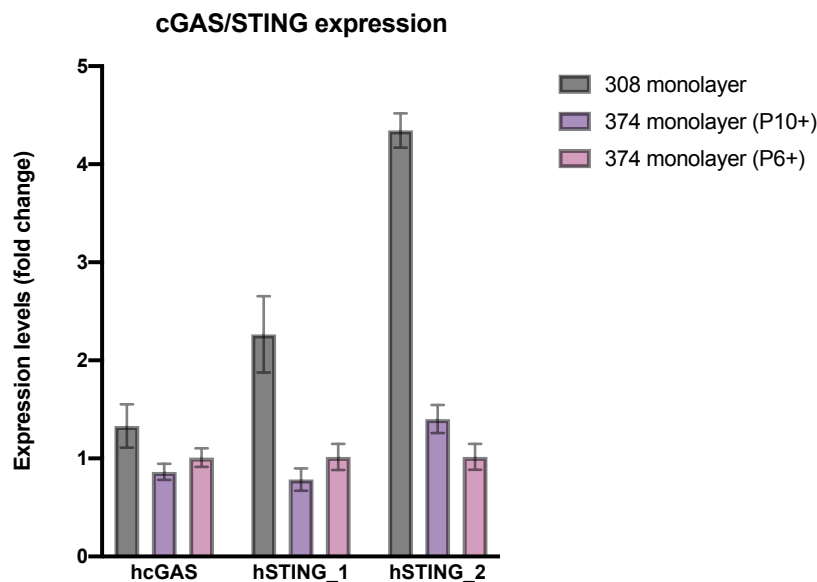


Figure 11: RT-PCR for evaluating the expression levels of human cGAS/STING in HK-374 and HK-308 glioma cell lines (adherent monolayer cells). N=3 independent repeats for all conditions. Data represented as mean +/- SEM.

Using one set of human specific primers for cGAS (hcGAS) and two different primer sets for testing STING expression (hSTING_1/2) (specific sequences can be found in **Supplementary Table 12**) expression of cGAS and STING was established in our glioma lines. To explore the potential involvement of the cGAS/STING signaling pathway further, we next performed ELDAs using select human cGAS and STING inhibitors (**Table 1**) and evaluated their effects on sphere forming capacity and stem cell frequency (**Figures 12-14**).

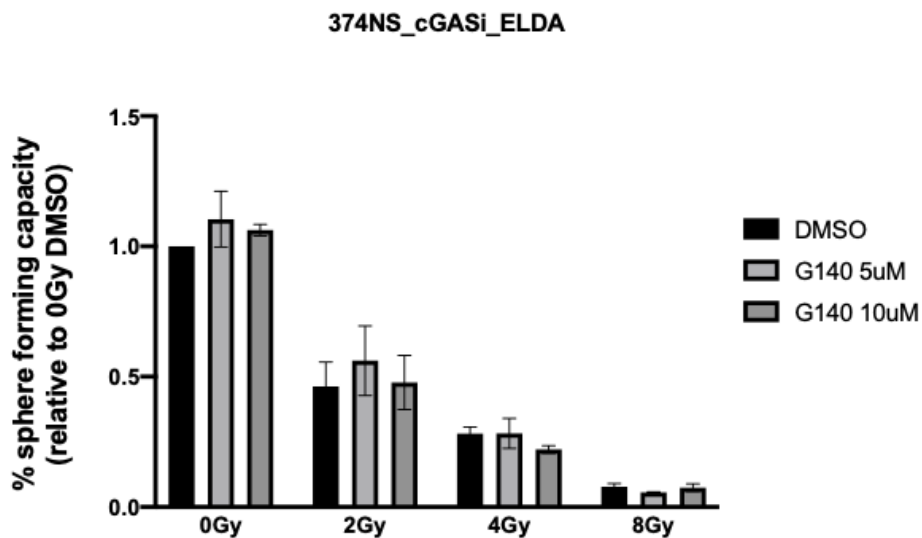


Figure 12: Sphere forming capacity for HK-374 glioma spheres treated (1x) with hcGASi (G140) as determined by ELDA. N=3, data represented as mean +/- SEM. New G140 solution used. Two-way ANOVA analysis with no statistically significant differences observed between the various conditions represented here.

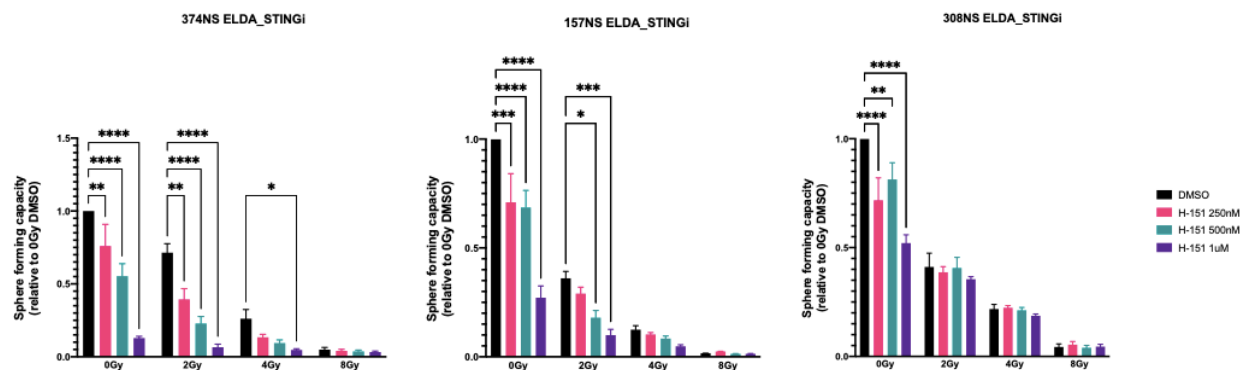


Figure 13: Sphere forming capacity for HK-374, HK-157 and HK-308 glioma spheres treated (1x) with human STINGi (H-151) as determined by ELDA. For 374: N=5 for 0/4/8 Gy, N=3 for 2 Gy. For 157 and 308 cells: N=3 biologically independent repeats for all conditions. New H-151 solution used. Data represented as mean +/- SEM. Two-way ANOVA analysis where 0.1234 (ns), 0.00332 (*), 0.0021 (**), 0.0002 (***) and <0.0001 (****).

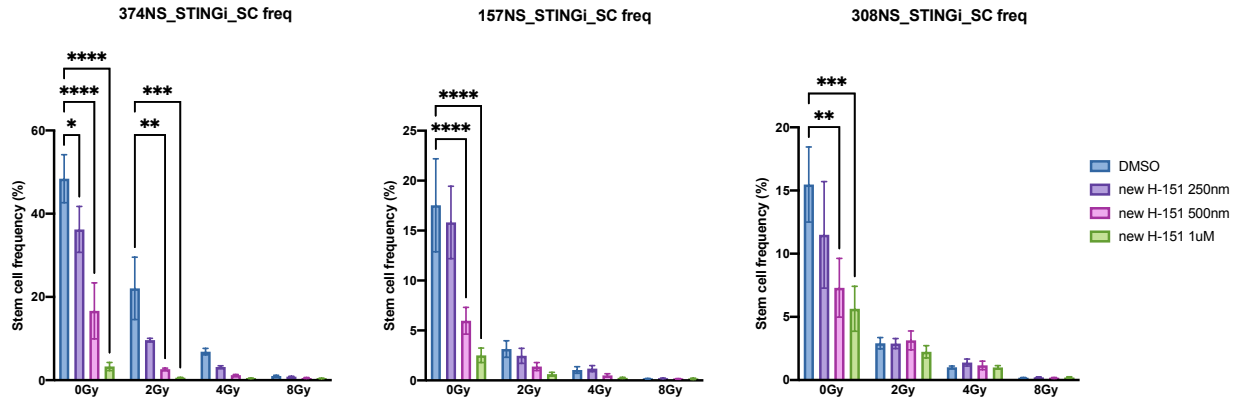


Figure 14: Stem cell frequency as determined by ELDA analysis in HK-374, HK-157 and HK-308 glioma spheres treated with (Guey et al.)STINGi (H-151) (1x). For 374: N=5 for 0/4/8 Gy, N=3 for 2 Gy, while for 157 and 308 N=3 biological independent repeats for all conditions tested. Data represented as mean +/- SEM. Two-way ANOVA analysis where 0.1234 (ns), 0.00332 (*), 0.0021 (**), 0.0002 (***) and <0.0001 (****).

cGAS inhibition did not decrease sphere formation or stem cell frequencies (**Figure 12, Supplementary Table 13**). In contrast, STINGi combined with radiation resulted in a statistically significant dose-dependent decrease in the sphere forming capacity of HK-374 and HK-157 glioma sphere cells (adjusted p-values for 2 Gy DMSO vs 2 Gy H151 (1uM) were <0.0001 and 0.0006 for HK-374 and HK-157 respectively, while for 4 Gy DMSO vs 4 Gy H151 (1uM) this value was 0.0146 for HK-374 cells; **Figures 13, 14**). For HK-308 cells, a statistically significant decrease in sphere forming capacity in a dose dependent manner was seen only in the non-irradiated samples, which was also evident for the other cell lines tested. This likely suggests that inhibition of steady state STING signaling is affecting stem cell self-renewal, proliferation and/or survival, or possibly this observation is the result of off-target effects from the inhibitor used. A complete overview of this two-way ANOVA multiple comparisons analysis can be found in **Supplementary Tables 14-16**. Analysis of the changes in stem cell frequencies of ELDA treated with the STINGi showed a statistically significant decrease in stem cell frequency at the highest STINGi concentration in combination with 2 Gy irradiation for HK-374 cells (adjusted p-value of 0.0008), while such a decrease was only evident in the absence of radiation for the other two cell lines

tested. **Supplementary Tables 17-19** contain the full set of results for this statistical analysis. These results suggest that radiation-induced cellular plasticity possibly functions through a cGAS-independent, but STING-dependent manner.

To gain further insight regarding the effects of STING inhibition at the transcriptomic level, RNA seq analysis was performed on HK-374 cells at 48h post 4 Gy irradiation. Using the integrated Differential Expression and Pathway analysis, iDEP, (Ge et al., 2018) web application, differential gene expression analysis identified 145 genes and 1853 genes upregulated by 4 Gy + STINGi (denoted as IR + STINGi) relative to irradiation (IR, 4 Gy) and unirradiated (DMSO, 0 Gy) samples respectively. 1937 genes and 2688 genes were downregulated in the combination treatment group relative to 4 Gy and 0 Gy respectively (**Table 2**).

Table 2. Differentially expressed genes (DEGs) as determined by DESeq2 analysis using FDR: 0.1 and min. fold change: 2, based on iDEP software.

| Comparison | Up | Down |
|---------------------|------|------|
| IR + STINGi vs IR | 145 | 1937 |
| IR + STINGi vs DMSO | 1853 | 2688 |
| IR vs DMSO | 641 | 75 |

Pathway analysis for differentially expressed genes identified from RNAseq (**Figure 15**) for the irradiation vs control conditions showed downregulation of G2M checkpoint and E2F targets. These are in accordance with radiation's expected effects on cell cycle and DNA replication pathways. Among pathways shown to be enriched in the irradiation group, epithelial mesenchymal transition, KRAS signaling, p53 pathway, coagulation, inflammatory response, apoptosis, TNF α signaling via NF κ B, angiogenesis, complement and hypoxia were identified. Upregulation of these pathways hinted at the diverse effects radiation has on cellular processes,

with an emphasis on inflammatory signaling responses. **Table 3** summarizes these findings in detail.

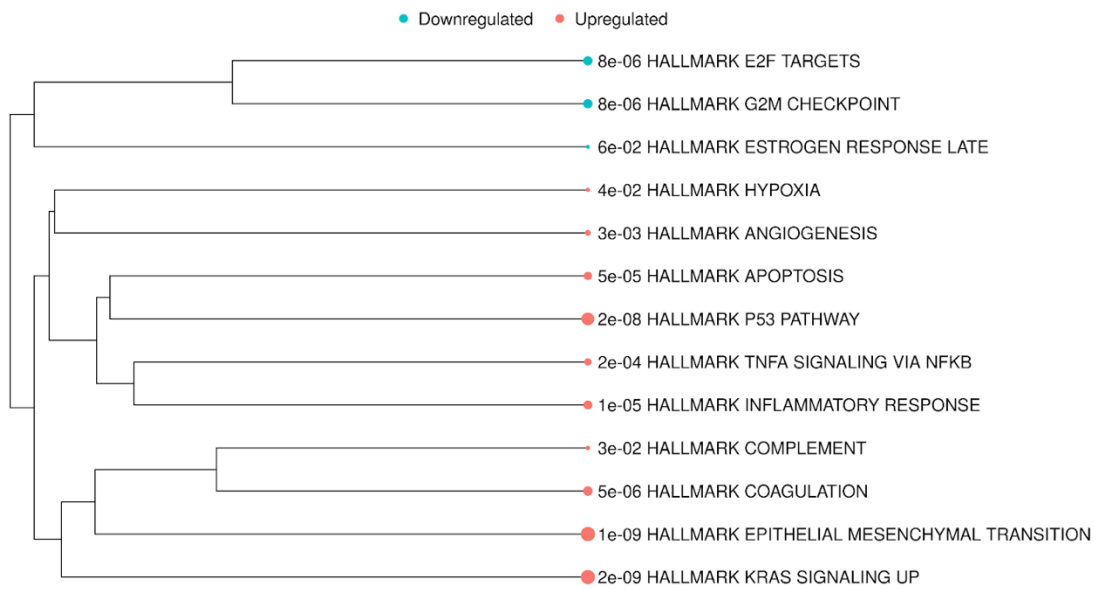


Figure 15. Pathway analysis of DEGs identified from RNAseq comparing irradiation (4 Gy) vs control (0 Gy) in HK-374 monolayer samples 48h post irradiation. Pathway database used: hallmark.MSigDB from iDEP software.

Table 3. Pathway analysis of DEGs identified from RNAseq comparing irradiation (4 Gy) vs control (0 Gy) in HK-374 monolayer samples 48h post irradiation. Pathway database used: hallmark.MSigDB from iDEP software.

| | group | FDR | nGenes | Pathway size | Fold enriched | Pathway |
|----|---------------|----------|--------|--------------|---------------|--|
| 1 | Upregulated | 1.15E-09 | 40 | 200 | 3.09 | HALLMARK EPITHELIAL MESENCHYMAL TRANSITION |
| 2 | Upregulated | 1.53E-09 | 34 | 200 | 3.39 | HALLMARK KRAS SIGNALING UP |
| 3 | Upregulated | 1.66E-08 | 36 | 200 | 2.95 | HALLMARK P53 PATHWAY |
| 4 | Upregulated | 5.39E-06 | 20 | 138 | 3.48 | HALLMARK COAGULATION |
| 5 | Upregulated | 1.4E-05 | 24 | 200 | 2.87 | HALLMARK INFLAMMATORY RESPONSE |
| 6 | Upregulated | 4.58E-05 | 25 | 161 | 2.60 | HALLMARK APOPTOSIS |
| 7 | Upregulated | 2.24E-04 | 27 | 200 | 2.27 | HALLMARK TNFA SIGNALING VIA NFKB |
| 8 | Upregulated | 3.3E-03 | 8 | 36 | 3.98 | HALLMARK ANGIOGENESIS |
| 9 | Upregulated | 2.93E-02 | 18 | 200 | 1.90 | HALLMARK COMPLEMENT |
| 10 | Upregulated | 3.9E-02 | 20 | 200 | 1.76 | HALLMARK HYPOXIA |
| 11 | Downregulated | 7.58E-06 | 9 | 200 | 7.43 | HALLMARK G2M CHECKPOINT |
| 12 | Downregulated | 7.58E-06 | 9 | 200 | 7.47 | HALLMARK E2F TARGETS |
| 13 | Downregulated | 6.44E-02 | 4 | 200 | 4.32 | HALLMARK ESTROGEN RESPONSE LATE |

Performing a similar pathway analysis for the DEGs from the IR + STINGi vs IR comparison (**Figure 16**) identified many of the same downregulated pathways as those listed above, with the addition of mitotic spindle, spermatogenesis and protein secretion. mTORC1 signaling, xenobiotic metabolism and p53 pathway were found to be upregulated in the IR + STINGi group relative to 4 Gy. **Table 4** provides details for the pathways identified under this paradigm. Ultimately, these pathway analyses point to inflammatory processes being upregulated and cell cycle/DNA repair pathways being downregulated following irradiation, with the inhibition of STING leading to similar outcomes, likely due to the more prominent role of radiation in this context.

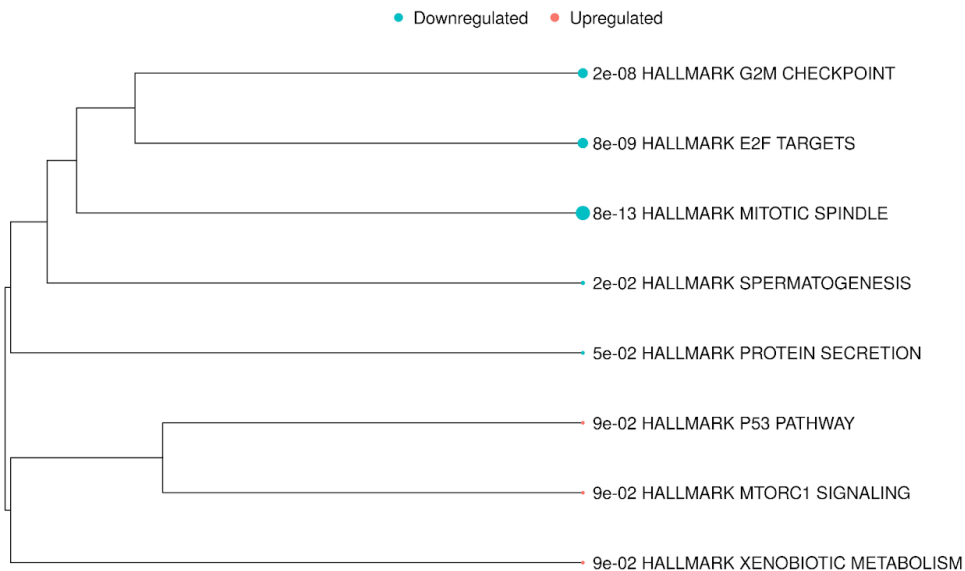


Figure 16. Pathway analysis of DEGs identified from RNAseq comparing IR + STINGi (4 Gy + 1uM H151) vs irradiation (4 Gy) in HK-374 monolayer samples 48h post irradiation. Pathway database used: hallmark.MSigDB from iDEP software.

Table 4. Pathway analysis of DEGs identified from RNAseq comparing IR + STINGi (4 Gy + 1uM H151) vs irradiation (4 Gy) in HK-374 monolayer samples 48h post irradiation. Pathway database used: hallmark.MSigDB from iDEP software.

| | group | FDR | nGenes | Pathway size | Fold enriched | Pathway |
|---|---------------|----------|--------|--------------|---------------|--------------------------------|
| 1 | Upregulated | 9.33E-02 | 7 | 200 | 2.91 | HALLMARK MTORC1 SIGNALING |
| 2 | Upregulated | 9.33E-02 | 6 | 200 | 3.27 | HALLMARK XENOBIOTIC METABOLISM |
| 3 | Upregulated | 9.33E-02 | 7 | 200 | 3.06 | HALLMARK P53 PATHWAY |
| 4 | Downregulated | 8.03E-13 | 61 | 199 | 2.70 | HALLMARK MITOTIC SPINDLE |
| 5 | Downregulated | 7.91E-09 | 55 | 200 | 2.32 | HALLMARK E2F TARGETS |
| 6 | Downregulated | 2.04E-08 | 54 | 200 | 2.27 | HALLMARK G2M CHECKPOINT |
| 7 | Downregulated | 1.78E-02 | 19 | 135 | 2.05 | HALLMARK SPERMATOGENESIS |
| 8 | Downregulated | 4.83E-02 | 20 | 96 | 1.82 | HALLMARK PROTEIN SECRETION |

Brief evaluation of the role select epigenetic factors might be playing in radiation-induced cellular plasticity

So far, our experimental explorations have provided some insight regarding potential receptors and downstream pathways engaged following irradiation that mediate cellular plasticity events,

either in terms of stem cell self-renewal capacity or *de novo* stem cell induction. Nevertheless, for cellular plasticity to occur, specific gene regulatory networks downstream of the receptors engaged need to be differentially turned on/off. Epigenetic mechanisms have been shown to play a critical role in regulating such processes (Paksa & Rajagopal, 2017). The proper epigenetic landscape and subsequent chromatin architecture need to exist for efficient cell fate transitions. Histone modifying enzymes and ATP-dependent chromatin remodeling complexes work in a coordinated fashion to this end (Tang et al., 2010).

The original papers by Cooke and colleagues showed that activation and signaling through TLR3 and RLRs led to rapid, global changes in the expression patterns of epigenetic modifiers involved in chromatin remodeling (Cooke, 2019; Cooke & Lai, 2023; Lee et al., 2012; Shu Meng et al., 2016; S. Meng et al., 2017; Sayed et al., 2017). These included 1) acquisition of open chromatin states at the promoter regions of Oct4 and Sox2, as evidenced by the gain/loss of permissive/restrictive histone marks respectively at these sites and 2) expression changes in histone modifying enzymes. While such changes were shown to enhance reprogramming, one of the main questions left unanswered was specifically how chromatin remodeling was achieved.

The SWItch/Sucrose Non-Fermentable (SWI/SNF) chromatin remodeling complex, one class of ATP-dependent chromatin remodeling complexes (Tang et al., 2010), has been implicated in cancer development (Roberts & Orkin, 2004), somatic cell reprogramming and stem cell maintenance (Ganguly et al., 2018; L. He et al., 2012; Hiramatsu et al., 2017). As such, components of this complex were evaluated by exploring available RNA sequencing datasets of HK-374 monolayer cells, 48h post 4 Gy irradiation.

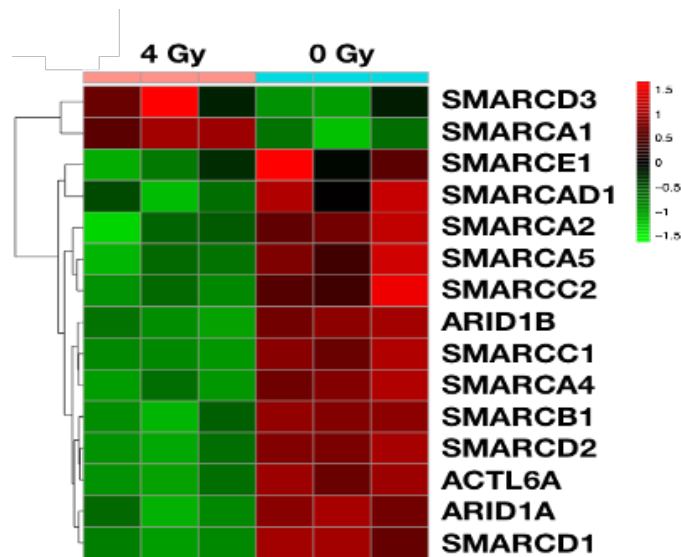


Figure 17: Heatmap representation of differentially expressed genes corresponding to chromatin remodeling complex components (log₂ fold changes) as determined from RNAseq analysis in HK-374 monolayer cells 48h post 4 Gy irradiation (QTP dataset). SMARCA1 and SMARCD3 upregulation following irradiation seen here was used as rationale for further investigating expression of these chromatin remodeling complex components in HK-374 cells.

Radiation causes changes in the expression of specific components of the SWI/SNF chromatin remodeling complexes, histones and their posttranslational modifications. More specifically, from the representative heatmap showing log₂ fold changes of differentially expressed chromatin remodeling complex components, SWI/SNF Related, Matrix Associated, Actin Dependent Regulator Of Chromatin, Subfamily A, Member 1 (SMARCA1) and SWI/SNF Related, Matrix Associated, Actin Dependent Regulator Of Chromatin, Subfamily D, Member 3 (SMARCD3) were upregulated following irradiation (**Figure 17**). To further investigate the role of these two chromatin remodeling complex subunits, RT-PCR experiments were performed on cells treated with TLR3/4i or CQ (**Figure 18**). Specific primer sequences used can be found in **Supplementary Table 20**. Sorted ZsGreen-negative cells (i.e. non-stem cells) were used and relative gene expression changes were evaluated 48h post irradiation to specifically address how the interventions employed affect the radiation-induced stem cell population at this critical time point previously

shown to be associated with epigenetic remodeling, de-differentiation and multipotency through re-expression of Yamanaka transcription factors (K. Bhat, Saki, et al., 2020; Lagadec et al., 2012).

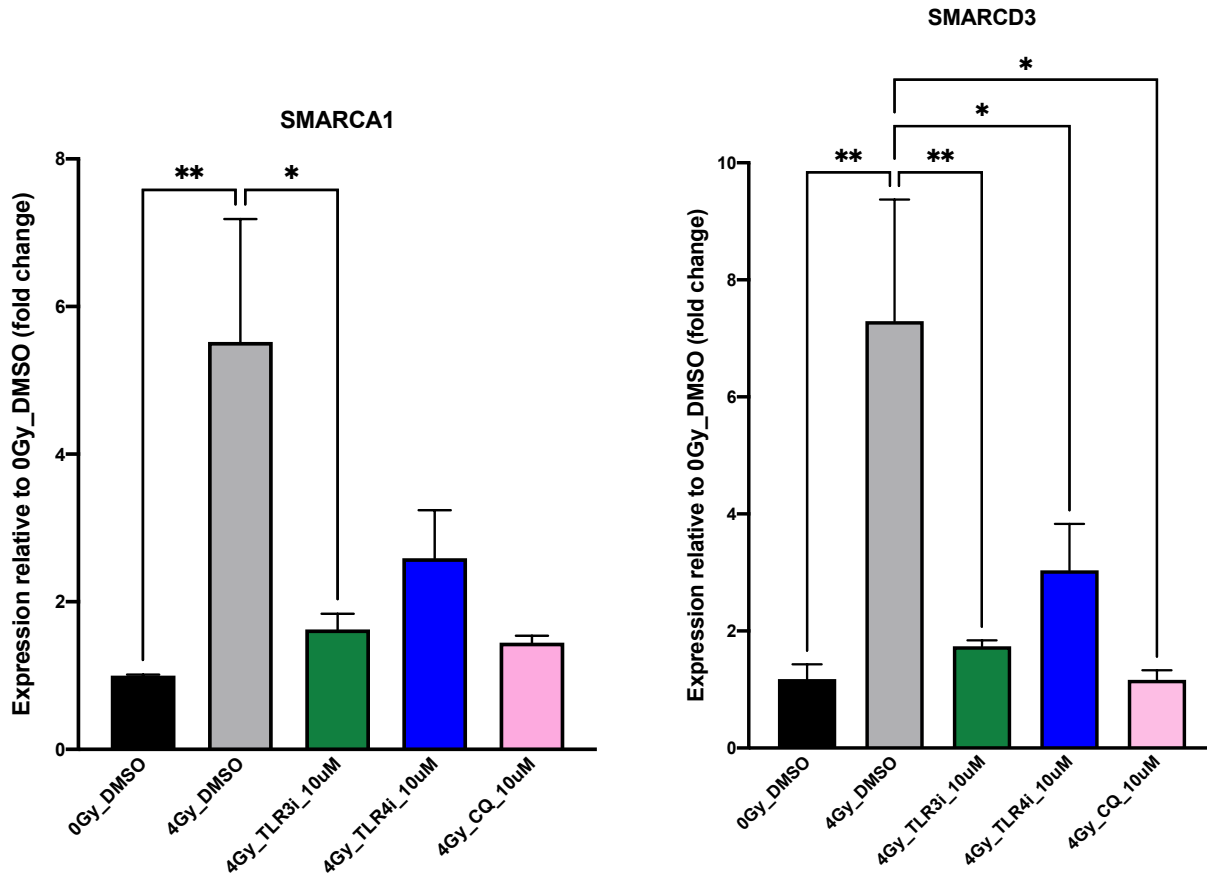


Figure 18: RT-PCR analysis showing the relative expression of chromatin remodeling complex components, SMARCA1 and SMARCD3, in HK-374 monolayers (ZsGreen negative sorted cells) irradiated with 4 Gy and treated with TLR3, TLR4 inhibitors and CQ. RT-PCR analysis performed 48h post irradiation. N>3 biologically independent repeats for all conditions. Data represented as mean +/- SEM. One-way ANOVA analysis was performed where 0.1234 (ns), 0.00332 (*), 0.0021 (**), 0.0002 (***) and <0.0001 (****).

Relative to unirradiated controls (0 Gy DMSO), both SMARCA1 and SMARCD3 showed a statistically significant upregulation following irradiation (adjusted p-values of 0.0091 and 0.0036 for SMARCA1 and SMARCD3 respectively), and combination treatment of radiation with TLR3/4i or CQ did not lead to a statistically significant change for either factor. However, when compared to the irradiation control (4 Gy DMSO), there was a statistically significant decrease in the relative

expression of SMARCA1 and SMARCD3 under the 4 Gy TLR3i (10uM) condition (adjusted p-values of 0.0184 and 0.0049 for SMARCA1 and SMARCD3 respectively). Such a decrease was also evident for the 4 Gy TLR4i (10uM) and 4 Gy CQ (10uM) conditions in the case of SMARCD3 (adjusted p-values of 0.0262 and 0.0228 respectively). Tables showing the complete one-way ANOVA analysis results for this RT-PCR can be found in **Supplementary Tables 21, 22**.

Downregulation of SMARCA1 and SMARCD3 following combination of radiation with TLR3/4i or CQ suggested that downstream signaling from TLR3/4 and possibly other receptors affected by CQ, could be altering epigenetic modifiers and subsequently affecting chromatin remodeling processes, steps essential for efficient reprogramming to occur. Similar experiments carried out with TLR9i did not show statistically significant changes in the expression levels of either SMARCA1 or SMARCD3 when comparing irradiated (4 Gy HycloneWater) and unirradiated (0Gy HycloneWater) control samples. Only 4 Gy TLR9i (5uM) led to a significant upregulation of SMARCD3 relative to the unirradiated control (adjusted p-value of 0.0048). This effect however was lost at the highest inhibitor concentration tested (**Figure 19**). For a complete list of the one-way ANOVA analysis results, information can be found in **Supplementary Tables 23, 24**.

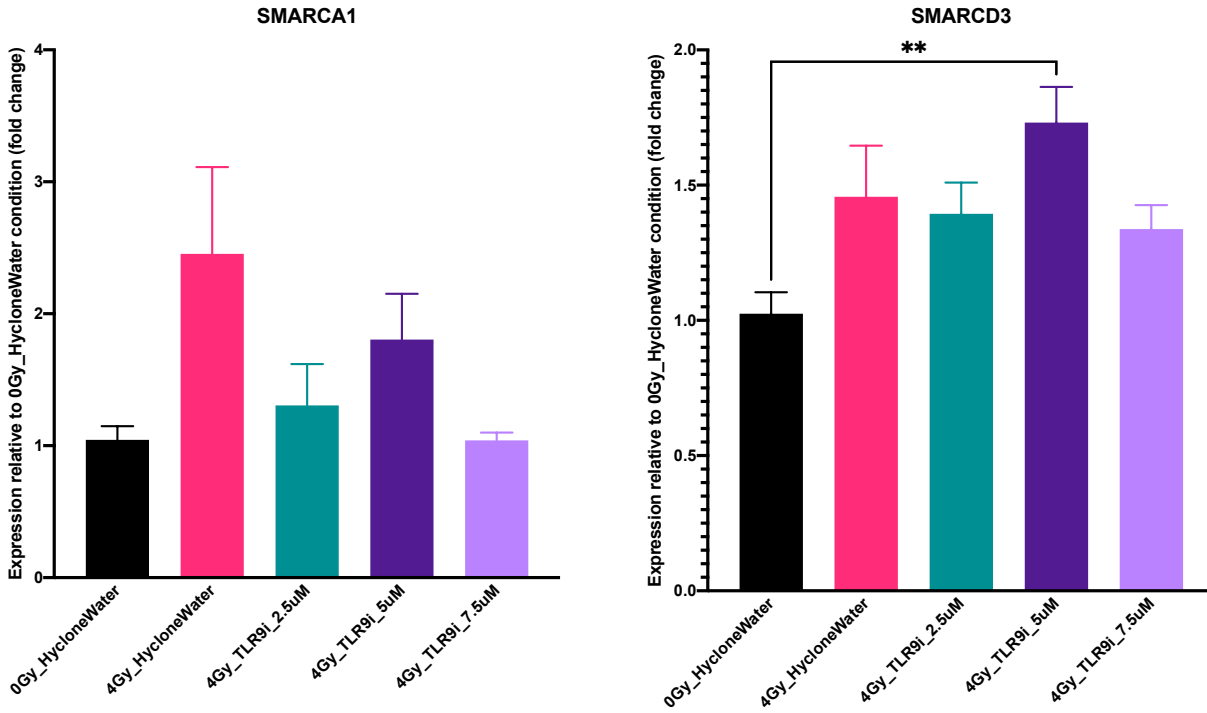


Figure 19: RT-PCR analysis showing the relative expression of chromatin remodeling complex components, SMARCA1 and SMARCD3, in HK-374 monolayers (ZsGreen negative sorted cells) irradiated with 4 Gy and treated with TLR9 inhibitor. N=3 biological repeats for all conditions. Data represented as mean +/- SEM. One-way ANOVA analysis was done where 0.1234 (ns), 0.00332 (*), 0.0021 (**), 0.0002 (***) and <0.0001 (****).

2.3 DISCUSSION

Cellular plasticity, an umbrella term encompassing reprogramming and radiation-induced phenotypic conversion events, allows cells to effectively respond to triggers that would otherwise compromise their functional and genomic integrity. In recent years, it has become increasingly clear that there exists a tight link between innate immunity, and specifically receptors of this cellular response machinery, and reprogramming, or else the ability of cells to switch from one state to another (Chanda et al., 2019; Cooke, 2019; Cooke & Lai, 2023; Lee et al., 2012; Shu Meng et al., 2016; S. Meng et al., 2017; Sayed et al., 2017; Sayed et al., 2015; Zhou et al., 2016). Specifically, studies by Cooke and colleagues have demonstrated the important role select TLRs and RLRs play in enabling and further facilitating the reprogramming of somatic cells into induced pluripotent stem cells (iPSCs). In the context of cancer, phenotypic plasticity, or else the ability of cells to evade or escape terminal differentiation through dedifferentiation, transdifferentiation or blocked differentiation, has been recently added into the Hallmarks of Cancer (Hanahan, 2022). This is a conceptual toolkit of common characteristics and functional capabilities normal cells acquire as they progress into malignancy. Probing at the underlying molecular drivers facilitating the acquisition of hallmark traits has also identified non-mutational epigenetic reprogramming as an important enabling characteristic in this process. As such, the combination of these findings highlights the significance of studying cellular plasticity.

For the purposes of this dissertation project, we were interested in exploring receptors governing the generation of cancer stem cells from non-stem cancer cells following irradiation. As a proxy for understanding how this phenotypic conversion is achieved, cancer cell stemness was studied in the context of stem cell maintenance/self-renewal (SFAs, ELDA) and *de novo* stem cell induction (cancer stem cell induction assays: reprogramming assays). Several TLR receptors as well as components of the free cytosolic DNA sensing machinery, the cGAS/STING pathway,

were evaluated for their potential involvement. Our main study findings were as follows: 1) stem cell maintenance following irradiation is mediated through cGAS-independent STING signaling, with potential crosstalk with TLR4 and TLR9, 2) *de novo* stem cell induction following irradiation implicates TLR3 signaling and potentially other receptors (e.g. cGAS/STING, RIG-1, endosomal TLRs) and processes (e.g. autophagy, IL6 production downstream of TLR9) affected by chloroquine.

i) RNAseq datasets: identification of DAMPs/PRRs upregulated following irradiation

From the analysis of available GBM RNAseq datasets (**Figure 1**), several DAMPs and PRRs were found to be differentially expressed following irradiation. Of the IR upregulated DAMP/PRR related genes, TLR4 was pursued further given previous research implicating TLR signaling in reprogramming (Cooke, 2019; Lee et al., 2012; Shu Meng et al., 2016; S. Meng et al., 2017). Evaluating the role of other components identified in this analysis would be of use in future experiments, particularly with regards to identifying the potential DAMP(s) responsible for radiation-induced cellular plasticity events. Of note, while from this exploration HMGB1, a common DAMP released following irradiation (Baatout Sarah, 2023), was shown to be slightly downregulated compared to unirradiated controls, this could be explained by the conditions used for this specific RNAseq experiment such as the time point (48h), irradiation dose (4 Gy - might not have been sufficient to induce detectable upregulation) and/or the cells used. This RNAseq analysis functioned more as a roadmap to help us identify candidate targets of interest, rather than a definitive representation of the exact, concrete processes relating to plasticity events occurring within the cells following irradiation. Thereafter, this heatmap was generated using a curated list of DAMPs/PRRs (Roh & Sohn, 2018) which was not necessarily exhaustive. Thus, it is possible that DAMPs/PRRs beyond those shown here are actually involved in radiation-induced phenotypic conversion. Additionally, RNAseq is limited to gene expression changes. As such, DAMPs (mainly nucleic acids) such as those recognized by cGAS/STING and endocytic TLRs:

TLR3/7/8/9 and RLRs (Gong et al., 2020) might have been missed since it was not possible to check for them in the differentially expressed genes list. It is also possible that receptors already present in the cells, and not upregulated at the mRNA level, could very much be at play here, as was seen from research by Jesenko and colleagues (Jesenko et al., 2020).

The present RT-PCR validation experiment (**Figure 2**) was able to only partially recapitulate the heatmap findings for some of the top IR upregulated genes identified. This discrepancy could be attributed to the cell populations used in RNAseq vs RT-PCR experiments. On the one hand, RNAseq was done using cells from a sorted population containing only cells with stem cell like characteristics. On the other hand, RT-PCR experiments were performed on bulk, unsorted cell populations for which the stem cell-like population accounts for only a small proportion. As such, potential effects of interest might have been masked. Nevertheless, bulk populations were chosen in this latter approach to more closely recapitulate which DAMPs/PRRs are related to radiation rather than being the result of potential mechanical stress from sorting. Future experiments could try matching experimental conditions across different techniques to more accurately validate and support findings.

ii) **TLR4 & TLR9 involvement in stem cell maintenance/self-renewal**

From the SFAs and ELDA's performed using select TLR inhibitors (**Figures 3, 5, 6, Supplementary Figure 2**) it was determined that stem cell maintenance and self-renewal following exposure to radiation, likely involve TLR4 and TLR9 signaling. TLR4 has the potential to signal through both MyD88-dependent and -independent (TRIF/TIRAP) means, while TLR9 engages MyD88 adaptor protein for its downstream signaling (Kashani et al., 2021). TLR3 inhibitor was shown to have no effect on sphere forming capacity as determined in our experiments. This receptor functions solely through a MyD88-independent manner (Kashani et al., 2021). The combination of these results suggests that a MyD88-dependent signaling cascade

downstream of TLRs is likely implicated in radiation-induced stem cell maintenance. Thereafter, seeing how both TLR4i and TLR9i were able to affect stem cell self-renewal, but only one of them reduced the frequency of these cells (**Figure 7, Supplementary Figures 3, 4**) highlights that signaling through these receptors could possibly be affecting cells in different ways following irradiation. Additional repeats for each of these assays would be required to verify this.

At a first glance, our results from SFAs and ELDA's showing a decrease in sphere forming capacity following TLR4i treatment appear to be in contrast with literature suggesting glioma stem cells downregulate this receptor to maintain their self-renewal capabilities. Specifically, research by Alvarado et al. showed that signaling through the TLR4-TBK1 axis (MyD88-independent) leads to the inhibition of retinoblastoma binding protein 5 (RBBP5). This transcription factor was elevated in glioma stem cells, and was shown to be necessary and sufficient for their maintenance, as evidenced by the effects shRNA against RBBP5 had in decreasing Sox2, Nanog and Oct4 expression at both the mRNA and protein levels (Alvarado et al., 2017). Mechanistically, downregulation of TLR4 in this context removes the inhibitory effect of TBK1 on RBBP5. This in turn allows for the expression of pluripotency genes and subsequent stem cell maintenance. The discrepancy with our data could be explained by: i) cell line heterogeneity (different lines used in our experiments vs the study and bulk vs sorted populations studied respectively) and/or ii) the TLR4 inhibitor used having broader effects beyond simply interfering with TLR4 leading to SFA/ELDA results reflecting off target effects. To address these possibilities further we could: i) perform similar experiments as those described by Alvarado et al. to determine the relative expression of TLR4 in our cell lines, ii) repeat SFAs/ELDA's using additional inhibitors, iii) knock down TLR4 by means of siRNA and repeat the assays in question and iv) supplement our SFAs/ELDA's with secondary and tertiary versions of these assays as a confirmation that the spheres formed under the different treatment paradigms are indeed the result of stem cells vs cell aggregates, to further support or refute our findings. At any rate, while understanding the

implications of TLR4 and its downstream signaling would be important, there is some consensus in that both our data and that provided by Alvarado and colleagues point to a MyD88-dependent pathway likely being involved, at least in part, in stem cell maintenance and self-renewal.

iii) Chloroquine treatment implications for stemness maintenance

In the case of chloroquine treatment (**Figure 4**), we observed a statistically significant, dose-dependent decrease in sphere forming capacity at steady state (i.e. in the absence of radiation). A similar trend was also seen at 4 Gy, in line with TLR9i data (**Figures 5, 6**). Chloroquine has been shown to inhibit endosomal TLRs and MyD88 signaling by decreasing interleukin 1 receptor associated kinase 4 (IRAK4) and interferon regulatory factor 7 (IRF7) molecules, and inhibiting interferon α (IFN α) synthesis (Al-Bari, 2017). The proposed mechanism of action for inhibition of endosomal TLRs involves i) raising endosomal pH which in turn compromises TLRs' ability to interact with their respective ligands (acidic conditions required) and ii) directly binding to nucleic acids, changing their conformation and thus preventing their recognition by TLRs. Specifically for TLR9, CQ has been shown to inhibit CpG mediated TLR9 activation and downstream production of tumor necrosis factor α (TNF α) and interleukin 6 (IL6) (Gies et al., 2020). Studies evaluating the role of specific histone demethylases in the promotion of somatic cell reprogramming of human fibroblasts to iPSCs have highlighted the important role of IL6 in enhancing reprogramming (Q. Jiang et al., 2020). Beyond endosomal TLRs, CQ can also interfere with other receptors, specifically the cGAS/STING and RIG-1/MAVS signaling pathways which play important roles in the recognition of cytosolic DNA and RNA respectively. In the case of cGAS/STING, CQ blocks dsDNA binding to cGAS thus preventing cGAMP mediated STING activation. For RIG-1/MAVS, while the exact mechanism of action is not known, it is suggested that CQ may be inhibiting type I interferon induction downstream of RIG-1 signaling. Additionally, being a weak base, CQ can accumulate in lysosomes and inhibit their function. This ultimately leads to lysosomal membrane destabilization, release of lysosomal enzymes in the intracellular

space and inability of lysosome-autophagosome fusion, impairing thus the autophagic machinery. Autophagy is an important cellular mechanism allowing for the sequestration and subsequent degradation of cytoplasmic components (Gies et al., 2020), and this process has also been implicated in reprogramming (S. Wang et al., 2013). Use of chloroquine in the present assays gave us insight about receptors, pathways and overall cellular processes that might be at play in the radiation-induced phenotypic conversion response.

Given the general consensus regarding CQ's ability to interfere with endosomal TLRs and their signaling, there are two potential discrepancies that arise here: 1) CQ showing a trend towards decreasing stem cell self-renewal capacity while TLR3 inhibition has no effect, and 2) lack of a statistically significant decrease following irradiation in the CQ data as compared to our TLR9i findings. In the case of (1) this could be explained by the fact that the TLR3 inhibitor used was more specific whereas CQ had much broader effects beyond potentially interfering with TLR3, an endosomal TLR. For (2), this could be attributed to: i) the essential role TLR9 plays in glioma stem cell maintenance (Herrmann et al., 2014), ii) chloroquine having broader effects which in turn might be affecting optimal receptor/process levels required for seeing a statistically significant effect. In a way, suboptimal receptor/process interference by CQ might be compensating for the TLR9 inhibition effects. Optimal levels of signaling components was previously established as a requirement for efficient reprogramming (Cooke & Lai, 2023), and/or iii) the presence of receptors specifically engaged upon irradiation, but not affected by CQ, similarly masking the effect of CQ-mediated TLR9 inhibition in **Figure 4**. Rodent studies have shown that the effects of CQ administration and TLR9 inhibition on survival, renal injury and cytokine production match, suggesting CQ administration effects are largely mediated through inhibition of TLR9. While these studies were addressing a very different question and were carried out in mice, the possibility that CQ administration was not affecting TLR9 in our experiments is rather unlikely.

iv) TLR3 & CQ-affected receptors/processes mediate cancer stem-cell induction following irradiation

Having evaluated the role of select TLRs in stem cell maintenance, their potential involvement in cellular reprogramming was also studied (**Figure 9**). Unlike stemness maintenance post irradiation which implicated TLR4/TLR9 (MyD88-dependent signaling) receptors, the induction of stemness following irradiation was found to function through a TLR3 (MyD88-independent) pathway instead, and/or other processes and receptors affected by chloroquine. CQ is broadly used to inhibit endosomal TLRs (Yasuda et al., 2008), which may or may not use MyD88 as their adaptor molecule. Because treatment of cells with CQ inhibited radiation-induced reprogramming more effectively than did our specific TLR3 inhibitor, this raises the possibility that other endosomal TLRs beyond TLR3, and/or other non-TLR receptors affected by CQ administration, might be implicated in this process. This later notion further supports our previous findings regarding the important role of TLR9 in radiation-induced cellular plasticity. To this end, reprogramming experiments using TLR9i would be beneficial in delineating our CQ findings. It is of interest to note that autophagy, TLR3/RIG-1 signaling as well as IL6 production downstream of TLR9, all of which are inhibited by CQ (Gies et al., 2020), have been previously identified as crucial components required for efficient reprogramming (Cooke, 2019; Cooke & Lai, 2023; Q. Jiang et al., 2020; Lee et al., 2012; Shu Meng et al., 2016; S. Meng et al., 2017; Sayed et al., 2017). Hence, while it is possible for radiation-induced reprogramming to be functioning through a single/distinct receptor, the CQ data would suggest that multiple receptors, pathways and/or processes are potentially involved/engaged. Some of these might be common with ones previously highlighted.

Of note, the fact that radiation effects as evaluated by means of SFAs/ELDAs and reprogramming assays do not necessarily diverge on the same receptors (TLR4/TLR9 vs TLR3) is not surprising. The two assays are by nature looking at two distinct processes. On the one hand SFAs/ELDAs

look at the formation of new stem cells from already existing stem cell enriched populations, while reprogramming assays start off with a non-stem cell population and look at newly generated stem like cells. Both of these however fall under the umbrella of cellular plasticity.

v) YF expression levels are affected by radiation and TLR3/TLR4 receptor inhibition

Previous research in the lab has shown that radiation-induced phenotypic conversion is associated with re-expression of YFs and acquisition of an open chromatin state at their respective promoter regions 48h post 4 Gy (K. Bhat, Saki, et al., 2020; Lagadec et al., 2012) As such, we were interested in seeing whether interference with some of the receptors we have identified so far as potential candidates could recapitulate these findings. To this end, we would expect inhibition of receptors crucial for radiation-driven cellular plasticity to result in decreased YF expression levels. While from our present experiments this was only partially supported (**Figure 10**), seeing that there was a trend for decreased expression in the case of Klf4, c-Myc, and to a lesser extent for Oct4 and Sox2, with Nanog expression showing a significant decrease, we can infer that TLR3 and TLR4 could be playing some role in radiation-induced phenotype conversion. These experiments were carried out using sorted ZsGreen negative cells (i.e. non-cancer stem cells) to determine the effects of radiation in combination with receptor inhibition on radiation-induced glioma stem cells. Following this treatment scheme however we once more end up with a bulk population composed of non-glioma stem cells and radiation-induced glioma stem cells. This latter population still makes up a smaller proportion of the bulk, potentially masking a significant decrease in YF expression levels. Additionally, since decreased expression was not significant across all factors, this also raises the possibility that TLR3 and TLR4 are not the sole mediators of radiation-induced cellular plasticity events. Instead, similarly to what we have seen from previous data, multiple receptors might be involved here, with receptor crosstalk playing an important, facilitating role. Moving forward, it would be of value to include similar experiments with some of the other receptors we have identified since that would provide additional validation for

the proposed multi-receptor engagement. Such a scenario would not be surprising since several distinct molecules functioning as DAMPs can be released following irradiation. Each of these can then engage either a single, unique receptor or a combination of different receptors (Gong et al., 2020), and in doing so activate important downstream signaling cascades.

vi) cGAS-independent STING involvement in radiation-induced cellular plasticity

Some common examples of IR-induced DAMPs include: 1) fragments of dsDNA in the cytosol of irradiated cells, 2) micronuclei and 3) nucleotides (Baatout Sarah, 2023). As such, the engagement of cGAS/STING, a pathway readily involved in the detection of free cytosolic DNA (Hopfner & Hornung, 2020), was evaluated for its potential role in radiation-induced plasticity events. Using select human cGAS and STING inhibitors, data generated from ELDA (Figures 12, 13) suggested that radiation-induced cellular plasticity functions through a cGAS-independent, STING-dependent manner. While cGAS/STING signaling is typically studied in its canonical form, whereby recognition of dsDNA by cGAS leads to the catalytic formation of secondary messenger cGAMP which in turn binds to and activates STING to further promote downstream signaling cascades (Kumar et al., 2023), there is evidence pointing to the existence of non-canonical STING activation achieved in a cGAS-independent manner (Dunphy et al., 2018; Holm et al., 2016; Vashi & Bakhoun, 2021). Our present findings would be in accordance with this latter case and highlight a novel possibility for cellular plasticity events following irradiation. Given the magnitude of effects seen following STING inhibition in ELDA performed, inclusion of reprogramming assays using cGAS/STING inhibitors would be of great value.

Pathway analysis performed on DEGs from irradiated and combination treated samples (IR + STINGi), showed many of the same pathways being upregulated and downregulated, regardless of STING inhibition (Figures 15, 16). This likely supports the notion of radiation having a more prominent role in this case and as a result potentially masking STING inhibition effects. Generally,

pathways relating to cell cycle and DNA repair were found to be downregulated, while inflammatory response pathways were enriched, data in accordance with radiation's effects. Beyond radiation having a more dominant effect here, other factors could have contributed to the absence of unique pathways following STING inhibition. For instance, it is possible that genes not differentially expressed, and thus not included in this pathway analysis, might still be having important functions in IR-induced plasticity events for which we propose STING involvement. Thus, absence of distinct pathways seen here could be justified by the nature of the analysis. Additionally, the use of a bulk cell population rather than a sorted ZsGreen negative one could also be a limitation. Given that the radiation-induced glioma stem cell population accounts for only a small proportion of the bulk cells, potential inhibitor effects could have been masked. Moving forward, it would be beneficial to evaluate the effects of STING inhibition at the transcriptomic level using either sorted or post treatment and radiation re-sorted populations instead. In doing so, it would be easier to make inferences regarding the differentially affected genes and subsequently pathways involved in the radiation-induced phenotype conversion response.

vii) Receptor crosstalk considerations in radiation-induced phenotype conversion

So far our data has implicated TLR4, TLR9 and STING signaling in aspects of the radiation-induced cellular plasticity response. Looking at the different cell lines used for our experimental approaches, TLR4 and TLR9 inhibition data were consistent across both classical (HK-374) and mesenchymal (HK-308/345) cell lines tested. STINGi data seemed to work in classical (HK-374) and proneural (HK-157) lines, and to a lesser extent in the mesenchymal (HK-308) line. The differential response seen could be explained by i) a need for additional repeats from each line to determine if effect size of TLR4/TLR9/STING inhibition is cell line classification independent and/or ii) having to include additional lines from each subtype to determine if there is indeed a preferential signaling pathway being engaged following irradiation, dependent on cell line classification. Irrespective of subtype however, inhibitors for TLR4, TLR9 and STING were all

shown to effectively decrease sphere forming capacity as evidenced by the SFAs/ELDAs performed. This could suggest that radiation-induced effects are governed by receptor crosstalk rather than being mediated by a single, unique receptor and/or pathway. Given the variety of DAMPs and their respective sensors, it comes as no surprise that receptor crosstalk exists. Under cellular stress/insult conditions, this feature allows cells to mount orchestrated inflammatory responses. For instance, recognition of the same DAMP by multiple receptors (either in parallel or in a successive manner) enables synergistic downstream action characterized by the activation of multiple signaling pathways. In turn, diverse responses can be mounted to address the cellular challenge more effectively. Synergistic response can also arise from interaction between the downstream signaling cascades activated by distinct DAMPs. More specifically, activation of DAMP-sensing receptors can lead to the production of proinflammatory molecules. These in turn can further stimulate DAMP release and receptor expression, allowing thus for a more amplified response (Gong et al., 2020). Radiation being a genotoxic stressor, can very much be having many of the same functional implications on the cells' danger/insult sensing machinery. Therefore, as a next step it would be important to look at the downstream signaling cascades engaged during radiation-induced cellular plasticity events to better understand how these processes come about. Exploration of NF κ B and interferon (IRF3/IRF7) pathways would be essential. Signaling through the receptors identified here activates many of the same downstream signaling cascades, meaning there is some inherent convergence expected. Consequently, it would come as no surprise if both signaling pathways are found to play a role, granted at varying degrees.

viii) Chromatin remodeling in radiation-induced cellular plasticity

While identifying which receptors are initially responding to radiation is important for understanding what downstream signaling pathways are being engaged, ultimately, cellular plasticity is readily dependent upon epigenetic changes. The appropriate, permissive epigenetic environment has to first be established in order for phenotypic conversion of non-stem cells to

stem-like cells to occur. By principle, segments of DNA are tightly wrapped around a core histone octamer to form the nucleosome, the fundamental subunit of chromatin (Roberts & Orkin, 2004). At any given moment, genes might have to be activated or repressed. This comes about through a highly coordinated process characterized by chromatin remodeling through the action of histone modifying enzymes as well as ATP-dependent chromatin remodeling complexes. While histone-modifying enzymes recognize and mark histone tails with different residues, ATP-dependent chromatin remodeling complexes recognize these marks and by hydrolyzing ATP, unwrap, mobilize, exchange or displace nucleosomes, facilitating thus the recruitment of the required transcriptional machinery to the particular DNA segment of interest (Tang et al., 2010). SWItch/Sucrose Non-Fermentable (SWI/SNF) is one such class of ATP-dependent chromatin remodeling complexes. There is evidence in the literature pointing to the important role components of this complex have in cancer development (Roberts & Orkin, 2004) as well as somatic cell reprogramming and stem cell maintenance (Ganguly et al., 2018; L. He et al., 2012; Hiramatsu et al., 2017). Therefore, in an attempt to address what potential epigenetic machinery might be driving cellular plasticity events downstream of the receptors identified earlier, we briefly explored the involvement of select components of the SWI/SNF chromatin remodeling complex shown to be upregulated by radiation (**Figure 17**).

In combination with our earlier findings from receptor inhibition assays, the downregulation of SMARCA1 and SMARCD3 following combination of radiation with TLR3/4i and CQ (**Figure 18**), would suggest that signaling downstream of TLR3/4, and possibly other receptors affected by CQ, leads to cellular plasticity events and that these are potentially mediated through the action of SMARCA1 and SMARCD3. More specifically, the fact that combined treatment of radiation with the three inhibitors (TLR3/4i and CQ) showed no differences in SMARCA1 and SMARCD3 expression levels relative to unirradiated controls, and either a trend or an actual statistically significant decrease when compared to irradiated controls, points to radiation acting through the

inhibited receptors to induce epigenetic reprogramming (involving SMARCA1, SMARCD3) downstream. At the same time, the uniform effects on SMARCA1 and SMARCD3 expression levels seen across inhibitors tested could further substantiate our earlier findings regarding the somewhat distinct receptors involved in self-renewal vs *de novo* stem cell induction, tying everything together. This RT-PCR data provides a more holistic view of the different receptors being engaged to bring about radiation-induced cellular plasticity events. The lack of statistical significance for some of the 4 Gy DMSO vs 4 Gy + inhibitor conditions seen in the case of SMARCA1 could potentially be restored (i.e. reach statistical significance beyond just seeing a trend towards decreased relative expression) by inclusion of additional repeats.

Thereafter, while our previous SFAs/ELDAs had pointed to TLR9 involvement in radiation-induced cellular plasticity events, SMARCA1 and SMARCD3 expression levels were not downregulated in cells treated with radiation and TLR9i (**Figure 19**). If anything, we actually observed a statistically significant upregulation at the 5uM concentration tested in the case of SMARCD3. Assuming i) the observed effects would remain following the addition of experimental repeats to detect the expected upregulation in the irradiation control group (expected based on our RNAseq findings, **Figure 17**), and that ii) TLR9 is indeed involved in radiation-induced cellular plasticity events, the lack of SMARCA1 downregulation could suggest that other epigenetic machinery, not SMARCA1, is acting downstream of TLR9. Under the same premise, SMARCD3 upregulation seen after 4 Gy TLR9i (5uM) could suggest epigenetic remodeling downstream of TLR9 functioning through SMARCD3-independent means. Alternatively, the observed upregulation could be a consequence of TLR9's role in glioma stem cell maintenance (Herrmann et al., 2014). More specifically, if TLR9 has a critical role in stem cell maintenance and its function is indispensable for cellular plasticity, inhibition of this pathway would render cells vulnerable. To overcome such effects, cells might in turn upregulate components of the epigenetic remodeling machinery, in this case SMARCD3, to re-establish their plasticity and stem cell-like

characteristics. Regardless, for either interpretation, the resultant upregulation could be simply reflecting compensatory action of functional TLR3, TLR4 and/or other receptors affected by CQ, all of which were previously shown to mediate radiation-induced cellular plasticity events, and be associated with SMARCD3 (**Figure 18**). Finally, lack of SMARCD3 upregulation following combination treatment of radiation and TLR3/4i could be the result of unaffected, functional TLR9 signaling being present. This would support radiation-induced epigenetic remodeling downstream of TLR3 and TLR4 being SMARCD3-dependent vs -independent in the case of TLR9. Nevertheless, given that increased SMARCD3 expression was only seen at the middle TLR9i dose tested, it would be necessary to include additional repeats to further strengthen this potential finding.

Combinations of the 15 known mammalian subunits of the SWI/SNF family of chromatin remodelers allows for considerable compositional diversity in these complexes (Kadoch & Crabtree). Taking this into consideration, looking at individual subunits is likely not going to reflect all radiation-induced epigenetic changes. Therefore, while only SMARCA1 and SMARCD3 were evaluated here, it is possible that other SWI/SNF chromatin remodeling complex components and/or different epigenetic remodeling processes are driving radiation-induced cellular plasticity. Moving forward it would be of essence to study such possibilities to establish a better understanding about the underlying mechanisms at play. Ultimately, the results from the present experiments point to an intricate balance between different receptor/pathways orchestrating the phenotypic plasticity events following irradiation.

2.4 FUTURE DIRECTIONS

The present experiments provide insight regarding receptors and epigenetic machinery engaged following irradiation that may be contributing to the radiation-induced phenotypic conversion of non-stem glioma cells to glioma stem cells. While informative, these findings are based on assays done using select inhibitors. As such, more confirmatory loss-of-function/gain-of function studies would be required before attributing a definitive role to these receptors in the radiation-induced cellular plasticity response. To fully comprehend the underlying cellular and molecular drivers, several questions still remain that warrant further investigation. Some such examples include: 1) what specific DAMP(s) released following irradiation is/are binding to and activating the receptors identified, 2) are other receptors beyond the ones studied here implicated (e.g. RIG-1), 3) what specific downstream signaling pathways (e.g. NFκB and/or IRF3/7) are mediating these responses, 4) is there receptor crosstalk happening between TLRs and/or STING, which would suggest radiation acting through a combination of receptors rather than a distinct one, 5) are other processes previously shown to be essential for reprogramming (e.g. autophagy (S. Wang et al., 2013), optimal ROS/RNS levels, altered bioenergetic demands of cells linking metabolism with epigenetic regulation (Cooke & Lai, 2023)) involved here, 6) what other key epigenetic changes occurring specifically following radiation are crucial for cellular plasticity and 7) are *in vitro* results recapitulated *in vivo*? **Figure 20** provides a schematic representation of some of the questions addressed in our present studies, as well as future directions that would be of interest.

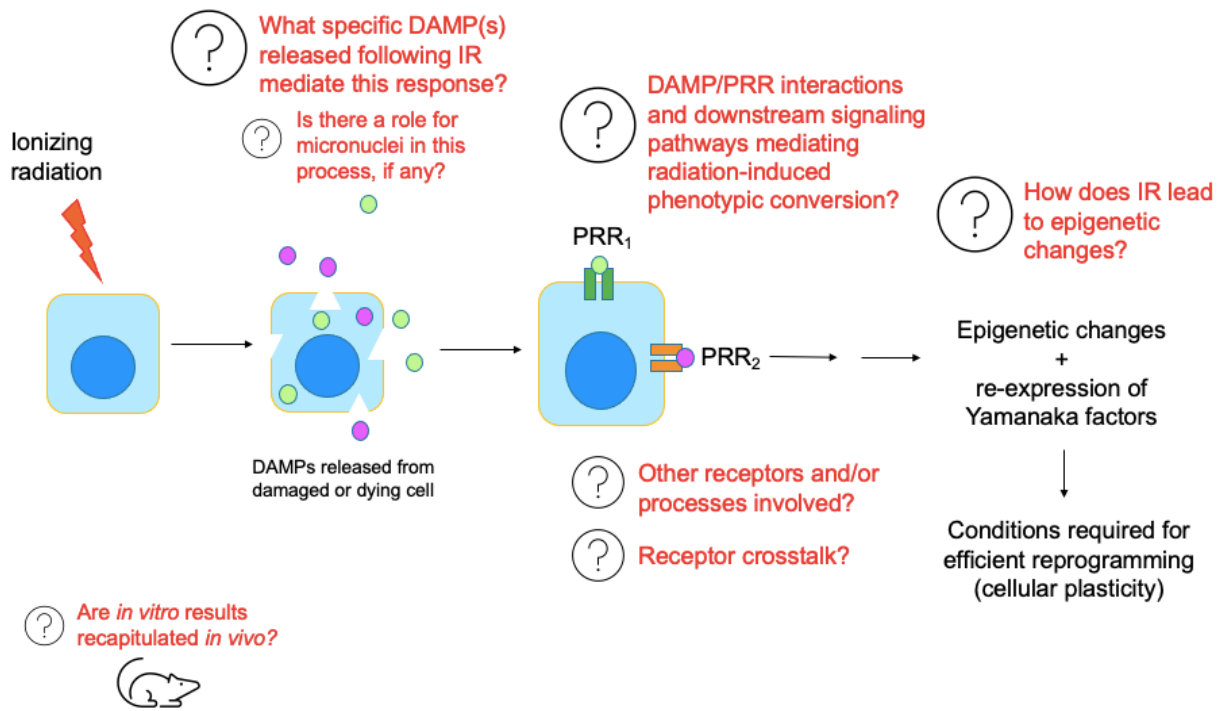


Figure 20: Graphical representation of research questions presently explored and useful future avenues to consider for better understanding how radiation-induced cellular plasticity events come about.

Firstly, to determine which DAMP(s) is/are mediating the response of interest following radiation, it would be essential to initially confirm the role of the signaling components identified in our experiments. This can be achieved through loss-of-function/gain-of-function studies using either si/shRNA interference or CRISPR methods, followed by re-evaluation of the parameters studied in SFAs/ELDAs and reprogramming assays, and subsequent rescue experiments (e.g. through overexpression of the knocked-out components). Once the suggested receptors are confirmed, as a first exploratory avenue, it would be of interest to determine whether micronuclei (MN) formed following irradiation are actually acting as DAMPs in this context. While involvement of other DAMPs could be evaluated by subjecting cell lysates from irradiated cells (collected at an optimal time point after irradiation) to specific Enzyme-Linked Immunosorbent Assays (ELISAs) for putative DAMPs for the receptors confirmed above, focusing on MN could be very informative. These structures formed during anaphase, encapsulate DNA in the form of lagging chromosomes or chromosomal fragments not successfully incorporated into a daughter cell nucleus during cell

division, separating it thus from the primary nucleus (Krupina, Goginashvili, & Cleveland, 2021). Looking at MN is of value since i) they can be generated following irradiation (Baatout Sarah, 2023; Jesenko et al., 2020), ii) there is evidence for greater MN induction post IR in stem cells vs non-stem cells, suggesting a potential link between stemness and MN formation (Y. Wang et al., 2018), iii) they are tightly linked to genomic integrity and chromatin remodeling processes, and iv) they can be recognized and lead to the activation of DNA sensors within the cell (Agustinus et al., 2023; Krupina et al., 2021). Therefore, it is possible that MN could be functioning as ligands mediating radiation-induced phenotypic conversion of non-stem glioma cells to glioma stem-like cells through engagement of DNA sensing receptors (e.g. TLR9, cGAS/STING, AIM2, IFI16 (Briard, Place, & Kanneganti, 2020)).

More specifically, for exploring the role of MN we could perform a Cytokinesis-block micronucleus cytome assay (Fenech, 2007) using sorted ZsGreen negative cells (i.e. non-stem cells, similar to those used as a starting material for the reprogramming assays described earlier) to see whether MN formation following irradiation is preferentially seen in cells that phenotype convert (i.e. cells that express ZsGreen fluorescence after radiation; IR-induced stem cells). Such a finding would suggest a potential link between MN formation and cellular plasticity. Similar experiments using combination treatments of radiation with select receptor inhibitors, could then further support the involvement of the targeted receptors in mediating these cellular plasticity events.

Next, to address the questions pertaining to downstream signaling pathways involved and whether there exists receptor crosstalk, the NF κ B and IRF pathways acting downstream of both TLRs and STING could be evaluated. Initially, NF κ B and/or IRF3/7 nuclear translocation following irradiation (which we would use as a proxy for activation of these pathways) could be explored by means of immunofluorescence assays using antibodies specific to the targets of interest. Subsequently, more specific assays could be used to identify the exact signaling components

implicated. For instance, the TransAM[®] NFκB Family kit (Active Motif, Cat# 43296), which is a colorimetric assay used for detecting NFκB subunits p50, p52, p65, c-Rel and RelB, could be used to determine which NFκB pathway(s), canonical and/or non-canonical, is/are activated specifically during radiation-induced cellular plasticity events. Similarly, colorimetric ELISA kits specific for p-IRF3/IRF3 (Abcam, Cat# ab279834) and/or IRF3 Transcription Factor assays (Abcam, ab207210) could be used to study IRF3 signaling activation in this context.

Given that our results point to diverse receptors potentially playing a role in radiation-induced cellular plasticity, it would not be surprising if both NFκB and IRF3 pathways are found to be activated. In that case, it would be of interest to understand the relative contribution of each. This could be achieved by specifically knocking-down pathway components unique to NFκB or IRF3 and seeing how such interventions are affecting the radiation-mediated response of interest. Based on evidence from previous research in the lab showing YF re-expression (Oct4, Sox2, Klf4, c-Myc) 48h post 4 Gy, establishment of an open chromatin state at the promoter regions of these transcription factors, as well as radiation-induced changes in histone methylation, acetylation and phosphorylation (K. Bhat, Saki, et al., 2020), experiments such as Chromatin Immunoprecipitation Polymerase Chain Reaction (ChIP-PCR; Cell Signaling Technologies, Danvers, MA) could be employed here. This would allow us to determine the state of YF promoter regions following interventions affecting the identified NFκB and/or IRF3 signaling components. Specifically, radiation could be combined with i) select receptor inhibitors, ii) receptor KD/KO (for receptors whose engagement and activation we have deemed essential for the radiation-specific cellular plasticity response to occur) and/or iii) KD of NFκB/IRF3 signaling components. Doing so would provide additional confirmation for the involvement of these receptors and hint at the relative contribution of each downstream signaling pathway. An Assay for Transposase-Accessible Chromatin (ATAC)-sequencing (Active Motif, Carlsbad, CA) could also be performed on irradiated sorted non-stem cells to determine transcription factor binding motifs for the signaling pathways

identified. Open chromatin state corresponds to locations where transcription factors can bind to and ultimately affect gene transcription, among other processes (Tsompana & Buck, 2014). Thus, studying the genomic regions containing open vs. closed chromatin states could inform us about the signaling pathways activated/engaged by radiation DAMP-receptor interactions. While some developmental pathways are expected to be found in an open chromatin state (K. Bhat, Saki, et al., 2020), other pathways not previously identified might be revealed here.

Having established the key receptor(s)/pathway(s) involved, we could then perform RNAseq experiments using irradiated sorted ZsGreen negative cells (i.e. non-stem cells) treated with specific receptor/pathway component inhibitors and look at different gene sets. Some such examples could be: autophagy related genes, epigenetic remodeling machinery components, ROS/RNS and/or histone deacetylase- (HDAC), histone acetyltransferase- (HATs) related genes. Identifying differentially expressed genes from these sets might provide additional insight regarding how radiation-induced cellular plasticity is functioning via the TLR +/- STING +/- other receptor(s) and/or downstream signaling pathways.

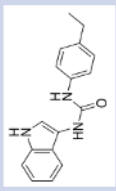
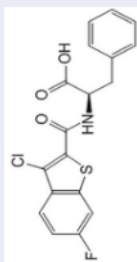
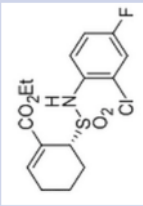
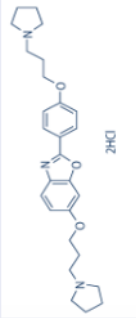
To study how other epigenetic changes might be at play in radiation-induced phenotype conversion, histone modifying enzymes, components of chromatin remodeling complexes, as well as proteins shown to be associated with these complexes, could be further explored by means of RT-PCR. For that we would need to use sorted ZsGreen negative cells (i.e. non-stem cells) and evaluate expression level changes following irradiation and/or treatment interventions targeting specific receptors or downstream signaling pathway components we previously confirmed for the radiation-induced response. Epigenetic modifiers shown to be implicated in this process could then be knocked down in sorted non-stem cells and the induction of phenotype conversion could be studied by means of reprogramming assays. Additionally, RT-PCR experiments looking at changes in histone expression levels, as well as ELISAs for evaluating post-translational

modifications occurring on histones following KD of the key epigenetic components identified above, could shed light on how epigenetic remodeling following irradiation, characterized by the re-expression of YFs (K. Bhat, Saki, et al., 2020), leads to radiation-induced cellular plasticity.

Lastly, after successfully confirming the signaling components mediating radiation-induced phenotypic conversion of non-stem glioma cells to glioma stem cells *in vitro*, it would be important studying these *in vivo*. Doing so would allow us to i) determine whether *in vitro* findings are recapitulated *in vivo* and ii) highlight potential therapeutic avenues. To this end, use of both immune competent (C57BL/6) and immunocompromised (NSG) animals would be beneficial. GFP-luc labeled murine glioma (GL261) or patient-derived GBM cells would be used in each mouse model respectively. Prior to implantation, receptors identified to play a role in radiation-induced cellular plasticity events would need to be knocked out by means of shRNA or CRISPR-Cas9 methods. Confirmation of successful receptor interference would need to be established at the protein and mRNA level. After cell implantation and confirmation of tumor engraftment by bioluminescence imaging, animals will be irradiated and cells will be allowed to grow for 3 weeks, time after which tumors will be harvested. At this point, digested tumor cells could be subjected to ELDAs, histologic evaluations and RNA extractions for subsequent RT-PCR and/or RNAseq experiments. Proposed treatment groups for this study would include animals receiving either non-engineered cells or receptor KO cells, in the presence of absence of radiation. An alternative approach would be to implant non-engineered murine glioma or patient-derived GBM cells in C57BL/6 and NSG mice respectively, confirm tumor grafting, treat animals with select inhibitors for the receptors deemed important, irradiate animals and subsequently collect and process cells as described above. Preliminary findings using LogBB_Pred (Shaker et al., 2023), a machine learning-based model for predicting the blood-brain-barrier (BBB) permeability of compounds, suggest that all but TLR3 inhibitor used in our experiments are BBB permeable (logBB values for TLR3i: -1.08279, TLR4i: -0.49653, TLR9i: 0.05719, STINGi: -0.30672; where logBB > -1 is

considered BBB permeable) (**Table 5**), meaning they could potentially be used here. For this latter experimental design however, care should be taken since administration of the receptor inhibitors could have much broader systemic effects beyond just affecting the implanted tumor cells and the radiation-induced response.

Table 5. Predicting blood-brain-barrier (BBB) permeability of select inhibitors. (SMILES: simplified molecular input line entry system)

| Inhibitor | SMILES | 2D depiction | logBB (values > -1 permeable) | BBB permeability |
|-----------|---|--|----------------------------------|-------------------|
| STINGi | <chem>O=C(NC(=CC1CC)=CC=1)NC(=CN1)C(=C1C=C1)C=C1</chem> |  | -0.30672 | BBB Permeable |
| TLR3i | <chem>C1C(=C(S1)C(=O)N[C@@H](CC(=CC=C2)C=C2)C(O)=O)C(=C1C=C1)C=C1</chem> |  | -1.08279 | BBB Non-permeable |
| TLR4i | <chem>C1C(=C1F)=C(NS(=O)=O)[C@@H](CC2)C(=CC2)C(=O)OCC)C=C1</chem> |  | -0.49653 | BBB Permeable |
| TLR9i | <chem>O(CCCN(CC1)CC1)C(=CC(=C1N2)OC=2C(C=CC2OCCCN(CC3)CC3)=CC=2)C=C1</chem> |  | 0.05719 | BBB Permeable |

All in all, better understanding what receptors, downstream pathways and epigenetic processes enable radiation to orchestrate the induction of phenotypic conversion could be of great value. In the context of cancer, it could highlight therapeutic avenues we could further pursue and target to address the inherent radioresistance of cancer stem-like cells, important players in tumor recurrence and therapy resistance. Conversely, in the case of tissue repair and regeneration, identified pathways could be exploited for their ability to restore compromised cellular compartments, providing thus important relief. Irrespective of the field of study, cancer or other, the benefits to be gained from this exploration are ample and hold great promise.

CHAPTER 3: Lab publications (3.1) & contributions (3.2)

3.1 Lab publications/papers

3.1.1 - Prevention of radiation-induced phenotypic conversion of non-stem glioma cells to glioma stem/initiating cells (GSCs/GICs)







Bhat, Kruttika, et al. "Dopamine receptor antagonists, radiation, and cholesterol biosynthesis in mouse models of glioblastoma." *JNCI: Journal of the National Cancer Institute* 113.8 (2021): 1094-1104.

He, Ling, et al. "Effects of the DRD2/3 antagonist ONC201 and radiation in glioblastoma." *Radiotherapy and Oncology* 161 (2021): 140-147.

He, Ling, et al. "Activation of the mevalonate pathway in response to anti-cancer treatments drives glioblastoma recurrences through activation of Rac-1." *bioRxiv* (2023).

A version of this work has been provisionally accepted in Cancer Research Communications (as of 5/20/2024).

Dopamine Receptor Antagonists, Radiation, and Cholesterol Biosynthesis in Mouse Models of Glioblastoma

Krutika Bhat, PhD,^{1,†} Mohammad Saki, PhD,^{1,†} Fei Cheng, PhD,¹ Ling He, DDS, PhD,¹ Le Zhang, MD, PhD,¹ Angeliki Ioannidis MS,¹ David Nathanson , PhD,² Jonathan Tsang BS,² Steven J. Bensinger, VMD, PhD,^{3,4,5} Phioanh Leia Nghiemphu , MD,^{5,6} Timothy F. Cloughesy , MD,^{5,6} Linda M. Liau , MD, PhD,^{5,7} Harley I. Kornblum, MD, PhD,^{5,2,7} Frank Pajonk , MD, PhD^{1,5*}

¹Department of Radiation Oncology, David Geffen School of Medicine at University of California Los Angeles (UCLA), Los Angeles, CA, USA; ²Department of Molecular and Medical Pharmacology at UCLA, Los Angeles, CA, USA; ³Department of Microbiology, Immunology and Molecular Genetics at UCLA, Los Angeles, CA, USA; ⁴UCLA Lipidomics Lab, Los Angeles, CA, USA; ⁵Jonsson Comprehensive Cancer Center at UCLA, Los Angeles, CA, USA; ⁶Department of Neurology at UCLA, Los Angeles, CA, USA and ⁷Department of Neurosurgery at UCLA, Los Angeles, CA, USA

†These authors contributed equally.

*Correspondence to: Frank Pajonk, MD, PhD, Department of Radiation Oncology, David Geffen School of Medicine at UCLA, NPI-Semel Institute for Neuroscience & Human Behavior at UCLA, 10833 Le Conte Ave, Los Angeles, CA 90095-1714, USA (e-mail: pajonk@ucla.edu).

Abstract

Background: Glioblastoma is the deadliest brain tumor in adults, and the standard of care consists of surgery followed by radiation and treatment with temozolomide. Overall survival times for patients suffering from glioblastoma are unacceptably low indicating an unmet need for novel treatment options. **Methods:** Using patient-derived HK-157, HK-308, HK-374, and HK-382 glioblastoma lines, the GL261 orthotopic mouse models of glioblastoma, and HK-374 patient-derived orthotopic xenografts, we tested the effect of radiation and the dopamine receptor antagonist quetiapine on glioblastoma self-renewal in vitro and survival in vivo. A possible resistance mechanism was investigated using RNA-sequencing. The blood-brain-barrier-penetrating statin atorvastatin was used to overcome this resistance mechanism. All statistical tests were 2-sided. **Results:** Treatment of glioma cells with the dopamine receptor antagonist quetiapine reduced glioma cell self-renewal in vitro, and combined treatment of mice with quetiapine and radiation prolonged the survival of glioma-bearing mice. The combined treatment induced the expression of genes involved in cholesterol biosynthesis. This rendered GL261 and HK-374 orthotopic tumors vulnerable to simultaneous treatment with atorvastatin and further statistically significantly prolonged the survival of C57BL/6 (n = 10 to 16 mice per group; median survival not reached; log-rank test, $P < .001$) and NOD Scid gamma mice (n = 8 to 21 mice per group; hazard ratio = 3.96, 95% confidence interval = 0.29 to 12.40; log-rank test, $P < .001$), respectively. **Conclusions:** Our results indicate promising therapeutic efficacy with the triple combination of quetiapine, atorvastatin, and radiation treatment against glioblastoma without increasing the toxicity of radiation. With both drugs readily available for clinical use, our study could be rapidly translated into a clinical trial.

Despite decades of drug development and technical improvement in radiotherapy, glioblastoma is still the deadliest brain cancer in adults with almost all patients ultimately dying from the disease (1). Attempts to add chemotherapeutic drugs that serve as radiosensitizers have largely failed because of either lack of blood-brain-barrier (BBB) penetration or lack of a proper therapeutic window with temozolomide being the only radiosensitizer that has so far been included into the standard of care (2). However, median survival time under the current standard of care with gross tumor

resection, temozolomide, and radiotherapy is only 15-18 months, thus indicating an urgent need to develop novel strategies against glioblastoma. Glioblastomas are thought to be organized hierarchically with a small number of glioma-initiating cells and able to produce more differentiated progeny and to repopulate a tumor after sublethal treatment. The ability to identify glioma-initiating cells prospectively (3,4) and the recognition of their intrinsic radioresistance (5) have sparked research aiming to target glioma-initiating cells specifically (6).

Received: November 9, 2020; Revised: January 18, 2021; Accepted: February 1, 2021

© The Author(s) 2021. Published by Oxford University Press. All rights reserved. For permissions, please email: journals.permissions@oup.com

In a high-throughput screen of 83 000 compounds (7), we identified the first-generation dopamine receptor antagonist trifluoperazine as a Food and Drug Administration (FDA)-approved drug with known BBB penetration that interferes with the self-renewal of glioma cells alone and prevents the induction of a glioma-initiating cell phenotype in combination with radiation (11). Recently, dopamine receptor antagonists have generated considerable interest in their repurpose as anticancer agents with well-established pharmacological properties and demonstrated some single-agent anticancer activity (8-14). Considering the unfavorable clinical side effect profile of trifluoperazine, we have extended our studies to include second-generation dopamine receptor antagonists with milder side effects.

In this study, we hypothesized that a combination of quetiapine and radiation would have equal or better efficacy against self-renewal of patient-derived glioma-initiating cells in vitro than first-generation dopamine receptor antagonists and radiation and it would prolong survival in mouse models of glioblastoma in vivo. Furthermore, RNA-sequencing (RNA-Seq) uncover novel resistance mechanisms against this combination treatment that could be exploited to improve survival of glioblastoma-bearing mice.

Methods

An extended description of the materials and methods is provided in the [Supplementary Methods](#) (available online).

Cell Culture

Primary human glioblastoma cell lines were established at the University of California, Los Angeles (UCLA) as described previously (3). Characteristics of specific gliomasphere lines can be found in Laks et al. (15). The GL261 murine glioma cell line was obtained from Charles River Laboratories, Inc (Frederick, MD). Cells were grown as previously described (11).

Drug Treatment

After confirming tumor grafting via bioluminescence imaging, mice implanted with the HK-374 or GL261 specimen were injected subcutaneously (quetiapine 30 mg/kg) or intraperitoneally (atorvastatin 30 mg/kg) on a 5-days on, 2-days off schedule with quetiapine, combined quetiapine and atorvastatin, or saline until they reached euthanasia endpoints. Quetiapine was dissolved in acidified phosphate buffered saline (0.4% glacial acetic acid) at a concentration of 5 mg/ml. Atorvastatin was dissolved in corn oil containing 2.5% dimethyl sulfoxide at a concentration of 5 mg/mL.

Irradiation

Cells were irradiated as previously described (11). Corresponding controls were sham irradiated. Mice were irradiated as previously described (16). For the assessment of the effect of quetiapine and quetiapine plus atorvastatin in combination with irradiation in vivo, mice were treated with corresponding drugs 1 hour prior to irradiation. Animals received a single dose of 10 Gy on day 3 or day 7 after tumor implantation.

In Vitro Sphere Formation Assay

For the assessment of self-renewal in vitro, patient-derived glioblastoma cells (HK-374, HK-382, HK-308, and HK-157) were irradiated with (0, 2, 4, 6, or 8 Gy) and treated with daily doses of quetiapine (0, 5, or 10 μ M). Glioblastoma cells were treated with a single dose of quetiapine (0, 5, 10 μ M) and atorvastatin (0, 50, 100, 250, 500, 1000 nM) with or without irradiation at 0, 2, 4, 6, or 8 Gy. The number of spheres formed at each dose point was normalized against the control. The resulting data points were fitted using a linear-quadratic model.

For the tertiary sphere formation assay with quetiapine, the spheres from patient-derived specimens were seeded in 10-cm dishes and treated with daily doses of either solvent or quetiapine (5 or 10 μ M) for 5 days. The surviving spheres after the initial treatment were collected, dissociated, and subjected to additional 2 rounds of identical treatment to attain the tertiary sphere cells. These spheres were plated in a 96-well plate and treated with a single dose of control or quetiapine. Ten days after treatment, the number of spheres formed in each condition were counted, and the percentage of clonal cells forming spheres was calculated.

RNA-Seq

RNA was extracted from HK-374 cells using Trizol 48 hours after 0 or 4 Gy. RNA-Seq analysis was performed by Novogene (Chula Vista, CA) as previously described (11).

Shotgun Lipidomics Analysis

Forty-eight hours after irradiation with 0 or 4 Gy in the presence or absence of quetiapine, HK-374 cells were trypsinized and resuspended in 0.2 mL of 1X phosphate buffered saline. A small aliquot of cell suspension from each sample was saved for cell counting, and the remaining cell suspension was immediately stored at -80°C and subjected to shotgun lipidomics analysis at the UCLA Lipidomics Core.

Statistical Analysis

All data shown are represented as mean (95% confidence interval [CI]) and result from at least 3 biologically independent experiments. A P value of no more than .05 in an unpaired 2-sided Student t test or 2-way ANOVA test indicated a statistically significant difference. For sphere-forming assays, data points were fitted using linear-quadratic model (surviving fraction = $\exp(-\alpha \cdot \text{dose} - \beta \cdot \text{dose}^2)$). For Kaplan-Meier estimates, a P value of .05 in a log-rank test indicated a statistically significant difference. Hazard ratios (HRs) and 95% confidence intervals for the survival curves were calculated using the Mantel-Haenszel model. All statistical analyses were performed using the GraphPad Prism Software package (GraphPad Software, San Diego, CA). All tests were 2-sided.

Results

Quetiapine and Radiation-Induced Phenotype Conversion In Vitro

We had previously reported that radiation treatment induced a phenotype conversion of glioma cells into glioma-initiating cells through reexpression of Yamanaka factors. Furthermore, we

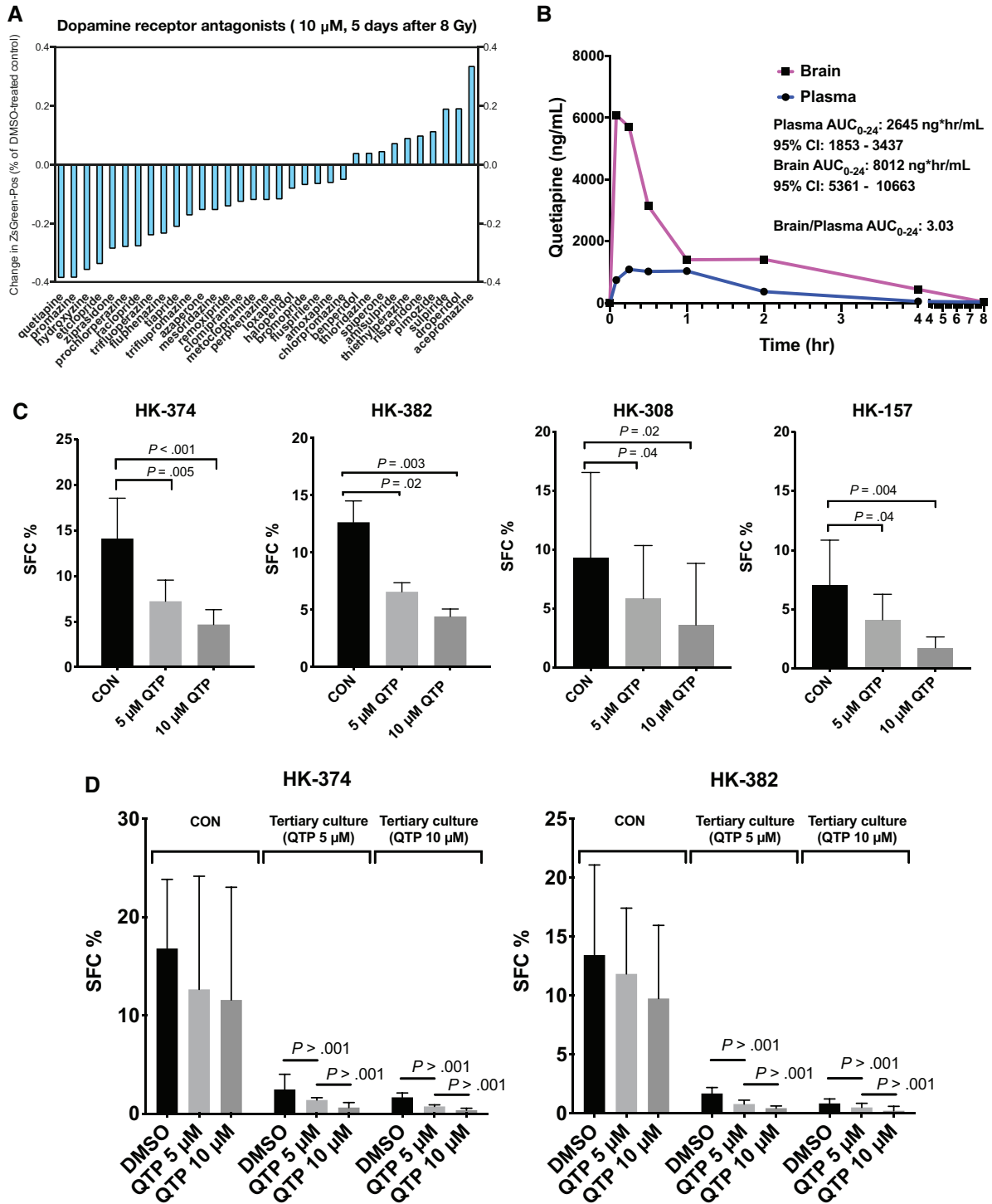


Figure 1. Quetiapine reduces self-renewal in patient-derived glioblastoma lines. (A) Inhibition of radiation-induced phenotype conversion by a panel of dopamine receptor antagonists. (B) Brain and plasma levels of quetiapine (QTP) in mice after a single injection (30 mg/kg, intraperitoneal) represented by Area Under Curve from 0-24 hours (AUC_{0-24}). (C) Sphere-forming capacity of patient-derived glioblastoma lines in quetiapine vs. control (CON) treated cells. (D) Tertiary sphere-forming assays with glioblastoma cells treated with quetiapine or control (DMSO). (E) Surviving fraction of spheres treated with radiation in the presence or absence of quetiapine. All experiments in this figure have been performed with at least 3 independent biological repeats. P values were calculated using 2-way ANOVA. CI = confidence interval.

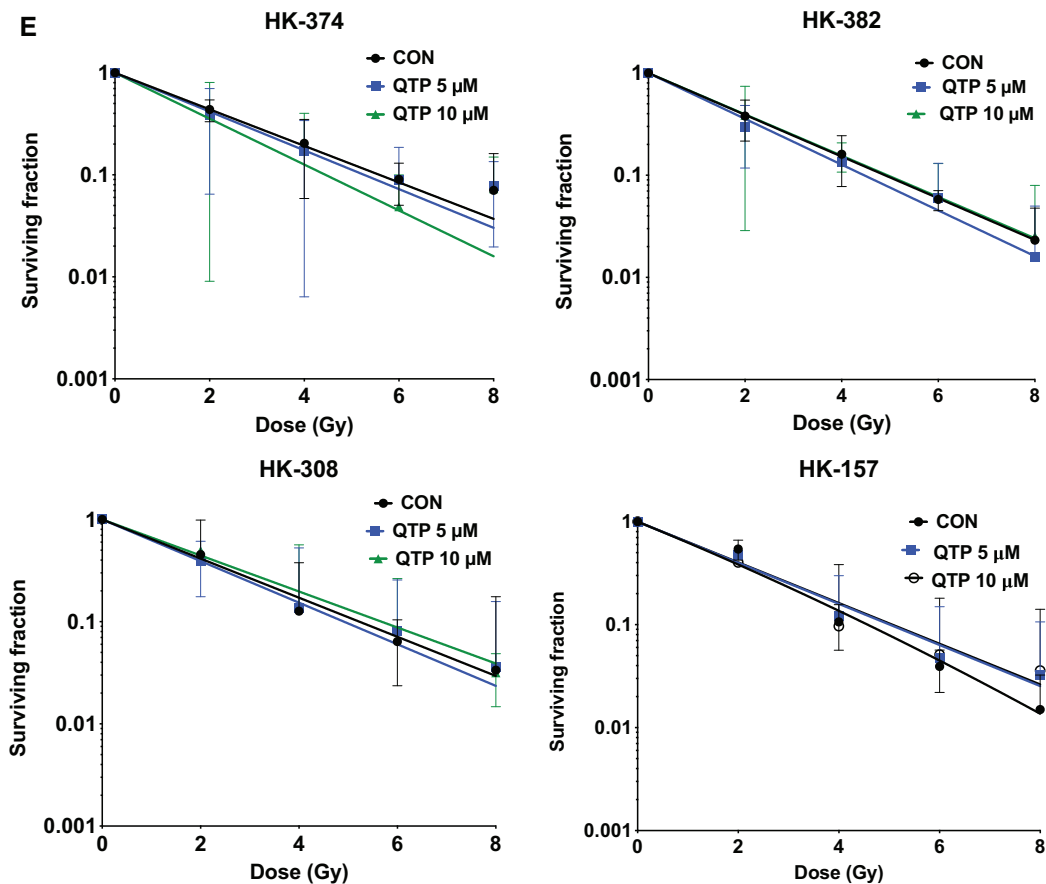


Figure 1. Continued

reported that treatment with the first-generation dopamine receptor antagonist trifluoperazine prevented this phenotype conversion and prolonged survival in a syngeneic GL261 model of glioblastoma and patient-derived orthotopic glioma xenografts (11).

Given the unfavorable side effect profile of trifluoperazine, we screened a panel of additional 32 dopamine receptor antagonists for their ability to interfere with the process of radiation-induced phenotype conversion. Compared with trifluoperazine, the second-generation dopamine receptor antagonist quetiapine, known for a milder side effect profile (17), showed higher efficacy against radiation-induced phenotype conversion than trifluoperazine in this screening assay (Figure 1, A).

Even though quetiapine is a psychotropic drug, we next ensured that quetiapine would penetrate into the central nervous system at relevant levels. Animals were treated with the mouse equivalent of 25% of the human maximum tolerated dose via intraperitoneal injection (30 mg/kg). Blood and brains were harvested at various time points after injection and subjected to mass spectrometry. Quetiapine rapidly crossed the BBB with a threefold higher Area Under Curve from 0-24 hours (AUC_{0-24}) compared with plasma levels (Figure 1, B).

To test the effects of quetiapine on the self-renewal of patient-derived glioblastoma specimens, we treated gliomaspheres of the HK-374, HK-382, HK-308, or HK-157 lines with 5 daily doses of quetiapine at 0, 5, or 10 μ M. Quetiapine caused a statistically significant dose-dependent reduction in sphere formation in all 4 cell lines (all $P < .05$) (Figure 1, C). To further evaluate the efficacy of quetiapine in inhibiting the self-renewal

capacity of gliomaspheres, we performed tertiary sphere-forming assays and observed a statistically significant exhaustion in sphere-forming capacity in glioblastoma cells treated with quetiapine (all $P < .001$) (Figure 1, D). Next, we combined a single dose of radiation with 5 daily doses of quetiapine to assess if quetiapine would act as a radiosensitizer in gliomaspheres. Quetiapine did not sensitize glioblastoma cells to radiation in the 4 patient-derived lines tested, suggesting that quetiapine treatment would not increase the toxicity of radiation (Figure 1, E; Supplementary Table 1, available online).

Effects of Quetiapine on Survival in Mouse Models of Glioblastoma

We next grafted GL261 cells into the striatum of C57BL/6 mice. Finding a statistically significant gain in the median survival in response to quetiapine but no clear dose dependency (Figure 2, A), we performed all subsequent *in vivo* experiments with quetiapine at 30 mg/kg (median survival: saline 23 days, quetiapine 31 days; HR = 1.34, 95% CI = 0.53 to 3.39; $P = .02$, log-rank test). Treatment of mice bearing GL261-StrawberryRed tumors with 5 daily injections of quetiapine for 1 or 2 weeks statistically significantly reduced the sphere-forming capacity of the surviving tumor cells *in vitro*, thus indicating the efficacy of quetiapine against glioma-initiating cells *in vivo* (Figure 2, B).

Considering that quetiapine did not act as a radiosensitizer, we decided to treat all animals with a single, sublethal dose of radiation, reflecting the inability of radiation to locally control

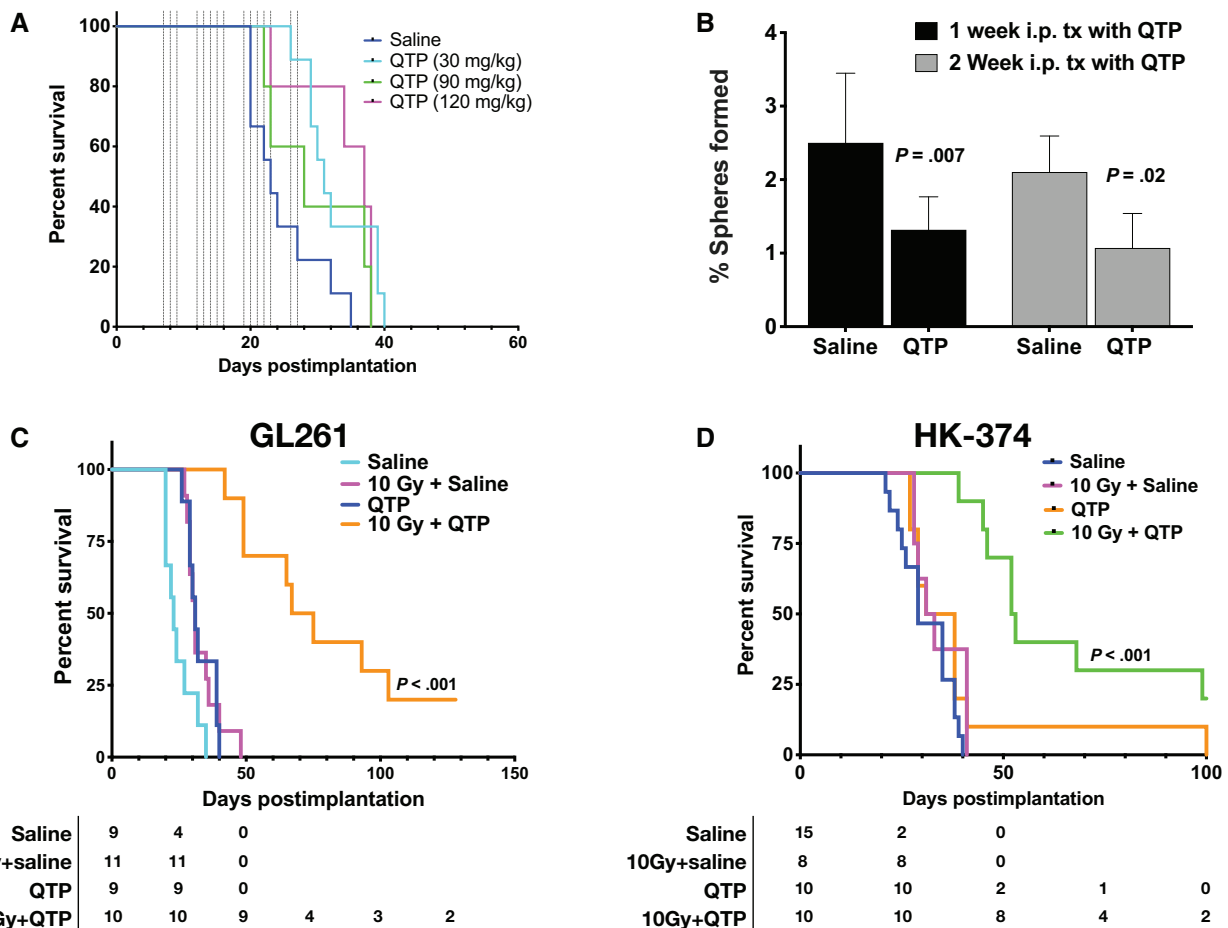


Figure 2. A combination of quetiapine and radiation prolongs survival in mouse models of glioblastoma. (A) Dose escalation of quetiapine (QTP) in GL261 tumor-bearing C57BL/6 mice. Seven days after injection of the tumor cells the animals were treated with escalating doses of quetiapine. Five daily doses of quetiapine per week for 3 weeks led to a statistically significant gain in the median survival (hazard ratio [HR] of control vs quetiapine = 2.64, 95% confidence interval [CI] = 0.93 to 7.44) with no clear dose dependency. (B) Treatment of GL261 tumor-bearing C57BL/6 mice with quetiapine reduces the sphere-forming capacity of surviving tumor cells. This experiment has been performed with at least 2 independent biological repeats (unpaired Student *t* test). (C and D) A single dose of 10 Gy or daily injection of quetiapine alone had small effects on medical survival (HR of control vs 10 Gy = 2.66, 95% CI = 0.94 to 7.49; HR control vs quetiapine = 3.96, 95% CI = 0.29 to 12.40). A combination of radiation (10 Gy) and daily injections of quetiapine statistically significantly prolongs survival in the GL261 glioma mouse model (HR of control vs quetiapine and 10 Gy = 5.46, 95% CI = 1.54 to 19.32) (C). Likewise, in mice carrying patient-derived orthotopic xenografts, radiation or quetiapine alone led to only small increases in median survival (HR of control vs quetiapine = 1.95; control vs 10 Gy = 1.77), whereas the combined treatment statistically significantly prolonged median survival from 27.5 to 52.5 days (log-rank HR = 4.70, 95% CI = 1.90 to 11.62) (D). All statistical tests were 2-sided. i.p. = intraperitoneal; tx = treatment.

glioblastoma in patients instead of using fractionated radiotherapy, which would normally be used to explore a therapeutic window for a radiosensitizer (18). A single radiation dose of 10 Gy (equivalent to 18 Gy in 2 Gy fractions in glioblastoma considering an alpha to beta ratio of 8 Gy), 7 days after orthotopic implantation of GL261 cells in mice, led to a small increase in median survival (23 days saline, 31 days 10 Gy, HR of control vs 10 Gy = 2.66, 95% CI = 0.94 to 7.49), comparable to the effect of quetiapine-alone treatment (23 days saline, 31 days quetiapine, HR control vs quetiapine = 3.96, 95% CI = 0.29 to 12.40). However, irradiation with 10 Gy rendered the tumors vulnerable to 5 daily injections of quetiapine per week, leading to a statistically significant increase in median survival (23 days saline, 71 days quetiapine and 10 Gy, HR of control vs quetiapine and 10 Gy = 5.46, 95% CI = 1.54 to 19.32; $P < .001$, log-rank test; Figure 2, C).

Next, we verified these findings using patient-derived orthotopic xenografts. Three days after orthotopic implantation of HK-374 glioblastoma cells in mice, animals were treated with a single dose of 0 or 10 Gy followed by daily injection of

quetiapine (30 mg/kg) or saline (5 days on, 2 days off schedule). Although NOD-scid IL2Rgamma^{null} mice are deficient in DNA repair via nonhomologous end joining, normal brain tissue toxicity from radiation does not differ from that in immune-competent mice (19). Again, quetiapine treatment or irradiation alone led to only small increases in median survival (29 days saline, 34.5 days quetiapine, HR of control vs quetiapine = 1.95, 95% CI = 0.78 to 4.88; 29 days saline, 32 days 10 Gy HR of control vs 10 Gy = 1.77, 95% CI = 0.82 to 5.57). However, the combination of a single radiation dose of 10 Gy followed by treatment with quetiapine statistically significantly increased the median survival (29 days saline, 52.5 days quetiapine and 10 Gy, HR = 4.70, 95% CI = 1.90 to 11.62; $P < .001$, log-rank test; Figure 2, D).

Dopamine Receptor Inhibition, Radiation, and Cholesterol Biosynthesis

Although the combined treatment with radiation and quetiapine statistically significantly improved the median survival

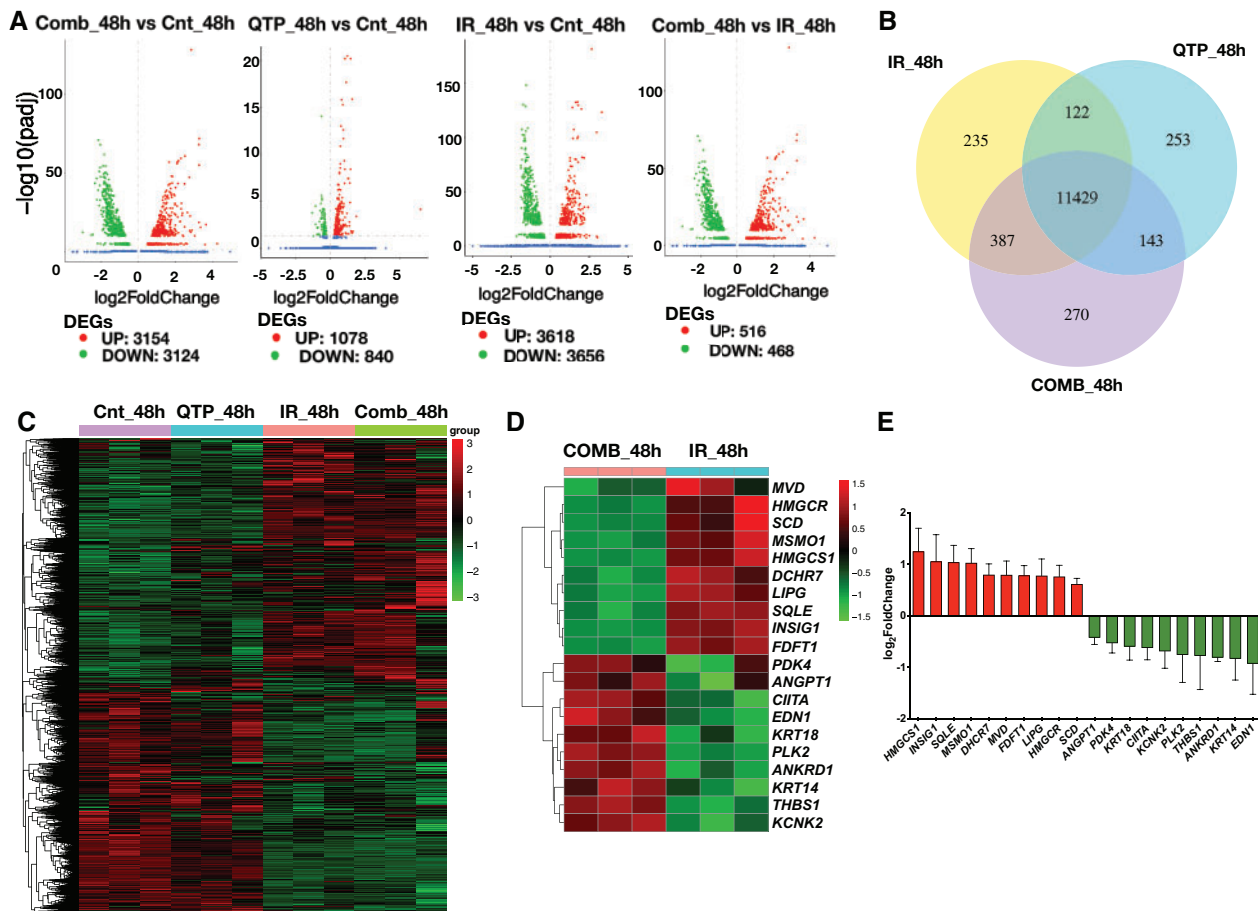


Figure 3. RNA-Seq analysis of glioma cells treated with quetiapine and radiation. (A) Volcano diagrams of differentially expressed genes (DEG) in HK-374 cells, 48 hours after treatment with radiation (IR, 4 Gy, RT), quetiapine (QTP), or quetiapine and radiation (Comb) compared with untreated control (Cnt) cells. (B) Venn diagrams of differentially expressed genes in HK-374 cells, 48 hours after treatment with radiation, quetiapine, or quetiapine and radiation. (C) Heatmap of differential expression genes in HK-374 cells, 48 hours after treatment with radiation, quetiapine, or quetiapine and radiation. (D) Top 10 up- and downregulated genes and their validation by qRT-PCR (E). Top 20 gene ontology gene set overlapping with genes differentially up- or downregulated in HK-374 cells, 48 hours after treatment with radiation and quetiapine (F). Genes involved in the biosynthesis of cholesterol are upregulated in HK-374 (G), HK-217, and HK-382 (H) cells, 48 hours after treatment with radiation (4 Gy) and quetiapine or radiation. Genes of the first-level regulator network of SREBF2, the master regulator of cholesterol biosynthesis, are upregulated in HK-374 (I), HK-217, and HK-382 (J) cells, 48 hours after treatment with radiation (4 Gy) and quetiapine or radiation.

of the animals, almost all animals eventually succumbed to the implanted tumor, thus suggesting that the tumor cells initiated a response to the treatment that led to resistance to quetiapine. To study this possibility in more detail, we next performed RNA-Seq on HK-374 cells at 48 hours after irradiation and/or quetiapine treatment to assess changes in the expression of genes in response to combined treatment. When compared with samples irradiated with a single dose of 4 Gy, the combined treatment with radiation and quetiapine led to the differential upregulation of 516 and the downregulation of 468 genes (Figure 3, A, last panel). The combination of quetiapine and radiation led to the differential expression of 122 unique genes (Figure 3, B), and irradiated samples showed a distinct genes expression profile (Figure 3, C). The top 10 up- and downregulated genes are presented as a heatmap (Figure 3, D) and were validated using qRT-PCR (Figure 3, E). Gene ontology enrichment analysis revealed overlap of the differentially downregulated genes in the samples treated with radiation and quetiapine with gene sets involved in DNA-dependent DNA replication, G1/S transition of the mitotic cell cycle, double-strand break repair, and cell cycle DNA replication (Figure 3, F).

The most prominent genes set that overlapped with genes differentially upregulated after combined treatment was involved in cholesterol, sterol, and lipid biosynthesis (Figure 3, F). The majority of genes involved in the cholesterol biosynthesis pathway were upregulated by quetiapine treatment, but this effect was enhanced when quetiapine treatment was combined with radiation (Figure 3, G). Analysis of the same set of genes in a second RNA-Seq data set of HK-374 cells treated with radiation, trifluoperazine, or a combination of trifluoperazine and radiation at the 48-hour timepoint showed a similar upregulation of genes involved in cholesterol biosynthesis after combined treatment and trifluoperazine treatment alone, thus indicating that this effect was not restricted to quetiapine alone (Supplementary Figure 1, A and B, available online).

Most of the genes in this pathway are under the control of sterol regulatory element binding transcription factor 2 (SREBF2) (20), and our analysis found SREBF2 as well as several genes of the SREBF2 first-level regulatory network upregulated in cells treated with quetiapine (Figure 3, I). To demonstrate that these effects of radiation and dopamine receptor antagonist were not cell-line specific, we performed qRT-PCR using specific primers for all genes in this pathway on 2 additional

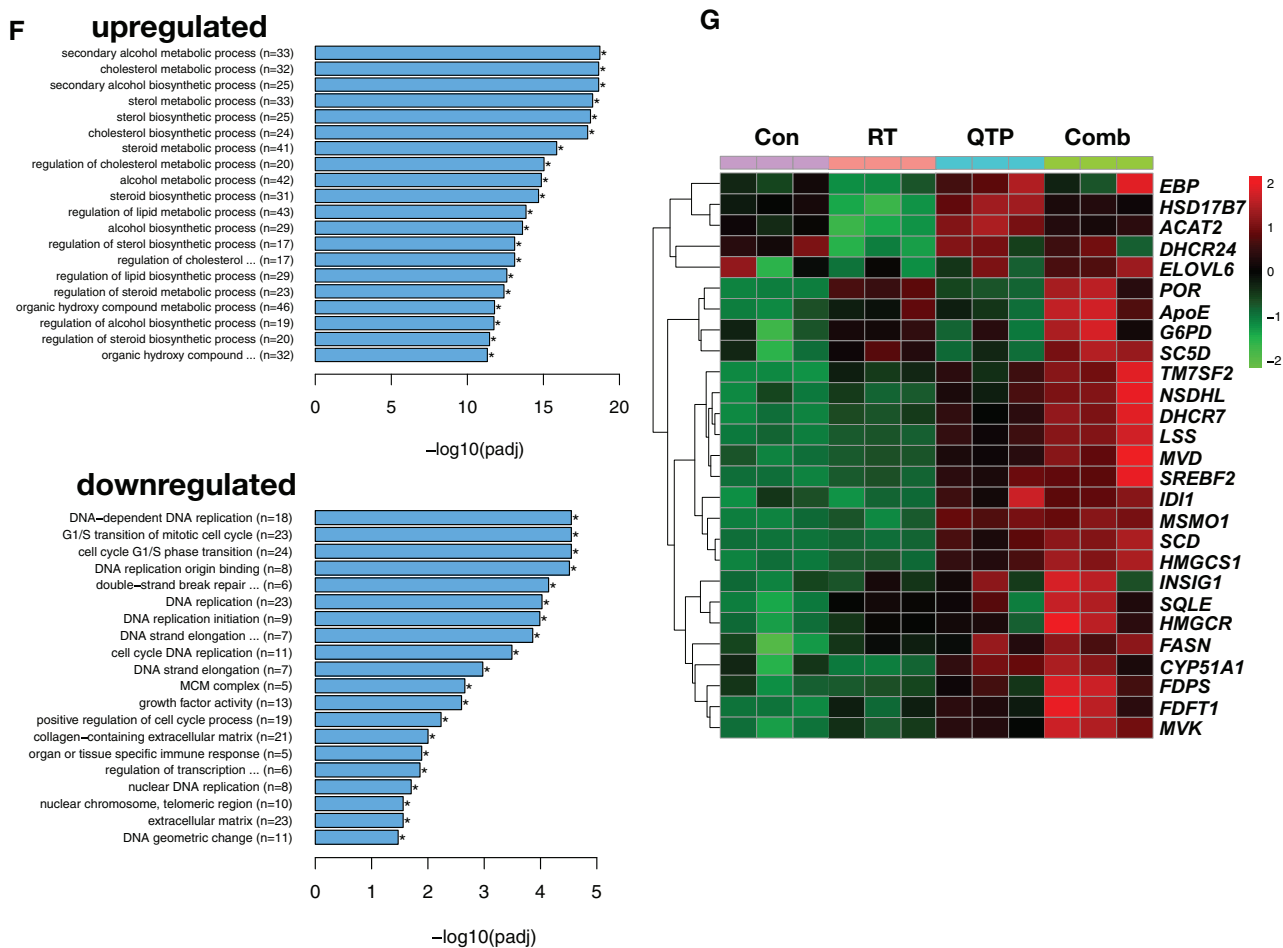


Figure 3. Continued.

patient-derived glioblastoma lines—HK-217 and HK-382—which confirmed the upregulation of the expression of key enzymes in the cholesterol biosynthesis pathway and the first-level regulatory network of SREBF2 (Figure 3, H and J).

Inhibition of Cholesterol Biosynthesis in Combination With Quetiapine and Radiation in Glioblastoma

Results from our RNA-Seq study led us to hypothesize that the upregulation of cholesterol biosynthesis is part of a defense mechanism of glioblastoma cells against radiation combined with dopamine receptor inhibition. We therefore tested if treatment with quetiapine and radiation would render glioblastoma cells vulnerable to treatment with the 3-hydroxy-3-methylglutaryl-CoA reductase inhibitor atorvastatin, a well-established and FDA-approved statin. Using the same 4 patient-derived glioblastoma specimens in sphere-formation assays, we reduced the very effective 5 daily treatments with quetiapine to only 1 treatment and combined it with atorvastatin at 0.1, 0.25, 0.5, or 1 μ M concentrations. Whereas a single dose of quetiapine had limited inhibitory effect on the self-renewal of gliospheres, the addition of atorvastatin to quetiapine treatment led to a statistically significant, dose-dependent reduction in sphere formation (all $P < .02$) (Figure 4, A). When combined with

radiation, the addition of atorvastatin did not radiosensitize gliospheres in the presence or absence of quetiapine (Figure 4, B; Supplementary Table 1, available online). Performing shotgun lipidomics on HK-374 cells after irradiation, quetiapine, or combined treatment, we found the lipid species of free fatty acids, diglycerides or diacylglycerols, and cholesterol esters upregulated, which agreed with our RNA-Seq findings. Addition of atorvastatin reversed the effects of the combined radiation and quetiapine treatment on those 3 lipid species while globally upregulating all other lipids (Figure 4, C). In agreement with our in vitro findings, daily treatment with quetiapine and atorvastatin (5 days on, 2 days off schedule) after a single dose of 10 Gy (Figure 4, D) statistically significantly increased the survival of C57Bl/6 mice implanted with GL261 cells with 90% of the animals surviving 157 days (median survival = 22 days saline, 31 days quetiapine, 34.5 10 Gy, 71 days quetiapine and 10 Gy, median survival not reached for quetiapine and atorvastatin and 10 Gy; HR of control vs 10 Gy and quetiapine and atorvastatin = 8.33, 95% CI = 2.50 to 27.77; $P < .001$, log-rank test; Figure 4, E). In mice-bearing HK-374 patient-derived orthotopic xenografts, the same combination treatment statistically significantly increased the median survival to 154 days (median survival = 39 days saline, 34.5 quetiapine, 33 days atorvastatin, 35.5 days quetiapine and atorvastatin, 43 days 10 Gy and saline, 64 days quetiapine and 10 Gy, 84 days atorvastatin and 10 Gy,

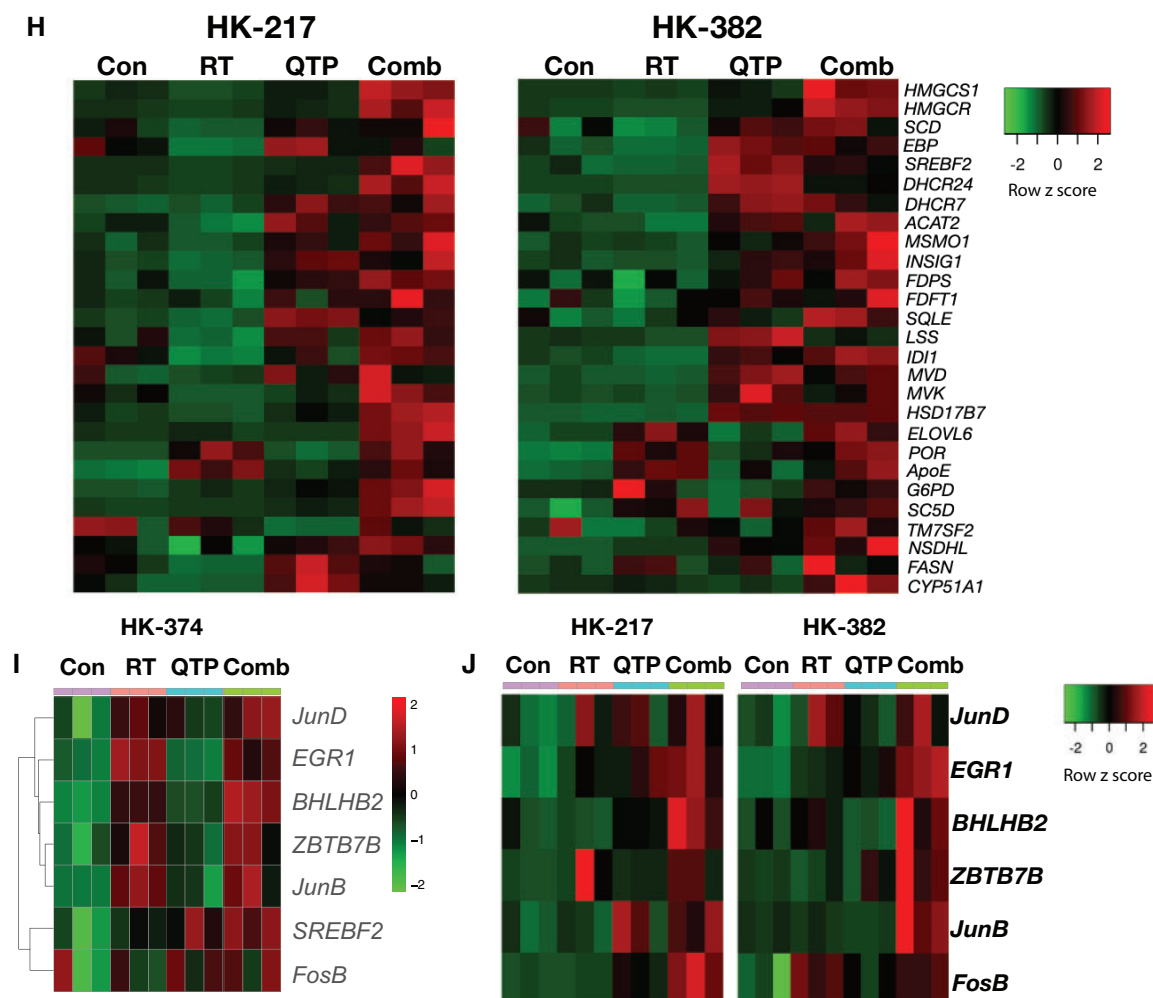


Figure 3. Continued.

154 days quetiapine and atorvastatin and 10 Gy; HR of control vs 10 Gy and quetiapine and atorvastatin = 5.94, 95% CI = 2.21 to 15.95; $P < .001$, log-rank test; Figure 4, F).

Discussion

Radiotherapy is one of the main pillars in the standard of care for patients suffering from glioblastoma and one of the few modalities that robustly prolongs the survival of the patients over surgery alone (21). Out of many attempts that added conventional chemotherapy or targeted therapies to the standard of care, so far only temozolomide met the threshold to be included in the treatment regimen (22). However, despite decades of effort, the overall survival of patients with glioblastoma remains unacceptably low, thus indicating an unmet need for novel treatment options against glioblastoma.

Recent reports in the literature have suggested an antitumor activity of dopamine receptor type 2 antagonists against glioblastoma (9,23-25), and dopamine receptors have been found to be expressed in various tumor types including glioblastoma (8). However, the antitumor efficacy of dopamine receptor

antagonists as single agents was found to be limited in preclinical (26) and clinical studies (14).

We have recently reported that a combination of a single high dose of radiation and continuous application of the first-generation dopamine receptor antagonist trifluoperazine improved survival in mouse models of glioblastoma (11). Here, we report that quetiapine, a second-generation dopamine receptor antagonist with a more favorable side effect profile than trifluoperazine, combined with radiation also shows efficacy against glioma-initiating cells in vitro and prolongs survival in mouse models of glioblastoma without affecting the radiation sensitivity of glioma cells. Although the effect on survival was highly statistically significant and meaningful, most animals eventually showed tumor progression and ultimately succumbed to the disease. Our search for a possible resistance mechanism analyzing data obtained by RNA-Seq revealed an upregulation of key components of the cholesterol biosynthesis pathway in the response of glioblastoma cells to the combination of quetiapine and radiation.

Antipsychotics like quetiapine, commonly used for the treatment of mental disorders, have been associated with

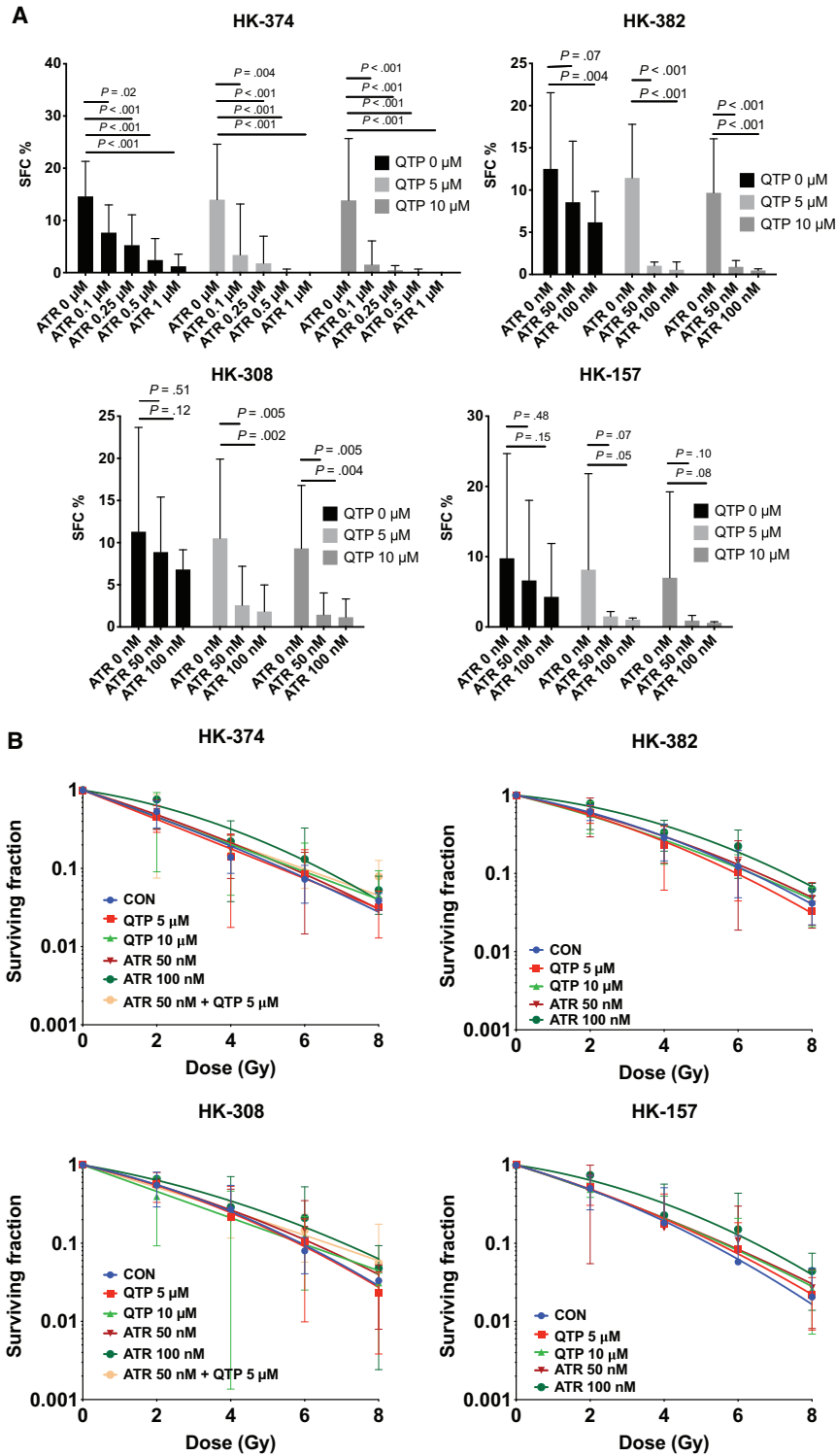


Figure 4. A combination of quetiapine and radiation with atorvastatin improves survival in mouse models of glioblastoma. (A) Quetiapine (QTP) and atorvastatin (ATR) synergistically decreases sphere-forming capacities (SFC) in patient-derived glioblastoma lines. All experiments in this figure have been performed with at least 3 independent biological repeats. (Two-way ANOVA; P values are indicated in the figure). (B) QTP, ATR, or a combination of both does not alter the radiation sensitivity of patient-derived glioblastoma lines. (C) Shotgun lipidomics analysis was performed with HK-374 cells treated with either control (CON), 4 Gy, 4 Gy + QTP, or 4 Gy + QTP + ATR that included at least 3 independent biological repeats. Radiation and quetiapine upregulated fatty acid, diglyceride or diacylglycerol, and cholesterol ester synthesis, and this effect was reversed by the addition of atorvastatin. (D) Treatment plan for patient-derived orthotopic xenografts using an image-guided small animal irradiator. A combination of QTP and ATR (both 30 mg/kg) with a single dose of radiation (10 Gy) statistically significantly prolongs survival in the GL261 glioma mouse model (hazard ratio [HR] of control vs 10 Gy and quetiapine and atorvastatin = 8.33, 95% confidence interval [CI] = 2.50 to 27.77) (E) and HK-374 patient-derived orthotopic xenografts (F) (log-rank HR of control vs 10 Gy and quetiapine and atorvastatin = 5.94, 95% CI = 2.21 to 15.95). All statistical tests were 2-sided.

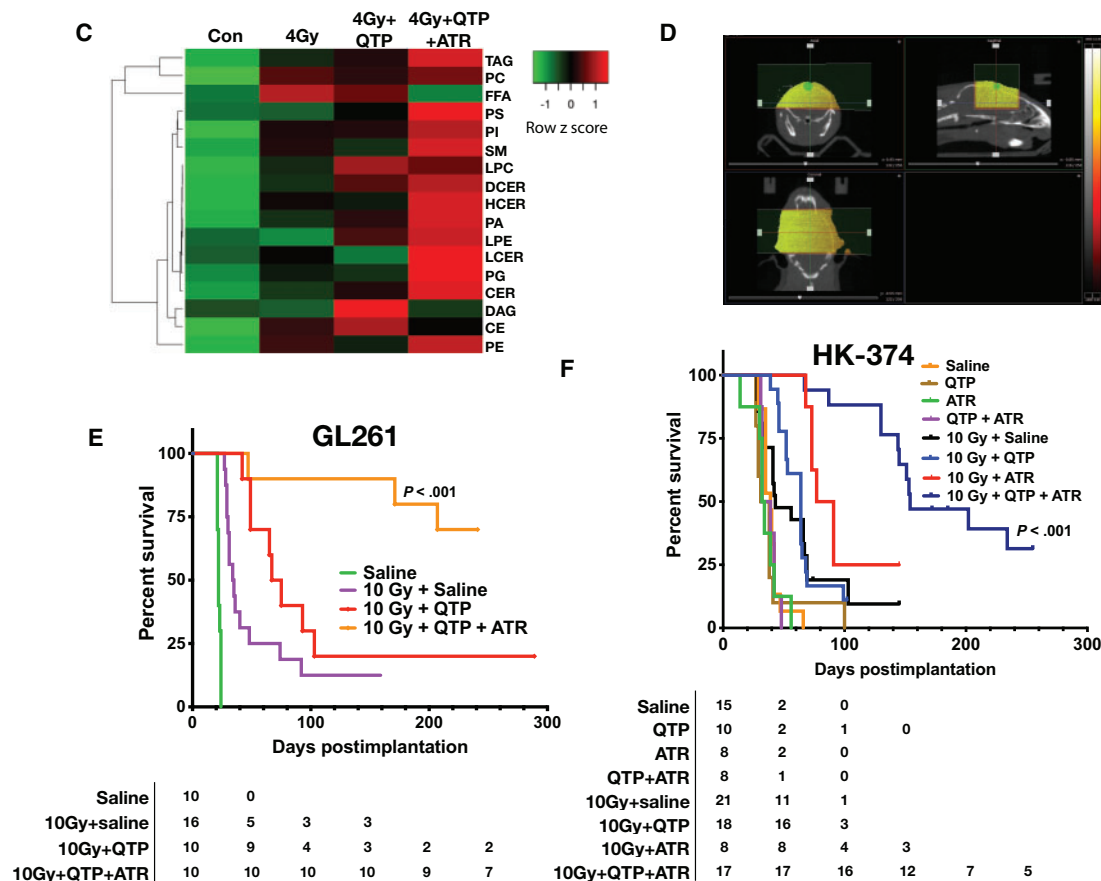


Figure 4. Continued.

dyslipidemia (27,28) and are known to cause an upregulation in serum lipid levels (29,30). However, even high concentrations of quetiapine alone are not able to induce the cholesterol and fatty acid synthesis pathway in *in vitro* (31). The microenvironmental and molecular changes that drive this dyslipidemic effect of quetiapine are incompletely understood but have recently been linked to the activation of the Pregnane X Receptor signaling in the intestines (27).

Survival of Glioblastoma cells is known to depend on cholesterol (32). The potential beneficial impact of statin use in glioblastoma patients is discussed controversially (33-36), but a recent meta-analysis did not indicate a beneficial effect of statins in glioblastoma under the current standard of care (37). We report here that quetiapine treatment of glioblastoma cells but not irradiation alone led to a moderate upregulation of the key components of the cholesterol biosynthesis. This effect was statistically significantly amplified when quetiapine and radiation were combined and led to an upregulation of the intracellular levels of fatty acids and cholesterol esters species. Additionally, although the normal brain contains cholesterol, only its free form, sterol esters, has long been known to be specific for glioblastomas (38). In agreement with the literature, inhibition of the cholesterol biosynthesis using atorvastatin by itself had some effect on the self-renewal capacity of glioma-initiating cells *in vitro*, and this was enhanced by the addition of quetiapine but failed to radiosensitize glioma-initiating cells. However, the combined treatment with radiation and quetiapine rendered the glioma-initiating cells and tumors sensitive

to the addition of atorvastatin, resulting in statistically significantly reduced self-renewal capacity of glioma-initiating cells and increased median survival in mouse models of glioblastoma. Our study falls short of identifying the specific cholesterol esters that facilitate the survival in glioblastoma after combined treatment and the pathways they engage. Future studies will potentially identify novel targets in this pathway that interfere with this resistance mechanism more specifically.

In summary, we conclude that dopamine receptor antagonists are readily available, FDA-approved drugs with well-known toxicity profiles that enhance the efficacy of radiotherapy. Furthermore, the addition of atorvastatin can further improve survival, a treatment combination that can be easily tested in future clinical trials.

Funding

FP was supported by a grant from the National Cancer Institute (R01CA200234). DN, PLN, TC, LL, HK, and FP were supported by a grant from the National Cancer Institute (P50CA211015).

Notes

Role of the funder: The National Cancer Institute played no role in the design and conduct of the study; the collection, management, analysis, and interpretation of the data; preparation,

review, or approval of the manuscript; and decision to submit the manuscript for publication.

Disclosures: TFC is cofounder, major stock holder and board member of Katmai Pharmaceuticals, Member of the board for the 501c3 Global Coalition for Adaptive Research, holds stock option of Notable Labs, has provided consulting services to QED, Roche, Trizel, Medscape, Bayer, Amgen, Odonate Therapeutics, Pascal Biosciences, Bayer, Del Mar Pharmaceuticals, Tocagen, Karyopharm, GW Pharma, Kiyatec, Abbvie, Boehringer Ingelheim, VBI, Deciphera, VBL, Agios, Merck, Roche, Genocoea, Celgene, Puma, Lilly, BMS, Cortice, Wellcome Trust, Novocure, Novogen, Boston Biomedical, Sunovion, Human Longevity, Insys, ProNai, Pfizer, Notable labs, Medqia and has contracts with UCLA for the Brain Tumor Program with Amgen, Abbvie, DNatrix, Beigene, BMS, AstraZeneca, Kazia, Agios, Boston Biomedical, Deciphera, Tocagen, Orbus, AstraZeneca, Karyopharm. No potential conflicts of interests are disclosed by the other authors.

Author contributions: FP, PLN, TFC conceived of the study. KB, MS, FC, LH, LZ, AI, DN, JT, SJB performed the experiments, KB, MS and FP analyzed the data, LML and HIK provided materials, FP and KB drafted the manuscript. All authors contributed to the writing of the manuscript

Data Availability

All data generated and analyzed in this study are available from the corresponding author on reasonable request. The RNA-Seq data are accessible through GSE165624 (quetiapine) and GSE146358 (trifluoperazine).

References

- van Linde ME, Brahm CG, de Witt Hamer PC, et al. Treatment outcome of patients with recurrent glioblastoma multiforme: a retrospective multicenter analysis. *J Neurooncol*. 2017;135(1):183–192.
- Cohen RJ, Mehta MP. Role of radiosensitizers in radiation treatment of gliomas. *Prog Neurol Surg*. 2018;31:102–115.
- Hemmati HD, Nakano I, Lazareff JA, et al. Cancerous stem cells can arise from pediatric brain tumors. *Proc Natl Acad Sci USA*. 2003;100(25):15178–15183.
- Singh SK, Clarke ID, Terasaki M, et al. Identification of a cancer stem cell in human brain tumors. *Cancer Res*. 2003;63(18):5821–5828.
- Bao S, Wu Q, McLendon RE, et al. Glioma stem cells promote radioresistance by preferential activation of the DNA damage response. *Nature*. 2006;444(7120):756–760.
- Spencer DA, Auffinger BM, Murphy JP, et al. Hitting a moving target: glioma stem cells demand new approaches in glioblastoma therapy. *Curr Cancer Drug Targets*. 2017;17(3):236–254.
- Zhang L, Bochkur Dratver M, Yazal T, et al. Mebendazole potentiates radiation therapy in triple-negative breast cancer. *Int J Radiat Oncol Biol Phys*. 2019;103(1):195–207.
- Caragher SP, Shireman JM, Huang M, et al. Activation of dopamine receptor 2 prompts transcriptomic and metabolic plasticity in glioblastoma. *J Neurosci*. 2019;39(11):1982–1993.
- Pinheiro T, Otrocka M, Seashore-Ludlow B, et al. A chemical screen identifies trifluoperazine as an inhibitor of glioblastoma growth. *Biochem Biophys Res Commun*. 2017;494(3–4):477–483.
- Brami-Cherrier K, Valjent E, Garcia M, et al. Dopamine induces a PI3-kinase-independent activation of Akt in striatal neurons: a new route to cAMP response element-binding protein phosphorylation. *J Neurosci*. 2002;22(20):8911–8921.
- Bhat K, Saki M, Vlashi E, et al. The dopamine receptor antagonist trifluoperazine prevents phenotype conversion and improves survival in mouse models of glioblastoma. *Proc Natl Acad Sci USA*. 2020;117(20):11085–11096.
- Hall MD, Odia Y, Allen JE, et al. First clinical experience with DRD2/3 antagonist ONC201 in H3 K27M-mutant pediatric diffuse intrinsic pontine glioma: a case report. *J Neurosurg Pediatr*. 2019;5:1–7.
- Prabhu VV, Morrow S, Rahman Kawakibi A, et al. ONC201 and imipridones: anti-cancer compounds with clinical efficacy. *Neoplasia*. 2020;22(12):725–744.
- Chi AS, Tarapore RS, Hall MD, et al. Pediatric and adult H3 K27M-mutant diffuse midline glioma treated with the selective DRD2 antagonist ONC201. *J Neurooncol*. 2019;145(1):97–105.
- Laks DR, Crisman TJ, Shih MY, et al. Large-scale assessment of the glioma-sphere model system. *Neuro Oncol*. 2016;18(10):1367–1378.
- Saki M, Bhat K, Sodhi SS, et al. Effects of brain irradiation in immune-competent and immune-compromised mouse models. *Radiat Res*. 2019;193(2):186–194.
- Yang SY, Kao Yang YH, Chong MY, et al. Risk of extrapyramidal syndrome in schizophrenic patients treated with antipsychotics: a population-based study. *Clin Pharmacol Ther*. 2007;81(4):586–594.
- Holthusen H. Erfahrungen über die Verträglichkeitsgrenze für Röntgenstrahlen und deren Nutzenanwendung zur Verhütung von Schäden. *Strahlentherapie*. 1936;57(7):254–269.
- Saki M, Bhat K, Sodhi SS, et al. Effects of brain irradiation in immune-competent and immune-compromised mouse models. *Radiat Res*. 2020;193(2):186–194.
- Eberle D, Hegarty B, Bossard P, et al. SREBP transcription factors: master regulators of lipid homeostasis. *Biochimie*. 2004;86(11):839–848.
- Walker MD, Strike TA, Sheline GE. An analysis of dose-effect relationship in the radiotherapy of malignant gliomas. *Int J Radiat Oncol Biol Phys*. 1979;5(10):1725–1731.
- Stupp R, Mason WP, van den Bent MJ, et al. Radiotherapy plus concomitant and adjuvant temozolomide for glioblastoma. *N Engl J Med*. 2005;352(10):987–996.
- Liu Z, Jiang X, Gao L, et al. Synergistic suppression of glioblastoma cell growth by combined application of temozolomide and dopamine D2 receptor antagonists. *World Neurosurg*. 2019;128:e468–e477.
- Chen X, Luo X, Cheng Y. Trifluoperazine prevents FOXO1 nuclear excretion and reverses doxorubicin-resistance in the SHG44/DOX drug-resistant glioma cell line. *Int J Mol Med*. 2018;42(6):3300–3308.
- Kang S, Lee JM, Jeon B, et al. Repositioning of the antipsychotic trifluoperazine: synthesis, biological evaluation and in silico study of trifluoperazine analogs as anti-glioblastoma agents. *Eur J Med Chem*. 2018;151:186–198.
- Zhang X, Xu R, Zhang C, et al. Trifluoperazine, a novel autophagy inhibitor, increases radiosensitivity in glioblastoma by impairing homologous recombination. *J Exp Clin Cancer Res*. 2017;36(1):118.
- Meng Z, Gwag T, Sui Y, et al. The atypical antipsychotic quetiapine induces hyperlipidemia by activating intestinal PXR signaling. *JCI Insight*. 2019;4(3).
- Olfson M, Marcus SC, Corey-Lisle P, et al. Hyperlipidemia following treatment with antipsychotic medications. *Am J Psychiatry*. 2006;163(10):1821–1825.
- Meyer JM, Koro CE. The effects of antipsychotic therapy on serum lipids: a comprehensive review. *Schizophr Res*. 2004;70(1):1–17.
- de Leon J, Susce MT, Johnson M, et al. A clinical study of the association of antipsychotics with hyperlipidemia. *Schizophr Res*. 2007;92(1–3):95–102.
- Lauressergues E, Staels B, Valeille K, et al. Antipsychotic drug action on SREBPs-related lipogenesis and cholesterologenesis in primary rat hepatocytes. *Naunyn-Schmied Arch Pharmacol*. 2010;381(5):427–439.
- Villa GR, Hulce JJ, Zanca C, et al. An LXR-cholesterol axis creates a metabolic co-dependency for brain cancers. *Cancer Cell*. 2016;30(5):683–693.
- Seliger C, Schaertl J, Gerken M, et al. Use of statins or NSAIDs and survival of patients with high-grade glioma. *PLoS One*. 2018;13(12):e0207858.
- Shojaei S, Alizadeh J, Thliveris J, et al. Statins: a new approach to combat temozolomide chemoresistance in glioblastoma. *J Invest Med*. 2018;66(8):1083–1087.
- Bhavsar S, Hagan K, Arunkumar R, et al. Preoperative statin use is not associated with improvement in survival after glioblastoma surgery. *J Clin Neurosci*. 2016;31:176–180.
- Gaist D, Hallas J, Friis S, et al. Statin use and survival following glioblastoma multiforme. *Cancer Epidemiol*. 2014;38(6):722–727.
- Happold C, Gorlia T, Nabors LB, et al.; for the EORTC Brain Tumor Group and on behalf of the CENTRIC and CORE Clinical Trial Groups. Do statins, ACE inhibitors or sartans improve outcome in primary glioblastoma? *J Neurooncol*. 2018;138(1):163–171.
- White HB Jr, Smith RR. Cholesteryl esters of the glioblastoma. *J Neurochem*. 1968;15(4):293–299.



Published in final edited form as:

Radiother Oncol. 2021 August ; 161: 140–147. doi:10.1016/j.radonc.2021.05.027.

Effects of the DRD2/3 Antagonist ONC201 and Radiation in Glioblastoma

Ling He¹, Kruttika Bhat¹, Angeliki Ioannidis¹, Le Zhang¹, Nhan T. Nguyen¹, Joshua E. Allen², Phioanh Leia Nghiemphu^{3,4}, Timothy F. Cloughesy^{3,4}, Linda M. Liau^{3,5}, Harley I. Kornblum^{3,6}, Frank Pajonk^{1,3,*}

¹Department of Radiation Oncology, David Geffen School of Medicine at UCLA

²Oncocoetics Inc., Philadelphia, Pennsylvania

³Jonsson Comprehensive Cancer Center at UCLA

⁴Department of Neurology at UCLA

⁵Department of Neurosurgery at UCLA

⁶NPI-Semel Institute for Neuroscience & Human Behavior at UCLA

Abstract

Background—Glioblastoma (GBM) is the deadliest of all brain cancers in adults. The current standard-of-care is surgery followed by radiotherapy and temozolomide, leading to a median survival time of only 15 months. GBM are organized hierarchically with a small number of glioma-initiating cells (GICs), responsible for therapy resistance and tumor recurrence, suggesting that targeting GICs could improve treatment response. ONC201 is a first-in-class anti-tumor agent with clinical efficacy in some forms of high-grade gliomas. Here we test its efficacy against GBM in combination with radiation.

Methods—Using patient-derived GBM lines and mouse models of GBM we test the effects of radiation and ONC201 on GBM self-renewal *in vitro* and survival *in vivo*. A possible resistance mechanism is investigated using RNA-Sequencing.

Results—Treatment of GBM cells with ONC201 reduced self-renewal, clonogenicity and cell viability *in vitro*. ONC201 exhibited anti-tumor effects on radioresistant GBM cells indicated by

* **Correspondence address:** Frank Pajonk, MD, PhD, Department of Radiation Oncology, David Geffen School of Medicine at UCLA, 10833 Le Conte Ave, Los Angeles, CA 90095-1714, Phone: +1 310 206 8733, Fax: +1 310 206 1260, pajonk@ucla.edu.

Authorship: LH, KB, AI, LZ performed the experiments and collected the data. LML and HIK provided the patient-derived specimen. JEA provided ONC201, FP designed the experiments, FP conceived of the study, LH and FP analyzed the data and wrote the manuscript. All authors edited and approved of the final version of the manuscript.

Conflict of Interest: J.E.A. is an employee and shareholder of Oncocoetics and has ownership interest (including patents) in Oncocoetics. F.P. holds stock in Chimerix Inc.. T.F.C. is cofounder, major stock holder and board member of Katmai Pharmaceuticals, Member of the board for the 501c3 Global Coalition for Adaptive Research, holds stock option of Notable Labs, has provided consulting services to QED, Roche, Trizel, Medscape, Bayer, Amgen, Odonate Therapeutics, Pascal Biosciences, Bayer, Del Mar Pharmaceuticals, Tocagen, Karyopharm, GW Pharma, Kiyatec, Abbvie, Boehringer Ingelheim, VBI, Deciphera, VBL, Agios, Merck, Roche, Genoece, Celgene, Puma, Lilly, BMS, Cortice, Wellcome Trust, Novocure, Novogen, Boston Biomedical, Sunovion, Human Longevity, Insys, ProNai, Pfizer, Notable labs, Medqia and has contracts with UCLA for the Brain Tumor Program with Amgen, Abbvie, DNAtrix, Beigene, BMS, AstraZeneca, Kazia, Agios, Boston Biomedical, Deciphera, Tocagen, Orbus, AstraZeneca, Karyopharm. No potential conflicts of interests are disclosed by the other authors.

reduced self-renewal in secondary and tertiary glioma spheres. Combined treatment with ONC201 and radiation prolonged survival in syngeneic and patient-derived orthotopic xenograft mouse models of GBM. Subsequent transcriptome analyses after combined treatment revealed shifts in gene expression signatures related to quiescent GBM populations, GBM plasticity, and GBM stem cells.

Conclusions—Our findings suggest that combined treatment with the DRD2/3 antagonist ONC201 and radiation improves the efficacy of radiation against GBM *in vitro* and *in vivo* through suppression of GICs without increasing toxicity in mouse models of GBM. A clinical assessment of this novel combination therapy against GBM is further warranted.

Keywords

Glioblastoma; radiotherapy; dopamine receptor antagonist; transcriptome analyses; quiescent glioblastoma cells

Introduction

GBM is the deadliest of all brain cancers in adults and all patients ultimately succumb to the tumor. The standard-of-care involves surgical removal of the bulk tumor followed by radiotherapy and temozolomide treatment [1]. Reasons for treatment failure include the spread of tumor cells into the normal parenchyma far beyond the detectable tumor, radio- and chemo-therapy resistance of the tumor cells and intratumoral heterogeneity and plasticity of GBM [2-6]. Past attempts to improve survival using classical chemotherapeutic drugs or immunotherapy have been hampered by the inability of many drugs or biologics to cross the blood brain barrier (BBB) [7-9].

ONC201 is the first member of a novel class of anti-cancer small molecules called imipridones, originally discovered by screening for p53-independent inducers of the immuno-surveillance cytokine TNF-related apoptosis-inducing ligand (TRAIL) and tumor cell death in human colorectal cancer cells [10, 11]. With p53-independency, low toxicity and excellent BBB penetration, ONC201 is currently being evaluated in multiple clinical trials for select advanced malignancies [12-19].

Emerging data suggest that a hierarchical organization within glioblastoma plays a crucial role in tumor development, therapy resistance and tumor recurrence [20-23] and interactions between tumor cells and the microenvironment are involved in tumor progression and the invasive nature of GBM [24]. Strategies to eradicate GICs at the apex of this hierarchy could be a valid approach for developing novel therapeutic approaches or modifying existing treatment regimen. Furthermore, GBM comprises of both a fast-dividing population and a relatively quiescent population, while conventional chemo- and radio-therapy largely target only the proliferative cell population [25-28]. Hence, mobilizing the quiescent cell population into proliferation to further sensitize them to existing therapies could be an approach to improve GBM treatment outcome.

In this study we demonstrate that the first-in-class compound of imipridones ONC201 in combination with radiation has anti-tumor efficacy against GBM *in vitro* and prolongs

overall survival in mouse models of GBM *in vivo*. Transcriptome analyses revealed shifts in gene signatures in response to radiation and ONC201, indicating effects of the combination treatment on quiescent GBM cells and their ability to interact with the extracellular matrix (ECM).

Material and Methods

Reagents

ONC201 was kindly provided by Oncoceutics, Inc. (Philadelphia, PA, USA). A 10 mM stock solution was prepared with dimethylsulfoxide (DMSO) for all *in vitro* experiments and stored in aliquots at -20°C . For *in vivo* studies, ONC201 was freshly prepared with sterile saline at a concentration of 5.5 mg/mL before injection.

Drug treatment

After confirming tumor grafting via bioluminescent imaging, mice bearing GL261 tumors or HK-374 specimen were injected intraperitoneally (i.p.) on a weekly basis either with ONC201 (50 mg/kg) or saline until they reached the euthanasia endpoint.

A detailed description of the cell culture conditions, *in-vitro* limiting dilution assay, clonogenic and cell viability assays, *in-vivo* bioluminescent imaging, irradiation procedures, immunohistochemistry, immunofluorescent staining, western blot, quantitative reverse transcription-PCR and RNA-sequencing is available in Supplementary Material. Primers are listed in Supplementary Table 1. The RNA-Seq data are available via GEO accession number GSE153982.

TCGA data mining and analysis

The TCGA Provisional dataset (captured June 1, 2020) was accessed via cBioPortal [29, 30]. Kaplan-Meier estimates were calculated for patients with upregulation (z -score >1.5) in one or more genes enriched in qGBM cells (gene list is available in Supplementary Material) and compared to patients with no alterations in the expression of those genes.

Statistics

All data were represented as means \pm standard error mean for at least 3 independent biological samples. All analyses were performed in the GraphPad Prism 8.0 software. An unpaired two-sided Student's t -test or Two-way ANOVA with a post hoc Bonferroni adjustment were used for comparisons. A log-rank test was used for Kaplan-Meier estimates. A p -value ≤ 0.05 was considered as statistically significant.

Results

ONC201 has been previously studied in diffuse intrinsic pontine gliomas (DIPG) carrying the H3K27 mutation and is a known inhibitor of DRD2/3 and an agonist of ClpP. In order to demonstrate target engagement after treatment of glioma cells that do not carry the H3K27 mutation we treated HK-374 and HK-382 glioma cells with ONC201 for 1 hour and performed Western blotting for Erk/p-Erk and Akt/p-Akt. ONC201 down-regulated

p-Akt and -to a lesser extent- pErk indicating that ONC201 inhibited DRD2/3 in both lines [31]. Likewise, treatment with ONC201 for 24 hours increased protein levels of ATF4 and TRAIL, consistent with an activation of ClpP [31] (Supplementary Fig. 1).

A radiobiological gold-standard for assessing the radiosensitizing properties of drugs is the clonogenic survival assay. Treatment of both HK-374 and HK-382 cells with ONC201 led to a significant, dose-dependent reduction in plating efficiency. Normalized to 0 Gy controls, ONC201 (0.5 μ M) decreased the surviving fraction from $33.1 \pm 3\%$ to $1.5 \pm 0.7\%$ ($p=1.2 \times 10^{-6}$) in HK-374 cells (Fig. 1A), while ONC201 (1 μ M) decreased the surviving fraction from $22.2 \pm 1.5\%$ to $0.7 \pm 0.12\%$ ($p=3.9 \times 10^{-3}$) in HK-382 cells (Fig. 1B). Higher concentrations of ONC201 in combination with 2 Gy prevented colony formation completely (Fig. 1C/D, Supplementary Fig. 2).

In order to assess an effect of ONC201 on DNA repair, we irradiated HK374 GBM in the presence/absence of ONC201. Using γ H2AX foci as surrogate markers for DNA double strand breaks (DSBs) we found that combined treatment of radiation and ONC201 significantly increased the number of initial DSBs at 1 hour when compared to the DMSO or radiation controls. Likewise, the combination treatment significantly increase the number of residual DSBs at 24 hours (Fig. 1 C/D), thus indicating interference of ONC201 with DNA DSB repair.

Gliomaspheres are known to enrich for GICs and gliomasphere formation from a single cell is a functional measure of self-renewal capacity [32, 33]. To assess the effect of ONC201 on self-renewal capacity, we first performed an *in vitro* limiting dilution assay using the patient-derived GBM lines HK-382, HK-374, HK-157, HK-345 and HK-308 (Table 1). Cells were treated with a single dose of radiation (0, 2, 4, 6 or 8 Gy) in the presence or absence of ONC201 (0, 0.5, 1 or 2.5 μ M). Treatment with ONC201 led to a dose-dependent reduction in sphere-formation (Fig. 1E/G, Supplementary Fig. 3B/D/F). Curve fitting of the sphere-forming data using a linear-quadratic model indicated that ONC201 did not radiosensitize GICs (Fig. 1F/H, Supplementary Fig. 3C/E/G).

Radiotherapy prolongs the survival of GBM patients, but the tumors almost always recur. In order to test if ONC201 inhibits self-renewal of GBM cells surviving combined treatment of a sublethal dose of radiation and ONC201 we performed secondary and tertiary sphere-formation assays in the absence and presence of ONC201 (Supplementary Fig. 3H). Combined treatment reduced primary, secondary and tertiary sphere-formation in both, the HK-374 line (established from a primary GBM) (Fig. 1I) and the HK-308 line (established from a recurrent GBM) (Fig. 1J) when compared to spheres formed from cells treated with 4 Gy only.

In order to better understand the effects of ONC201 in combination with radiation, we performed RNA-Sequencing on HK-374 cells. Principal component analysis showed that biologically-independent replicates of each experimental group clustered closely, indicating reproducibility of the results (Supplementary Fig. 4A). Hierarchical clustering of differentially expressed genes revealed a distinct gene expression profile after combined treatment (Supplementary Fig. 4B). Radiation caused differential up-regulation of 1711

genes and down-regulation of 1680 genes when compared to DMSO control, while combined treatment led to 3048 differentially up-regulated and 3156 down-regulated genes when compared to radiation only. We also compared combination-treated samples and ONC201-treated samples to DMSO-treated controls and found 3190 differentially up-regulated and 3158 down-regulated genes in combination-treated, and 2989 differentially up-regulated and 3223 down-regulated genes in ONC201-treated cells (Supplementary Fig. 4C). The top 10 up- and down-regulated genes with their \log_2 -fold changes are shown in Supplementary Fig. 4D. The top up- and down-regulated genes in cells after combined treatment compared to irradiated only were validated using qRT-PCR (Supplementary Fig. 4E).

Next, we performed a GO enrichment analysis of DEGs in irradiated versus control samples. Differentially up-regulated genes overlapped with gene sets containing ECM components (Supplementary Fig. 4F, **Top**), while down-regulated genes overlapped with gene sets involved in DNA replication, chromatin binding, and mitotic nuclear division (Supplementary Fig. 4F, **Bottom**). DEGs in combination-treated versus irradiated cells, overlapped with gene sets involved in catabolism, cellular response to extracellular stimuli, and DNA-binding transcription repressor activity (Supplementary Fig. 4G, **Top**), while down-regulated DEGs overlapped with gene sets involved in cell adhesion, mitotic nuclear division, and DNA replication (Supplementary Fig. 4G, **Bottom**).

Assessing global gene expression changes using GSEA in combination-treated versus irradiated cells we found DEGs in combination-treated cells overlapping with the Hallmark gene sets of apoptosis and the p53 pathway (Fig. 2A), consistent with the pro-apoptotic properties of ONC201 and a p53 response to radiation. Furthermore, DEGs up-regulated in response to combined treatment overlapped with gene sets of the unfolded protein response, TNF α and IL-6/Stat3 and mTORC1 signaling, IFN γ response, xenobiotic and heme metabolism, genes up-regulated in response to UV and an inflammatory response (Supplementary Fig. 4H). Down-regulated DEGs in combination-treated cells overlapped with the gene sets of E2F targets, G2M checkpoint, mitotic spindle, apical surface, epithelial mesenchymal transition (EMT) and myogenesis (Fig. 2B, Supplementary Fig. 4J). Heat maps of genes contributing to the leading edge of each gene set are shown in Supplementary Fig. 4I/K.

GBM are known for their intratumoral heterogeneity. A recent study reported the presence of a relatively quiescent cell population in GBM (qGBM) that exhibited self-renewal capacity comparable to its proliferative counterparts (pGBM) but showed higher therapeutic resistance and distinct gene expression signatures [25]. We had previously confirmed the presence of quiescent and proliferating cells with self-renewal capacity in GBM and also reported recruitment of qGICs cells into the cell cycle in response to radiation [34]. Analyzing our transcriptome data, we observed pattern changes in gene sets associated with cell cycle growth, EMT, metabolism, mitochondria, and stress pathway in response to radiation (Supplementary Fig. 4L, **left**) consistent with the recruitment of qGICs into the cell cycle. Treatment of the cells with ONC201 led to a down-regulation of genes involved in the G2/M checkpoint, EMT-related genes and genes involved in oxidative phosphorylation, consistent with ClpP agonism, while up-regulating angiogenesis,

mTORC1 signaling, UV response, apoptosis, unfolded protein response, TNF α and IL2/Stat5 signaling (Supplementary Fig. 4L, **right**). Compared to radiation alone, combined treatment reduced the expression of genes involved in G2/M checkpoint control, protein secretion, EMT, oxidative phosphorylation and DNA repair, while increasing the expression of Myc target genes, hypoxia-related genes, genes involved in xenobiotic metabolism, UV response, TNF α , IL2/Stat5, TGF β and inflammatory response (Fig. 2C). A subpopulation of GBM cells is thought to acquire and maintain quiescence through ECM organization and interaction with niche factors [25].

When compared to irradiated samples, the combined treatment significantly down-regulated genes involved in ECM interaction, while irradiation or treatment with ONC201 alone did not significantly affect the expression of these genes (Fig. 2D). Western blotting confirmed this effect in a subset of proteins down- or up-regulated in qGICs (Fig. 2E). Lastly, when compared to radiation alone, the combined treatment reduced the expression of genes overlapping with gene sets of GBM plasticity, glioma stem cells and targets of the developmental transcription factor Oct4 (Fig. 2F, Supplementary Fig. 4M).

Based on the *in-vitro* effect of ONC201 on the self-renewal capacity, we tested whether ONC201 also had anti-tumor activity in a murine model of GBM *in vivo*. In C57BL/6 mice bearing orthotopic GL261 tumors, a single radiation dose of 10 Gy three days after implantation led to a significant increase in survival (10 Gy + Saline *v.s.* Saline: 120.5 *v.s.* 24 days, $p < 0.0001$). Weekly treatment with ONC201 alone had a smaller but significant effect on median survival (ONC201 *v.s.* Saline: 42 *v.s.* 24 days, $p < 0.0001$; ONC201 *v.s.* 10 Gy + Saline: 42 *v.s.* 120.5 days, $p < 0.0001$). However, a single dose of 10 Gy combined with weekly ONC201 treatments led to a significant increase in survival compared to irradiation or ONC201 alone (10 Gy + ONC201 *v.s.* 10 Gy + Saline: $p = 0.0173$, median survival not reached in 10 Gy + ONC201 group) with 80 % of the animals showing no signs of tumor growth 240 days after the start of the experiment (Fig. 3A) and no toxicity (Fig. 3B). Bioluminescence imaging of the tumors at day 3 (pre-treatment) and at day 28 (days post-implantation) showed a reduction of signal intensity after combined treatment, consistent with the observed increase in survival (Fig. 3C). Likewise, a single dose of 10 Gy led to a central necrosis of the tumors and ONC201 treatment alone had little effect, while the combined treatment caused an almost complete regression of the tumors (Fig. 3D). Ki67 staining of coronal brain sections of mice that reached euthanasia endpoints did not indicate a reduction in proliferation by radiation or ONC201 alone. However, the combined treatment decreased the number of proliferating cells at the injection site (Fig. 3E), which was in line with the observed reduction of the bioluminescence signal (Fig. 3C), the reduced tumor size (Fig. 3D) and the improved survival after combined treatment (Fig. 3A).

Furthermore, immunohistochemistry staining revealed induction of c-Myc expression by radiation, which agreed with our previous report on radiation-induced acquisition of a GIC phenotype of non-tumorigenic cells [34]. This was also seen after ONC201 treatment but was completely abolished after combined treatment (Fig. 3F). A single dose of 10 Gy or ONC201 treatment reduced the number of CD133-positive cells in GL261 tumors. Combined treatment with radiation and ONC201 further reduced the number of CD133-positive and reduced the number of Ki67-positive cells (Fig. 3G).

Next, we verified these findings using patient-derived orthotopic xenografts. The same implantation and treatment procedures were performed with HK-374 glioblastoma cells in NSG mice. Again, ONC201 treatment led to a small increase in median survival (ONC201 *v.s.* Saline: 60.5 *v.s.* 34 days, $p < 0.0001$), while 10 Gy alone did not significantly prolong median survival (10 Gy + Saline *v.s.* Saline: 100 *v.s.* 34 days, $p = 0.1155$; 10 Gy + Saline *v.s.* ONC201: 100 *v.s.* 60.5 days, $p = 0.1472$). However, the combined treatment increased overall survival when compared to 10 Gy group (10 Gy + ONC201 *v.s.* 10 Gy + Saline: $p = 0.0059$, median survival not reached in 10 Gy + ONC201 group) with 70% of the animals showing no signs of tumors growth 250 days after start of the experiment (Fig. 3H) and toxicity (Fig. 3I).

To further investigate whether qGBM-enriched ECM-related gene expression is indeed associated with clinical outcome in GBM, we analyzed overall survival (OS) and progression-free survival (PFS) data from 206 GBM patients in the TCGA Provisional Dataset, stratified into subgroups with altered or unaltered expression of one or more ECM-related genes over-expressed in qGBM cells. Patients with increased expression of ECM-related genes showed an inferior median PFS (5.4 *v.s.* 8.2 months, $p\text{-value} = 6.745e-3$) and OS (11.9 *v.s.* 14.3 months, $p\text{-value} = 0.0357$) compared to those with unaltered expression of these genes (Fig. 4A/B).

Discussion

Despite decades of research aimed at improving the treatment outcome for GBM patients, OS for this disease still remain dismal. The current standard-of-care with postoperative radiotherapy and temozolomide treatment prolongs PFS by only 3 months and almost all tumors recur [35]. Reasons for treatment failure include the lack of BBB penetration of drugs, the infiltrative nature of GBMs, cellular plasticity and intratumoral heterogeneity [4, 36, 37] with a small number of therapy-resistant GICs able to re-grow a tumor [38-40].

Previous studies have shown expression of DRD2 in GBM, with elevated DRD2 expression in the GIC population [41, 42]. DRD2 signaling is involved in maintaining self-renewal [42], activating hypoxia response and functionally altering metabolism of GBM in a potentially autocrine manner [41], indicating that DRD2 could be a therapeutic target in GBM.

So far, clinical trials using ONC201 against GBM have shown pharmacodynamic activity in biomarker-defined recurrent GBM patients, as well as in pediatric and adult H3 K27M-mutant glioma [13, 17, 18].

We have recently reported that radiation in combination with the first-generation dopamine receptor antagonist trifluoperazine prolonged survival in mouse GBM models [34]. Here we show that radiation in combination with ONC201 reduced the viability of bulk cells, radiosensitized clonogenic GBM cells and reduced the self-renewal capacity of GICs *in vitro*. Combined treatment led to distinct changes in gene expression, consistent with an induction of cell death, downregulation of DNA repair and elimination of GICs. Furthermore, combined treatment prevented the radiation-induced expression of gene sets correlated with GBM plasticity, glioma stem cells, Oct4 targets and interfered with cell

growth, ECM interaction and EMT genes, thought to be involved in neural-to-mesenchymal transition, and the metabolism of GBM cells. This agreed with a previous study reporting effects of ONC201 on glioma stem cells [43].

In vivo, a single dose of radiation combined with continuous, weekly ONC201 treatment translated into significantly prolonged median survival in mouse models of GBM. This was accompanied by tumor regression and loss of Ki67 and c-Myc staining, which was consistent with our *in-vitro* data and indicated a previously unknown efficacy of ONC201 in combination with radiation. Most importantly, the combined treatment was well tolerated and did not lead to treatment-related toxicity.

Our data suggest that the combination of radiation with ONC201 counteracts defense mechanisms of GBM cells against radiation without acting as a classical radiosensitizer against GICs but only non-stem GBM cells. We conclude that ONC201 in combination with radiation could be a promising new strategy against GBM that should be tested in clinical trials.

Supplementary Material

Refer to Web version on PubMed Central for supplementary material.

Funding:

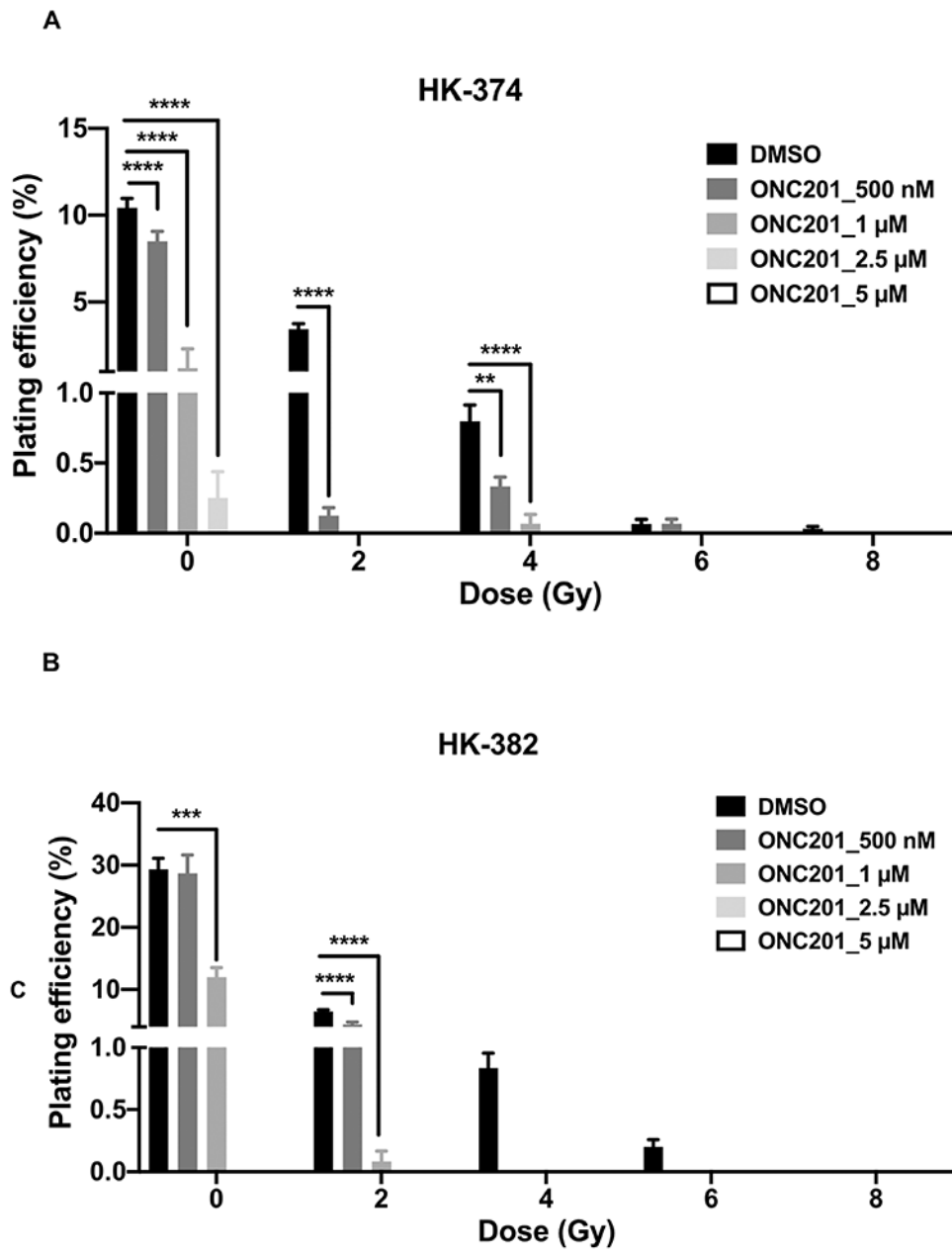
FP was supported by a grant from the *National Cancer Institute* (R01CA200234). PLN, TFC, LML, HIK, and FP were supported by a grant from the *National Cancer Institute* (UCLA Brain Tumor SPORE P50CA211015).

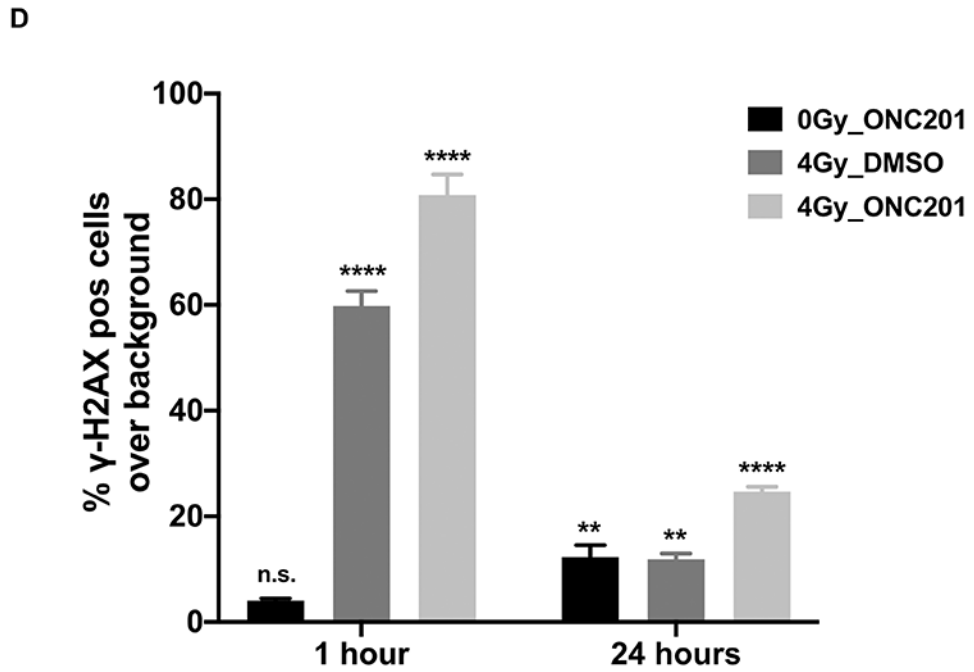
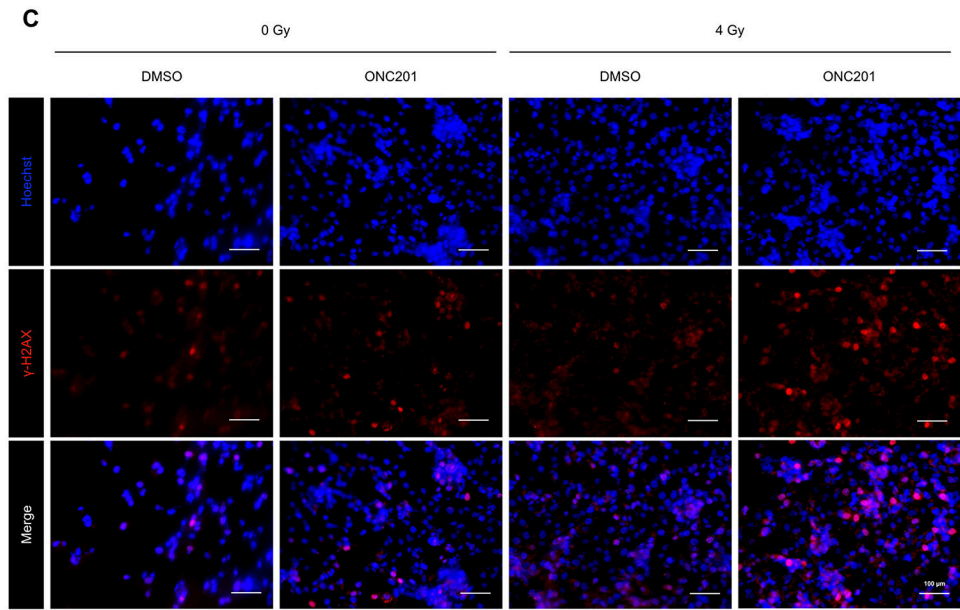
References

1. Laperriere N, et al., Radiotherapy for newly diagnosed malignant glioma in adults: a systematic review. *Radiother Oncol*, 2002. 64(3): p. 259–73. [PubMed: 12242114]
2. Chan JL, et al., Survival and failure patterns of high-grade gliomas after three-dimensional conformal radiotherapy. *J Clin Oncol*, 2002. 20(6): p. 1635–42. [PubMed: 11896114]
3. Osuka S and Van Meir EG, Overcoming therapeutic resistance in glioblastoma: the way forward. *J Clin Invest*, 2017. 127(2): p. 415–426. [PubMed: 28145904]
4. Dirkse A, et al., Stem cell-associated heterogeneity in Glioblastoma results from intrinsic tumor plasticity shaped by the microenvironment. *Nat Commun*, 2019. 10(1): p. 1787. [PubMed: 30992437]
5. Auffinger B, et al., The role of glioma stem cells in chemotherapy resistance and glioblastoma multiforme recurrence. *Expert Rev Neurother*, 2015. 15(7): p. 741–52. [PubMed: 26027432]
6. Shergalis A, et al., Current Challenges and Opportunities in Treating Glioblastoma. *Pharmacol Rev*, 2018. 70(3): p. 412–445. [PubMed: 29669750]
7. Drean A, et al., Blood-brain barrier, cytotoxic chemotherapies and glioblastoma. *Expert Rev Neurother*, 2016. 16(11): p. 1285–1300. [PubMed: 27310463]
8. Laquintana V, et al., New strategies to deliver anticancer drugs to brain tumors. *Expert Opin Drug Deliv*, 2009. 6(10): p. 1017–32. [PubMed: 19732031]
9. Wang D, et al., A comprehensive review in improving delivery of small-molecule chemotherapeutic agents overcoming the blood-brain/brain tumor barriers for glioblastoma treatment. *Drug Deliv*, 2019. 26(1): p. 551–565. [PubMed: 31928355]
10. Allen JE, et al., Dual inactivation of Akt and ERK by TIC10 signals Foxo3a nuclear translocation, TRAIL gene induction, and potent antitumor effects. *Sci Transl Med*, 2013. 5(171): p. 171ra17.

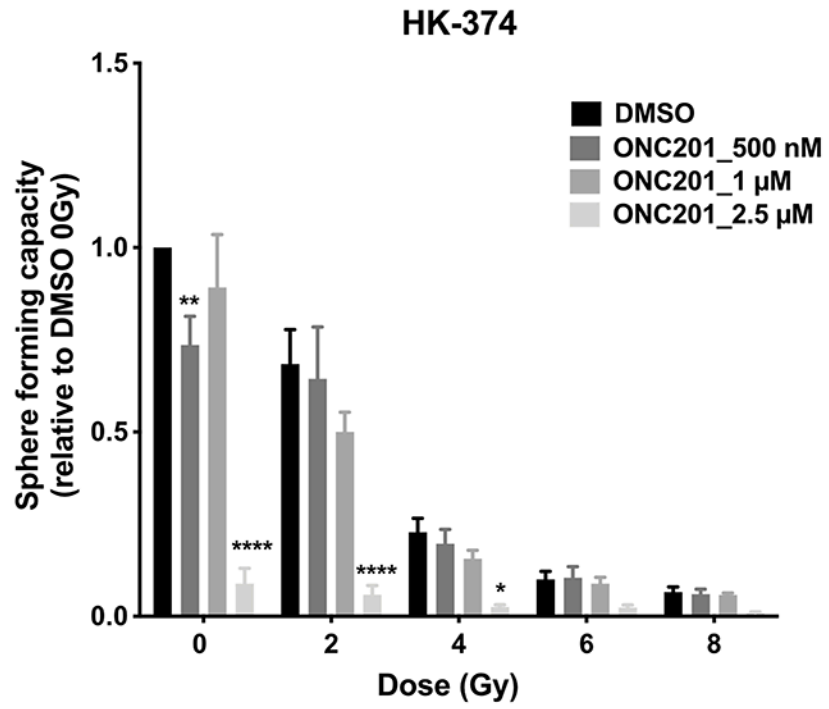
11. Allen JE, et al., Identification of TRAIL-inducing compounds highlights small molecule ONC201/TIC10 as a unique anti-cancer agent that activates the TRAIL pathway. *Mol Cancer*, 2015. 14: p. 99. [PubMed: 25927855]
12. Arrillaga-Romany I, et al., Biological activity of weekly ONC201 in adult recurrent glioblastoma patients. *Neuro Oncol*, 2020. 22(1): p. 94–102. [PubMed: 31702782]
13. Arrillaga-Romany I, et al., A phase 2 study of the first imipridone ONC201, a selective DRD2 antagonist for oncology, administered every three weeks in recurrent glioblastoma. *Oncotarget*, 2017. 8(45): p. 79298–79304. [PubMed: 29108308]
14. Stein MN, et al., Safety and enhanced immunostimulatory activity of the DRD2 antagonist ONC201 in advanced solid tumor patients with weekly oral administration. *J Immunother Cancer*, 2019. 7(1): p. 136. [PubMed: 31118108]
15. Prabhu VV, et al., Single agent and synergistic combinatorial efficacy of first-in-class small molecule imipridone ONC201 in hematological malignancies. *Cell Cycle*, 2018. 17(4): p. 468–478. [PubMed: 29157092]
16. Stein MN, et al., First-in-Human Clinical Trial of Oral ONC201 in Patients with Refractory Solid Tumors. *Clin Cancer Res*, 2017. 23(15): p. 4163–4169. [PubMed: 28331050]
17. Hall MD, et al., First clinical experience with DRD2/3 antagonist ONC201 in H3 K27M-mutant pediatric diffuse intrinsic pontine glioma: a case report. *J Neurosurg Pediatr*, 2019: p. 1–7.
18. Chi AS, et al., Pediatric and adult H3 K27M-mutant diffuse midline glioma treated with the selective DRD2 antagonist ONC201. *J Neurooncol*, 2019. 145(1): p. 97–105. [PubMed: 31456142]
19. Romaguera JE, et al., Integrated stress response and immune cell infiltration in an ibrutinib-refractory mantle cell lymphoma patient following ONC201 treatment. *Br J Haematol*, 2019. 185(1): p. 133–136. [PubMed: 29740811]
20. Hemmati HD, et al., Cancerous stem cells can arise from pediatric brain tumors. *Proc Natl Acad Sci U S A*, 2003. 100(25): p. 15178–83. [PubMed: 14645703]
21. Singh SK, et al., Identification of human brain tumour initiating cells. *Nature*, 2004. 432(7015): p. 396–401. [PubMed: 15549107]
22. Bao S, et al., Glioma stem cells promote radioresistance by preferential activation of the DNA damage response. *Nature*, 2006. 444(7120): p. 756–60. [PubMed: 17051156]
23. Eramo A, et al., Chemotherapy resistance of glioblastoma stem cells. *Cell Death Differ*, 2006. 13(7): p. 1238–41. [PubMed: 16456578]
24. Matarredona ER and Pastor AM, Extracellular Vesicle-Mediated Communication between the Glioblastoma and Its Microenvironment. *Cells*, 2019. 9(1).
25. Tejero R, et al., Gene signatures of quiescent glioblastoma cells reveal mesenchymal shift and interactions with niche microenvironment. *EBioMedicine*, 2019. 42: p. 252–269. [PubMed: 30952620]
26. Moore N and Lyle S, Quiescent, slow-cycling stem cell populations in cancer: a review of the evidence and discussion of significance. *J Oncol*, 2011. 2011.
27. Gasch C, et al., Catching moving targets: cancer stem cell hierarchies, therapy-resistance & considerations for clinical intervention. *Mol Cancer*, 2017. 16(1): p. 43. [PubMed: 28228161]
28. Ahmed AU, Auffinger B, and Lesniak MS, Understanding glioma stem cells: rationale, clinical relevance and therapeutic strategies. *Expert Rev Neurother*, 2013. 13(5): p. 545–55. [PubMed: 23621311]
29. Cerami E, et al., The cBio cancer genomics portal: an open platform for exploring multidimensional cancer genomics data. *Cancer Discov*, 2012. 2(5): p. 401–4. [PubMed: 22588877]
30. Gao J, et al., Integrative analysis of complex cancer genomics and clinical profiles using the cBioPortal. *Sci Signal*, 2013. 6(269): p. p11. [PubMed: 23550210]
31. Ishizawa J, et al., Mitochondrial ClpP-Mediated Proteolysis Induces Selective Cancer Cell Lethality. *Cancer Cell*, 2019. 35(5): p. 721–737 e9. [PubMed: 31056398]
32. Lathia JD, et al., Cancer stem cells in glioblastoma. *Genes Dev*, 2015. 29(12): p. 1203–17. [PubMed: 26109046]

33. Pastrana E, Silva-Vargas V, and Doetsch F, Eyes wide open: a critical review of sphere-formation as an assay for stem cells. *Cell Stem Cell*, 2011. 8(5): p. 486–98. [PubMed: 21549325]
34. Bhat K, et al., The dopamine receptor antagonist trifluoperazine prevents phenotype conversion and improves survival in mouse models of glioblastoma. *Proc Natl Acad Sci U S A*, 2020. 117(20): p. 11085–11096. [PubMed: 32358191]
35. Fernandes C, et al., Current Standards of Care in Glioblastoma Therapy, in *Glioblastoma*, De Vleeschouwer S, Editor. 2017: Brisbane (AU).
36. Harder BG, et al., Developments in Blood-Brain Barrier Penetrance and Drug Repurposing for Improved Treatment of Glioblastoma. *Front Oncol*, 2018. 8: p. 462. [PubMed: 30406029]
37. Lemee JM, Clavreul A, and Menei P, Intratumoral heterogeneity in glioblastoma: don't forget the peritumoral brain zone. *Neuro Oncol*, 2015. 17(10): p. 1322–32. [PubMed: 26203067]
38. Goffart N, Kroonen J, and Rogister B, Glioblastoma-initiating cells: relationship with neural stem cells and the micro-environment. *Cancers (Basel)*, 2013. 5(3): p. 1049–71. [PubMed: 24202333]
39. Ikushima H, et al., Autocrine TGF-beta signaling maintains tumorigenicity of glioma-initiating cells through Sry-related HMG-box factors. *Cell Stem Cell*, 2009. 5(5): p. 504–14. [PubMed: 19896441]
40. Niibori-Nambu A, et al., Glioma initiating cells form a differentiation niche via the induction of extracellular matrices and integrin alphaV. *PLoS One*, 2013. 8(5): p. e59558. [PubMed: 23704872]
41. Caragher SP, et al., Activation of Dopamine Receptor 2 Prompts Transcriptomic and Metabolic Plasticity in Glioblastoma. *J Neurosci*, 2019. 39(11): p. 1982–1993. [PubMed: 30651332]
42. Li Y, et al., Paired related homeobox 1 transactivates dopamine D2 receptor to maintain propagation and tumorigenicity of glioma-initiating cells. *J Mol Cell Biol*, 2017. 9(4): p. 302–314. [PubMed: 28486630]
43. Prabhu VV, et al., Cancer stem cell-related gene expression as a potential biomarker of response for first-in-class imipridone ONC201 in solid tumors. *PLoS One*, 2017. 12(8): p. e0180541. [PubMed: 28767654]

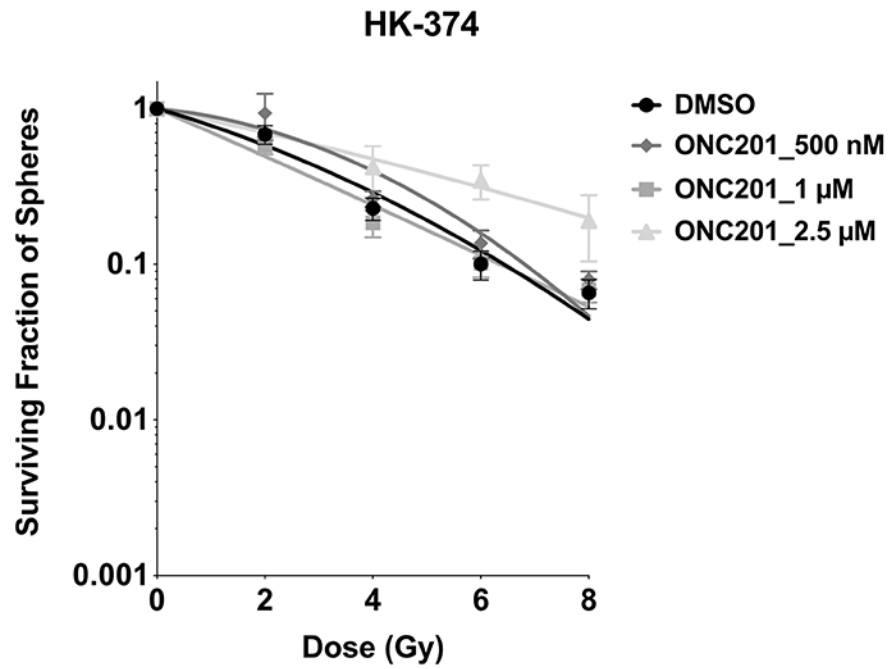




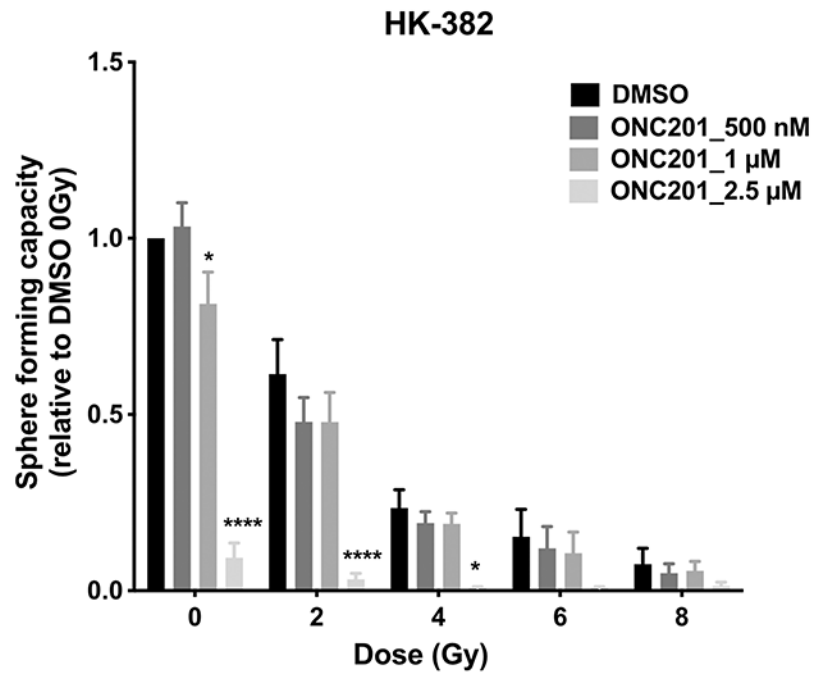
E



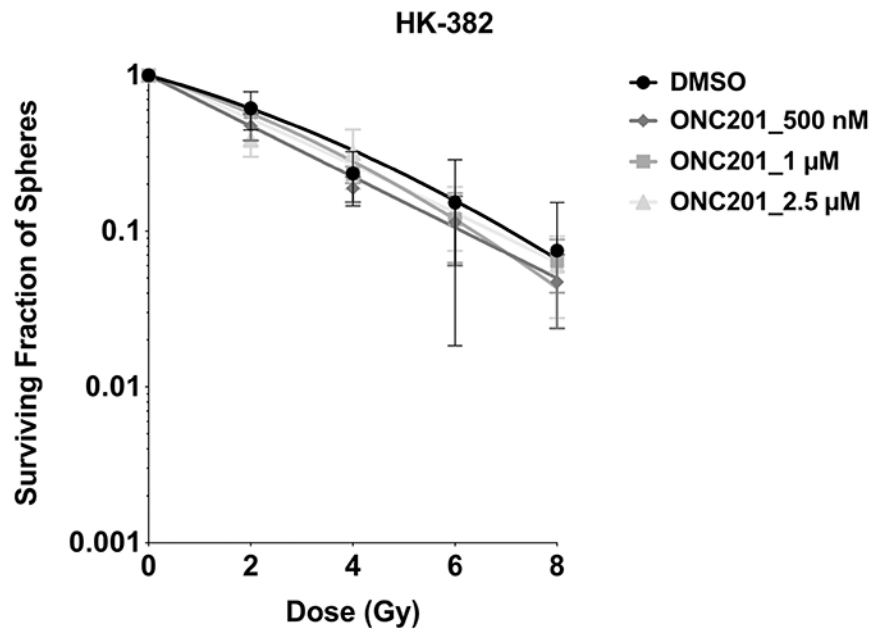
F



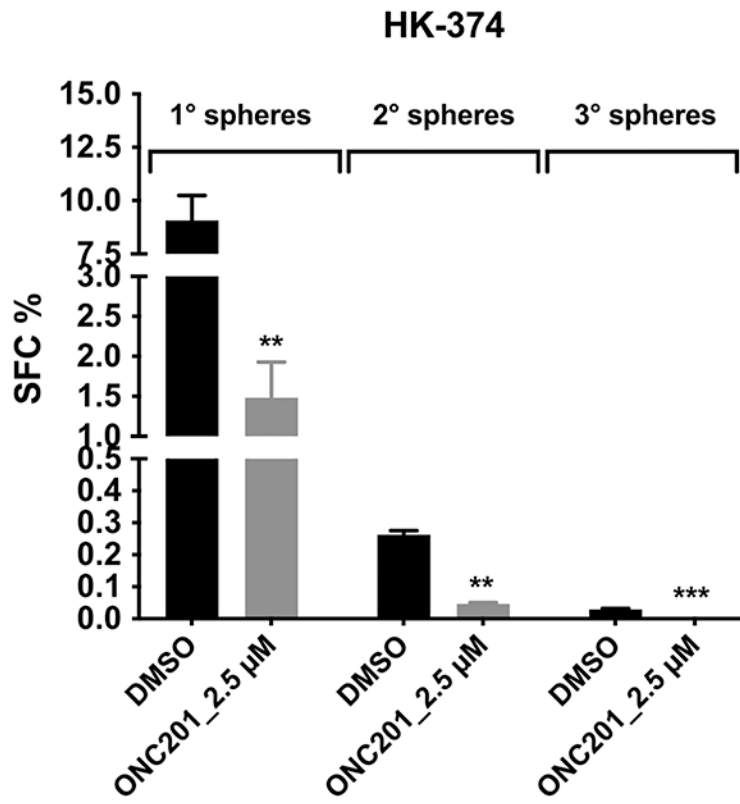
G



H



I.



J.

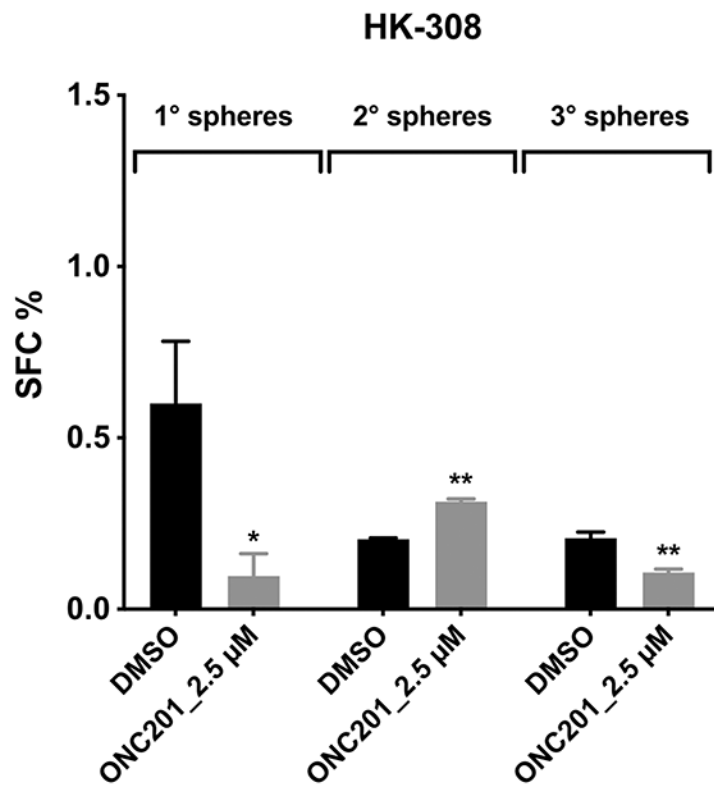
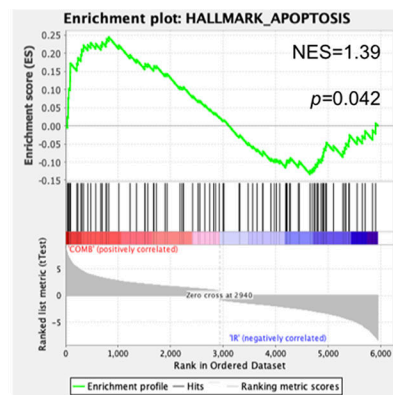
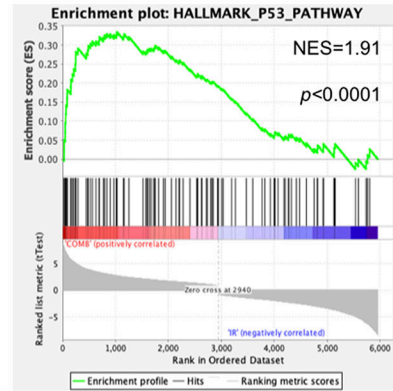


Figure 1. Effects of ONC201 on GBM cells *in vitro*.

(A/B) Clonogenic assay of patient-derived primary HK-374 and HK-382 GBM cells treated with ONC201 (500 nM, 1 μ M, 2.5 μ M and 5 μ M) or solvent control (DMSO) in combination with a single dose of radiation (0, 2, 4, 6 or 8 Gy). The colony number was counted and presented as the percentage relative to the initial number of cells plated. (C) γ H2AX immunofluorescent staining of HK-374 GBM cells treated with 2.5 μ M ONC201 or DMSO in combination with a single dose of radiation (4 Gy) for 24 hours. (D) Quantification of the percentage of γ H2AX positive cells over background at 1 hour and 24 hours after radiation, respectively. (E-H) Patient-derived HK-374 and HK-382 GBM cells were used to perform sphere-forming assays with sham-irradiated or irradiated cells in the presence or absence of ONC201 (500 nM, 1 μ M, 2.5 μ M). The spheres were cultured in suspension for 7-10 days. The number of spheres formed under each condition were counted and presented as percentage spheres formed and normalized against the sham-irradiated control. (I/J) Sphere-forming capacity (SFC%) was evaluated using HK-374 and HK-308 derived secondary and tertiary spheres in the presence or absence of 2.5 μ M ONC201 using a limiting dilution assay. All experiments have been performed with at least 3 biological independent repeats. *p*-values were calculated using two-way ANOVA for A-H; multiple Student's *t*-tests for J and K. * *p*-value<0.05, ** *p*-value<0.01, *** *p*-value<0.001 and **** *p*-value<0.0001.

A



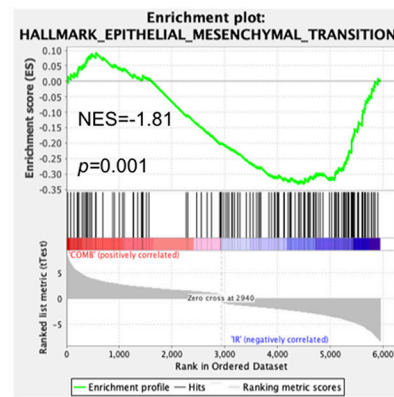
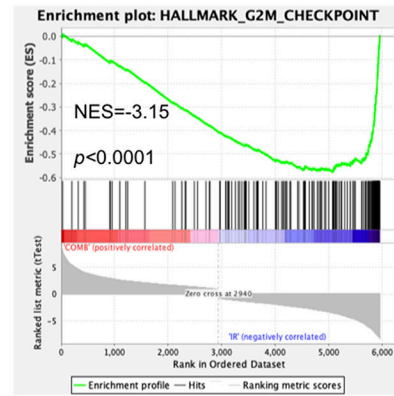
B

Author Manuscript

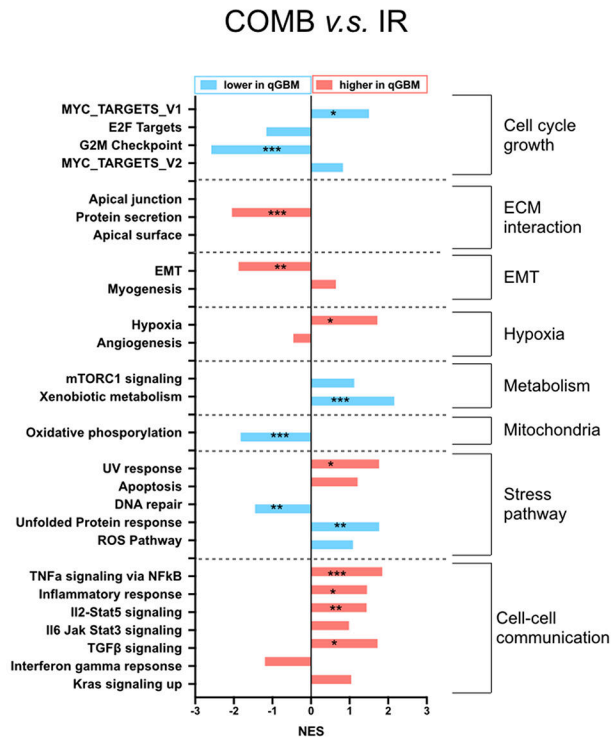
Author Manuscript

Author Manuscript

Author Manuscript



C



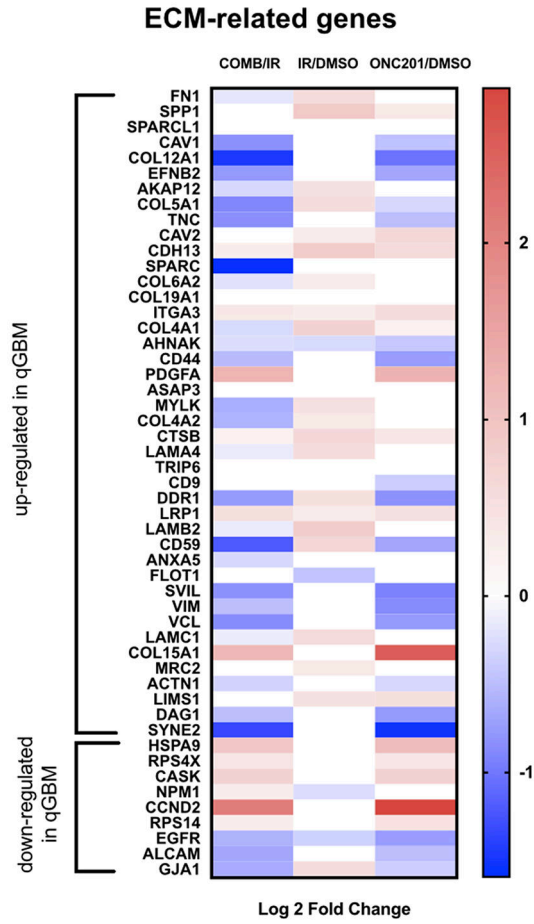
Author Manuscript

Author Manuscript

Author Manuscript

Author Manuscript

D



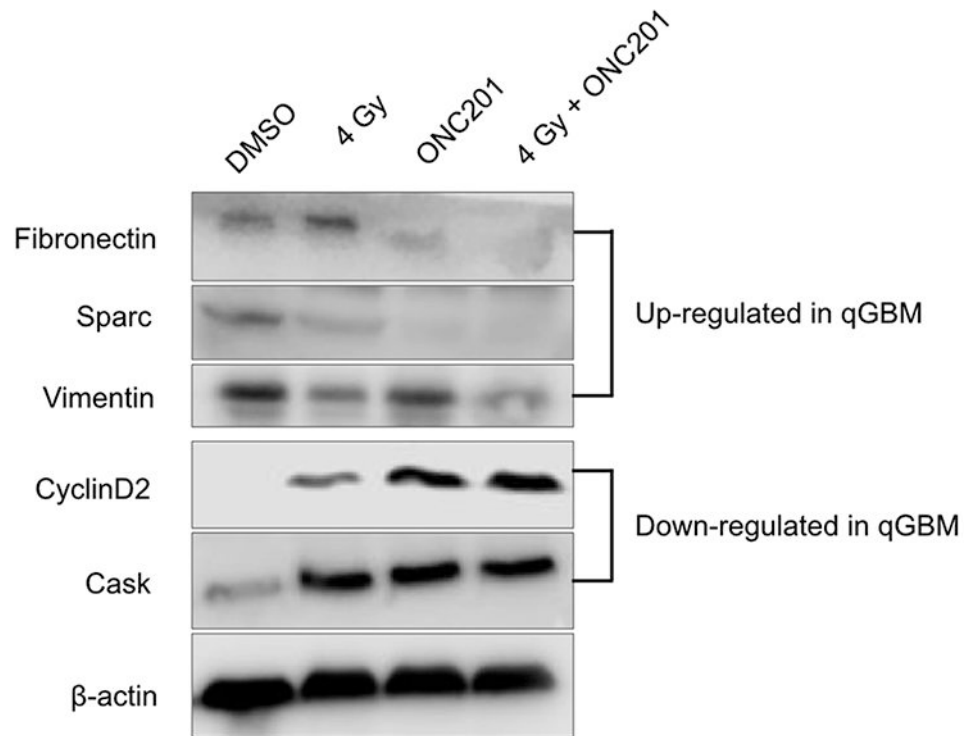
Author Manuscript

Author Manuscript

Author Manuscript

Author Manuscript

E



F

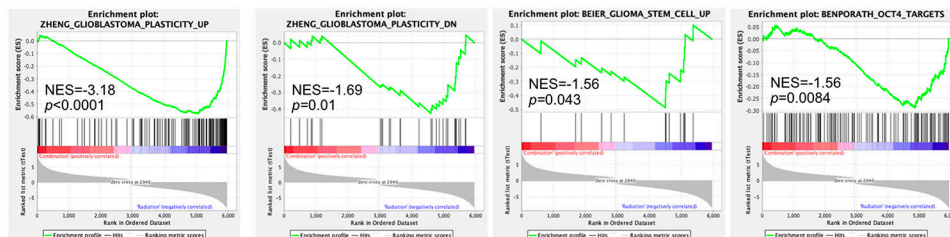


Figure 2. RNA-Seq analysis of glioma cells treated with ONC201 and radiation. (A/B) GSEA results of the gene sets that are positively or negatively enriched in the combination of ONC201 and radiation as compared to radiation alone. NES, normalized enrichment score. (C) GSEA of quiescent GBM (qGBM) gene signatures in the comparisons COMB *v.s.* IR, displayed with normalized enrichment scores. Red indicates the gene sets highly expressed in qGBM, while the blue represents gene sets with low expression in qGBM. The nominal *p*-value was labeled with * <0.05 ; ** <0.01 ; *** <0.001 . (D) Heatmap of ECM-related gene expressions in the comparisons, e.g., IR *v.s.* DMSO, COMB *v.s.* IR, ONC201 *v.s.* DMSO, stratified by whether these genes are up- and down-regulated in qGBM. (E) Western blot verification of selected up-regulated ECM-related proteins (Fibronectin, Sparc and Vimentin) and down-regulated ECM-related proteins (CyclinD2 and Cask) in qGICs, with β -actin as a loading control. Proteins were extracted from HK374

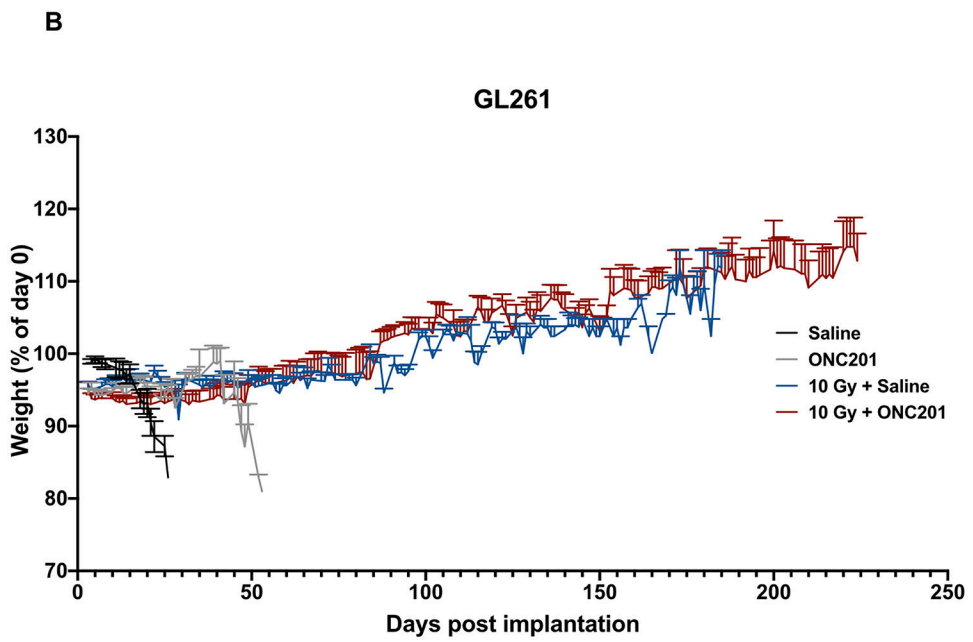
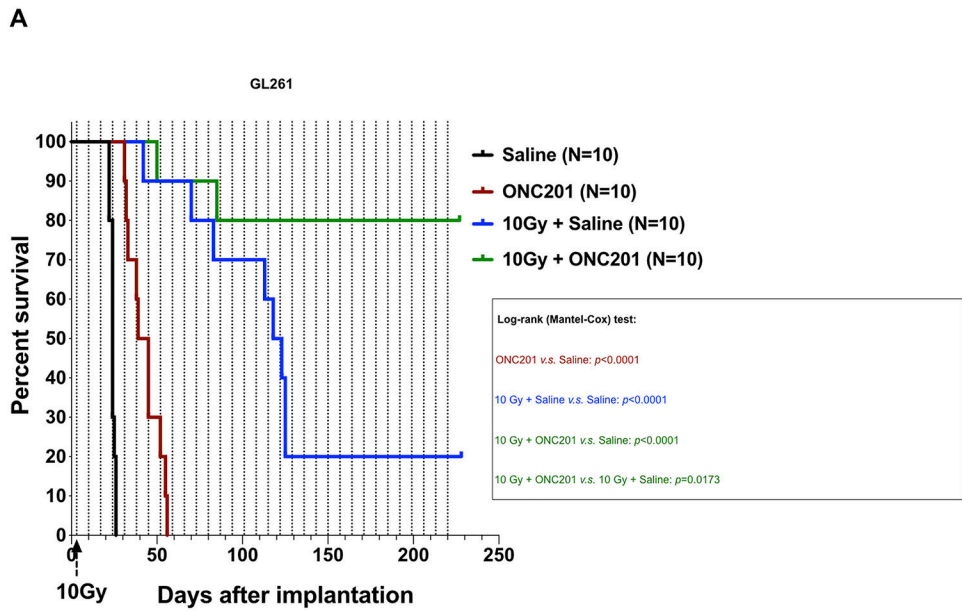
spheres treated with 2.5 μM ONC201 or DMSO in combination with a single dose of radiation (4 Gy) for 48 hours. (F) GSEA results of the gene sets of glioblastoma plasticity, glioma stem cells and targets of the developmental transcription factor Oct4 in the combined treatment of ONC201 and radiation (COMB) compared to radiation alone (IR), displayed with Enrichment plots.

Author Manuscript

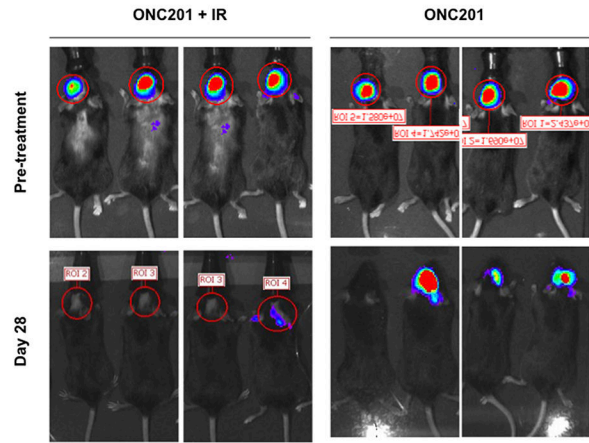
Author Manuscript

Author Manuscript

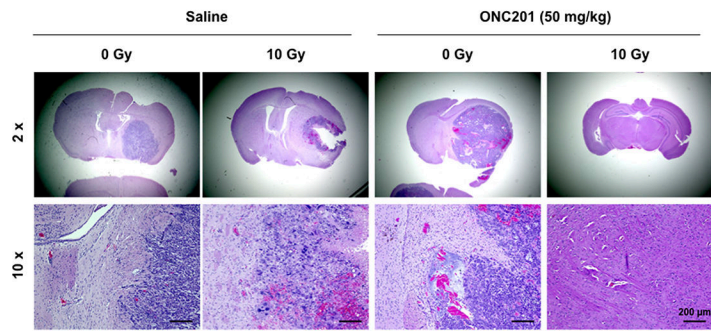
Author Manuscript



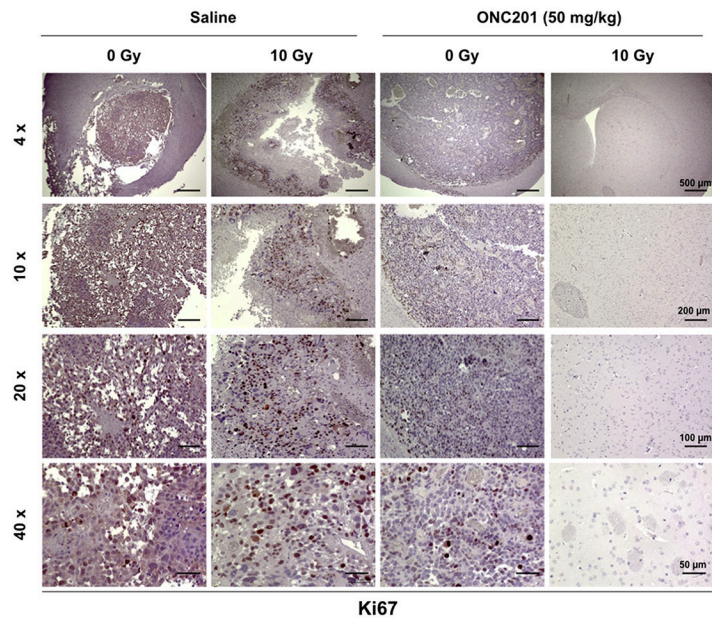
C



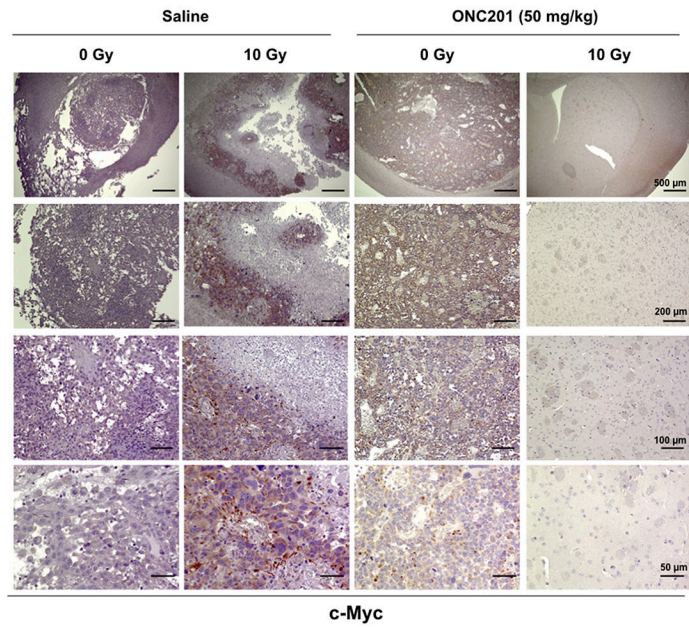
D

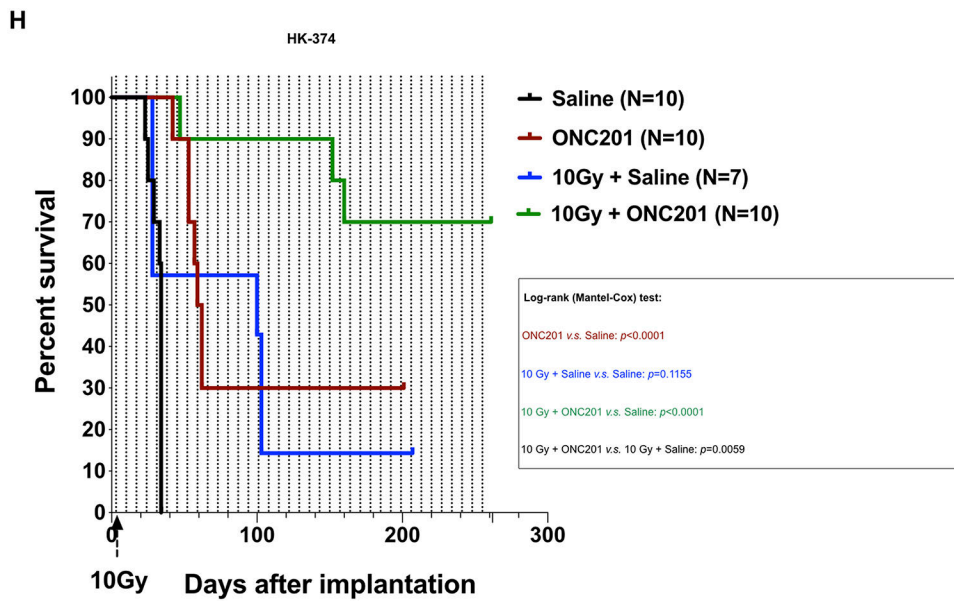
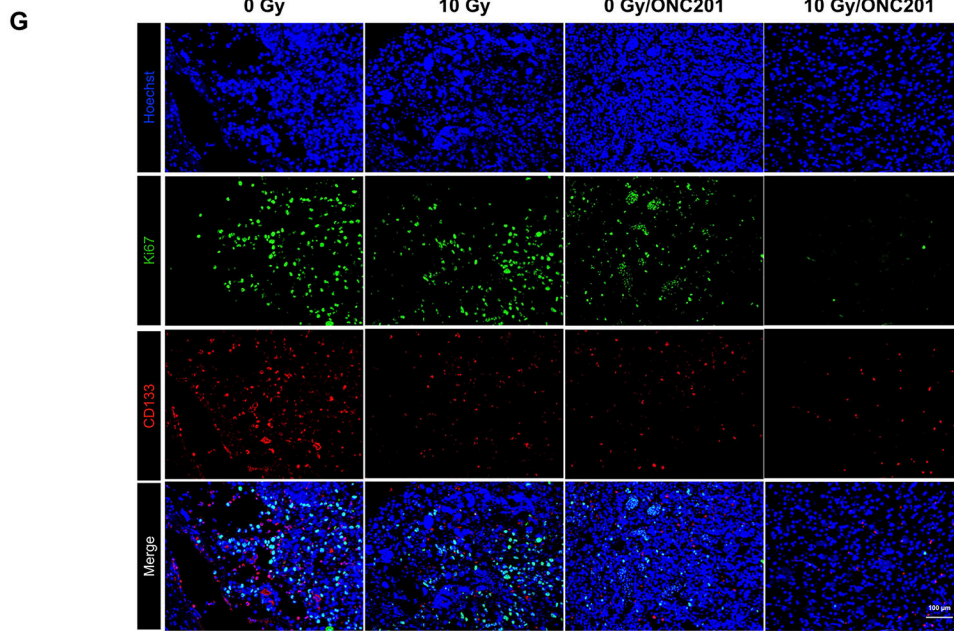


E



F





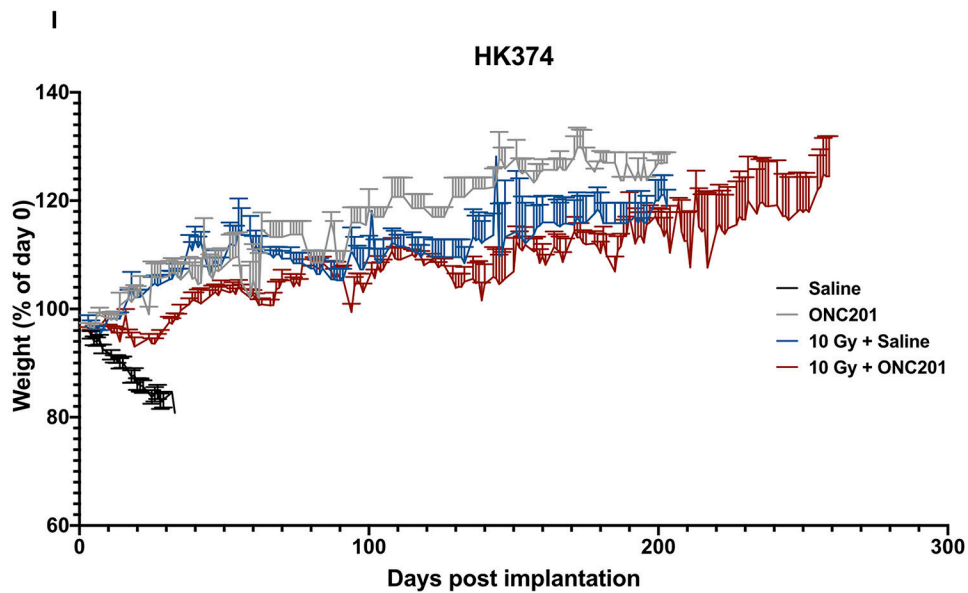


Figure 3. Combination of ONC201 and radiation prolongs survival in mouse models of glioblastoma.

(A) Survival curves for C57BL/6 mice implanted intra-cranially with 2×10^5 GL261-GFP-Luciferase mouse glioma cells. Tumors were grown for 3 days for successful grafting. Mice were irradiated with a single fraction of 0 or 10 Gy and weekly treated with Saline or ONC201 (50 mg/kg, i.p.) continuously until they reached the study endpoint. Log-rank (Mantel-Cox) test for comparison of Kaplan-Meier survival curves indicated significant differences in the ONC201 treated mice compared to their respective controls. ONC201 *v.s.* Saline (**** p -value<0.0001), 10 Gy + Saline *v.s.* Saline (**** p -value<0.0001), 10 Gy + ONC201 *v.s.* Saline (**** p -value<0.0001), 10 Gy + ONC201 *v.s.* 10 Gy + Saline (* p -value=0.0173). (B) Weight curves for the C57BL/6 mice in the different treatment groups. (C) Bio-luminescence images of mice bearing tumors obtained at day 3 (pre-treatment) and at day 28 (days post implantation). (D) H&E stained coronal sections of the C57BL/6 mice brains implanted with GL261-GFP-Luc cells which were treated continuously with either ONC201 or saline until they met the criteria for study endpoint. (E/F) 4x, 10x, 20x and 40x images of Ki67 and c-Myc stained coronal sections of brains from C57BL/6 mice implanted with GL261-GFP-Luc cells and treated with either ONC201 (50 mg/kg) or saline in the presence or absence of a single dose of radiation (10 Gy) at the study endpoint. The brain samples for ONC201 in combination with radiation were from the mice at post-op day 227 (the mice did not reach the study endpoint). (G) Double immunofluorescent staining of GBM stem cell marker CD133 (red) and proliferating marker Ki67 (green) in coronal sections of brains from C57BL/6 mice implanted with GL261-GFP-Luc cells, treated with either ONC201 (50 mg/kg) or saline in the presence or absence of a single dose of radiation (10 Gy), at the study endpoint. (H) Survival curves for NSG mice implanted intra-cranially with 3×10^5 HK374-GFP-Luciferase patient-derived GBM cells. Tumors were grown for 3 days for successful grafting. Mice were irradiated with a single fraction of 0 or 10 Gy and weekly treated with Saline or ONC201 (50 mg/kg, i.p.) continuously until they reached the study endpoint. Log-rank (Mantel-Cox) test for comparison of Kaplan-Meier survival curves indicated significant differences in the ONC201 treated mice compared to

their respective controls. ONC201 *v.s.* Saline (**** p -value<0.0001), 10 Gy + Saline *v.s.* Saline (n.s. p -value=0.1155), 10 Gy + ONC201 *v.s.* Saline (**** p -value<0.0001), 10 Gy + ONC201 *v.s.* 10 Gy + Saline (** p -value=0.0059). **(I)** Weight curves for the NSG mice in the different treatment groups.

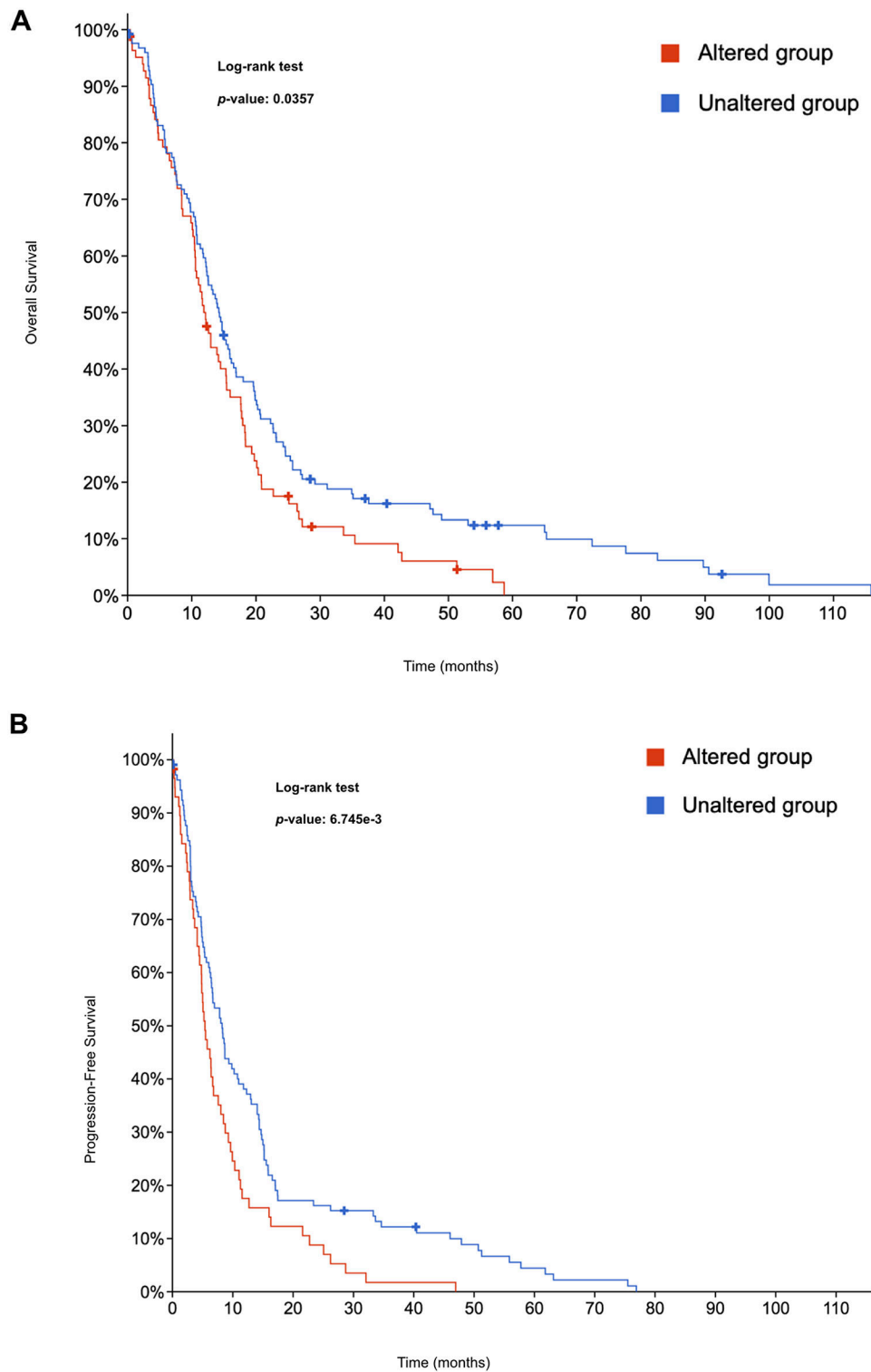


Figure 4. Evaluation of qGBM-enriched ECM-related gene signatures in TCGA glioblastoma patients.

(A) The overall survival (OS) in glioblastoma patients from TCGA stratified by qGBM-enriched ECM-related gene expression. OS in qGBM-enriched ECM-related gene altered

group (higher expression) was significantly worse than that of the unaltered group (log rank test, p -value=0.0357). **(B)** The progression-free survival (PFS) in glioblastoma patients from TCGA stratified by qGBM-enriched ECM-related gene expression. PFS in qGBM-enriched ECM-related gene altered group (higher expression) was significantly worse than that of the unaltered group (log rank test, p -value=6.745e-3).

Table 1.

Patient demographics and TCGA-classification of GBM subtypes.

| Line | Origin | Age | Gender | TCGA subtype | Culture P53 CN | EGFRvIII | PTEN | MGMT |
|--------|---------------|-----|--------|--------------|----------------|----------|----------|----------------|
| HK-374 | Primary GBM | 45 | Male | classical | Loss "mosaic" | Positive | Positive | not methylated |
| HK-345 | Recurrent GBM | 26 | Female | mesenchymal | wt | Negative | Positive | not methylated |
| HK-157 | Primary GBM | 54 | Female | proneural | wt | Negative | Positive | Unknown |
| HK-382 | Primary GBM | 66 | Male | classical | Loss "mosaic" | Negative | Positive | methylated |
| HK-308 | Recurrent GBM | 50 | Female | mesenchymal | Unknown | Positive | Positive | not methylated |

1 **Activation of the mevalonate pathway in response to anti-cancer**
2 **treatments drives glioblastoma recurrences through activation of Rac-1**

3
4 ¹Ling He, D.D.S., Ph.D., ¹Angeliki Ioannidis, M.S., ¹Evelyn Arambula, ¹Carter J. Hoffman,
5 M.S., ¹Purva Joshi, B.S., ¹Anoushka Kathiravan, ^{2,3}Julian Whitelegge, Ph.D., ^{2,4}Linda M.
6 Liau, M.D., Ph.D., ^{2,3}Harley I. Kornblum, M.D., Ph.D., and ^{1,2}Frank Pajonk, M.D., Ph.D.**

7
8 ¹Department of Radiation Oncology, David Geffen School of Medicine at UCLA

9 ²Jonsson Comprehensive Cancer Center at UCLA

10 ³Department of Psychiatry and Human Behavior, David Geffen School of Medicine at
11 UCLA

12 ⁴Department of Neurosurgery, David Geffen School of Medicine at UCLA

13
14
15 ****Correspondence address:** Frank Pajonk, MD, PhD, Department of Radiation
16 Oncology, David Geffen School of Medicine at UCLA, 10833 Le Conte Ave, Los Angeles,
17 CA 90095-1714, Phone: +1 310 206 8733, Fax: +1 310 206 1260, email:
18 pajonk@ucla.edu

19
20 **Funding:** FP was supported by grants from the *National Cancer Institute* (R01CA200234,
21 R01CA260886, R01CA281682). FP and HIK were supported by the California Institute
22 for Regenerative Medicine (CIRM; DISC2-14083) and the American Cancer Society

23 (CSCC-Team-23-980262-01-CSCC). LML, HIK, and FP were supported by a grant from
24 the *National Cancer Institute* (UCLA Brain Tumor SPORE P50CA211015).

25

26 **Author contributions:** FP conceived of the study. LH, AI, EA, CH, PJ, AK performed the
27 experiments, JW performed mass spectrometry, LML and HIK provided materials, FP and
28 LH analyzed the data and drafted the manuscript. All authors contributed to and approved
29 the final version of the manuscript.

30

31 **Abstract**

32 Glioblastoma is the deadliest adult brain cancer. Under the current standard of care
33 almost all patients succumb to the disease and novel treatments are urgently needed.
34 Dopamine receptor antagonists have been shown to target cancer cell plasticity in GBM
35 and repurposing these FDA-approved drugs in combination with radiation improves the
36 efficacy of radiotherapy in glioma models. In cells surviving this combination treatment
37 the mevalonate pathway is upregulated at the transcriptional and functional level.
38 Here we report that glioblastoma treatments that converge in the immediate early
39 response to radiation through activation of the MAPK cascade universally upregulate the
40 mevalonate pathway and increase stemness of GBM cells through activation of the Rho-
41 GTPase Rac-1. Activation of the mevalonate pathway and Rac-1 is inhibited by statins,
42 which leads to improved survival in mouse models of glioblastoma when combined with
43 radiation and drugs that target the glioma stem cell pool and plasticity of glioma cells.

44 **Introduction**

45 Glioblastoma (GBM) is the deadliest adult brain cancer. The standard-of-care, surgery
46 followed by radiation therapy and temozolomide (TMZ) almost always fails and the tumors
47 progress or recur, thus leading to unacceptable low 5-year survival rates. Despite
48 iterations in radiotherapy protocols and techniques, introduction of targeted therapies and
49 biologics, the survival rates have not changed in almost two decades and strategies
50 against GBM have hit a critical barrier. Understanding mechanisms underlying this
51 treatment resistance holds the key to develop novel approaches against GBM.

52 GBMs are thought to be governed by a hierarchical organization of tumor cells with
53 a small number of glioma stem cells (GSCs) at the top of this hierarchy, giving rise to the
54 bulk of more differentiated glioma cells. GSCs have been reported to resist many
55 chemotherapeutic agents [1] and are relatively resistant to ionizing radiation [2].
56 Consequently, a portion of the GSC population survives treatment and can repopulate
57 the tumor. This led to efforts specifically targeting the GSC population of GBMs but so far
58 this has not successfully translated into the clinic.

59 Recently, we reported an additional novel aspect of GBM biology in response to
60 radiation. Non-stem glioma cells surviving irradiation converted into glioma-initiating cells
61 in a radiation dose-dependent manner. Compounds that counteract this phenomenon
62 improved median survival in patient-derived orthotopic xenograft (PDOX) and syngeneic
63 models of GBM [3-5]. Yet, the efficacy was not 100% and bulk RNA-sequencing revealed
64 that surviving cells upregulated gene expression of the mevalonate pathway, followed by
65 upregulation of its enzymatic function *in vitro*. This hinted at a novel metabolic vulnerability
66 that could be exploited by the addition of a statin, but it was unclear if the same effects

67 could be observed *in vivo* and how the mevalonate pathway affects stemness of glioma
68 cells. In the present study we report that combination treatments that synergize with
69 radiation in activating the immediate early response through the mitogen-activated protein
70 kinase (MAPK) cascade upregulate the mevalonate pathway *in vivo*, thereby triggering
71 repopulation of gliomas through prenylation of the Rho GTPase Rac-1.

72 **Results**

73 *Upregulation of the mevalonate pathway in response to anti-cancer treatments in vivo is*
74 *restricted to glioma cells.*

75 We previously reported that combinations of radiation and dopamine receptor antagonists
76 upregulated genes in the mevalonate pathway and increased cholesterol biosynthesis in
77 GBM cells *in vitro* [3, 4]. Genes in this pathway are under control of sterol regulatory
78 element-binding protein 2 (SREBP-2 also called SREBF-2), a transcription factor under
79 control of the MAPK cascade through AP-1, a pathway well known to be activated during
80 the immediate-early response to radiation [6]. Its components JunB, JunD, and FosB, are
81 all part of the first-order regulatory network of SREBP-2. JunB and JunD have weak
82 transactivation domains and can be considered repressors in the presence of the strong
83 transcriptional activator FosB. All three are regulated by GSK-3 [7], the kinase
84 downstream of dopamine receptors, thus explaining synergistic effects of radiation and
85 dopamine receptor antagonists on the mevalonate pathway.

86 TMZ, part of the current standard-of-care against GBM is known to activate the
87 MAPK cascade in GBM [8]. Likewise, vincristine, a component of the PCV chemotherapy
88 regimen against GBM, activates this pathway [9]. Western blots of patient-derived HK374
89 and HK217 glioma cells (**Supplementary Table 1**) confirmed that radiation, quetiapine
90 (QTP; a dopamine receptor antagonist), TMZ and vincristine activated the MAPK cascade
91 in our model system (**Fig. 1a-c, Suppl. Fig. 1a/b**). Next, we tested if radiation in
92 combination with TMZ, vincristine, or QTP would also up-regulate the mevalonate
93 pathway. As expected, combining radiation and TMZ upregulated gene expression of key
94 enzymes in this pathway (**Fig. 1d/e**). Similar results were found when combining radiation

95 and vincristine (**Fig. 1f/g**). We have previously reported the upregulation of mevalonate
96 pathway in HK374 cells upon combination treatment of radiation plus QTP [3]. Here,
97 similar results were also observed in HK217 cells (**Suppl. Fig. 1c**). This indicated that
98 combination therapies that converge on the immediate-early response to radiation [10]
99 through activation of the MAPK cascade universally upregulate the mevalonate pathway,
100 thereby creating a metabolic vulnerability in cells surviving the sublethal DNA damage
101 caused by radiation.

102 Our previous studies investigated the effects of radiation and dopamine receptor
103 antagonists on the mevalonate pathway in patient derived GBM lines *in vitro* [3]. To test
104 if this effect could also be observed in the presence of a tumor microenvironment, we next
105 implanted HK374 glioma cells into the striatum of NSG mice. After 2 weeks of grafting
106 and tumor growth, mice were treated with a single dose of 4 Gy and 2 consecutive doses
107 of QTP (**Fig. 2a**). Tumor tissue was harvested, mRNA extracted and subjected to qRT-
108 PCR using human- and mouse-specific primers for genes in the mevalonate pathway.
109 Gene expression of enzymes in the mevalonate pathway in tumors cells confirmed data
110 obtained in our *in vitro* studies showing upregulation of gene expression in response to
111 radiation in combination with QTP. Using mouse-specific primers for the corresponding
112 murine genes we did not observe an upregulation of these genes in normal cells in the
113 tumor microenvironment, thus indicating that this response was specific to GBM cells
114 (**Fig. 2b**).

115 In *in vitro* shotgun lipidomics experiments we previously demonstrated that
116 radiation in combination with QTP upregulated cholesterol and free fatty acids production
117 [3]. To test if these pathways were also functionally upregulated in response to the

118 combination therapy *in vivo*, we next quantified cholesterol and free fatty acids levels in
119 tumor tissues. Compared to radiation alone, the combination of radiation and QTP
120 significantly upregulated free and total cholesterol levels in the tumor tissue (**Fig. 2c**) but
121 did not affect free fatty acid levels (**Fig. 2d**), confirming that the mevalonate pathway was
122 not only transcriptionally but also functionally activated. However, the increases in
123 cholesterol synthesis were unexpectedly small, thus hinting that other branches of the
124 mevalonate pathway could be involved in mediating the survival of GBM cells.

125

126 *Statins reduce treatment-induced upregulation of cholesterol biosynthesis in PDOXs*

127 Statins are a class of FDA-approved drugs that target 3-hydroxy-3-methylglutaryl-CoA
128 reductase (HMGCR), the rate-limiting enzyme in the mevalonate pathway. Designed to
129 lower cholesterol levels in the periphery, data on blood-brain barrier (BBB) penetration in
130 the literature is sparse and often conflicting. Our *in vivo* data indicated that the addition of
131 statins to a combination of radiation and QTP could significantly improve median survival
132 in mouse models of GBM [3]. Therefore, we next tested if statins could be detected in
133 normal brain tissue and if statin treatment would alter the mevalonate pathway in PDOXs.
134 We had previously used atorvastatin at a dose of 30 mg/kg in mice, and at this dose we
135 were able to detect atorvastatin in brain tissue and plasma of mice with a brain to plasma
136 ratio of 1.6 (**Fig. 3a**). *In silico* calculations predicted better BBB penetration for simvastatin
137 (**Suppl. Fig. 2**) [11]. However, simvastatin is a prodrug with a short half-life and subject
138 to first pass elimination [12, 13]. When we treated mice with simvastatin at 7 mg/kg, the
139 murine equivalent dose [14] of the currently recommended human dose of 40 mg/day,
140 mass spectrometry analysis of brain tissue and plasma could only detect plasma levels

141 of simvastatin (**Fig. 3b**). However, both -atorvastatin and simvastatin- reduced free and
142 total cholesterol but not free fatty acid levels in orthotopic gliomas (**Fig. 3c/d**) and
143 prevented upregulation of gene expression of genes in the mevalonate pathway by
144 radiation combined with QTP in tumor tissues (**Fig. 3e**). This indicated that both statins
145 crossed the BBB in pharmacologically relevant concentrations or that there is sufficient
146 diminution of the BBB in xenografts to let it it..

147

148 *Statins improve median survival in mouse models of GBM undergoing fractionated*
149 *irradiation*

150 In previous *in vitro* studies we reported that the dopamine receptor antagonists
151 trifluoperazine (TFP) and QTP prevented radiation-induced phenotype conversion of non-
152 stem glioma cells into glioma stem cells, but induced gene expression of the mevalonate
153 pathway in surviving cells, thereby creating a metabolic vulnerability that could be
154 exploited with the use of atorvastatin to further improve median survival [3]. At 7 mg/kg,
155 equivalent to the recommended human dose of 40 mg, simvastatin also significantly
156 prolonged the median survival of glioma-bearing mice when combined with radiation and
157 QTP (10 Gy + QTP: 64 days vs. 10 Gy + QTP + simvastatin: 120.5 days, $p < 0.0001$, Log-
158 rank test; **Fig. 3f**) and was well-tolerated with animals gaining weight during treatment
159 (**Fig 3g**). We previously reported that the atypical dopamine receptor 2/3 antagonist and
160 caseinolytic protease P (ClpP) activator ONC201 [15], now in clinical trials against
161 pediatric glioma, also prevented radiation-induced phenotype conversion of non-stem
162 glioma cells into glioma stem cells and prolonged median survival in mouse models of
163 GBM [5]. Here we report that similar to TFP and QTP, ONC201 in combination with

164 radiation also upregulates the mevalonate pathway, although with different kinetics,
165 reflective of the longer half-life of ONC201 (**Fig. 4a**). Importantly, the addition of a statin
166 significantly improved median survival compared to animals treated with radiation and
167 ONC201 alone (10 Gy + ONC201 + atorvastatin vs. 10 Gy + ONC201, $p=0.0193$, Log-
168 rank test; **Fig. 4b**), and led to smaller tumors or no signs of residual tumor in some animals
169 as shown in H&E staining (**Fig. 4c**).

170 Next, we repeated the experiment with fractionated irradiation (5 daily fractions of
171 3 Gy) in GL261 glioma bearing mice. In parallel, mice were treated with daily doses of
172 either corn oil, QTP, or QTP plus atorvastatin. After completion of the radiation treatment
173 all animals were treated with QTP plus atorvastatin until they reached criteria for
174 euthanasia (**Fig. 4d**). Kaplan-Meier estimates for the 3 treatment arms did not differ
175 significantly but showed a trend for improved median survival for animals receiving QTP
176 or QTP + atorvastatin during radiation treatment (**Fig. 4e**) in line with QTP preventing
177 radiation-induced phenotype conversion of non-stem GBM cells into GSCs and
178 atorvastatin affecting the mevalonate pathway in surviving cells. Histologically, the triple
179 combination of radiation, QTP and atorvastatin led to smaller tumor sizes or no signs of
180 residual tumor in some animals (**Fig. 4f**).

181
182 *Treatment-induced upregulation of the mevalonate pathway in glioma affects stemness*
183 *through prenylation of Rac-1*

184 The mevalonate pathway is the fundamental pathway in the cholesterol biosynthesis.
185 While the uptake of exogenous cholesterol has been shown to be essential for glioma
186 [16] other metabolites in the mevalonate pathway contribute to normal cell function

187 through farnesylation and geranylgeranylation to the prenylation of small GTPases [17,
188 18]. To determine which of the pathway components' upregulation contributes to glioma
189 stemness, we employed an inhibitor-based approach (**Fig. 5a**). Using clonal sphere-
190 forming capacity assay, we found that inhibition of geranylgeranylation (**Fig. 5b**) but not
191 inhibition of the cholesterol biosynthesis (**Fig. 5c/d**) or farnesylation (**Fig. 5e**) further
192 reduced sphere formation when combined with radiation and QTP.

193 Since geranylgeranylation of Rho GTPases is fundamental for their downstream
194 effects on cytoskeletal reorganization [19], which mediates the interaction of cancer stem
195 cells (CSCs) with the tumor microenvironment, maintenance of stemness and CSC
196 migration [20] we next tested which Rho GTPase would affect the self-renewal capacity
197 of GBM cells (**Fig. 5a**). Inhibition of Rac GTPases (**Fig. 5f**) but not Rho or Cdc42 GTPases
198 (**Fig. 5g-i**) significantly reduced sphere formation in a dose-dependent fashion when
199 combined with radiation and QTP.

200 In agreement with our inhibitor studies, Rac-1 pulldown assays revealed a
201 significant activation of Rac-1 after combined treatment with QTP and radiation (**Fig.**
202 **6a/b**). *In vitro*, surviving cells treated with radiation and QTP showing significantly
203 increased migratory capacity (**Fig. 6c/d**), known to require remodeling of the cytoskeleton
204 [21]. The addition of atorvastatin inhibited Rac-1 activation (**Fig. 6a**) and diminished the
205 increased migratory capacity seen in cells surviving the combination treatment (**Fig.**
206 **6c/d**). Microtubules are part of the cytoskeleton, a structural network within the cell's
207 cytoplasm which helps to support cell shape, as well as cell migration and cell division.
208 Using a microtubule stain we showed that the surviving cells treated with radiation and
209 QTP had more filopodia (**Fig. 6e, white arrowheads**), which support cell migration by

210 promoting cell–matrix adhesiveness at the leading edge, as well as increased numbers
211 of tunneling nanotubes (TNTs) (**Fig. 6e, yellow arrowheads**). TNTs are known to
212 mediate protein and mitochondrial transfer between distant cells as part of the radiation
213 response of GBM cells and are suspected to drive GBM growth and treatment resistance
214 [22, 23]. This suggested more active Rac-1-mediated cytoskeleton remodeling in cells
215 surviving the combination of radiation and QTP. Importantly, the observed effects on
216 cytoskeleton remodeling were inhibited with the additional atorvastatin (**Fig. 6e**).

217 Lastly, we performed loss-of-function experiments to demonstrate that
218 radiation/QTP-induced Rac-1 activation is indeed a driver for stemness maintenance in
219 surviving GSCs. With the efficient transient knock down of Rac-1 in HK374 cells (**Fig.**
220 **6f/g**), we tested its role in both, clonogenicity survival and self-renewal capacity of the
221 cells surviving from radiation and/or QTP and the effect of atorvastatin. While treatment
222 with radiation and QTP significantly reduced the formation of adherent clonal colonies
223 (**Fig. 6h**), sphere-forming capacity (**Fig. 6i**) and stem cell frequency (**Tables 1 and 2**),
224 additional treatment with atorvastatin did not further diminish these three parameters after
225 knock-down of Rac-1, thus suggesting that all three traits are Rac-1-driven in cells
226 surviving radiation and QTP.

227

228 **Discussion**

229 To date, surgery and radiotherapy remain the most effective treatment modalities against
230 GBM. Temozolomide, the only chemotherapeutic agent added to the standard-of-care
231 during the past two decades [24, 25], only marginally improves patient outcome and the
232 median and long-term survival rates of patients suffering from GBM remain unacceptably
233 low. Attempts to increase the tumoricidal efficacy of radiotherapy through e.g., alternative
234 fractionation schemes or radiosensitizers have largely failed [26], in part due to the
235 dispersion of glioma cells into the normal parenchyma beyond the visible tumor and
236 because many compounds lacked BBB penetration or increased normal tissue toxicity.
237 Likewise, targeted therapies had little effects as GBMs escape through utilization of
238 alternate signaling pathways [27].

239 The DNA-damaging effects of radiation unfold in milliseconds after irradiation and
240 the repair of DNA double-strand breaks is completed within the first few hours.
241 Compounds that increase the amount of initial DNA damage or interfere with its repair
242 mainly operate during this short timeframe. While it is desirable to eliminate all malignant
243 cells this way, current therapies against GBM fail in achieving this goal and almost all
244 patients succumb to progressive or recurrent disease. Over the past two decades it
245 became evident that a small population of cancer stem cells, relatively resistant to radio-
246 and chemo-therapy, maintains the growth of tumors [28-30] and shows enrichment after
247 treatment [2, 31, 32]. Recurrent or progressing gliomas are likely caused by GSCs that
248 survive these sublethal treatments and the pathways that drive them to proliferate, invade,
249 and repopulate the tumor are not necessarily identical with the pathways that helped them
250 to survive the genotoxic insults.

251 With the discovery of radiation-induced phenotype conversion of non-stem cancer
252 cells into cancer stem cells we have reported a novel major factor for radiation treatment
253 failure [33]. In an unbiased phenotypic high-throughput screen we identified compounds
254 that -unlike TMZ, which enhances it- prevented this unwanted effect of radiation, and we
255 demonstrated that repurposing FDA-approved drugs identified in this screen prolonged
256 median survival in PDOX models of glioma [3, 4].

257 The mevalonate pathway is one of the key metabolic pathways known to be
258 dysregulated in GBM [34]. Statins, developed to lower cholesterol levels in the periphery
259 target HMGCR, the rate-limiting enzyme in this pathway and affect glioma biology in
260 multiple ways, from interfering with the dependence of GBM on cholesterol to inhibition
261 of farnesylation of Ras or geranylgeranylation of GTPases with effects on cell proliferation
262 and survival, cell cycle progression, migration and invasion [35]. Recognized as a
263 potential target, the mevalonate pathway has been probed in several preclinical and
264 clinical studies repurposing statins against brain tumors with largely disappointing results.
265 While statins showed robust anti-tumor activities *in vitro* [35-37], previous rodent
266 pharmacokinetic studies were not able to achieve therapeutic drug concentrations in the
267 central nervous system (CNS) [38, 39]. A recent clinical phase II study, which added
268 atorvastatin to the current standard-of-care, radiotherapy and TMZ, showed no beneficial
269 effects on progression-free or overall survival when compared to historic controls treated
270 with radiotherapy and TMZ [40]

271 Clinically, the biodistribution of TMZ into the brain is less than 20% and peak
272 concentrations after single doses of 75-200 mg/m² were predicted to reach only 1.8-3.7
273 µg/ml or 9.2 to 19.1 µM [41]. At these concentrations TMZ has only minimal if any effects

274 *in vitro* and most preclinical studies use TMZ in the high micromolar to millimolar range
275 [42, 43]. Although TMZ is a known activator of the MAPK cascade, our *in vitro* data did
276 not indicate effects of TMZ on the mevalonate pathway unless drug concentrations were
277 raised to 1 mM. The lack of upregulation of the mevalonate pathway in response to low
278 TMZ concentrations agreed with the lack of clinical benefits of statins in combination with
279 radiation and TMZ, which was not surprising given that 23% of the human body's
280 cholesterol are located in the brain [44] and that GBM cells rely on exogenous cholesterol
281 and not on cholesterol biosynthesis [16].

282 In contrary, dopamine receptor antagonists activate the MAPK cascade via GSK-
283 3 at low concentrations and synergize with radiation by targeting tumor cell plasticity and
284 glioma stem cells [4, 5]. Designed as psychotropic drugs they easily cross the blood-brain
285 barrier and reach therapeutic concentrations in the CNS. Here we show that dopamine
286 receptor antagonists robustly created a metabolic vulnerability in surviving cells through
287 upregulation of the mevalonate pathway *in vivo*.

288 Tumors outpace cell loss with proliferation, thereby creating a need for
289 macromolecular building blocks to not only replicate DNA but also to double the cellular
290 mass before and during mitosis. To serve this need, cancer cells utilize aerobic glycolysis,
291 known as the Warburg effect, to channel glucose into the biosynthesis of macromolecules
292 including the mevalonate pathway to produce cholesterol. The cell cycle and the
293 mevalonate pathway are tightly intervened with non-sterol isoprenoids initiating the
294 transition from G₁- to S-phase and cholesterol being required during the G₂- and M phase
295 of the cell cycle. Very high cholesterol concentration are toxic for cells and cholesterol
296 biosynthesis is limited by a negative feedback loop [45]. And since GBM cells primarily

297 rely on uptake of exogenous cholesterol [16] it is not surprising that the radiation/QTP-
298 induced upregulation of the mevalonate pathway reported here only slightly increased
299 cholesterol biosynthesis in GBM cells.

300 Consequently, the inhibition of this branch of the mevalonate pathway did not affect
301 the self-renewal of surviving GBM cells beyond the effects of radiation and dopamine
302 receptor antagonists. Instead of upregulating cholesterol production, surviving cells
303 increased their migratory and invasive capacity through activation of Rac-1, a major
304 regulator of cytoskeleton reorganization. A role for Rac-1 in stemness and tumorigenicity
305 had been previously reported for U87MG and U373 glioma cells [46] and our results
306 confirmed these findings with a significant reduction in clonogenic survival, sphere-
307 forming capacity and glioma stem cell frequency when Rac-1 was knocked down.
308 Likewise, the treatment of cells with a geranylation inhibitor or inhibition of Rac-1
309 synergized with radiation and QTP in reducing the sphere-forming capacity of the cells.

310

311 We conclude that the upregulation of the mevalonate pathway is part of the
312 immediate-early response to glioma treatments that converge in activating the MAPK
313 cascade, effectively diminish the GSC pool and interfere with glioma cell plasticity.
314 Surviving GSCs rely on activation of Rac-1 through the mevalonate pathway to maintain
315 stemness and to repopulate the tumors. This generates a metabolic vulnerability that can
316 be exploited through the addition of statins to further improve the efficacy of radiotherapy.
317 Furthermore, upregulation of the mevalonate pathway seemed to be restricted to tumor
318 tissue, indicating the presence of a therapeutic window for statins in combination with
319 radiation and repurposed, FDA-approved dopamine receptor antagonists.

320 These effects on the mevalonate pathway are not seen after treatment with
321 radiation and TMZ, the current standard of care, and the addition of statins is not expected
322 to provide an anti-tumor effect in this situation.

323

324

325

326

327

328

329

330

331

332

333

334

335 **Methods**

336 *Cell lines*

337 Primary human glioma cell lines were established at UCLA as described in [29];
338 Characteristics of specific gliomasphere lines can be found in [47]. Primary GBM cells
339 were propagated as gliomaspheres in serum-free conditions in ultra-low adhesion plates
340 in DMEM/F12, supplemented with SM1 Neuronal Supplement (#05177, STEMCELL
341 Technology, Kent, WA) EGF (#78006, STEMCELL Technology), bFGF (#78003,
342 STEMCELL Technology) and heparin (1,000 USP Units/mL, NDC0409-2720-31, Lake
343 Forest, IL) as described previously [29, 47, 48]. GL261 cells were cultured in log-growth
344 phase in DMEM supplemented with 10% fetal bovine serum, penicillin and streptomycin
345 (P/S). All cells were grown in a humidified atmosphere at 37°C with 5% CO₂. The unique
346 identity of all patient-derived specimens was confirmed by DNA fingerprinting (Laragen,
347 Culver City, CA). All lines were routinely tested for mycoplasma infection (#G238, Applied
348 biological Materials, Ferndale, WA).

349

350 *Animals*

351 6–8-week-old C57BL/6 mice, or NOD-*scid* IL2Rgamma^{null} (NSG) originally obtained from
352 The Jackson Laboratories (Bar Harbor, ME) were re-derived, bred and maintained in a
353 pathogen-free environment in the American Association of Laboratory Animal Care-
354 accredited Animal Facilities of Department of Radiation Oncology, University of California,
355 Los Angeles, in accordance with all local and national guidelines for the care of animals.
356 2×10^5 GL261-GFP-Luc or 3×10^5 HK374-GFP-Luc cells were implanted into the right
357 striatum of the brains of mice using a stereotactic frame (Kopf Instruments, Tujunga, CA)

358 and a nano-injector pump (Stoelting, Wood Dale, IL). Injection coordinates were 0.5 mm
359 anterior and 2.25 mm lateral to the bregma, at a depth of 3.0 mm from the surface of the
360 brain. Weight of the animals was recorded daily. Tumors were grown for 3 days for HK374
361 cells and 7 days for GL261 cells with successful grafting confirmed by bioluminescence
362 imaging. Mice that developed neurological deficits or lost 20% of their body weights
363 requiring euthanasia were sacrificed.

364

365 *Drug treatment*

366 For *in vivo* studies, after confirming tumor grafting via bioluminescence imaging, mice
367 implanted with HK374 cells were injected subcutaneously with quetiapine (QTP; #KS-
368 1099, Key Organics, Cornwall, UK) at 30 mg/kg and/or intraperitoneally with simvastatin
369 at 7 mg/kg on a 5-days on / 2-days off schedule until they reached euthanasia endpoints.
370 QTP was dissolved in acidified PBS (0.4% Glacial acetic acid) at a concentration of 5
371 mg/ml. Simvastatin (#S1792, Selleck Chemicals, Houston, TX) was dissolved in corn oil
372 containing 2.5% DMSO at a concentration of 5 mg/ml. Mice bearing GL261 tumors were
373 injected intraperitoneally on a weekly basis either with ONC201 at 50 mg/kg and/or
374 intraperitoneally with atorvastatin (#10493, Cayman Chemical, Ann Arbor, MI) at 30
375 mg/kg until they reached the euthanasia endpoint. ONC201 was kindly provided by
376 Oncoceutics, Inc. (Philadelphia, PA) and dissolved in sterile saline at a concentration of
377 5.5 mg/ml. Atorvastatin was dissolved in corn oil containing 2.5% DMSO at a
378 concentration of 5 mg/ml.

379 To determine the optimal timing of the drug treatments during fractionated radiotherapy.
380 Mice bearing GL261 tumors received 5 daily fractions of 3 Gy. In parallel, mice were

381 treated with daily doses of either saline, QTP (30 mg/kg, subQ), or QTP + atorvastatin
382 (30 mg/kg, i.p.). After completion of the radiation treatment all animals were treated with
383 QTP + atorvastatin until they reached criteria for euthanasia.

384 To explore the activation of MAPK pathway *in vitro*, HK374 cells were serum
385 starved and the following day treated with a single dose of 10 Gy in the absence or
386 presence of QTP (10 μ M), temozolomide (1 mM; #14163, Cayman Chemical) or
387 Vincristine (250 nM; #HY-N0488, MedChem Express, Monmouth Junction, NJ). 2 hours
388 after the irradiation, cell lysates were harvested for western blotting.

389 To determine, which part of the mevalonate pathways synergizes with radiation
390 and QTP to affect self-renewal, HK374 cells were plated under sphere forming conditions
391 in an *in-vitro* limiting dilution assay. Cells were irradiated with a single dose of 4 Gy in the
392 presence of QTP (10 μ M) and treated either with zaragozic acid (squalene synthase
393 inhibitor; #17452, Cayman Chemical), GGTI-298 (GGTase inhibitor; #16176, Cayman
394 Chemical), YM-53601 (squalene synthase inhibitor; #18113, Cayman Chemical),
395 Lonafarnib (farnesyltransferase inhibitor, #SML1457, Sigma, St. Louis, MO) at 100 nM,
396 500 nM, and 1 μ M or Rhosin (RhoA-specific inhibitor; #555460, Sigma), Y27632
397 (ROCK1/2 inhibitor; #S1049, Selleck Chemicals), EHop-016 (Rac GTPase inhibitor;
398 #S7319, Selleck Chemicals), CID44216842 (Cdc42-selective inhibitor; #S6000, Selleck
399 Chemicals) at 500 nM, 1 μ M, 5 μ M and 10 μ M. All drugs were dissolved in DMSO at 10
400 mM for stock and were replenished daily for 5 days.

401

402 *Migration Assay*

403 HK374 cells were treated with 10 μ M QTP, 1 μ M atorvastatin, or QTP and atorvastatin
404 and irradiated with 0 or 4 Gy. 48 hours after irradiation, cells were serum-starved for 12
405 hours. 5×10^5 cells were then plated into 12-well Transwell[®] insert with 8 μ m pore size
406 (Corning, New York, NY). After 24 hours, membranes were washed with PBS, cells fixed
407 with 10% formalin, stained with 1% crystal violet, and counted using ImageJ.

408

409 *In-vitro* limiting dilution assay

410 For the assessment of self-renewal capacity *in vitro*, HK374 cells were seeded at clonal
411 densities under serum-free conditions into non-tissue-culture-treated 96-well plates in
412 DMEM/F12 media, supplemented with SM1 Neuronal Supplement, EGF, bFGF and
413 heparin. The next day, the cells were treated with drugs and one hour later irradiated with
414 a single dose of 4 Gy. Growth factors were supplemented every two days. Glioma spheres
415 were counted 10 days later and presented as the percentage of the initial number of cells
416 plated.

417

418 *Irradiation*

419 Cells were irradiated with at room temperature using an experimental X-ray irradiator
420 (Gulmay Medical Inc. Atlanta, GA) at a dose rate of 5.519 Gy/min. Control samples were
421 sham-irradiated. The X-ray beam was operated at 300 kV and hardened using a 4 mm
422 Be, a 3 mm Al, and a 1.5 mm Cu filter and calibrated using NIST-traceable dosimetry.
423 Corresponding controls were sham irradiated.

424 For *in vivo* irradiation experiments, mice were anesthetized prior to irradiation with an
425 intra-peritoneal injection of 30 μ L of a ketamine (100 mg/mL, Phoenix, MO) and xylazine

426 (20 mg/mL, AnaSed, Lake Forest, IL) mixture (4:1) and placed on their sides into an
427 irradiation jig that allows for irradiation of the midbrain while shielding the esophagus,
428 eyes, and the rest of the body. For survival experiments, animals implanted with GL261
429 cells received a single dose of 10 Gy on day 7 or 5 fractions of 3 Gy each starting 7 days
430 after tumor implantation. Animals injected with HK374 glioma specimen received a single
431 dose of 10 Gy on day 3 after tumor implantation.

432

433 *Quantitative Reverse Transcription-PCR*

434 Total RNA was isolated using TRIZOL Reagent (Invitrogen, Waltham, MA) cDNA
435 synthesis was carried out using the SuperScript Reverse Transcriptase IV (Invitrogen).
436 Quantitative PCR was performed in the QuantStudio™ 3 Real-Time PCR System
437 (Applied Biosystems, Carlsbad, CA, USA) using the PowerUp™ SYBR™ Green Master
438 Mix (Applied Biosystems). C_t for each gene was determined after normalization to PPIA
439 and $\Delta\Delta C_t$ was calculated relative to the designated reference sample. Gene expression
440 values were then set equal to $2^{-\Delta\Delta C_t}$ as described by the manufacturer of the kit (Applied
441 Biosystems). All PCR primers were synthesized by Invitrogen with PPIA as the
442 housekeeping gene (for primer sequences see **Supplementary Table 2**).

443

444 *Cholesterol and free fatty acid quantification*

445 3×10^5 HK374-GFP-Luc cells were intracranially implanted and grafted for 2 weeks to
446 achieve the appropriate size of tumor to start with. Mice were irradiated with a single dose
447 of 4 Gy and treated with daily with either corn oil, QTP (30 mg/kg), QTP + atorvastatin
448 (30 mg/kg) or QTP + simvastatin (7 mg/kg). After 2 and 5 days of drug treatments, the

449 mice were euthanized, and brain tumor samples were collected and weighted. PBS (20
450 μ l/mg) was added to mince the brain tumor tissues with a pellet pestle® tissue grinder
451 (#749521-1590, DWK Life Sciences, Rockwood, TN). Equal volumes of homogenized
452 tumor specimens were subsequently subjected to Cholesterol/Cholesterol Ester-GLo™
453 assay (#J3190, Promega, Madison, WI) and Free Fatty Acid assay (ab65341, Abcam,
454 Cambridge, UK) following the manufacturers' instructions.

455

456 *Western Blotting*

457 HK374 and HK217 cells were serum starved overnight and the following day treated with
458 10 μ M QTP, 1 mM TMZ, or 250 nM Vincristine for one hour and then irradiated with a
459 single dose of 10 Gy. Two hours after irradiation, the cells were lysed in 150 μ l of ice-cold
460 RIPA lysis buffer (10 mM Tris-HCl (pH 8.0), 1 mM EDTA, 1 % Triton X- 100, 0.1 % Sodium
461 Deoxycholate, 0.1 % SDS, 140 mM NaCl, 1 mM PMSF) containing protease inhibitor
462 (#A32955, Thermo Fisher Scientific, Waltham, MA) and phosphatase inhibitor (#A32957,
463 Thermo Fisher Scientific). The protein concentration in each sample was determined by
464 BCA protein assay (Thermo Fisher Scientific) and samples were denatured in 4X
465 Laemmli sample buffer (Bio-Rad) containing 10% β - mercaptoethanol for 10 mins at 95°C.
466 Equal amounts of protein were loaded onto 10% SDS-PAGE gels (1X Stacking buffer -
467 1.0 M Tris-HCl, 0.1% SDS, pH 6.8, 1X Separating buffer - 1.5 M Tris-HCl, 0.4% SDS, pH
468 8.8) and were subjected to electrophoresis in 1X Running buffer (12.5 mM Tris-base, 100
469 mM Glycine, 0.05% SDS), initially at 50 V for 30 min followed by 100 V for 2 hours.
470 Samples were then transferred onto 0.45 μ m nitrocellulose membrane (Bio-Rad,
471 Hercules, CA) for 2 hours at 80 V. Membranes were blocked in 1X TBST (20 mM Tris-

472 base, 150 mM NaCl, 0.2% Tween-20) containing 5% bovine serum albumin (BSA) for 30
473 min and then incubated with primary antibodies against p-ERK (#4370S, 1:1000, Cell
474 Signaling, Danvers, MA), p-P38 (#4511S, 1:1000, Cell Signaling), t-ERK (#5013S,
475 1:1000, Cell Signaling), t-P38 (#8690S, 1:1000, Cell Signaling), Rac1 (#ARC03, 1:500,
476 Cytoskeleton, Denver, CO), β -actin (#3700S, 1:1000, Cell Signaling) in 1X TBST
477 containing 5% BSA overnight at 4°C with gentle rocking. Membranes were then washed
478 three times for 5 min each with 1X TBST and incubated with secondary antibodies, 1:2000
479 anti-mouse or anti-rabbit horseradish peroxidase (HRP; Cell Signaling) in TBST for 2
480 hours at room temperature with gentle rocking. Membranes were washed again three
481 times for 5 min each with 1X TBST. Pierce ECL Plus Western Blotting Substrate (Thermo
482 Fisher Scientific) was added to each membrane and incubated at room temperature for
483 5 min. The blots were then scanned with Odyssey Fc Imaging system (LI-COR, Lincoln,
484 NB). β -actin was used as a loading control. The ratio of the gene of interest over its
485 endogenous control was calculated and expressed as relative intensity.

486

487 *Rac1 pulldown assay*

488 HK374 cells were serum starved overnight, treated with QTP (10 μ M) or QTP +
489 atorvastatin (1 μ M) and irradiated with a single dose of 4 Gy one hour after the drug
490 treatment. 48 hours after the treatment, the cells were lysed in 250 μ l cell lysis buffer
491 supplemented with protease inhibitors and subjected to a pull-down assay for activated
492 Rac1 (#BK035, Cytoskeleton). Briefly, the protein concentration in each sample was
493 determined using the BCA protein assay (Thermo Fisher Scientific) and 500 μ g cell lysate
494 was incubated with PAK-PBD beads at 4°C on a rotator for one hour. The beads were

495 pelleted by centrifugation, washed with 500 μ l wash buffer for two times, resuspended in
496 20 μ l of 2x Laemmli sample buffer and boiled at 100°C for 5 minutes. The pull-down
497 protein samples were then subjected to western blotting with the whole cell lysate and
498 His-tagged Rac1 protein (#RC01, Cytoskeleton) serving as the controls.

499

500 *siRNA and Extreme Limiting Dilution Analysis (ELDA)*

501 HK374 cells were seeded into 6-well tissue-culture plates and transfected with scramble
502 siRNA or Rac1 siRNA by incubation with RNAiMAX-siRNA Lipofectamine duplex
503 (#13778075, Thermo Fisher Scientific) in Opti-MEM medium overnight at 37°C with 5%
504 CO₂. The next day, cell culture medium was changed back to regular DMEM + 10% FBS
505 + 1% P/S. Two days after the transfection, the cells were trypsinized and plated into the
506 non-tissue-culture-treated 96-well plates in DMEM/F12 media, supplemented with SM1
507 Neuronal Supplement, EGF, bFGF and heparin. The next day, the cells were treated with
508 DMSO or QTP (10 μ M) or QTP + atorvastatin (1 μ M) and irradiated with a single dose of
509 4 Gy one hour after the drug treatment. Growth factors were supplemented every two
510 days. Glioma spheres were counted 5 days later (day 7 after siRNA transfection) and
511 presented as the percentage to the initial number of cells plated. The glioma stem cell
512 frequency was calculated using the ELDA software [49]. Both protein and RNA samples
513 were collected at day 2 and day 7 after transfection. Knockdown efficiency was confirmed
514 by RT-PCR and western blotting.

515

516 *Clonogenic assay*

517 Two days after the siRNA transfection, HK374 cells were trypsinized and plated at a
518 density of 100 cells per well in a 6-well plate. The next day, the cells were treated with
519 DMSO or QTP (10 μ M) or QTP + atorvastatin (1 μ M) and irradiated with a single dose of
520 4 Gy one hour after the drug treatment. The colonies were fixed and stained with 0.1%
521 crystal violet 5 days later (day 7 after siRNA transfection). Colonies containing at least 50
522 cells were counted in each group.

523

524 *Microtubule stain*

525 HK374 cells were plated into 35 mm dish (No. 1.5 Coverslip, 10 mm Glass
526 Diameter, Poly-D-Lysine coated; #P35GC-1.5-10-C, MatTek Ashland, MA) and the
527 following day treated with QTP (10 μ M) or QTP + atorvastatin (1 μ M) and irradiated with
528 a single dose of 4 Gy one hour after the drug treatment. 48 hours later, cells were stained
529 with ViaFluor® 488 live cell microtubule stains (#70062, Biotium, Fremont, CA) following
530 manufacturer's instructions. Specifically, the cells were washed with PBS and incubated
531 with medium containing probes (0.5 x ViaFluor® dye + 100 μ M verapamil) at 37°C for 30
532 minutes. Fluorescent images were then acquired using a confocal microscope (Nikon A1,
533 Melville, NY).

534

535 *Mass spectrometry*

536 Sample Preparation: Whole blood from mice was centrifuged to isolate plasma.
537 Atorvastatin or simvastatin was isolated by liquid-liquid extraction from plasma: 50 μ L
538 plasma was added to 2 μ L internal standard and 100 μ L acetonitrile. Mouse brain tissue
539 was washed with 2 mL cold saline and homogenized using a tissue homogenizer with

540 fresh 2 mL cold saline. Atorvastatin or simvastatin was then isolated and reconstituted in
541 a similar manner by liquid-liquid extraction: 100 μ L brain homogenate was added to 2 μ L
542 internal standard and 200 μ L acetonitrile. The samples were centrifuged, supernatant
543 removed and evaporated by a rotary evaporator and reconstituted in 100 μ L 50:50
544 water:acetonitrile.

545 Atorvastatin or Simvastatin Detection: Chromatographic separations were performed on
546 a 100 x 2.1 mm Phenomenex Kinetex C18 column (Phenomenex, Torrance, CA) using
547 the 1290 Infinity LC system (Agilent, Santa Clara, CA). The mobile phase was composed
548 of solvent A: 0.1% formic acid in Milli-Q water, and B: 0.1% formic acid in acetonitrile.
549 Analytes were eluted with a gradient of 5% B (0-4 min), 5-99% B (4-32 min), 99% B (32-
550 36 min), and then returned to 5% B for 12 min to re-equilibrate between injections.
551 Injections of 20 μ L into the chromatographic system were used with a solvent flow rate of
552 0.10 mL/min.

553 Mass spectrometry was performed on a 6460 triple quadrupole LC/MS system
554 (Agilent). Ionization was achieved by using positive ion electrospray ionization and data
555 acquisition was made in multiple reaction monitoring mode. Atorvastatin was monitored
556 with the transition from m/z 559.2 \rightarrow 250 with fragmentor settings at 45 V and a collision
557 energy of 17 and an accelerator voltage of 4V, and for Simvastatin m/z 419.2 \rightarrow 198.2 with
558 fragmentor settings at 85 V and a collision energy of 5 and an accelerator voltage of 4 V.
559 Atorvastatin brain concentrations were adjusted by 1.4% of the mouse brain weight for
560 the residual blood in the brain vasculature as described by Dai *et al.* [50].

561

562 *Statistics*

563 Unless stated otherwise all data shown are represented as mean \pm standard error mean
564 (SEM) of at least 3 biologically independent experiments. A p -value of ≤ 0.05 in an
565 unpaired two-sided t -test, One-way or Two-way ANOVA indicated a statistically significant
566 difference. For Kaplan-Meier estimates a p -value of 0.05 in a log-rank test indicated a
567 statistically significant difference.

568

569 **Competing interests**

570 The authors declare no competing interests.

571

572 **Availability of data and materials**

573 All data and methods are included in the manuscript. Patient-derived cell lines will be
574 made available upon reasonable request to the corresponding author.

575

576 **Figure legends**

577

578 **Figure 1.**

579 **Combination therapies that converge on the immediate-early response to radiation**
580 **through the MAPK cascade universally upregulate the mevalonate pathway.**

581 **(a/b)** Western blotting of *p*-ERK, total ERK, *p*-P38, and total P38 in patient-derived GBM
582 HK374 and HK217 cell lines upon radiation (a single dose of 10 Gy) in combination of
583 QTP (10 μ M) or TMZ (1 mM) or Vincristine (250 nM) at 2 hours after treatment. **(c)** The
584 densitometry measurements of *p*-ERK/total ERK and *p*-P38/total P38 using Image J.
585 **(d/e)** Heatmap showing the results of quantitative RT-PCR for the cholesterol
586 biosynthesis related genes in both HK374 and HK217 cells treated with radiation (a single
587 dose of 4 Gy) in the presence of absence of TMZ (1 mM) for two consecutive days. **(f/g)**
588 Heatmap showing the results of quantitative RT-PCR for the cholesterol biosynthesis
589 related genes in both HK374 and HK217 cells treated with radiation (a single dose of 4
590 Gy) in the presence of absence of Vincristine (250 nM) for 24 hours. All experiments have
591 been performed with at least 3 biological independent repeats. *p*-values were calculated
592 using One-way ANOVA. * *p*-value < 0.05, ** *p*-value < 0.01, *** *p*-value < 0.001, **** *p*-
593 value < 0.0001.

594

595 **Figure 2.**

596 **Upregulation of the mevalonate pathway in response to anti-cancer treatments *in***
597 ***vivo* is restricted to glioma cells.**

598 **(a)** Schematic of the experimental design underlying Figures 2 and 3. **(b)** Heatmap
599 showing the results of quantitative RT-PCR for the cholesterol biosynthesis related genes
600 in the tumor specimen harvested from the PDOX GBM mouse model at day 2 after the
601 treatment of radiation (a single dose of 4 Gy) in combination with QTP (30 mg/kg) or
602 solvent control using the human- and mouse-specific primers. **(c)** The levels of total, free
603 cholesterol and cholesterol-esters in the tumors harvested from the PDOX GBM mouse
604 model at day 2 after the treatments. **(d)** The concentration of free fatty acid in the tumors
605 harvested from the PDOX GBM mouse model at day 2 after the treatments. All
606 experiments have been performed with at least 3 biological independent repeats. *p*-
607 values were calculated using Unpaired Student's *t*-tests. * *p*-value < 0.05, ns: not
608 significant.

609

610 **Figure 3.**

611 **Statins reduce treatment-induced upregulation of cholesterol biosynthesis in**
612 **PDOXs.**

613 **(a/b)** Brain and plasma levels of atorvastatin and simvastatin in C57BL/6 mice after a
614 single injection (atorvastatin – 30 mg/kg, i.p.; simvastatin – 7 mg/kg, i.p.). **(c)** The levels
615 of total, free cholesterol and cholesterol-esters in the tumors harvested from the PDOX
616 GBM mouse model at day 5 after the treatment of radiation (a single dose of 4 Gy) in
617 combination with QTP (30 mg/kg), atorvastatin (30 mg/kg) or simvastatin (7 mg/kg). **(d)**
618 The concentration of free fatty acid in the tumors harvested from the PDOX GBM mouse
619 model at day 5 after the treatments. **(e)** Heatmap showing the results of quantitative RT-
620 PCR for the cholesterol biosynthesis related genes in the tumor specimen harvested from

621 the PDOX GBM mouse model at day 5 after the treatments using the human- and mouse-
622 specific primers. **(f)** Survival curves for NSG mice implanted intracranially with 3×10^5
623 HK374-GFP-Luciferase glioma cells and grafted for 3 days. Mice were irradiated with a
624 single fraction of 0 or 10 Gy and treated with corn oil or QTP (30 mg/kg, subQ, 5-day
625 on/2-day off schedule) or triple combination of 10 Gy plus QTP and simvastatin (7 mg/kg,
626 i.p., 5-day on/2-day off schedule) continuously until they reached the study endpoint. Log-
627 rank (Mantel-Cox) test for comparison of Kaplan-Meier survival curves. **(g)** Weight curves
628 for the NSG mice in different treatment groups. All experiments have been performed with
629 at least 3 biological independent repeats. *p*-values were calculated using One-way
630 ANOVA. * *p*-value < 0.05, **** *p*-value < 0.0001, ns: not significant.

631

632 **Figure 4.**

633 **Statins improve median survival in mouse models of GBM undergoing fractionated** 634 **irradiation.**

635 **(a)** Heat map showing the results of quantitative RT-PCR for the cholesterol biosynthesis
636 related genes in HK374 cells treated with radiation (a single dose of 4 Gy) in the presence
637 of absence of ONC201 (a single treatment of 2.5 μ M) at 48 and 72 hours. **(b)** Survival
638 curves for C57BL/6 mice implanted intracranially with 2×10^5 GL261-GFP-Luciferase
639 mouse glioma cells and grafted for 7 days. Mice were irradiated with a single fraction of
640 0 or 10 Gy and weekly treated with Saline or ONC201 (50 mg/kg, i.p.) or triple combination
641 of 10 Gy plus ONC201 (weekly) and atorvastatin (30 mg/kg, i.p., 5-day on/2-day off
642 schedule) continuously until they reached the study endpoint. Log-rank (Mantel-Cox) test
643 for comparison of Kaplan-Meier survival curves. **(c)** H&E-stained coronal sections of the

644 C57BL/6 mice brains implanted with GL261-GFP-Luc cells which were irradiated at 10
645 Gy and treated continuously with ONC201 in the presence of absence of atorvastatin until
646 they met the criteria for study endpoint. **(d)** Schematic of the experimental design of
647 fractionated irradiation in syngeneic mouse model of GBM. **(e)** Kaplan-Meier survival
648 curves for C57BL/6 mice implanted intracranially with GL261-GFP-Luciferase mouse
649 glioma cells and treated with either a single fraction of 0 or 10 Gy or 5 daily fractions of 3
650 Gy each and daily doses of either corn oil, QTP (30 mg/kg, subQ), or QTP plus
651 atorvastatin (30 mg/kg, i.p.). After completion of the radiation treatment all animals were
652 treated with QTP plus atorvastatin until they reached criteria for euthanasia. Log-rank
653 (Mantel-Cox) test for comparison of Kaplan-Meier survival curves. **(f)** H&E stained coronal
654 sections of the C57BL/6 mice brains from the groups of 5 x 3 Gy -> QTP + atorvastatin,
655 5 x 3 Gy + QTP -> QTP + atorvastatin and 5 x 3 Gy + QTP + atorvastatin -> QTP +
656 atorvastatin.

657

658 **Figure 5.**

659 **Identification of Rac1 as the potential contributor for maintaining the stemness of**
660 **surviving glioma cells.**

661 **(a)** Cholesterol biosynthesis pathway and the key selected inhibitors. **(b-e)** Sphere-
662 forming capacity of HK374 spheres treated either with GGTI-298 (GGTase inhibitor) or
663 YM-53601 (squalene synthase inhibitor) or Zaragozic acid (squalene synthase inhibitor)
664 or Lonafarnib (farnesyltransferase inhibitor) at 100, 500 nM, 1 μ M concentrations when
665 combined with radiation (a single dose of 4 Gy) and QTP (10 μ M). **(f-i)** Sphere-forming
666 capacity of HK374 spheres treated either with Ehop-016 (Rac GTPase inhibitor) or Rhosin

667 (RhoA-specific inhibitor) or Y27632 (ROCK1/2 inhibitor) or CID44216842 (Cdc42-
668 selective inhibitor) at 500 nM, 1, 5, 10 μ M concentrations when combined with radiation
669 and QTP. All experiments have been performed with at least 3 biological independent
670 repeats. *p*-values were calculated using One-way ANOVA. * *p*-value < 0.05, ** *p*-value <
671 0.01, *** *p*-value < 0.001, **** *p*-value < 0.0001.

672

673 **Figure 6.**

674 **Treatment-induced upregulation of the mevalonate pathway in glioma affects**
675 **stemness through prenylation of Rac1.**

676 **(a)** HK374 cells were treated with 0 or 4 Gy in the presence or absence of QTP (10 μ M)
677 and/or atorvastatin (1 μ M) for 48 hours. The activated Rac1 was immunoprecipitated by
678 10 μ g PAK-PBD agarose beads from the whole cell lysates and subjected to
679 immunoblotting against Rac1, along with the total proteins. His-tagged Rac1 protein
680 serves as the positive control. **(b)** The densitometry measurements of activated
681 Rac1/total Rac1 using Image J. **(c)** Transwell migration assay of HK374 cells pre-treated
682 with 0 or 4 Gy in the presence or absence of QTP (10 μ M) and/or atorvastatin (1 μ M) for
683 48 hours. **(d)** The quantification of migrated cells using Image J. **(e)** Confocal images of
684 microtubules in HK374 cells treated with 0 or 4 Gy in the presence or absence of QTP
685 (10 μ M) and/or atorvastatin (1 μ M) for 48 hours. White arrowheads: filopodia. Yellow
686 arrowheads: tunneling nanotubes (TNTs). **(f/g)** Rac1 knock-down efficiency was
687 evaluated at both mRNA (qRT-PCR) and protein (western blotting) levels at day 2 and
688 day 7 after siRNA transfection. β -actin was used as the loading control and the
689 densitometry measurements of Rac1 using Image J. **(h)** Clonogenic assay of siCtrl or

690 siRac1 transfected HK374 cells treated with 0 or 4 Gy in the presence or absence of QTP
691 (10 μ M) and/or atorvastatin (1 μ M) for 7 days. **(i)** Sphere-forming capacity of siCtrl or
692 siRac1 HK374 spheres treated with 0 or 4 Gy in the presence or absence of QTP (10 μ M)
693 and/or atorvastatin (1 μ M). All experiments have been performed with at least 3 biological
694 independent repeats. *p*-values were calculated using One-way ANOVA for **b, d**; Unpaired
695 Student's *t*-tests for **f, g**; Two-way ANOVA for **i**. * *p*-value < 0.05, ** *p*-value < 0.01, *** *p*-
696 value < 0.001, **** *p*-value < 0.0001, ns: not significant.

697

698

699 **References**

700

- 701 1. Eramo, A., et al., *Chemotherapy resistance of glioblastoma stem cells*. Cell
702 Death Differ, 2006. **13**(7): p. 1238-41.
- 703 2. Bao, S., *Glioma stem cells promote radioresistance by preferential activation of*
704 *the DNA damage response*. Nature, 2006. **444**: p. 756-760.
- 705 3. Bhat, K., et al., *Dopamine Receptor Antagonists, Radiation, and Cholesterol*
706 *Biosynthesis in Mouse Models of Glioblastoma*. J Natl Cancer Inst, 2021. **113**(8):
707 p. 1094-1104.
- 708 4. Bhat, K., et al., *The dopamine receptor antagonist trifluoperazine prevents*
709 *phenotype conversion and improves survival in mouse models of glioblastoma*.
710 Proc Natl Acad Sci U S A, 2020. **117**(20): p. 11085-11096.
- 711 5. He, L., et al., *Effects of the DRD2/3 antagonist ONC201 and radiation in*
712 *glioblastoma*. Radiother Oncol, 2021. **161**: p. 140-147.
- 713 6. Nishad, S. and A. Ghosh, *Gene expression of immediate early genes of AP-1*
714 *transcription factor in human peripheral blood mononuclear cells in response to*
715 *ionizing radiation*. Radiat Environ Biophys, 2016. **55**(4): p. 431-440.
- 716 7. Tullai, J.W., J.R. Graham, and G.M. Cooper, *A GSK-3-mediated transcriptional*
717 *network maintains repression of immediate early genes in quiescent cells*. Cell
718 Cycle, 2011. **10**(18): p. 3072-7.
- 719 8. Tomicic, M.T., et al., *Apoptosis induced by temozolomide and nimustine in*
720 *glioblastoma cells is supported by JNK/c-Jun-mediated induction of the BH3-only*
721 *protein BIM*. Oncotarget, 2015. **6**(32): p. 33755-68.

- 722 9. Xu, H., et al., *Vincristine Promotes Transdifferentiation of Fibroblasts Into*
723 *Myofibroblasts via P38 and ERK Signal Pathways*. *Front Pharmacol*, 2022. **13**: p.
724 901000.
- 725 10. Weichselbaum, R.R., et al., *Radiation induction of immediate early genes:*
726 *effectors of the radiation-stress response*. *Int J Radiat Oncol Biol Phys*, 1994.
727 **30**(1): p. 229-34.
- 728 11. Dyabina, A.S., et al., *Prediction of blood-brain barrier permeability of organic*
729 *compounds*. *Dokl Biochem Biophys*, 2016. **470**(1): p. 371-374.
- 730 12. Vickers, S., et al., *Metabolic disposition studies on simvastatin, a cholesterol-*
731 *lowering prodrug*. *Drug Metab Dispos*, 1990. **18**(2): p. 138-45.
- 732 13. Pedersen, T.R. and J.A. Tobert, *Simvastatin: a review*. *Expert Opin*
733 *Pharmacother*, 2004. **5**(12): p. 2583-96.
- 734 14. Nair, A.B. and S. Jacob, *A simple practice guide for dose conversion between*
735 *animals and human*. *J Basic Clin Pharm*, 2016. **7**(2): p. 27-31.
- 736 15. Graves, P.R., et al., *Mitochondrial Protease ClpP is a Target for the Anticancer*
737 *Compounds ONC201 and Related Analogues*. *ACS Chem Biol*, 2019. **14**(5): p.
738 1020-1029.
- 739 16. Villa, G.R., et al., *An LXR-Cholesterol Axis Creates a Metabolic Co-Dependency*
740 *for Brain Cancers*. *Cancer Cell*, 2016. **30**(5): p. 683-693.
- 741 17. Gendaszewska-Darmach, E., M.A. Garstka, and K.M. Blazewska, *Targeting*
742 *Small GTPases and Their Prenylation in Diabetes Mellitus*. *J Med Chem*, 2021.
743 **64**(14): p. 9677-9710.

- 744 18. Zhao, Y., et al., *The balance of protein farnesylation and geranylgeranylation*
745 *during the progression of nonalcoholic fatty liver disease*. J Biol Chem, 2020.
746 **295**(15): p. 5152-5162.
- 747 19. Waiczies, S., I. Bendix, and F. Zipp, *Geranylgeranylation but not GTP-loading of*
748 *Rho GTPases determines T cell function*. Sci Signal, 2008. **1**(12): p. pt3.
- 749 20. Li, Y., et al., *Cytoskeletal and Cytoskeleton-Associated Proteins: Key Regulators*
750 *of Cancer Stem Cell Properties*. Pharmaceuticals (Basel), 2022. **15**(11).
- 751 21. Yamaguchi, H. and J. Condeelis, *Regulation of the actin cytoskeleton in cancer*
752 *cell migration and invasion*. Biochim Biophys Acta, 2007. **1773**(5): p. 642-52.
- 753 22. Venkataramani, V., et al., *Disconnecting multicellular networks in brain tumours*.
754 Nat Rev Cancer, 2022. **22**(8): p. 481-491.
- 755 23. Pinto, G., et al., *Patient-derived glioblastoma stem cells transfer mitochondria*
756 *through tunneling nanotubes in tumor organoids*. Biochem J, 2021. **478**(1): p. 21-
757 39.
- 758 24. Stupp, R., et al., *Effects of radiotherapy with concomitant and adjuvant*
759 *temozolomide versus radiotherapy alone on survival in glioblastoma in a*
760 *randomised phase III study: 5-year analysis of the EORTC-NCIC trial*. Lancet
761 Oncol, 2009. **10**(5): p. 459-66.
- 762 25. Stupp, R., et al., *Radiotherapy plus concomitant and adjuvant temozolomide for*
763 *glioblastoma*. N Engl J Med, 2005. **352**(10): p. 987-96.
- 764 26. Laperriere, N., L. Zuraw, and G. Cairncross, *Radiotherapy for newly diagnosed*
765 *malignant glioma in adults: a systematic review*. Radiother Oncol, 2002. **64**(3): p.
766 259-73.

- 767 27. Bai, R.Y., V. Staedtke, and G.J. Riggins, *Molecular targeting of glioblastoma:*
768 *Drug discovery and therapies*. Trends Mol Med, 2011. **17**(6): p. 301-312.
- 769 28. Singh, S.K., et al., *Identification of human brain tumour initiating cells*. Nature,
770 2004. **432**(7015): p. 396-401.
- 771 29. Hemmati, H.D., et al., *Cancerous stem cells can arise from pediatric brain*
772 *tumors*. Proc Natl Acad Sci U S A, 2003. **100**(25): p. 15178-83.
- 773 30. Al-Hajj, M., et al., *Prospective identification of tumorigenic breast cancer cells*.
774 Proc. Natl Acad. Sci. USA, 2003. **100**: p. 3983-3988.
- 775 31. Woodward, W.A., et al., *WNT/beta-catenin mediates radiation resistance of*
776 *mouse mammary progenitor cells*. Proc Natl Acad Sci U S A, 2007. **104**(2): p.
777 618-23.
- 778 32. Phillips, T.M., W.H. McBride, and F. Pajonk, *The response of CD24(-/low)/CD44+*
779 *breast cancer-initiating cells to radiation*. J Natl Cancer Inst, 2006. **98**(24): p.
780 1777-85.
- 781 33. Lagadec, C., et al., *Radiation-induced reprogramming of breast cancer cells*.
782 Stem Cells, 2012. **30**(5): p. 833-44.
- 783 34. Lee, H., D. Kim, and B. Youn, *Targeting Oncogenic Rewiring of Lipid Metabolism*
784 *for Glioblastoma Treatment*. Int J Mol Sci, 2022. **23**(22).
- 785 35. Afshari, A.R., et al., *Effects of statins on brain tumors: a review*. Semin Cancer
786 Biol, 2021. **73**: p. 116-133.
- 787 36. Jiang, P., et al., *In vitro and in vivo anticancer effects of mevalonate pathway*
788 *modulation on human cancer cells*. Br J Cancer, 2014. **111**(8): p. 1562-71.

- 789 37. Fuentes-Fayos, A.C., et al., *Metformin and simvastatin exert additive antitumour*
790 *effects in glioblastoma via senescence-state: clinical and translational evidence.*
791 *EBioMedicine*, 2023. **90**: p. 104484.
- 792 38. Wood, W.G., et al., *Statins and neuroprotection: a prescription to move the field*
793 *forward.* *Ann N Y Acad Sci*, 2010. **1199**: p. 69-76.
- 794 39. Fracassi, A., et al., *Statins and the Brain: More than Lipid Lowering Agents?* *Curr*
795 *Neuropharmacol*, 2019. **17**(1): p. 59-83.
- 796 40. Altwaairgi, A.K., et al., *Atorvastatin in combination with radiotherapy and*
797 *temozolomide for glioblastoma: a prospective phase II study.* *Invest New Drugs*,
798 2021. **39**(1): p. 226-231.
- 799 41. Rosso, L., et al., *A new model for prediction of drug distribution in tumor and*
800 *normal tissues: pharmacokinetics of temozolomide in glioma patients.* *Cancer*
801 *Res*, 2009. **69**(1): p. 120-7.
- 802 42. Herbener, V.J., et al., *Considering the Experimental use of Temozolomide in*
803 *Glioblastoma Research.* *Biomedicines*, 2020. **8**(6).
- 804 43. Perry, J.R., et al., *Phase II trial of continuous dose-intense temozolomide in*
805 *recurrent malignant glioma: RESCUE study.* *J Clin Oncol*, 2010. **28**(12): p. 2051-
806 7.
- 807 44. Dietschy, J.M., *Central nervous system: cholesterol turnover, brain development*
808 *and neurodegeneration.* *Biol Chem*, 2009. **390**(4): p. 287-93.
- 809 45. Whitney, K.D., et al., *Regulation of cholesterol homeostasis by the liver X*
810 *receptors in the central nervous system.* *Mol Endocrinol*, 2002. **16**(6): p. 1378-85.

- 811 46. Yoon, C.H., et al., *The small GTPase Rac1 is involved in the maintenance of*
812 *stemness and malignancies in glioma stem-like cells*. FEBS Lett, 2011. **585**(14):
813 p. 2331-8.
- 814 47. Laks, D.R., et al., *Large-scale assessment of the gliomasphere model system*.
815 Neuro Oncol, 2016. **18**(10): p. 1367-78.
- 816 48. Vlashi, E., et al., *In vivo imaging, tracking, and targeting of cancer stem cells*.
817 Journal of the National Cancer Institute, 2009. **101**(5): p. 350-9.
- 818 49. Hu, Y. and G.K. Smyth, *ELDA: extreme limiting dilution analysis for comparing*
819 *depleted and enriched populations in stem cell and other assays*. J Immunol
820 Methods, 2009. **347**(1-2): p. 70-8.
- 821 50. Dai, H., et al., *Distribution of STI-571 to the brain is limited by P-glycoprotein-*
822 *mediated efflux*. J Pharmacol Exp Ther, 2003. **304**(3): p. 1085-92.
- 823

Table 1. Confidence intervals for stem cell frequency (%).

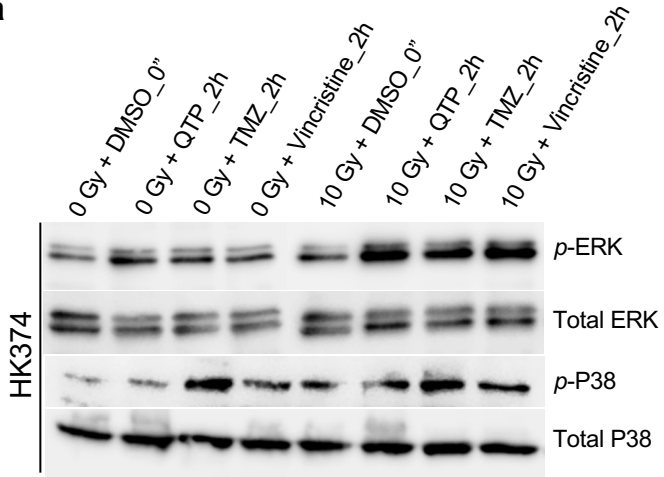
| Groups | Lower | Estimate | Upper |
|-----------------------------------|--------------|-----------------|--------------|
| siCtrl_0 Gy + DMSO | 7.246377 | 9.90099 | 13.45895 |
| siCtrl_4 Gy + DMSO | 3.584229 | 4.901961 | 6.697924 |
| siCtrl_4 Gy + QTP | 0.785546 | 1.079914 | 1.483239 |
| siCtrl_4 Gy + QTP + Atorvastatin | 0.403877 | 0.555247 | 0.762893 |
| siRac-1_0 Gy + DMSO | 4.608295 | 6.329114 | 8.613264 |
| siRac-1_4 Gy + DMSO | 2.083333 | 2.857143 | 3.913894 |
| siRac-1_4 Gy + QTP | 1.48368 | 2.040816 | 2.800336 |
| siRac-1_4 Gy + QTP + Atorvastatin | 0.816327 | 1.122334 | 1.541545 |

Table 2. Pairwise tests for differences in stem cell frequencies.

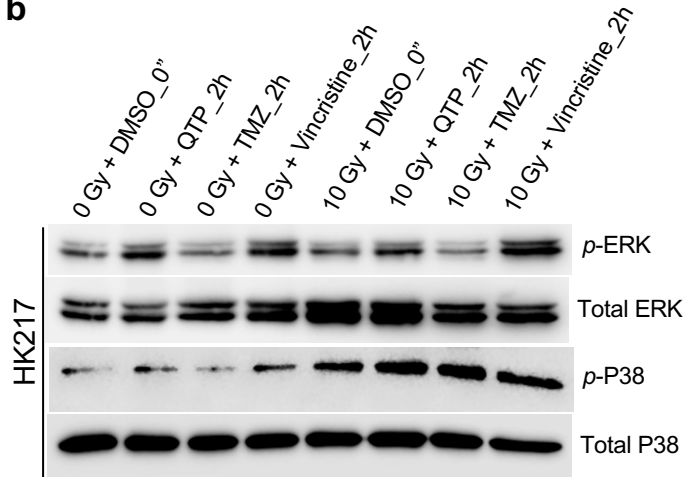
| Group 1 | Group 2 | Chisq | DF | Pr(>Chisq) |
|---------------------|-----------------------------------|--------------|-----------|----------------------|
| siCtrl_0 Gy + DMSO | siCtrl_4 Gy + DMSO | 8.81 | 1 | 0.003 |
| siCtrl_4 Gy + DMSO | siCtrl_4 Gy + QTP | 41 | 1 | 1.51e-10 |
| siCtrl_4 Gy + QTP | siCtrl_4 Gy + QTP + Atorvastatin | 7.86 | 1 | 0.00507 |
| siCtrl_0 Gy + DMSO | siRac-1_0 Gy + DMSO | 3.64 | 1 | 0.0562 |
| siCtrl_4 Gy + DMSO | siRac-1_4 Gy + DMSO | 4.95 | 1 | 0.0261 |
| siRac-1_0 Gy + DMSO | siRac-1_4 Gy + DMSO | 10.7 | 1 | 0.00105 |
| siRac-1_4 Gy + DMSO | siRac-1_4 Gy + QTP | 1.92 | 1 | 0.165 |
| siRac-1_4 Gy + QTP | siRac-1_4 Gy + QTP + Atorvastatin | 6.06 | 1 | 0.0138 |

Figure 1.

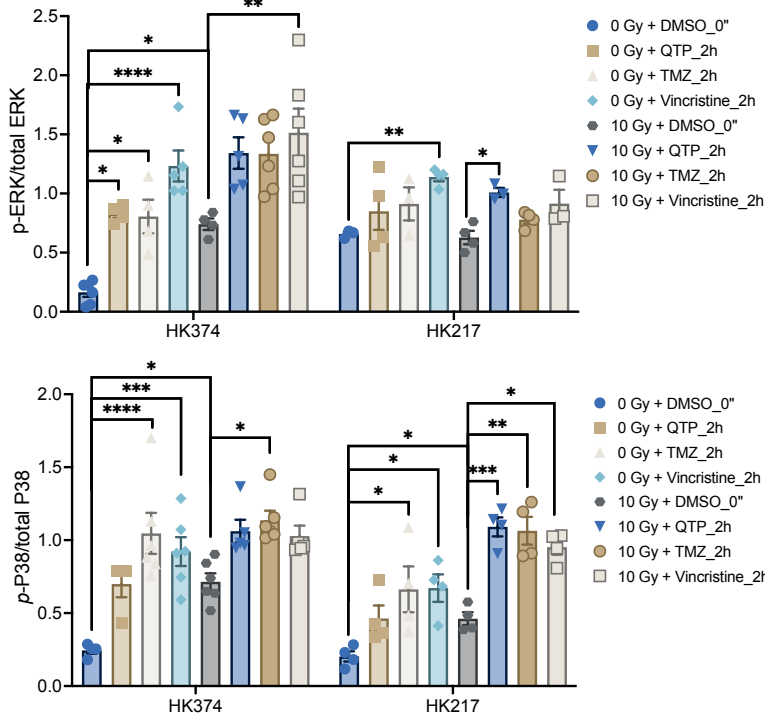
a



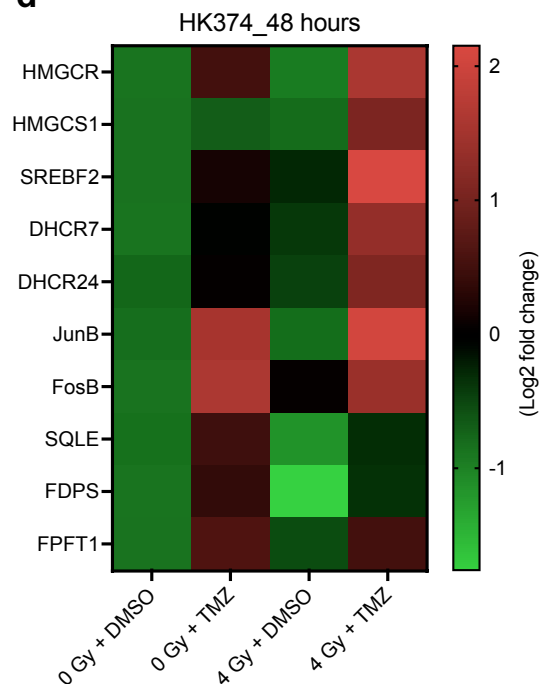
b



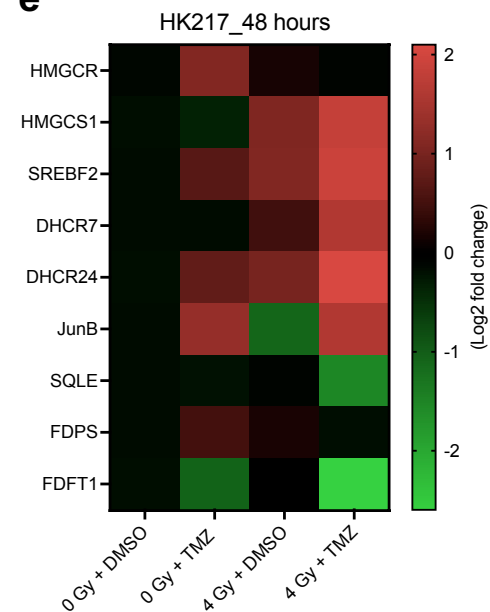
c



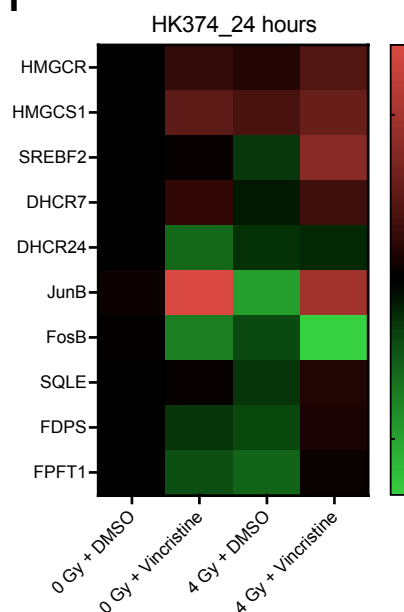
d



e



f



g

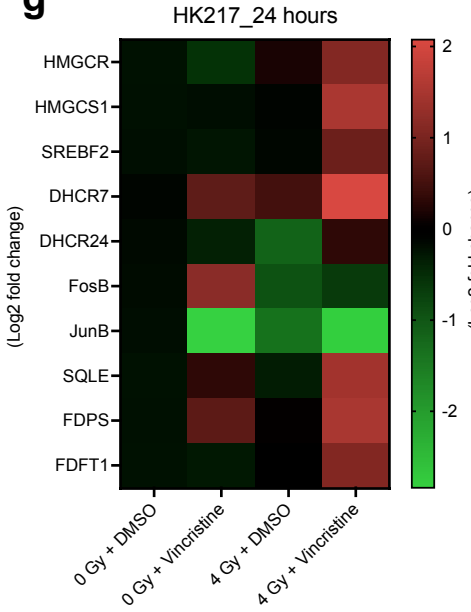
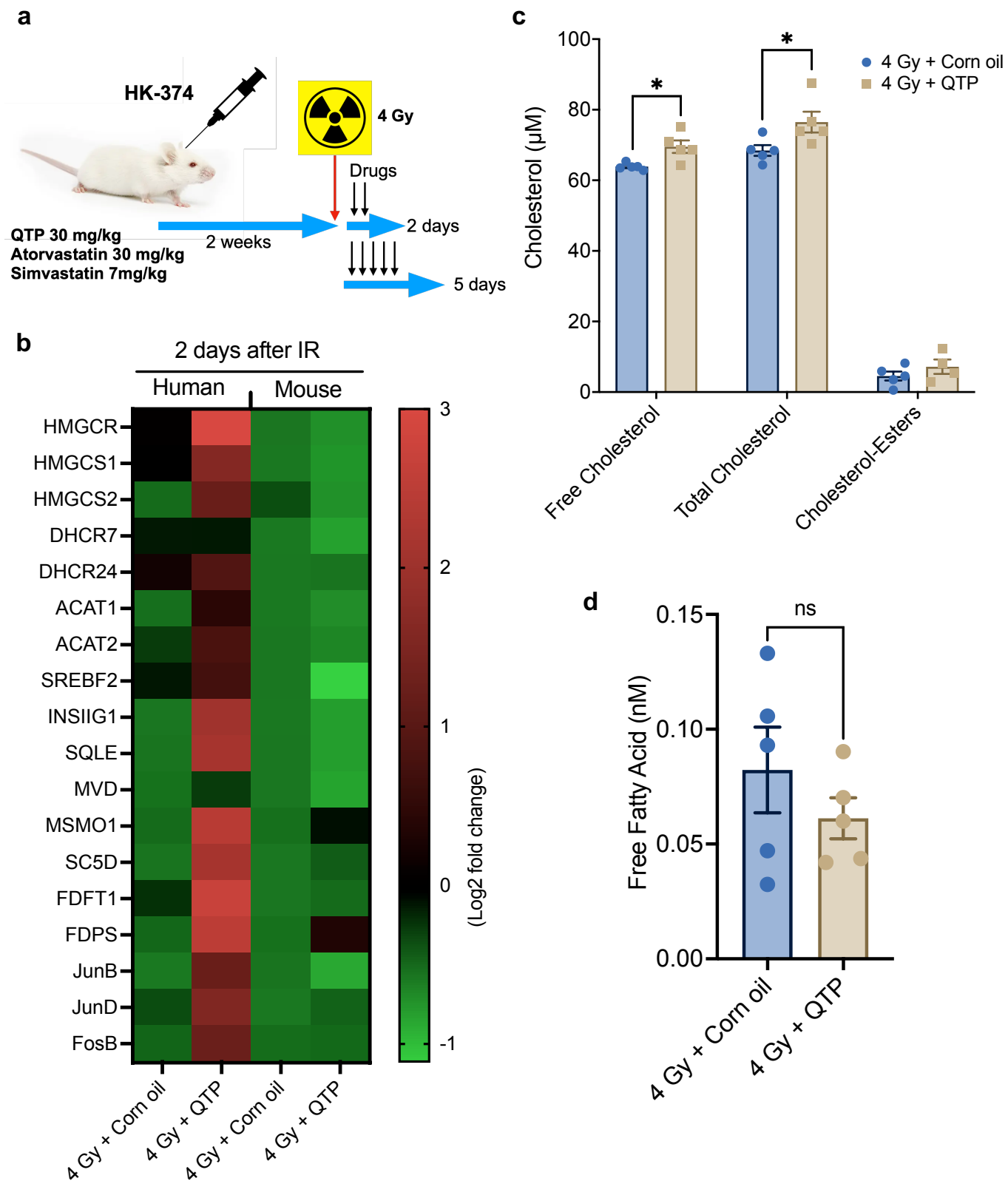
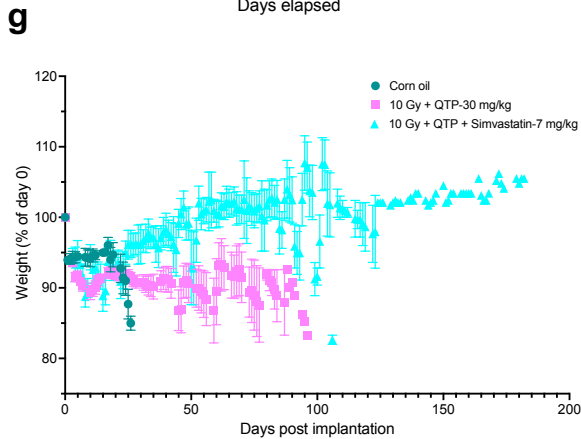
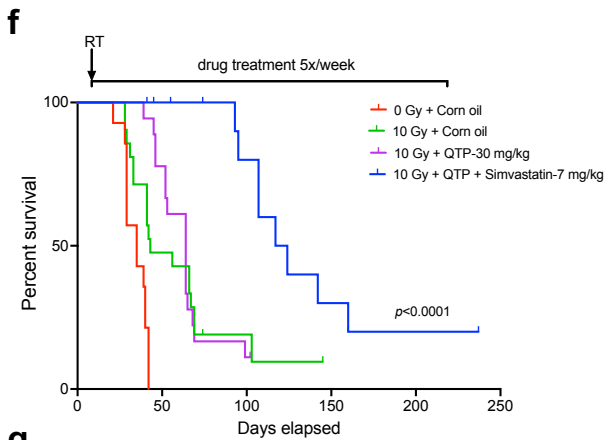
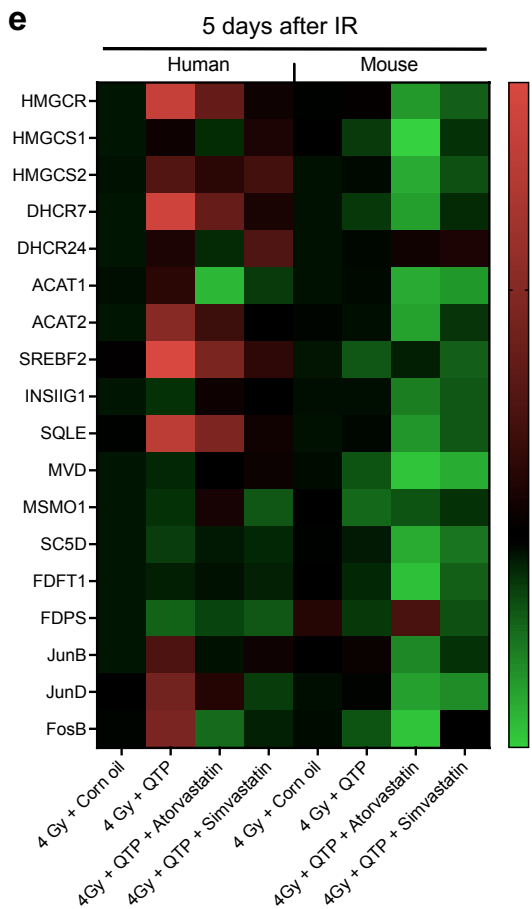
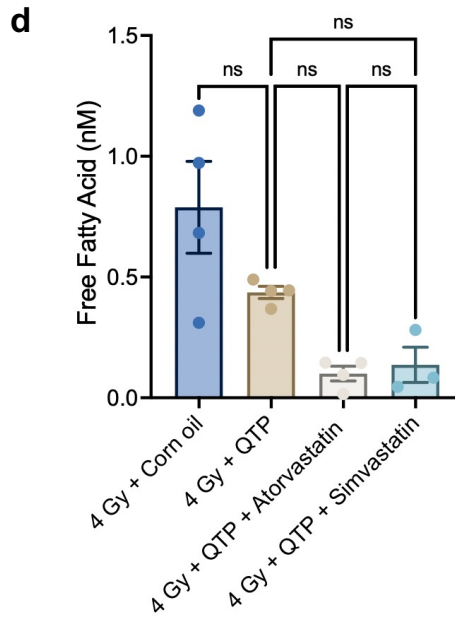
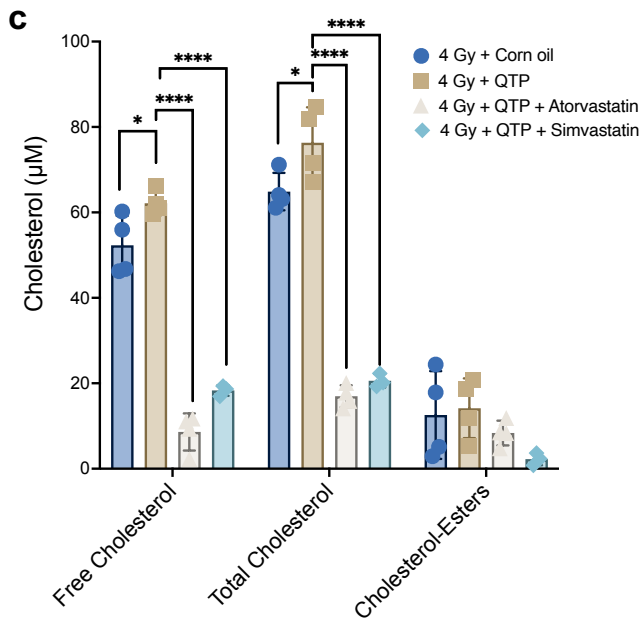
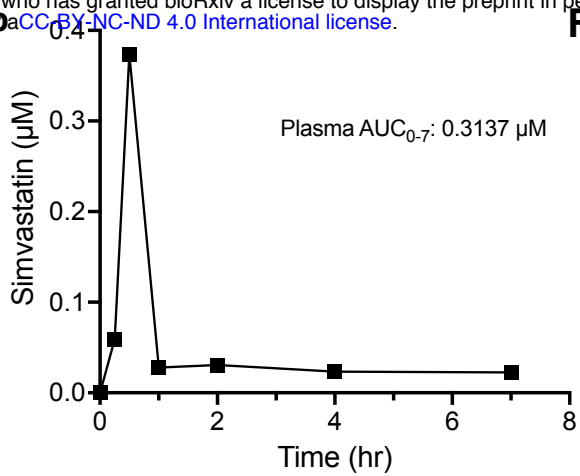
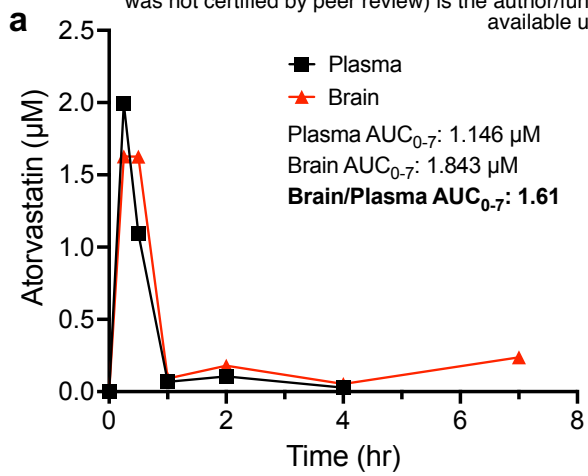


Figure 2.





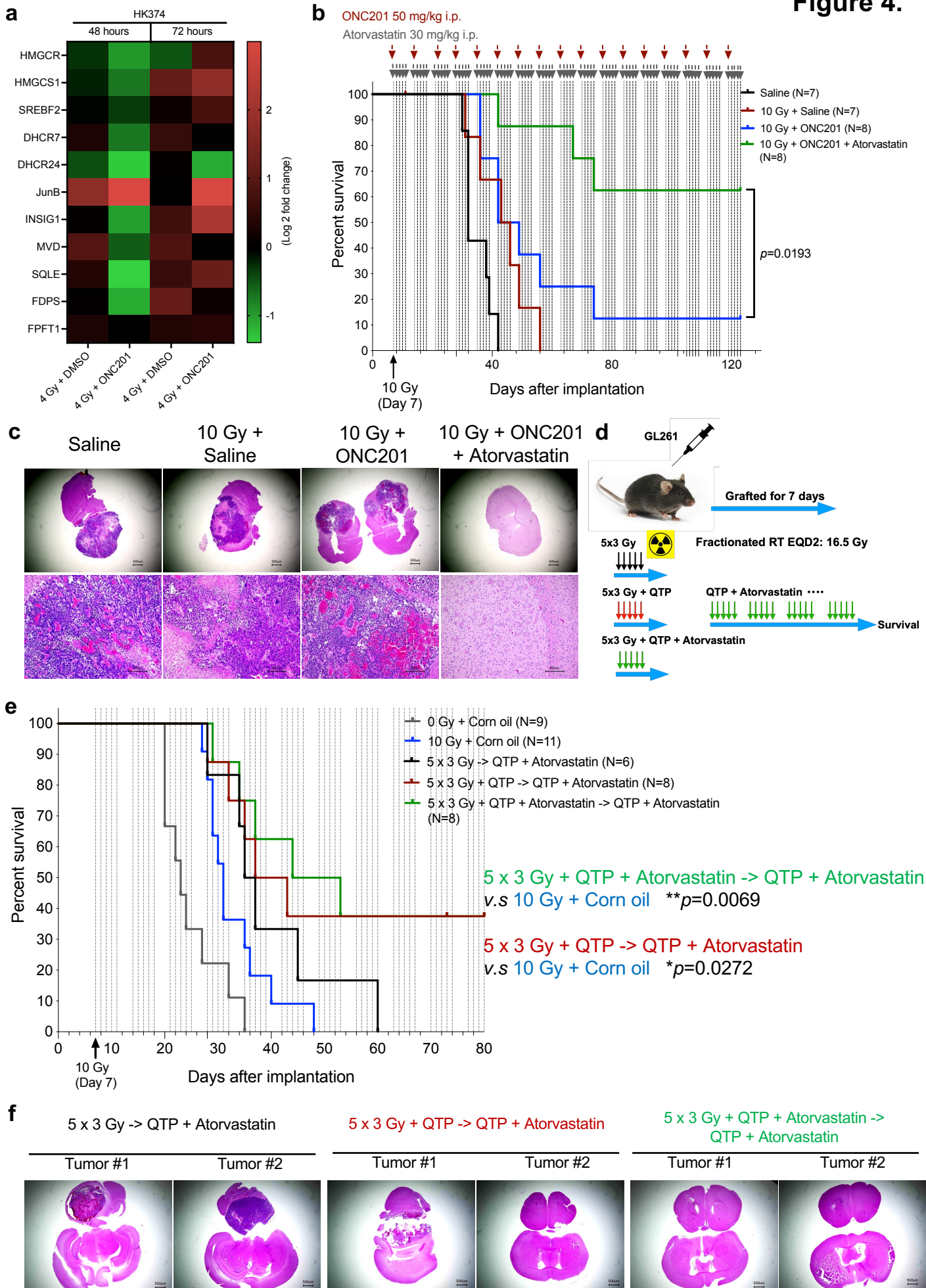
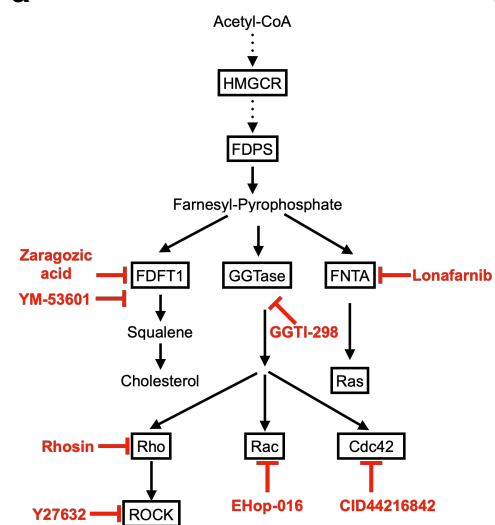
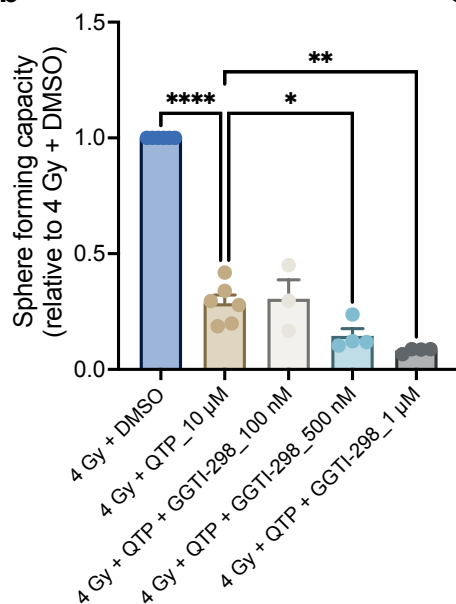


Figure 5.

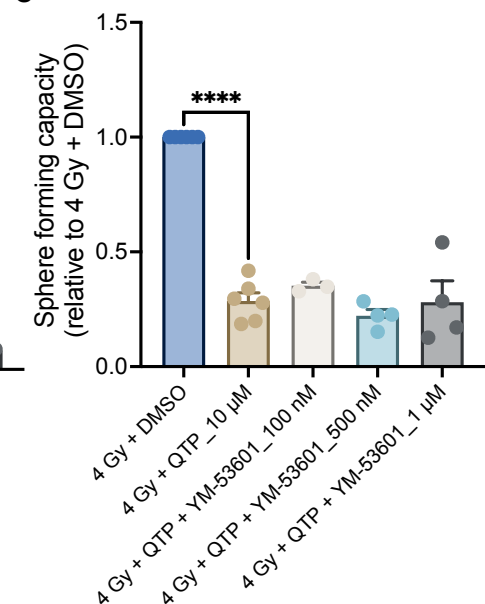
a



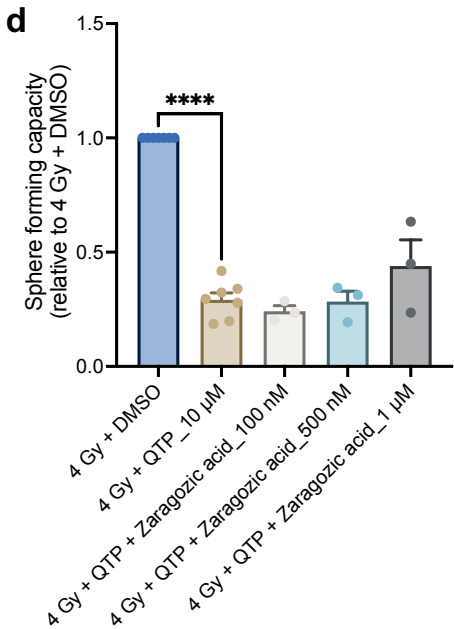
b



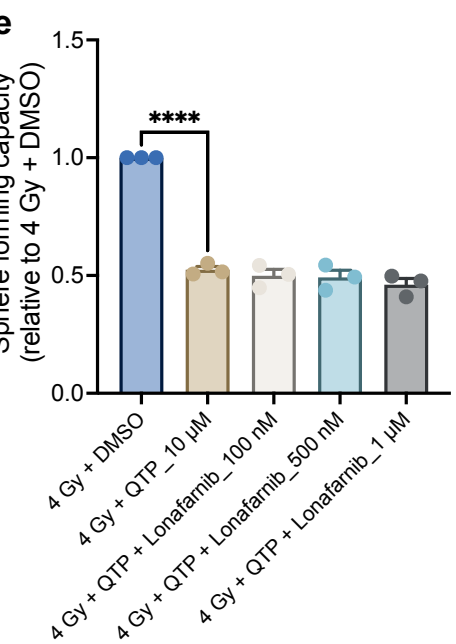
c



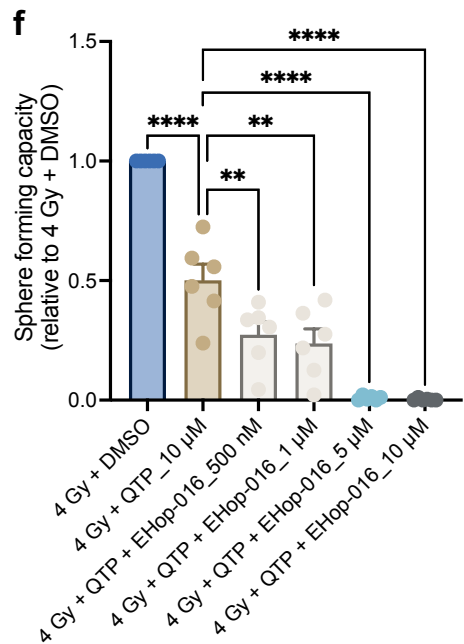
d



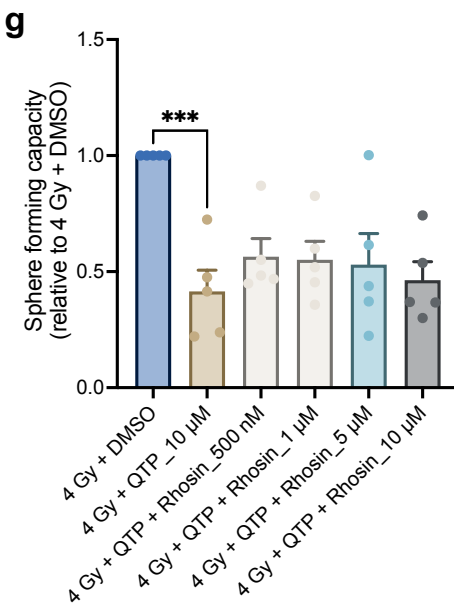
e



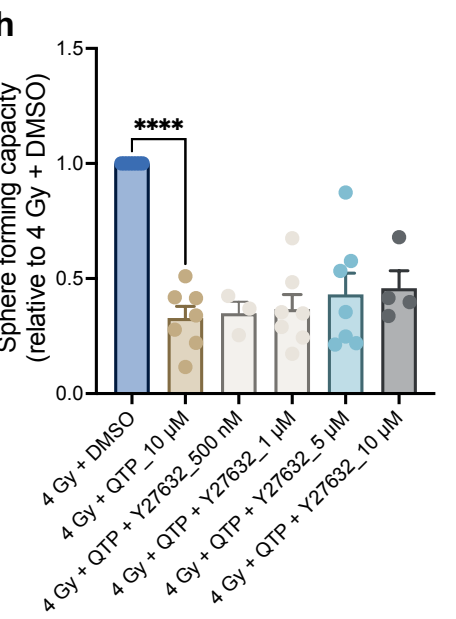
f



g



h



i

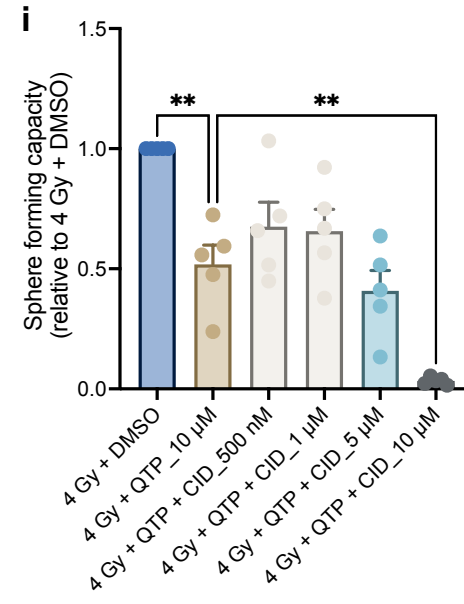
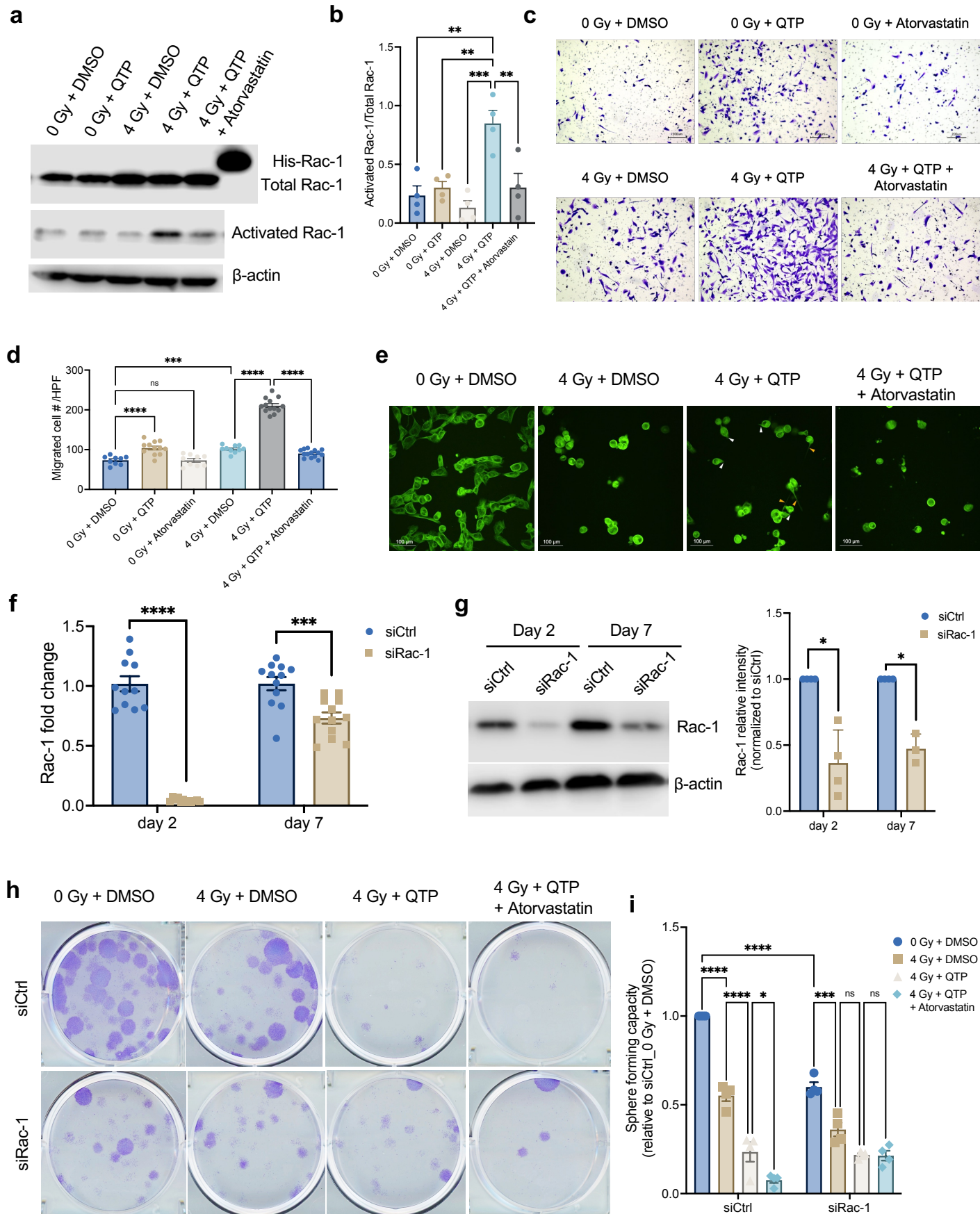
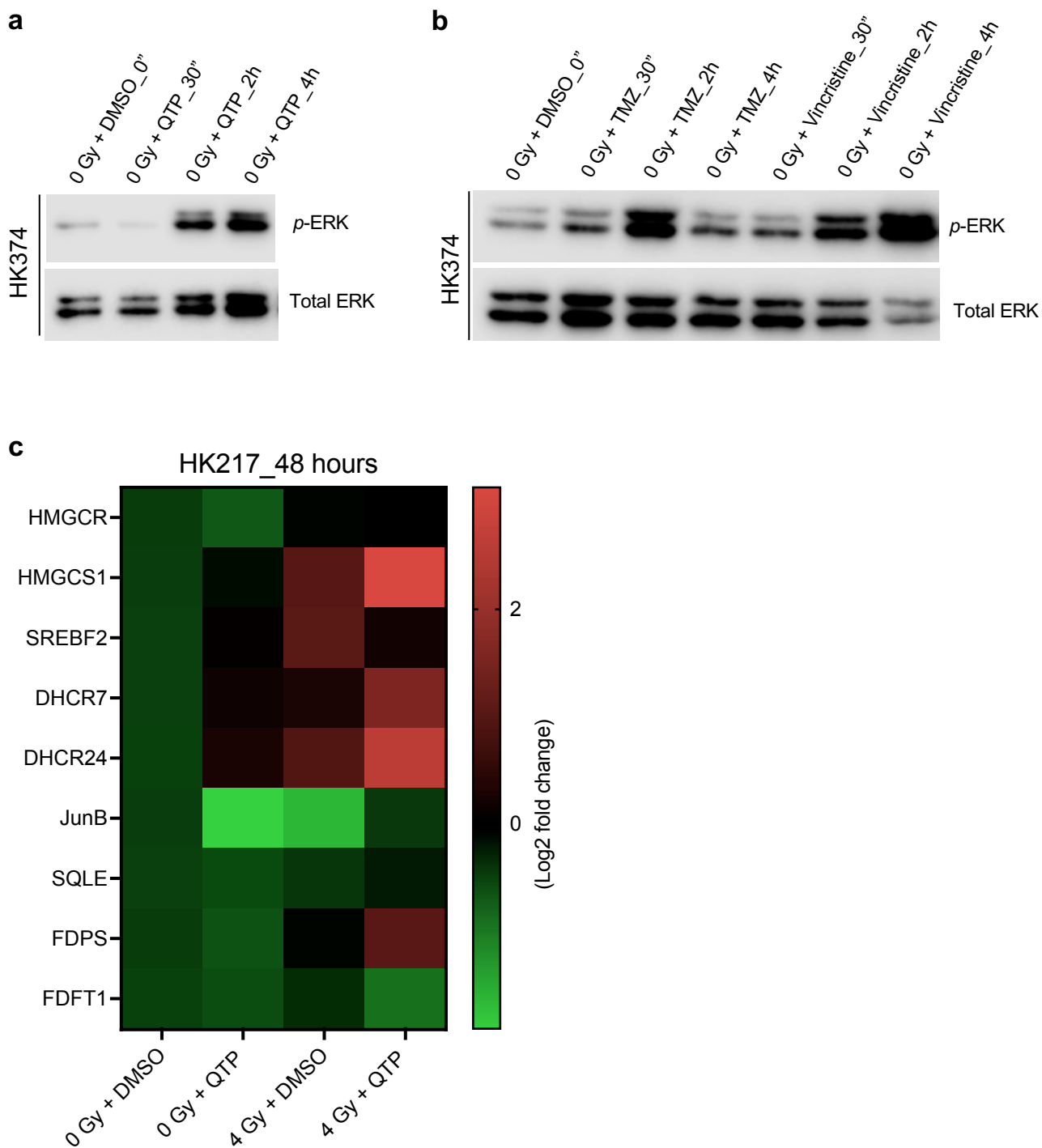


Figure 6.

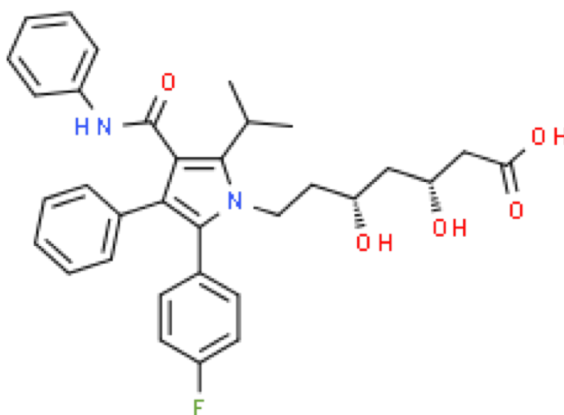


Supplementary Figure 1.

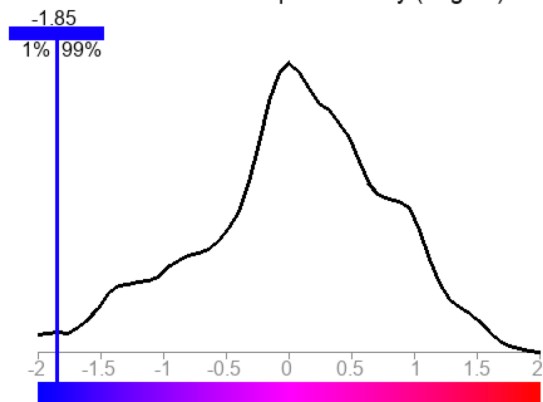


Supplementary Figure 2

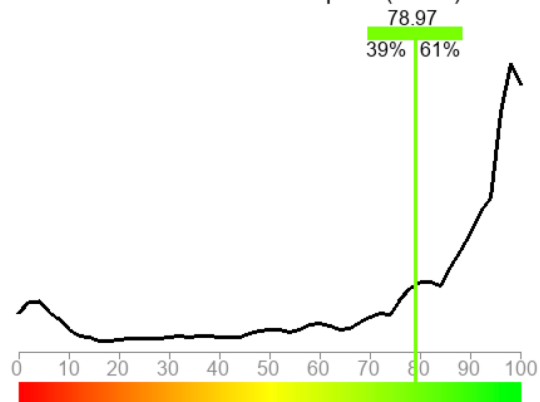
Atorvastatin



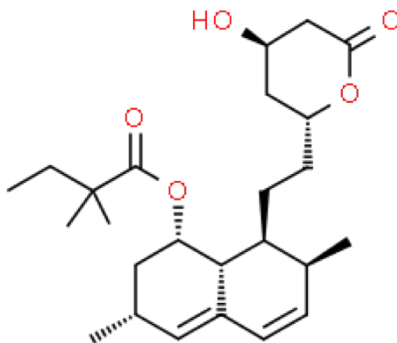
Blood-brain barrier permeability (LogBB)



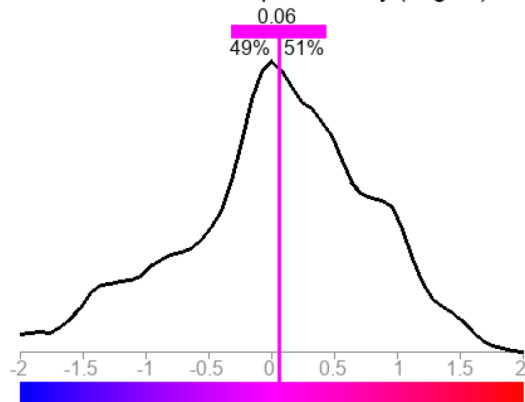
Human intestinal absorption (HIA%)



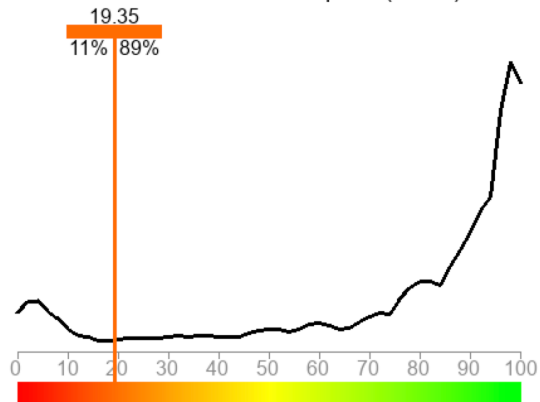
Simvastatin



Blood-brain barrier permeability (LogBB)



Human intestinal absorption (HIA%)



3.1.2 - Implications of drug treatments on normal tissue following irradiation

Bhat, Kruttika, et al. "1-[4-Nitrophenyl] sulfonyl]-4-phenylpiperazine treatment after brain irradiation preserves cognitive function in mice." *Neuro-oncology* 22.10 (2020): 1484-1494.

He, Ling, et al. "Effects of Dopamine Receptor Antagonists and Radiation on Mouse Neural Stem/Progenitor Cells." *bioRxiv* (2023): 2023-01.

A version of this work has been submitted for review.

1-[(4-Nitrophenyl)sulfonyl]-4-phenylpiperazine treatment after brain irradiation preserves cognitive function in mice

Kruttika Bhat, Paul Medina, Ling He, Le Zhang, Mohammad Saki, Angeliki Ioannidis, Nhan T. Nguyen, Sirajbir S. Sodhi, David Sung, Clara E. Magyar, Linda M. Liao, Harley I. Kornblum, and Frank Pajonk

Department of Radiation Oncology, David Geffen School of Medicine, University of California at Los Angeles, Los Angeles, California (K.B., P.M., L.H., L.Z., M.S., A.I., N.T.N., S.S.S., D.S., F.P.); Translational Pathology Core Laboratory, Image Analysis/Virtual Microscopy, Department of Pathology and Laboratory Medicine, Los Angeles, California (C.E.M.); Department of Neurosurgery, David Geffen School of Medicine, University of California at Los Angeles, Los Angeles, California (L.M.L.); NPI-Semel Institute for Neuroscience and Human Behavior at UCLA, Los Angeles, California (H.I.K.); Jonsson Comprehensive Cancer Center at UCLA, Los Angeles, California (L.M.L., H.I.K., F.P.)

Corresponding Author: Frank Pajonk, MD, PhD, Department of Radiation Oncology, David Geffen School of Medicine at UCLA, 10833 Le Conte Ave, Los Angeles, CA 90095–1714 (pajonk@ucla.edu).

Abstract

Background. Normal tissue toxicity is an inevitable consequence of primary or secondary brain tumor radiotherapy. Cranial irradiation commonly leads to neurocognitive deficits that manifest months or years after treatment. Mechanistically, radiation-induced loss of neural stem/progenitor cells, neuroinflammation, and demyelination are contributing factors that lead to progressive cognitive decline.

Methods. The effects of 1-[(4-nitrophenyl)sulfonyl]-4-phenylpiperazine (NSPP) on irradiated murine neurospheres, microglia cells, and patient-derived gliomaspheres were assessed by sphere-formation assays, flow cytometry, and interleukin (IL)-6 enzyme-linked immunosorbent assay. Activation of the hedgehog pathway was studied by quantitative reverse transcription PCR. The *in vivo* effects of NSPP were analyzed using flow cytometry, sphere-formation assays, immunohistochemistry, behavioral testing, and an intracranial mouse model of glioblastoma.

Results. We report that NSPP mitigates radiation-induced normal tissue toxicity in the brains of mice. NSPP treatment significantly increased the number of neural stem/progenitor cells after brain irradiation in female animals, and inhibited radiation-induced microglia activation and expression of the pro-inflammatory cytokine IL-6. Behavioral testing revealed that treatment with NSPP after radiotherapy was able to successfully mitigate radiation-induced decline in memory function of the brain. In mouse models of glioblastoma, NSPP showed no toxicity and did not interfere with the growth-delaying effects of radiation.

Conclusions. We conclude that NSPP has the potential to mitigate cognitive decline in patients undergoing partial or whole brain irradiation without promoting tumor growth and that the use of this compound as a radiation mitigator of radiation late effects on the central nervous system warrants further investigation.

Key Points

1. Patients undergoing radiotherapy for brain cancer experience cognitive decline over time after treatment.
2. NSPP targets hedgehog pathway to expand neural stem cells and progenitor cells without affecting the tumor cells in the brain.
2. In an animal model NSPP mitigates radiation-induced neuro-inflammation and cognitive impairment.

Importance of the Study

Successful radiotherapy of CNS malignancies inevitably leads to cognitive decline in cancer survivors, and treatment options to mitigate this side effect are limited. We present evidence that a piperazine compound can prevent cognitive decline in mice after total brain

irradiation without compromising the antitumor effect of radiation, suggesting that this compound could be used to mitigate radiation side effects in brain tumor patients undergoing radiotherapy.

Exposure of the CNS to ionizing radiation results in normal tissue toxicity.¹ With survival times for cancer patients steadily increasing over the past decades,² more and more patients are now at risk of experiencing late effects of radiotherapy. Patients receiving cranial irradiation—and among those in particular pediatric patients—are facing a decline in cognitive function later in life.^{3–5} The underlying mechanisms include neuroinflammation, diminished neuronal connectivity, and demyelination.¹ Earlier studies by Limoli and colleagues demonstrated that the functional consequences of brain irradiation can be mitigated by injection of neural stem cells into the brain and that newly derived neurons from this stem cell population integrate into the circuitry of the adult brain.⁶ Furthermore, activation of microglia is a critical factor for radiation-induced neuroinflammation, which ultimately leads to cognitive decline. These data indicate that mitigating radiation effects in the intrinsic neural stem/progenitor cell population and microglia cells could be exploited in the radiotherapy setting to prevent radiation-induced cognitive decline.

We previously reported that 1-[(4-nitrophenyl)sulfonyl]-4-phenylpiperazine (NSPP, formerly termed “Compound #5”^{7,8}) prevents the acute radiation syndrome in mice by activating the hedgehog signaling pathway.^{7,8} In this study we tested if NSPP has an effect on the neural stem/progenitor cell population. Our data show that NSPP when given after cranial irradiation preserves the neural stem/progenitor cell population, inhibits microglia activation, mitigates radiation-induced neuroinflammation, and prevents radiation-induced cognitive impairment in mice.

Materials and Methods

Animals

Nestin-enhanced green fluorescent protein (GFP) mice were a kind gift from Dr Grigori Enikolopov, Cold Spring Harbor Laboratory.⁹ C3Hf/Sed/Kam were originally obtained from The MD Anderson Cancer Center. All experiments were performed in accordance with all local and national guidelines for the care of animals.

For orthotopic tumor grafting, 2×10^5 GL261-Luciferase cells were implanted into the right striatum of the brains of female C57BL/6 mice using a stereotactic frame (Kopf Instruments) and a nano-injector pump (Stoelting). Injection coordinates were 0.5 mm anterior and 2.25 mm lateral to the bregma, at a depth of 3.5 mm from the surface of the brain. Tumors were grown for 7 days, after which successful grafting was confirmed by bioluminescence imaging.

Cell Culture

A detailed description of the culture conditions for murine neural stem/progenitor cells, microglia cells, glioblastoma (GBM) cells, and human patient-derived lines is provided in [Supplementary methods](#).

Quantitative Reverse Transcription PCR

Total RNA was isolated using TRIzol reagent (Invitrogen). Synthesis of cDNA was carried out using SuperScript Reverse Transcription IV (Invitrogen). Quantitative PCR was performed in the QuantStudio 3 (Applied Biosystems, Thermo Fisher) using the PowerUp SYBR Green Master mix (Applied Biosystems, #A25742). Cycle threshold (C_t) for each gene was determined after normalization to hypoxanthine-guanine phosphoribosyltransferase (HPRT; mouse) and glyceraldehyde 3-phosphate dehydrogenase (GAPDH; human), and $\Delta\Delta C_t$ was calculated relative to the designated reference sample. Gene expression values were then set equal to $2^{-\Delta\Delta C_t}$ as described by the manufacturer of the kit (Applied Biosystems). All PCR primers were synthesized by Invitrogen and designed for the murine and human sequences of Ptch1, Ptch2, Gli1, Gli2, and the housekeeping genes HPRT and GAPDH ([Supplementary table](#)).

IL-6 Enzyme-Linked Immunosorbent Assays

Enzyme-linked immunosorbent assays (ELISAs) were performed by following the manufacturer's instructions (Mouse IL-6 Quantikine ELISA Kit, Fisher Scientific, #M6000B). The absorbance was read at 450 nm (Spectramax M5, Molecular Devices). A wavelength correction was performed by subtracting readings at 600 nm from those at 450 nm.

Irradiation

Neurosphere cultures were irradiated with 0, 2, or 4 Gy at room temperature using an experimental X-ray irradiator (Gulmay Medical) at a dose rate of 5.519 Gy/min. Control samples were sham irradiated. The X-ray beam was operated at 300 kV and hardened using a 4 mm Be, a 3 mm Al, and a 1.5 mm Cu filter.

Eight-week-old mice were anesthetized with isoflurane, cone beam CT images were acquired, and individual treatment plans were calculated for each mouse using the SmART Plan software package. Subsequently, for the in

vivo experiments the right hemisphere of the brain was irradiated with 4 Gy or 10 Gy using a single beam. For behavioral studies, the whole brain was irradiated with 10 Gy using 2 opposing beams. The X-ray beam was operated at 225 kV.

Dosimetry traceable by NIST (National Institute of Standards and Technology) on both X-ray machines was performed using a micro-ionization chamber.

In Vitro Drug Treatment

NSPP (Vitascreen) was solubilized in dimethyl sulfoxide (DMSO). Three hours after irradiation, neurosphere cultures were treated with NSPP (10 μ M) or DMSO.

In Vivo Drug Administration

In vivo neural stem/progenitor experiments: 0.55 mg of NSPP was dissolved in 15 μ L DMSO and then suspended in 1 mL of 1% Cremophor EL (CrEL; Sigma-Aldrich). Starting 24 hours after irradiation, mice received 5 daily subcutaneous injections of 5 mg/kg of NSPP or DMSO/CrEL.

For behavioral studies, starting immediately after 10 Gy whole brain irradiation, mice received 5 daily subcutaneous injections of 5 mg/kg NSPP or DMSO/CrEL.

In Vitro Assays with Patient-Derived GBM Specimens

For the assessment of self-renewal in vitro, HK-374, HK-157, and HK-382 cells were irradiated with 0 or 4 Gy. Three hours after irradiation, cells were treated with either DMSO or NSPP. The medium was supplemented with DMSO or NSPP every other day for 2 weeks. The number of spheres formed in each treatment group was normalized against the non-irradiated control.

Brain Dissociation

Five days after drug treatment, the brains of the mice were harvested and placed on the Acrylic Mouse Brain Slicer Matrix (Zivic Instruments, #BSMAA001-1). Coronal sections starting from 2 mm anterior to 2 mm posterior of the bregma were cut and the left hemisphere was separated from the right. The brain tissue was minced into very small pieces using a scalpel and the cells were isolated as mentioned in [Supplementary methods](#) (neural stem cell culture). The cells were then used for either flow cytometric analysis to assess the percentage of Nestin-GFP⁺ cells in different treatment groups or to quantify self-renewal capacity in neurosphere formation assays.

Behavioral Testing

All of the behavioral experiments (Novel Object Recognition [NOR], Object in Place [OIP], Fear Conditioning [FC]) were conducted in the Behavioral Testing Core at UCLA. A detailed description is provided in [Supplementary methods](#).

Flow Cytometry

Passage #2 neurospheres established from the brains of Nestin-GFP mice were harvested and dissociated into single cell suspension as described in [Supplementary methods](#). Single cell suspensions were either subjected to fluorescence activated cell sorting (FACS) (Flow Cytometry Core, Terasaki, BD FACS ARIA) for GFP-high, -medium, and -low cell populations or analyzed for GFP expression using a MACSQuant Analyzer (Miltenyi Biosciences) and the FlowJo software package v10.

Neurosphere-Formation Assay

In order to assess self-renewal capacity, passage #2 neurospheres from Nestin-GFP mice were trypsinized and plated into 96-well nontreated plates containing 1x complete NeuroCult media, at a range from 1 to 1000 cells/well. Growth factors (epidermal and basic fibroblast), were added every 3 days, and the cells were allowed to form neurospheres for 14 days. The number of spheres formed per well was then counted and expressed as a percentage of the initial number of cells plated.

Immunohistochemistry

Immunohistochemistry was performed using standard protocols. A detailed description is included in [Supplementary methods](#).

Statistical Analysis

All statistical analyses were performed using the GraphPad Prism software package. Unless stated otherwise, results were derived from 3 biological replicates or at least 3 animals per group. A *P*-value ≤ 0.05 in a Student's *t*-test or one-way ANOVA was considered statistically significant. Kaplan–Meier estimates were calculated using GraphPad Prism, and a *P*-value of 0.05 in log-rank test indicated a statistically significant difference.

Results

Radiation Mitigation in Neural Stem/Progenitor Cells In Vitro

Passage #2 neurospheres from Nestin-GFP mice, in which most cells were Nestin-GFP⁺, were used for all in vitro experiments ([Figure 1A](#)). In order to test the self-renewing capacity of the sorted GFP-high, -medium, and -low cells from neurospheres we performed in vitro limiting dilution assays. Nestin-GFP^{high} cells showed 4.3-fold higher sphere formation than Nestin-GFP^{med} cells and 13.5-fold higher sphere formation than Nestin-GFP^{low} cells ([Figure 1B](#)), thus supporting the neural stem/progenitor phenotype of Nestin-GFP^{high} cells. Irradiation of the neurospheres with 0, 2, or 4 Gy preferentially reduced the size of the Nestin-GFP^{high} cell population ([Figure 1C](#)). This was in line with

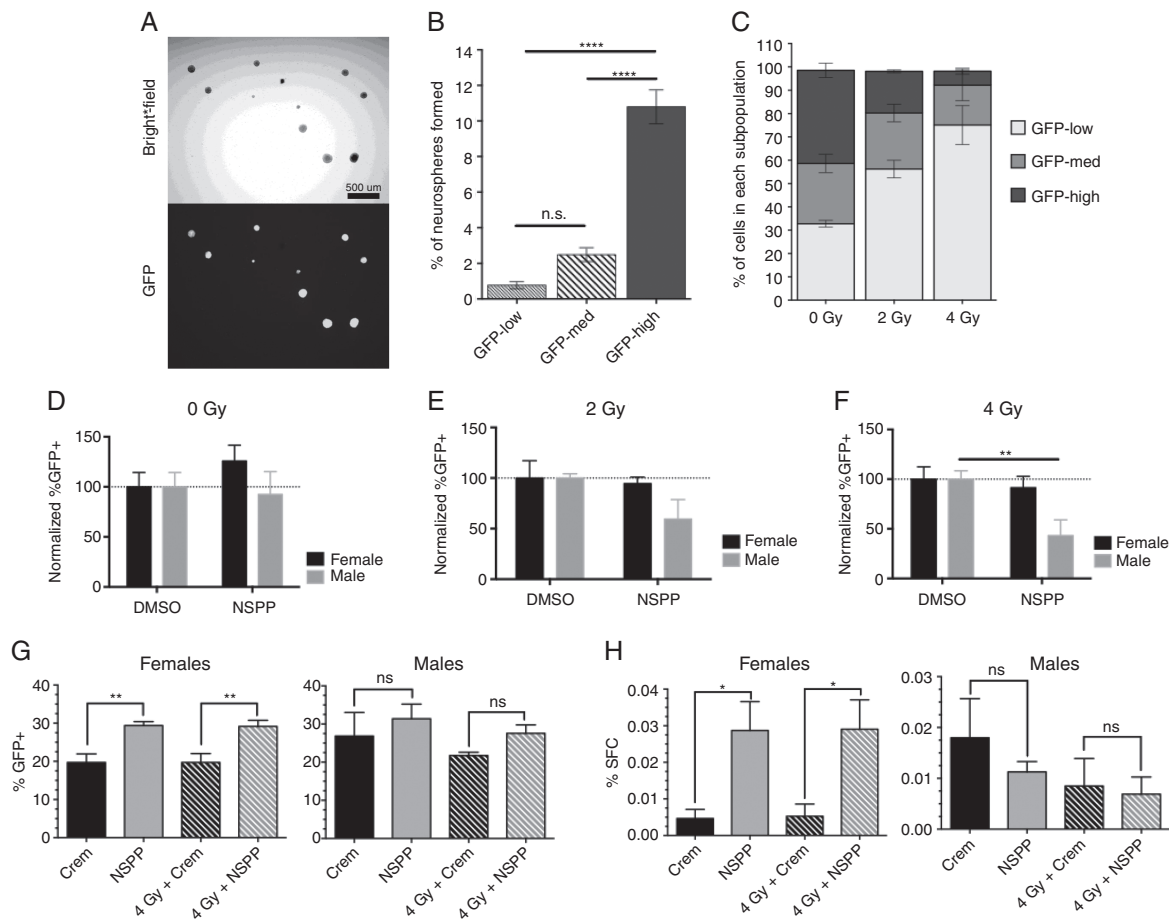


Figure 1. Radiation mitigation in neural/progenitor cells in vitro and in vivo. (A) Representative images of neurosphere cultures established from the brains of Nestin-GFP mice. Bright-field and GFP image (4x). (B) Sorted GFP^{high}, _{medium}, and _{low} cells were subjected to an in vitro limiting dilution assay. (C) Effect of radiation (0, 2, or 4 Gy) on 3 different subpopulations of Nestin-GFP neurospheres. Neurospheres (passage #2) from male or female newborn pups were subjected to 0 (D), 2 (E), or 4 Gy (F) followed by a single treatment with either DMSO or NSPP (10 μ M) 3 hours post irradiation. Eight-week-old Nestin-GFP male and female mice were sham irradiated or irradiated with 4 Gy. After 24 hours, mice were treated with DMSO/CrEL or NSPP (5 mg/kg) subcutaneously for 5 days. The brains of the mice were harvested, dissociated, and analyzed by FACS (G) or sphere forming assays (H). All experiments in this figure have been performed with at least 3 independent biological repeats. (Unpaired *t*-test. **P* < 0.05, ***P* < 0.01, *****P* < 0.0001.)

a previous report on radiation-induced differentiation of neural stem/progenitor cells.¹⁰

Next, we irradiated neurospheres with 0, 2, or 4 Gy and treated the cells with NSPP. NSPP failed to increase the size of the population of Nestin-GFP^{high} neural stem/progenitor cells (Figure 1D–F). While NSPP did not show any effect on the neurospheres derived from the female newborn pups, it significantly reduced the Nestin-GFP^{high} population of cells derived from the male newborn pups, especially in the 4 Gy treated groups.

Radiation Mitigation in Neural Stem/Progenitor Cells In Vivo

We next considered the possibility that our lead compound targets neural stem/progenitor cells indirectly, which, however, cannot be easily tested in the absence of the correct

microenvironment in vitro. To investigate this, 8-week-old male and female Nestin-GFP mice were irradiated with a dose of 4 Gy to the right brain hemisphere. The radiation treatment plan ensured sparing of the contralateral hemisphere from irradiation, thus allowing for an internal unirradiated control for each individual mouse. 24 hours later the animals began treatment with 5 daily injections of CrEL/DMSO or NSPP. The brains were harvested, digested, and analyzed for the number of Nestin-GFP^{high} stem/progenitor cells, and the self-renewing capacity of the isolated cells was evaluated.

NSPP significantly increased the number of Nestin-GFP^{high} stem/progenitor cells in female mice (Figure 1G, left panel). In male mice we observed a similar trend but the effect was not significant (Figure 1H, left panel). In in vitro limiting dilution assays we observed a significant increase in sphere-forming capacity in cells obtained from female mice treated with NSPP but not in cells obtained

from male mice (Figure 1G, H, right panel). Therefore, all remaining studies were conducted in female mice.

NSPP Mitigates Radiation-Induced Neuroinflammation

Six-week-old female C3H mice were treated with a single fraction of 4 or 10 Gy to the right brain hemisphere (Figure 2A). Starting 24 hours after irradiation, the mice were treated with either DMSO/CrEL or NSPP for 5 days. The brains were harvested, fixed in formalin, and embedded in paraffin, and 4 μ m sections were subjected to immunohistochemistry. Sections were either stained with hematoxylin and eosin (H&E) or stained against glial fibrillary acidic protein (GFAP; marker for reactive astrocytes marker), Iba1 (ionized calcium binding adaptor molecule 1; an activated microglia marker), and Ki67 (proliferation

marker) and subjected to an automated image analysis (Figure 2B–E).

The slides were scored for positively stained cells in the cortex, corpus callosum, *cornu ammonis* 1 stratum pyramidale (CA1sp), and the dentate gyrus. In the non-irradiated group, NSPP did not show significant changes in GFAP, Iba1, or Ki67 expression. When NSPP was given on 5 consecutive days starting 24 hours after irradiation, it led to a significant reduction in GFAP and Iba1 expression, thus indicating mitigation of radiation-induced neuroinflammation (Figure 3A).

To further confirm the anti-inflammatory effect of NSPP, we collected conditioned media from EOC20 microglia cells 24 hours after exposure to irradiation with 0 or 10 Gy and treatment with DMSO or NSPP in vitro. IL-6 secretion levels were assessed using ELISA. In line with the well-known pro-inflammatory effect of radiation, we observed a significant

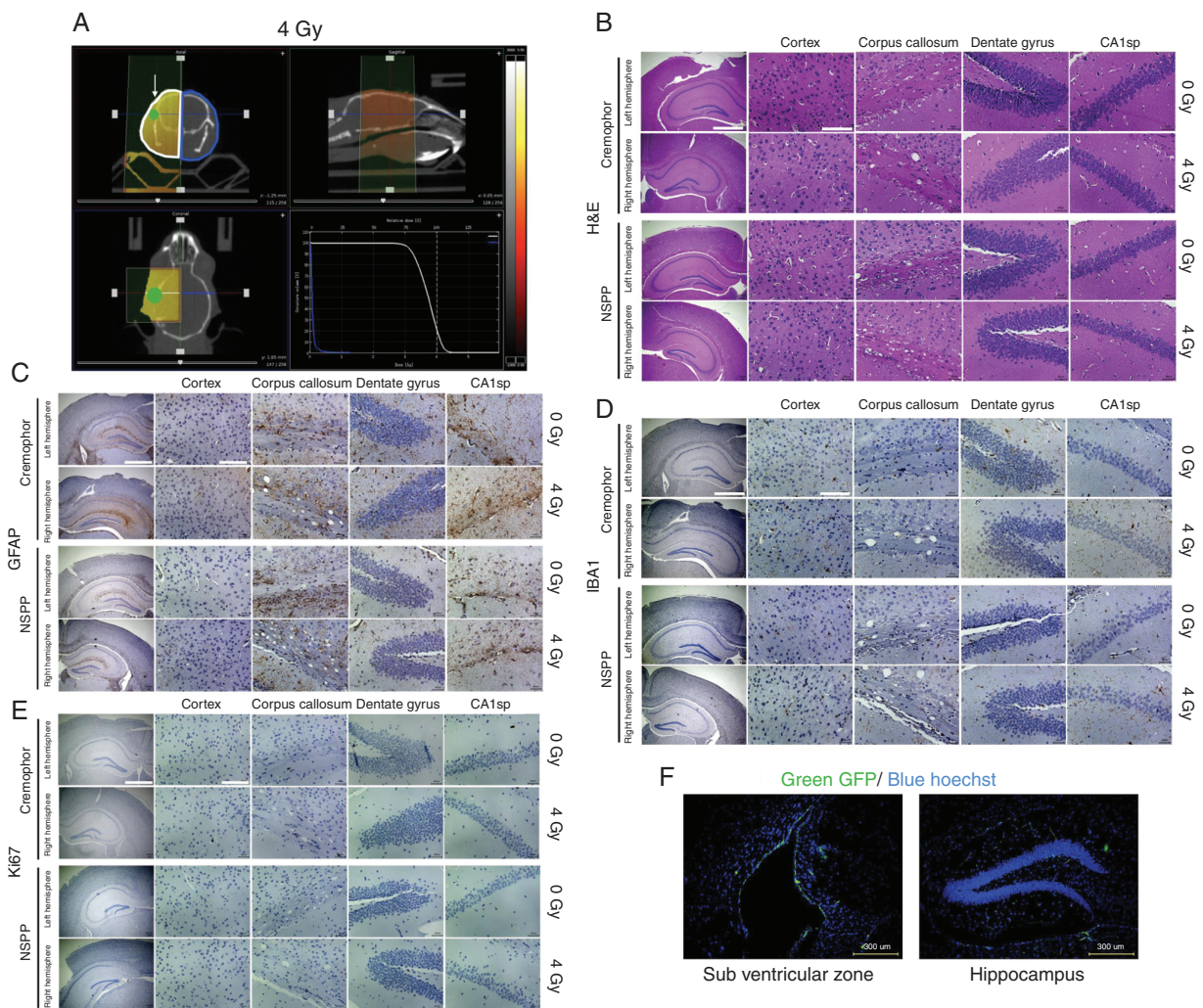


Figure 2. Radiation treatment plans and immunohistochemistry images. (A) Six-week-old C3H female mice were irradiated with 0 or 4 Gy and treated with DMSO/CrEL or NSPP (5 mg/kg, s.c.) for 5 days. Coronal sections were stained with H&E (B) or labeled with antibodies against GFAP (C), Iba1 (D), or Ki67 (E). Scale bars in low power images (4x, left columns): 1000 μ m. Scale bars in high power images (40x): 100 μ m. (F) Representative images (10x) of the subventricular zone and hippocampus region of 8-week-old Nestin-GFP mice labeled for GFP.

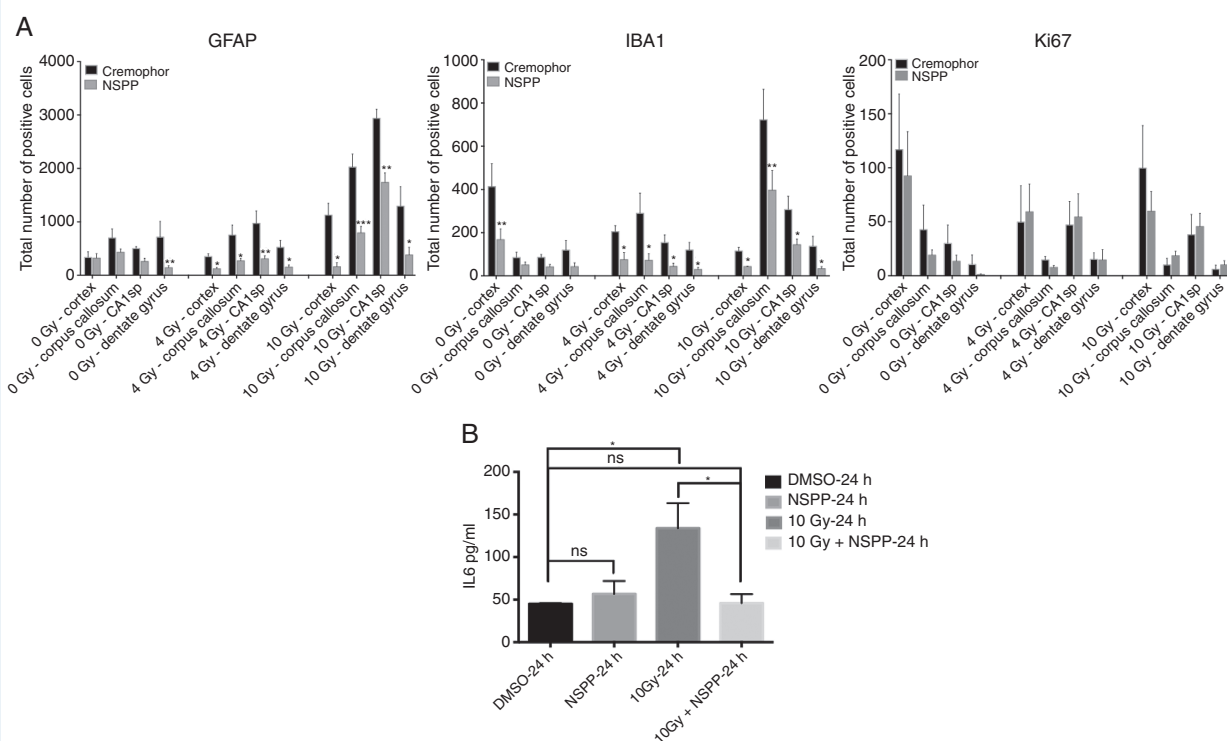


Figure 3. NSPP mitigates radiation-induced neuroinflammation. (A) Coronal sections stained against GFAP (left panel), Iba1 (center panel), and Ki67 (right panel) were quantified for the total number of positive cells in the cortex, corpus callosum, CA1sp, and dentate gyrus regions of the brain in the unirradiated and irradiated mice. (B) ELISA for IL-6 using conditioned media from normal EOC20 microglia cells 24 hours after exposing them to 0 or 10 Gy irradiation and treatment with either DMSO or NSPP. (Unpaired *t*-test. * $P < 0.05$, ** $P < 0.01$, *** $P < 0.001$.)

increase in the secretion of IL-6 in cells treated with 10 Gy. Consistent with an anti-inflammatory effect, NSPP significantly reduced IL-6 secretion levels (10 Gy: 2-fold, $P = 0.0425$) compared with the DMSO control group (Figure 3B).

Preservation of Cognitive Function in Irradiated Mice

Ionizing radiation to the brain has long been known to cause neuroinflammation, which ultimately leads to a decline in cognitive function.^{11,12} Our short-term experiments indicated that NSPP mitigates neuroinflammation. Next, we sought to test if treatment with NSPP also translated into improved cognitive function. After total brain irradiation with 10 Gy (Figure 4A), animals were treated with either DMSO/CrEL or NSPP (5 mg/kg) for 5 days. One month after irradiation the animals were subjected to unbiased cognitive testing (Figure 4B). NOR and OIP tests were performed to evaluate impairments in the prefrontal and perirhinal cortices, as well as hippocampus regions. This was followed by FC tasks for studying deficits in memory function dependent on the hippocampal regions.

Mice receiving DMSO/CrEL after cranial irradiation of 10 Gy demonstrated a significant behavioral deficit on both NOR and OIP tasks compared with unirradiated controls, as indicated by their impaired preference for novel object (Figure 4C) or place (Figure 4D). However, in the NSPP-treated

group, mice showed significantly improved performance in identifying the novel object (Figure 4C) or place (Figure 4D). Furthermore, the discrimination index (DI) between the unirradiated and the combined treatment groups (10 Gy + DMSO/CrEL or 10 Gy + NSPP) were statistically insignificant, indicating that NSPP had successfully mitigated the radiation effects. In the FC task, the baseline freezing levels were comparable among the 3 treatment groups. All groups also showed an increased freezing behavior post 3 tone-shock pairings (context fear bars). Baseline freezing levels 48 hours post-training were significantly decreased in irradiated mice compared with the unirradiated control mice. Administration of NSPP to the irradiated mice reduced the cognitive deficits (Figure 4E). Treatment of the irradiated mice with NSPP led to an increased freezing behavior compared with the DMSO/CrEL-treated irradiated group, indicating preservation of hippocampal function (Figure 4E).

Effects of NSPP on GBM Cells In Vitro and In Vivo

Radiation mitigators or protectors always bear the risk of radiation protection or mitigation not only in normal tissues but also in tumors. To test the effect of NSPP on GBM cells in vitro we performed sphere-forming capacity assays using 3 different patient-derived GBM cell lines: HK-374, HK-157, and HK-382 in the presence (10 μ M) or absence of NSPP in combination with irradiation at 0 or 4 Gy. The

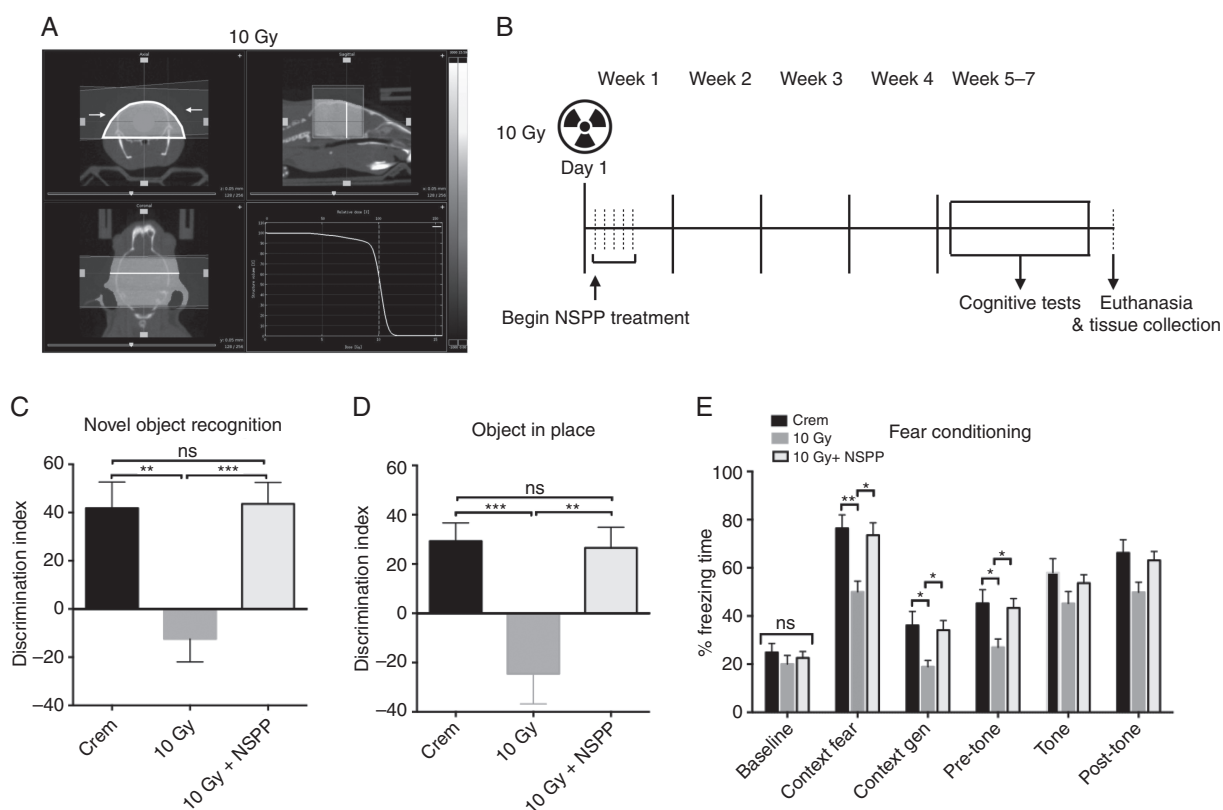


Figure 4. Preservation of cognitive function in irradiated mice. Groups ($n = 10$) of 6-week-old female C3H mice were irradiated with 0 or 10 Gy (A) and treated with NSPP (5 mg/kg) or DMSO/CrEL for 5 days. Schematic representation of the behavioral testing schedule (B). Starting week 5 the mice were tested for cognitive functions by performing NOR (C), OIP (D), and FC (E) tasks. (Unpaired t -test. * $P < 0.05$, ** $P < 0.01$, *** $P < 0.001$.)

gliomaspheres were treated with DMSO or NSPP every other day for 2 weeks, at the end of which the number of spheres formed was counted and presented as the percentage of spheres formed. In HK-374 GBM cells NSPP significantly reduced the cells' self-renewing capacity with or without irradiation (Figure 5A, left panel), while in the HK-157 and HK-382 cell lines NSPP had no effect (Figure 5A, center and right panels).

To test if NSPP interferes with the effects of tumor irradiation in vivo, 2×10^5 GL261-luciferase mouse glioma cells were intracranially injected in C57BL/6 mice. Seven days after implantation, tumor grafting was confirmed by bioluminescence imaging (BLI), and the tumors were either sham irradiated or irradiated with 10 Gy. Immediately after irradiation, the mice were treated with either DMSO/CrEL or NSPP (5 mg/kg) subcutaneously. The treatment was given on a 5-days-on/2-days-off schedule for 3 weeks. Weights of the mice were recorded every day until the study endpoint. Kaplan–Meier survival estimates showed no effects of NSPP alone or in combination with radiation (Figure 5B). Importantly, NSPP did not show any toxicity and did not lead to weight loss (Figure 5C). Tumor growth was monitored by BLI of the tumors at day 7 (pretreatment) and at day 23 (days post implantation; Figure 5D) and indicated no tumor-promoting effects of NSPP.

Effects of NSPP on the hedgehog Pathway in Microglia and GBM Cells

Recent publications have shown that deregulated developmental pathways play a key role in GBM progression and tumorigenesis by conferring drug resistance to the tumor cells and that inhibition of the hedgehog pathway induces apoptosis in GBM cells.^{13–15} We had previously demonstrated that NSPP activates the hedgehog pathway by binding to the transmembrane domain of Smoothened.¹⁶ Therefore, we sought to test whether the different sensitivities of microglia and GBM to NSPP would explain its differential effect in normal tissues and tumors. Quantitative RT-PCR for hedgehog target genes was performed in normal microglia cells (EOC20) and HK-374 patient-derived GBM tumor cells 24 hours after treatment with different concentrations of NSPP. The results obtained are presented as a ratio of fold changes of the genes in EOC20 over HK-374 cells. Low doses of NSPP (500 nM to 1 μ M) induced the expression of the hedgehog pathway target genes *Ptch1*, *Ptch2*, *Gli1*, and *Gli2* in microglia cells more efficiently compared with HK-374 GBM cells, both alone and in combination with radiation (Figure 6A–D), suggesting that microglia cells are more sensitive to NSPP than HK-374 glioma cells.

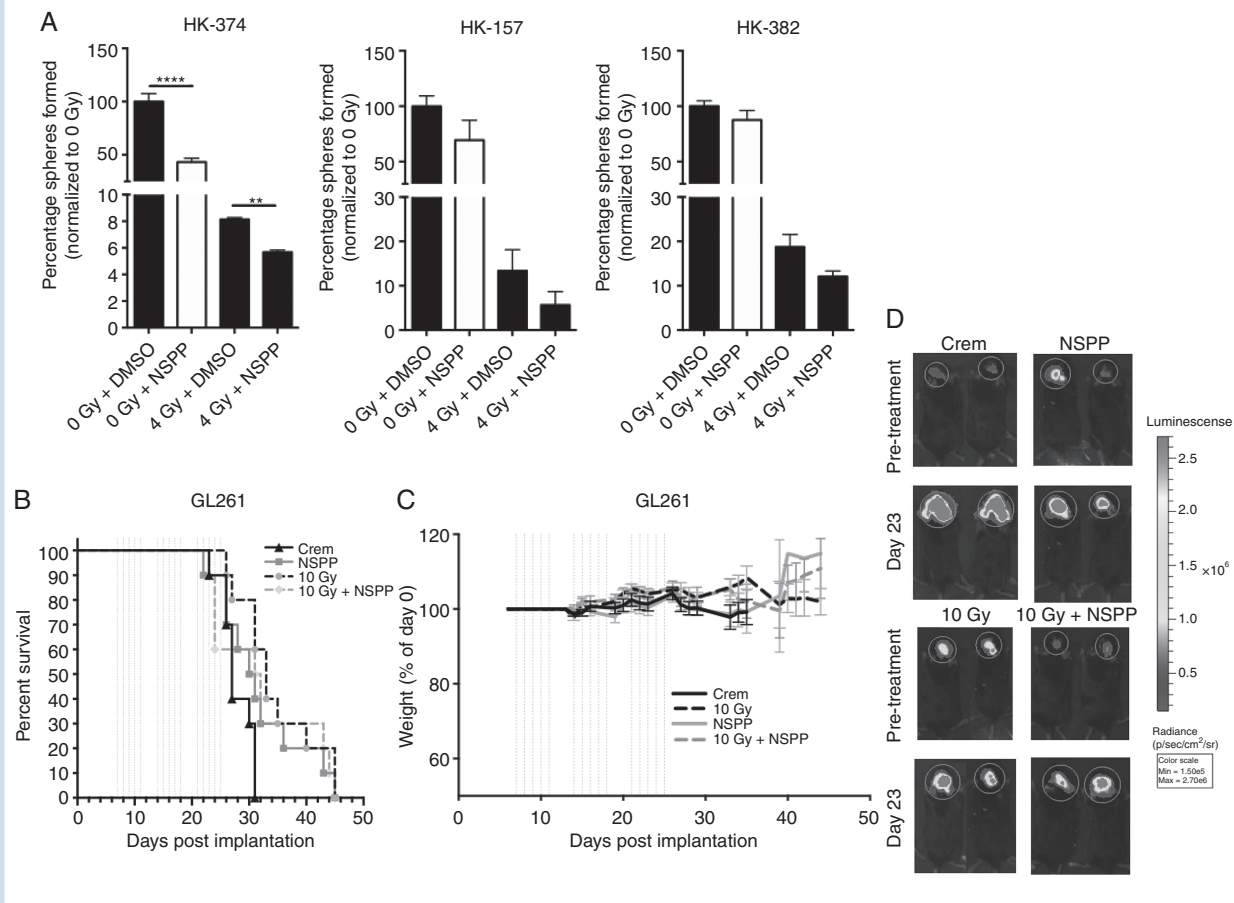


Figure 5. Effects of NSPP on GBM cells in vitro and in vivo. (A) Patient-derived HK-374 (left panel), HK-157 (center panel), and HK-382 (right panel) GBM cells were used to perform sphere-forming assays with sham-irradiated or irradiated cells in the presence or absence of NSPP (10 μ M). The cells were treated every other day for 2 weeks. The number of spheres formed under each condition was counted and presented as percentage spheres formed. (Unpaired *t*-test. ** $P < 0.01$, **** $P < 0.0001$.) (B) 2×10^5 GL261-Luciferase mouse glioma cells were implanted intracranially into six-week-old female C57BL/6 mice. Animals were irradiated with 0 or 10 Gy and treated with DMSO/CrEL or NSPP (5 mg/kg, s.c.) for 3 weeks. The effect of NSPP on survival in tumor-bearing mice was assessed using Kaplan–Meier estimates. (C) Weight curves for the mice in the different treatment groups. (D) Bioluminescence images of mice bearing tumors obtained at day 7 (pretreatment) and at day 23 (days post implantation). Each group had $n = 10$ mice.

Discussion

Aside from surgery, radiotherapy is one of the most effective cancer treatments for patients suffering from brain cancer or cancer metastases to the brain. However, with 5-year survival rates steadily increasing, more and more patients experience long-term treatment side effects, which in the case of cranial irradiation manifest in impaired cognitive functions. Symptoms arise months and years after completion of radiotherapy and are particularly detrimental in childhood cancer survivors where despite tumor control rates often being excellent, the cognitive decline can amount to a loss of 1–2 IQ points per year.¹⁷

Some experimental approaches, while difficult to translate into the clinic, have shown promising results.^{18–20} Approved clinical treatment options for preventing the late sequelae of cerebral radiotherapy are few and are mostly limited to radiation treatment volume reduction²¹ or sparing

of critical brain structures from irradiation.²² Previous pharmacological radioprotection studies using, for example, amifostine have been hindered by the lack of blood–brain barrier penetration of the drugs and the general concern of simultaneous protection of tumor cells.²³

Few pharmacological treatment attempts have been made to mitigate radiation effects to the CNS after completion of treatment, and those are mostly limited to corticosteroids, which are routinely used to acutely reduce edema but are not sustainable as a long-term treatment option. So far experimental approaches have had limited²⁴ or no success.²⁵

We had previously reported that NSPP mitigates the acute intestinal radiation syndrome when given 24 hours or later after a lethal dose of radiation through activation of the hedgehog pathway.^{7,16} Motivated by reports in the literature that hedgehog signaling also affects neural stem cells,^{26–28} we sought to test if NSPP would mitigate radiation injury in brain tissues.

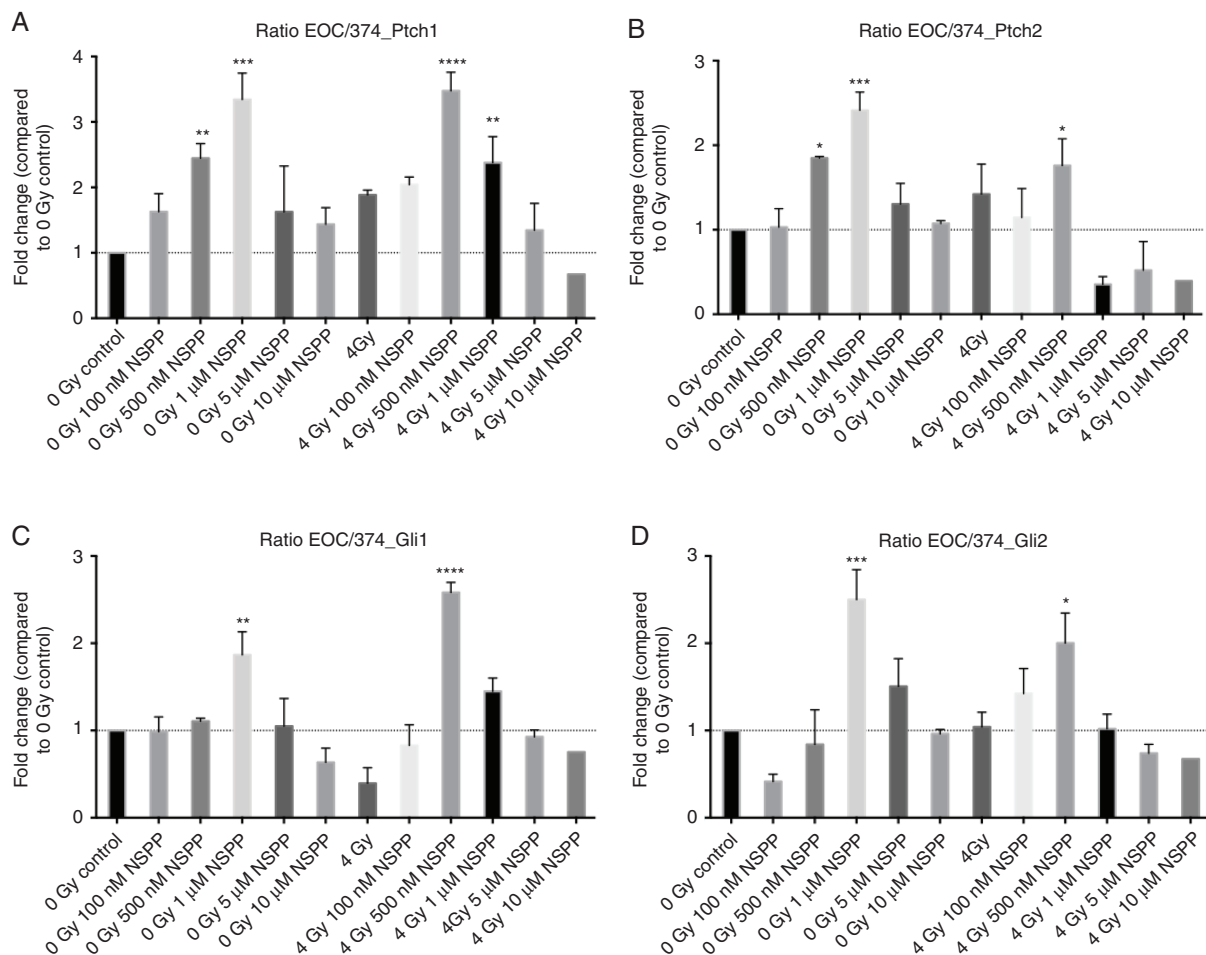


Figure 6. Effects of NSPP on hedgehog signaling in microglia and GBM cells. QRT-PCR for hedgehog target genes Ptch1 (A), Ptch2 (B), Gli1 (C), and Gli2 (D) in EOC20 microglia and HK-374 glioma cells 24 hours after irradiation and treatment with DMSO or NSPP. Fold changes are presented as a ratio of EOC20 microglia cells over HK-374 cells. (Unpaired one-way ANOVA. * $P < 0.05$, ** $P < 0.01$, *** $P < 0.001$, **** $P < 0.0001$.)

NSPP is not soluble in water and it was therefore solubilized in DMSO/CrEL. Clinically, CrEL is known for having side effects when drugs like paclitaxel are dissolved in 50% CrEL, and large amounts of CrEL are co-injected with the drug.²⁹ In our study, CrEL was only used in *in vivo* experiments as a solvent for NSPP at a concentration of 1%. The total volume injected per animal was on average 225 μ L, which amounted to a small total amount of CrEL per animal and did not cause adverse effects.

When given after total brain irradiation, NSPP increased the number of Nestin-GFP+ cells and their self-renewal capacity of the cells in the brains of female mice while it had no effect on male mice. It is noteworthy that the self-renewal of Nestin-GFP+ cells from male mice exceeded that of female mice, both at baseline and after 4 Gy, and that the number and self-renewal capacity of Nestin-GFP+ cells in female mice were not affected by a single dose of 4 Gy. Estrogen dependency of embryonic but not adult neural stem/progenitor cell proliferation and differentiation has been previously described.³⁰ At the age of 8 weeks, one can assume that the young-adult animals in our study still had

active neurogenesis. We speculate that the reported interplay of hedgehog and estrogen signaling³¹ could explain the striking sex differences in efficacy for the Smoothed activator NSPP.⁸

Attempts to show the effect of NSPP on passage #2 neural stem/progenitor cells *in vitro* failed irrespective of sex, indicating that NSPP does not have a direct effect on neural stem/progenitor cells but that it rather affects the microenvironment. The possibility of indirect effects was further supported by data showing a reduction of radiation-induced IL-6 production by microglia cells *in vitro* and reduction of radiation-induced astrogliosis (GFAP) and microglia activation (Iba1) *in vivo*.

It is important to point out that NSPP showed efficacy when given 24 hours after exposure of the animals to radiation and when repair of radiation-induced DNA damage has long been completed.³² Previous attempts to preserve cognitive function have mostly relied upon radioprotectors like amifostine that have to be given before treatment to limit radiation toxicity to the normal tissue and always bear the risk of tumor tissue protection. In our study, NSPP did

not attenuate the effects of radiation on glioma cells in vitro or in vivo, even when given 3 hours after or concurrently with radiation, respectively.

An explanation for the differential effects of NSPP on normal and malignant cells could be that the hedgehog signaling pathway is utilized at a different threshold in gliomas, resulting in differential responses to activators of this pathway. Furthermore, Smoothed agonists are known to inhibit hedgehog signaling at higher concentrations,³³ and the bioavailability of NSPP in normal brain tissues and GBM is likely to differ based on differences between the blood–brain barrier and the blood–tumor barrier.³⁴ Taken together, the data suggest the possibility of a therapeutic window for NSPP and indicates that NSPP could be safely administered during or after the completion of radiotherapy in patients suffering from GBM, where the presence of residual tumor cells after completion of surgery and radiotherapy is almost always inevitable.

Cranial irradiation is known to disrupt hippocampal neurogenesis in rodents as well as in humans.³⁵ The resulting decline in cognitive function manifests in memory loss. Using 3 different cognitive tests, we demonstrated that a dose of 10 Gy had profound effects on hippocampal-dependent memory function. In line with the observed effects of NSPP on neuroinflammation and neural stem/progenitor cell populations, NSPP treatment translated into preservation of cognitive function in the animals, with results in irradiated, NSPP-treated animals being statistically indistinguishable from non-irradiated animals.

Despite the promising nature of NSPP as an agent that allows for radiation mitigation and preservation of cognitive function following radiotherapy, there are still some questions that need to be addressed. First, we demonstrated inhibition of radiation-induced neuroinflammation by NSPP after a single dose of 4 or 10 Gy. It remains to be seen if NSPP when given daily during the typical course of fractionated radiotherapy with 30 fractions of 2 Gy still preserves cognitive function. Second, our studies on cognitive function used a single dose of 10 Gy. Based on an alpha/beta ratio of 2 for the CNS,³⁶ this dose amounts to a biologically effective dose (BED) of only 60 Gy. Although falling short of the BED of 120 Gy calculated for 60 Gy in 2 Gy fractions given in GBM patients, our dose more closely resembled the BED for cranial irradiation in children with leukemia, a patient population most vulnerable to the normal tissue effects of radiation.³⁷ However, the dose of 10 Gy given in our study accounted for a substantial normal tissue toxicity. Finally, radiation-induced toxicity to the CNS is multifactorial and affects multiple tissue compartments, including demyelination of neurons, activation of microglia, and microvascular damage that all contribute to a decline in cognitive function over time. We demonstrated a reduction in early onset of neuroinflammation and preservation of cognitive function 6 weeks after irradiation but did not test whether NSPP will mitigate cognitive decline at later time points. Future studies will be needed to evaluate if continued application of NSPP over an extended period of time will continue to mitigate radiation-induced cognitive impairment.

In summary, we conclude that NSPP has the potential to mitigate radiation effects to the normal brain when given during or after radiotherapy and warrants further investigation.

Supplementary Material

Supplementary data are available at *Neuro-Oncology* online.

Keywords

cognitive function | neural stem cells | radiation | radiation mitigation

Funding

FP, LML, and HIK were supported by a grant from the National Cancer Institute (P50CA211015). FP was supported by grants from the National Cancer Institute (R01CA200234) and the National Institute of Allergies and Infectious Diseases (U19AI067769).

Conflict of interest statement. The authors declare no conflict of interest.

Authorship statement. KB, PM, LH, LZ, MS, AI, NTN, SSS, DS performed the experiments and collected the data. CEM performed the immunohistochemical analysis, LML and HIK provided materials. KB and FP analyzed the data and wrote the manuscript. FP conceived of the study. All authors edited and approved of the final version of the manuscript.

References

- Jellinger K. Human central nervous system lesions following radiation therapy. *Zentralbl Neurochir.* 1977;38(2):199–200.
- SEER. Cancer Stat Facts: Brain and Other Nervous System Cancer. <https://seer.cancer.gov/statfacts/html/brain.html>. Accessed March 7, 2020.
- Tso WWY, Liu APY, Lee TMC, et al. Neurocognitive function, performance status, and quality of life in pediatric intracranial germ cell tumor survivors. *J Neurooncol.* 2019;141(2):393–401.
- Szentes A, Erős N, Kekecs Z, et al. Cognitive deficits and psychopathological symptoms among children with medulloblastoma. *Eur J Cancer Care (Engl).* 2018;27(6):e12912.
- Doger de Speville E, Robert C, Perez-Guevara M, et al. Relationships between regional radiation doses and cognitive decline in children treated with crani-spinal irradiation for posterior fossa tumors. *Front Oncol.* 2017;7:166.
- Smith SM, Limoli CL. Stem cell therapies for the resolution of radiation injury to the brain. *Curr Stem Cell Rep.* 2017;3(4):342–347.
- Bhat K, Duhachek-Muggy S, Ramanathan R, et al. 1-(4-Nitrobenzenesulfonyl)-4-piperazine increases the number of Peyer's patch-associated regenerating crypts in the small intestines after radiation injury. *Radiother Oncol.* 2019;132:8–15.

8. Duhachek-Muggy S, Bhat K, Medina P, et al. Radiation mitigation of the intestinal acute radiation injury in mice by 1-[[4-nitrophenyl]sulfonyl]-4-phenylpiperazine. *Stem Cells Transl Med.* 2020;9(1):106–119.
9. Mignone JL, Kukekov V, Chiang AS, Steindler D, Enikolopov G. Neural stem and progenitor cells in nestin-GFP transgenic mice. *J Comp Neurol.* 2004;469(3):311–324.
10. Konirova J, Cupal L, Jarosova S, et al. Differentiation induction as a response to irradiation in neural stem cells in vitro. *Cancers (Basel).* 2019;11(7):1–13.
11. Parihar VK, Acharya MM, Roa DE, Bosch O, Christie LA, Limoli CL. Defining functional changes in the brain caused by targeted stereotaxic radiosurgery. *Transl Cancer Res.* 2014;3(2):124–137.
12. Acharya MM, Green KN, Allen BD, et al. Elimination of microglia improves cognitive function following cranial irradiation. *Sci Rep.* 2016;6:31545.
13. Wang K, Chen D, Qian Z, Cui D, Gao L, Lou M. Hedgehog/Gli1 signaling pathway regulates MGMT expression and chemoresistance to temozolomide in human glioblastoma. *Cancer Cell Int.* 2017;17:117.
14. Melamed JR, Morgan JT, Ioele SA, Gleghorn JP, Sims-Mourtada J, Day ES. Investigating the role of hedgehog/GLI1 signaling in glioblastoma cell response to temozolomide. *Oncotarget.* 2018;9(43):27000–27015.
15. Ulasov IV, Nandi S, Dey M, Sonabend AM, Lesniak MS. Inhibition of sonic hedgehog and Notch pathways enhances sensitivity of CD133(+) glioma stem cells to temozolomide therapy. *Mol Med.* 2011;17(1-2):103–112.
16. Duhachek-Muggy S, Bhat K, Medina P, et al. Radiation mitigation of the intestinal acute radiation injury in mice by 1-[[4-nitrophenyl]sulfonyl]-4-phenylpiperazine. *Stem Cells Transl Med.* 2020;9(1):106–119.
17. Kahalley LS, Ris MD, Grosshans DR, et al. Comparing intelligence quotient change after treatment with proton versus photon radiation therapy for pediatric brain tumors. *J Clin Oncol.* 2016;34(10):1043–1049.
18. Leavitt RJ, Limoli CL, Baulch JE. miRNA-based therapeutic potential of stem cell-derived extracellular vesicles: a safe cell-free treatment to ameliorate radiation-induced brain injury. *Int J Radiat Biol.* 2019;95(4):427–435.
19. Hinzman CP, Baulch JE, Mehta KY, et al. Plasma-derived extracellular vesicles yield predictive markers of cranial irradiation exposure in mice. *Sci Rep.* 2019;9(1):9460.
20. Baulch JE, Acharya MM, Allen BD, et al. Cranial grafting of stem cell-derived microvesicles improves cognition and reduces neuropathology in the irradiated brain. *Proc Natl Acad Sci U S A.* 2016;113(17):4836–4841.
21. Brown PD, Jaeckle K, Ballman KV, et al. Effect of radiosurgery alone vs radiosurgery with whole brain radiation therapy on cognitive function in patients with 1 to 3 brain metastases: a randomized clinical trial. *JAMA.* 2016;316(4):401–409.
22. Gondi V, Pugh SL, Tome WA, et al. Preservation of memory with conformal avoidance of the hippocampal neural stem-cell compartment during whole-brain radiotherapy for brain metastases (RTOG 0933): a phase II multi-institutional trial. *J Clin Oncol.* 2014;32(34):3810–3816.
23. Lindegaard JC, Grau C. Has the outlook improved for amifostine as a clinical radioprotector? *Radiother Oncol.* 2000;57(2):113–118.
24. Brown PD, Pugh S, Laack NN, et al; Radiation Therapy Oncology Group (RTOG). Memantine for the prevention of cognitive dysfunction in patients receiving whole-brain radiotherapy: a randomized, double-blind, placebo-controlled trial. *Neuro Oncol.* 2013;15(10):1429–1437.
25. Rapp SR, Case LD, Peiffer A, et al. Dexamethasone for irradiated brain tumor survivors: a phase III randomized placebo-controlled clinical trial. *J Clin Oncol.* 2015;33(15):1653–1659.
26. Kume M, Chiyoda H, Kontani K, Katada T, Fukuyama M. Hedgehog-related genes regulate reactivation of quiescent neural progenitors in *Caenorhabditis elegans*. *Biochem Biophys Res Commun.* 2019;520(3):532–537.
27. Klein SD, Nguyen DC, Bhakta V, et al. Mutations in the sonic hedgehog pathway cause macrocephaly-associated conditions due to crosstalk to the PI3K/AKT/mTOR pathway. *Am J Med Genet A.* 2019;179(12):2517–2531.
28. Yang H, Liu C, Fan H, et al. Sonic hedgehog effectively improves Oct4-mediated reprogramming of astrocytes into neural stem cells. *Mol Ther.* 2019;27(8):1467–1482.
29. Gelderblom H, Verweij J, Nooter K, Sparreboom A, Cremophor EL: the drawbacks and advantages of vehicle selection for drug formulation. *Eur J Cancer.* 2001;37(13):1590–1598.
30. Brännvall K, Korhonen L, Lindholm D. Estrogen-receptor-dependent regulation of neural stem cell proliferation and differentiation. *Mol Cell Neurosci.* 2002;21(3):512–520.
31. Diao Y, Azatyan A, Rahman MF, et al. Blockade of the hedgehog pathway downregulates estrogen receptor alpha signaling in breast cancer cells. *Oncotarget.* 2016;7(44):71580–71593.
32. Berthel E, Ferlazzo ML, Devic C, Bourguignon M, Foray N. What does the history of research on the repair of DNA double-strand breaks tell us?—a comprehensive review of human radiosensitivity. *Int J Mol Sci.* 2019;20(21):1–15.
33. Chen JK, Taipale J, Young KE, Maiti T, Beachy PA. Small molecule modulation of Smoothened activity. *Proc Natl Acad Sci U S A.* 2002;99(22):14071–14076.
34. Arvanitis CD, Ferraro GB, Jain RK. The blood-brain barrier and blood-tumour barrier in brain tumours and metastases. *Nat Rev Cancer.* 2020;20(1):26–41.
35. Monje ML, Vogel H, Masek M, Ligon KL, Fisher PG, Palmer TD. Impaired human hippocampal neurogenesis after treatment for central nervous system malignancies. *Ann Neurol.* 2007;62(5):515–520.
36. Kondziolka D, Shin SM, Brunswick A, Kim I, Silverman JS. The biology of radiosurgery and its clinical applications for brain tumors. *Neuro Oncol.* 2015;17(1):29–44.
37. Pinnix CC, Yahalom J, Specht L, Dabaja BS. Radiation in central nervous system leukemia: guidelines from the International Lymphoma Radiation Oncology Group. *Int J Radiat Oncol Biol Phys.* 2018;102(1):53–58.

Effects of Dopamine Receptor Antagonists and Radiation on Mouse Neural Stem/Progenitor Cells

¹Ling He, DDS, Ph.D.*; ¹Krutika Bhat, Ph.D.; ¹Angeliki Ioannidis, M.S., and ^{1,2,3}Frank Pajonk, MD, Ph.D.

¹Department of Radiation Oncology, David Geffen School of Medicine at UCLA

²Jonsson Comprehensive Cancer Center at UCLA

³Department of Neurosurgery, David Geffen School of Medicine at UCLA

***Correspondence:** Ling He, DDS, Ph.D. (linghe@mednet.ucla.edu). Department of Radiation Oncology, David Geffen School of Medicine at UCLA, 10833 Le Conte Ave, Los Angeles, CA 90095-1714, Phone: +1 310-825-6852.

1 **Abstract**

2 *Background:* Dopamine receptor antagonists have recently been identified as potential
3 anti-cancer agents in combination with radiation, and a first drug of this class is in clinical
4 trials against pediatric glioma. Radiotherapy is known to cause cognitive impairment in
5 patients receiving cranial irradiation through the elimination of neural stem/progenitor
6 cells and subsequent loss of neurogenesis. Therefore, we tested the combined effects of
7 dopamine receptor antagonists and radiation on neural stem/progenitor cells.

8 *Methods:* Using transgenic mice that report the presence of neural stem/progenitor cells
9 through Nestin promoter-driven expression of enhanced green fluorescent protein, the
10 effects of dopamine receptor antagonists alone or in combination with radiation on murine
11 neural stem/progenitor cells were assessed in sphere-formation assays, extreme limiting
12 dilution assays, flow cytometry and immunofluorescence *in vitro* and *in vivo* in both sexes.

13 *Results:* We report that several dopamine receptor antagonists show sex-dependent
14 effects on neural stem/progenitor cells both *in vitro* and *in vivo*. Hydroxyzine,
15 trifluoperazine, amisulpride, nemonapride or quetiapine alone or in combination with
16 radiation significantly increased the number of neural stem/progenitor cells in
17 neurospheres established from females but not male mice. Dopamine receptor
18 antagonists either protected neural stem/progenitor cells from radiation or expanded the
19 stem cell pool, thus indicating that this combination therapy against glioblastoma will not
20 increase radiation-induced cognitive decline through increasing elimination of neural
21 stem/progenitor cells and subsequent loss of neurogenesis.

22 *Conclusion:* We conclude that a therapeutic window for dopamine receptor antagonists
23 in combination with radiation potentially exists, making it a novel combination therapy

24 against glioblastoma. Normal tissue toxicity following this treatment scheme likely differs
25 depending on age and sex and should be taken into consideration when designing clinical
26 trials.

27

28 **Keywords:** dopamine receptor antagonists; neural stem/progenitor cells; radiation;
29 gender difference; combination therapy.

Highlights

- Neural stem/progenitor cells show sex-dependent sensitivity to dopamine receptor antagonists
- Dopamine receptor antagonists show sex-dependent effects on neural stem/progenitor cells either by protecting neural stem/progenitor cells from radiation or inducing an expansion of the stem cell pool
- Normal tissue toxicity of this combination potentially differs depending on age and sex and should be further explored in clinical trials

30 **Introduction**

31 Neurotransmitters and their receptors were originally described in neuronal tissues
32 (1, 2) but have since been found to be expressed in many solid cancers including brain
33 tumors (3, 4). While dopamine receptors are primarily associated with neurotransmission,
34 emerging research has suggested their involvement in cancer progression and identified
35 them as potential targets for cancer therapy (5-7), including for brain tumors (8-10).
36 Dopamine receptor antagonists (DRAs) are psychotropic drugs originally developed
37 against a broad range of psychiatric disorders. Brain tumors often cause cognitive deficits
38 and psychiatric comorbidity and therefore, psychotropic drugs are commonly used in this
39 patient population. DRAs have well known side effect profiles in normal tissues and their
40 pharmacokinetic and pharmacodynamic properties are well established. Given their
41 ability to cross the blood-brain barrier (BBB), these FDA-approved drugs can be readily
42 repurposed to treat intracranial malignancies.

43 Treatment with DRAs by itself has shown limited efficacy against tumors in that
44 past (6, 11, 12), but we recently reported significantly improved survival in mouse models
45 of glioblastoma (GBM) when DRAs were combined with radiotherapy (RT) (8-10). RT is
46 known for causing cognitive impairment in patients receiving cranial irradiation. This side
47 effect is most pronounced in children (13) but also observed in adult patients and at least
48 in part thought to be caused by the loss of neurogenesis (14, 15). However, the specific
49 combined effects of radiation and DRAs on neural stem/progenitor cells (NSPCs) are not
50 well studied in the literature. We recently reported that the combined treatment with
51 radiation and DRAs eliminated glioma-initiating cells (GICs) both *in vitro* and *in vivo* (8-
52 10). Because NSPCs and GICs share certain traits we sought to investigate whether

53 DRAs alone or in combination with radiation would adversely affect NSPCs. Taking into
54 account that sex differences exist in the prevalence, presentation, and severity of
55 neurodevelopmental and neuropsychiatric disorders (16, 17), we incorporated sex as a
56 biological variable to our studies to assess if sex-specific pattern exists in the response
57 to radiation, DRAs or combined treatment in NSPCs.

58 **Materials and Methods**

59 *Animals*

60 Nestin-EGFP mice were a kind gift from Dr. Grigori Enikolopov, Cold Spring Harbor
61 Laboratory (18). C3Hf/Sed/Kam mice were originally obtained from the MD Anderson
62 Cancer Center. Mice were re-derived, bred and maintained in a pathogen-free
63 environment in the American Association of Laboratory Animal Care-accredited Animal
64 Facilities of the Department of Radiation Oncology, University of California (Los Angeles,
65 CA) in accordance with all local and national guidelines for the care of animals. Sex of
66 newborn animals was determined as described in (19).

67

68 *Neural stem cell culture*

69 The cells were harvested from the newborn Nestin-EGFP mice as described in our
70 previous publication (20). Details of the procedures can be found in **Supplementary**

71 **Materials.**

72

73 *Irradiation*

74 Neurosphere cultures were irradiated with 0, 2 or 4 Gy using an experimental X-ray
75 irradiator (Gulmay Medical Inc) at a dose rate of 5.519 Gy/min. Control samples were
76 sham-irradiated. The X-ray beam was operated at 300 kV and hardened using a 4-mm
77 Be, a 3-mm Al, and a 1.5-mm Cu filter and calibrated using NIST-traceable dosimetry.

78

79 *Drug treatment*

80 The full list of DRAs and the drug treatment details can be found in **Supplementary**
81 **Materials**.

82

83 *Flow cytometry*

84 P2 neurospheres established from the Nestin-EGFP mice were dissociated into single
85 cell suspension as described above. Single cell suspensions were either subjected to
86 FACS (Flow Cytometry Core, Broad Stem Cell Research Center at UCLA) for EGFP-high,
87 -medium, and -low cell populations as described in (20) or analyzed for total EGFP
88 expression using a MACSQuant Analyzer (Miltenyi Biosciences) and the FlowJo software
89 package (FlowJo v10). Drug-treated samples were normalized against the corresponding
90 solvent-treated controls.

91

92 *Neurosphere-formation assay*

93 To assess self-renewal capacity, P2 neurospheres from Nestin-EGFP mice were
94 dissociated and plated in an *in-vitro* limiting dilution assay into 96-well non-treated plates
95 at a range of 1 to 1,024 cells/well. Growth factors, EGF and bFGF, were added every 3
96 days, and the cells were allowed to form neurospheres for 14 days. The number of
97 spheres formed per well was then counted and expressed as a percentage of the initial
98 number of cells plated.

99

100 *Extreme Limiting Dilution Assay (ELDA)*

101 P2 neurospheres were plated at a range of 1 to 512 cells/well. They were pre-treated
102 either with 1 μ M Temozolomide (TMZ, #T2577, Sigma, St. Louis, MO) or 1 μ M ONC201

103 (Oncoceutics, Inc. Philadelphia, PA) or 1 μ M amisulpride one hour before a single dose
104 of 4 Gy irradiation. ONC201 was added twice a week while both TMZ and amisulpride
105 were added every other day. Neurospheres were counted 14 days later and presented
106 as a percentage relative to the initial number of cells plated. The stem cell frequency was
107 calculated using the ELDA software (21).

108

109 *Quantitative Reverse Transcription-PCR*

110 Total RNA, cDNA synthesis and qRT-pCR were carried out using standard protocols
111 (**Supplementary Materials**; primer sequences **Supplementary Table 1**).

112

113 *Brain dissection*

114 Five days after drug treatment, the brains of mice were harvested and placed on the
115 Acrylic Mouse Brain Slicer Matrix (Zivic Instruments, # BSMAA001-1). 1 mm thick coronal
116 sections starting from 2 mm anterior to 2 mm posterior of the bregma were cut. The brain
117 tissue was minced into very small pieces using a scalpel and the cells were isolated in
118 Neural Stem Cell culture media as described above. Cells were then used for flow
119 cytometric analysis to assess the percentage of Nestin-EGFP⁺ cells in different treatment
120 groups (20).

121

122 *Immunofluorescence*

123 The brain sections were stained with the protocol described in our previous publication
124 (9). Details of the staining procedures can be found in **Supplementary Materials**.

125

126 *Statistics*

127 Unless stated otherwise all data shown are represented as mean \pm standard error mean
128 of at least 3 biologically independent experiments. A p -value of ≤ 0.05 in an unpaired two-
129 sided t -test or two-sided ANOVA test for multiple comparisons indicated a statistically
130 significant difference.

131 **Results**

132 *Dopamine receptor antagonists show sex-dependent effects on neural stem/progenitor*
133 *cells in vitro*

134 In a first set of experiments, we tested if DRAs affect the number of NSPCs *in vitro*.
135 Nestin-EGFP⁺ NSPCs were harvested from both male and female newborn pups and
136 cultured as neurospheres. We have previously reported that Nestin promoter driven
137 EGFP expression in this mouse strain correlates with self-renewal capacity (20). Passage
138 2 (P2) neurospheres were pretreated with DRAs (**Table 1**) at 1 μ M concentrations,
139 irradiated with 0, 2 or 4 Gy and cultured for 2 weeks during which DRAs were added
140 3x/week (**Fig. 1A**).

141 At the conclusion of this experiment, two weeks post treatment initiation, we
142 observed baseline differences in the number of Nestin-EGFP^{high} NSPCs in neurospheres
143 established from male and female mice with female mice showing a higher trend of stem
144 cell content [female: 37 ± 12.6 % (DMSO), 34.7 ± 8.6 % (PBS); male: 28.6 ± 9.3 %
145 (DMSO), 28.4 ± 8.7 % (PBS); N=3] (**Fig. 1B/C**). In response to DRA treatment alone we
146 found unexpected differences between neurospheres established from male and female
147 mice, with those from female mice in general showing larger reductions in the number of
148 EGFP⁺ NSPCs. However, the number of EGFP⁺ NSPCs from individual animals of the
149 same sex varied and none of the observed differential effects of DRAs between sexes
150 reached the level of statistical significance (**Fig. 1D**). In agreement with our previous
151 report (20), radiation predominately eliminated the Nestin-EGFP^{high} population of cells
152 from neurospheres, consistent with the known exquisite radiation sensitivity of neural
153 stem cells (22, 23). The differences between sexes in the total number of EGFP⁺ cells in

154 response to individual DRAs became smaller with increasing radiation doses in alignment
155 with the generally non-sex-specific cell killing effects of ionizing radiation (**Fig. 1E/F**).

156

157 Next, we tested if the DRAs that showed the largest effects on the number of
158 Nestin-EGFP⁺ cells in neurospheres established from either male or female mice also
159 affected the self-renewal capacity of NSPCs from the same P2 neurospheres. Cells were
160 plated at clonal density in an *in vitro* limiting dilution assay, irradiated and treated with
161 DRAs. The number of clonal spheres formed was counted two weeks later (**Fig. 2A**).
162 Compared to corresponding irradiated, solvent-treated controls, cells from neurospheres
163 established from male mice showed a significant reduction in sphere-formation after
164 irradiation with 0, 2, or 4 Gy when treated with perphenazine, fluphenazine,
165 thiethylperazine, prochloroperazine or zuclopenthixol, but not after treatment with
166 hydroxyzine, trifluoperazine, amisulpride or nemonapride (**Fig. 2B/C**). At the same time,
167 treatment with quetiapine significantly increased sphere-formation after irradiation with 2
168 Gy (**Fig. 2C**). Cells from neurospheres established from female mice, treated with
169 hydroxyzine, trifluoperazine, amisulpride, nemonapride or quetiapine showed a
170 significant increase in sphere-formation after irradiation with 0, 2, or 4 Gy compared to
171 the corresponding irradiated, solvent-treated controls (**Fig. 2D/E**).

172

173 *Dopamine receptor antagonists show sex-dependent effects on neural stem/progenitor*
174 *cells in vivo*

175 To test if DRAs that increase neurosphere-formation *in vitro* would also affect
176 NPSCs *in vivo*, we treated 8-week-old Nestin-EGFP mice with five daily i.p. injections of

177 trifluoperazine, hydroxyzine, quetiapine, nemonapride or amisulpride and harvested the
178 brains at day 5 post treatment initiation. To enrich frequencies of NSPCs, we collected
179 brain sections from the subventricular zones of the lateral ventricles, regions known to
180 contain stem cells niches, digested these sections into single cells suspensions and
181 analyzed them for the number of Nestin-EGFP⁺ cells by flow cytometry (**Fig. 3A**). In cell
182 suspensions from these enriched regions we found baseline frequencies of NSPCs
183 reaching 20 % of the total cell population. Treatment with trifluoperazine significantly
184 increased the number of NSPCs in female mice. The same trend was seen in male mice,
185 but the effect was small and did not reach statistical significance (**Fig. 3B**). Likewise,
186 treatment of the animals with hydroxyzine, quetiapine, or nemonapride significantly
187 increased the number of NSPCs in combined male and female cohorts, with similar trends
188 seen in the individual sexes (**Fig. 3C-E**). Lastly, treatment with amisulpride significantly
189 increased NSPCs numbers in both sexes (**Fig. 3F**). This was validated by staining of the
190 corresponding brain section with an anti-EGFP antibody. Image-based quantification
191 showed a significant increase in the number of EGFP⁺ cells compared to the control
192 group in both female and male mice (**Fig. 3G/H**).

193

194 *Sex differences in dopamine receptor expressions and their response to radiation*

195 To investigate whether the observed sex-dependent effects were associated with
196 differences in dopamine receptor expression levels, we evaluated the baseline
197 expression of all dopamine receptors in neurospheres derived from female and male
198 neonatal pups. Our analysis revealed that both dopamine receptor D1 (DRD1) and DRD2
199 were highly expressed in the neurospheres, while the expression levels of DRD3, DRD4

200 and DRD5 were detected at very low levels in both sexes. Notably, despite differences in
201 the overall expression levels of these receptor subtypes, no significant differences were
202 observed in any dopamine receptor subtype expression levels between sexes (**Fig. 4A**).

203 Next, we sought to study the impact of radiation exposure on receptor subtypes,
204 with a specific focus on DRD1 and DRD2. Twenty-four hours after radiation exposure, we
205 observed a significant increase in DRD1 expression levels, while no significant changes
206 were observed for DRD2 expression. These changes were consistent across both sexes
207 (**Fig. 4B/C**). Notably, when we compared DRD1 and DRD2 expression levels after
208 radiation exposure between sexes, no significant differences were observed (**Fig. 4D**).

209 Temozolomide (TMZ), is part of the current standard-of-care against GBM and the
210 novel DRA ONC201 is currently in clinical trials against glioma in pediatric patients. And
211 peak TMZ concentration in human brain tissue adjacent to tumors have been reported to
212 be $3.1 \pm 1.5 \mu\text{M}$ (24). In this final part of our study we tested the effects of TMZ or ONC201
213 on NSPCs alone or in combination with radiation, and compared it to amisulpride at
214 equimolar concentrations.

215 Neither TMZ nor ONC201 had an effect on neural stem/progenitor cells in male or
216 female mice when compared to the DMSO controls (**Fig. 4E-H**). However, amisulpride
217 consistently increased sphere forming capacity (**Fig. 4E**) and stem cell frequency (**Fig.**
218 **4F-H**) in both sexes when compared to DMSO or irradiated controls, which was in line
219 with findings shown in **Fig 3F-H**.

220 **Discussion**

221 GBM is a deadly form of brain cancer. The current standard-of-care, surgery
222 followed by RT and temozolomide only provides a limited advantage to patients, with the
223 5-year survival rate for pediatric patients being 20 % and less than 5 % for adults. These
224 unacceptably low survival rates highlight an urgent need for novel treatment strategies.
225 So far, targeted agents and biologics have not been successful in meeting this need, often
226 due to their inability to cross the BBB. Furthermore, RT and chemotherapy cause
227 cognitive deficits and neurological sequelae (14, 25), especially in pediatric patients (26-
228 28). These detrimental effects become more severe and apparent as overall survival from
229 the brain tumors improves. In a high-throughput screen (8) we previously identified DRAs
230 as FDA-approved psychotropic, BBB-penetrating drugs able to target GICs in mouse
231 models of GBM, leading to significantly improved overall survival when combined with
232 radiation (8-10). While this combination was well tolerated, its effects on normal stem cells
233 in the CNS are not known and were evaluated in our present study.

234 While most studies in mice are done in male animals we included sex as biological
235 variable in our experiments. Our data indicate a trend for higher baseline numbers of
236 NSPC in female newborn mice when compared to age-matched male mice. Even though
237 the variability between batches of mice was large and the differences did therefore not
238 reach statistical significance, the observed sex differences were consistent. This agreed
239 with previous studies that explored the role of sexual dimorphism in regulating the
240 ventricular-subventricular zone (V-SVZ), one of the locations in which neural stem cells
241 (NSCs) reside (29, 30). Neurogenesis was found to be more prominent in female mice
242 compared to age-matched males with higher proliferating rates and lower numbers of

243 apoptotic cells seen in the V-SVZ of adult mice (30). Moreover, males showed significant
244 decline in NSPC numbers, progenitor cell proliferation, and more disorganized migrating
245 neuroblast chains with age when compared to age-matched females, indicating sex
246 differences indeed exist in the process of neurogenesis and decline with age, at least in
247 adults (29).

248 DRAs alone or in combination with radiation exhibited sex-dependent effects on
249 NSPCs both *in vitro* and *in vivo*. It's known that sex hormones play crucial roles in
250 neurogenesis and neuronal function (31). It's possible that DRAs interact with these
251 hormonal pathways in a sex-dependent manner, leading to differential effects on NSPCs
252 (32). Furthermore, the interaction of dopamine receptor signaling pathways with other
253 neurotransmitter systems (33, 34) as well as differences in stem cell niches due to
254 hormonal (35, 36), metabolic (37, 38), or other factors (39, 40) could lead to the sex-
255 specific effects of DRAs on NSPCs. Understanding these sex differences has
256 translational relevance in cases where DRAs are used as anti-cancer agents in
257 combination with radiotherapy or are given concurrently with cranial irradiation as anti-
258 psychotic treatments.

259 Our observation that the DRAs trifluoperazine and quetiapine elevated NSPC
260 numbers was contrast to our previous studies using the trifluoperazine and quetiapine in
261 glioma where we found both drugs preventing glioma cell plasticity and targeting GICs (8,
262 10). The differential response of GICs and NSPCs is most likely grounded in their
263 differential reliance on developmental signaling pathways. In our previous studies, the
264 induction of GICs from non-stem glioma cells by radiation relied on the re-expression of
265 Yamanaka factors (Sox2, Klf4, c-Myc, and Oct4). This induction was prevented by

266 trifluoperazine or quetiapine in a DRD2-dependent manner (8, 10), which led to a loss of
267 the inactivating Ser9/21 phosphorylation of Glycogen synthase kinase $3\alpha/\beta$ (GSK3 α/β),
268 subsequent degradation of β -catenin, reduced self-renewal capacity of patient-derived
269 GBM lines and prolonged median survival in PDOX bearing mice (8). While also
270 dependent on Wnt/ β -catenin signaling (41-43), NSPCs are maintained by additional
271 developmental signaling pathways, including Notch (44-46) and Shh (47, 48), and these
272 pathways are also modulated by GSK3 α/β (49, 50).

273 In the brain, both GSK3 α and GSK3 β are expressed (51), and disruption of GSK3
274 signaling has been implicated in a number of neurological diseases, such as
275 schizophrenia (52), bipolar disorder (53), and neurodegenerative diseases (54).
276 However, studies have shown that GSK3 α and GSK3 β play overlapping but distinct roles
277 in neocortex development (55), with GSK3 β acting as the master kinase in the regulation
278 of NSPC behavior (56). GSK3 β -dependent regulation of NSPC includes the maintenance
279 of self-renewal (57), the control of cell differentiation (58, 59), and their plasticity (60) and
280 GSK3 α/β signaling is known to have differential effects in naïve and primed embryonic
281 stem cells (61, 62).

282 It's also well known that NSPCs are highly sensitive to RT due to their proliferative
283 nature and active cell cycle (22, 63), whereas GICs exhibit intrinsic resistance to RT and
284 other traditional treatments, leading to therapeutic failure and tumor recurrence (64, 65).
285 GICs represent a subpopulation of tumor cells that are in a dormant or slow-cycling state,
286 which exhibit altered dopamine signaling pathways compared to proliferating tumor cells
287 (6, 66). Further, dopamine signaling within the GICs niche modulates interactions
288 between quiescent GICs and their microenvironment, promoting tumor dormancy and

289 therapy resistance (67). DRAs could disrupt these interactions by targeting the altered
290 dopamine receptors expressed on GICs or stromal cells within the niche, leading to the
291 exit of GICs from dormancy and induce their differentiation into more vulnerable cell
292 states and sensitize them to therapies. Differences in dopamine receptor utilization
293 between GICs and NSPCs could potentially explain to the differential responses to DRAs
294 alone or in combination with radiation.

295 A limitation of our study is its restriction to a murine *in vivo* model. Species
296 differences in the dependence of stem cell populations on developmental pathways have
297 been reported before (61, 68, 69). While the effects of some DRAs and selected other
298 psychotropic drugs have been tested in human NSPCs, *in vivo* responses will most likely
299 also include effects on the microenvironment and cannot easily be assessed in the human
300 setting.

301 To the best of our knowledge, our study is the first to investigate the combined
302 effects of DRAs and radiation in NSPCs. The unexpected finding that DRAs either
303 protected irradiated NSPCs from radiation or caused an expansion of the NSPC pool
304 indicates that this effective combination therapy against GBM (8-10) will not increase
305 radiation-induced cognitive decline through further increasing the elimination of NSPCs
306 and subsequent loss of neurogenesis.

307 In conclusion, our published data (8, 10) and data presented in this study suggest
308 the existence of a therapeutic window for DRAs in combination with radiation as a novel
309 combination therapy against GBM. Normal tissue toxicity of this combination potentially
310 differs depending on age and sex and should be taken into consideration when designing
311 clinical trials.

312 **Acknowledgements**

313 Not applicable.

314

315 **Authors' contributions**

316 LH, KB, AI performed the experiments and collected the data. HK participated in the
317 project discussion and edited the manuscript. LH and FP analyzed the data and wrote the
318 manuscript. FP conceived of the study. All authors edited and approved of the final
319 version of the manuscript.

320

321 **Funding**

322 FP was supported by grants from the *National Cancer Institute* (R01CA200234,
323 R01CA260886, UCLA SPORE in Brain Cancer P50CA211015).

324

325 **Data Availability**

326 Research data are stored in an institutional repository and will be shared upon request to
327 the corresponding author.

328

329 **Abbreviations**

330 DRAs, dopamine receptor antagonists; GBM, glioblastoma; RT, radiotherapy; NSPCs,
331 neural stem/progenitor cells; GICs, glioma initiating cells; ELDA, extreme limiting dilution
332 assay; TMZ, temozolomide; DRD, dopamine receptor domain; BBB, blood brain barrier;
333 PDOX, patient-derived orthotopic xenograft; GSK3 α/β , Glycogen synthase kinase 3 α/β .

334 **Figure Legends**

335 **Figure 1. Dopamine receptor antagonists show sex-dependent effects on neural**
336 **stem/progenitor cell populations *in vitro*.**

337 **(A)** Schematic of the experimental design for Figure 1. **(B, C)** The brains from male or
338 female newborn pups were harvested, dissociated, and analyzed for EGFP^{-high}, ^{-medium}
339 and ^{-low} subpopulations by flow cytometry (N=3). **(D-F)** Neurospheres (Passage #2) from
340 male or female newborn pups were pre-treated with either controls (DMSO/PBS) or DRAs
341 (1 μ M) and subjected to irradiation with 0 **(D)**, 2 **(E)** or 4 Gy **(F)**. DRAs were added 3 times
342 per week for two weeks, time after which the neurospheres were subjected for flow
343 cytometry and analyzed for the total percentage of EGFP⁺ cells in each sample (N=3).
344 Percentages shown are normalized to the corresponding solvent control (DMSO or PBS).

345

346 **Figure 2. Dopamine receptor antagonists show sex-dependent effects on self-**
347 **renewal capacity in neural stem/progenitor cells.**

348 **(A)** Schematic of experimental design for Figure 2. **(B-E)** Sphere forming capacity of
349 neurospheres (Passage #2) from male **(B, C)** or female **(D, E)** newborn pups pre-treated
350 with a single treatment of either solvent controls (DMSO/PBS) or DRAs (1 μ M) and
351 subjected to 0, 2 or 4 Gy irradiation. (Unpaired Student's t-tests. * p -value < 0.05, ** p -
352 value < 0.01, *** p -value < 0.001, **** p -value < 0.0001).

353

354 **Figure 3. Dopamine receptor antagonists show sex-dependent effects on neural**
355 **stem/progenitor cells *in vivo*.**

356 **(A)** Schematic of experimental design for Figure 3. **(B-F)** The percentage of EGFP+ cells
357 in dissociated brain samples from 8-week-old Nestin-EGFP male and female mice treated
358 with either Control (Saline/Cremophor) or DRAs (20 mg/kg of trifluoperazine, 30 mg/kg of
359 quetiapine, 20 mg/kg of hydroxyzine dihydrochloride, 1 mg/kg of nemonapride or 1 mg/kg
360 of amisulpride) i.p. for five days. **(G)** Immunofluorescent staining for EGFP in coronal
361 sections of brains from 8-week-old Nestin-EGFP male and female mice treated with either
362 Cremophor (control) or 1 mg/kg of amisulpride i.p. for five days. **(H)** Quantification of the
363 percentage of EGFP+ cells over DAPI-stained cells. (N=3; Unpaired Student's t-tests).

364

365 **Figure 4. Sex differences in dopamine receptor expressions and their response to**
366 **radiation.**

367 **(A)** Dopamine receptor (DRD1, DRD2, DRD3, DRD4 and DRD5) expression levels in the
368 Passage #1 neurospheres harvested from male and female newborn pups. **(B, C)**
369 Expression levels of DRD1 and DRD2 in Passage #1 neurospheres at 24 hours after
370 irradiating with a single dose of 4 Gy relative to non-treated samples. **(D)** Expression
371 levels of DRD1 and DRD2 in the 4 Gy-treated neurospheres from both male and female
372 newborn pups. **(E, F)** Sphere forming capacity **(E)** and stem cell frequency **(F)** of Passage
373 #2 neurospheres treated with 1 μ M amisulpride or 1 μ M ONC201 or 1 μ M temozolomide
374 (TMZ) in the absence or presence of a single dose of 4 Gy irradiation. (Unpaired Student's
375 t-tests for **B** and **C**; One-way ANOVA for **E-H**).

Figure 1.

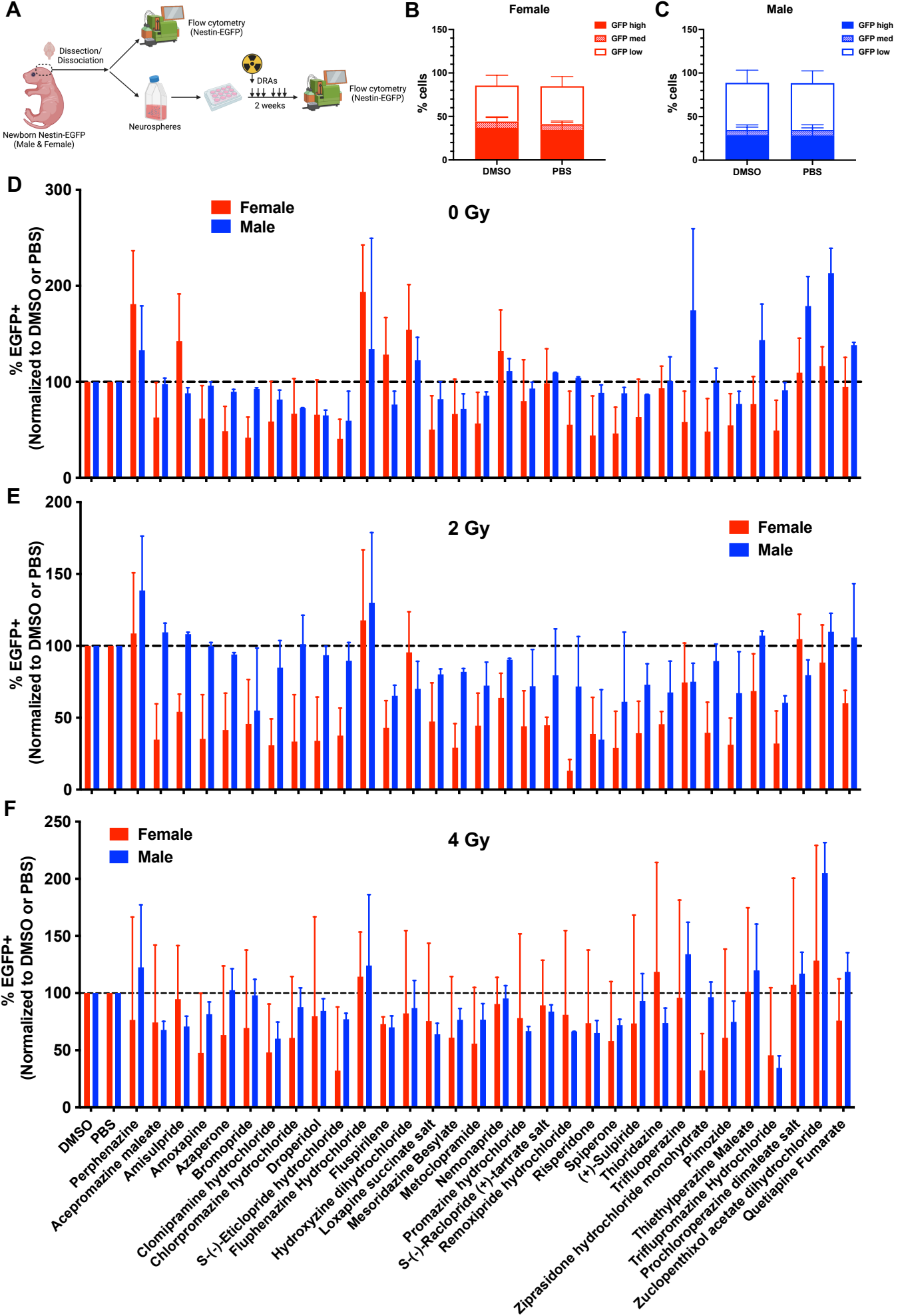


Figure 2.

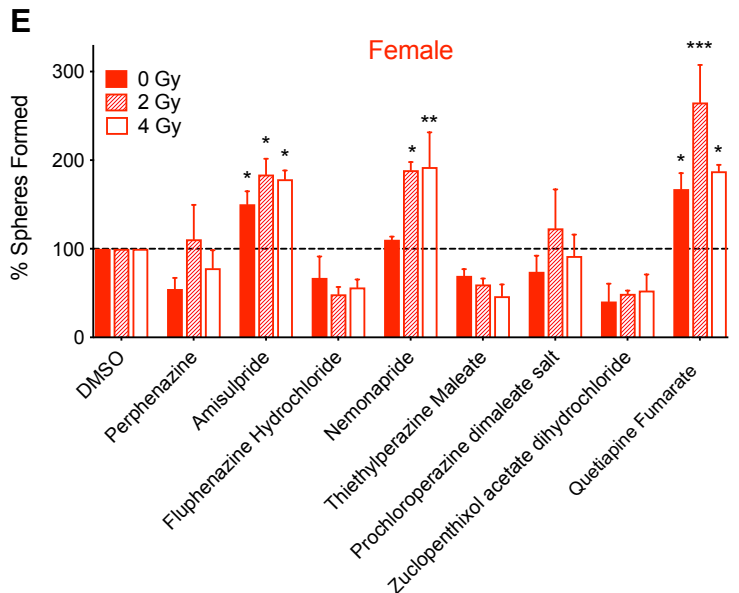
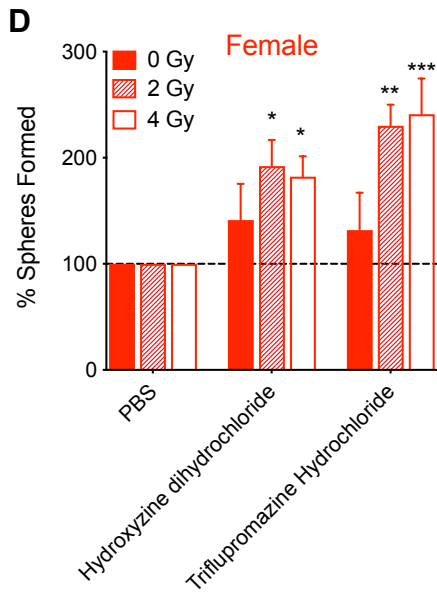
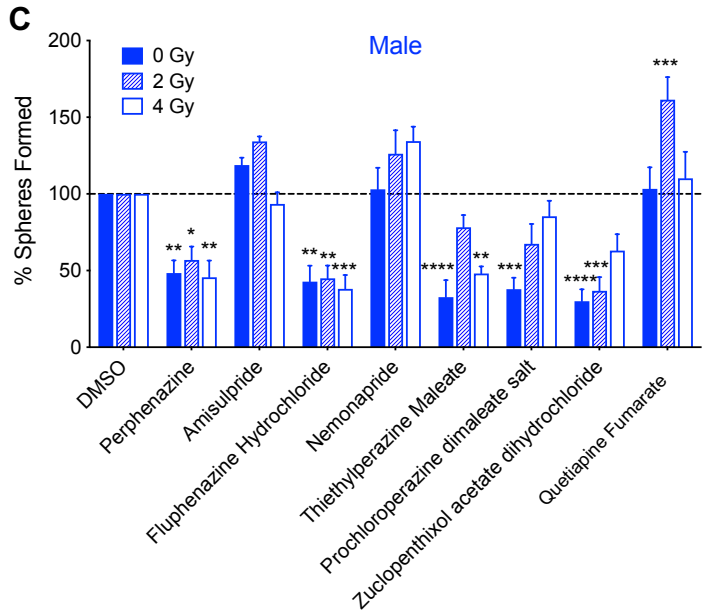
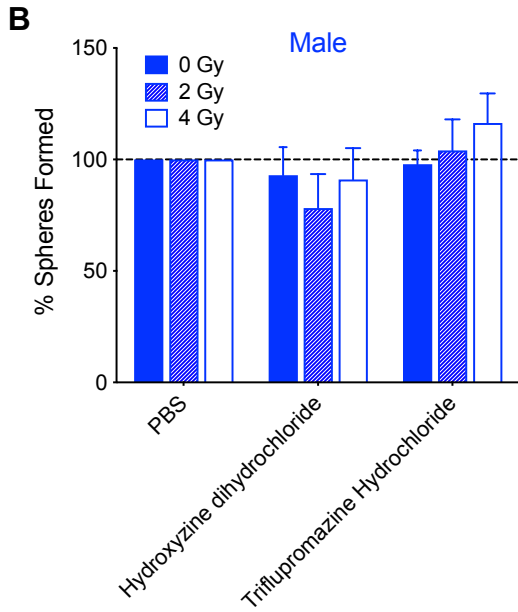
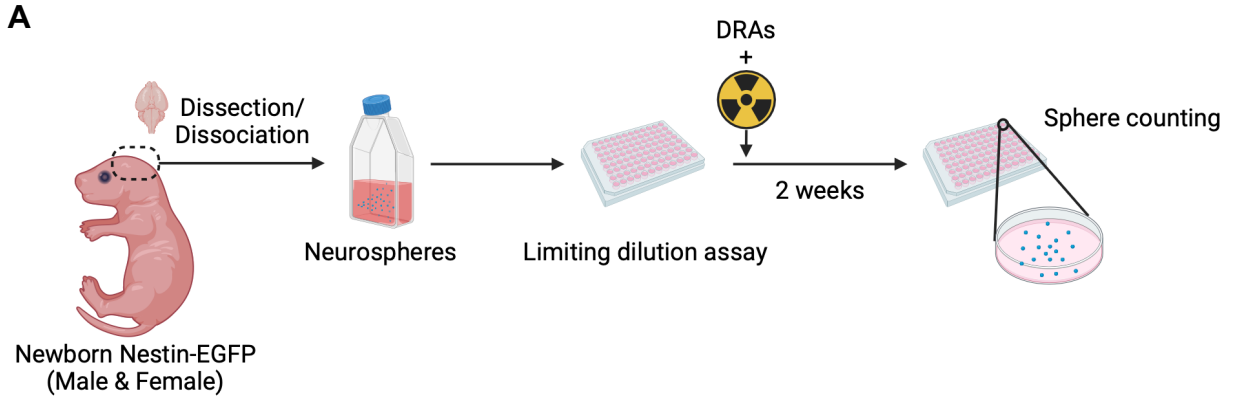


Figure 3.

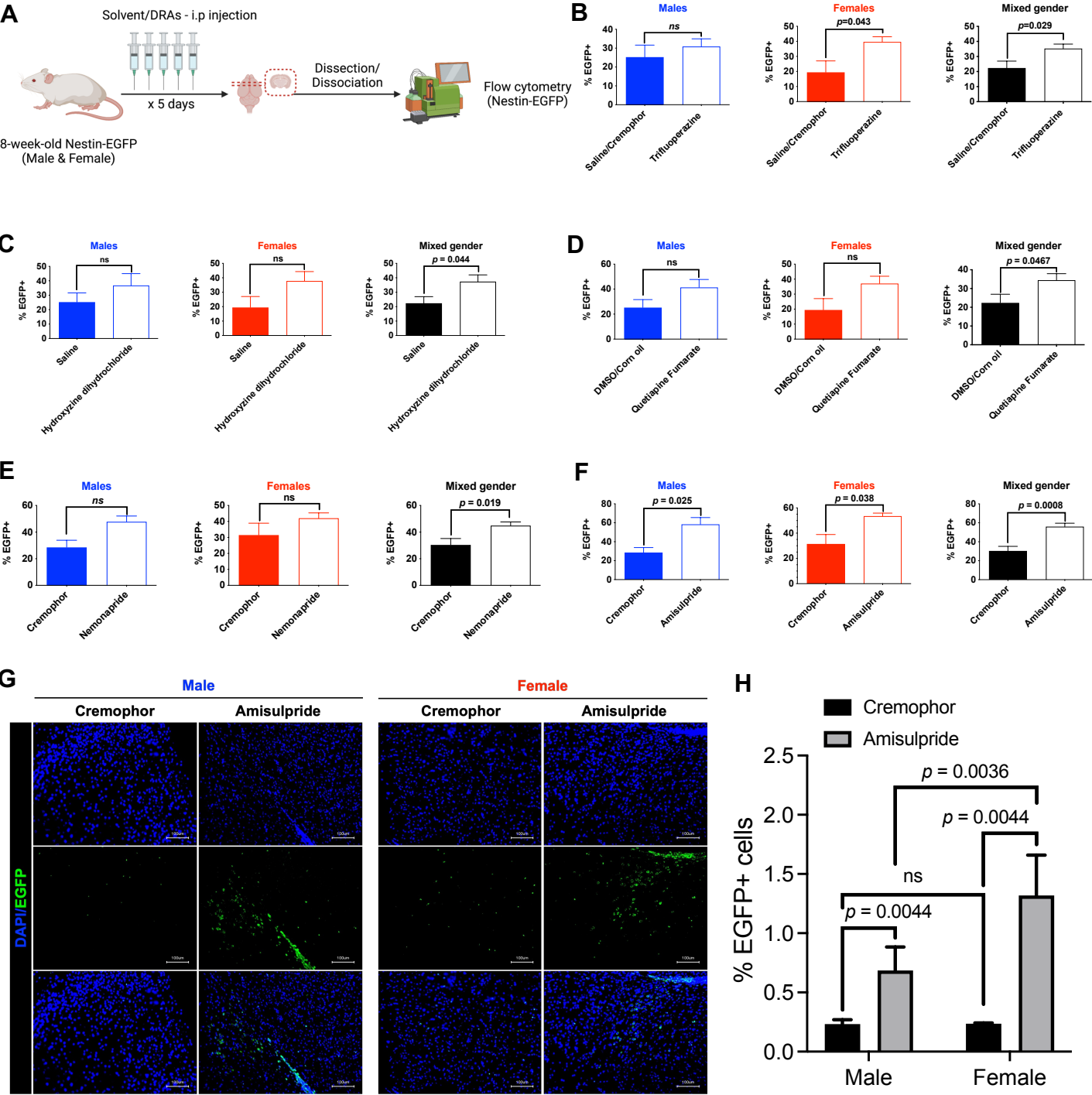


Figure 4.

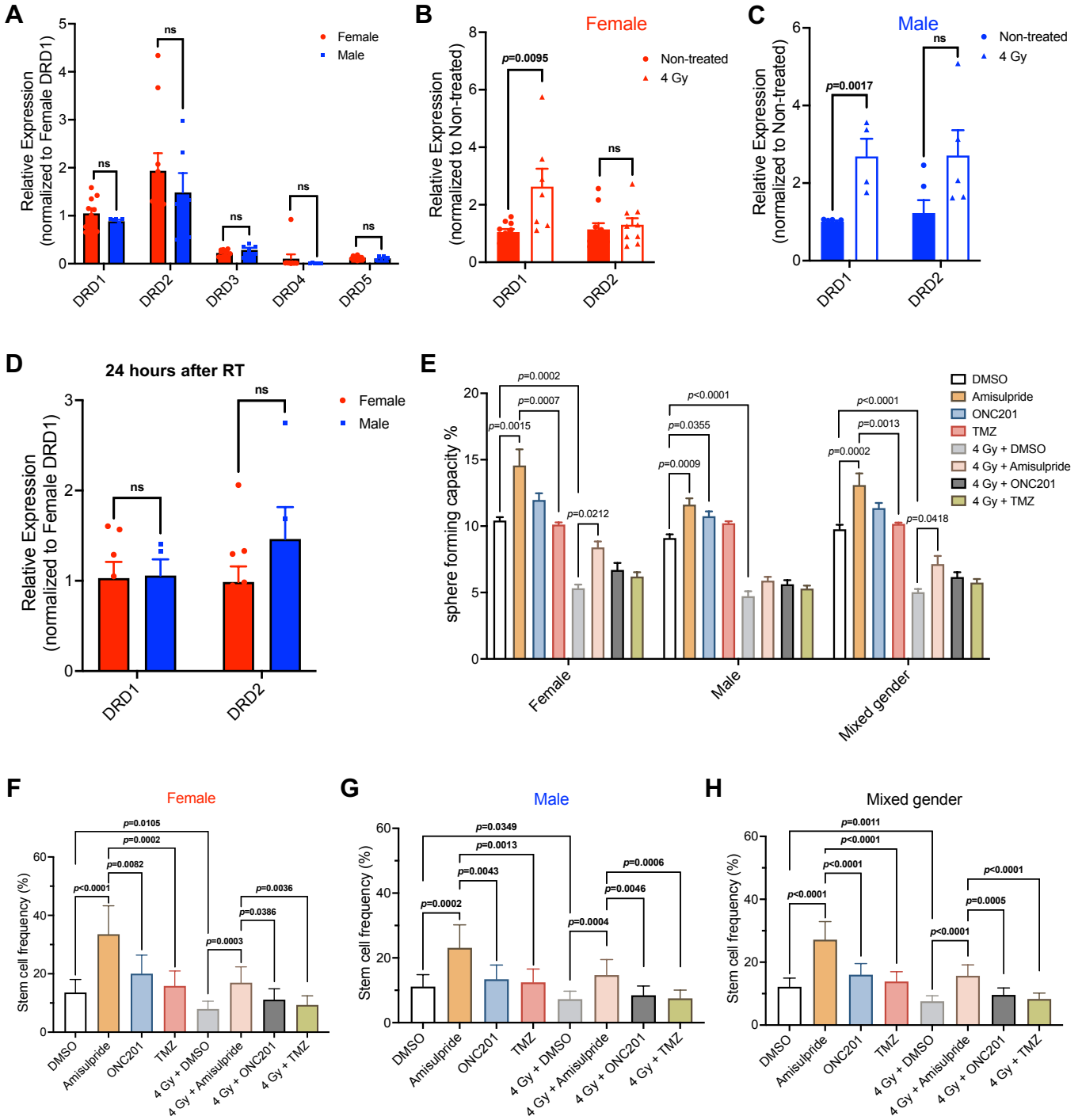


Table 1. List of dopamine receptor antagonists and their binding receptor(s)

| Drug name | Dopamine-1 (D1) receptor | Dopamine-2 (D2) receptor |
|--|--------------------------|--------------------------|
| Perphenazine | | Ö |
| Acepromazine maleate | | Ö |
| Amisulpride | | Ö |
| Amoxapine | | Ö |
| Azaperone | Ö | Ö |
| Bromopride | | Ö |
| Clomipramine hydrochloride | | Ö |
| Chlorpromazine hydrochloride | | Ö |
| Droperidol | | Ö |
| S-(-)-Eticlopride hydrochloride | | Ö |
| Fluphenazine Hydrochloride | Ö | Ö |
| Fluspirilene | | Ö |
| Hydroxyzine dihydrochloride | | Ö |
| Loxapine succinate salt | | Ö |
| Mesoridazine Besylate | | Ö |
| Metoclopramide | | Ö |
| Nemonapride | | Ö |
| Promazine hydrochloride | Ö | Ö |
| S-(-)-Raclopride (+)-tartrate salt | Ö | Ö |
| Remoxipride hydrochloride | | Ö |
| Risperidone | | Ö |
| Siperone | | Ö |
| (+)-Sulpiride | | Ö |
| Thioridazine | | Ö |
| Trifluoperazine | | Ö |
| Ziprasidone hydrochloride monohydrate | | Ö |
| Pimozide | | Ö |
| Thiethylperazine Maleate | | Ö |
| Triflupromazine Hydrochloride | Ö | Ö |
| Prochloroperazine dimaleate salt | | Ö |
| Zuclopenthixol acetate dihydrochloride | Ö | Ö |
| Quetiapine Fumarate | | Ö |
| ONC201 | | Ö |

376 **References**

377

- 378 1. Ledeen RW, Golly F, Haley JE. Axon-myelin transfer of phospholipids and
379 phospholipid precursors. Labeling of myelin phosphoinositides through axonal transport.
380 *Mol Neurobiol.* 1992;6(2-3):179-90.
- 381 2. Belachew S, Rogister B, Rigo JM, Malgrange B, Moonen G. Neurotransmitter-
382 mediated regulation of CNS myelination: a review. *Acta Neurol Belg.* 1999;99(1):21-31.
- 383 3. Hanoun M, Maryanovich M, Arnal-Estape A, Frenette PS. Neural regulation of
384 hematopoiesis, inflammation, and cancer. *Neuron.* 2015;86(2):360-73.
- 385 4. Boilly B, Faulkner S, Jobling P, Hondermarck H. Nerve Dependence: From
386 Regeneration to Cancer. *Cancer Cell.* 2017;31(3):342-54.
- 387 5. Weissenrieder JS, Neighbors JD, Mailman RB, Hohl RJ. Cancer and the
388 Dopamine D(2) Receptor: A Pharmacological Perspective. *J Pharmacol Exp Ther.*
389 2019;370(1):111-26.
- 390 6. Rosas-Cruz A, Salinas-Jazmin N, Velazquez MAV. Dopamine Receptors in
391 Cancer: Are They Valid Therapeutic Targets? *Technol Cancer Res Treat.*
392 2021;20:15330338211027913.
- 393 7. Wang X, Wang ZB, Luo C, Mao XY, Li X, Yin JY, et al. The Prospective Value of
394 Dopamine Receptors on Bio-Behavior of Tumor. *J Cancer.* 2019;10(7):1622-32.
- 395 8. Bhat K, Saki M, Vlashi E, Cheng F, Duhachek-Muggy S, Alli C, et al. The
396 dopamine receptor antagonist trifluoperazine prevents phenotype conversion and
397 improves survival in mouse models of glioblastoma. *Proc Natl Acad Sci U S A.*
398 2020;117(20):11085-96.

- 399 9. He L, Bhat K, Ioannidis A, Zhang L, Nguyen NT, Allen JE, et al. Effects of the
400 DRD2/3 antagonist ONC201 and radiation in glioblastoma. *Radiother Oncol*.
401 2021;161:140-7.
- 402 10. Bhat K, Saki M, Cheng F, He L, Zhang L, Ioannidis A, et al. Dopamine Receptor
403 Antagonists, Radiation, and Cholesterol Biosynthesis in Mouse Models of Glioblastoma.
404 *J Natl Cancer Inst*. 2021;113(8):1094-104.
- 405 11. Huang J, Zhao D, Liu Z, Liu F. Repurposing psychiatric drugs as anti-cancer
406 agents. *Cancer Lett*. 2018;419:257-65.
- 407 12. Moura C, Vale N. The Role of Dopamine in Repurposing Drugs for Oncology.
408 *Biomedicines*. 2023;11(7).
- 409 13. Roman DD, Sperduto PW. Neuropsychological effects of cranial radiation:
410 current knowledge and future directions. *Int J Radiat Oncol Biol Phys*. 1995;31(4):983-
411 98.
- 412 14. Greene-Schloesser D, Robbins ME, Peiffer AM, Shaw EG, Wheeler KT, Chan
413 MD. Radiation-induced brain injury: A review. *Front Oncol*. 2012;2:73.
- 414 15. Pazzaglia S, Briganti G, Mancuso M, Saran A. Neurocognitive Decline Following
415 Radiotherapy: Mechanisms and Therapeutic Implications. *Cancers (Basel)*. 2020;12(1).
- 416 16. Williams OOF, Coppolino M, Perreault ML. Sex differences in neuronal systems
417 function and behaviour: beyond a single diagnosis in autism spectrum disorders. *Transl*
418 *Psychiatry*. 2021;11(1):625.
- 419 17. DuMont M, Agostinis A, Singh K, Swan E, Buttle Y, Tropea D. Sex representation
420 in neurodegenerative and psychiatric disorders' preclinical and clinical studies.
421 *Neurobiol Dis*. 2023;184:106214.

- 422 18. Mignone JL, Kukekov V, Chiang AS, Steindler D, Enikolopov G. Neural stem and
423 progenitor cells in nestin-GFP transgenic mice. *J Comp Neurol.* 2004;469(3):311-24.
- 424 19. Wolterink-Donselaar IG, Meerding JM, Fernandes C. A method for gender
425 determination in newborn dark pigmented mice. *Lab Anim (NY).* 2009;38(1):35-8.
- 426 20. Bhat K, Medina P, He L, Zhang L, Saki M, Ioannidis A, et al. 1-[(4-
427 Nitrophenyl)sulfonyl]-4-phenylpiperazine treatment after brain irradiation preserves
428 cognitive function in mice. *Neuro Oncol.* 2020;22(10):1484-94.
- 429 21. Hu Y, Smyth GK. ELDA: extreme limiting dilution analysis for comparing depleted
430 and enriched populations in stem cell and other assays. *J Immunol Methods.*
431 2009;347(1-2):70-8.
- 432 22. Michaelidesova A, Konirova J, Bartunek P, Zikova M. Effects of Radiation
433 Therapy on Neural Stem Cells. *Genes (Basel).* 2019;10(9).
- 434 23. Prise KM, Saran A. Concise review: stem cell effects in radiation risk. *Stem Cells.*
435 2011;29(9):1315-21.
- 436 24. Portnow J, Badie B, Chen M, Liu A, Blanchard S, Synold TW. The
437 neuropharmacokinetics of temozolomide in patients with resectable brain tumors:
438 potential implications for the current approach to chemoradiation. *Clin Cancer Res.*
439 2009;15(22):7092-8.
- 440 25. Greene-Schloesser D, Robbins ME. Radiation-induced cognitive impairment--
441 from bench to bedside. *Neuro Oncol.* 2012;14 Suppl 4(Suppl 4):iv37-44.
- 442 26. Butler RW, Mulhern RK. Neurocognitive interventions for children and
443 adolescents surviving cancer. *J Pediatr Psychol.* 2005;30(1):65-78.

- 444 27. Moore BD, 3rd. Neurocognitive outcomes in survivors of childhood cancer. *J*
445 *Pediatr Psychol.* 2005;30(1):51-63.
- 446 28. Palmer SL, Reddick WE, Gajjar A. Understanding the cognitive impact on
447 children who are treated for medulloblastoma. *J Pediatr Psychol.* 2007;32(9):1040-9.
- 448 29. Zhao X, Wang Y, Wait E, Mankowski W, Bjornsson CS, Cohen AR, et al. 3D
449 Image Analysis of the Complete Ventricular-Subventricular Zone Stem Cell Niche
450 Reveals Significant Vasculature Changes and Progenitor Deficits in Males Versus
451 Females with Aging. *Stem Cell Reports.* 2021;16(4):836-50.
- 452 30. Ponti G, Farinetti A, Marraudino M, Panzica G, Gotti S. Sex Steroids and Adult
453 Neurogenesis in the Ventricular-Subventricular Zone. *Front Endocrinol (Lausanne).*
454 2018;9:156.
- 455 31. McEwen BS, Milner TA. Understanding the broad influence of sex hormones and
456 sex differences in the brain. *J Neurosci Res.* 2017;95(1-2):24-39.
- 457 32. Barth C, Villringer A, Sacher J. Sex hormones affect neurotransmitters and
458 shape the adult female brain during hormonal transition periods. *Front Neurosci.*
459 2015;9:37.
- 460 33. Beaulieu JM, Gainetdinov RR, Caron MG. The Akt-GSK-3 signaling cascade in
461 the actions of dopamine. *Trends Pharmacol Sci.* 2007;28(4):166-72.
- 462 34. Boyd KN, Mailman RB. Dopamine receptor signaling and current and future
463 antipsychotic drugs. *Handb Exp Pharmacol.* 2012(212):53-86.
- 464 35. Bramble MS, Vashist N, Vilain E. Sex steroid hormone modulation of neural stem
465 cells: a critical review. *Biol Sex Differ.* 2019;10(1):28.

- 466 36. Koutmani Y, Karalis KP. Neural stem cells respond to stress hormones:
467 distinguishing beneficial from detrimental stress. *Front Physiol.* 2015;6:77.
- 468 37. Angelopoulos I, Gakis G, Birmpas K, Kyrousi C, Habeos EE, Kaplani K, et al.
469 Metabolic regulation of the neural stem cell fate: Unraveling new connections,
470 establishing new concepts. *Front Neurosci.* 2022;16:1009125.
- 471 38. Scandella V, Petrelli F, Moore DL, Braun SMG, Knobloch M. Neural stem cell
472 metabolism revisited: a critical role for mitochondria. *Trends Endocrinol Metab.*
473 2023;34(8):446-61.
- 474 39. Fawal MA, Davy A. Impact of Metabolic Pathways and Epigenetics on Neural
475 Stem Cells. *Epigenet Insights.* 2018;11:2516865718820946.
- 476 40. Kazanis I, Lathia J, Moss L, ffrench-Constant C. The neural stem cell
477 microenvironment. *StemBook.* Cambridge (MA)2008.
- 478 41. Kalani MY, Cheshier SH, Cord BJ, Bababegy SR, Vogel H, Weissman IL, et al.
479 Wnt-mediated self-renewal of neural stem/progenitor cells. *Proc Natl Acad Sci U S A.*
480 2008;105(44):16970-5.
- 481 42. Bengoa-Vergniory N, Kypka RM. Canonical and noncanonical Wnt signaling in
482 neural stem/progenitor cells. *Cell Mol Life Sci.* 2015;72(21):4157-72.
- 483 43. Chavali M, Klingener M, Kokkosis AG, Garkun Y, Felong S, Maffei A, et al. Non-
484 canonical Wnt signaling regulates neural stem cell quiescence during homeostasis and
485 after demyelination. *Nat Commun.* 2018;9(1):36.
- 486 44. Imayoshi I, Sakamoto M, Yamaguchi M, Mori K, Kageyama R. Essential roles of
487 Notch signaling in maintenance of neural stem cells in developing and adult brains. *J*
488 *Neurosci.* 2010;30(9):3489-98.

- 489 45. Mizutani K, Yoon K, Dang L, Tokunaga A, Gaiano N. Differential Notch signalling
490 distinguishes neural stem cells from intermediate progenitors. *Nature*.
491 2007;449(7160):351-5.
- 492 46. Kageyama R, Ohtsuka T, Shimojo H, Imayoshi I. Dynamic regulation of Notch
493 signaling in neural progenitor cells. *Curr Opin Cell Biol*. 2009;21(6):733-40.
- 494 47. Fuccillo M, Joyner AL, Fishell G. Morphogen to mitogen: the multiple roles of
495 hedgehog signalling in vertebrate neural development. *Nat Rev Neurosci*.
496 2006;7(10):772-83.
- 497 48. Garcia ADR, Han YG, Triplett JW, Farmer WT, Harwell CC, Ihrie RA. The
498 Elegance of Sonic Hedgehog: Emerging Novel Functions for a Classic Morphogen. *J*
499 *Neurosci*. 2018;38(44):9338-45.
- 500 49. Ocasio JK, Bates RDP, Rapp CD, Gershon TR. GSK-3 modulates SHH-driven
501 proliferation in postnatal cerebellar neurogenesis and medulloblastoma. *Development*.
502 2019;146(20).
- 503 50. Zheng L, Conner SD. Glycogen synthase kinase 3beta inhibition enhances
504 Notch1 recycling. *Mol Biol Cell*. 2018;29(4):389-95.
- 505 51. Yao HB, Shaw PC, Wong CC, Wan DC. Expression of glycogen synthase
506 kinase-3 isoforms in mouse tissues and their transcription in the brain. *J Chem*
507 *Neuroanat*. 2002;23(4):291-7.
- 508 52. Emamian ES, Hall D, Birnbaum MJ, Karayiorgou M, Gogos JA. Convergent
509 evidence for impaired AKT1-GSK3beta signaling in schizophrenia. *Nat Genet*.
510 2004;36(2):131-7.

- 511 53. Chenn A, Walsh CA. Regulation of cerebral cortical size by control of cell cycle
512 exit in neural precursors. *Science*. 2002;297(5580):365-9.
- 513 54. Hooper C, Killick R, Lovestone S. The GSK3 hypothesis of Alzheimer's disease.
514 *J Neurochem*. 2008;104(6):1433-9.
- 515 55. Ma YX, Wang XL, Chen JQ, Li B, Hur EM, Saijilafu. Differential Roles of
516 Glycogen Synthase Kinase 3 Subtypes Alpha and Beta in Cortical Development. *Front*
517 *Mol Neurosci*. 2017;10:391.
- 518 56. Racaud-Sultan C, Vergnolle N. GSK3beta, a Master Kinase in the Regulation of
519 Adult Stem Cell Behavior. *Cells*. 2021;10(2).
- 520 57. Patel P, Woodgett JR. Glycogen Synthase Kinase 3: A Kinase for All Pathways?
521 *Curr Top Dev Biol*. 2017;123:277-302.
- 522 58. Huang J, Zhang Y, Bersenev A, O'Brien WT, Tong W, Emerson SG, et al. Pivotal
523 role for glycogen synthase kinase-3 in hematopoietic stem cell homeostasis in mice. *J*
524 *Clin Invest*. 2009;119(12):3519-29.
- 525 59. Tsuchiya K, Nakamura T, Okamoto R, Kanai T, Watanabe M. Reciprocal
526 targeting of Hath1 and beta-catenin by Wnt glycogen synthase kinase 3beta in human
527 colon cancer. *Gastroenterology*. 2007;132(1):208-20.
- 528 60. Schwabe RF, Brenner DA. Role of glycogen synthase kinase-3 in TNF-alpha-
529 induced NF-kappaB activation and apoptosis in hepatocytes. *Am J Physiol Gastrointest*
530 *Liver Physiol*. 2002;283(1):G204-11.
- 531 61. Singh AM, Bechard M, Smith K, Dalton S. Reconciling the different roles of
532 Gsk3beta in "naive" and "primed" pluripotent stem cells. *Cell Cycle*. 2012;11(16):2991-
533 6.

534 62. Wang W, Lu G, Su X, Tang C, Li H, Xiong Z, et al. Pten-mediated Gsk3beta
535 modulates the naive pluripotency maintenance in embryonic stem cells. *Cell Death Dis.*
536 2020;11(2):107.

537 63. Jacobs KM, Misri S, Meyer B, Raj S, Zobel CL, Sleckman BP, et al. Unique
538 epigenetic influence of H2AX phosphorylation and H3K56 acetylation on normal stem
539 cell radioresponses. *Mol Biol Cell.* 2016;27(8):1332-45.

540 64. Yalamarty SSK, Filipczak N, Li X, Subhan MA, Parveen F, Ataide JA, et al.
541 Mechanisms of Resistance and Current Treatment Options for Glioblastoma Multiforme
542 (GBM). *Cancers (Basel).* 2023;15(7).

543 65. Wu W, Klockow JL, Zhang M, Lafortune F, Chang E, Jin L, et al. Glioblastoma
544 multiforme (GBM): An overview of current therapies and mechanisms of resistance.
545 *Pharmacol Res.* 2021;171:105780.

546 66. Mancino M, Ametller E, Gascon P, Almendro V. The neuronal influence on tumor
547 progression. *Biochim Biophys Acta.* 2011;1816(2):105-18.

548 67. Liebelt BD, Shingu T, Zhou X, Ren J, Shin SA, Hu J. Glioma Stem Cells:
549 Signaling, Microenvironment, and Therapy. *Stem Cells Int.* 2016;2016:7849890.

550 68. Sanz-Ezquerro JJ, Munsterberg AE, Stricker S. Editorial: Signaling Pathways in
551 Embryonic Development. *Front Cell Dev Biol.* 2017;5:76.

552 69. Montero JA, Lorda-Diez CI, Francisco-Morcillo J, Chimal-Monroy J, Garcia-
553 Porrero JA, Hurle JM. Sox9 Expression in Amniotes: Species-Specific Differences in the
554 Formation of Digits. *Front Cell Dev Biol.* 2017;5:23.

555

Supplementary Materials for

Effects of Dopamine Receptor Antagonists and Radiation on Mouse

Neural Stem/Progenitor Cells

Table of contents:

- Supplementary Figures
- Supplementary Tables
- Supplementary Materials and Methods

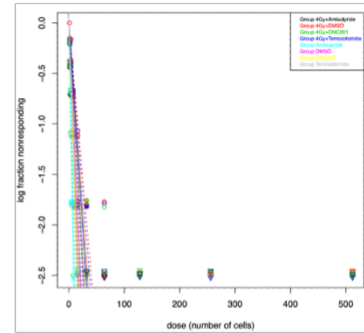
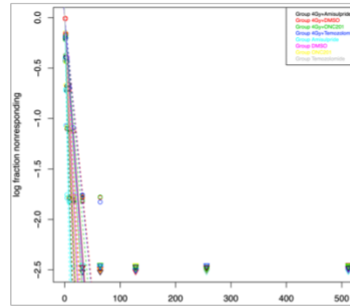
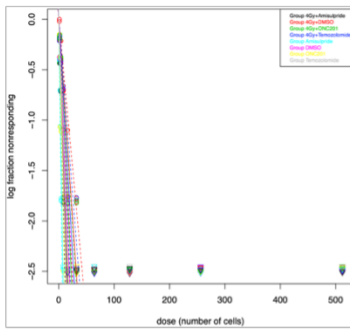
Supplementary Figure 1.

A

Female

Male

Mixed gender



B

Plot results has been checked
Confidence intervals for
1/(stem cell frequency)

| Group | Lower | Estimate | Upper |
|------------------|-------|----------|-------|
| 4Gy+Amisulpride | 7.89 | 5.91 | 4.47 |
| 4Gy+DMSO | 16.91 | 12.60 | 9.42 |
| 4Gy+ONC201 | 12.02 | 8.98 | 6.74 |
| 4Gy+Temozolomide | 14.39 | 10.73 | 8.04 |
| Amisulpride | 3.92 | 2.98 | 2.31 |
| DMSO | 9.84 | 7.36 | 5.54 |
| ONC201 | 6.64 | 4.99 | 3.79 |
| Temozolomide | 8.44 | 6.32 | 4.77 |

Plot results has been checked
Confidence intervals for
1/(stem cell frequency)

| Group | Lower | Estimate | Upper |
|------------------|-------|----------|-------|
| 4Gy+Amisulpride | 9.09 | 6.80 | 5.13 |
| 4Gy+DMSO | 18.47 | 13.75 | 10.28 |
| 4Gy+ONC201 | 15.86 | 11.82 | 8.84 |
| 4Gy+Temozolomide | 17.87 | 13.31 | 9.95 |
| Amisulpride | 5.75 | 4.33 | 3.31 |
| DMSO | 12.04 | 8.99 | 6.75 |
| ONC201 | 9.97 | 7.46 | 5.62 |
| Temozolomide | 10.75 | 8.03 | 6.04 |

Plot results has been checked
Confidence intervals for
1/(stem cell frequency)

| Group | Lower | Estimate | Upper |
|------------------|-------|----------|-------|
| 4Gy+Amisulpride | 7.81 | 6.38 | 5.22 |
| 4Gy+DMSO | 16.24 | 13.19 | 10.73 |
| 4Gy+ONC201 | 12.81 | 10.41 | 8.48 |
| 4Gy+Temozolomide | 14.83 | 12.05 | 9.81 |
| Amisulpride | 4.47 | 3.68 | 3.04 |
| DMSO | 10.08 | 8.21 | 6.70 |
| ONC201 | 7.65 | 6.24 | 5.12 |
| Temozolomide | 8.84 | 7.21 | 5.89 |

C

Pairwise tests for differences in stem cell frequencies

| Group 1 | Group 2 | Chisq | DF | Pr(>Chisq) |
|------------------|------------------|-------|----|------------|
| 4Gy+Amisulpride | 4Gy+DMSO | 13.4 | 1 | 0.00255 |
| 4Gy+Amisulpride | 4Gy+ONC201 | 4.28 | 1 | 0.0386 |
| 4Gy+Amisulpride | 4Gy+Temozolomide | 8.47 | 1 | 0.00362 |
| 4Gy+Amisulpride | Amisulpride | 12 | 1 | 0.000535 |
| 4Gy+Amisulpride | DMSO | 1.13 | 1 | 0.287 |
| 4Gy+Amisulpride | ONC201 | 0.729 | 1 | 0.393 |
| 4Gy+Amisulpride | Temozolomide | 0.108 | 1 | 0.742 |
| 4Gy+DMSO | 4Gy+ONC201 | 2.71 | 1 | 0.0996 |
| 4Gy+DMSO | 4Gy+Temozolomide | 0.592 | 1 | 0.442 |
| 4Gy+DMSO | Amisulpride | 49.2 | 1 | 2.28e-12 |
| 4Gy+DMSO | DMSO | 6.55 | 1 | 0.0105 |
| 4Gy+DMSO | ONC201 | 20.4 | 1 | 6.15e-06 |
| 4Gy+DMSO | Temozolomide | 11 | 1 | 0.000891 |
| 4Gy+ONC201 | 4Gy+Temozolomide | 0.765 | 1 | 0.382 |
| 4Gy+ONC201 | Amisulpride | 30.4 | 1 | 3.49e-08 |
| 4Gy+ONC201 | DMSO | 0.939 | 1 | 0.333 |
| 4Gy+ONC201 | ONC201 | 8.65 | 1 | 0.00327 |
| 4Gy+ONC201 | Temozolomide | 3 | 1 | 0.0833 |
| 4Gy+Temozolomide | Amisulpride | 39.8 | 1 | 2.88e-10 |
| 4Gy+Temozolomide | DMSO | 3.28 | 1 | 0.0699 |
| 4Gy+Temozolomide | ONC201 | 14.3 | 1 | 0.000159 |
| 4Gy+Temozolomide | Temozolomide | 6.63 | 1 | 0.01 |
| Amisulpride | DMSO | 19.9 | 1 | 7.95e-06 |
| Amisulpride | ONC201 | 6.99 | 1 | 0.00821 |
| Amisulpride | Temozolomide | 14.3 | 1 | 0.000158 |
| DMSO | ONC201 | 3.66 | 1 | 0.0557 |
| DMSO | Temozolomide | 0.542 | 1 | 0.461 |
| ONC201 | Temozolomide | 1.4 | 1 | 0.237 |

Pairwise tests for differences in stem cell frequencies

| Group 1 | Group 2 | Chisq | DF | Pr(>Chisq) |
|------------------|------------------|--------|----|------------|
| 4Gy+Amisulpride | 4Gy+DMSO | 12.5 | 1 | 0.000416 |
| 4Gy+Amisulpride | 4Gy+ONC201 | 8.03 | 1 | 0.0046 |
| 4Gy+Amisulpride | 4Gy+Temozolomide | 11.7 | 1 | 0.000635 |
| 4Gy+Amisulpride | Amisulpride | 5.59 | 1 | 0.018 |
| 4Gy+Amisulpride | DMSO | 2.03 | 1 | 0.154 |
| 4Gy+Amisulpride | ONC201 | 0.229 | 1 | 0.633 |
| 4Gy+Amisulpride | Temozolomide | 0.736 | 1 | 0.391 |
| 4Gy+DMSO | 4Gy+ONC201 | 0.578 | 1 | 0.447 |
| 4Gy+DMSO | 4Gy+Temozolomide | 0.0262 | 1 | 0.872 |
| 4Gy+DMSO | Amisulpride | 34 | 1 | 5.65e-09 |
| 4Gy+DMSO | DMSO | 4.45 | 1 | 0.0349 |
| 4Gy+DMSO | ONC201 | 9.57 | 1 | 0.00198 |
| 4Gy+DMSO | Temozolomide | 7.26 | 1 | 0.00704 |
| 4Gy+ONC201 | 4Gy+Temozolomide | 0.367 | 1 | 0.544 |
| 4Gy+ONC201 | Amisulpride | 26.8 | 1 | 2.23e-07 |
| 4Gy+ONC201 | DMSO | 1.93 | 1 | 0.165 |
| 4Gy+ONC201 | ONC201 | 5.67 | 1 | 0.0172 |
| 4Gy+ONC201 | Temozolomide | 3.92 | 1 | 0.0477 |
| 4Gy+Temozolomide | Amisulpride | 33 | 1 | 9.35e-09 |
| 4Gy+Temozolomide | DMSO | 3.91 | 1 | 0.0481 |
| 4Gy+Temozolomide | ONC201 | 8.84 | 1 | 0.00295 |
| 4Gy+Temozolomide | Temozolomide | 6.6 | 1 | 0.0102 |
| Amisulpride | DMSO | 14.2 | 1 | 0.000167 |
| Amisulpride | ONC201 | 8.17 | 1 | 0.00425 |
| Amisulpride | Temozolomide | 10.4 | 1 | 0.00129 |
| DMSO | ONC201 | 0.926 | 1 | 0.336 |
| DMSO | Temozolomide | 0.33 | 1 | 0.566 |
| ONC201 | Temozolomide | 0.149 | 1 | 0.699 |

Pairwise tests for differences in stem cell frequencies

| Group 1 | Group 2 | Chisq | DF | Pr(>Chisq) |
|------------------|------------------|--------|----|------------|
| 4Gy+Amisulpride | 4Gy+DMSO | 25.7 | 1 | 3.97e-07 |
| 4Gy+Amisulpride | 4Gy+ONC201 | 12.3 | 1 | 0.000452 |
| 4Gy+Amisulpride | 4Gy+Temozolomide | 20.3 | 1 | 6.76e-06 |
| 4Gy+Amisulpride | Amisulpride | 16.2 | 1 | 5.8e-05 |
| 4Gy+Amisulpride | DMSO | 3.19 | 1 | 0.074 |
| 4Gy+Amisulpride | ONC201 | 0.0231 | 1 | 0.879 |
| 4Gy+Amisulpride | Temozolomide | 0.769 | 1 | 0.38 |
| 4Gy+DMSO | 4Gy+ONC201 | 2.73 | 1 | 0.0994 |
| 4Gy+DMSO | 4Gy+Temozolomide | 0.388 | 1 | 0.533 |
| 4Gy+DMSO | Amisulpride | 80.8 | 1 | 2.54e-19 |
| 4Gy+DMSO | DMSO | 10.7 | 1 | 0.00108 |
| 4Gy+DMSO | ONC201 | 27.8 | 1 | 1.33e-07 |
| 4Gy+DMSO | Temozolomide | 17.7 | 1 | 2.54e-05 |
| 4Gy+ONC201 | 4Gy+Temozolomide | 1.07 | 1 | 0.3 |
| 4Gy+ONC201 | Amisulpride | 56.5 | 1 | 5.74e-14 |
| 4Gy+ONC201 | DMSO | 2.82 | 1 | 0.093 |
| 4Gy+ONC201 | ONC201 | 13.7 | 1 | 0.000216 |
| 4Gy+ONC201 | Temozolomide | 6.91 | 1 | 0.00858 |
| 4Gy+Temozolomide | Amisulpride | 71.6 | 1 | 2.58e-17 |
| 4Gy+Temozolomide | DMSO | 7.2 | 1 | 0.00731 |
| 4Gy+Temozolomide | ONC201 | 22.1 | 1 | 2.58e-06 |
| 4Gy+Temozolomide | Temozolomide | 13.2 | 1 | 0.000282 |
| Amisulpride | DMSO | 33.2 | 1 | 8.46e-09 |
| Amisulpride | ONC201 | 15.3 | 1 | 9.3e-05 |
| Amisulpride | Temozolomide | 23.9 | 1 | 1e-06 |
| DMSO | ONC201 | 3.83 | 1 | 0.0505 |
| DMSO | Temozolomide | 0.844 | 1 | 0.358 |
| ONC201 | Temozolomide | 1.08 | 1 | 0.299 |

Supplementary Figure 1. Extreme limiting dilution assay (ELDA) was performed with the Passage 2 neurospheres isolated from both female and male pups. The neurospheres were treated with a single dose of 4 Gy radiation in the presence or absence of ONC201 (1 μ M) or Temozolomide (1 μ M) or Amisulpride (1 μ M). Wells with neurospheres were counted at 7 days post initial culturing. Results were analyzed using freely available software for predicting stem cell frequency <http://bioinf.wehi.edu.au/software/elda/>. The

amount of initially seeded cells (x-axis) is plotted against the log fraction of non-responders corresponding to wells without any detected neurospheres (y-axis). The slope of the line represents the log-active cell fraction (**A**). Confidence intervals for 1/stem cell frequency (%) (**B**) and Pairwise tests for differences in stem cell frequencies (**C**) were also obtained from the software.

Supplementary Table 1

| Species | Gene name | Primer sequence (5'-3') |
|---------|-----------|---|
| Mouse | DRD1 | Forward: CCAAGAACGTGAGGGGCTAAG Reverse: TGAGGATGCGAAAGGAGAAG |
| Mouse | DRD2 | Forward: ACCACTCAAGGGCAACTG Reverse: TGACAGCATCTCCATTTCCAG |
| Mouse | DRD3 | Forward: TTCACTATCAGCATGGCACC Reverse: GGTTGGAGATGGAGCAGATG |
| Mouse | DRD4 | Forward: GCTGCCTCTCTTTGTCTACTC Reverse: AACCTGTCCACGCTGATG |
| Mouse | DRD5 | Forward: AAAATCTCACCCTCACC Reverse: AAGCATAAGCACACCAGGAG |
| Mouse | GAPDH | Forward: AGGTCGGTGTGAACGGATTTG Reverse: CCCTGGCACATGAATCCTGG |

Supplementary Materials and Methods

Neural stem cell culture

The entire brains of the newborn Nestin-EGFP mice were harvested, minced and transferred to a tube with 1-ml of 0.05 % trypsin-EDTA (Thermo Fisher, # 25300-054), mixed and incubated at 37 °C for 7 minutes. Trypsin was inhibited by adding 1-ml of trypsin inhibitor (Sigma-Aldrich, # T6522), then centrifuged at 110 x g for 5 minutes with supernatant discarded. The tissue was resuspended in 200- μ l of NeuroCult (Stem Cell Technologies, # 05702), then diluted with 10 ml NeuroCult media and passed through a 70 μ m cell strainer. The cell suspension was centrifuged, the supernatant discarded, and the cell pellet resuspended in 2-ml of ACK lysing buffer (Lonza, # 10-548E). After centrifugation, cells from the final pellet were cultured in 1X complete NeuroCult media (45-ml of base NeuroCult media, 5-ml of supplement, 1- μ l of EGF, 20- μ l of bFGF, 3130 U/ml of heparin) under standard conditions (37 °C, 5 % CO₂) and labeled as Passage #1 (P1). All experiments were performed with P2 cells.

Drug treatment

For *in vitro* studies DRAs were solubilized in DMSO or PBS. The neurosphere cultures were pre-treated either with 1 μ M DRAs or solvent control one hour before a single dose of 0, 2 or 4 Gy irradiation. In *in vivo* experiments mice received daily i.p. injections of 20 mg/kg of trifluoperazine, 30 mg/kg of quetiapine, 20 mg/kg of hydroxyzine dihydrochloride, 1 mg/kg of nemonapride or 1 mg/kg of amisulpride for five consecutive days. Trifluoperazine was prepared with saline/cremophor, nemonapride and amisulpride

were prepared with cremophor, while hydroxyzine dihydrochloride was dissolved in saline and quetiapine was solubilized in DMSO/corn oil.

Immunofluorescence

Brains were explanted, fixed and embedded in paraffin. 4- μ m blank sections were baked at 65 °C for 30 minutes, dewaxed in two successive Xylene for 5 minutes each and then hydrated for 5 minutes each using an alcohol gradient. Antigen retrieval was performed using Heat Induced Epitope Retrieval in citrate buffer (10 mM sodium citrate, 0.05 % tween20, pH=6) with heating to 95 °C for 10 minutes. After cooling down, the slides were blocked with 10 % goat serum containing 1 % BSA at room temperature for 30 minutes and then incubated with the primary antibody against EGFP (Abcam, ab184601, 1:100) overnight at 4 °C. The next day, the secondary antibody Alexa Fluor 488 Goat Anti-mouse IgG (H/L) antibody [1:1,000 (Invitrogen)] was applied for 60 minutes. Slides were mounted with ProLong[®] Gold Antifade Reagent with DAPI (Cell signaling, #8961S). Images were captured and merged at 20X using a digital microscope (BZ-9000, Keyence) and the percentages of Nestin-EGFP⁺ cells were quantified using Image J.

Quantitative Reverse Transcription-PCR

Total RNA was isolated using TRIZOL. cDNA synthesis was carried out using the SuperScript Reverse Transcriptase IV (Invitrogen). Quantitative PCR was performed in the QuantStudio[™] 3 Real-Time PCR System (Applied Biosystems, Carlsbad, CA, USA) using the PowerUp[™] SYBR[™] Green Master Mix (Applied Biosystems). C_t for each gene was determined after normalization to PPIA and $\Delta\Delta C_t$ was calculated relative to the

designated reference sample. Gene expression values were then set equal to $2^{-\Delta\Delta C_t}$ as described by the manufacturer of the kit (Applied Biosystems). All PCR primers were synthesized by Invitrogen with GAPDH as the housekeeping gene.

Drug list - Dopamine receptor antagonists (DRAs)

Perphenazine (#P6402, Sigma, Saint Louis, MO)

Acepromazine maleate (#A71111, Sigma)

Amisulpride (#A2729, Sigma)

Amoxapine (#A129, Sigma)

Azaperone (#Y0000029, Sigma)

Bromopride (#SC-217793, Santa Cruz Biotechnology, Dallas, TX)

Clomipramine hydrochloride (#C7291, Sigma)

Chlorpromazine hydrochloride (#31679, Sigma)

Droperidol (#D1414, Sigma)

S-(-)-Eticlopride hydrochloride (#E101, Sigma)

Fluphenazine Hydrochloride (#PHR1792, Sigma)

Fluspirilene (#Y0000236, Sigma)

Hydroxyzine dihydrochloride (#H8885, Sigma)

Loxapine succinate salt (#L106, Sigma)

Mesoridazine Besylate (#1393005, Sigma)

Metoclopramide (#32473, Sigma)

Nemonapride (#1746, Tocris, Minneapolis, MN)

Promazine hydrochloride (#46674, Sigma)

S-(-)-Raclopride (+)-tartrate salt (#R121, Sigma)
Remoxipride hydrochloride (#0916, Tocris)
Risperidone (#PHR1631, Sigma)
Spiperone (#S7395, Sigma)
(+)-Sulpiride (#S8010, Sigma)
Thioridazine (#1662504, Sigma)
Trifluoperazine (#T6062, Sigma)
Ziprasidone hydrochloride monohydrate (#Y0001286, Sigma)
Pimozide (#P1793, Sigma)
Thiethylperazine Maleate (#1658008, Sigma)
Triflupromazine Hydrochloride (#1686003, Sigma)
Prochloroperazine dimaleate salt (#P9178, Sigma)
Zuclopenthixol acetate dihydrochloride (#Y0000534, Sigma)
Quetiapine Fumarate (#AS-12050, Key Organics, Cornwall, UK)

3.1.3 - Leveraging the radiation-induced state of multipotency to drive surviving GBM cells towards a mitotically incompetent, neuron-like state

He, Ling, et al. "Radiation-Induced Cellular Plasticity: A Strategy for Combatting Glioblastoma." *bioRxiv* (2024): 2024-05.

A version of this work has been submitted for review.

Radiation-Induced Cellular Plasticity: A Strategy for Combatting Glioblastoma

^{1,2}Ling He, D.D.S. Ph.D., ³Daria Azizad, ¹Kruttika Bhat, Ph.D., ¹Angeliki Ioannidis, M.S.,
¹Carter J. Hoffmann, M.S., ¹Evelyn Arambula, ^{2, 3}Aparna Bhaduri, Ph.D., ^{2,4}Harley I.
Kornblum, M.D., Ph.D and ^{1,2,5}Frank Pajonk, M.D., Ph.D.*

¹Department of Radiation Oncology, David Geffen School of Medicine at UCLA

²Jonsson Comprehensive Cancer Center at UCLA

³Department of Biological Chemistry at UCLA

⁴NPI-Semel Institute for Neuroscience & Human Behavior at UCLA

⁵Department of Neurosurgery, David Geffen School of Medicine at UCLA

***Correspondence address:** Frank Pajonk, MD, PhD, Department of Radiation Oncology, David Geffen School of Medicine at UCLA, 10833 Le Conte Ave, Los Angeles, CA 90095-1714, Phone: +1 310 206 8733, Fax: +1 310 206 1260, email: pajonk@ucla.edu

Funding: FP was supported by grants from the *National Cancer Institute* (R01CA260886, R01CA281682) and the UCLA Eli and Edythe Broad Center of Regenerative Medicine and Stem Cell Research Award Program. FP and HIK were supported by the California Institute for Regenerative Medicine (CIRM; DISC2-14083).

AB, HIK and FP were supported by the American Cancer Society (CSCC-Team-23-980262-01-CSCC).

Summary

Glioblastoma is the deadliest brain cancer in adults and almost all patients succumb to the tumor. While surgery followed by chemo-radiotherapy significantly delays disease progression, these treatments do not lead to long-term tumor control and targeted therapies or biologics have so far failed to further improve survival.

Utilizing a transient radiation-induced state of multipotency we used the adenylylase activator forskolin to alter the cellular fate of glioma cells in response to radiation. The combined treatment induced the expression of neuronal markers in glioma cells, reduced proliferation and led to a distinct gene expression profile. scRNAseq revealed that the combined treatment forced glioma cells into a microglia- and neuron-like phenotypes. *In vivo* this treatment led to a loss of glioma stem cells and prolonged median survival in mouse models of glioblastoma. Collectively, our data suggest that revisiting a differentiation therapy with forskolin in combination with radiation could lead to clinical benefit.

Keywords

Glioblastoma, radiation, forskolin, cAMP, scRNAseq, differentiation therapy, mouse model, survival

Introduction

Glioblastoma (GBM) is the deadliest brain tumor in adults. The current standard of care, surgery followed by chemo-radiotherapy has not changed in almost two decades and the median survival times of 15-18 months are unacceptably low. A large body of literature supports the hierarchical organization of GBM with glioma stem cells (GSCs) at the top of this hierarchy, able to regrow the tumor and to give rise to more differentiated GBM cells [1, 2]. Importantly, GSCs resist established anti-cancer therapies making them a main culprit in treatment failure [3, 4].

The debate over the identity of the cell of origin for GBM is not settled but neural stem cells (NSCs) and oligodendrocyte precursor cells (OPCs) are likely candidates [5] and GSCs share stem cell traits with these cell populations. While the stem cell/precursor state of NSCs and OPCs depends on the association with a supporting niche environment, GSCs utilize the same niche factors but also carry a mutational burden that supports stemness [6] and actively modulate pro-differentiation signaling to maintain GSCs traits and to block differentiation [7]. Overcoming such differentiation blocks in solid cancers has been attempted in the past. While numerous approaches have been successful *in vitro* [8-13], few succeeded *in vivo* [11, 12] and even fewer prolonged survival [12]. In GBM, this situation is further complicated by the requirement for systemically administered drug-based differentiation therapies to cross the blood-brain barrier (BBB).

We recently reported that ionizing radiation -aside from inducing cell death- led to global epigenetic changes in surviving cells with a transient acquisition of an open chromatin state in the promoter region of developmental transcription factors [14, 15].

Subsequently, some surviving non-stem cancer cells converted their phenotype into induced cancer stem cells [16, 17] and some surviving GSCs trans-differentiated into pericyte- and vascular-like cells [18], thus suggesting that exposure to ionizing radiation transiently elevates glioma cells into a multipotent state, comparable to lineage committed normal stem/progenitor cells.

Ideally, a differentiative therapy would direct cells towards a mitotically incompetent state. E.g., sarcoma cells can be forced into erythrocyte-like cells *in vitro* that even expel their nucleus [19]. In the CNS neurons are terminally differentiated cells that have lost their capacity to divide, thus making them a desirable end-state for a differentiation therapy in GBM. In the present study we sought to use this effect of ionizing radiation in combination with forskolin, an established agent for neuronal differentiation, to drive glioma cells into terminal differentiation.

Materials and Methods

Cell lines

Primary human glioma cell lines were established at UCLA as described in [1]; Characteristics of specific gliomasphere lines can be found in [20]. Primary GBM cells were propagated as gliomaspheres in serum-free conditions in ultra-low adhesion plates in DMEM/F12, supplemented with SM1 Neuronal Supplement (#05177, STEMCELL Technology, Kent, WA), EGF (#78006, STEMCELL Technology), bFGF (#78003, STEMCELL Technology) and heparin (1,000 USP Units/mL, NDC0409-2720-31, Lake Forest, IL) as described previously [1, 20, 21]. GL261 cells were cultured in log-growth phase in DMEM supplemented with 10% fetal bovine serum, penicillin, and streptomycin. All cells were grown in a humidified atmosphere at 37°C with 5% CO₂. The unique identity of all patient-derived specimens was confirmed by DNA fingerprinting (Laragen, Culver City, CA). All lines were routinely tested for mycoplasma infection (#G238, Applied biological Materials, Ferndale, WA).

Extreme Limiting Dilution Analysis (ELDA)

3×10^5 HK-374 cells were intracranially implanted into the NSG mice as described above. Tumors were grown for 3 days for successful grafting. Tumor-bearing mice were then irradiated with a single dose of 4 Gy and injected intra-peritoneally on a 5-days on / 2-days off schedule for 2 weeks either with corn oil or forskolin starting 48 hours after the irradiation. The mice were then euthanized and tumor-bearing brains were dissected and further subjected for dissociation using mouse Tumor Dissociation Kit (Cat # 130-

096-730, Miltenyi, Auburn, CA) to get single cell suspension, as described in [15]. The cells were counted and plated into the non-tissue-culture-treated 96-well plates at a range of 1 to 512 cells/well. Growth factors (EGF and bFGF) were supplemented every two days. Glioma spheres were counted 10 days later and presented as the percentage to the initial number of cells plated. The glioma stem cell frequency was calculated using the ELDA software [22].

cAMP Assay

Primary GBM HK-374 monolayers were trypsinized and plated at a density of 5×10^4 cells/well in a surfaced treated 96-well plate, while the HK374 gliomaspheres were dissociated and plated at the same density in a non-treated 96-well plate. The following day, cells were treated with freshly prepared Forskolin (#F3917, Sigma, St. Louis, MO) at 0.1, 0.25, 0.5, 1, 5, 10, 50, and 100 μM concentrations, with DMSO serving as the solvent control. 15 minutes after the treatment, the adherent monolayers were incubated with 100 μl /well cell lysis buffer from the cAMP Direct Immunoassays Kit (Fluorometric, ab138880, Abcam, Cambridge, UK), while the gliomaspheres were collected, centrifuged down and further incubated with 100 μl cell lysis buffer at RT for 10 minutes. 25 μl cell lysates were used to quantify the cAMP concentration by comparing to the standard cAMP curve, all the procedures were performed following the manufacturer's guidelines.

Quantitative Reverse Transcription-PCR

Total RNA was isolated using TRIZOL Reagent (Invitrogen, Waltham, MA). cDNA synthesis was carried out using the SuperScript Reverse Transcription IV (Invitrogen). Quantitative PCR was performed in the QuantStudio™ 3 Real-Time PCR System (Applied Biosystems, Carlsbad, CA, USA) using the PowerUp™ SYBR™ Green Master Mix (Applied Biosystems). C_t for each gene was determined after normalization to PPIA and $\Delta\Delta C_t$ was calculated relative to the designated reference sample. Gene expression values were then set equal to $2^{-\Delta\Delta C_t}$ as described by the manufacturer of the kit (Applied Biosystems). All PCR primers were synthesized by Invitrogen and used with PPIA as housekeeping gene (for primer sequences see **Suppl. Table 1**).

Western Blotting

HK374 cells were plated and irradiated the next day with a single dose of 4 Gy. 48 hours after the irradiation, cells were daily treated with forskolin at 10 μ M for 5 days. The cells were then lysed in 150 μ l of ice-cold RIPA lysis buffer (10 mM Tris-HCl (pH 8.0), 1 mM EDTA, 1% Triton X-100, 0.1% Sodium Deoxycholate, 0.1% SDS, 140 mM NaCl, 1 mM PMSF) containing proteinase inhibitor (Thermo Fisher Scientific) and phosphatase inhibitor (Thermo Fisher Scientific). The protein concentration in each sample was determined by BCA protein assay (Thermo Fisher Scientific) and samples were denatured in 4x Laemmli sample buffer (Bio-Rad) containing 10% β -mercaptoethanol for 10 minutes at 95 °C. Equal amounts of protein were loaded onto 10% SDS-PAGE gels and subjected to electrophoresis for 2 hours. Samples were then transferred onto 0.45 μ m nitrocellulose membrane (Bio-Rad) and blocked in 1x TBST containing 5% bovine serum albumin (BSA) for 30 minutes at RT, followed by

incubation with primary antibodies against Neurofilament-L (#2837S, 1:1000, Cell Signaling Technology), GFAP (#12389S, 1:1000, Cell Signaling Technology), β 3-tubulin (#5568S, 1:1000, Cell Signaling Technology), and β -actin (#3700S, 1:1000, Cell Signaling Technology) in 1X TBST containing 5% BSA overnight at 4°C with gentle rocking. Membranes were then washed three times for 5 minutes each with 1X TBST and incubated with secondary antibodies, 1:5000 anti-mouse or anti-rabbit horseradish peroxidase (HRP; Cell Signaling) in TBST for two hours at RT with gentle rocking. Membranes were washed again three times for 5 minutes each with 1X TBST. Pierce ECL Plus Western Blotting Substrate (Thermo Fisher) was added to each membrane and incubated at RT for 5 minutes. The blots were then scanned with Odyssey Fc imaging system (LI-COR Biosciences, Lincoln, NE). β -actin was used as a loading control. Densitometry was performed using ImageJ. The ratio of the protein of interest over its endogenous control was calculated and expressed as relative intensity.

Immunofluorescence

For *in vitro* neuron marker staining, HK374 cells were trypsinized and plated onto the round glass coverslips in 6-well plate at a density of 2×10^4 cells/well. The following day, cells were irradiated at a single dose of 4 Gy and then daily treated with forskolin at 10 μ M for 5 days starting from the 48 hours after irradiation. At day 5, the coverslips were fixed in formalin at RT for 15 minutes and washed three times with PBS, then permeabilized by 0.5% Triton X-100 for 10 minutes at RT. After three-time PBS washing, the coverslips were blocked with 10% goat serum diluted in PBS for 1 hour at RT and then incubated with primary antibodies against Neurofilament-L (Cell Signaling

Technology, #2837, 1:100), and β 3-tubulin (Cell Signaling Technology, #5568s, 1:400) overnight at 4°C. The next day, the secondary antibodies Alexa Fluor 594 Goat Anti-rabbit immunoglobulin G (IgG) (H/L) antibody (1:1,000 (Invitrogen)) or Alexa Fluor 488 Goat Anti-rabbit IgG (H/L) antibody (1:1,000 (Invitrogen)) were applied for 60 min, with subsequent nuclear counterstaining of Hoechst 33342 (Invitrogen, Cat# H3570, 1:5000). The sections were sealed with VECTASHIELD® PLUS Antifade Mounting Medium (Vector Laboratories, Cat#H-1900) and images were taken with a digital microscope (BZ-9000, Keyence, Itasca, IL).

For *in vivo* EGFP and neuron marker co-staining, brain sections were baked for 30 minutes in an oven at 65 °C, deparaffinized in two successive Xylene baths for 5 minutes each and then hydrated for 5 minutes each using an alcohol gradient (ethanol 100%, 90%, 70%, 50%, 25%). Antigen retrieval was performed using Heat Induced Epitope Retrieval in a citrate buffer (10 mM sodium citrate, 0.05% tween20, pH 6) with heating to 95 °C in a steamer for 20 minutes. After cooling down, the slides were blocked with 10% goat serum plus 1% BSA at room temperature for 30 minutes and then incubated with the primary antibodies against EGFP (Abcam, ab184601, 1:100) mixed with Neurofilament-L (Cell Signaling Technology, #2837, 1:100) or EGFP (Abcam, ab184601, 1:100) mixed with β 3-tubulin (Cell Signaling Technology, #5568s, 1:400) overnight at 4°C. The secondary antibodies Alexa Fluor 594 Goat Anti-rabbit immunoglobulin G (IgG) (H/L) antibody (1:1,000 (Invitrogen)) and Alexa Fluor 488 Goat Anti-mouse IgG (H/L) antibody (1:1,000 (Invitrogen)) were applied followed by nuclear

counterstaining and mounting procedures as above. Fluorescent images were then acquired using a confocal microscope (Nikon A1, Melville, NY).

Animals

Female 6–8-week-old C57BL/6 mice, or NOD-*scid* IL2Rgamma^{null} (NSG) originally obtained from The Jackson Laboratories (Bar Harbor, ME) were re-derived, bred and maintained in a pathogen-free environment in the American Association of Laboratory Animal Care-accredited Animal Facilities of Department of Radiation Oncology, University of California, Los Angeles, in accordance with all local and national guidelines for the care of animals. Weight of the animals was recorded every day. 2×10^5 GL261-Luc or 3×10^5 HK-374-Luc cells were implanted into the right striatum of the brains of mice using a stereotactic frame (Kopf Instruments, Tujunga, CA) and a nano-injector pump (Stoelting, Wood Dale, IL). Injection coordinates were 0.5 mm anterior and 2.25 mm lateral to the bregma, at a depth of 3.0 mm from the surface of the brain. Tumors were grown for 3 days with successful grafting confirmed by bioluminescence imaging. Mice that lost 20% of their body weight or developed neurological deficits requiring euthanasia were sacrificed.

Drug treatment

For *in vitro* studies, HK374, HK308 or HK157 cells were plated to form monolayers or gliomaspheres and irradiated at a single dose of 4 Gy the next day. 48 hours after irradiation, the cells were then treated with dibutyryl cAMP (dbcAMP; #D0627, Sigma), a

cell-permeable analog of cyclic adenosine 3'5'-monophosphate (cAMP), at 1mM or forskolin at 10 μ M for 5 consecutive days.

For *in vivo* studies, tumor grafting was confirmed via bioluminescence imaging. Mice implanted with either HK374 cells or GL261 cells were injected intraperitoneally with forskolin (#F3917, Sigma) at 5 mg/kg on a 5-days on / 2-days off schedule starting 48 hours after irradiation until they reached euthanasia endpoints. Forskolin was dissolved in corn oil containing 2.5% DMSO at a concentration of 0.55 mg/ml and prepared freshly for the injection.

Irradiation

Cells were irradiated with at room temperature (RT) using an experimental X-ray irradiator (Gulmay Medical Inc. Atlanta, GA) at a dose rate of 5.519 Gy/min. Control samples were sham-irradiated. The X-ray beam was operated at 300 kV and hardened using a 4 mm Be, a 3 mm Al, and a 1.5 mm Cu filter and calibrated using NIST-traceable dosimetry. Corresponding controls were sham irradiated.

For *in vivo* irradiation experiments, mice were anesthetized prior to irradiation with an intra-peritoneal injection of 30 μ L of a ketamine (100 mg/mL, Phoenix, MO) and xylazine (20 mg/mL, AnaSed, IL) mixture (4:1) and placed on their sides into an irradiation jig that allows for irradiation of the midbrain while shielding the esophagus, eyes, and the rest of the body. Animals received a single dose of 10 Gy on day 3 after tumor implantation.

Cell cycle analysis

After forskolin (10 μ M) treatment, HK374 cells were trypsinized and rinsed with ice-cold PBS. The cells were then centrifuged at 500 x g for 4 minutes, resuspended in 200 μ l UltraPure RNase (Thermo Fisher, #12-091-021) and transferred to FACS tubes. 200 μ l Propidium Iodide solution (1 mg/ml, Thermo Fisher, #P1304MP) was added and incubated for 15 minutes in the dark at RT. At least 100,000 events were analyzed by flow cytometry (LSR Fortessa, BD, San Jose, CA) and analyzed in FlowJo v10.

Bulk RNA sequencing

For bulk RNA sequencing HK-374 cells were seeded into 6-well plates as monolayer cultures at 40k cells/well. 4 days after seeding the cells were irradiated with 4 Gy. Controls were sham irradiated. 48 hours later cells were treated with either forskolin (10 μ M) or DMSO for 5 consecutive days. Total RNA was harvested and isolated using Trizol. Bulk RNA sequencing (RNAseq) was performed by Novogene and reads were mapped to the human genome (hg38) following their standard pipeline [15]. Read counts were analyzed using the iDEP package (version 2.0) [23]. Differentially expressed genes were calculated using the DESeq2 algorithm with a minimum of a 2-fold change and a false discovery rate (FDR) of 0.1. Enrichment p -values were calculated based on a one-sided hypergeometric test. P -values were then adjusted for multiple testing using the Benjamini-Hochberg procedure and converted to FDR. Fold Enrichment was defined as the percentage of genes in the list belonging to a pathway, divided by the corresponding percentage in the background.

Single Cell RNA Sequencing

HK374 gliomaspheres were plated onto the Poly-D-Lysine/Laminin 6-well plate (#354595, Corning) and irradiated at a single dose of 4 Gy the next day. 48 hours after the irradiation, the cells were treated with forskolin at the concentration of 10 μ M daily for 5 consecutive days or 21 days. At day 5 or day 21, the gliomaspheres in the suspension culture will be collected and dissociated with TrypLE (no phenol red, Thermo Fisher Scientific), and the adherent differentiated cells were washed with HBSS and de-attached with Trypsin/EDTA (Cell Applications, Cat#090K). The cells were then pooled and filtered through a 40- μ m strainer and fixed with EvercodeTM Cell Fixation v2 kit (#ECF2101, Parse Biosciences, Seattle, WA) following the manufacturer's guidelines. The samples (n=3 for each condition) were then sent out to the Genomics High Throughput Facility (GHTF) at the University of California, Irvine for subsequent single cell RNA sequencing (scRNAseq) using the EvercodeTM Whole Transcriptome Mini kit (#EC-W01010, Parse Biosciences). Sequencing reads from the mRNA libraries were mapped to the human genome (hg38) using the Parse Biosciences pipeline (split-pipe vers. 1.1.1) to generate cell by gene counts matrices. Data analysis was performed using the R package Seurat (version 4.3.3). Matrices were filtered for cells with high mitochondrial and ribosomal gene count and doublets were removed using DoubletFinder R package. For the subsequent cluster annotation, we used three published gene sets associated with cell types in the developing brain as previously described [24]. The trajectory analysis was executed using the Python package scVelo (version 0.2.5) [25]. Engagement of transcription factors was determined using the R package BITFAM [26].

Statistics

Unless stated otherwise all data shown are represented as mean \pm standard error mean (SEM) of at least 3 biologically independent experiments. A p -value of ≤ 0.05 in an unpaired two-sided t -test or one-sided ANOVA for multiple testing indicated a statistically significant difference. Kaplan-Meier estimates were calculated using the GraphPad Prism Software package (version 10.2.0). For Kaplan-Meier estimates a p -value of 0.05 in a log-rank test indicated a statistically significant difference. For bulk RNAseq, differentially expressed genes were calculated with a minimum fold-change of 2 and a false discovery rate cut-off of 0.1.

Results

Treatment of irradiated glioma cells with cAMP leads to expression of neuronal markers

In a first set of experiments, we tested the hypothesis that radiation induced a state multipotency that could be used to direct glioma cells into a neuron-like state using dbcAMP, part of established differentiation protocols for the neuronal differentiation of iPS cells [27, 28]. Patient-derived HK-374 glioma cells were irradiated with 0 or 4 Gy. We had previously shown that 48 hours after a single dose of 4 Gy, epigenetic remodeling led to a multipotent state with gains in open chromatin in the promoter regions of developmental transcription factors [15]. Therefore, we treated irradiated and unirradiated cells with dbcAMP (daily, 1 mM), starting 48 hours after irradiation (**Figure 1A**). As early as 24 hours after start of the dbcAMP treatment both, dbcAMP-treated unirradiated and irradiated cells, showed elongated cell bodies reminiscent of neuron-like morphology (**Figure 1B, black arrows**) while control cells, not treated with dbcAMP, retained the morphology of untreated cells (**Figure 1B**).

After five daily treatments with dbcAMP, irradiated cells showed strong expression of the neuronal markers Tuj-1 and Neurofilament Light Chain (**Figure 1C, white arrows**), which agreed with the neuron-like morphology of the cells. Cells treated with radiation or dbcAMP alone only showed faint expression of both markers (**Figure 1C**).

The adenylate cyclase activator Forskolin induces neuron-like phenotype in irradiated glioma cells.

In vivo, direct application of dbcAMP is not a feasible approach to differentiate glioma cells. To overcome this limitation, we next tested if forskolin, a known activator of

adenylate cyclase [29] could increase cAMP levels in glioma cells. Glioma cells grown as monolayer cultures and gliomasphere cultures enriched for GSCs were treated with forskolin at concentrations of 0.1, 0.25, 0.5, 1, 5, 10, 50 or 100 μ M. Differentiated cells and cells enriched for GSCs both showed a dose-dependent increase in cAMP production, thus confirming that forskolin can induce cAMP production in glioma cells, including GSCs. Induced intracellular cAMP concentrations did not reach mM concentrations used in dbcAMP experiments but plateaued below 200 nM after 15 minutes of forskolin treatment (**Figure 2A**).

Next, we tested if treatment of irradiated glioma cells with forskolin would also induce the expression of neuronal markers. Quantitative RT-PCR 24 hours and 5 days after the start of forskolin treatment revealed that combined treatment with radiation and forskolin increased the expression of the neuronal markers β 3-tubulin, CHAT, Neurofilament light chain (NF-LC), and MAG, thus indicating possible induction of a differentiated cell state (**Figure 2B/C**). We further confirmed the induction of neuronal markers NF-LC and β 3-tubulin on day 5 after irradiation and forskolin treatment by western blotting (**Figure 2D/E**) and immunofluorescence staining (**Figure 2F, white arrows**). However, expression of these markers was less uniform than after treatment with dbcAMP, consistent with much lower intracellular cAMP concentrations (**Figure 2A**). Forskolin alone or in combination with radiation induced changes in cell morphology with elongation of some of the cells' bodies (**Figure 2G, black arrows**). Considering the distinct characteristics of different TCGA subtypes in GBM, we included another two patient-derived GBM lines (**Suppl. Table 2**) to assess the effect of radiation plus forskolin on neuron-like differentiation. In HK-308 cells (mesenchymal subtype)

combined treatment with radiation and forskolin showed similar induction of neuronal markers (**Suppl. Figure 1A**), while these effects were less notable in HK-157 cells (proneural subtype) (**Suppl. Figure 1B**).

Forskolin in combination with radiation impacts cell proliferation and cell cycle in glioma cells.

True differentiation towards a neuronal phenotype would result in a loss of mitotic capacity. To test the proliferative capacity of cells treated with radiation and/or forskolin, HK-374, HK-308 or HK-157 patient-derived glioma cells were seeded and treated with 0 or 4 Gy of radiation the following day. After an additional 48 hours, cells were treated with DMSO or forskolin (daily at 10 μ M). Cell numbers were counted on day 5, 10, 15 and 20 after forskolin treatment initiation. While radiation or forskolin alone reduced cell numbers and/or slowed proliferation in all three lines to some extent, the combination of radiation and forskolin had additive effects on cell numbers from day 5 on (**Figure 2H, Suppl. Figure 2A/B**), thus suggesting that the combined effect is not cell line specific. Forskolin is known to affect cell cycle progression through specific inhibition of G₁-to-S phase progression [30]. To study the lack of proliferation in more details we next performed a cell cycle analysis. On day 5, forskolin treatment led to an arrest in the G₁/G₀ phase of the cell cycle. Irradiation with a single dose of 4 Gy decreased the number of cells in the G₁/G₀- and G₂/M-phase and increased the population of cells in S-phase, consistent with the well-known initial arrest at the G₁/G₀ and G₂/M checkpoints and the subsequent release after DNA repair. Combined treatment with radiation and

forskolin decreased the number of cells in G₁/G₀ while elevating the size of the S- and G₂/M-phase cell populations (**Figure 2I**).

On day 10, the G₁/G₀ population of untreated control cells increased, consistent with growth inhibition in confluent monolayer cultures. The cell cycle distribution of forskolin treated cells was similar to the distribution on day 5, while irradiated cells continued to redistribute, matching distributions of untreated control cells. Irradiated cells treated with forskolin appeared to be arrested at the G₁-to-S transition of the cell cycle (**Figure 2J**).

Bulk RNA sequencing

After observing the effects of increased neuronal differentiation in GBM cells in response to radiation combined with forskolin treatment, in order to assess which pathways were activated in cells irradiated and subsequently treated with forskolin and if surviving cells would display gene expression profiles associated with neuronal differentiation, we performed bulk RNA sequencing on HK-374 cells cultured as monolayers. Compared to unirradiated controls, cells irradiated with 4 Gy had 421 differentially expressed genes (DEGs) at least 2-fold (FDR 0.1) up- and 865 genes down-regulated. After combined treatment we found 1,471 genes differentially up- and 2,058 genes down-regulated when compared to untreated control cells. Compared to irradiated cells, we found 945 DEGs up- and 704 genes down-regulated in cells treated with radiation and forskolin (**Figure 3A/B**), thus leading to a distinct gene expression profile for cells treated with radiation and forskolin (**Figure 3C**).

Enrichment analysis of upregulated DEGs found in irradiated samples compared to unirradiated control cells using the Hallmark.MSigDB gene set revealed overlap with

genes associated with proinflammatory pathways, epithelial-to-mesenchymal transition, and activation of the p53-dependent response (**Figure 3D**), all consistent with the well-known effects of ionizing radiation [31]. The inflammatory response was amplified by the addition of forskolin and suppression of genes in Hedgehog signaling.

Enrichment analysis of upregulated DEGs in cells treated with radiation and forskolin and compared to control cells using the Celltype.MSigDB gene set showed overlap with genes associated with Manno Midbrain Neurotypes HMGL, Descartes Fetal Cerebrum and Cerebellum Microglia gene sets, as well as Descartes Fetal Cerebrum and Cerebellum Vascular Endothelial Cells while suppressing expression of genes associated with Manno midbrain neurotypes HOPC, HNBGABA, HDA1/2, HRGL2A, HAD, HNBML1/5 HSERT, HRGL2b/C, HRN, HOMTN, HRGL1 and Descartes fetal cerebellum oligodendrocytes (**Figure 3E**).

Single cell RNA sequencing

Our qRT-PCR indicated that monolayer cultures, primarily consisting of more differentiated cells, increased neuronal marker expression in response to radiation combined with forskolin treatment. However, the effect was less pronounced when performed with gliomaspheres in suspension culture which are enriched for GSCs (**Suppl. Figure 3A/B**). We consider that the differentiated cells grown out from the surviving populations would die by anoikis under the suspension culture conditions [32]. To allow for studying GSCs and more differentiated cells in parallel we first tested if gliomaspheres grown on Poly-D-Lysine/Laminin-coated plates would still respond to irradiation combined with forskolin treatment in similar ways as mostly differentiated

monolayer cells. These culture conditions maintained viable cells for 21 days irrespective of the treatment arm (**Suppl. Table 3**). The addition of forskolin to unirradiated or irradiated cells induced neuronal marker expression (**Figure 4A, Suppl. Figure 3C/D**) and morphological changes with elongated cell bodies (**Figure 4B, black arrows**). qRT-PCR for neuronal markers revealed a significant increase in β 3-tubulin expression (**Figure 4C**), and neurofilament light chain expression (**Figure 4D**). Furthermore, we observed a significant increase in the expression of the microglia marker TMEM119 (**Figure 4E**). Expression of neurofilament light chain and β 3-tubulin at the protein level was confirmed by Western blotting (**Figure 4F-H**).

Our bulk RNAseq data has shown that the gene expression profile in cells treated with radiation and forskolin overlapping with a gene set associated not only with a neuronal signature but also fetal microglia and vascular endothelial cells was rather unexpected, and we therefore sought to study differences in cell fate in more details. We next performed scRNAseq using 20,028 cells treated with 0 (6,738) or 4 Gy (5,403), forskolin (5,494), or irradiation and forskolin (2,393), grown on Poly-D-Lysine/Laminin-coated plates for 5 days. Lovain clustering identified 24 unique clusters of cells that could be assigned to the different treatment arms of the study (**Suppl. Figure 4A**). While there was some overlap between control cells (DMSO-treated) and irradiated cells and – to a lesser extent – control and forskolin-treated cells, cells treated with radiation and forskolin separated into 3 unique clusters (2, 17 and 18) (**Figure 5A**). We next compared marker genes of the identified clusters to gene expression signatures of the adult and developing brain as described previously [24]. Correlation coefficients were generally low, and the closest normal brain cell type was assigned to individual

GBM clusters (**Figure 5B**). The main clusters in untreated control cells were primarily comprised of glycolytic- (33.4 %), inhibitory neuron- (15.3 %), NPC- (15.3 %), OPC- (13 %), and neuron-like cells (11.4 %). 5 Days after the initial forskolin treatment (7 Days after treatment with a single dose of 4 Gy) the dominant cell populations were NPC-like cells (30.2 %), inhibitory neuron-like (22.8 %) and 22.8 % of cells of low quality, the latter consistent with radiation-induced cell death. The relative increase in NPC-like cells agreed with the known radioresistant phenotype of glioma stem cells [3] and the decrease of the glycolytic-like cell population to 1.3 % was in line with our previous reports of metabolic heterogeneity and metabolic plasticity [33, 34]. Likewise, neuron-like and OPC-like cells dropped to 2 % and 3.4 %, respectively. After treatment with forskolin for five days the dominant cell clusters were vascular-like cells (37.7 %), neuron-like cells (28.3 %), astrocyte-like cells (18.1 %) and outer radial glia-like cells (oRG, 4.7 %). Combined treatment with radiation and forskolin led to the occurrence of microglia-like cells (59.1 %), neuron-like cells (22.7 %), cells in the G1/S-phase of the cell cycle (“Dividing”, 16.2 %) and a reduction in NPC-like cells (0.17 %), OPC-like cells (0.22 %) and oRG-like cells (0 %) (**Suppl. Table 4**). Although microglia-like cells expressed immune-related genes they lacked expression of classical microglia markers (**Suppl. Figure 5**). Notably, microglia-like cells were the rarest cell population in control cells and cells treated with radiation or forskolin alone (**Figure 5C, Suppl. Table 4**). Violin plots of marker genes for the different cell types are shown in **Figure 5D**.

In consideration of the notable shifts in cluster composition between the different treatments we next sought to perform a trajectory analysis of the data based on RNA

splicing information at day 5. Comparing the amount of spliced and unspliced RNA we found 70 % of the RNA in control cells and forskolin-treated cells unspliced, while irradiated cells showed 68 % of unspliced RNA. The amount of unspliced RNA dropped to 62 % in cells treated with radiation and forskolin (**Figure 5E**). Next, we used scVelo's dynamical model to compute cell trajectories based on RNA expression and splicing information by calculating RNA velocities, dynamical genes, and latent time [25] for the three different treatments and the control sample cells that were used as starting point. UMAP plots of latent time suggested that control cells and cells treated with radiation or forskolin originated from dividing cells while cells treated with radiation and forskolin branched from the microglia-like cell population (**Figure 5F**). We observed cascading dynamical genes over inferred latent time for all four conditions suggesting progression through differentiation or dedifferentiation steps (**Figure 5G**), which was supported by the trajectory analysis of the cells (**Figure 5H**). The trajectory analysis indicated dynamic conversion of cell types in untreated control cells consistent with the known intratumoral cellular heterogeneity of GBM (**Figure 5H**). As expected, cells in the control sample developed into the different phenotypes from the dividing cell population. The main trajectory led to glycolytic cells from which a subset further developed into OPC-like, neuron-like and NPC-like cells and into inhibitory neuron-like cells. This trajectory was maintained in irradiated cells, except for the occurrence of 'low quality' cells originating directly from the dividing cell population (**Figure 5H**). Treatment of the cells with forskolin caused a deviation from this trajectory with dividing cells transitioning into vascular-like cells, neuron-like cells, astrocyte-like cells, and outer radial glia-like cells (**Figure 5H**).

Lastly, treatment with radiation and forskolin completely altered the trajectory of the cells with the appearance of microglia-like cells and dividing cells leading into neuron-like cells, thereby omitting all other phenotypes (**Figure 5H**). The top 5 driver genes for each condition are shown in **Figure 5I**.

Next we sought to identify transcription factors engaged in changes of gene expression profiles in individual cell types using a Bayesian model [26] (**Figure 5J**). For microglia-like cells we calculated engagement of HAND2, MITF, MYC, ATF3, JUNB, SMAD1, RBPJ, NFE2L1, FOXG1, CAVIN1, AHR, TAL1, ESR1, FOXO1, SNAI2, PML, FOXM1, GATA2 and PBX1. None of these transcription factors are defining microglia cells but rather pointed to proinflammatory signaling (MYC, ATF3, JUNB, SMAD1, FOXO1, AHR, ESR1) [35-41].

For neuron-like cells we calculated engagement of MAFK, CBX3, Rad21, COBLL1, RUNX2, NSD2, NFIA, ETS2, HLF, GLIS3, SKIL, EZH2, GLIS1, HAND2, MITF, FOXG1, HIF1A, HMGB2, BATF, NR3C1, ZSCAN31, HDGF, SNAI2, YBX1, TET3, THRB, FOSL2 and. EZH2 [42] and FOSL2 [43] are associated with synaptic plasticity and FOXG1 [44], DLX2 [45], THRB [46] participate in CNS development.

Finally, we studied how stable these phenotypes would be over time. Repeating the scRNAseq experiment with cells treated for 21 days (25 unique clusters of cells were identified by Lovain clustering, **Suppl. Figure 4B**) and projecting cell types identified in day 5 samples onto clusters from day 21 (**Figure 6A**), we observed that the culture conditions changed the overall composition of control cells with mesenchymal-like cells (25.8 %), dividing cells (19.3 %), NPC-like cells (13.4 %), astrocyte-like cells

(12.7 %), or neuron-like cells (10.6 %) as the dominant cell types and oRG-like and OPC-like cells no longer present in any of the treatment arms. At day 21, irradiated cells had largely redistributed to match the cluster distribution of control cells but still maintained an increase in NPC-like cells (19.8 %). Forskolin-treated cells predominantly showed an astrocyte-like (38.2 %), neuron-like (25.3 %), mesenchymal-like (11.4 %), or NPC-like (10.7 %) phenotype. The dominant phenotypes in cells treated with radiation plus forskolin remained microglia-like cells (39 %), followed by NPC-like (15.5 %), and neuron-like cells (10.2 %) (**Figure 6B/C; Suppl. Table 5**).

A combination of radiation and forskolin improves median survival in vivo

In silico, forskolin has an estimated LogBB of -0.24 [47], indicating its ability to cross the blood-brain barrier [48]. Therefore, we tested if the combination of radiation and forskolin would affect the number of GSCs *in vivo*. HK374 cells were implanted into the striatum of NSG mice. After 3 days of grafting, tumors were irradiated with 0 or 4 Gy. After 48 hours, the animals were treated with daily forskolin injections (5 mg/kg) on a 5-day on/2-day off schedule for 2 weeks. Tumors were harvested, digested into single cell suspensions, and subjected to clonal sphere-formation assays for 10 days (**Figure 7A**). The combination of 4 Gy and Forskolin led to a significant reduction in sphere-forming capacity from 5.25 % to 0.24 % ($p=0.015$). Treatment with radiation alone also significantly reduced sphere-formation, while forskolin alone had no significant effect (**Figure 7B/C**). Next, we calculated GSC frequencies using an ELDA. Both irradiation and forskolin treatment significantly reduced the number of GSCs, while the combination of radiation and forskolin significantly reduced GSC numbers to 0.04 %, 95

% class interval: 0.03 % to 0.05 %, $p < 0.0001$ (**Figure 7D/E, Suppl. Tables 6/7**). Confocal imaging of corresponding tumor sections revealed that forskolin treatment and combined treatment with radiation and forskolin induced the expression of neurofilament light chain and Tuj1 in GFP-expressing GBM cells *in vivo* (**Figure 7F, white arrows**).

Finally, we tested if the combination of radiation and forskolin would lead to an improved median survival in mouse models of glioma. HK374 cells were implanted into the striatum of NSG mice. After 3 days of grafting, PDOXs were irradiated with a single dose of 10 Gy, equivalent to a total dose of 18 Gy in 2 Gy fractions. Control mice were sham irradiated. Forty-eight hours later, mice were treated with forskolin at 5 mg/kg (5 days on/2 days off schedule) until they reached euthanasia criteria. Control animals were treated with solvent only. While radiation or forskolin treatment alone had no effect in this highly aggressive and rapidly growing PDOX, the combination of radiation and forskolin significantly increased the median survival of the animals from 34 to 48 days (**Figure 7G**; $p < 0.0001$, Log-Rank test). Forskolin treatment was well tolerated, and animals continued to gain weight after combined treatment (**Figure 7H**).

In the syngeneic GL261 glioma model in C57Bl/6 mice control mice had a median survival of 36 days. Median survival was increased to 43.5 days in irradiated mice (not significant), to 64 days in mice treated with forskolin ($p = 0.001$, Log-Rank test) and to 129 days in mice receiving the combination of radiation and forskolin (**Figure 7I**; $p = 0.0021$, Log-Rank test). As in NSG mice the addition of forskolin was well tolerated (**Figure 7J**).

Discussion

In our current study we hypothesized that glioma cells, that survive irradiation, go through a transient state of multipotency that can be exploited to drive GBM cells into a postmitotic neuron-like state. Our hypothesis was based on our previous observations that differentiated non-stem glioma cells that survive exposure to ionizing radiation respond with a phenotype conversion into induced GSCs [15] while surviving, preexisting GSCs transdifferentiated into endothelial- and pericyte-like cells [18]. The underlying mechanisms were global epigenetic remodeling through changes in histone methylation and acetylation and subsequent changes in open chromatin [15, 18], with the latter mediated by the histone acetyltransferase EP300 [18]. Induced GSCs and transdifferentiated pericyte- and endothelial-like cells contributed to tumor recurrences and treatment resistance [15, 18] and preventing phenotype conversion or transdifferentiation prolonged median survival in PDOXs mouse models of GBM [15, 18, 49, 50]. We show here that the addition of forskolin to radiation drives GBM cells into microglia- and neuron-like states, reduced cell proliferation and the number of functional GSCs *in vitro* and *in vivo* and prolonged the median survival in syngeneic and PDOX mouse models of GBM.

Several previous studies have attempted differentiation therapies for GBM. Most studies succeeded to some extent *in vitro* and cells showed decreased tumorigenicity when implanted into mice. For example, all-trans retinoic acid (ATRA) successfully differentiated GSCs *in vitro* and reduced their tumorigenicity *in vivo* [51] but clinical translation targeting GBM with ATRA has consistently failed [52, 53]. Another study

induced GSC differentiation through stereotactical injection of a WNT inhibitor, an SHH inhibitor and BMP [54]. While effective, the intracranial application route could be clinically challenging and is likely to miss GBM cells, dispersed into the normal parenchyma that are not in reach of the injections.

Forskolin and cAMP have long been known to induce glioma differentiation *in vitro* [55, 56] and the use of forskolin or dbcAMP to induce terminal neuronal differentiation of glioma *in vivo* has been previously reported [57]. Like in our current study, this treatment alone had minimal effects on median survival even when combined with a Wnt inhibitor and even though dbcAMP was given at a high dose [57]. Our scRNAseq data indicate that forskolin treatment alone not only induced neuron-, astrocyte-, and vascular-like cells but also a small number of cells with an outer radial glia-like cell state (4.7 %), a cell population present in small numbers in control and irradiated cells but completely absent in cells treated with radiation and forskolin. It was previously reported that oRG cells have glioma stem cells features [24] and this observation could explain why dbcAMP or forskolin treatment alone have limited impact on median survival in glioma models.

Radiation therapy is and -for the foreseeable time- will remain the most effective treatment modality against GBM and any novel treatment modality will most likely be added to standard of care, surgery, and radiation, or will at least be benchmarked against it. Our discovery, that radiation induces a transient multipotent state added a previously unknown facet to the radiation response of cancer, that leads to increased cellular plasticity, which is increasingly recognized as an emerging hallmark of cancer [58]. This increase in plasticity leads to dedifferentiation or transdifferentiation and is by itself

detrimental with respect to tumor control. By exploiting radiation-induced multipotency our approach highjacks a unique feature of surviving cells that is inevitably induced by a main pillar of the current standard of care. With the addition of forskolin to radiation treatment we utilize an established method that forces iPS cells into neuronal differentiation.

However, GBM cells, that gain a certain level of multipotency, and iPS cells do not share the same level of multipotency, drastically differ in mutational burden and irradiated GBM cells continue to signal through the DNA damage response. Hence, it is not expected that forced differentiation of GBM cell yields in *bona fide* induced neurons. Our finding that the combination of radiation and forskolin predominately led to the occurrence of microglia-like cells and to a lesser extent to neuron-like cells was unexpected. The role of this predominant immune cell-like phenotype in the presence of an intact immune system needs further investigation. However, a combination of radiation and forskolin was superior to their individual effects on inducing neuronal marker expression and inhibiting cell proliferation of GBM cells, reducing self-renewal capacity of GSCs and GSC frequency and prolonging median survival of glioma-bearing mice and leading to long term tumor control in some of the mice. This suggested that this combination therapy induced cell phenotype that can no longer sustain tumor growth. The very low dose of forskolin used here was well tolerated and the human equivalent dose (25 mg for 60 kg body weight) is far below the usual supplement dose of 50mg/day for forskolin. With forskolin crossing the blood-brain barrier and its long use in ayurvedic medicine, this combination therapy can easily be translated into a clinical trial.

Acknowledgements

This work used computational and storage services associated with the Hoffman2 Shared Cluster provided by UCLA Office of Advanced Research Computing's Research Technology Group.

This work was made possible, in part, through access to the following: the Genomics Research and Technology Hub (formerly Genomics High-Throughput Facility) Shared Resource of the Cancer Center Support Grant (P30CA-062203), the Single Cell Analysis Core shared resource of Complexity, Cooperation and Community in Cancer (U54CA217378), the Genomics-Bioinformatics Core of the Skin Biology Resource Based Center @ UCI (P30AR075047) at the University of California, Irvine and NIH shared instrumentation grants 1S10RR025496-01, 1S10OD010794-01, and 1S10OD021718-01.

References

1. Hemmati, H.D., et al., *Cancerous stem cells can arise from pediatric brain tumors*. Proc Natl Acad Sci U S A, 2003. **100**(25): p. 15178-83.
2. Singh, S.K., et al., *Identification of a cancer stem cell in human brain tumors*. Cancer Res, 2003. **63**(18): p. 5821-8.
3. Bao, S., *Glioma stem cells promote radioresistance by preferential activation of the DNA damage response*. Nature, 2006. **444**: p. 756-760.
4. Eramo, A., et al., *Chemotherapy resistance of glioblastoma stem cells*. Cell Death Differ, 2006. **13**(7): p. 1238-41.
5. Yao, M., et al., *Cellular origin of glioblastoma and its implication in precision therapy*. Cell Mol Immunol, 2018. **15**(8): p. 737-739.
6. Swartling, F.J., et al., *Deregulated proliferation and differentiation in brain tumors*. Cell Tissue Res, 2015. **359**(1): p. 225-54.
7. Yan, K., et al., *Glioma cancer stem cells secrete Gremlin1 to promote their maintenance within the tumor hierarchy*. Genes Dev, 2014. **28**(10): p. 1085-100.
8. Yan, M., et al., *IKKalpha restoration via EZH2 suppression induces nasopharyngeal carcinoma differentiation*. Nat Commun, 2014. **5**: p. 3661.
9. Munster, P.N., et al., *The histone deacetylase inhibitor suberoylanilide hydroxamic acid induces differentiation of human breast cancer cells*. Cancer Res, 2001. **61**(23): p. 8492-7.

10. Basu-Roy, U., et al., *PPARgamma agonists promote differentiation of cancer stem cells by restraining YAP transcriptional activity*. *Oncotarget*, 2016. **7**(38): p. 60954-60970.
11. Ishay-Ronen, D., et al., *Gain Fat-Lose Metastasis: Converting Invasive Breast Cancer Cells into Adipocytes Inhibits Cancer Metastasis*. *Cancer Cell*, 2019. **35**(1): p. 17-32 e6.
12. Storm, E.E., et al., *Targeting PTPRK-RSPO3 colon tumours promotes differentiation and loss of stem-cell function*. *Nature*, 2016. **529**(7584): p. 97-100.
13. Ishay-Ronen, D. and G. Christofori, *Targeting Cancer Cell Metastasis by Converting Cancer Cells into Fat*. *Cancer Res*, 2019. **79**(21): p. 5471-5475.
14. Lagadec, C., et al., *Radiation-induced reprogramming of breast cancer cells*. *Stem Cells*, 2012. **30**(5): p. 833-44.
15. Bhat, K., et al., *The dopamine receptor antagonist trifluoperazine prevents phenotype conversion and improves survival in mouse models of glioblastoma*. *Proc Natl Acad Sci U S A*, 2020. **117**(20): p. 11085-11096.
16. Pisco, A.O. and S. Huang, *Non-genetic cancer cell plasticity and therapy-induced stemness in tumour relapse: 'What does not kill me strengthens me'*. *Br J Cancer*, 2015. **112**(11): p. 1725-32.
17. Chen, X., et al., *Induced cancer stem cells generated by radiochemotherapy and their therapeutic implications*. *Oncotarget*, 2017. **8**(10): p. 17301-17312.
18. Muthukrishnan, S.D., et al., *P300 promotes tumor recurrence by regulating radiation-induced conversion of glioma stem cells to vascular-like cells*. *Nat Commun*, 2022. **13**(1): p. 6202.

19. Zhang, X., et al., *Terminal differentiation and loss of tumorigenicity of human cancers via pluripotency-based reprogramming*. *Oncogene*, 2013. **32**(18): p. 2249-60, 2260 e1-21.
20. Laks, D.R., et al., *Large-scale assessment of the gliomasphere model system*. *Neuro Oncol*, 2016. **18**(10): p. 1367-78.
21. Vlashi, E., et al., *In vivo imaging, tracking, and targeting of cancer stem cells*. *Journal of the National Cancer Institute*, 2009. **101**(5): p. 350-9.
22. Hu, Y. and G.K. Smyth, *ELDA: extreme limiting dilution analysis for comparing depleted and enriched populations in stem cell and other assays*. *J Immunol Methods*, 2009. **347**(1-2): p. 70-8.
23. Ge, S.X., E.W. Son, and R. Yao, *iDEP: an integrated web application for differential expression and pathway analysis of RNA-Seq data*. *BMC Bioinformatics*, 2018. **19**(1): p. 534.
24. Bhaduri, A., et al., *Outer Radial Glia-like Cancer Stem Cells Contribute to Heterogeneity of Glioblastoma*. *Cell Stem Cell*, 2020. **26**(1): p. 48-63 e6.
25. Bergen, V., et al., *Generalizing RNA velocity to transient cell states through dynamical modeling*. *Nat Biotechnol*, 2020. **38**(12): p. 1408-1414.
26. Gao, S., Y. Dai, and J. Rehman, *A Bayesian inference transcription factor activity model for the analysis of single-cell transcriptomes*. *Genome Res*, 2021. **31**(7): p. 1296-1311.
27. Li, W., et al., *Rapid induction and long-term self-renewal of primitive neural precursors from human embryonic stem cells by small molecule inhibitors*. *Proc Natl Acad Sci U S A*, 2011. **108**(20): p. 8299-304.

28. Chambers, S.M., et al., *Highly efficient neural conversion of human ES and iPS cells by dual inhibition of SMAD signaling*. Nat Biotechnol, 2009. **27**(3): p. 275-80.
29. Seamon, K.B. and J.W. Daly, *Forskolin: its biological and chemical properties*. Adv Cyclic Nucleotide Protein Phosphorylation Res, 1986. **20**: p. 1-150.
30. Muraguchi, A., et al., *Inhibition of human B cell activation by diterpine forskolin: interference with B cell growth factor-induced G1 to S transition of the B cell cycle*. J Immunol, 1984. **133**(3): p. 1283-7.
31. McBride, W.H., et al., *NF-kappa B, cytokines, proteasomes, and low-dose radiation exposure*. Mil Med, 2002. **167**(2 Suppl): p. 66-7.
32. Ray, S., *Tumorsphere Formation Assay: A Cancer Stem-Like Cell Characterization in Pediatric Brain Cancer Medulloblastoma*. Methods Mol Biol, 2023. **2701**: p. 253-259.
33. Vlashi, E., et al., *Metabolic state of glioma stem cells and nontumorigenic cells*. Proceedings of the National Academy of Sciences of the United States of America, 2011. **108**(38): p. 16062-16067.
34. Vlashi, E., et al., *Metabolic differences in breast cancer stem cells and differentiated progeny*. Breast Cancer Res Treat, 2014. **146**(3): p. 525-34.
35. Gao, L., et al., *Baicalein Attenuates Neuroinflammation in LPS-Treated BV-2 Cells by Inhibiting Glycolysis via STAT3/c-Myc Pathway*. Neurochem Res, 2023. **48**(11): p. 3363-3377.

36. Zhang, Y., et al., *Microglia-specific transcriptional repression of interferon-regulated genes after prolonged stress in mice*. *Neurobiol Stress*, 2022. **21**: p. 100495.
37. Woo, M.S., et al., *Selective modulation of lipopolysaccharide-stimulated cytokine expression and mitogen-activated protein kinase pathways by dibutyryl-cAMP in BV2 microglial cells*. *Brain Res Mol Brain Res*, 2003. **113**(1-2): p. 86-96.
38. Huang, W., et al., *TGF-beta1/SMADs signaling involved in alleviating inflammation induced by nanoparticulate titanium dioxide in BV2 cells*. *Toxicol In Vitro*, 2022. **80**: p. 105303.
39. Li, Z., et al., *Foxo1-mediated inflammatory response after cerebral hemorrhage in rats*. *Neurosci Lett*, 2016. **629**: p. 131-136.
40. Quintana, F.J., *Regulation of central nervous system autoimmunity by the aryl hydrocarbon receptor*. *Semin Immunopathol*, 2013. **35**(6): p. 627-35.
41. Sarvari, M., et al., *Estrogens regulate neuroinflammatory genes via estrogen receptors alpha and beta in the frontal cortex of middle-aged female rats*. *J Neuroinflammation*, 2011. **8**: p. 82.
42. Zhang, M., et al., *Neuronal Histone Methyltransferase EZH2 Regulates Neuronal Morphogenesis, Synaptic Plasticity, and Cognitive Behavior in Mice*. *Neurosci Bull*, 2023. **39**(10): p. 1512-1532.
43. Levran, O., et al., *Synaptic Plasticity and Signal Transduction Gene Polymorphisms and Vulnerability to Drug Addictions in Populations of European or African Ancestry*. *CNS Neurosci Ther*, 2015. **21**(11): p. 898-904.

44. Hettige, N.C. and C. Ernst, *FOXP1 Dose in Brain Development*. Front Pediatr, 2019. **7**: p. 482.
45. Bulfone, A., et al., *Spatially restricted expression of Dlx-1, Dlx-2 (Tes-1), Gbx-2, and Wnt-3 in the embryonic day 12.5 mouse forebrain defines potential transverse and longitudinal segmental boundaries*. J Neurosci, 1993. **13**(7): p. 3155-72.
46. Jones, I., et al., *The thyroid hormone receptor beta gene: structure and functions in the brain and sensory systems*. Thyroid, 2003. **13**(11): p. 1057-68.
47. Shaker, B., et al., *A machine learning-based quantitative model (LogBB_Pred) to predict the blood-brain barrier permeability (logBB value) of drug compounds*. Bioinformatics, 2023. **39**(10).
48. Dyabina, A.S., et al., *Prediction of blood-brain barrier permeability of organic compounds*. Dokl Biochem Biophys, 2016. **470**(1): p. 371-374.
49. Bhat, K., et al., *Dopamine Receptor Antagonists, Radiation, and Cholesterol Biosynthesis in Mouse Models of Glioblastoma*. J Natl Cancer Inst, 2021. **113**(8): p. 1094-1104.
50. He, L., et al., *Effects of the DRD2/3 antagonist ONC201 and radiation in glioblastoma*. Radiother Oncol, 2021. **161**: p. 140-147.
51. Campos, B., et al., *Differentiation therapy exerts antitumor effects on stem-like glioma cells*. Clin Cancer Res, 2010. **16**(10): p. 2715-28.
52. Kaba, S.E., et al., *The treatment of recurrent cerebral gliomas with all-trans-retinoic acid (tretinoin)*. J Neurooncol, 1997. **34**(2): p. 145-51.

53. Phuphanich, S., et al., *All-trans-retinoic acid: a phase II Radiation Therapy Oncology Group study (RTOG 91-13) in patients with recurrent malignant astrocytoma*. J Neurooncol, 1997. **34**(2): p. 193-200.
54. Jin, X., et al., *Inhibition of ID1-BMP2 Intrinsic Signaling Sensitizes Glioma Stem Cells to Differentiation Therapy*. Clin Cancer Res, 2018. **24**(2): p. 383-394.
55. Chen, T.C., et al., *Up-regulation of the cAMP/PKA pathway inhibits proliferation, induces differentiation, and leads to apoptosis in malignant gliomas*. Lab Invest, 1998. **78**(2): p. 165-74.
56. Sharma, S.K. and A.B. Raj, *Transient increase in intracellular concentration of adenosine 3':5'-cyclic monophosphate results in morphological and biochemical differentiation of C6 glioma cells in culture*. J Neurosci Res, 1987. **17**(2): p. 135-41.
57. Chen, Z., et al., *Disruption of beta-catenin-mediated negative feedback reinforces cAMP-induced neuronal differentiation in glioma stem cells*. Cell Death Dis, 2022. **13**(5): p. 493.
58. Hanahan, D., *Hallmarks of Cancer: New Dimensions*. Cancer Discov, 2022. **12**(1): p. 31-46.

Figure Legends

Figure 1 Neuronal marker induction by dbcAMP

Schematic of the experimental design for Figure 1 (A). Cells showed morphology changes into neuron-like cells (black arrows) as early as 24 hours after dbcAMP treatment start (B). The combination of radiation and dbcAMP but not radiation or dbcAMP treatment alone induced expression of neurofilament light chain (NF_L) and Tuj-1 (white arrows) (C). All experiments have been performed with at least 3 biological independent repeats.

Figure 2 Forskolin effects on glioma cells

Treatment of HK-374 glioma monolayer cells and glioma spheres with forskolin leads to a dose-dependent induction of intracellular cAMP levels (A) and expression of neuronal markers at 24 h (B) and 5 days after start of forskolin treatment (C). Representative Western blot for neurofilament light chain and β 3-tubulin (D) shows a significant induction of both proteins after treatment with radiation and forskolin (E). Immunofluorescent imaging of glioma cells treated with radiation and forskolin shows expression of neurofilament light chain, and Tuj-1 in a subset of cells with elongated cell bodies (white arrows) (F). Morphology changes after irradiation and forskolin treatment could be observed as early as 24 hours after start of forskolin treatment (G, black arrows). Treatment of HK-374 glioma cells with radiation and consecutive treatment with forskolin for 5, 10 15 or 20 days significantly inhibits cell proliferation (H) and alters the cell cycle distribution (I, day 5; J, day 10). All experiments have been performed with at least 3 biological independent repeats. *p*-values were calculated using One-way

ANOVA for **A, E, H**; The p -values listed in the heatmaps were from the comparison of RT + Forskolin to RT + DMSO. * p -value < 0.05, ** p -value < 0.01, *** p -value < 0.001, **** p -value < 0.0001.

Figure 3 Bulk RNAseq of cells treated with radiation and forskolin

Treatment with radiation and forskolin induced the upregulation (**A**) of 220 and downregulation (**B**) of 143 unique differentially expressed genes leading to a distinctive gene expression profile. Heatmap showing the top 200 differentially expressed genes (**C**). Enrichment analysis using the Hallmark.MSigDB gene set and the differentially expressed genes indicated enhancement of proinflammatory signaling after treatment with radiation and forskolin when compared to radiation alone, induction of reactive oxygen species and inhibition of Shh and Kras signaling (**D**). Compared to unirradiated control cells the combination of radiation and forskolin led to gene expression profiles overlapping with those of microglia, neurons, and endothelial cells (Celltype.MSig.DB) (**E**). Abbrev. RT+Fsk represents RT + forskolin.

Figure 4 Glioma cells grown on poly-D-lysine/laminin-coated plates maintain the response to irradiation and forskolin treatment

Heatmaps showing the results of quantitative RT-PCR for the neuronal markers in HK-374 glioma spheres treated with radiation (a single dose of 4 Gy) in the presence or absence of forskolin (10 μ M) for 24 hours and 5 consecutive days under suspension culture in ultra-low adhesion plates (**A**). Neuron-like cell morphology changes in HK-374 glioma spheres grown on Poly-D-Lysine/Laminin coated plates upon combine treatment

of radiation and forskolin for 5, 14 and 21 days (black arrows showed the elongation of cell bodies) **(B)**. Cells could be maintained under these culture conditions for 21 days with persisting significantly increased β 3-tubulin, and neurofilament light chain marker expression after irradiation and forskolin treatment **(C/D)**. Additionally, we found a significant increase of the microglia marker TMEM119 after treatment with radiation and forskolin **(E)**. The significant increase in neuronal marker expression was confirmed in Western blots **(F-H)**. All experiments have been performed with at least 3 biological independent repeats. *p*-values were calculated using One-way ANOVA for **C-F, G, H**; The *p*-values listed in the heatmaps were from the comparison of RT + Forskolin to RT + DMSO. * *p*-value < 0.05, ** *p*-value < 0.01, *** *p*-value < 0.001, **** *p*-value < 0.0001.

Figure 5 scRNAseq of HK-374 glioma cells (day 5)

UMAP plots **(A)** of 24 identified clusters that could be attributed to the different treatments. Cell type annotations are shown in **B**. Stacked columns show the distribution of the different cell types for each treatment condition **(C)**. Violin plots of marker genes for the identified cell types are shown in **D**. Percentage of spliced and unspliced RNA in all samples and in each treatment condition **(E)**. UMAP plot of latent time for all 4 conditions **(F)**. Plot of dynamical genes against inferred latent time for all samples **(G)**. Trajectory analysis for all four conditions **(H)**. Expression of the top 5 driver genes for each condition over latent time **(I)**. Transcription factor engagement for all predicted cell types calculated using a Bayesian model (BITFAM) **(J)**.

Figure 6 scRNAseq of HK-374 glioma cells (day 21)

UMAP plot of clusters identified 21 days after start of forskolin treatment attributed to the four different conditions (A) and projection of cell types identified on day 5 (B). Stacked columns show the distribution of the different cell types for each treatment condition (C).

Figure 7 A combination of radiation and forskolin eliminates GSC *in vivo* and prolongs median survival in mouse models of glioblastoma

Schematic of the experimental design for Figure 7 (A). Single cell suspension from the tumors harvested showed a significant reduction in sphere-formation for animals treated with radiation, while a combination of radiation and forskolin almost completely prevented sphere-formation (B/C). Using an ELDA we found that forskolin treatment and irradiation alone significantly reduced the frequency of GSCs, while the combined treatment with radiation and forskolin nearly eliminated all GSCs (D/E). Confocal imaging of tumor section of the animals revealed expression of neurofilament light chain and Tuj-1 in a subset of GFP-expressing tumor cells (F, white arrows: colocalization of double stained cells). Treatment of HK-374 PDOXs in NSG mice (G/H) and intracranial syngeneic GL261 tumors in C57Bl/6 mice (I/J) with a single dose of 10 Gy and forskolin (5 mg/kg) was well tolerated and significantly prolonged the median survival of the animals. All experiments have been performed with at least 3 biological independent repeats. *p*-values were calculated using One-way ANOVA for C; *p*-values were calculated and generated by ELDA software for D; Log-rank (Mantel-Cox) test for comparison of Kaplan-Meier survival curves in G, I. * *p*-value < 0.05, ** *p*-value < 0.01, *** *p*-value < 0.001.

Figure 1.

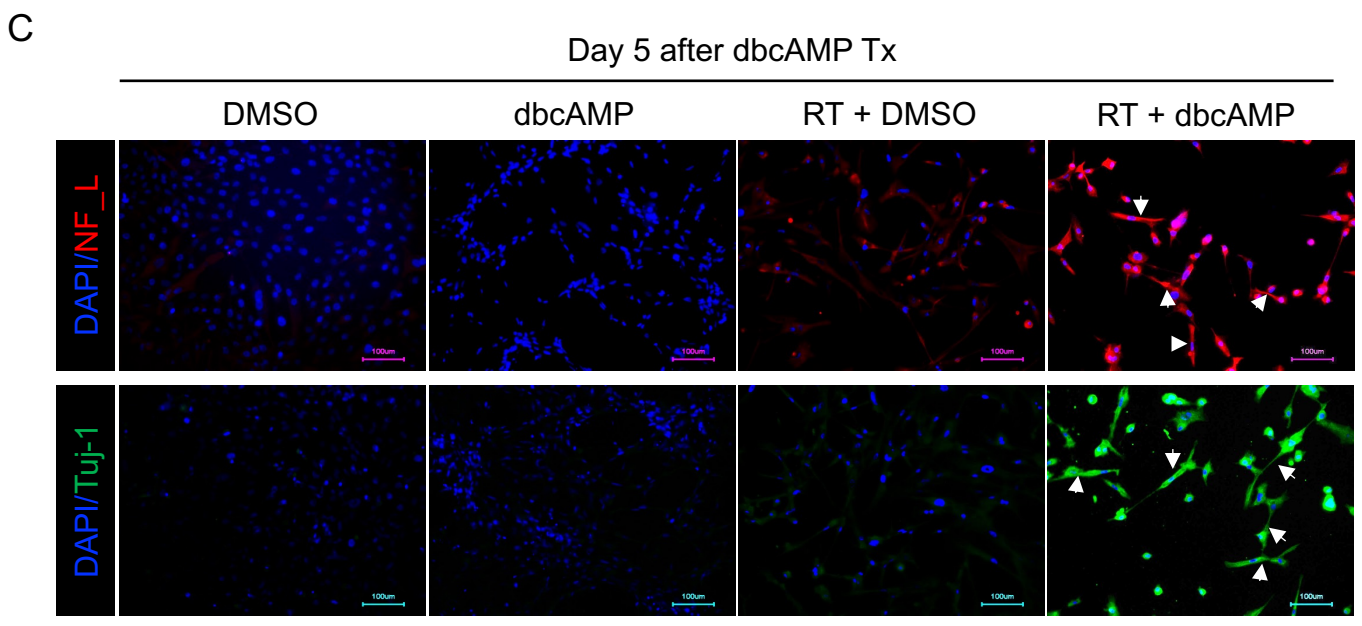
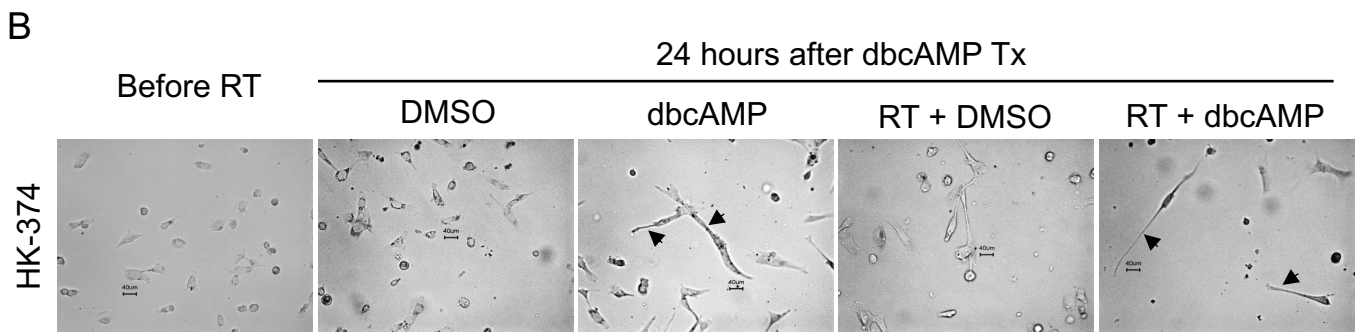
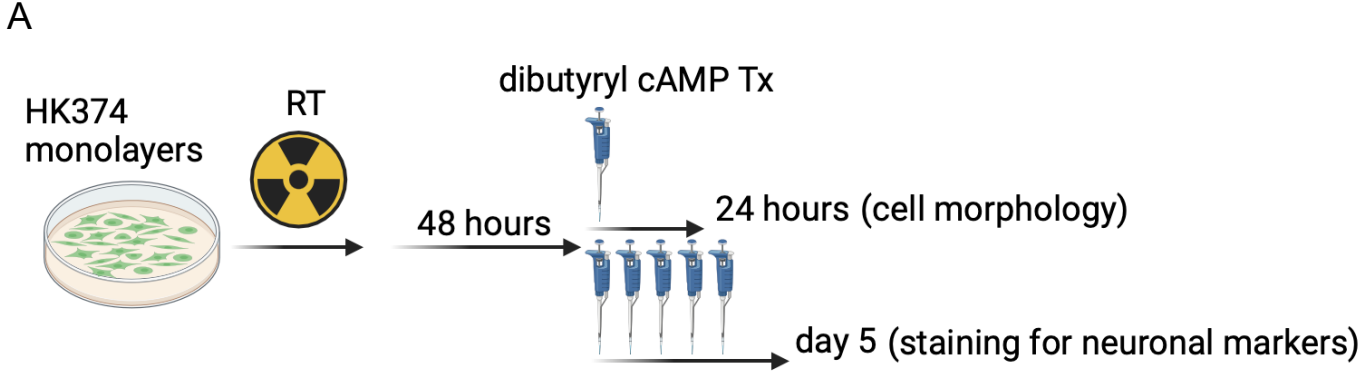


Figure 2.

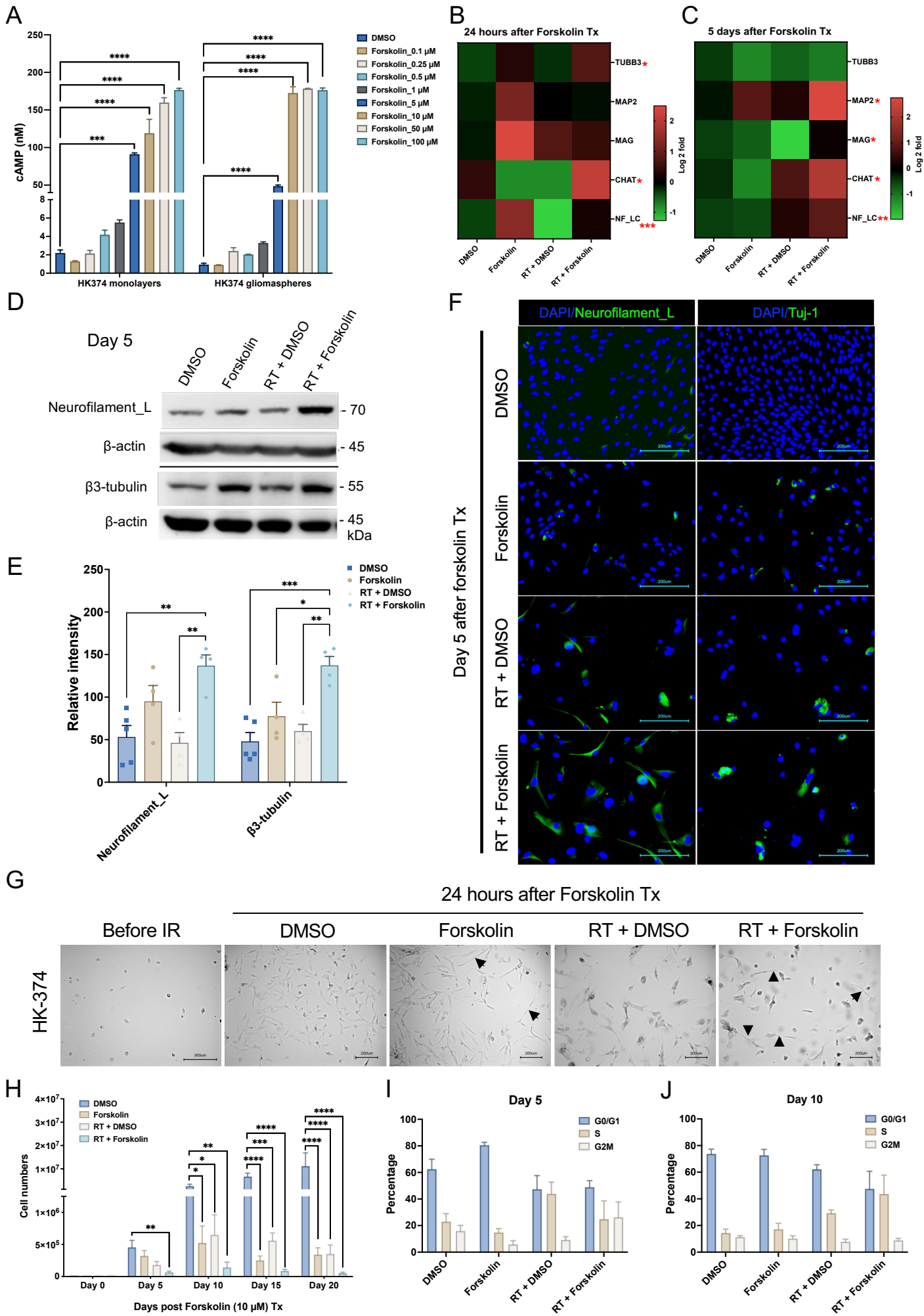
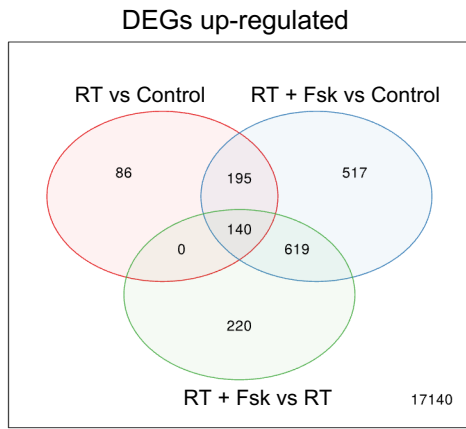
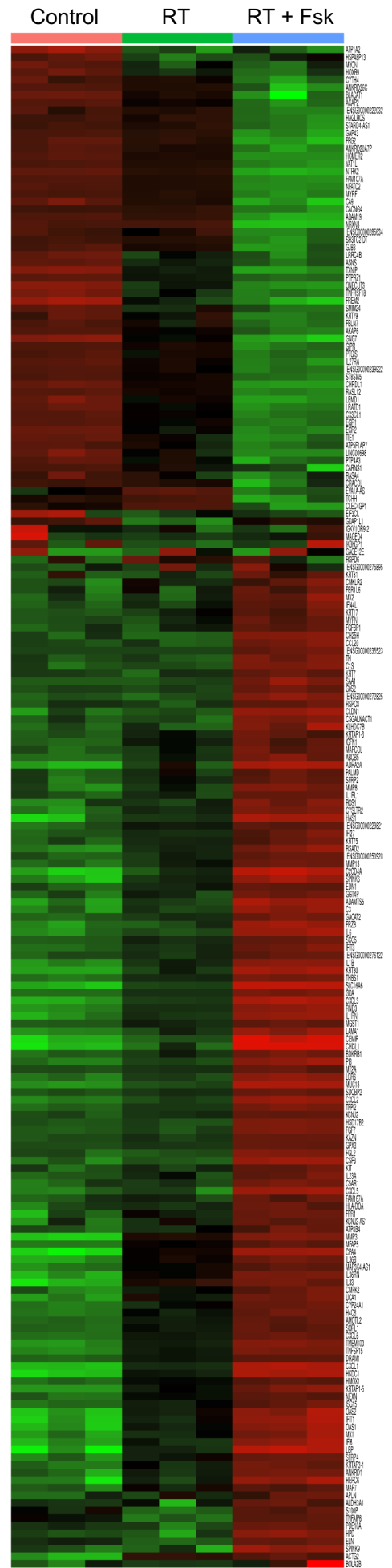


Figure 3.

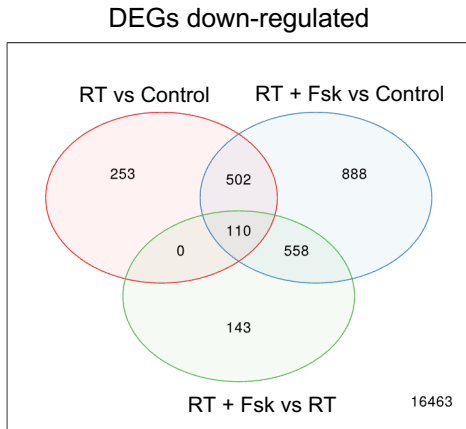
A



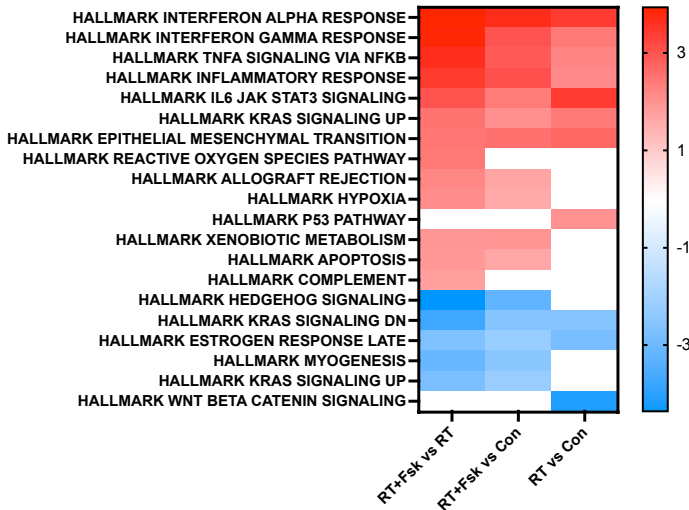
C



B



D



E

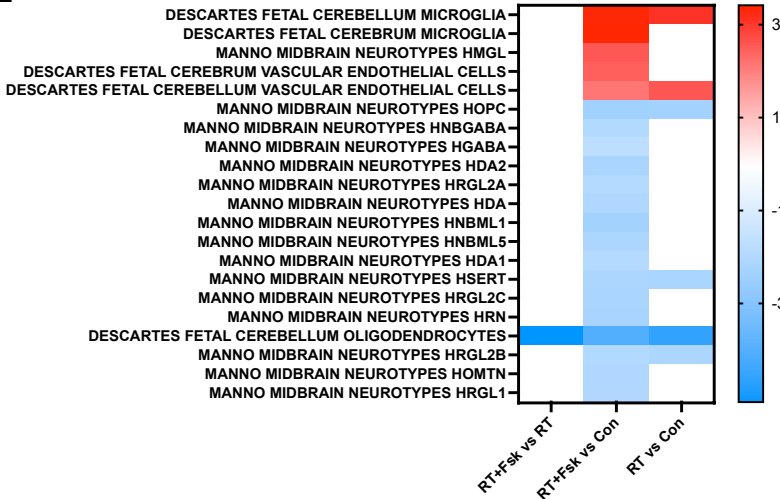
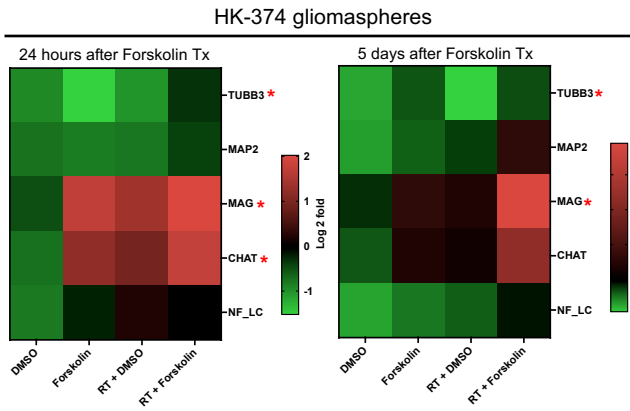
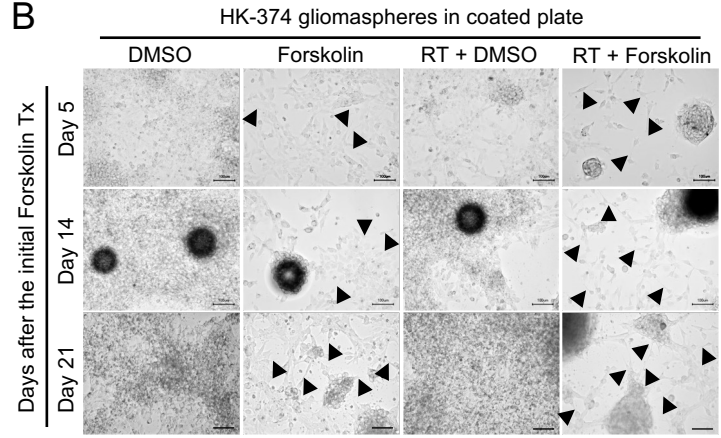


Figure 4.

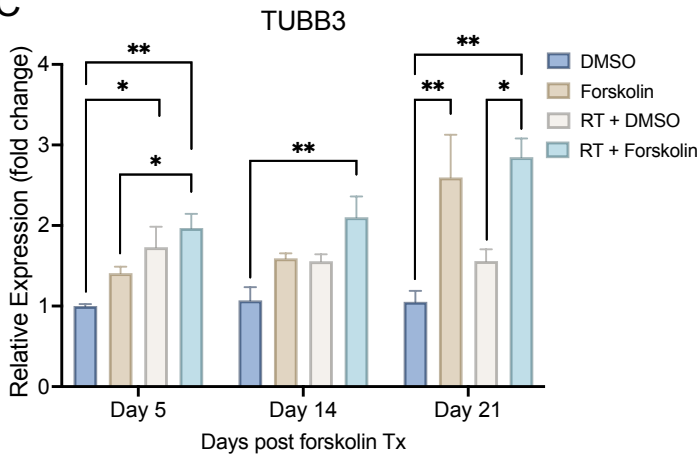
A



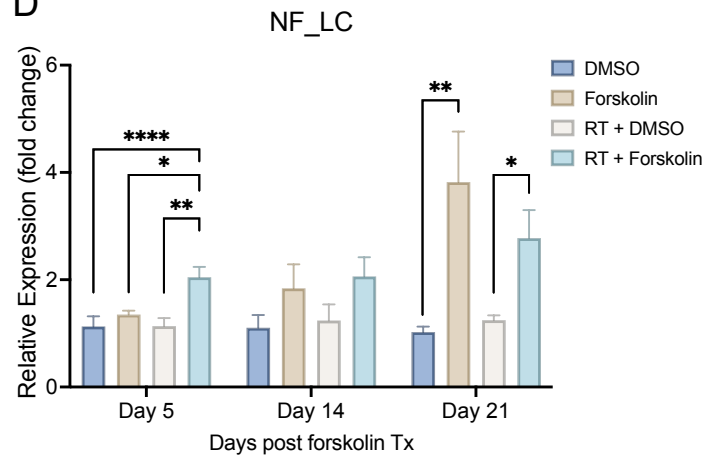
B



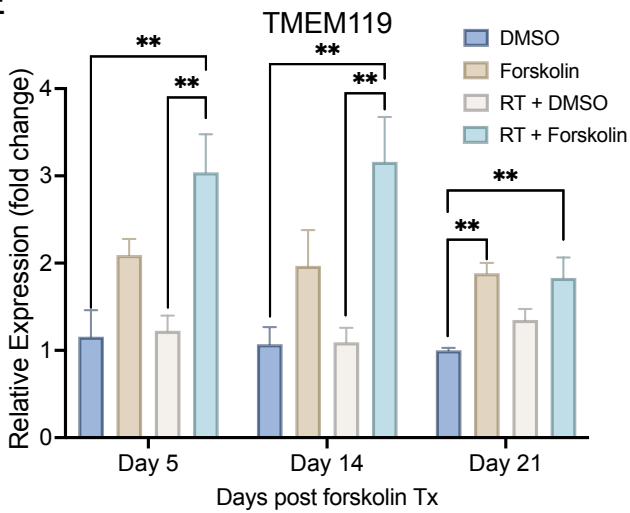
C



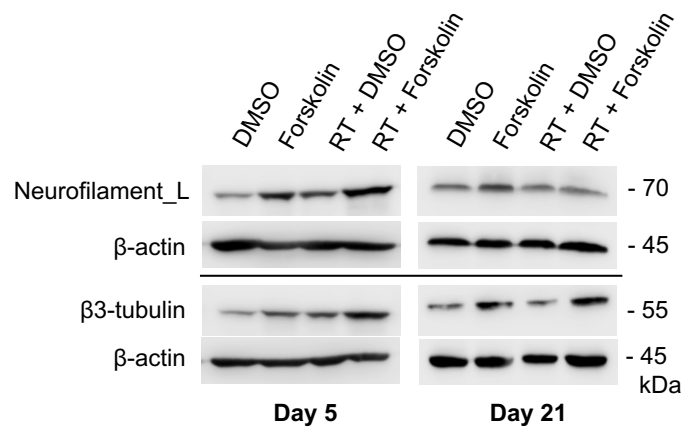
D



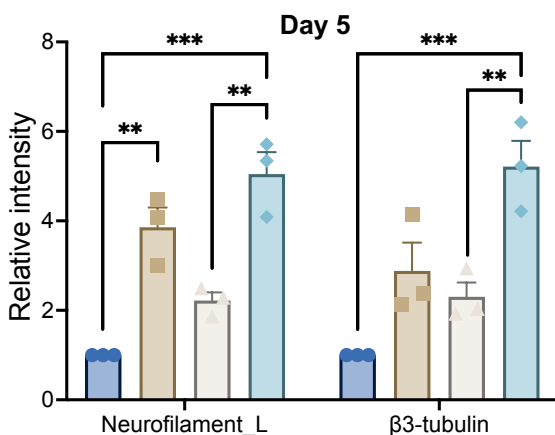
E



F



G



H

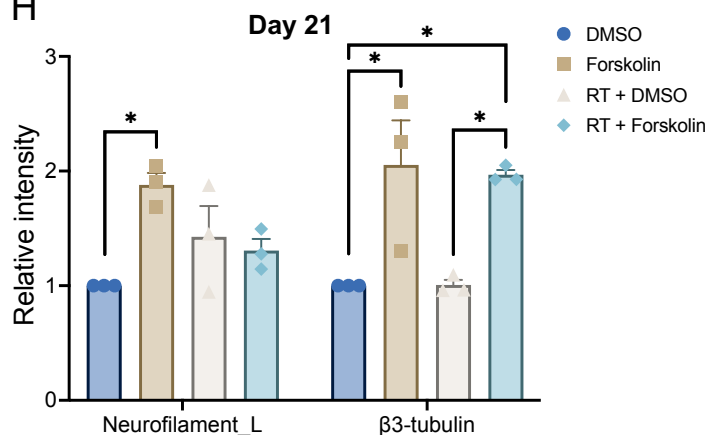
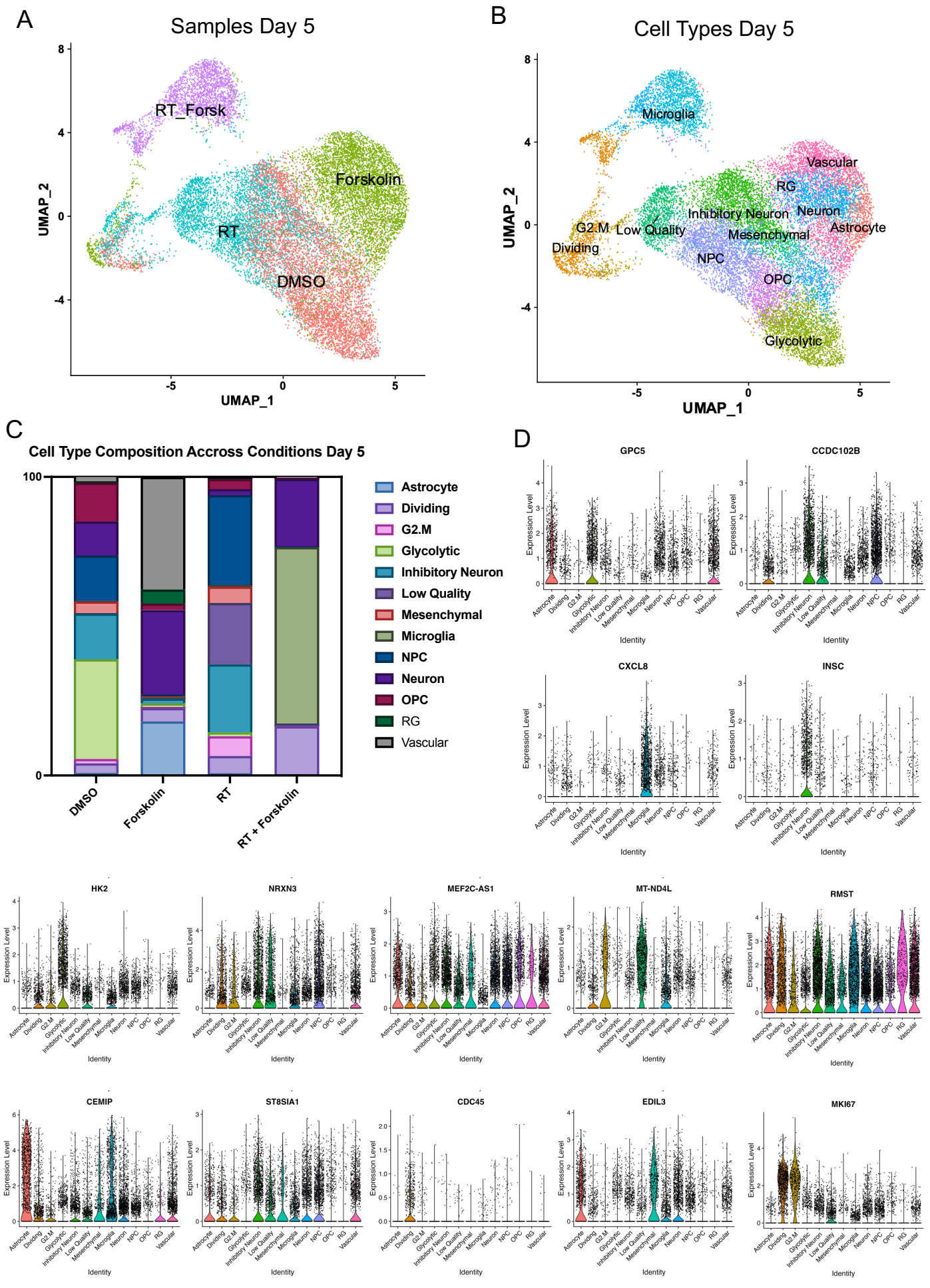
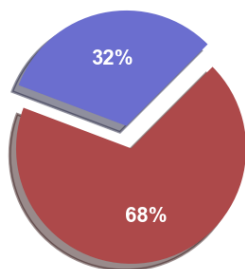


Figure 5.

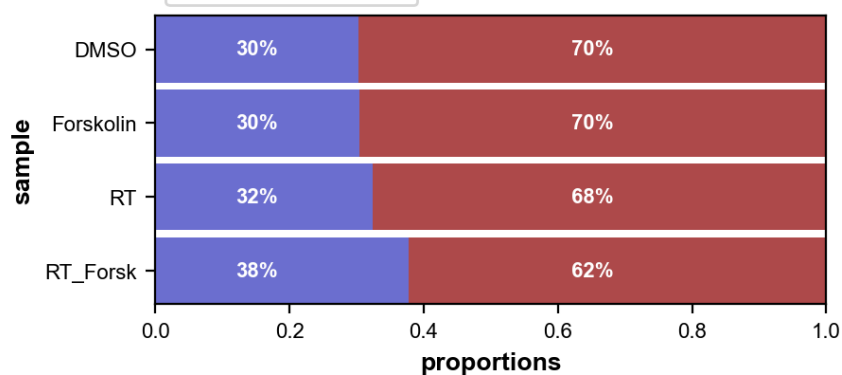


E

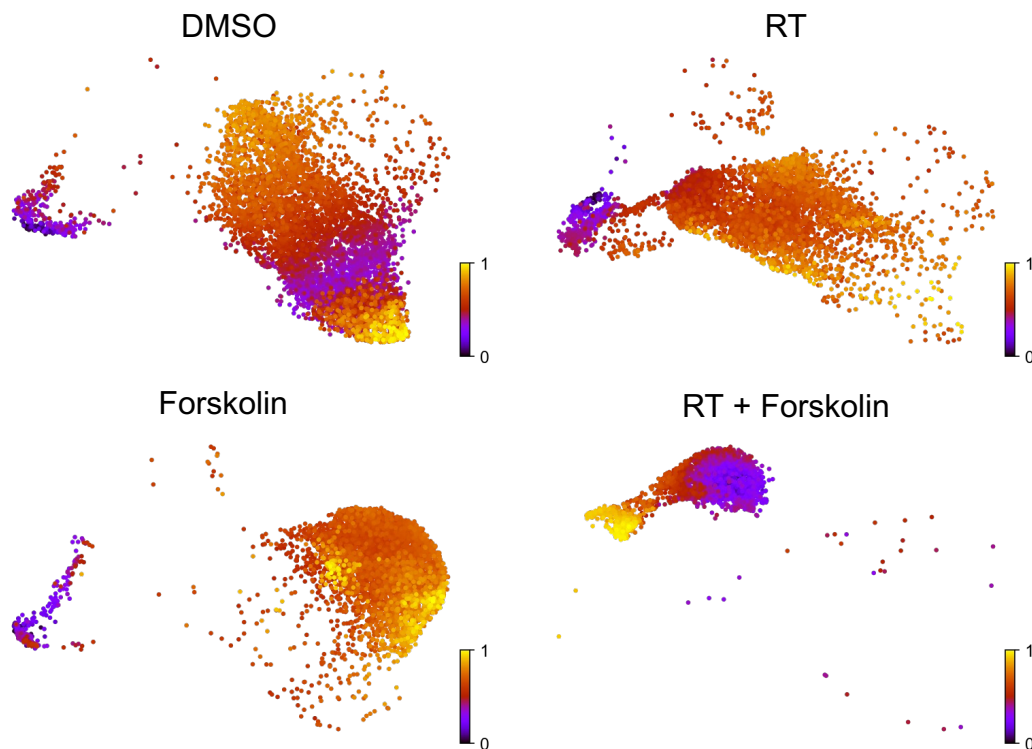
■ spliced ■ unspliced



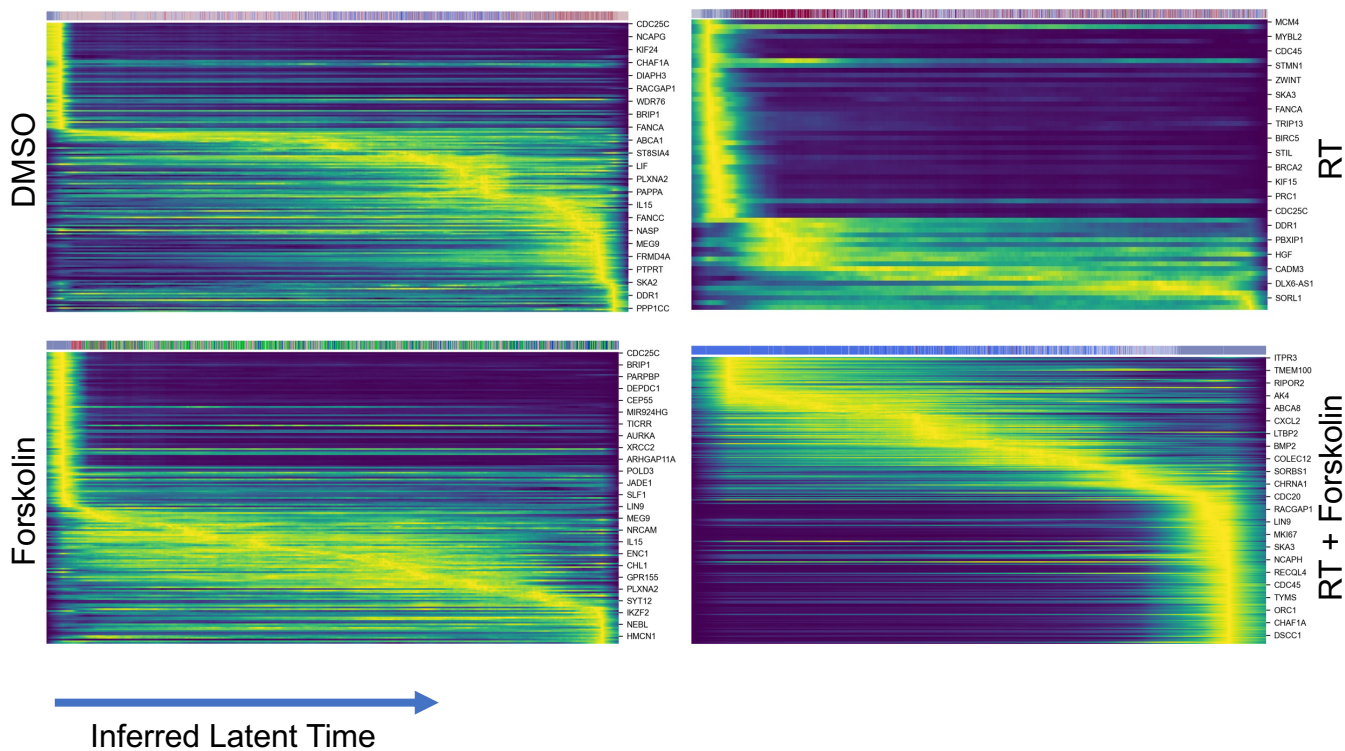
■ spliced ■ unspliced



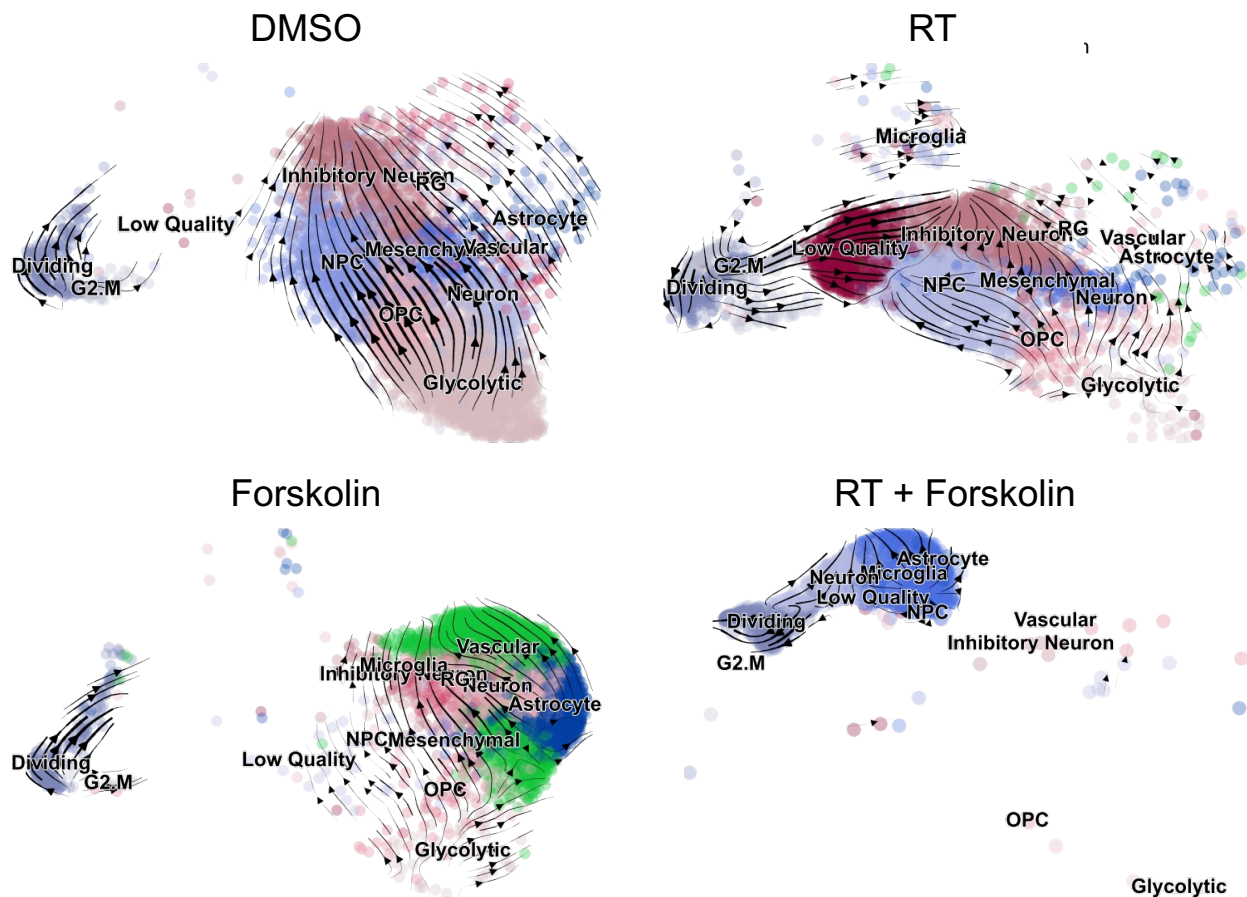
F



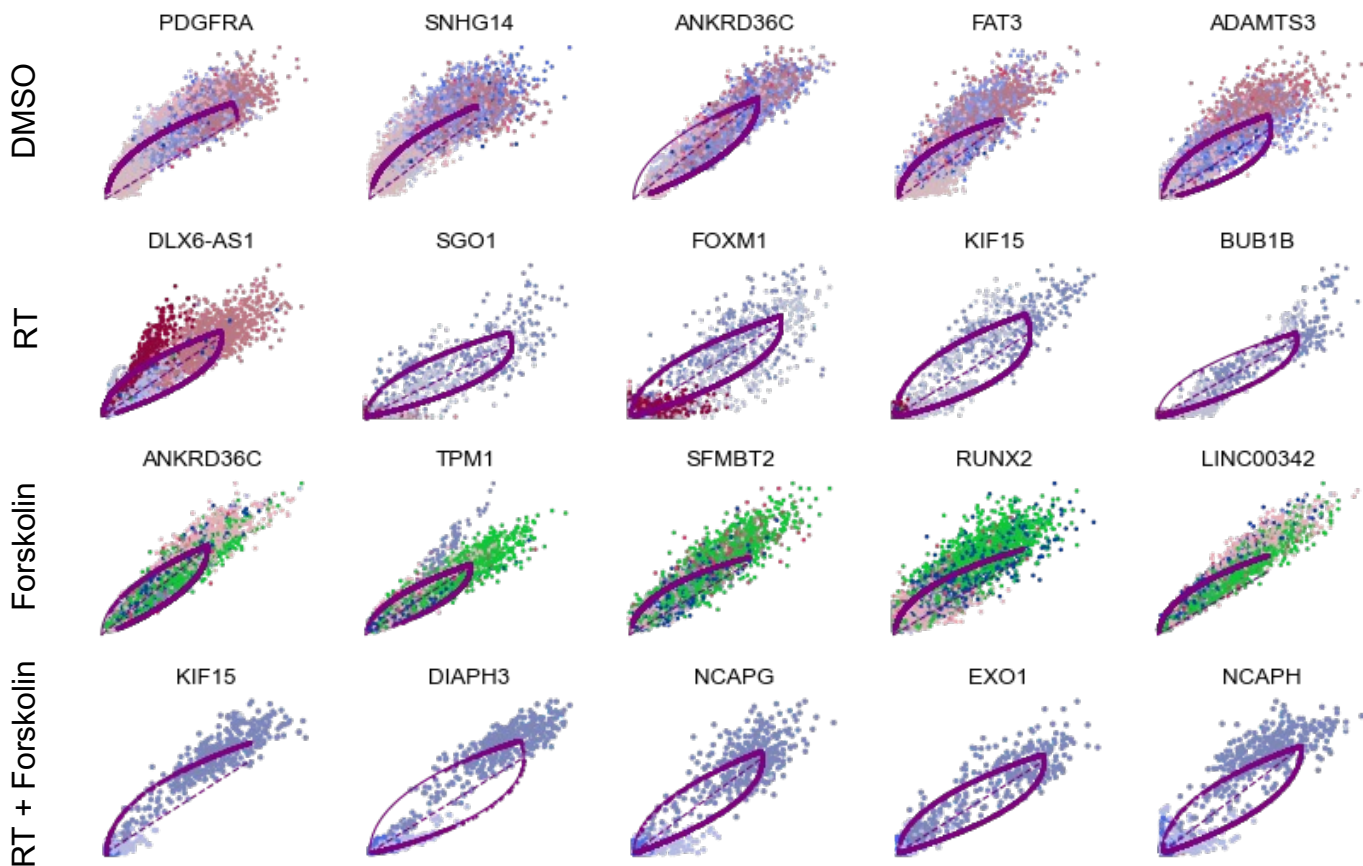
G



H



I



J

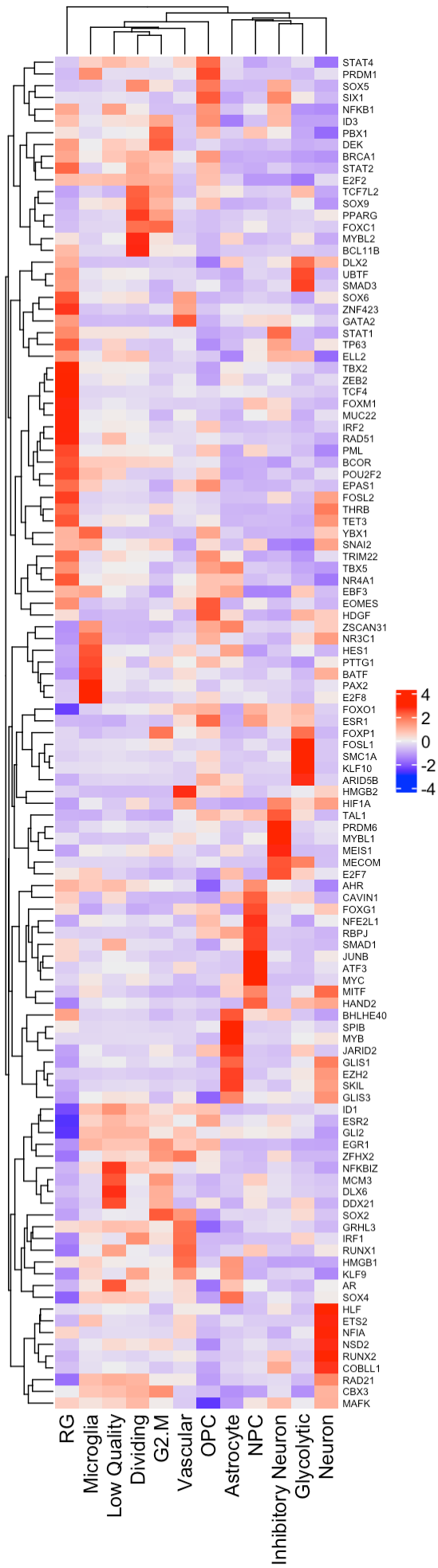


Figure 6.

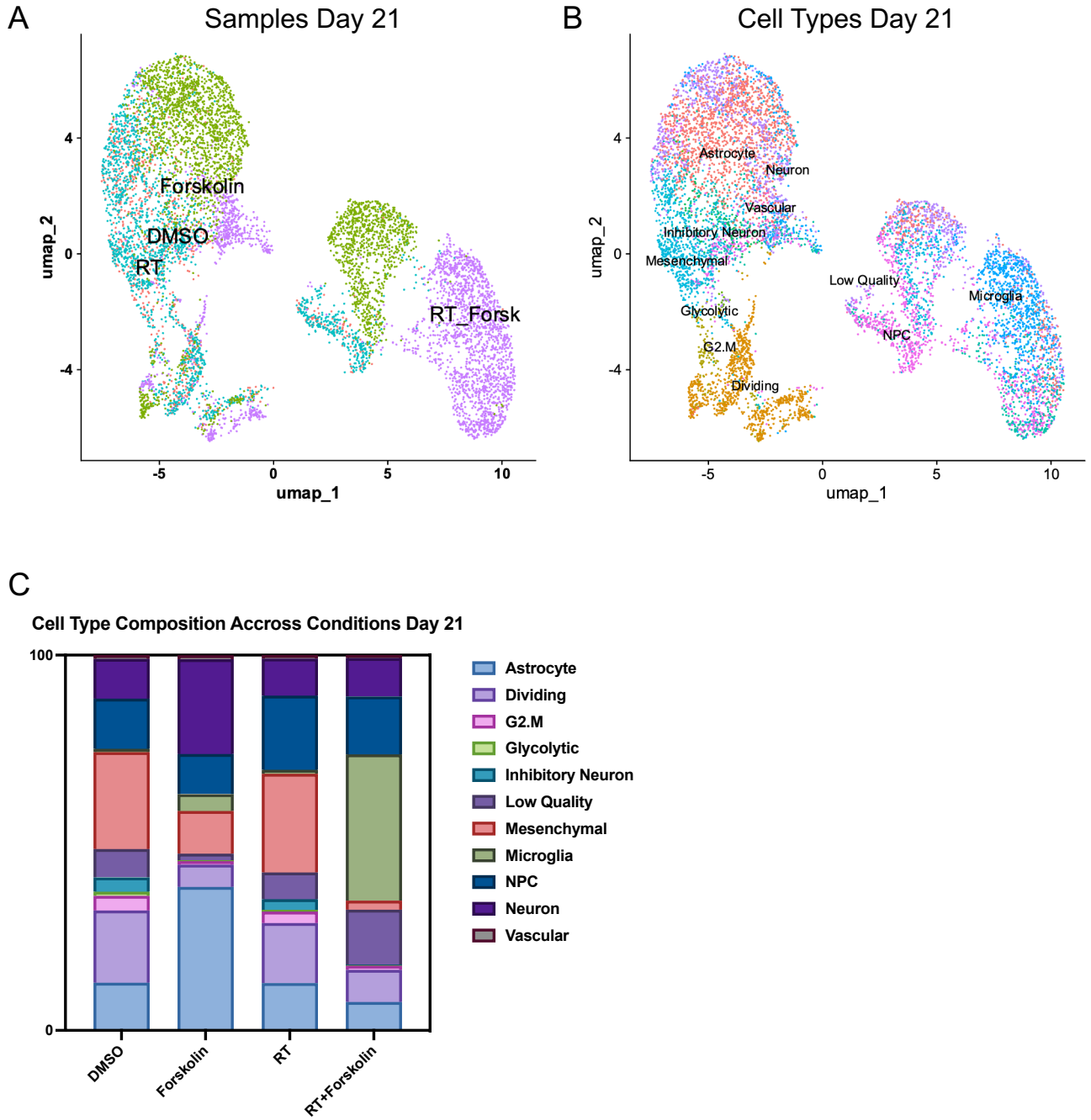
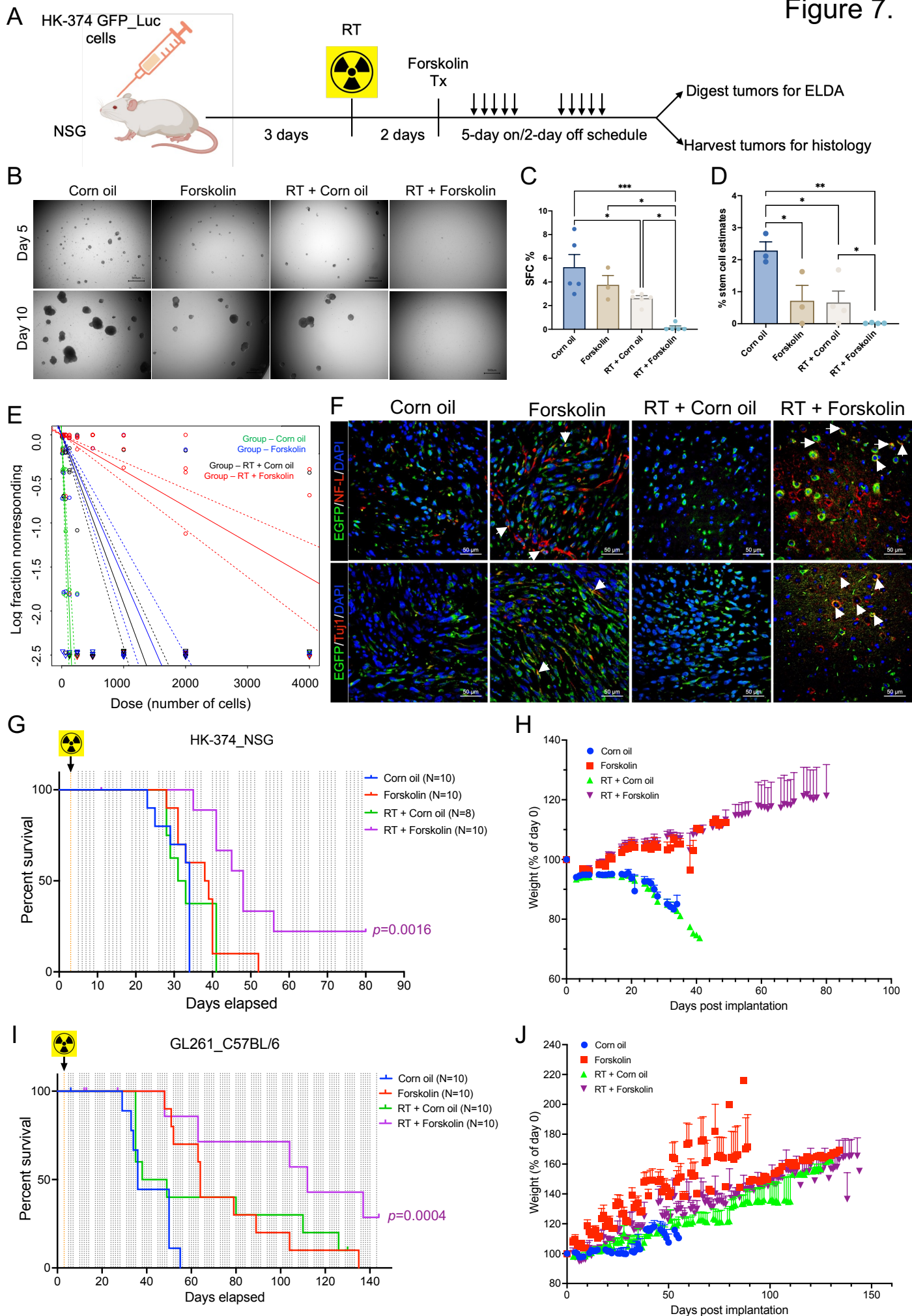


Figure 7.



3.1.4 - Pro-inflammatory signaling in mammary gland development and carcinogenesis

He, Ling, et al. "Tumor necrosis factor receptor signaling modulates carcinogenesis in a mouse model of breast cancer." *Neoplasia* 23.2 (2021): 197-209.

Tumor necrosis factor receptor signaling modulates carcinogenesis in a mouse model of breast cancer



Ling He^a; Kruttika Bhat^a; Sara Duhacheck-Muggy^a;
Angeliki Ioannidis^a; Le Zhang^a; Nhan T. Nguyen^a;
Neda A. Moatamed^{b,c}; Frank Pajonk^{a,c,*}

^a Department of Radiation Oncology, David Geffen School of Medicine, University of California Los Angeles, Los Angeles, CA, USA

^b Department of Pathology and Laboratory Medicine, David Geffen School of Medicine at UCLA, Los Angeles, CA, USA

^c Jonsson Comprehensive Cancer Center, University of California Los Angeles, Los Angeles, CA, USA

Abstract

Pro-inflammatory conditions have long been associated with mammary carcinogenesis and breast cancer progression. The underlying mechanisms are incompletely understood but signaling of pro-inflammatory cytokine TNF α through its receptors TNFR1 and TNFR2 is a major mediator of inflammation in both obesity and in the response of tissues to radiation, 2 known risk factors for the development of breast cancer. Here, we demonstrated the loss of one TNFR2 allele led to ductal hyperplasia in the mammary gland with increased numbers of mammary epithelial stem cell and terminal end buds. Furthermore, loss of one TNFR2 allele increased the incidence of breast cancer in MMTV-Wnt1 mice and resulted in tumors with a more aggressive phenotype and metastatic potential. The underlying mechanisms include a preferential activation of canonical NF- κ B signaling pathway and autocrine production of TNF α . Analysis of the TCGA dataset indicated inferior overall survival for patients with down-regulated TNFR2 expression. These findings unravel the imbalances in TNFR signaling promote the development and progression of breast cancer, indicating that selective agonists of TNFR2 could potentially modulate the risk for breast cancer in high-risk populations.

Neoplasia (2021) 23, 197–209

Keywords: Breast cancer, Mammary epithelial stem cells, Tumor necrosis factor alpha receptor, NF- κ B signaling

Introduction

Since 1975, the incidence of breast cancer in the United States has been steadily rising. For 2019, 268,600 new cases were estimated, making up 15.2% of all new cancer cases in the United States. At the same time, 5-year survival rates increased from 75.3% to 89.9% in 2015 (<https://seer.cancer.gov/statfacts/html/breast.html>).

Total 41,760 women in the United States are predicted to die from breast cancer in 2019 accounting for 6.9% of all cancer deaths in the country.

Major risk factors for the development of breast cancer aside from gender and age are obesity [1] and thoracic radiotherapy during puberty [2]. Both obesity and radiotherapy cause systemic or local pro-inflammatory conditions with elevated TNF α levels in adipose tissue [3] or within normal tissues exposed to radiation [4]. TNF α signals through binding to its receptors, TNFR1 (also called p55 or TNFRSF1A) and TNFR2 (p75 or TNFRSF1B), with distinct and common pathways downstream of TNFR1 and TNFR2 affecting cell death and/or survival [5].

TNF α , mainly derived from activated macrophages, is a well-known pro-inflammatory cytokine that regulates the inflammatory processes in tumor development and progression [6]. High level of TNF α is associated with an aggressive behavior and a poor prognosis in many malignant cancers, including breast cancer [6,7]. In tumor cells, TNF α activates I κ B kinases (I κ Ks), c-Jun N-terminal kinase (c-JNK), and mitogen-activated protein kinase signaling to stimulate the nuclear translocation of transcription factors including nuclear factor kappa B (NF- κ B), which involves in inflammation, cellular transformation, survival, proliferation, angiogenesis, invasion, and metastasis [8]. The NF- κ B family of transcription factors includes 5 members: RelA (p65), NF κ B1 (p50), NF κ B2 (p52), RelB, and c-Rel,

Abbreviations: c-Myc, myelocytoma; CXCL1, C-X-C Motif chemokine ligand 1; DTT, dithiothreitol; ELISA, enzyme-linked immunosorbent assay; GAPDH, glyceraldehyde 3-phosphate dehydrogenase; IFN- γ , interferon gamma; IKK, the inhibitor of nuclear factor- κ B (I κ B) kinase; IL-1 α , interleukin 1 alpha; IL-12, interleukin 12; iNOS, inducible nitric oxide synthase; Klf4, Krüppel-like factor 4; Oct4, octamer-binding transcription factor 4; NF- κ B, nuclear factor kappa-light-chain-enhancer of activated B cells; PMSE, phenylmethylsulfonyl fluoride; Sox2, SRY (sex determining region Y)-box 2; TNF α , tumor necrosis factor alpha; TNFR, tumor necrosis factor receptor.

* Corresponding author.

E-mail address: pajonk@ucla.edu (F. Pajonk).

Received 1 December 2020; received in revised form 18 December 2020; accepted 21 December 2020

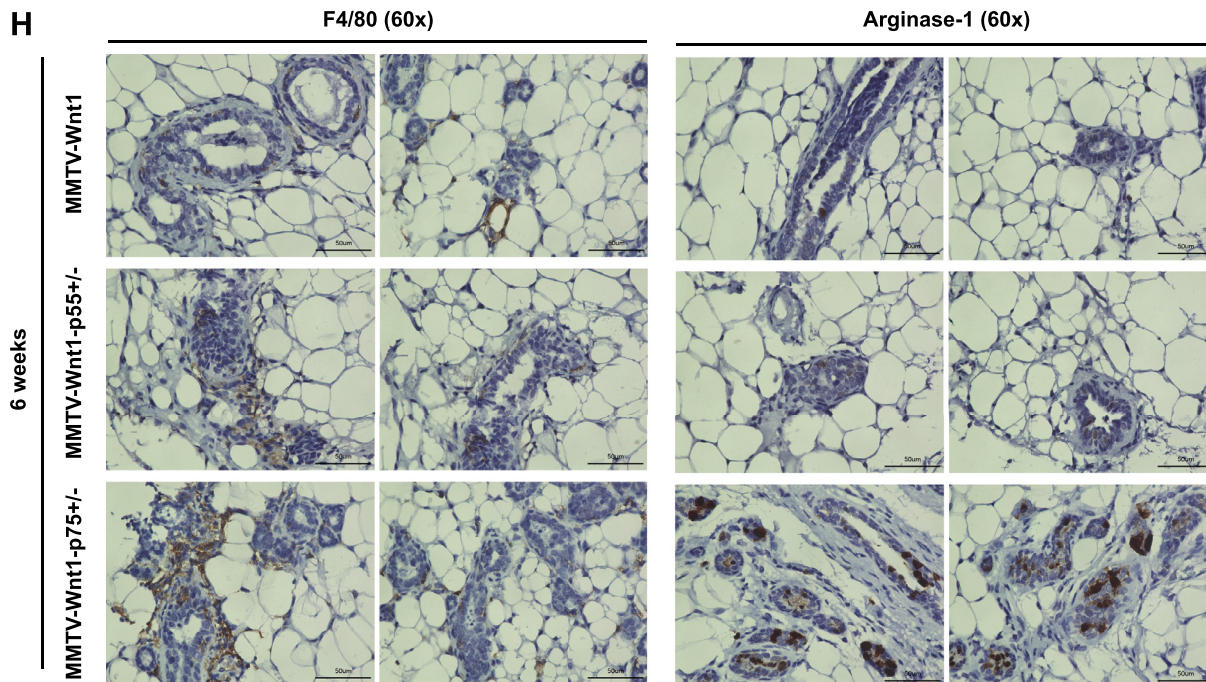


Fig. 1. TNFR1/TNFR2 imbalances affect mammary gland development. (A) #4 mammary glands were isolated from 6-wk-old female C57BL/6 wt, p55 or p75 KO mice, and mounted (LN: lymph node). (B, C) Mammary gland ductal outgrowth was quantified by measuring whole mammary gland area using ImageJ and the number of terminal end buds (TEBs) and side-buds was counted, respectively. (D) Whole mount staining of #4 mammary glands dissected from MMTV-Wnt1, MMTV-Wnt1-p55^{+/-}, and MMTV-Wnt1-p75^{+/-} females. (E) Mammary gland ductal outgrowth was quantified by whole mammary gland area using ImageJ. (F) Mammary epithelial stem cells were isolated from 6-wk-old MMTV-Wnt1 and MMTV-Wnt1-p75^{+/-} females. Mammosphere-forming capacity was evaluated after 2-wk and 3-wk mammosphere culture. (G, H) Immunohistochemistry staining of mammary gland sections from 6-wk-old MMTV-Wnt1, MMTV-Wnt1-p55^{+/-}, and MMTV-Wnt1-p75^{+/-} mice using the macrophage markers F4/80, iNOS (M1) and Arginase-1 (M2). All experiments have been performed with at least 3 biological independent repeats. *P* values were calculated using a one-way ANOVA for B and C; un-paired student's *t* test for E and F. **P* value < 0.05, ***P* value < 0.01, ****P* value < 0.001, and *****P* value < 0.0001.

which are expressed in nearly all cell types and regulate genes with different functions [9]. The activation of diverse NF- κ B subunits can induce either the canonical or non-canonical NF- κ B pathways, which plays distinct roles in both development of normal tissues and malignancies. Abnormal constitutive activation of NF- κ B pathway has been widely reported to be associated with breast cancer development and progression [10]. However, the intracellular signaling cascades through distinct TNFRs (TNFR1 or TNFR2), specifically the NF- κ B pathway have not been clearly demonstrated in the development of mammary gland and breast cancer in literature. However, recent reports indicated a specific role of TNFR2 in tumor metastasis and progression through immunosuppression [11].

In this study, we tested the hypothesis that TNF α signaling contributes to the development of breast cancer. Using a transgenic mouse model for spontaneous breast cancer development crossed with TNFR1 or TNFR2 knockout animals we demonstrated that loss of one TNFR2 allele not only affects mammary gland development, but also significantly increases the incidence of breast cancer and leads to a more aggressive tumor phenotype.

Materials and methods

Animals

MMTV-Wnt1, p55 and p75 knockout (KO) mice were originally obtained from the Jackson Laboratories (Bar Harbor, ME). All mice were re-derived, bred, and maintained in a pathogen-free environment in the American Association of Laboratory Animal Care-accredited Animal Facilities of the Department of Radiation Oncology, University of California

(Los Angeles, CA) in accordance to all local and national guidelines for the care of animals. Due to extensive ductal hyperplasia, the female MMTV-Wnt1 transgenic mice cannot lactate, so we crossed the male MMTV-Wnt1 (+) mice with female p55 KO or p75 KO mice to generate heterozygous MMTV-Wnt1-p55^{+/-} and MMTV-Wnt1-p75^{+/-} offspring. Genotyping was performed for the MMTV-Wnt1 transgene. Mice were monitored regularly and tumors were harvested before exceeding humane endpoints.

Whole mammary gland mounting

The mammary glands from 6-wk-old female mice were carefully excised and spread directly onto a glass slide without changing their original in situ shape. The tissue was fixed by immersing in Carnoy's fixative solution (100%EtOH, chloroform, glacial acetic acid; 6:3:1) at 4°C overnight. Glands were hydrated and stained with carmine alum overnight at room temperature. The stained tissues were then dehydrated and cleared in xylene. Images were captured and merged at 4 \times using a digital microscope (BZ-9000, Keyence, Itasca, IL). Ductal outgrowth was quantified by measurement of the area (mm²) covered by the ductal tree in merged images of the mammary gland whole mounts in ImageJ and the terminal end buds (TEBs) and side-buds were counted manually in an unbiased manner.

Cell lines

The human SUM159PT breast cancer cell line was purchased from Asterand (Detroit, MI). Human MCF-7 breast cancer cell line was purchased from American Type Culture Collection (Manassas, VA).

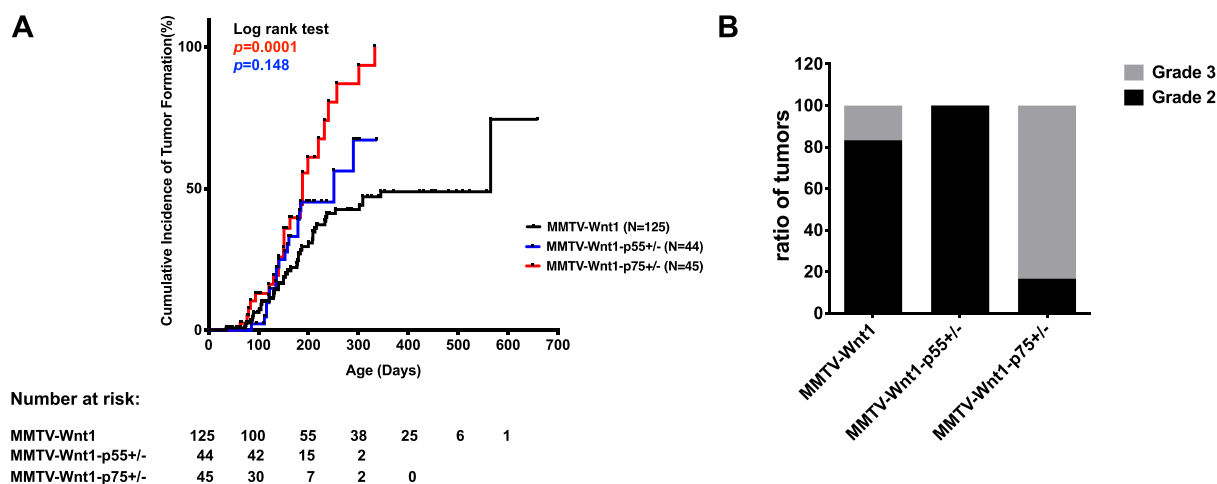


Fig. 2. Loss of one allele of TNFR2 increases BCICs and promotes tumor vasculature with greater metastatic potential. (A) Cumulative incidence curves for breast cancers in MMTV-Wnt1, MMTV-Wnt1-p55^{+/-} and MMTV-Wnt1-p75^{+/-} females. Breast tumors were observed and measured until they reached the study endpoint. Log-rank (Mantel-Cox) test for comparisons of Kaplan-Meier survival curves indicated significant difference between MMTV-Wnt1-p75^{+/-} and MMTV-Wnt1 mice (P value = 0.0001). (B) Tumors were harvested, fixed and embedded in paraffin and cut into 4 μ m sections. H&E staining was performed and the stained slides were graded blind by a clinical pathologist. (C) Representative gross view of the tumors from MMTV-Wnt1, MMTV-Wnt1-p55^{+/-}, and MMTV-Wnt1-p75^{+/-} mice. (D) Immunohistochemistry staining of Vimentin and Snail (EMT markers) for the MMTV-Wnt1, MMTV-Wnt1-p55^{+/-}, and MMTV-Wnt1-p75^{+/-} tumor sections. (E) qRT-PCR for EMT-related genes Vimentin, Snail and Slug in MMTV-Wnt1, MMTV-Wnt1-p55^{+/-}, and MMTV-Wnt1-p75^{+/-} primary tumor cell lines. (F, G) Immunohistochemistry staining of Ki67 (proliferating marker) for the MMTV-Wnt1, MMTV-Wnt1-p55^{+/-}, and MMTV-Wnt1-p75^{+/-} tumor sections, with the slides graded by clinical pathologist for the percentage of tumor cells positive for nuclear Ki67. (H, I) Migration and invasion assays of primary tumor cells isolated from MMTV-Wnt1, MMTV-Wnt1-p55^{+/-}, and MMTV-Wnt1-p75^{+/-} mice. The migrated and invaded cell numbers were counted and quantified by ImageJ, respectively. (J) Mammosphere forming capacity of primary tumor spheres isolated from MMTV-Wnt1, MMTV-Wnt1-p55^{+/-}, and MMTV-Wnt1-p75^{+/-} mice. The number of spheres formed was counted and calculated as a ratio to the initial number of cells plated, and then normalized to the MMTV-Wnt1 value. (K) Clonogenic assay of primary tumor cells extracted from MMTV-Wnt1, MMTV-Wnt1-p55^{+/-}, and MMTV-Wnt1-p75^{+/-} mice. The colony number was counted and presented as the percentage relative to the initial number of cells plated. All experiments have been performed with at least 3 biological independent repeats. P values were calculated using 1-way ANOVA for E, G-K; Log-rank (Mantel-Cox) test for A. * P value < 0.05, ** P value < 0.01, and **** P value < 0.0001.

SUM159PT cells were cultured in log-growth phase in F12 Medium (Invitrogen, Carlsbad, CA) supplemented with 5% fetal bovine serum, penicillin (100 units/mL), streptomycin (100 μ g/mL), 5 μ g/mL insulin (Eli Lilly, Indianapolis, IN), 0.1% 1M HEPES buffer (4-(2-hydroxyethyl)-1-piperazineethanesulfonic acid, Invitrogen) and 1 μ g/mL hydrocortisone (Pfizer, New York, NY). MCF-7 cells were cultured in log-growth phase in Dulbecco's Modified Eagle Medium (DMEM) (Invitrogen, Carlsbad, CA) supplemented with 10% fetal bovine serum, penicillin, and streptomycin. All cells were grown in a humidified incubator at 37°C with 5% CO₂ and routinely tested for mycoplasma infection (MycAlert, Lonza). The identity of the cell line was confirmed by DNA fingerprinting (Laragen, Culver City, CA).

ZsGreen-cODC expressing cells were obtained as described in [12]. Briefly, cells were infected with a lentiviral vector coding for a fusion protein between the fluorescent protein ZsGreen and the C-terminal decon of murine ornithine decarboxylase. The latter targets ZsGreen to ubiquitin-independent degradation by the 26S proteasome, thus reporting lack of proteasome function through accumulation of ZsGreen-cODC. We previously reported that cancer cell populations lacking proteasome activity are enriched for tumor-initiating cells in glioblastoma, breast cancer, and cancer of the head and neck region [12–15] and others have confirmed these findings independently in tumors of the liver, lung, cervix, pancreas, osteosarcoma, and colon [16–21]. After infection with the lentivirus, cells expressing the ZsGreen-cODC fusion protein were further selected with G418 for 5 d. Successful infection was verified using the proteasome inhibitor MG132 (Sigma, MO).

Primary breast tumor cell culture

Breast tumor tissues were extracted from MMTV-Wnt1, MMTV-Wnt1-p55^{+/-}, or MMTV-Wnt1-p75^{+/-} female mice and washed 3 times with PBS/1% Penicillin/Streptomycin. For tumor dissociation, Miltenyi C tubes (gentleMACS C tubes, Cat # 130-093-237, Auburn, CA, USA) were preloaded with 100 μ L enzyme D, 50 μ L enzyme R and 12.5 μ L enzyme A provided in the mouse Tumor Dissociation Kit (Cat # 130-096-730, Miltenyi, Auburn, CA) in 2.35 mL of F12 media. The breast tumor tissues were finely chopped with a scalpel and transferred into the C tubes. Tumor tissues were further dissociated by running the m_impTumor_02 program once on the gentleMACS Dissociator (Cat# 130-093-235, Miltenyi). The tubes were next placed in a shaker incubator at 37°C for 60 min. After incubation, the tubes were once again placed in the gentleMACS Dissociator and subjected twice to the same dissociation program as described above. The tubes were briefly centrifuged at 300 \times g to collect the digested cells at the bottom of the tube. The cells were re-suspended in the enzyme-containing medium and filtered through a 70- μ m filter into a 50 mL conical tube. The filter was washed with 10 mL F12 media and centrifuged at 300 \times g for 7 min. The supernatant was aspirated, and the pellet was re-suspended in 2 mL of ACK lysis buffer (Cat # 10-548E, BioWhittaker, Walkersville, MD) to lyse the red blood cells. After 2 min, the conical tubes were centrifuged at 300 \times g for 7 min and the supernatant was aspirated. The cell pellet was resuspended in 1 to 2 mL F12 media and cell numbers were counted using a hemocytometer. Subsequently, the cells were plated onto 100 mm dishes in

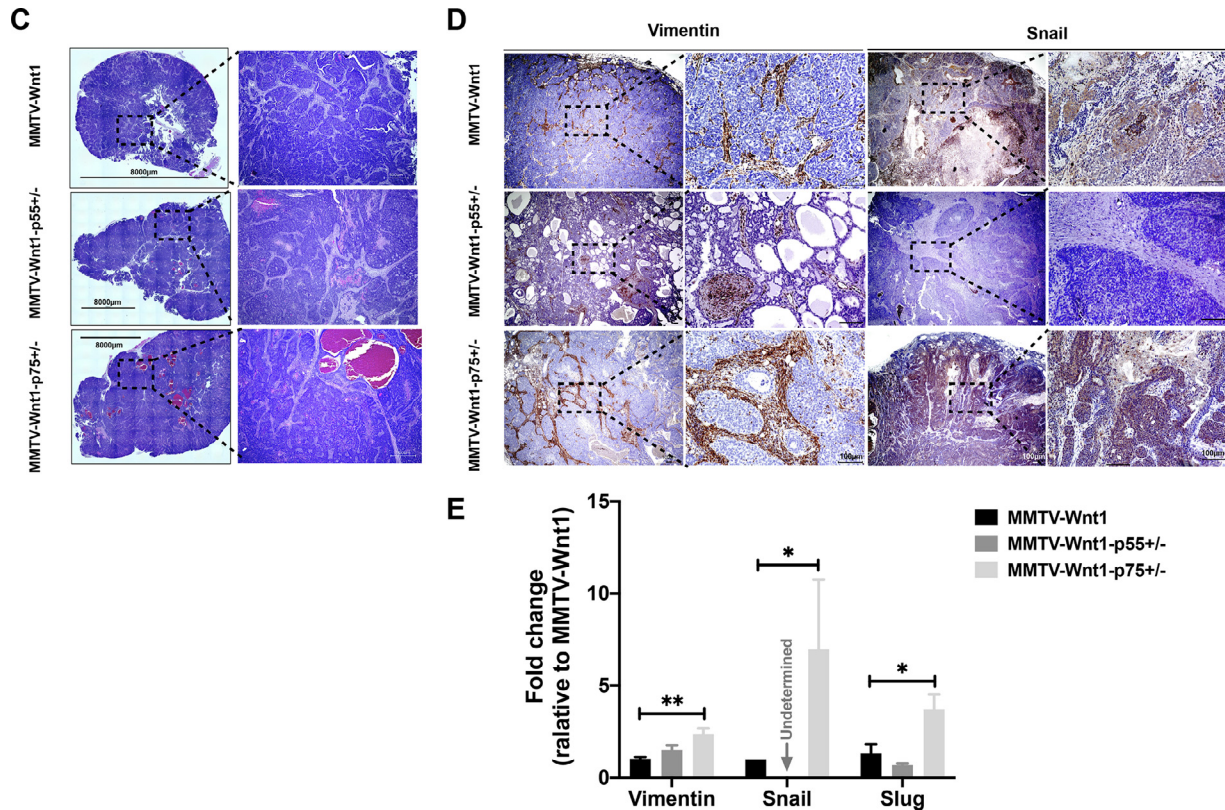


Fig. 2. Continued

SUM159PT culture medium supplemented with plasmocin and grown in a humidified incubator at 37°C with 5% CO₂.

Irradiation

Cells were irradiated at room temperature using an experimental X-ray irradiator (Gulmay Medical Inc. Atlanta, GA) at a dose rate of 5.519 Gy/min for the time required to apply a prescribed dose. The X-ray beam was operated at 300 kV and hardened using a 4 mm Be, a 3 mm Al, and a 1.5 mm Cu filter and calibrated using NIST-traceable dosimetry. Corresponding controls were sham irradiated.

In vitro limiting dilution assays

SUM159PT and MCF-7 spheres were dissociated by TrypLE and plated in mammosphere media (DMEM-F12, 10 mL/500 mL B27 [Invitrogen], 5 µg/mL bovine insulin [Sigma], 4 µg/mL heparin [Sigma], 20 ng/mL basic fibroblast growth factor [bFGF, Sigma], and 20 ng/mL epidermal growth factor [EGF, Sigma]) into 96-well ultra-low adhesion plates, ranging from 1 to 256 cells per well, along with a single dose of TNFα (1, 2.5, 5, 10, 50, 100 ng/mL) or vehicle (0.1% bovine serum albumin [BSA]), respectively. Growth factors (EGF and bFGF) were added every 3 days. The number of spheres formed per well was then counted and expressed as a percentage of the initial number of cells plated.

MMTV-Wnt1, MMTV-Wnt1-p55^{+/-}, and MMTV-Wnt1-p75^{+/-} mammospheres were cultured from their corresponding monolayer cells. The cells were detached with Trypsin and plated in SUM159PT mammosphere media for sphere formation. The spheres were then dissociated by TrypLE and plated into 96-well ultra-low adhesion plates, ranging from 2 to 512 cells per well, along with a single dose of TNFα (1, 10, 100 ng/mL) or vehicle (0.1% BSA) applied. Growth factors (EGF and bFGF) were added every 3

d. The number of spheres formed per well was then counted, expressed as the percentage of the initial number of cells plated, and normalized to the counts in the MMTV-Wnt1 0.1% BSA-treated control group.

Clonogenic survival assay

MMTV-Wnt1, MMTV-Wnt1-p55^{+/-}, and MMTV-Wnt1-p75^{+/-} monolayer cells were trypsinized and plated in 6-well plates at a density of 2000 cells for MMTV-Wnt1, and 200 cells for both MMTV-Wnt1-p55^{+/-} and MMTV-Wnt1-p75^{+/-} per well. The cell culture media was changed every 3 d. After 2 wk, the colonies were fixed and stained with 0.1% crystal violet. Colonies consisting of at least 50 cells were counted in each group and presented as percentage of the initial number of cells plated.

SUM159PT and MCF-7 monolayer cells were trypsinized and plated in 6-well plates at a density of 200 cells per well with the presence of TNFα (1, 2.5, 5, 10, 50, 100 ng/mL) or vehicle (0.1% BSA). After 2 wk, the colonies were fixed and stained with 0.1% crystal violet. Colonies consisting of at least 50 cells were counted in each group and presented as percentage of the initial number of cells plated.

Cell migration/invasion assay

Cell migration was quantified using Transwell plates (8 µm pore size; Corning). After 12 h of serum starvation, 1 × 10⁵ MMTV-Wnt1, MMTV-Wnt1-p55^{+/-}, or MMTV-Wnt1-p75^{+/-} primary cells were placed in the insert, with 750 µL cell culture medium containing 5% FBS as the induction medium in the lower chamber. After 16 h of incubation, unmigrated cells on the upper surface of the insert were removed with a cotton swab. Migrated cells were fixed with formalin and stained with crystal violet. Images were taken randomly on a digital microscope (BZ-9000, Keyence) with 4×

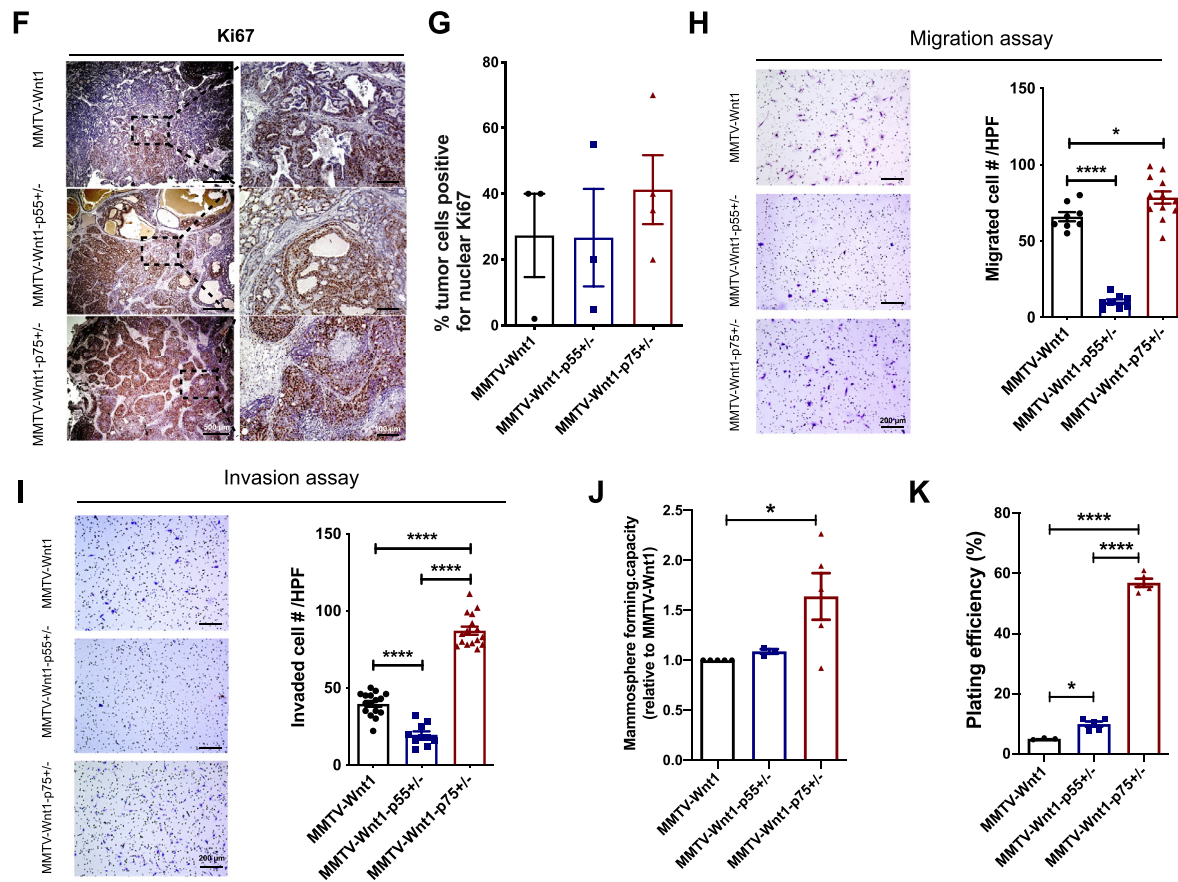


Fig. 2. Continued

magnification and the migrated cell number was counted and quantified by ImageJ.

For the cell invasion assay, 8 μ m porous Transwell chamber membranes were pre-coated with 100 μ L diluted Matrigel matrix solution (dilute with F12 medium to final Matrigel concentration of 200-300 μ g/mL). Plates with coated invasion chambers were incubated at 37°C for 2 hours and the remaining coating buffer was removed. The cell preparation, seeding, fixation, and staining procedures were the same as the migration procedures described above. Images were randomly taken on a digital microscope and migrated cell number was counted and quantified by ImageJ.

Flow cytometry

Breast cancer-initiating cells (BCICs) were identified based on their low proteasome activity using the ZsGreen-cODC reporter system [14]. Five days after irradiation, cells were trypsinized and ZsGreen-cODC expression was assessed by flow cytometry (MACSQuant Analyzer, Miltenyi). Cells were defined as "ZsGreen-cODC positive" if the fluorescence in the FL-1H channel exceeded the level of 99.9% of the parental control cells.

Immunohistochemistry

Formalin-fixed tissue samples were embedded in paraffin and 4 μ m sections were stained with hematoxylin and eosin (H&E) using standard protocols. Additional sections were baked for 1 h in an oven at 65°C, dewaxed in 2 successive Xylene baths for 5 min each and then hydrated for 5 min each using an alcohol gradient (ethanol 100%, 90%, 70%, 50%, 25%). The

slides were incubated in 3% hydrogen peroxide/methanol solution for 10 min. Antigen retrieval was performed using Heat Induced Epitope Retrieval in a citrate buffer (10 mM sodium citrate, 0.05% Tween-20, pH 6) with heating to 95°C in a steamer for 25 min. After cooling down, the slides were blocked with 10% goat serum plus 1% BSA at room temperature for 30 min and then incubated with the primary antibody against Ki67 (Abcam, Cat #15580, 1:200), Vimentin (Cell Signaling, Cat #5741S, 1:200), Snail (Abcam, Cat# 85931, 1:400), F4/80 (Cell Signaling, Cat #70076S, 1:400), iNOS (Thermo Fisher Scientific, PA1-036, 1:400) or Arginase-1 (Cell Signaling, Cat #93668S 1:400) overnight at 4°C. The next day, the slides were rinsed with PBS and then incubated with ready-to-use IHC detection reagent (Cell signaling, Danvers, MA; 10 μ L) at room temperature for 1 h, rinsed, and then incubated with DAB (Cell Signaling) for 3 to 5 min. Tissues were counterstained with Harris modified Hematoxylin (Fisher scientific, Waltham, MA) for 30 s, dehydrated via an alcohol gradient (ethanol 25%, 50%, 70%, 90%, 100%) and soaked twice into Xylene. A drop of Premount mounting media (Fisher Scientific) was added on the top of each section before covering up with a coverslip.

Protein extraction and western blotting

The total protein was extracted from FACS sorted ZsGreen-cODC-negative SUM159PT cells treated with TNF α and/or irradiation. Briefly, the cells were lysed in ice-cold RIPA lysis buffer containing proteinase inhibitor (Sigma, #P8340) and phosphatase inhibitor (EMD Millipore, MA, #524629). The protein concentration in each sample was determined using the BCA protein assay (Thermo Fisher Scientific) and samples were denatured

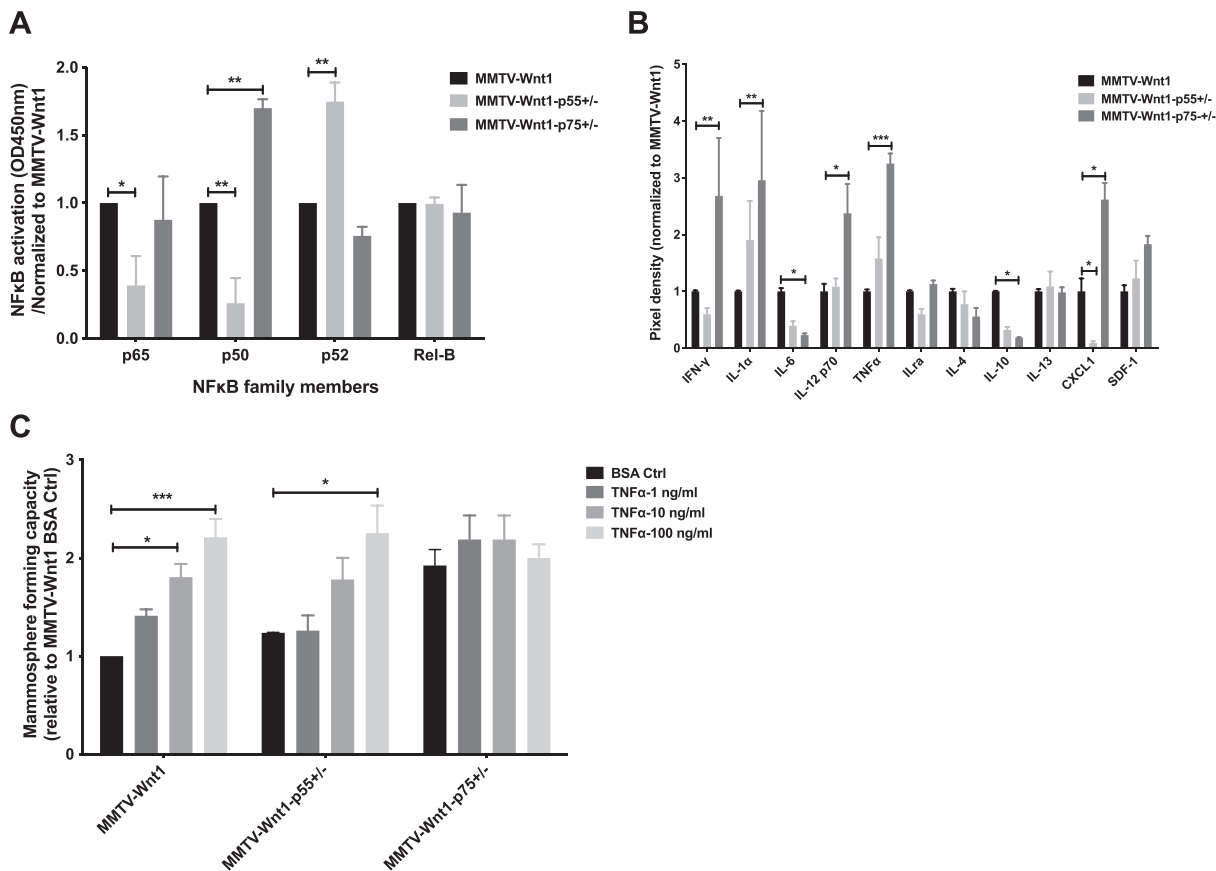


Fig. 3. Loss of 1 TNFR2 allele activates p50/NF- κ B transcriptional activity with more abundant secretion of pro-inflammatory cytokines. (A) Nuclear extracts prepared from MMTV-Wnt1, MMTV-Wnt1-p55^{+/-}, and MMTV-Wnt1-p75^{+/-} primary tumor cells were assayed at 5 μ g/well for p65, p50, p52, and Rel-B activity using the Trans AM NF- κ B Family Kit. The assay uses immobilized DNA-double strands with the consensus NF- κ B binding motif for this transcription factor family to measure the DNA-binding activity of its subunits instead of their simple presence. Bound transcription factors are then detected using specific antibodies against the NF- κ B subunits and a secondary, horseradish-peroxidase-conjugated secondary antibody. The absorbance was normalized to each subunit positive values and subsequently normalization to MMTV-Wnt1 values. (B) Proteome profiler cytokine array for nuclear extracts from MMTV-Wnt1, MMTV-Wnt1-p55^{+/-}, and MMTV-Wnt1-p75^{+/-} primary tumor cell lines. Pixel density was analyzed and normalized to MMTV-Wnt1 by ImageJ. (C) Mammosphere-forming capacity of primary tumor spheres isolated from MMTV-Wnt1, MMTV-Wnt1-p55^{+/-}, and MMTV-Wnt1-p75^{+/-} mice upon a single dose of TNF α (1, 10, 100 ng/mL) or vehicle (0.1% BSA) treatment. The number of spheres formed was counted, calculated as a ratio to the initial number of cells plated, and then normalized to the MMTV-Wnt1 vehicle control value. All experiments have been performed with at least 3 biological independent repeats. *P* values were calculated using 2-way ANOVA. **P* value < 0.05, ***P* value < 0.01, and ****P* value < 0.001.

in 4X Laemmli sample buffer containing 10% β -mercapto-ethanol for 10 min at 95°C. Equal amounts of protein were loaded onto 10% SDS-PAGE gels (1X Stacking buffer - 1.0 M Tris-HCl, 0.1% SDS, pH 6.8, 1X Separating buffer - 1.5 M Tris-HCl, 0.4% SDS, pH 8.8) and were subjected to electrophoresis in 1X Running buffer (12.5 mM Tris-base, 100 mM Glycine, 0.05% SDS), initially at 40 V for 30 min followed by 80 V for 2 h. Samples were then transferred onto 0.45 μ m nitrocellulose membrane (Bio-Rad) for 2 h at 80 V. Membranes were blocked in 1X TBST (20 mM Tris-base, 150 mM NaCl, 0.2% Tween-20) containing 5% BSA for 30 min and then washed with 1X TBST. These were then incubated with primary antibodies against Sox2 (Cell Signaling, Cat# 14962S, 1:1000), Oct4 (Cell Signaling, Cat # 2750S, 1:1000), Klf4 (Cell Signaling, Cat # 4038S, 1:1000), cMyc (Cell Signaling, Cat # 5605S, 1:1000) or GAPDH (Abcam, Cat# 9484, 1:1000) in 1X TBST containing 5% BSA overnight at 4°C with gentle rocking. Membranes were then washed three times for 5 min each with 1X TBST and incubated with a secondary anti-rabbit horseradish peroxidase-conjugated antibody (Cell Signaling, Cat # 7074S, 1:2000) in 5% BSA for 2 h at room

temperature with gentle rocking. Membranes were washed again 3 times for 5 min each with 1X TBST. Pierce ECL Plus Western Blotting Substrate (Thermo Fisher Scientific) was added to each membrane and incubated at room temperature for 5 min. The blots were then used to expose X-ray films (Agfa X-Ray film, VWR, Cat # 11299-020) in a dark room. GAPDH was used as a loading control. The bands that developed were scanned and their density was measured using ImageJ software. The ratio of the gene of interest over its endogenous loading control was calculated and expressed as relative intensity.

Nuclear proteins were extracted from MMTV-Wnt1, MMTV-Wnt1-p55^{+/-} and MMTV-Wnt1-p75^{+/-} cells. Briefly, the cells were detached and the pellet resuspended in cell lysis buffer with PMSE, DTT and protease inhibitor, incubated on ice for 20 min with intermittent tapping and inverting, then vortexed and centrifuged at 12,000 \times *g* at 4°C for 10 min. The cytoplasmic supernatant was discarded and the remaining pellet washed and resuspended in nuclear extraction buffer supplemented with PMSE, DTT, and protease inhibitor, along with 2-time sonication. The samples were

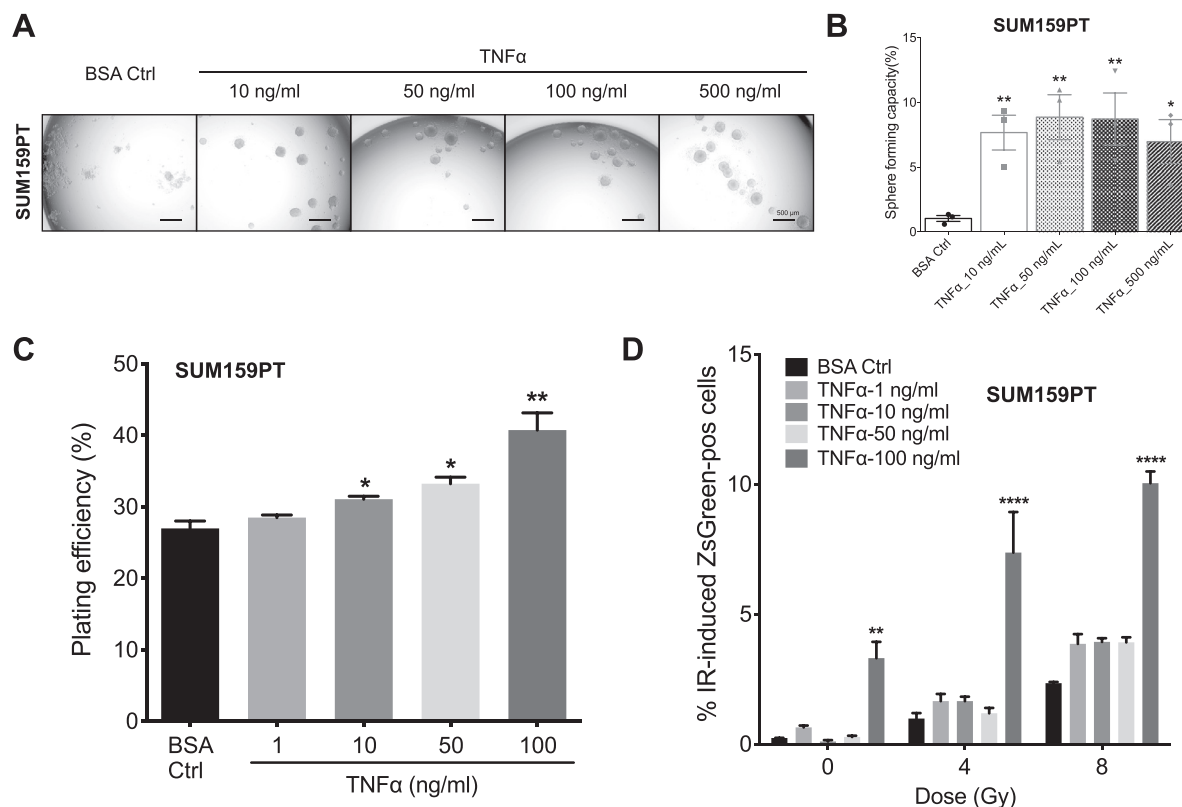


Fig. 4. TNF α increases breast cancer initiating cells and induces phenotype conversion in breast cancer cells. (A, B) Mammosphere formation assay was performed using SUM159PT mammospheres plated in a 96-well plate and treated with different concentrations of TNF α (10, 50, 100, 500 ng/mL) or vehicle (0.1% BSA). The number of mammospheres formed in each condition was counted and normalized against the vehicle control. Representative images of mammospheres in each condition (A) with the percentage of mammospheres formed (B) quantified. (C) The SUM159PT cells were plated at a density of 200 cells per well in a 6-well plate, then treated with a single dose of TNF α (1, 10, 50, 100 ng/mL) or vehicle (0.1% BSA) and cultured for 14 d. The resulting data were presented as plating efficiency with the percentage of colonies formed. (D) Sorted ZsGreen-cODC-negative SUM159PT ZsGreen-cODC vector expressing cells were plated at a density of 50,000 cells per well in a 6-well plate and the following day were pretreated with either with TNF α (1, 10, 50, 100 ng/mL) or vehicle (0.1% BSA) 1 h before irradiation at a single dose of 0, 4 or 8 Gy. Five days later, the cells were trypsinized and analyzed for ZsGreen-cODC-positive population by flow cytometry, with noninfected parental SUM159PT cells used as controls. (E) Sorted ZsGreen-cODC-negative SUM159PT cells were plated and pre-treated with 100 ng/mL TNF α or vehicle (0.1% BSA) 1 h before irradiation at a single dose of 0 or 4 or 8 Gy. The proteins were extracted 5 d later and were subjected to western blotting. The blots were analyzed for Oct4, Sox2, c-Myc, Klf4, and GAPDH, with GAPDH as the loading control. (F) The intensity of each band was quantified using ImageJ and presented as density ratio of gene over GAPDH. (G) Mammosphere formation assay were performed plating MCF-7 cells into 96-well plates, treated with different concentrations of TNF α (1, 2.5, 5, 10, 50, 100 ng/mL) or vehicle (0.1% BSA). The number of mammospheres formed in each condition was counted and quantified. (H) Sorted ZsGreen-cODC-negative MCF-7-ZsGreen-cODC cells were plated and the following day pretreated with either with TNF α (1, 2.5, 5, 10 ng/mL) or vehicle (0.1% BSA) 1 h before irradiation using a single dose of 0, 4 or 8 Gy. Five days later, the cells were trypsinized and analyzed for ZsGreen-cODC-positive cells by flow cytometry. (I, J) The MCF-7 cells were plated at a density of 200 cells per well into 6-well plates, treated with a single dose of TNF α (1, 2.5, 5, 10 ng/mL) or vehicle (0.1% BSA) and cultured for 14 d. Colony formation is shown in (I) and quantified and expressed as percentage of the number of cells plated in (J). All experiments have been performed with at least 3 biological independent repeats. *P* values were calculated using 1-way ANOVA for B, C, G, and I; 2-way ANOVA for D, F, and H. **P* value < 0.05, ***P* value < 0.01, ****P* value < 0.001, and *****P* value < 0.0001.

incubated on ice for 30 min, centrifuged at $12,000\times g$ at 4°C for 15 min and the supernatant containing the nuclear proteins was transferred into fresh tubes and quantified using the BCA protein assay (Thermo Fisher Scientific).

Quantitative reverse transcription-PCR

Total RNA was isolated using TRIZOL Reagent (Invitrogen). cDNA synthesis was carried out using the SuperScript Reverse Transcription IV (Invitrogen). Quantitative PCR was performed in the QuantStudio 3 Real-Time PCR System (Applied Biosystems, Carlsbad, CA) using the PowerUp SYBR™ Green Master Mix (Applied Biosystems). C_t for each gene was determined after normalization to GAPDH and $\Delta\Delta C_t$ was

calculated relative to the designated reference sample. Gene expression values were then set equal to $2^{-\Delta\Delta C_t}$ as described by the manufacturer of the kit (Applied Biosystems). All PCR primers were synthesized by Invitrogen with GAPDH as housekeeping genes (for primer sequences see Supplementary Table 1).

NF- κ B DNA-binding assay

The DNA-binding activity of NF- κ B was quantified by enzyme-linked immunosorbent assay using the TransAM NF- κ B family activation assay kit (Active Motif North America, Carlsbad, CA) to specifically detect and quantify the DNA-binding capacity of the NF- κ B subunits p65, p50,

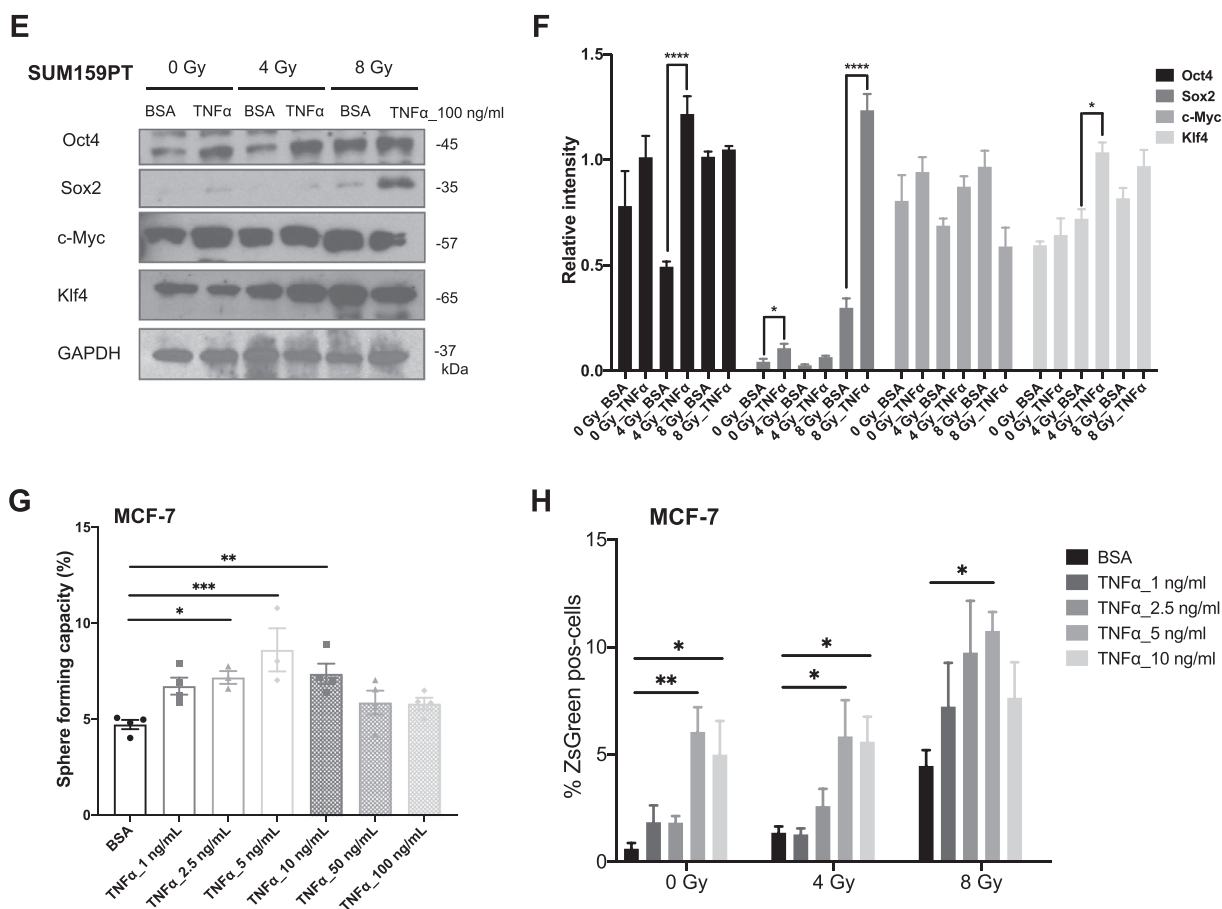


Fig. 4. Continued

p52, and Rel-B. The assay was performed according to the manufacturer's protocol and analyzed using a microplate absorbance reader (Spectramax M5, Molecular Devices, San Jose, CA).

Proteome Profiler cytokine array

The MMTV-Wnt1, MMTV-Wnt1-p55^{+/-}, and MMTV-Wnt1-p75^{+/-} primary tumor cells were plated, serum-starved overnight and placed into fresh serum-free medium the next day. Twenty-four h later, the cell culture medium was collected and centrifuged to remove insoluble materials. Secreted cytokines were measured using the Proteome Profiler Mouse Cytokine Panel A Array Kit (R&D Systems, Minneapolis, MN) according to the manufacturer's instructions. The kit consists of a nitrocellulose membrane containing 40 different anti-cytokine/chemokine antibodies spotted in duplicate. Briefly, membranes were incubated with blocking buffer at room temperature for 1 h. Cell supernatants (1 mL) were mixed with a biotinylated detection antibody cocktail at room temperature for 1 h, and then each was incubated with a membrane overnight at 4°C. The arrays were then washed 3 times for 10 min and subsequently incubated with horseradish peroxidase-conjugated streptavidin for 30 min at room temperature. The arrays were exposed to peroxidase substrate (ECL Western blotting detection reagent; Amersham Bioscience). Luminescence was detected using X-ray films, the films were scanned, and signals were quantified using the ImageJ software package. The data were normalized using the internal controls included on each array.

TCGA data mining and analysis

The Cancer Genome Atlas (TCGA) data set was accessed via the cBioPortal [22,23] and the TCGA Provisional dataset (captured December 10, 2019) was interrogated. The overall survival data and the expression data (RNA-Seq V2 RSEM Z scores for TCGA Provisional data) for TNFRSF1A and TNFRSF1B, which encode the TNFR1 and TNFR2 receptors respectively, were downloaded. Patients with both gene expression and survival data accessible were used for analysis (N = 1078). Kaplan-Meier survival analysis was performed using a Z-score cut-off of 1.0, and the patients were stratified into subgroups with over-expression, under-expression, or normal expression for each receptor. Overall survival times were used to calculate Kaplan-Meier estimates.

Statistics

All analyses were performed in the GraphPad Prism 8.0 software package. A 2-sided Student's *t* test was used for un-paired comparisons, and a 1-way or 2-way ANOVA with a post hoc Bonferroni adjustment was used for comparisons between 3 or more groups. A log-rank test was used to determine the *P* value for the Kaplan-Meier survival curves. A *P* value <0.05 was considered as statistically significant. All in vitro experiments were performed in at least 3 independent biological samples.

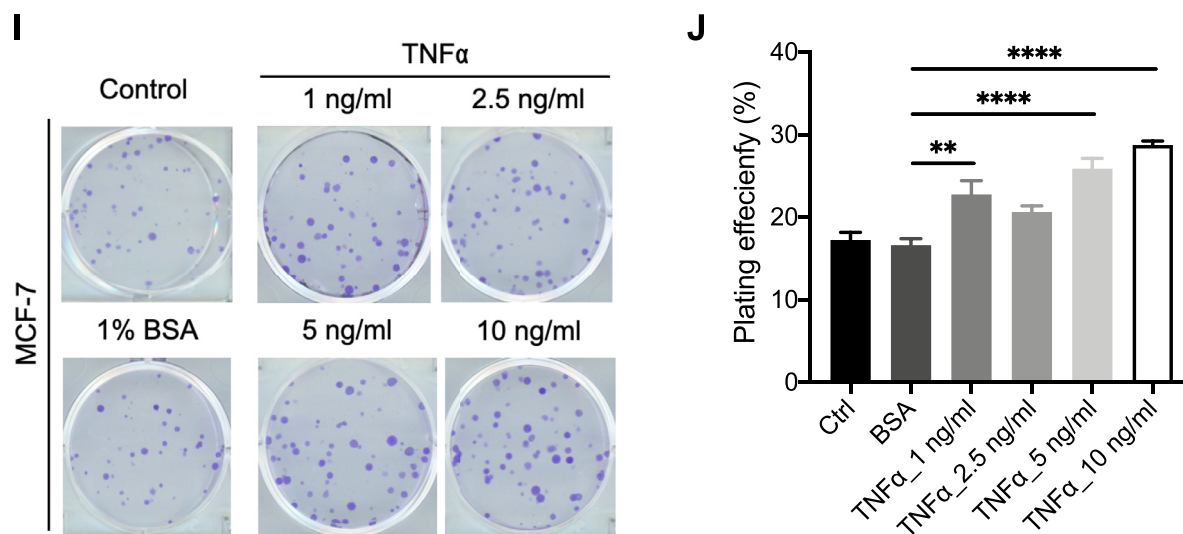


Fig. 4. Continued

Results

Loss of TNFR2 signaling impacts mammary gland development

In order to explore if TNF α , a major mediator of inflammation, affects the normal mammary gland development via TNF α /TNFR signaling, we utilized knockout mouse strains for the TNF receptors. Using whole mounts of the fourth mammary gland of prepubescent, 6-wk-old female C57BL/6, TNFR1 (p55) KO or TNFR2 (p75) KO animals (Figure 1A), we found a significant increase in the mammary gland area in both, p55 (3.1-fold, P value = 0.0001) and p75 (3.6-fold, P value < 0.0001) KO animals (Figure 1B). Compared to C57BL/6 wild-type animals, p55 KO animals had slightly decreased number of terminal end buds (TEBs), while showing a significant 2.3-fold (P value < 0.0001) increase in the number of side-buds. However, both TEBs and side-buds were significantly enriched in p75KO mice, with 3-fold (P value < 0.0001) increase in the number of TEBs and 1.8-fold (P value = 0.0003) increase in side-buds (Figure 1C). Expression of the MMTV-Wnt1 transgene leads to robust breast cancer formation in C57BL/6 mice [24]. A comparison of the mammary gland areas between 6-wk-old C57BL/6 wild type and MMTV-Wnt1 transgenic animals showed a 1.9-fold (P value = 0.0225) increase in MMT-Wnt1 animals, consistent with the published hyperproliferative phenotype of the mammary epithelium in this strain [24]. In order to test if p55 or p75 affects tumor formation under a genetic background prone to mammary carcinogenesis we next crossed MMTV-Wnt1 animals with p55 or p75 KO animals leading to animals with a hemizygous loss of the p55 or p75 gene and expression of the MMTV-Wnt1 transgene.

Mammary gland areas in MMTV-Wnt1-p75^{+/-} mice were significantly larger than in MMTV-Wnt1 mice (1.7-fold, P value = 0.0075; Figure 1D/E) but did not differ from MMTV-Wnt1-p55^{+/-} mice (P value = 0.429). The number of TEBs in MMTV-Wnt1 mice was highly increased over those in wild-type mice and drastically increased in MMTV-Wnt1-p75^{+/-} mice, which made their quantification impossible (Figure 1A/D). This suggested that hemizygous loss of either the p55 or p75 allele impacts mammary gland development when crossed with the MMTV-Wnt1 strain. In order to test for effects of the TNF receptors on the function of mammary epithelial stem cells we isolated the epithelial cells from the fat pads and subjected them to mammosphere formation assays. Mammary epithelial cells (MECs) from MMTV-Wnt1-p75^{+/-} mice showed a 10.3-fold increase (P value = 0.0003)

and a 6.6-fold increase (P value < 0.0001) in mammosphere formation at 2 wk and 3 wk in culture respectively, when compared to MECs from MMTV-Wnt1 mice (Figure 1F), which is consistent with increased numbers of TEBs and indicative of increased number of mammary epithelial stem cells [25].

As macrophages are indispensable regulators for ductal outgrowth during mammary gland development, so we assessed the number of macrophages in mammary glands of 6-wk-old MMTV-Wnt1, MMTV-Wnt1-p55^{+/-}, or MMTV-Wnt1-p75^{+/-} animals. Using the macrophage marker F4/80, the M1 activated macrophage marker iNOS and the M2 activated macrophage marker Arginase-1 we found elevated number of total macrophages as well as activated M1 and M2 macrophages associated with the mammary gland ductal system of MMTV-Wnt1-p75^{+/-} mice when compared to MMTV-Wnt1 or MMTV-Wnt1-p55^{+/-} animals (Figure 1G, H).

Loss of one TNFR2 allele accelerates breast cancer development in female MMTV-Wnt1 transgenic mice

Next, we assessed the tumor incidences in MMTV-Wnt1 mice and MMTV-Wnt1 mice crossed with p55 and p75 KO animals. Half of the female MMTV-Wnt1 mice developed mammary tumors over the course of 2 y, which was consistent with tumor incidences reported for this strain in the literature [24]. MMTV-Wnt1-p55^{+/-} mice showed a slightly higher incidence of mammary tumors but this difference was not statistically significant (Figure 2A). However, in MMTV-Wnt1-p75^{+/-} mice mammary tumors developed more rapidly with all animals showing breast tumors within the first year (P value = 0.0001; Figure 2A). Histologically, tumors in MMTV-Wnt1 and MMTV-Wnt1-p55^{+/-} mice were grade 2 breast cancers while tumors in MMTV-Wnt1-p75^{+/-} mice were less differentiated and predominantly grade 3 carcinomas (Figure 2B). Furthermore, tumors from MMTV-Wnt1-p75^{+/-} mice showed higher degrees of vascularization (Figure 2C), as well as the epithelial-mesenchymal transition (EMT) markers Vimentin and Snail (Figure 2D). In order to test if EMT markers originated from tumor cells and not only from cancer-associated fibroblasts, we assessed EMT-related gene expression levels in primary tumor cell lines established from the tumors. In accordance with the immunohistochemistry staining, the MMTV-Wnt1-p75^{+/-} tumor cell lines showed significantly enhanced Vimentin, Snail, and Slug expression levels when compared to MMTV-Wnt1 cell lines, thus indicating increased EMT in MMTV-Wnt1-p75^{+/-} tumors (Figure 2E). Interestingly, Snail was barely detected in MMTV-Wnt1-p55^{+/-}

tumor cell lines, which was in line with the minimal signal observed after immunohistochemistry staining. Furthermore, grading of the tumor sections by a clinical breast cancer pathologist showed a trend for increased numbers of proliferating tumor cells positive for nuclear Ki67 in MMTV-Wnt1-p75^{+/-} tumors (Figure 2F/G).

Next, we validated the more aggressive phenotype of tumors in MMTV-Wnt1-p75^{+/-} mice using a functional trans-well assay. A comparison of tumor cells from breast cancer lines established from tumors of MMTV-Wnt1, MMTV-Wnt1-p55^{+/-} or MMTV-Wnt1-p75^{+/-} mice revealed higher migration and invasion capacity in lines established from MMTV-Wnt1-p75^{+/-} breast cancers (Figure 2H/I). Furthermore, cells derived from MMTV-Wnt1-p75^{+/-} tumors exhibited increased mammosphere formation (Figure 2J) and clonogenic plating efficiency (Figure 2K) when compared to both MMTV-Wnt1 and MMTV-Wnt1-p55^{+/-} cell lines, thus indicating higher numbers of BCICs and clonogenic cells, respectively.

Loss of one TNFR2 allele activates canonical NF-κB signaling

To gain insight into the mechanisms of how knockout of one p75 allele affects mammary gland development and breast carcinogenesis, we next compared the DNA-binding activity of NF-κB family subunits among the primary tumor cell lines using an ELISA-based assay. Nuclear extracts from MMTV-Wnt1-p75^{+/-} cell lines exhibited significantly higher activation of the p50 NF-κB subunit than MMTV-Wnt1 cell lines, while the MMTV-Wnt1-p55^{+/-} cell lines had higher activity of the p52 NF-κB subunit and reduced activity of p65 and p50 subunits (Figure 3A). Together this suggested preferential signaling through the canonical NF-κB signaling pathway in MMTV-Wnt1-p75^{+/-} cell lines.

To further explore the activation of the canonical NF-κB signaling pathway in MMTV-Wnt1-p75^{+/-} cell lines, we next assessed its pro-inflammatory downstream targets [26,27] using cytokine arrays. Compared to MMTV-Wnt1-derived lines, MMTV-Wnt1-p75^{+/-} cell lines showed more abundant secretion of pro-inflammatory cytokines IFN-γ (2.68-fold, *P*value = 0.0097), IL-1α (2.96-fold, *P*value = 0.0023), TNFα (3.25-fold, *P*value = 0.0004), and IL-12 p70 (2.37-fold, *P*value = 0.0393), while the anti-inflammatory cytokine IL-10 (0.19-fold, *P*value = 0.0409) was significantly diminished (Figure 3B). Consistent with increased migratory capacity and increased expression of EMT markers, the level of the chemotaxis-related chemokine CXCL1 was increased in MMTV-Wnt1-p75^{+/-} cell lines (2.62-fold, *P*value = 0.0133, Figure 3B).

Finding 3-fold increase of tumor-derived TNFα secretion in MMTV-Wnt1-p75^{+/-} cell lines, we next explored the effects of exogenous TNFα ligand on self-renewal capacity of MMTV-Wnt1, MMTV-Wnt1-p55^{+/-} and MMTV-Wnt1-p75^{+/-} tumor cell lines. Using mammosphere formation assay, we observed a significant increase in mammosphere formation in response to TNFα treatment in MMTV-Wnt1 and MMTV-Wnt1-p55^{+/-} cell lines, suggesting TNFα could promote self-renewal capacity in breast cancer cells (Figure 3C). However, this effect of TNFα was not notable in MMTV-Wnt1-p75^{+/-} cell lines.

TNFα induces phenotype conversion in human breast cancer cells

Next, we sought to test the effects of TNFα on both SUM159PT human triple-negative and MCF-7 human luminal breast cancer cells. Treatment with TNFα caused a significant increase in mammosphere formation suggesting that self-renewal in breast cancer cells is regulated by TNFα (Figure 4A/B and G). This effect of TNFα extended to an increased plating efficiency in a classic clonogenic survival assay (Figure 4C/I). We had previously reported that irradiation of nontumorigenic breast cancer cells led to the induction of a BCIC phenotype [13]. Using a reporter system that marks BCICs through accumulation of the fluorescent protein ZsGreen [12,14,28] we removed preexisting BCICs by FACS and irradiated

the remaining non-BCICs with 0, 4 or 8 Gy in the presence or absence of TNFα. After 5 d in culture, we observed a radiation-induced phenotype conversion of non-BCICs into induced BCICs and an amplification of this effect in the presence of TNFα (Figure 4D/H). This phenotype conversion correlated with the induction of the Yamanaka transcription factors Oct4, Sox2, and Klf4 (Figure 4E/F), which can be used to reprogram somatic cells into induced pluripotent stem cells (iPSCs) [29].

Down-regulated TNFR2 expression is associated with decreased overall survival in breast cancer patients

To further investigate whether TNFR expression is associated with the clinical outcome of breast cancer patients, we analyzed overall survival data from 1078 breast cancer patients in the TCGA Provisional dataset, stratified into subgroups with up-, down-regulated or unchanged expression of TNFR1 and 2 using a Z-score cut-off of 1.0. The median survival of patients in the subgroup with up-regulated TNFR1 expression was significantly higher (211.09 months, *P*value = 0.0366) than that of patients in the subgroup with normal expression (127.23 months), while the median survival of patients with down-regulated TNFR1 expression was 114.06 months (*P*value = 0.8783; Figure 5A/B). On the contrary, patients with down-regulated expression of TNFR2 showed an inferior median overall survival 89.09 months when compared to the median survival of 127.23 months for patients with normal receptor expression (*P*value = 0.0376). The median survival of patients with upregulated TNFR2 expression was 244.91 months, but this was not statistically significant (*P*value = 0.146) when compared to the median survival of patients with normal receptor expression (Figure 5C/D).

Discussion

Pro-inflammatory conditions are in large part driven by TNFα and have long been known to promote the development of malignancies including breast cancer [30,31]. In tumors, TNFα plays a critical role in proliferation, angiogenesis, invasion and metastasis via signaling through the TNFα/NF-κB axis [32]. However, it has been unclear, which signaling events downstream of TNFα receptors affect tumorigenesis.

In this study, we show that the homozygous knockout of either TNFR1 or TNFR2 alone increased the mammary epithelial stem cell numbers and led to accelerated prepubescent mammary gland development with hyperplastic ductal outgrowth and larger gland areas when compared to age-matched C57BL/6 wild-type animals. However, with over the past 20 years of breeding p55 and p75 KO animals we have never observed an increase in spontaneous breast cancer in either of the TNFR knock-out strains, consistent with the resistance of their genetic C57BL/6 background strain against spontaneous breast cancer development [33]. When p75 or p55 knock-out animals were crossed with MMTV-Wnt1 transgenic animals to study the effects of TNF receptors on spontaneous breast carcinogenesis, MMTV-Wnt1-p75^{+/-} animals not only exhibited enhanced ductal outgrowth and greater mammary gland area, but also showed increased numbers of total, and both, M1 and M2 macrophages. Macrophages were associated with mammary epithelial cells, consistent with the important role of the microenvironment in ductal outgrowth. Our study did not investigate if hemizygous loss of p55 or p75 in the absence of the MMTV-Wnt1 transgene affects mammary gland development and this needs to be explored in future studies. Furthermore, in the litters of TNFR2 KO mice that were crossed with MMTV-Wnt1 transgenic animals, prone to develop mammary tumors [24], the onset of breast cancer was significantly accelerated and the tumors showed a more aggressive phenotype. This was also reflected in increased numbers of Ki67-, Vimentin- and Snail-positive cells. Vimentin-positive cells were primarily located at the invasive front of the tumors. In contrast, Snail-positive cells were located in the core of the tumors and were almost completely absent in

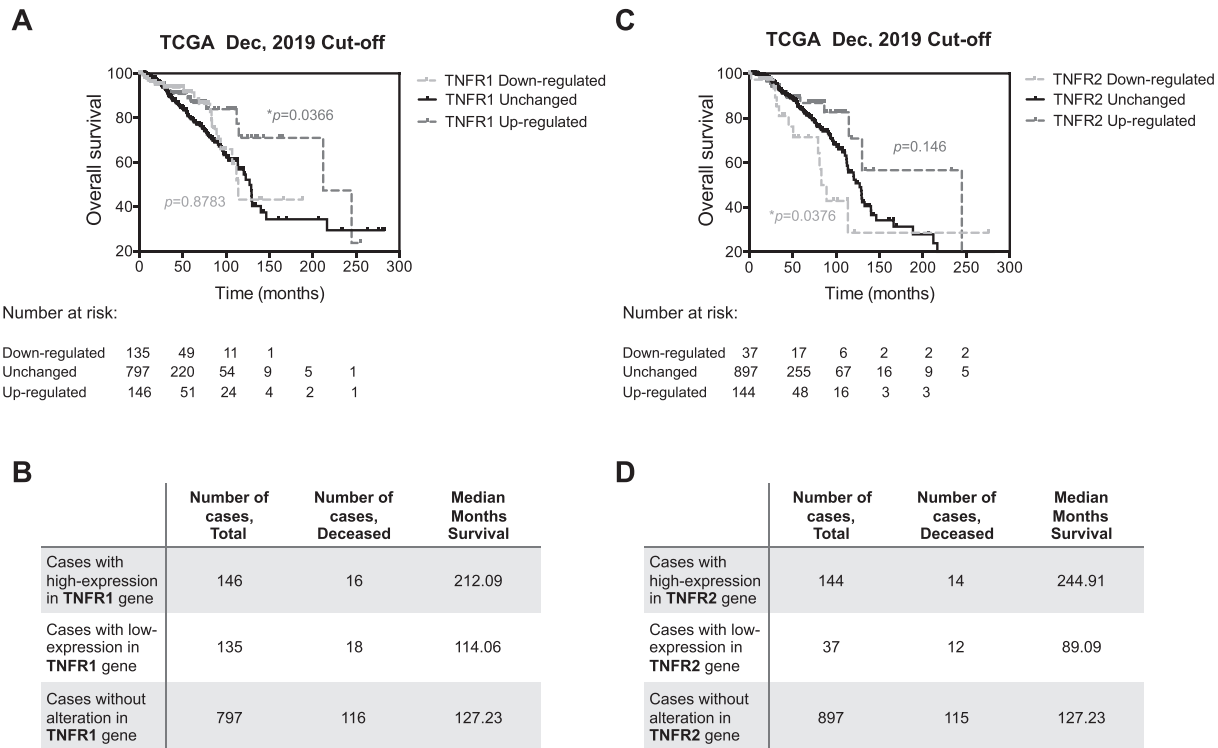


Fig. 5. Overall survival evaluation of TNFR1 and TNFR2 signature in TCGA breast cancer patients. (A) The overall survival (OS) in breast cancer patients from TCGA stratified by TNFR1 mRNA expression. The light gray dotted line indicates patients with down-regulated expression of TNFR1, the dark gray dotted line represents the patients with up-regulated TNFR1 expression and the black line represents the unchanged population. OS in TNFR1 up-regulated subgroup was significantly better than that of the unchanged group (log rank test, P value = 0.0366). (B) The total case number, the deceased case number and the median survival of patients with down-regulated, unchanged or up-regulated TNFR1 expression. (C) OS in breast cancer patients from TCGA stratified by TNFR2 mRNA expression. The light gray dotted line indicates patients with down-regulated expression of TNFR2, the dark gray dotted line represents the patients with up-regulated TNFR2 expression and the black line represents the unchanged population. OS in TNFR2 down-regulated subgroup was significantly worse than that of the unchanged group (log rank test, P value = 0.0376). The number of patients at risk is listed below the Kaplan-Meier curves. (D) The total case number, the deceased case number, and the median survival time of patients with down-regulated, unchanged, or up-regulated TNFR2 expression. P values were calculated using Log-rank (Mantel-Cox) test. * P value < 0.05.

tumors from MMTV-Wnt1-p55^{+/-} mice, consistent with a less aggressive phenotype. Previous reports demonstrated TNF α -induced EMT via Snail [34,35], an important transcriptional repressor of E-cadherin. Loss of E-cadherin is a hallmark of EMT during which epithelial cells lose their polarity, cell-cell adhesion, epithelial characteristics and acquire migratory and invasive mesenchymal properties. The absence of Snail in tumors from MMTV-Wnt1-p55^{+/-} mice suggested a possible role of TNFR2 but not TNFR1 in TNF α /Snail axis of EMT.

Compared to less aggressive tumors developing in MMTV-Wnt1 animals, tumors in MMTV-Wnt1-p75^{+/-} animals showed elevated DNA-binding capacity of the NF- κ B subunit p50, which indicated a preferential response of these tumors to TNF α and Interleukine-1 (IL-1) through NF- κ B p50/p50 homodimers and the canonical NF- κ B signaling pathway. In contrast, tumors in MMTV-Wnt1-p55^{+/-} animals showed elevated DNA-binding capacity of the NF- κ B subunit p52, which signals through the noncanonical NF- κ B pathway, does not respond to TNF α , and exclusively depends on IKK α but not IKK β and IKK γ [36].

Consistent with an activation of the canonical NF- κ B signaling pathway, tumor cell lines derived from MMTV-Wnt1-p75^{+/-} mammary tumors showed significantly upregulated levels of the pro-inflammatory cytokines IFN- γ , IL-1 α , TNF α , IL-12 and the chemotaxis-related CXCL1 chemokine. Treatment of tumor cell lines derived from MMTV-Wnt1 and MMTV-Wnt1-p55^{+/-} breast tumors as well as the triple-negative human breast cancer

line SUM159PT with exogenous TNF α led to a dose-dependent increase in mammosphere formation and also an increased plating efficacy in the colony-forming assays. On the contrary, tumor cell lines derived from MMTV-Wnt1-p75^{+/-} breast tumors did not respond to TNF α but showed higher baseline mammosphere formation comparable to that of MMTV-Wnt1 and MMTV-Wnt1-p55^{+/-} cell lines stimulated with high concentrations of TNF α , results consistent with an autocrine pro-inflammatory loop. It is noteworthy that when BCICs were purged from SUM159PT cells as described previously [14], treatment with TNF α or radiation led to re-expression of the developmental transcription factors Oct4, Sox2, and Klf4 and that coincided with a phenotype conversion in some of the remaining non-BCICs into induced BCICs. The combined treatment with radiation and a high concentration of TNF α appeared to have an additive effect. These findings were in line with our previous report on radiation-induced phenotype conversion in breast cancer [13]. Inflammatory breast cancer is a rare and aggressive form of the disease with worse survival than other types of breast cancer [37]. Our observation of TNF α -induced phenotype conversion could be one aspect of the aggressive phenotype of inflammatory breast cancer.

Finally, we analyzed the overall survival of 1078 breast cancer patients in the TCGA Provisional dataset. Patients with upregulated TNFR1 expression showed significantly increased overall survival while patients with down-regulated TNFR2 expression had a significantly reduced overall survival, thus supporting the clinical significance of our experimental findings. A shortfall

of our study is that the TCGA data are based on gene expression changes in the bulk tumor material. However, while this material will certainly also contain mRNA from immune cells, one can assume that those changes in TNFR1 and TNFR2 expression primarily reflect expression changes in tumor cells, indicating a role for TNFR signaling imbalances in modulating the aggressiveness of breast cancer cells directly and not necessarily through immunomodulation alone. Future studies should employ single cell or single nuclei RNA-Sequencing to further clarify this question.

We are not the first to report an effect of TNF α on the mammary gland. TNF α has been shown to increase the growth of both normal and malignant mammary epithelial cells in experimental models [38,39] and has been associated with tumorigenesis by affecting stem cell fate and inducing the transformation of normal stem cells [40,41]. TNF α exerts its activity by stimulation of its receptors TNFR1 and TNFR2. These 2 receptors trigger distinct and common signaling pathways that control cell apoptosis and survival [5]. However, to our best knowledge, the effects of imbalances in TNFR1 and TNFR2 signaling on mammary gland development and carcinogenesis have never been studied as per the literature.

In our present study, we elucidated the role of TNFRs in mammary gland development and carcinogenesis using genetic mouse models. While expression of the MMTV-Wnt1 transgene in our model was restricted to the mammary epithelium, TNFRs were knocked out globally, suggesting that the effects observed were not just from the changes in the mammary epithelium and the tumor cells derived from it or the surrounding microenvironment, but could also have rather also accounted for systemic changes of immunity and inflammation. By testing the effects of TNF α on mammary epithelial cells and mammary tumor cells derived from our different mouse strains in vitro we were able to separate these effects, demonstrating a clear role for TNF α in the self-renewal of normal mammary epithelial stem cells as well as BCICs.

Macrophages are important regulators of mammary gland developmental processes, especially during puberty stage when they are recruited to the neck region of the TEBs and guide the mammary gland ducts out-branching [42]. Furthermore, macrophages are mediators of inflammation, play an indispensable role in modulating innate immune responses and interacting as tumor-associated macrophages with the surrounding microenvironment [43]. However, the effects of both the resident macrophages and the tumor-associated macrophages on tumorigenesis or progression are still incompletely understood. In our present study, we did not perform longitudinal studies to address whether macrophages were responsible for increased ductal outgrowth and numbers of TEBs or if instead TNFR signaling imbalances in epithelial cells were the primary cause for this phenotype with macrophages secondarily associating with the ductal system. Future studies are warranted to address these outstanding questions.

Conclusions

We conclude that the roles of TNFR1 and TNFR2 in breast cancer development and progression are rather complex and go far beyond the pro-inflammatory properties of TNF α . It still needs to be determined if selective targeting of the receptors by e.g., specific TNFR2 agonists or TNF α inhibitors [44–46] can modulate mammary carcinogenesis and disease progression.

Availability of data and materials

All data and methods are included in the manuscript. Tumor-derived cell lines will be made available from the corresponding author upon reasonable request.

Author contributions

LH, KB, SD, AI, LZ performed the experiments and collected the data. NTN helped capturing immunohistochemistry and transwell images. NAM performed the tumor grading analysis. LH and FP analyzed the data and wrote the manuscript. FP conceived of the study. All authors edited and approved of the final version of the manuscript.

Funding

FP was supported by grants from the National Cancer Institute (R01CA161294, 5R01CA200234, P50CA211015) and a grant from the National Institute of Allergy and Infectious Diseases (AI067769).

Conflict of interest

The authors declare no competing interests.

Supplementary materials

Supplementary material associated with this article can be found, in the online version, at [doi:10.1016/j.neo.2020.12.007](https://doi.org/10.1016/j.neo.2020.12.007).

References

- [1] Jiralerspong S, Goodwin PJ. Obesity and breast cancer prognosis: evidence, challenges, and opportunities. *J Clin Oncol* 2016;**34**:4203–16.
- [2] Travis LB, Hill D, Dores GM, Gospodarowicz M, van Leeuwen FE, Holowaty E, Glimelius B, Andersson M, Pukkala E, Lynch CF, et al. Cumulative absolute breast cancer risk for young women treated for Hodgkin lymphoma. *J Natl Cancer Inst* 2005;**97**:1428–37.
- [3] Hotamisligil GS, Spiegelman BM. Tumor necrosis factor alpha: a key component of the obesity-diabetes link. *Diabetes* 1994;**43**:1271–8.
- [4] Chiang CS, McBride WH. Radiation enhances tumor necrosis factor alpha production by murine brain cells. *Brain Res* 1991;**566**:265–9.
- [5] Wajant H, Sigmund D. TNFR1 and TNFR2 in the control of the life and death balance of macrophages. *Front Cell Dev Biol* 2019;**7**:91.
- [6] Balkwill F. Tumour necrosis factor and cancer. *Nat Rev Cancer* 2009;**9**:361–71.
- [7] Miles DW, Happerfield LC, Naylor MS, Bobrow LG, Rubens RD, Balkwill FR. Expression of tumour necrosis factor (TNF alpha) and its receptors in benign and malignant breast tissue. *Int J Cancer* 1994;**56**:777–82.
- [8] Hagemann T, Wilson J, Kulbe H, Li NF, Leinster DA, Charles K, Klemm F, Pukrop T, Binder C, Balkwill FR. Macrophages induce invasiveness of epithelial cancer cells via NF-kappa B and JNK. *J Immunol* 2005;**175**:1197–205.
- [9] Ghosh S, May MJ, Kopp EB. NF-kappa B and Rel proteins: evolutionarily conserved mediators of immune responses. *Annu Rev Immunol* 1998;**16**:225–60.
- [10] Wang W, Nag SA, Zhang R. Targeting the NFkappaB signaling pathways for breast cancer prevention and therapy. *Curr Med Chem* 2015;**22**:264–89.
- [11] Sheng Y, Li F, Qin Z. TNF receptor 2 makes tumor necrosis factor a friend of tumors. *Front Immunol* 2018;**9**:1170.
- [12] Vlashi E, Kim K, Lagadee C, Donna LD, McDonald JT, Eghbali M, Sayre JW, Stefani E, McBride W, Pajonk F. In vivo imaging, tracking, and targeting of cancer stem cells. *J Natl Cancer Inst* 2009;**101**:350–9.
- [13] Lagadee C, Vlashi E, Della Donna L, Dekmezian C, Pajonk F. Radiation-induced reprogramming of breast cancer cells. *Stem Cells* 2012;**30**:833–44.
- [14] Bhat K, Sandler K, Duhachek-Muggy S, Alli C, Cheng F, Moatamed NA, Magyar CE, Du L, Li G, McCloskey S, et al. Serum erythropoietin levels, breast cancer and breast cancer-initiating cells. *Breast Cancer Res* 2019;**21**:17.
- [15] Lagadee C, Vlashi E, Bhuta S, Lai C, Mischel P, Werner M, Henke M, Pajonk F. Tumor cells with low proteasome subunit expression predict overall survival in head and neck cancer patients. *BMC Cancer* 2014;**14**:152.

- [16] Muramatsu S, Tanaka S, Mogushi K, Adikrisna R, Aihara A, Ban D, Ochiai T, Irie T, Kudo A, Nakamura N, et al. Visualization of stem cell features in human hepatocellular carcinoma reveals in vivo significance of tumor-host interaction and clinical course. *Hepatology* 2013;**58**:218–28.
- [17] Pan J, Zhang Q, Wang Y, You M. 26S proteasome activity is down-regulated in lung cancer stem-like cells propagated in vitro. *PLoS One* 2010;**5**:e13298.
- [18] Hayashi K, Tamari K, Ishii H, Konno M, Nishida N, Kawamoto K, Koseki J, Fukusumi T, Kano Y, Nishikawa S, et al. Visualization and characterization of cancer stem-like cells in cervical cancer. *Int J Oncol* 2014;**45**:2468–74.
- [19] Adikrisna R, Tanaka S, Muramatsu S, Aihara A, Ban D, Ochiai T, Irie T, Kudo A, Nakamura N, Yamaoka S, et al. Identification of pancreatic cancer stem cells and selective toxicity of chemotherapeutic agents. *Gastroenterology* 2012;**143**:234–45 e237.
- [20] Tamari K, Hayashi K, Ishii H, Kano Y, Konno M, Kawamoto K, Nishida N, Koseki J, Fukusumi T, Hasegawa S, et al. Identification of chemoradiation-resistant osteosarcoma stem cells using an imaging system for proteasome activity. *Int J Oncol* 2014;**45**:2349–54.
- [21] Qian Y, Wu X, Yokoyama Y, Okuzaki D, Taguchi M, Hirose H, Wang J, Hata T, Inoue A, Hiraki M, et al. E-cadherin-Fc chimera protein matrix enhances cancer stem-like properties and induces mesenchymal features in colon cancer cells. *Cancer Sci* 2019;**110**:3520–32.
- [22] Cerami E, Gao J, Dogrusoz U, Gross BE, Sumer SO, Aksoy BA, Jacobsen A, Byrne CJ, Heuer ML, Larsson E, et al. The cBio cancer genomics portal: an open platform for exploring multidimensional cancer genomics data. *Cancer Discov* 2012;**2**:401–4.
- [23] Gao J, Aksoy BA, Dogrusoz U, Dresdner G, Gross B, Sumer SO, Sun Y, Jacobsen A, Sinha R, Larsson E, et al. Integrative analysis of complex cancer genomics and clinical profiles using the cBioPortal. *Sci Signal* 2013;**6**:pl1.
- [24] Li Y, Hively WP, Varmus HE. Use of MMTV-Wnt-1 transgenic mice for studying the genetic basis of breast cancer. *Oncogene* 2000;**19**:1002–9.
- [25] Bandyopadhyay A, Dong Q, Sun LZ. Stem/progenitor cells in murine mammary gland: isolation and functional characterization. *Methods Mol Biol* 2012;**879**:179–93.
- [26] Lawrence T. The nuclear factor NF-kappa B pathway in inflammation. *Cold Spring Harb Perspect Biol* 2009;**1**:a001651.
- [27] Hoesel B, Schmid JA. The complexity of NF-kappa B signaling in inflammation and cancer. *Mol Cancer* 2013;**12**:86.
- [28] Duhachek-Muggy S, Bhat K, Medina P, Cheng F, He L, Alli C, Saki M, Muthukrishnan SD, Ruffenach G, Eghbali M, et al. Radiation mitigation of the intestinal acute radiation injury in mice by 1-[(4-nitrophenyl)sulfonyl]-4-phenylpiperazine. *Stem Cells Transl Med* 2020;**9**:106–19.
- [29] Yamanaka S, Blau HM. Nuclear reprogramming to a pluripotent state by three approaches. *Nature* 2010;**465**:704–12.
- [30] Coussens LM, Werb Z. Inflammation and cancer. *Nature* 2002;**420**:860–7.
- [31] Grivennikov SI, Greten FR, Karin M. Immunity, inflammation, and cancer. *Cell* 2010;**140**:883–99.
- [32] Ham B, Fernandez MC, D'Costa Z, Brodt P. The diverse roles of the TNF axis in cancer progression and metastasis. *Trends Cancer Res* 2016;**11**:1–27.
- [33] Medina D. Of mice and women: a short history of mouse mammary cancer research with an emphasis on the paradigms inspired by the transplantation method. *Cold Spring Harb Perspect Biol* 2010;**2**:a004523.
- [34] Wang H, Wang HS, Zhou BH, Li CL, Zhang F, Wang XF, Zhang G, Bu XZ, Cai SH, Du J. Epithelial-mesenchymal transition (EMT) induced by TNF-alpha requires AKT/GSK-3beta-mediated stabilization of snail in colorectal cancer. *PLoS One* 2013;**8**:e56664.
- [35] Wang Y, Zhou BP. Epithelial-mesenchymal transition in breast cancer progression and metastasis. *Chin J Cancer* 2011;**30**:603–11.
- [36] Oeckinghaus A, Ghosh S. The NF-kappa B family of transcription factors and its regulation. *Cold Spring Harb Perspect Biol* 2009;**1**:a000034.
- [37] Menta A, Fouad TM, Lucci A, Le-Petross H, Stauder MC, Woodward WA, Ueno NT, Lim B. Inflammatory breast cancer: what to know about this unique, aggressive breast cancer. *Surg Clin North Am* 2018;**98**:787–800.
- [38] Varela LM, Ip MM. Tumor necrosis factor-alpha: a multifunctional regulator of mammary gland development. *Endocrinology* 1996;**137**:4915–24.
- [39] Warren MA, Shoemaker SF, Shealy DJ, Bshar W, Ip MM. Tumor necrosis factor deficiency inhibits mammary tumorigenesis and a tumor necrosis factor neutralizing antibody decreases mammary tumor growth in neu/erbB2 transgenic mice. *Mol Cancer Ther* 2009;**8**:2655–63.
- [40] Wang L, Zhao Y, Liu Y, Akiyama K, Chen C, Qu C, Jin Y, Shi S. IFN-gamma and TNF-alpha synergistically induce mesenchymal stem cell impairment and tumorigenesis via NF kappa B signaling. *Stem cells* 2013;**31**:1383–95.
- [41] Afify SM, Seno M. Conversion of stem cells to cancer stem cells: undercurrent of cancer initiation. *Cancers (Basel)* 2019;**11**:345.
- [42] Gouon-Evans V, Lin EY, Pollard JW. Requirement of macrophages and eosinophils and their cytokines/chemokines for mammary gland development. *Breast Cancer Res* 2002;**4**:155–64.
- [43] DeNardo DG, Coussens LM. Inflammation and breast cancer. Balancing immune response: crosstalk between adaptive and innate immune cells during breast cancer progression. *Breast Cancer Res* 2007;**9**:212.
- [44] Leung CH, Zhong HJ, Yang H, Cheng Z, Chan DS, Ma VP, Abagyan R, Wong CY, Ma DL. A metal-based inhibitor of tumor necrosis factor-alpha. *Angew Chem Int Ed Engl* 2012;**51**:9010–14.
- [45] Mercogliano MF, Bruni S, Elizalde PV, Schillaci R. Tumor necrosis factor alpha blockade: an opportunity to tackle breast cancer. *Front Oncol* 2020;**10**:584.
- [46] Kang TS, Mao Z, Ng CT, Wang M, Wang W, Wang C, Lee SM, Wang Y, Leung CH, Ma DL. Identification of an iridium (III)-based inhibitor of tumor necrosis factor-alpha. *J Med Chem* 2016;**59**:4026–31.

3.2 SUMMARIES & CONTRIBUTIONS

Research in the Pajonk lab aims to address important questions relating to radiobiology, cancer stem cells, drug discovery and radiation mitigation, primarily using glioblastoma and breast cancer models. Since joining the lab, I have actively contributed to projects in these areas of research, resulting in co-authorship on the publications (some pending journal review) discussed in this chapter. More specifically, the papers presented hereafter can be divided into four main categories: i) prevention of radiation-induced phenotypic conversion of non-stem cancer cells to cancer stem/initiating cells in the context of glioblastoma, ii) implications of drug treatments (radiation mitigators or compounds that prevent radiation-induced phenotypic conversion) on normal tissue following irradiation, iii) leveraging radiation-induced multipotency to drive surviving GBM cells towards a mitotically incompetent, neuron-like state, and iv) pro-inflammatory signaling in mammary gland development and carcinogenesis. While my own research project aiming to identify the mechanism(s) by which radiation leads to cellular plasticity and reprogramming more closely relates to categories i & iii described above, its exploration of inflammatory signaling pathways as potential mediators of the radiation-induced cellular plasticity events can be viewed as a common, unifying theme for all categories. In the following pages I will provide an overview of each category followed by a brief study rationale/summary, and lastly include my contributions to each paper.

i) Prevention of radiation-induced phenotypic conversion of non-stem glioma cells to glioma stem/initiating cells (GSCs/GICs)

Previous research in the lab identified that radiation leads to the induction of cancer stem cells from non-stem cancer cells (K. Bhat, Saki, et al., 2020; Lagadec et al., 2012). This coincided

with the re-expression of Yamanaka factors and the acquisition of an open chromatin state at the respective YF promoter regions, pointing to radiation-induced epigenetic remodeling. Additionally, cancer stem cells are intrinsically chemo- and radiotherapy-resistant, posing an extra challenge to therapy success. Given the significant implications of this cellular population for tumor growth, therapy resistance and recurrence, a high throughput screen of 83,000 compounds was carried out to identify compounds that could potentially interfere with this process (L. Zhang et al., 2019). Among those, select dopamine receptor antagonists (DRAs) such as trifluoperazine (TFP) and quetiapine (QTP), both Food and Drug Administration (FDA)-approved drugs, were identified. Further studies were also carried out using ONC201, a novel small molecule from the imipridone class, which has shown promising clinical efficacy against high-grade diffuse pediatric gliomas. The role of these compounds in preventing radiation-induced cellular plasticity events was evaluated in glioblastoma models. Rationale behind studying DRAs is based on the fact that dopamine receptors (DRs), and specifically DRD2, have been shown to be expressed in GBM cells, and at higher levels in glioma-initiating cells (Caragher et al., 2019; Y. Li et al., 2017). Additionally, dopamine receptor signaling has been implicated in self-renewal maintenance (Y. Li et al., 2017), response to hypoxia and metabolic shifts in GBM (Caragher et al., 2019), further supporting targeting these receptors as a potential therapeutic avenue.

Paper #1: Dopamine Receptor Antagonists, Radiation, and Cholesterol Biosynthesis in Mouse Models of Glioblastoma (K. Bhat et al., 2021).

In this paper, the effects of quetiapine on radiation-induced phenotype conversion were investigated *in vitro* and *in vivo*. This was a follow-up study to the TFP paper from the lab (K. Bhat, Saki, et al., 2020) aimed at identifying a dopamine receptor antagonist with a more

favorable side effect profile than TFP, which was however still able to effectively interfere with the radiation-induced cellular plasticity events. QTP, a second-generation dopamine receptor antagonist and FDA approved drug, fit this criteria. Here we showed that while the combination of radiation with QTP was able to prevent phenotype conversion, eventually all animals succumbed to the tumor, suggesting that glioma cells became resistant to QTP. Through an RNAseq analysis it was determined that GBM cells upregulate cholesterol, sterol and lipid biosynthesis pathways as a defense mechanism. To overcome this, the use of statins in combination with IR and QTP was explored. Statins are widely used to lower cholesterol levels, as such their addition into the treatment scheme aimed at rendering GBM cells once more vulnerable to the IR+QTP treatment by inhibiting this defense mechanism. Indeed, the triple combination showed significant reduction in self-renewal capacity *in vitro* and improved median survival *in vivo*.

For this publication, I was involved with cell culture maintenance, sphere forming assays and relevant data interpretation under the guidance of my postdoc (currently assistant project scientist in the lab) mentor at the time, Dr. He. I also independently explored the RNAseq datasets using similar methods and approaches to those presented in the paper in order to address other questions of interest pertinent to my own project. Specifically, I queried the list of differentially expressed genes (DEGs) identified in the irradiation and control conditions in order to identify differentially expressed damage associated molecular patterns (DAMPs) and pattern recognition receptors (PRRs). Some receptors identified from this search were further explored to identify the pathway(s) driving radiation-induced cellular plasticity and reprogramming events. Lastly, I helped review and edit the manuscript prior to publication.

Paper #2: Effects of the DRD2/3 antagonist ONC201 and radiation in glioblastoma (L. He, Bhat, Ioannidis, et al., 2021).

Having previously established a role for DRAs in preventing the radiation-induced conversion of non-stem glioma cells to GICs, ONC201, another antagonist of dopamine receptors D2 and D3 (DRD2/3) was studied in the context of glioblastoma. Combination of this small molecule with radiation was able to prevent phenotypic conversion, reduce self-renewal, clonogenic capacity and cell viability *in vitro*. *In vivo*, combined treatment was able to prolong survival in both syngeneic and patient-derived orthotopic xenograft mouse models of GBM. GBMs are characterized by intratumoral heterogeneity as evidenced by the presence of both a proliferative and a quiescent population of cells. While both populations have comparable self-renewal capabilities, the quiescent population is thought to be more resistant to treatments (Tejero et al., 2019). Previous research in the lab had shown radiation recruiting quiescent GBM cells into the cell cycle through interference with gene sets relating to extracellular matrix (ECM) organization and cell cycle growth, both important factors for the acquisition and maintenance of GBM quiescence (K. Bhat, Saki, et al., 2020). Being able to specifically target this population of cells is of value given the poor prognosis seen in patients with increased ECM-related genes. In the present study, the combination of IR+ONC201 led to a significant downregulation in gene sets relating to GBM quiescence, cellular plasticity and stem cells. This supported the idea that while radiation recruits the quiescent GBM population into the cell cycle, addition of ONC201 to the treatment scheme is able to specifically target this otherwise resistant population of cells. These findings point to an added benefit resulting from the use of ONC201 in combination with radiation, extending beyond its ability to interfere with radiation-induced phenotypic conversion.

Regarding my contributions for this publication, I was involved with setting up and analyzing clonogenic assays for determining the radiosensitizing properties of ONC201. Additionally, I helped with the immunofluorescence experimental procedure aiming to assess the effects of ONC201 on DNA repair through the evaluation of γ H2AX foci. I also assisted with setting up, treating and counting primary sphere forming assays for determining the effects of combination treatment on the self-renewal capacity of glioma sphere samples. Thereafter, under the guidance of my mentor, Dr. He, I helped with protein isolation and quantification, as well as steps of the Western blotting procedure used for identifying ECM-related proteins pertinent to our exploration of the quiescent GBM population. While I was not directly involved in the generation of the gene set enrichment analysis (GSEA) graphs shown in this paper, I independently analyzed the RNAseq dataset we had to explore questions for my own research proposal. Through this analysis I found that compared to unirradiated controls, irradiated samples showed enrichment for pathways relating to inflammatory response, tumor necrosis factor alpha (TNF α) signaling via nuclear factor kappa beta (NF κ B), cytokine-cytokine receptor interactions and response to interleukin 1 α (IL-1 α), highlighting the role of inflammatory pathways in the radiation-induced response. Finally, I helped revise and edit the manuscript and figures prior to publication.

Paper #3: Activation of the mevalonate pathway in response to anti-cancer treatments drives glioblastoma recurrences through activation of Rac-1 (L. He, Ioannidis, et al., 2023).

In the present research paper, the upregulation of the mevalonate pathway, downstream of which is cholesterol biosynthesis, seen in cells surviving combination treatment of radiation with QTP, ONC201 as well as standard of care temozolomide (TMZ), was probed further to identify the underlying mechanism driving GBM stemness and recurrence. More specifically, given that

cholesterol is essential in helping support GBM's increased bioenergetic demands, the metabolic vulnerability created by the combination treatment of radiation with DRAs was exploited through the use of statins to determine whether effects previously established *in vitro* could also be recapitulated *in vivo*. While combination therapies converging on the immediate-early response to radiation through MAPK signaling activation were all able to upregulate the mevalonate pathway *in vitro*, these effects were limited to IR+QTP *in vivo*, and were associated with relatively small increases in cholesterol levels, unlike what was previously seen in *in vitro* shotgun lipidomic studies. Given this relatively small upregulation it was postulated that other branches of the mevalonate pathway, beyond cholesterol biosynthesis, might actually be driving GBM stemness. Through a combination of inhibitor and loss of function studies we determined that instead of upregulating cholesterol biosynthesis, cells surviving combination treatment of IR+DRAs activate Rac-1, a small GTPase, to reorganize their cytoskeleton and increase their migratory and invasive potential. Cytoskeleton organization plays a crucial role in allowing cancer stem cells to interact with their microenvironment, migrate and maintain their stemness capabilities (Y. Li et al., 2022). Use of statins in this scenario was able to inhibit Rac-1 activation and diminish surviving cells' migratory potential. As such, even though *in vitro* findings were only partially recapitulated *in vivo*, this study highlighted the underlying mechanism driving the defense response GBM cells mount against combination treatments.

For this paper I was actively involved in the generation of data for the following figures. Figure 1: I assisted with sample preparation (cell culture, plating, treating), protein isolation, quantification and subsequent Western blot analysis steps used for determining activation of MAPK signaling pathway components following combination treatments with QTP, TMZ and Vincristine. I also helped with sample preparations, RNA isolation and RT-PCR analyses for the various mevalonate pathway genes under this treatment scheme. Figure 2: I prepared samples treated with QTP and processed them for RNA isolation and RT-PCR analysis using human and mouse

specific primers for mevalonate pathway genes. Figure 3: I plated, treated and processed RNA samples for RT-PCR analysis of Day 5 samples investigating the effects of combination treatments (IR+QTP as well as IR+QTP+statins) on the expression of mevalonate pathway genes. Figure 4: Once more was involved with the entire process of preparing samples, isolating RNA and performing RT-PCRs for evaluating the effects of IR+ONC201 combination treatment. Figure 5: Performed sphere forming assays with all the mevalonate pathway inhibitors shown to determine which specific pathway component's upregulation drives glioma stemness following combination treatments of IR+QTP. Figure 6: I was involved with plating, treating, isolating and quantifying protein samples for use in Rac-1 pulldown and siRNA experiments, as well as subsequent Western blotting analysis steps used for establishing the role of Rac-1 in GBM stemness resulting following combination therapies. I also helped prepare the migration assay samples (plating, treating, processing/staining) used for demonstrating the increased migratory potential of cells treated with QTP and IR+QTP, effects rescued by the addition of atorvastatin. Supplementary Figure 1: for this figure, I helped with plating, treating, and isolating protein for some of the time points shown, and subsequent Western blotting steps. Given that this paper is currently under review, I will be providing comments and edits prior to its publication.

Overall, the combination of the three publications in this category explored the concept of how radiation-induced phenotype conversion of non-stem glioma cells to GICs can be targeted, and further identified the underlying mechanism by which surviving glioma cells are able to drive tumor recurrence following combination treatments. Understanding how these processes come about is of value in providing new therapeutic targets and treatment modalities against GBM.

ii) Implications of drug treatments on normal tissue following irradiation

Whereas the papers discussed in the previous section were exploring therapeutic avenues for targeting glioma stem/initiating cells, in this section the effects of combination treatments were evaluated in the context of normal tissues. Specifically, normal tissue toxicity is an inevitable consequence of brain irradiation that is associated with progressive cognitive decline due to loss of neural stem/progenitor cells, inflammation and demyelination (Jellinger, 1977). This is of great concern, particularly for pediatric patients for whom neurological effects have more time to develop. As such, identifying ways by which these adverse effects can be mitigated and/or avoided is of paramount importance. Compounds previously identified as radiation mitigators or that were shown to effectively target cancer stem cells when combined with irradiation were further probed to see if and how they might be affecting the normal brain. Specifically, the following two studies aimed to evaluate the effects of these compounds on neural stem/progenitor cells.

Paper #4: 1-[(4-Nitrophenyl)sulfonyl]-4-phenylpiperazine treatment after brain irradiation preserves cognitive function in mice (K. Bhat, Medina, et al., 2020).

Previous research in the lab identified 1-[(4-Nitrophenyl)sulfonyl]-4-phenylpiperazine (NSPP) as a radiation mitigator. NSPP was able to expand the intestinal stem cell pool, promote regeneration of intestinal crypts and prevent gastrointestinal acute radiation syndrome following exposure to a lethal dose of radiation. This was achieved through activation of the Hedgehog (hh) signaling pathway (Kruttika Bhat et al., 2019; Duhachek-Muggy et al., 2020). Given evidence pointing to the involvement of hh signaling in neural stem/progenitor cells, the effects of NSPP in mitigating radiation-induced cognitive decline in mice were evaluated in this

publication. Specifically, while treatment with NSPP after irradiation did not directly affect neural stem/progenitor cells, administration of this compound resulted in beneficial changes in the surrounding microenvironment as evidenced by a decrease in neuroinflammation. Mice treated with NSPP also showed improved cognitive function when compared to their irradiated counterparts. Thereafter, a general challenge posed by the use of radiation mitigators is the possibility for these agents to protect not only the normal tissue (goal of interest), but also the tumor (side effect). Here, NSPP was able to preferentially protect the normal tissue, without compromising radiation's antitumor effects. All in all, activation of the hh signaling pathway following NSPP treatment resulted in the effective mitigation of radiation-induced effects as those related to neural stem/progenitor cells and cognitive function.

Given that the majority of the work for this paper had already been underway prior to me joining the lab, my contributions were limited to assisting with cell culture maintenance as well as actively following along experimental procedures for sphere formation assays, including plating, treating and counting plates for determining the effects of NSPP on neural stem/progenitor cells' self-renewal. My role was more informative in the process of reviewing and editing the manuscript and accompanying figures.

Paper #5: Effects of Dopamine Receptor Antagonists and Radiation on Mouse Neural Stem/Progenitor Cells (L. He, Bhat, Ioannidis, & Pajonk, 2023).

Papers discussed in the previous category established a promising role for the use of DRAs in combination with radiation in effectively targeting glioma initiating cells, a population contributing to tumor growth, therapy resistance and recurrence. Nevertheless, effects of such combination treatments on normal tissue were not demonstrated at the time. Given the fact that similarities

exist between GICs and neural stem/progenitor cells (NSPCs) in terms of their dependence on glycogen synthase kinase-3 (GSK3) signaling (K. Bhat, Saki, et al., 2020; Kim & Snider, 2011), studying if and how DRAs affect this cellular population was of interest. Additionally, radiation is known to lead to cognitive decline by affecting NSPCs and subsequent neurogenesis. Thus, if combination treatments of radiation with DRAs were to further compromise neural stem/progenitor cells, justifying the benefits of this treatment modality would be challenged. Using transgenic mice engineered to express a green fluorescent version of Nestin, a neuronal stem cell marker, allowed for tracking of NSPCs and evaluation of the effects of treatment interventions on this population. Through this approach it was determined that several DRAs (e.g. TFP and QTP) previously shown to effectively prevent GICs, were also able to protect NSPCs from the effects of radiation, and in some instances even induce the expansion of this cellular population. Of interest, sex-dependent differences in NSPCs were identified in the process. Overall, the differential response seen between GICs and NSPCs following treatment with radiation and select DRAs was attributed to the underlying differential reliance of these populations on developmental signaling pathways implicating GSK3. Results from this study were beneficial in highlighting the therapeutic advantages of these combination treatments.

Regarding my contributions to this study, in experiments using samples collected from newborn pups, I assisted with the preparation of neurosphere cultures from the harvested brains and subsequent *in vitro* limiting dilution assays (SFAs) used for determining the effects of DRAs on the self-renewal ability of neural stem/progenitor cells. Additionally, I was involved with helping prepare neurosphere cultures from brain dissections performed in 3 week and 8 week old mice. Lastly, I helped revise and edit the manuscript and accompanying figures.

In this category, normal tissue toxicity as this relates to effects on neural stem/progenitor cells, was evaluated for combination treatments previously identified as radiation mitigators or inhibitors of the radiation-induced phenotypic conversion response. Understanding how normal tissues might be affected under different treatment schemes is of paramount importance as benefits of combination therapies against tumors should not come to the detriment of normal tissues, or if possible should have limited, and ideally manageable, adverse effects.

iii) Leveraging radiation-induced multipotency to drive surviving GBM cells towards a mitotically incompetent, neuron-like state

The highly aggressive nature of GBMs and the inability of currently available treatments to provide a survival benefit beyond the very dismal 12-18 months (Batchelor; Cheray et al., 2017), are largely attributed to the inherent heterogeneity and highly infiltrative nature of GBMs, as well as the presence of cancer stem cells (CSCs) (Cheray et al., 2017). Adding to this complexity, radiation-induced phenotype conversion of non-stem cancer cells to cancer stem-like cells, further contributes to the enrichment of this CSC population which plays important roles in tumor recurrence and therapy resistance. This phenotypic conversion is characterized by great plasticity as evidenced by the accompanying global epigenetic changes (e.g. re-expression of developmentally silenced transcription factors resulting from the acquisition of an open chromatin state in the respective promoters) (K. Bhat, Saki, et al., 2020; Lagadec et al., 2012). In line with this radiation-induced response, it has been shown that some of the pre-existing glioma CSCs surviving radiation acquire vascular endothelial- and pericyte-like traits, contributing thus to tumor proliferation (Muthukrishnan et al., 2022). As such, it follows that radiation leads to the acquisition of a transient state of multipotency, which depending on the presence of appropriate intrinsic/extrinsic cues, can result in changes promoting tumor growth

and therapy resistance. Given the complexity of GBMs, the ability to prevent radiation-induced phenotypic conversion and/or harness the underlying epigenetically permissive environment established to push cells towards differentiation (ideally a postmitotic, neuron-like state), both provide great promise in addressing the limited treatment success for this devastating disease.

Paper #6: Radiation-Induced Cellular Plasticity: A Strategy for Combatting Glioblastoma

(Ling He et al., 2024)

In the present study, the radiation-induced transient state of multipotency was exploited through the use of forskolin, an adenylate cyclase activator (Seamon & Daly, 1986) and known component of neuronal differentiation protocols (Hansen, Rehfeld, & Nielsen, 2000; Jang, Cho, Cho, Park, & Jeong, 2010), in an attempt to drive radiation-surviving glioma cells towards terminal differentiation. It was established that combination treatment of radiation and forskolin resulted in increased expression of neuronal markers, suggestive of neuronal differentiation. This was further accompanied by morphological changes in the treated cells, resembling the elongated neuron cell morphology. Interestingly, effects of combination treatment were found to be consistent across TCGA subtypes, granted at varying degrees. Additionally, combination treatment led to reduced cell proliferation through inhibition of G1-to-S phase progression, a known function of forskolin (Muraguchi, Miyazaki, Kehrl, & Fauci, 1984), as well as the establishment of distinct gene expression profiles. More specifically, bulk RNA sequencing identified upregulation of genes relating to brain neurotypes, microglia and vascular endothelial cells, hinting at cell fate changes. Probing further into the underlying cell fate transitions occurring following combination treatment, scRNAseq experiments revealed that surviving glioma cells were pushed towards a microglia- and neuron-like state. Importantly, treatment of cells with radiation and forskolin was able to decrease the self-renewal capacity and frequency of glioma CSCs, and improve median survival *in vivo*. The findings above

highlighted the possibility of using forskolin in combination with radiation as a novel differentiation therapy in the context of glioblastoma.

For this paper, I was actively involved with performing the majority of *in vitro* drug treatments used for establishing the effects of the different interventions on i) the expression of neuronal markers, ii) morphological changes of cells, iii) cell count numbers and cell proliferation, as well as iv) self-renewal capacity and stem cell-frequency changes. More specifically, I plated, treated and subsequently processed and used the corresponding samples to perform RT-PCR, Western blotting and ELDA experiments addressing the points discussed above. Lastly, I provided comments and edits for the manuscript and accompanying figures.

Ultimately, harnessing the radiation-induced transient state of multipotency to push GBM cells towards a mitotically incompetent, neuron-like state holds great promise in providing a much needed therapeutic relief. So far our data suggests a translatable clinical benefit that could be further explored to address some of the inherent challenges of GBMs.

iv) Pro-inflammatory signaling in mammary gland development and carcinogenesis

Inflammatory signaling has been regarded as an important enabling characteristic described in the Hallmarks of Cancer, a conceptual toolkit originally proposed by Dr. Hanahan enlisting common characteristics and functional capabilities normal cells acquire as they progress into malignancy. While hallmarks refer to normal cellular functions that become dysregulated and corrupted to assist in the progression of malignancy, enabling characteristics are traits arising during tumorigenesis that allow cells to acquire the aforementioned hallmarks (Hanahan, 2022). More specifically, inflammatory conditions and specifically factors released into the tumor microenvironment can help cells proliferate, evade apoptosis, promote angiogenesis, invasion

and metastasis, all while increasing their genetic instability and subsequently tumorigenic potential. Therefore, inflammatory signaling plays a key role in contributing to the acquisition of many of the fundamental hallmark capabilities (Hanahan & Weinberg, 2011). Additionally, as evidenced by recent studies by Cooke and colleagues, inflammatory signaling is readily involved in cellular plasticity and reprogramming events (Chanda et al., 2019; Cooke, 2019; Cooke & Lai, 2023; Lee et al., 2012; Shu Meng et al., 2016; S. Meng et al., 2017; Sayed et al., 2017; Sayed et al., 2015; Zhou et al., 2016), further highlighting the important and diverse roles inflammatory signaling cascades have. As such, studying inflammatory pathways and how these can potentially mediate and/or contribute to carcinogenesis is of essence.

Paper #7: Tumor necrosis factor receptor signaling modulates carcinogenesis in a mouse model of breast cancer (L. He, Bhat, Duhacheck-Muggy, et al., 2021).

Pro-inflammatory conditions such as obesity (Jiralerspong & Goodwin, 2016) and thoracic radiotherapy during puberty (Travis et al., 2005), both known risk factors in breast cancer development, are associated with elevated levels of inflammatory cytokines, particularly TNF α . This proinflammatory cytokine mediates its downstream effects by engaging tumor necrosis factor receptors 1 and 2 (TNFR1/2), thus suggesting a potential role for these receptors in breast cancer development. The present research paper aimed to address the implications of TNFR1 and TNFR2 imbalances in normal mammary gland development and breast carcinogenesis. More specifically, loss of either TNFR resulted in abnormal mammary gland development, with effects being more prominent when TNFR2 was knocked out. Using a transgenic mouse model prone to spontaneous breast cancer development (MMTV-Wnt1), loss of TNFR2 allele resulted in increased mammary carcinogenesis, characterized by a more aggressive phenotype as evidenced by the enhanced migratory and invasive potential of the resulting tumors. TNF α effects in this case were found to be mediated through canonical NF κ B

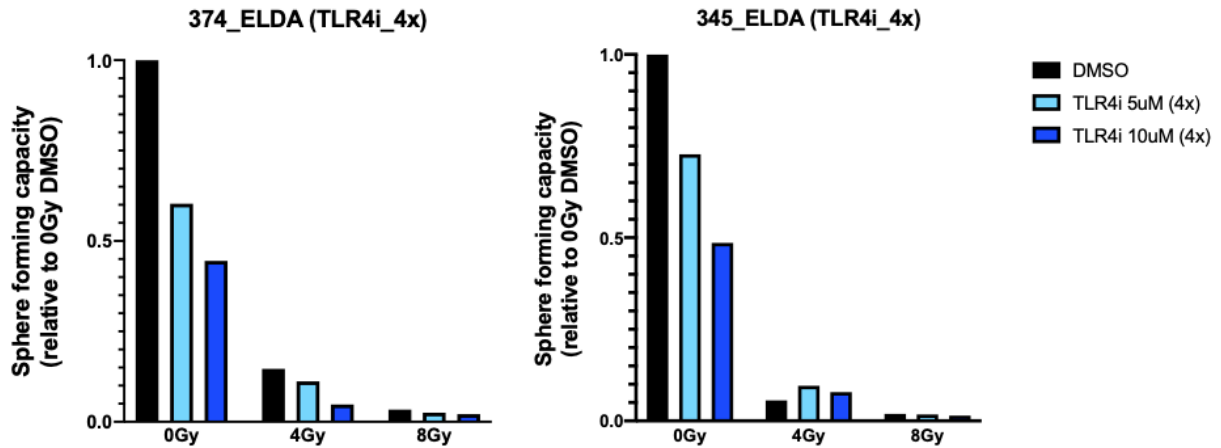
signaling (p50 homodimers). Of particular interest was the finding that exogenous supplementation of TNF α enhanced the radiation-induced phenotypic conversion of non-stem breast cancer cells to breast cancer initiating cells, providing additional validation for why inflammatory breast cancer has such an aggressive phenotype. In summary, TNFR signaling imbalances were found to play an important role in breast cancer development and progression.

In this publication, I assisted with the preparation of sphere forming assays used for evaluating the self-renewal capacity of cells collected from MMTV-Wnt1 TNFR knockout crosses. I also helped set up and process clonogenic assays for these cells as a means of identifying how TNFR imbalances affect cells' clonogenic potential. Thereafter, I helped with steps of the protein isolation and subsequent protein quantification for samples used for determining NF κ B subunit activation following TNFR knock down, as well as samples used in the proteome profiler cytokine array employed to further validate activation of the NF κ B signaling cascades identified. Next, while I did not independently perform the flow cytometric analysis steps used in the reprogramming assay of SUM159 cells for determining the effects of exogenous TNF α supplementation on the induction of phenotypic conversion, I shadowed my mentors Drs. Bhat and He during this procedure. Subsequently, I helped with the preparation of samples for Western blot analysis of Yamanaka factor protein levels in the presence or absence of TNF α , used to further supplement our earlier reprogramming assay findings showing enhancement of the radiation-induced phenotypic conversion response upon TNF α addition. Finally, I contributed to the revision and editing of the manuscript prior to its publication.

All in all, while this paper was focused on breast cancer and studies discussed in previous categories, including my own project, evaluated glioblastoma and/or normal brain models, studying of inflammatory pathways and the exploration of radiation-induced effects are common,

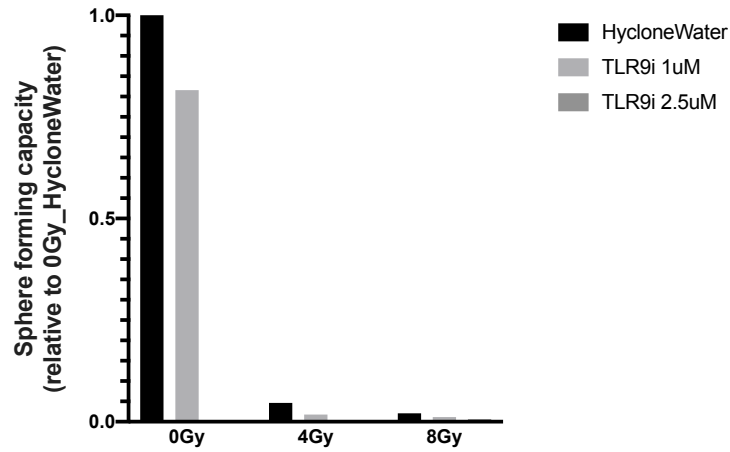
unifying themes. Through my involvement in these research papers I gained invaluable mentorship and hands-on experience, and familiarized myself with diverse experimental techniques, the principles of which I was able to later apply in my own research project

SUPPLEMENTARY FIGURES



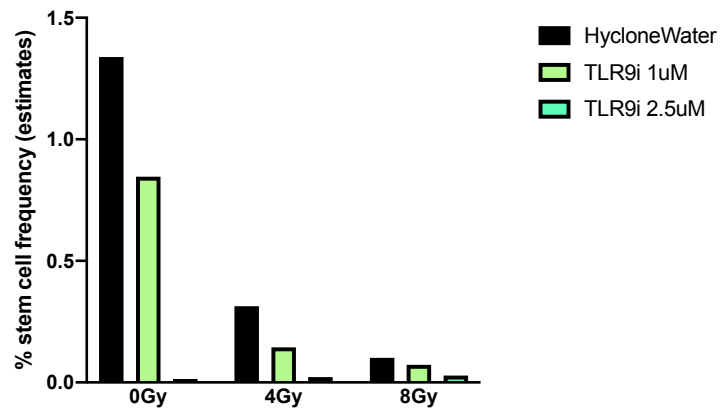
Supplementary Figure 1: Sphere forming capacity as determined from extreme limiting dilution assays (ELDAs) for HK-374 and HK-345 glioma sphere samples treated (4x) with TLR4 inhibitor. N=1 biological repeat for each line.

345_ELDA (TLR9i)

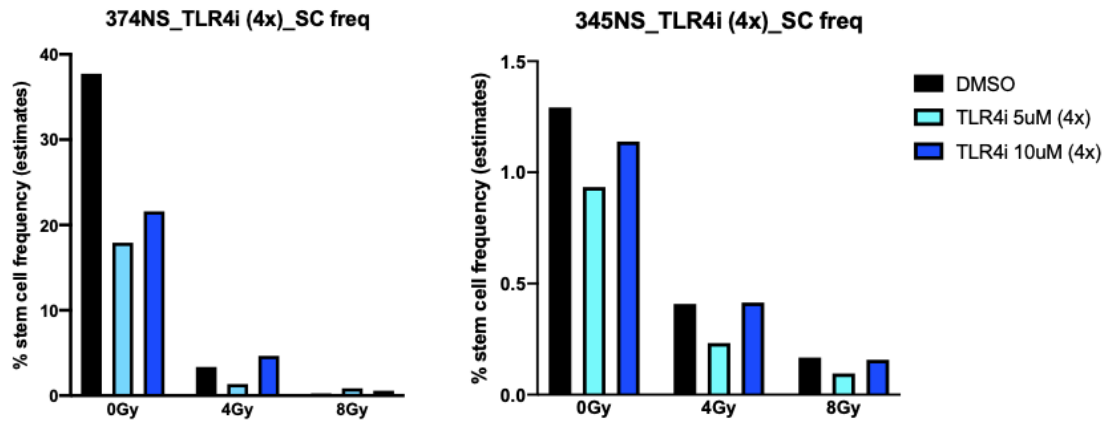


Supplementary Figure 2: Sphere forming capacity as determined from extreme limiting dilution assays (ELDAs) for HK-345 glioma sphere samples treated with TLR9 inhibitor (1x). N=1 biological repeat.

345NS_TLR9i_SC freq



Supplementary Figure 3: Stem cell frequency as determined by ELDA analysis in HK-345 glioma spheres treated with TLR9 inhibitor (1x). N=1 biological repeat.



Supplementary Figure 4: Stem cell frequency as determined by ELDA analysis in HK-374 and HK-345 glioma spheres treated with TLR9 (1x) and TLR4 inhibitors (4x treatment). N=1 for each inhibitor.

SUPPLEMENTARY TABLES

Supplementary Table 1. Primer sequences (Integrated DNA Technologies) used for RT-PCR validation experiments represented in Figure 2 (RT-PCR for select DAMPs/PRRs identified in RNAseq heatmap).

| | |
|----------------|-------------------------------|
| APBB2 | |
| Forward | TGCCTTCTGAGCTTTGTACC |
| Reverse | TGAAATATGAGCTGCCTGGAC |
| | |
| GPC1 | |
| Forward | GACTATTGCCGAAATGTGCTC |
| Reverse | GCTGCCGATGACACTCTC |
| | |
| SDC3 | |
| Forward | AGAGTATCCTGGAGCGGAAG |
| Reverse | CGATAGATGAGCAGTGTGACC |
| | |
| VCAN | |
| Forward | CAGTCATAGCAACTCCAGAGC |
| Reverse | CTCCTGCCTTTCCCATCTTATC |
| | |
| H2BC4 | (alternative name: HIST1H2BC) |
| Forward | TCCAGGGAGATCCAGACG |
| Reverse | AGGTGTTAAGACGCTTACTTGG |
| | |
| TLR4 | |
| Forward | TGCGTGAGACCAGAAAGC |
| Reverse | TTAAAGCTCAGGTCCAGGTTC |
| | |
| HMGB1 | |
| Forward | GATATGGCAAAAGCGGACAAG |
| Reverse | GGCGATACTCAGAGCAGAAG |
| | |
| HSPA12A | |
| Forward | GCCCTTCTCCTTCATTGACTAC |
| Reverse | TTCATGGCATCTGGACTCATC |
| | |
| SNCA | |
| Forward | CTGGAAGATATGCCTGTGGATC |
| Reverse | AGCACTTGTACAGGATGGAAC |

Supplementary Table 2. Two-way ANOVA analysis results of multiple comparisons for data represented in Figure 3 (SFAs of TLR3/4i).

| Dunnett's multiple comparisons test | Mean Diff. | 95.00% CI of diff. | Summary | Adjusted P Value |
|-------------------------------------|------------|--------------------|---------|------------------|
| 0Gy | | | | |
| DMSO vs. TLR3i 5uM | 0.08196 | -0.09831 to 0.2622 | ns | 0.6137 |
| DMSO vs. TLR3i 10uM | -0.1105 | -0.2908 to 0.06976 | ns | 0.3548 |
| DMSO vs. TLR4i 5uM | 0.3074 | 0.1272 to 0.4877 | *** | 0.0003 |
| DMSO vs. TLR4i 10uM | 0.5153 | 0.3350 to 0.6956 | **** | <0.0001 |
| 4Gy | | | | |
| DMSO vs. TLR3i 5uM | 0.02929 | -0.1510 to 0.2096 | ns | 0.9828 |
| DMSO vs. TLR3i 10uM | 0.04546 | -0.1348 to 0.2257 | ns | 0.9214 |
| DMSO vs. TLR4i 5uM | 0.1427 | -0.03756 to 0.3230 | ns | 0.1585 |
| DMSO vs. TLR4i 10uM | 0.2720 | 0.09175 to 0.4523 | ** | 0.0014 |
| 8Gy | | | | |
| DMSO vs. TLR3i 5uM | 0.003462 | -0.1768 to 0.1837 | ns | >0.9999 |
| DMSO vs. TLR3i 10uM | 0.01012 | -0.1701 to 0.1904 | ns | 0.9998 |
| DMSO vs. TLR4i 5uM | 0.03539 | -0.1449 to 0.2157 | ns | 0.9662 |
| DMSO vs. TLR4i 10uM | 0.06917 | -0.1111 to 0.2494 | ns | 0.7376 |

Supplementary Table 3. Two-way ANOVA analysis results of multiple comparisons for data represented in Figure 4 (SFA of CQ).

| Dunnett's multiple comparisons test | Mean Diff. | 95.00% CI of diff. | Summary | Adjusted P Value |
|-------------------------------------|------------|--------------------|---------|------------------|
| 0Gy | | | | |
| DMSO vs. CQ 1uM | 0.1354 | -0.06724 to 0.3380 | ns | 0.2544 |
| DMSO vs. CQ 5uM | 0.2541 | 0.05143 to 0.4567 | * | 0.0110 |
| DMSO vs. CQ 10uM | 0.4488 | 0.2462 to 0.6514 | **** | <0.0001 |
| 4Gy | | | | |
| DMSO vs. CQ 1uM | 0.05037 | -0.1523 to 0.2530 | ns | 0.8747 |
| DMSO vs. CQ 5uM | 0.08777 | -0.1149 to 0.2904 | ns | 0.5865 |
| DMSO vs. CQ 10uM | 0.1087 | -0.09393 to 0.3113 | ns | 0.4223 |
| 8Gy | | | | |
| DMSO vs. CQ 1uM | -0.01248 | -0.2151 to 0.1902 | ns | 0.9976 |
| DMSO vs. CQ 5uM | -0.005455 | -0.2081 to 0.1972 | ns | 0.9999 |
| DMSO vs. CQ 10uM | -0.01173 | -0.2144 to 0.1909 | ns | 0.9979 |

Supplementary Table 4. Two-way ANOVA analysis results of multiple comparisons for data represented in Figure 5 (SFA of TLR9i).

| Dunnett's multiple comparisons test | Predicted (LS) mean diff. | 95.00% CI of diff. | Summary | Adjusted P Value |
|-------------------------------------|---------------------------|--------------------|---------|------------------|
| 0Gy | | | | |
| HycloneWater vs. TLR9i 1uM | 0.1983 | 0.05135 to 0.3452 | ** | 0.0041 |
| HycloneWater vs. TLR9i 2.5uM | 0.3365 | 0.1335 to 0.5395 | *** | 0.0003 |
| HycloneWater vs. TLR9i 5uM | 0.8921 | 0.7452 to 1.039 | **** | <0.0001 |
| HycloneWater vs. TLR9i 7.5uM | 1.000 | 0.7970 to 1.203 | **** | <0.0001 |
| HycloneWater vs. TLR9i 10uM | 1.000 | 0.7970 to 1.203 | **** | <0.0001 |
| 4Gy | | | | |
| HycloneWater vs. TLR9i 1uM | 0.1354 | -0.01150 to 0.2823 | ns | 0.0814 |
| HycloneWater vs. TLR9i 2.5uM | 0.1711 | -0.03193 to 0.3741 | ns | 0.1287 |
| HycloneWater vs. TLR9i 5uM | 0.3871 | 0.2402 to 0.5341 | **** | <0.0001 |
| HycloneWater vs. TLR9i 7.5uM | 0.4061 | 0.2031 to 0.6091 | **** | <0.0001 |
| HycloneWater vs. TLR9i 10uM | 0.4070 | 0.2039 to 0.6100 | **** | <0.0001 |
| 8Gy | | | | |
| HycloneWater vs. TLR9i 1uM | 0.01042 | -0.1365 to 0.1573 | ns | 0.9997 |
| HycloneWater vs. TLR9i 2.5uM | -0.005347 | -0.2083 to 0.1977 | ns | >0.9999 |
| HycloneWater vs. TLR9i 5uM | 0.03626 | -0.1107 to 0.1832 | ns | 0.9595 |
| HycloneWater vs. TLR9i 7.5uM | 0.06098 | -0.1420 to 0.2640 | ns | 0.9132 |
| HycloneWater vs. TLR9i 10uM | 0.06089 | -0.1421 to 0.2639 | ns | 0.9137 |

Supplementary Table 5. Two-way ANOVA analysis results of multiple comparisons for HK-374 glioma sphere data represented in Figure 6 (ELDA of TLR9i).

| Dunnett's multiple comparisons test | Mean Diff. | 95.00% CI of diff. | Summary | Adjusted P Value |
|-------------------------------------|------------|---------------------|---------|------------------|
| 0Gy | | | | |
| HycloneWater vs. TLR9i 1uM | 0.4114 | 0.3463 to 0.4765 | **** | <0.0001 |
| HycloneWater vs. TLR9i 2.5uM | 0.7356 | 0.6705 to 0.8008 | **** | <0.0001 |
| 4Gy | | | | |
| HycloneWater vs. TLR9i 1uM | 0.07849 | 0.01337 to 0.1436 | * | 0.0181 |
| HycloneWater vs. TLR9i 2.5uM | 0.1391 | 0.07395 to 0.2042 | *** | 0.0001 |
| 8Gy | | | | |
| HycloneWater vs. TLR9i 1uM | -0.001270 | -0.06639 to 0.06385 | ns | 0.9984 |
| HycloneWater vs. TLR9i 2.5uM | 0.009709 | -0.05541 to 0.07483 | ns | 0.9116 |

Supplementary Table 6. Two-way ANOVA analysis results of multiple comparisons for HK-308 glioma sphere data represented in Figure 6 (ELDA of TLR9i).

| Dunnett's multiple comparisons test | Mean Diff. | 95.00% CI of diff. | Summary | Adjusted P Value |
|-------------------------------------|------------|--------------------|---------|------------------|
| 0Gy | | | | |
| HycloneWater vs. TLR9i 1uM | 0.2913 | 0.1328 to 0.4498 | *** | 0.0007 |
| HycloneWater vs. TLR9i 2.5uM | 0.5899 | 0.4314 to 0.7485 | **** | <0.0001 |
| 4Gy | | | | |
| HycloneWater vs. TLR9i 1uM | 0.1255 | -0.03302 to 0.2840 | ns | 0.1295 |
| HycloneWater vs. TLR9i 2.5uM | 0.2021 | 0.04364 to 0.3607 | * | 0.0127 |
| 8Gy | | | | |
| HycloneWater vs. TLR9i 1uM | -0.01601 | -0.1745 to 0.1425 | ns | 0.9581 |
| HycloneWater vs. TLR9i 2.5uM | 0.04615 | -0.1124 to 0.2047 | ns | 0.7122 |

Supplementary Table 7. Two-way ANOVA analysis results of multiple comparisons for HK-374 glioma sphere data represented in Figure 7 (SC freq for TLR9i ELDA).

| Dunnett's multiple comparisons test | Mean Diff. | 95.00% CI of diff. | Summary | Adjusted P Value |
|-------------------------------------|------------|--------------------|---------|------------------|
| 0Gy | | | | |
| Hyclone vs. TLR9i 1uM | 8.072 | -1.892 to 18.04 | ns | 0.1195 |
| Hyclone vs. TLR9i 2.5uM | 25.09 | 15.12 to 35.05 | **** | <0.0001 |
| 4Gy | | | | |
| Hyclone vs. TLR9i 1uM | 8.243 | -1.721 to 18.21 | ns | 0.1109 |
| Hyclone vs. TLR9i 2.5uM | 10.53 | 0.5648 to 20.49 | * | 0.0380 |
| 8Gy | | | | |
| Hyclone vs. TLR9i 1uM | -0.4670 | -10.43 to 9.498 | ns | 0.9908 |
| Hyclone vs. TLR9i 2.5uM | 0.09407 | -9.870 to 10.06 | ns | 0.9996 |

Supplementary Table 8. Two-way ANOVA analysis results of multiple comparisons for HK-308 glioma sphere data represented in Figure 7 (SC freq for TLR9i ELDA).

| Dunnett's multiple comparisons test | Mean Diff. | 95.00% CI of diff. | Summary | Adjusted P Value |
|-------------------------------------|------------|--------------------|---------|------------------|
| 0Gy | | | | |
| Hyclone vs. TLR9i 1uM | 3.091 | 0.4562 to 5.725 | * | 0.0213 |
| Hyclone vs. TLR9i 2.5uM | 12.57 | 9.938 to 15.21 | **** | <0.0001 |
| 4Gy | | | | |
| Hyclone vs. TLR9i 1uM | 0.6962 | -1.938 to 3.331 | ns | 0.7543 |
| Hyclone vs. TLR9i 2.5uM | 1.347 | -1.288 to 3.981 | ns | 0.3831 |
| 8Gy | | | | |
| Hyclone vs. TLR9i 1uM | -0.3444 | -2.979 to 2.290 | ns | 0.9311 |
| Hyclone vs. TLR9i 2.5uM | 0.2987 | -2.336 to 2.933 | ns | 0.9476 |

Supplementary Table 9. One-way ANOVA analysis results of multiple comparisons for data represented in Figure 9 (Reprogramming assay using TLR3/4i and CQ).

| Tukey's multiple comparisons test | Mean Diff. | 95.00% CI of diff. | Summary | Adjusted P Value |
|-----------------------------------|------------|--------------------|---------|------------------|
| 0Gy_DMSO vs. 0Gy_TLR3i_5uM | -0.02922 | -11.23 to 11.17 | ns | >0.9999 |
| 0Gy_DMSO vs. 0Gy_TLR3i_10uM | -0.2207 | -11.42 to 10.98 | ns | >0.9999 |
| 0Gy_DMSO vs. 0Gy_TLR4i_5uM | 0.08227 | -11.11 to 11.28 | ns | >0.9999 |
| 0Gy_DMSO vs. 0Gy_TLR4i_10uM | -0.8242 | -12.02 to 10.37 | ns | >0.9999 |
| 0Gy_DMSO vs. 0Gy_CQ_1uM | 0.1973 | -11.00 to 11.39 | ns | >0.9999 |
| 0Gy_DMSO vs. 0Gy_CQ_5uM | 0.5770 | -10.62 to 11.77 | ns | >0.9999 |
| 0Gy_DMSO vs. 0Gy_CQ_10uM | 0.3895 | -10.81 to 11.59 | ns | >0.9999 |
| 0Gy_DMSO vs. 4Gy_DMSO | -14.02 | -25.22 to -2.829 | ** | 0.0036 |
| 0Gy_DMSO vs. 4Gy_TLR3i_5uM | -7.188 | -18.38 to 4.008 | ns | 0.6122 |
| 0Gy_DMSO vs. 4Gy_TLR3i_10uM | -2.766 | -13.96 to 8.430 | ns | >0.9999 |
| 0Gy_DMSO vs. 4Gy_TLR4i_5uM | -16.13 | -27.33 to -4.936 | *** | 0.0004 |
| 0Gy_DMSO vs. 4Gy_TLR4i_10uM | -9.703 | -20.90 to 1.493 | ns | 0.1578 |
| 0Gy_DMSO vs. 4Gy_CQ_1uM | -0.2364 | -11.43 to 10.96 | ns | >0.9999 |
| 0Gy_DMSO vs. 4Gy_CQ_5uM | 0.7525 | -10.44 to 11.95 | ns | >0.9999 |
| 0Gy_DMSO vs. 4Gy_CQ_10uM | 0.7521 | -10.44 to 11.95 | ns | >0.9999 |
| 0Gy_TLR3i_5uM vs. 0Gy_TLR3i_10uM | -0.1914 | -11.39 to 11.00 | ns | >0.9999 |
| 0Gy_TLR3i_5uM vs. 0Gy_TLR4i_5uM | 0.1115 | -11.08 to 11.31 | ns | >0.9999 |
| 0Gy_TLR3i_5uM vs. 0Gy_TLR4i_10uM | -0.7950 | -11.99 to 10.40 | ns | >0.9999 |
| 0Gy_TLR3i_5uM vs. 0Gy_CQ_1uM | 0.2265 | -10.97 to 11.42 | ns | >0.9999 |
| 0Gy_TLR3i_5uM vs. 0Gy_CQ_5uM | 0.6063 | -10.59 to 11.80 | ns | >0.9999 |
| 0Gy_TLR3i_5uM vs. 0Gy_CQ_10uM | 0.4187 | -10.78 to 11.61 | ns | >0.9999 |
| 0Gy_TLR3i_5uM vs. 4Gy_DMSO | -14.00 | -25.19 to -2.800 | ** | 0.0037 |
| 0Gy_TLR3i_5uM vs. 4Gy_TLR3i_5uM | -7.159 | -18.35 to 4.037 | ns | 0.6186 |
| 0Gy_TLR3i_5uM vs. 4Gy_TLR3i_10uM | -2.737 | -13.93 to 8.459 | ns | >0.9999 |

| | | | | |
|-----------------------------------|----------|------------------|-----|---------|
| 0Gy_TLR3i_5uM vs. 4Gy_TLR4i_5uM | -16.10 | -27.30 to -4.907 | *** | 0.0004 |
| 0Gy_TLR3i_5uM vs. 4Gy_TLR4i_10uM | -9.674 | -20.87 to 1.522 | ns | 0.1611 |
| 0Gy_TLR3i_5uM vs. 4Gy_CQ_1uM | -0.2071 | -11.40 to 10.99 | ns | >0.9999 |
| 0Gy_TLR3i_5uM vs. 4Gy_CQ_5uM | 0.7818 | -10.41 to 11.98 | ns | >0.9999 |
| 0Gy_TLR3i_5uM vs. 4Gy_CQ_10uM | 0.7813 | -10.41 to 11.98 | ns | >0.9999 |
| 0Gy_TLR3i_10uM vs. 0Gy_TLR4i_5uM | 0.3029 | -10.89 to 11.50 | ns | >0.9999 |
| 0Gy_TLR3i_10uM vs. 0Gy_TLR4i_10uM | -0.6035 | -11.80 to 10.59 | ns | >0.9999 |
| 0Gy_TLR3i_10uM vs. 0Gy_CQ_1uM | 0.4179 | -10.78 to 11.61 | ns | >0.9999 |
| 0Gy_TLR3i_10uM vs. 0Gy_CQ_5uM | 0.7977 | -10.40 to 11.99 | ns | >0.9999 |
| 0Gy_TLR3i_10uM vs. 0Gy_CQ_10uM | 0.6101 | -10.59 to 11.81 | ns | >0.9999 |
| 0Gy_TLR3i_10uM vs. 4Gy_DMSO | -13.80 | -25.00 to -2.608 | ** | 0.0045 |
| 0Gy_TLR3i_10uM vs. 4Gy_TLR3i_5uM | -6.967 | -18.16 to 4.229 | ns | 0.6606 |
| 0Gy_TLR3i_10uM vs. 4Gy_TLR3i_10uM | -2.545 | -13.74 to 8.650 | ns | >0.9999 |
| 0Gy_TLR3i_10uM vs. 4Gy_TLR4i_5uM | -15.91 | -27.11 to -4.715 | *** | 0.0005 |
| 0Gy_TLR3i_10uM vs. 4Gy_TLR4i_10uM | -9.482 | -20.68 to 1.714 | ns | 0.1836 |
| 0Gy_TLR3i_10uM vs. 4Gy_CQ_1uM | -0.01571 | -11.21 to 11.18 | ns | >0.9999 |
| 0Gy_TLR3i_10uM vs. 4Gy_CQ_5uM | 0.9732 | -10.22 to 12.17 | ns | >0.9999 |
| 0Gy_TLR3i_10uM vs. 4Gy_CQ_10uM | 0.9728 | -10.22 to 12.17 | ns | >0.9999 |
| 0Gy_TLR4i_5uM vs. 0Gy_TLR4i_10uM | -0.9065 | -12.10 to 10.29 | ns | >0.9999 |
| 0Gy_TLR4i_5uM vs. 0Gy_CQ_1uM | 0.1150 | -11.08 to 11.31 | ns | >0.9999 |
| 0Gy_TLR4i_5uM vs. 0Gy_CQ_5uM | 0.4948 | -10.70 to 11.69 | ns | >0.9999 |
| 0Gy_TLR4i_5uM vs. 0Gy_CQ_10uM | 0.3072 | -10.89 to 11.50 | ns | >0.9999 |
| 0Gy_TLR4i_5uM vs. 4Gy_DMSO | -14.11 | -25.30 to -2.911 | ** | 0.0033 |
| 0Gy_TLR4i_5uM vs. 4Gy_TLR3i_5uM | -7.270 | -18.47 to 3.926 | ns | 0.5939 |
| 0Gy_TLR4i_5uM vs. 4Gy_TLR3i_10uM | -2.848 | -14.04 to 8.348 | ns | 0.9999 |
| 0Gy_TLR4i_5uM vs. 4Gy_TLR4i_5uM | -16.21 | -27.41 to -5.018 | *** | 0.0004 |
| 0Gy_TLR4i_5uM vs. 4Gy_TLR4i_10uM | -9.785 | -20.98 to 1.411 | ns | 0.1490 |

| | | | | |
|-----------------------------------|---------|------------------|-----|---------|
| 0Gy_TLR4i_5uM vs. 4Gy_CQ_1uM | -0.3186 | -11.51 to 10.88 | ns | >0.9999 |
| 0Gy_TLR4i_5uM vs. 4Gy_CQ_5uM | 0.6703 | -10.53 to 11.87 | ns | >0.9999 |
| 0Gy_TLR4i_5uM vs. 4Gy_CQ_10uM | 0.6698 | -10.53 to 11.87 | ns | >0.9999 |
| 0Gy_TLR4i_10uM vs. 0Gy_CQ_1uM | 1.021 | -10.17 to 12.22 | ns | >0.9999 |
| 0Gy_TLR4i_10uM vs. 0Gy_CQ_5uM | 1.401 | -9.795 to 12.60 | ns | >0.9999 |
| 0Gy_TLR4i_10uM vs. 0Gy_CQ_10uM | 1.214 | -9.982 to 12.41 | ns | >0.9999 |
| 0Gy_TLR4i_10uM vs. 4Gy_DMSO | -13.20 | -24.40 to -2.005 | ** | 0.0081 |
| 0Gy_TLR4i_10uM vs. 4Gy_TLR3i_5uM | -6.364 | -17.56 to 4.832 | ns | 0.7835 |
| 0Gy_TLR4i_10uM vs. 4Gy_TLR3i_10uM | -1.942 | -13.14 to 9.254 | ns | >0.9999 |
| 0Gy_TLR4i_10uM vs. 4Gy_TLR4i_5uM | -15.31 | -26.50 to -4.112 | *** | 0.0010 |
| 0Gy_TLR4i_10uM vs. 4Gy_TLR4i_10uM | -8.879 | -20.07 to 2.317 | ns | 0.2696 |
| 0Gy_TLR4i_10uM vs. 4Gy_CQ_1uM | 0.5878 | -10.61 to 11.78 | ns | >0.9999 |
| 0Gy_TLR4i_10uM vs. 4Gy_CQ_5uM | 1.577 | -9.619 to 12.77 | ns | >0.9999 |
| 0Gy_TLR4i_10uM vs. 4Gy_CQ_10uM | 1.576 | -9.620 to 12.77 | ns | >0.9999 |
| 0Gy_CQ_1uM vs. 0Gy_CQ_5uM | 0.3797 | -10.82 to 11.58 | ns | >0.9999 |
| 0Gy_CQ_1uM vs. 0Gy_CQ_10uM | 0.1922 | -11.00 to 11.39 | ns | >0.9999 |
| 0Gy_CQ_1uM vs. 4Gy_DMSO | -14.22 | -25.42 to -3.026 | ** | 0.0030 |
| 0Gy_CQ_1uM vs. 4Gy_TLR3i_5uM | -7.385 | -18.58 to 3.811 | ns | 0.5683 |
| 0Gy_CQ_1uM vs. 4Gy_TLR3i_10uM | -2.963 | -14.16 to 8.233 | ns | 0.9998 |
| 0Gy_CQ_1uM vs. 4Gy_TLR4i_5uM | -16.33 | -27.53 to -5.133 | *** | 0.0003 |
| 0Gy_CQ_1uM vs. 4Gy_TLR4i_10uM | -9.900 | -21.10 to 1.296 | ns | 0.1373 |
| 0Gy_CQ_1uM vs. 4Gy_CQ_1uM | -0.4337 | -11.63 to 10.76 | ns | >0.9999 |
| 0Gy_CQ_1uM vs. 4Gy_CQ_5uM | 0.5553 | -10.64 to 11.75 | ns | >0.9999 |
| 0Gy_CQ_1uM vs. 4Gy_CQ_10uM | 0.5548 | -10.64 to 11.75 | ns | >0.9999 |
| 0Gy_CQ_5uM vs. 0Gy_CQ_10uM | -0.1876 | -11.38 to 11.01 | ns | >0.9999 |
| 0Gy_CQ_5uM vs. 4Gy_DMSO | -14.60 | -25.80 to -3.406 | ** | 0.0020 |
| 0Gy_CQ_5uM vs. 4Gy_TLR3i_5uM | -7.765 | -18.96 to 3.431 | ns | 0.4845 |

| | | | | |
|----------------------------------|---------|------------------|-----|---------|
| 0Gy_CQ_5uM vs. 4Gy_TLR3i_10uM | -3.343 | -14.54 to 7.853 | ns | 0.9992 |
| 0Gy_CQ_5uM vs. 4Gy_TLR4i_5uM | -16.71 | -27.90 to -5.513 | *** | 0.0002 |
| 0Gy_CQ_5uM vs. 4Gy_TLR4i_10uM | -10.28 | -21.48 to 0.9160 | ns | 0.1038 |
| 0Gy_CQ_5uM vs. 4Gy_CQ_1uM | -0.8134 | -12.01 to 10.38 | ns | >0.9999 |
| 0Gy_CQ_5uM vs. 4Gy_CQ_5uM | 0.1755 | -11.02 to 11.37 | ns | >0.9999 |
| 0Gy_CQ_5uM vs. 4Gy_CQ_10uM | 0.1751 | -11.02 to 11.37 | ns | >0.9999 |
| 0Gy_CQ_10uM vs. 4Gy_DMSO | -14.41 | -25.61 to -3.218 | ** | 0.0024 |
| 0Gy_CQ_10uM vs. 4Gy_TLR3i_5uM | -7.577 | -18.77 to 3.619 | ns | 0.5256 |
| 0Gy_CQ_10uM vs. 4Gy_TLR3i_10uM | -3.156 | -14.35 to 8.040 | ns | 0.9996 |
| 0Gy_CQ_10uM vs. 4Gy_TLR4i_5uM | -16.52 | -27.72 to -5.325 | *** | 0.0003 |
| 0Gy_CQ_10uM vs. 4Gy_TLR4i_10uM | -10.09 | -21.29 to 1.104 | ns | 0.1194 |
| 0Gy_CQ_10uM vs. 4Gy_CQ_1uM | -0.6258 | -11.82 to 10.57 | ns | >0.9999 |
| 0Gy_CQ_10uM vs. 4Gy_CQ_5uM | 0.3631 | -10.83 to 11.56 | ns | >0.9999 |
| 0Gy_CQ_10uM vs. 4Gy_CQ_10uM | 0.3627 | -10.83 to 11.56 | ns | >0.9999 |
| 4Gy_DMSO vs. 4Gy_TLR3i_5uM | 6.837 | -4.359 to 18.03 | ns | 0.6886 |
| 4Gy_DMSO vs. 4Gy_TLR3i_10uM | 11.26 | 0.06279 to 22.45 | * | 0.0474 |
| 4Gy_DMSO vs. 4Gy_TLR4i_5uM | -2.107 | -13.30 to 9.089 | ns | >0.9999 |
| 4Gy_DMSO vs. 4Gy_TLR4i_10uM | 4.322 | -6.874 to 15.52 | ns | 0.9882 |
| 4Gy_DMSO vs. 4Gy_CQ_1uM | 13.79 | 2.593 to 24.98 | ** | 0.0046 |
| 4Gy_DMSO vs. 4Gy_CQ_5uM | 14.78 | 3.581 to 25.97 | ** | 0.0017 |
| 4Gy_DMSO vs. 4Gy_CQ_10uM | 14.78 | 3.581 to 25.97 | ** | 0.0017 |
| 4Gy_TLR3i_5uM vs. 4Gy_TLR3i_10uM | 4.422 | -6.774 to 15.62 | ns | 0.9854 |
| 4Gy_TLR3i_5uM vs. 4Gy_TLR4i_5uM | -8.944 | -20.14 to 2.252 | ns | 0.2592 |
| 4Gy_TLR3i_5uM vs. 4Gy_TLR4i_10uM | -2.515 | -13.71 to 8.681 | ns | >0.9999 |
| 4Gy_TLR3i_5uM vs. 4Gy_CQ_1uM | 6.952 | -4.244 to 18.15 | ns | 0.6640 |
| 4Gy_TLR3i_5uM vs. 4Gy_CQ_5uM | 7.940 | -3.255 to 19.14 | ns | 0.4468 |
| 4Gy_TLR3i_5uM vs. 4Gy_CQ_10uM | 7.940 | -3.256 to 19.14 | ns | 0.4469 |

| | | | | |
|-----------------------------------|------------|------------------|-----|---------|
| 4Gy_TLR3i_10uM vs. 4Gy_TLR4i_5uM | -13.37 | -24.56 to -2.170 | ** | 0.0069 |
| 4Gy_TLR3i_10uM vs. 4Gy_TLR4i_10uM | -6.937 | -18.13 to 4.259 | ns | 0.6672 |
| 4Gy_TLR3i_10uM vs. 4Gy_CQ_1uM | 2.530 | -8.666 to 13.73 | ns | >0.9999 |
| 4Gy_TLR3i_10uM vs. 4Gy_CQ_5uM | 3.519 | -7.677 to 14.71 | ns | 0.9986 |
| 4Gy_TLR3i_10uM vs. 4Gy_CQ_10uM | 3.518 | -7.678 to 14.71 | ns | 0.9986 |
| 4Gy_TLR4i_5uM vs. 4Gy_TLR4i_10uM | 6.429 | -4.767 to 17.62 | ns | 0.7712 |
| 4Gy_TLR4i_5uM vs. 4Gy_CQ_1uM | 15.90 | 4.700 to 27.09 | *** | 0.0005 |
| 4Gy_TLR4i_5uM vs. 4Gy_CQ_5uM | 16.88 | 5.688 to 28.08 | *** | 0.0002 |
| 4Gy_TLR4i_5uM vs. 4Gy_CQ_10uM | 16.88 | 5.688 to 28.08 | *** | 0.0002 |
| 4Gy_TLR4i_10uM vs. 4Gy_CQ_1uM | 9.467 | -1.729 to 20.66 | ns | 0.1855 |
| 4Gy_TLR4i_10uM vs. 4Gy_CQ_5uM | 10.46 | -0.7405 to 21.65 | ns | 0.0908 |
| 4Gy_TLR4i_10uM vs. 4Gy_CQ_10uM | 10.45 | -0.7410 to 21.65 | ns | 0.0908 |
| 4Gy_CQ_1uM vs. 4Gy_CQ_5uM | 0.9889 | -10.21 to 12.18 | ns | >0.9999 |
| 4Gy_CQ_1uM vs. 4Gy_CQ_10uM | 0.9885 | -10.21 to 12.18 | ns | >0.9999 |
| 4Gy_CQ_5uM vs. 4Gy_CQ_10uM | -0.0004362 | -11.20 to 11.20 | ns | >0.9999 |

Supplementary Table 10. Primer sequences (Integrated DNA Technologies) used for RT-PCR validation experiments represented in Figure 10 (RT-PCR for YFs following IR+TLR3/4i).

| | |
|--------------|----------------------------|
| Oct4 | |
| Forward | CATAGTCGCTGCTTGATCGCTTG |
| Reverse | GAGAACCGAGTGAGAGGCAACC |
| | |
| Sox2 | |
| Forward | TTGCGTGAGTGTGGATGGGATTGGTG |
| Reverse | GGGAAATGGGAGGGGTGCAAAGAGG |
| | |
| Klf4 | |
| Forward | GGTCCGACCTGGAAAATGCT |
| Reverse | ACCAGGCACTACCGTAAACACA |
| | |
| Nanog | |
| Forward | TGCGTCACACCATTGCTATTCTTC |
| Reverse | AATACCTCAGCCTCCAGCAGATG |
| | |
| cMyc | |
| Forward | CACTGTCCAACCTTGACCCTCTTG |
| Reverse | CGTCTCCACACATCAGCACAA |

Supplementary Table 11. Two-way ANOVA analysis results of multiple comparisons for HK-374 data represented in Figure 10 (RT-PCR for YFs following IR+TLR3/4i).

| Tukey's multiple comparisons test | Predicted (LS) mean diff. | 95.00% CI of diff. | Summary | Adjusted P Value |
|-----------------------------------|---------------------------|--------------------|---------|------------------|
| Oct4 | | | | |
| 0Gy_DMSO vs. 4Gy_DMSO | -0.9651 | -2.768 to 0.8382 | ns | 0.5061 |
| 0Gy_DMSO vs. 4Gy_TLR3i_5uM | -0.02787 | -1.674 to 1.618 | ns | >0.9999 |
| 0Gy_DMSO vs. 4Gy_TLR4i_5uM | -0.1613 | -1.808 to 1.485 | ns | 0.9942 |
| 4Gy_DMSO vs. 4Gy_TLR3i_5uM | 0.9373 | -0.7089 to 2.583 | ns | 0.4514 |
| 4Gy_DMSO vs. 4Gy_TLR4i_5uM | 0.8038 | -0.8424 to 2.450 | ns | 0.5831 |
| 4Gy_TLR3i_5uM vs. 4Gy_TLR4i_5uM | -0.1334 | -1.606 to 1.339 | ns | 0.9954 |
| Sox2 | | | | |
| 0Gy_DMSO vs. 4Gy_DMSO | -0.4973 | -2.301 to 1.306 | ns | 0.8899 |
| 0Gy_DMSO vs. 4Gy_TLR3i_5uM | 0.07439 | -1.572 to 1.721 | ns | 0.9994 |
| 0Gy_DMSO vs. 4Gy_TLR4i_5uM | 0.1882 | -1.458 to 1.834 | ns | 0.9908 |
| 4Gy_DMSO vs. 4Gy_TLR3i_5uM | 0.5717 | -1.074 to 2.218 | ns | 0.8028 |
| 4Gy_DMSO vs. 4Gy_TLR4i_5uM | 0.6855 | -0.9607 to 2.332 | ns | 0.7001 |
| 4Gy_TLR3i_5uM vs. 4Gy_TLR4i_5uM | 0.1138 | -1.359 to 1.586 | ns | 0.9971 |
| Klf4 | | | | |
| 0Gy_DMSO vs. 4Gy_DMSO | -2.507 | -4.310 to -0.7035 | ** | 0.0024 |
| 0Gy_DMSO vs. 4Gy_TLR3i_5uM | -1.061 | -2.708 to 0.5848 | ns | 0.3394 |
| 0Gy_DMSO vs. 4Gy_TLR4i_5uM | -0.9295 | -2.576 to 0.7167 | ns | 0.4589 |
| 4Gy_DMSO vs. 4Gy_TLR3i_5uM | 1.445 | -0.2008 to 3.092 | ns | 0.1068 |
| 4Gy_DMSO vs. 4Gy_TLR4i_5uM | 1.577 | -0.06888 to 3.224 | ns | 0.0656 |
| 4Gy_TLR3i_5uM vs. 4Gy_TLR4i_5uM | 0.1319 | -1.340 to 1.604 | ns | 0.9955 |
| Nanog | | | | |
| 0Gy_DMSO vs. 4Gy_DMSO | -3.336 | -5.139 to -1.533 | **** | <0.0001 |
| 0Gy_DMSO vs. 4Gy_TLR3i_5uM | -0.1864 | -1.833 to 1.460 | ns | 0.9911 |

| | | | | |
|---------------------------------|---------|--------------------|------|---------|
| 0Gy_DMSO vs. 4Gy_TLR4i_5uM | -0.4116 | -2.058 to 1.235 | ns | 0.9151 |
| 4Gy_DMSO vs. 4Gy_TLR3i_5uM | 3.150 | 1.503 to 4.796 | **** | <0.0001 |
| 4Gy_DMSO vs. 4Gy_TLR4i_5uM | 2.924 | 1.278 to 4.571 | **** | <0.0001 |
| 4Gy_TLR3i_5uM vs. 4Gy_TLR4i_5uM | -0.2252 | -1.698 to 1.247 | ns | 0.9786 |
| cMyc | | | | |
| 0Gy_DMSO vs. 4Gy_DMSO | -1.882 | -3.685 to -0.07849 | * | 0.0372 |
| 0Gy_DMSO vs. 4Gy_TLR3i_5uM | -0.6269 | -2.273 to 1.019 | ns | 0.7547 |
| 0Gy_DMSO vs. 4Gy_TLR4i_5uM | -0.5266 | -2.173 to 1.120 | ns | 0.8389 |
| 4Gy_DMSO vs. 4Gy_TLR3i_5uM | 1.255 | -0.3913 to 2.901 | ns | 0.1994 |
| 4Gy_DMSO vs. 4Gy_TLR4i_5uM | 1.355 | -0.2910 to 3.001 | ns | 0.1453 |
| 4Gy_TLR3i_5uM vs. 4Gy_TLR4i_5uM | 0.1003 | -1.372 to 1.573 | ns | 0.9980 |

Supplementary Table 12. Primer sequences used for evaluating the expression levels of human cGAS/STING, as shown in Figure 11. Note: designation “h” indicates human specific primer.

| | |
|-----------------|-----------------------------|
| hcGAS | Integrated DNA Technologies |
| Forward | AGGAAGCAACTACGACTAAAGC |
| Reverse | TCACAGCACGTTTTAGATTTTCC |
| | |
| hSTING_1 | Integrated DNA Technologies |
| Forward | TCAAGGATCGGGTTTACAGC |
| Reverse | GCTTGACTGTATTGTGACATGG |
| | |
| hSTING_2 | Origene |
| Forward | CCTGAGTCTCAGAACAACCTGCC |
| Reverse | GGTCTTCAAGCTGCCACAGTA |

Supplementary Table 13. Two-way ANOVA analysis results of multiple comparisons for data represented in Figure 12 (ELDA for cGASi).

| Dunnett's multiple comparisons test | Mean Diff. | 95.00% CI of diff. | Summary | Adjusted P Value |
|--|-------------------|---------------------------|----------------|-------------------------|
| 0Gy | | | | |
| DMSO vs. G140 5uM | -0.1047 | -0.3269 to 0.1176 | ns | 0.4464 |
| DMSO vs. G140 10uM | -0.06260 | -0.2849 to 0.1597 | ns | 0.7354 |
| 2Gy | | | | |
| DMSO vs. G140 5uM | -0.09900 | -0.3213 to 0.1233 | ns | 0.4828 |
| DMSO vs. G140 10uM | -0.01533 | -0.2376 to 0.2069 | ns | 0.9810 |
| 4Gy | | | | |
| DMSO vs. G140 5uM | -0.001352 | -0.2236 to 0.2209 | ns | 0.9999 |
| DMSO vs. G140 10uM | 0.06053 | -0.1617 to 0.2828 | ns | 0.7495 |
| 8Gy | | | | |
| DMSO vs. G140 5uM | 0.02182 | -0.2004 to 0.2441 | ns | 0.9619 |
| DMSO vs. G140 10uM | 0.003459 | -0.2188 to 0.2257 | ns | 0.9990 |

Supplementary Table 14. Two-way ANOVA analysis results of multiple comparisons for HK-374 glioma sphere data represented in Figure 13 (ELDA for STINGi).

| Dunnett's multiple comparisons test | Predicted (LS) mean diff. | 95.00% CI of diff. | Summary | Adjusted P Value |
|-------------------------------------|---------------------------|--------------------|---------|------------------|
| 0Gy | | | | |
| DMSO vs. H-151 250nM | 0.2400 | 0.06115 to 0.4188 | ** | 0.0057 |
| DMSO vs. H-151 500nM | 0.4465 | 0.2677 to 0.6254 | **** | <0.0001 |
| DMSO vs. H-151 1uM | 0.8710 | 0.6922 to 1.050 | **** | <0.0001 |
| 2Gy | | | | |
| DMSO vs. H-151 250nM | 0.3203 | 0.08943 to 0.5512 | ** | 0.0041 |
| DMSO vs. H-151 500nM | 0.4860 | 0.2551 to 0.7169 | **** | <0.0001 |
| DMSO vs. H-151 1uM | 0.6491 | 0.4182 to 0.8800 | **** | <0.0001 |
| 4Gy | | | | |
| DMSO vs. H-151 250nM | 0.1279 | -0.05098 to 0.3067 | ns | 0.2128 |
| DMSO vs. H-151 500nM | 0.1672 | -0.01164 to 0.3460 | ns | 0.0719 |
| DMSO vs. H-151 1uM | 0.2148 | 0.03595 to 0.3936 | * | 0.0146 |
| 8Gy | | | | |
| DMSO vs. H-151 250nM | 0.008023 | -0.1708 to 0.1869 | ns | 0.9991 |
| DMSO vs. H-151 500nM | 0.01169 | -0.1672 to 0.1905 | ns | 0.9972 |
| DMSO vs. H-151 1uM | 0.01672 | -0.1621 to 0.1956 | ns | 0.9920 |

Supplementary Table 15. Two-way ANOVA analysis results of multiple comparisons for HK-157 glioma sphere data represented in Figure 13 (ELDA for STINGi).

| Dunnett's multiple comparisons test | Mean Diff. | 95.00% CI of diff. | Summary | Adjusted P Value |
|-------------------------------------|------------|--------------------|---------|------------------|
| 0Gy | | | | |
| DMSO vs. H-151 250nM | 0.2902 | 0.1378 to 0.4426 | *** | 0.0001 |
| DMSO vs. H-151 500nM | 0.3141 | 0.1617 to 0.4665 | **** | <0.0001 |
| DMSO vs. H-151 1uM | 0.7285 | 0.5761 to 0.8809 | **** | <0.0001 |
| 2Gy | | | | |
| DMSO vs. H-151 250nM | 0.07060 | -0.08179 to 0.2230 | ns | 0.5334 |
| DMSO vs. H-151 500nM | 0.1811 | 0.02873 to 0.3335 | * | 0.0168 |
| DMSO vs. H-151 1uM | 0.2611 | 0.1087 to 0.4135 | *** | 0.0006 |
| 4Gy | | | | |
| DMSO vs. H-151 250nM | 0.02204 | -0.1304 to 0.1744 | ns | 0.9700 |
| DMSO vs. H-151 500nM | 0.04105 | -0.1113 to 0.1934 | ns | 0.8455 |
| DMSO vs. H-151 1uM | 0.07677 | -0.07563 to 0.2292 | ns | 0.4688 |
| 8Gy | | | | |
| DMSO vs. H-151 250nM | -0.007944 | -0.1603 to 0.1444 | ns | 0.9985 |
| DMSO vs. H-151 500nM | 0.002831 | -0.1496 to 0.1552 | ns | >0.9999 |
| DMSO vs. H-151 1uM | 0.002830 | -0.1496 to 0.1552 | ns | >0.9999 |

Supplementary Table 16. Two-way ANOVA analysis results of multiple comparisons for HK-308 glioma sphere data represented in Figure 13 (ELDA for STINGi).

| Dunnett's multiple comparisons test | Mean Diff. | 95.00% CI of diff. | Summary | Adjusted P Value |
|-------------------------------------|------------|--------------------|---------|------------------|
| 0Gy | | | | |
| DMSO vs. H-151 250nM | 0.2823 | 0.1404 to 0.4242 | **** | <0.0001 |
| DMSO vs. H-151 500nM | 0.1871 | 0.04519 to 0.3291 | ** | 0.0075 |
| DMSO vs. H-151 1uM | 0.4791 | 0.3371 to 0.6210 | **** | <0.0001 |
| 2Gy | | | | |
| DMSO vs. H-151 250nM | 0.02493 | -0.1170 to 0.1669 | ns | 0.9485 |
| DMSO vs. H-151 500nM | 0.004924 | -0.1370 to 0.1469 | ns | 0.9995 |
| DMSO vs. H-151 1uM | 0.05644 | -0.08549 to 0.1984 | ns | 0.6429 |
| 4Gy | | | | |
| DMSO vs. H-151 250nM | -0.005924 | -0.1479 to 0.1360 | ns | 0.9992 |
| DMSO vs. H-151 500nM | 0.005658 | -0.1363 to 0.1476 | ns | 0.9993 |
| DMSO vs. H-151 1uM | 0.03063 | -0.1113 to 0.1726 | ns | 0.9111 |
| 8Gy | | | | |
| DMSO vs. H-151 250nM | -0.01104 | -0.1530 to 0.1309 | ns | 0.9950 |
| DMSO vs. H-151 500nM | 0.003566 | -0.1384 to 0.1455 | ns | 0.9999 |
| DMSO vs. H-151 1uM | -0.001506 | -0.1434 to 0.1404 | ns | >0.9999 |

Supplementary Table 17. Two-way ANOVA analysis results of multiple comparisons for HK-374 glioma sphere data represented in Figure 14 (SC freq for STINGi ELDAAs).

| Dunnett's multiple comparisons test | Predicted (LS) mean diff. | 95.00% CI of diff. | Summary | Adjusted P Value |
|-------------------------------------|---------------------------|--------------------|---------|------------------|
| 0Gy | | | | |
| DMSO vs. new H-151 250nm | 12.19 | 1.878 to 22.51 | * | 0.0165 |
| DMSO vs. new H-151 500nm | 31.77 | 21.46 to 42.09 | **** | <0.0001 |
| DMSO vs. new H-151 1uM | 45.13 | 34.82 to 55.45 | **** | <0.0001 |
| 2Gy | | | | |
| DMSO vs. new H-151 250nm | 12.42 | -0.8966 to 25.74 | ns | 0.0727 |
| DMSO vs. new H-151 500nm | 19.41 | 6.093 to 32.73 | ** | 0.0025 |
| DMSO vs. new H-151 1uM | 21.46 | 8.146 to 34.78 | *** | 0.0008 |
| 4Gy | | | | |
| DMSO vs. new H-151 250nm | 3.705 | -6.610 to 14.02 | ns | 0.7186 |
| DMSO vs. new H-151 500nm | 5.634 | -4.681 to 15.95 | ns | 0.4165 |
| DMSO vs. new H-151 1uM | 6.423 | -3.892 to 16.74 | ns | 0.3130 |
| 8Gy | | | | |
| DMSO vs. new H-151 250nm | 0.1582 | -10.16 to 10.47 | ns | >0.9999 |
| DMSO vs. new H-151 500nm | 0.4771 | -9.838 to 10.79 | ns | 0.9990 |
| DMSO vs. new H-151 1uM | 0.5766 | -9.738 to 10.89 | ns | 0.9982 |

Supplementary Table 18. Two-way ANOVA analysis results of multiple comparisons for HK-157 glioma sphere data represented in Figure 14 (SC freq for STINGi ELDAAs).

| Dunnett's multiple comparisons test | Mean Diff. | 95.00% CI of diff. | Summary | Adjusted P Value |
|-------------------------------------|------------|--------------------|---------|------------------|
| 0Gy | | | | |
| DMSO vs. new H-151 250nm | 1.714 | -3.716 to 7.144 | ns | 0.7775 |
| DMSO vs. new H-151 500nm | 11.55 | 6.124 to 16.98 | **** | <0.0001 |
| DMSO vs. new H-151 1uM | 15.02 | 9.591 to 20.45 | **** | <0.0001 |
| 2Gy | | | | |
| DMSO vs. new H-151 250nm | 0.6832 | -4.747 to 6.113 | ns | 0.9797 |
| DMSO vs. new H-151 500nm | 1.754 | -3.676 to 7.184 | ns | 0.7659 |
| DMSO vs. new H-151 1uM | 2.517 | -2.913 to 7.947 | ns | 0.5330 |
| 4Gy | | | | |
| DMSO vs. new H-151 250nm | -0.1392 | -5.569 to 5.291 | ns | 0.9999 |
| DMSO vs. new H-151 500nm | 0.5467 | -4.883 to 5.977 | ns | 0.9894 |
| DMSO vs. new H-151 1uM | 0.7925 | -4.638 to 6.223 | ns | 0.9692 |
| 8Gy | | | | |
| DMSO vs. new H-151 250nm | -0.02856 | -5.459 to 5.402 | ns | >0.9999 |
| DMSO vs. new H-151 500nm | 0.02078 | -5.409 to 5.451 | ns | >0.9999 |
| DMSO vs. new H-151 1uM | 0.01684 | -5.413 to 5.447 | ns | >0.9999 |

Supplementary Table 19. Two-way ANOVA analysis results of multiple comparisons for HK-308 glioma sphere data represented in Figure 14 (SC freq for STINGi ELDA).s).

| Dunnett's multiple comparisons test | Mean Diff. | 95.00% CI of diff. | Summary | Adjusted P Value |
|-------------------------------------|------------|--------------------|---------|------------------|
| 0Gy | | | | |
| DMSO vs. new H-151 250nm | 3.980 | -1.295 to 9.255 | ns | 0.1729 |
| DMSO vs. new H-151 500nm | 8.174 | 2.899 to 13.45 | ** | 0.0016 |
| DMSO vs. new H-151 1uM | 9.838 | 4.563 to 15.11 | *** | 0.0002 |
| 2Gy | | | | |
| DMSO vs. new H-151 250nm | 0.02501 | -5.250 to 5.300 | ns | >0.9999 |
| DMSO vs. new H-151 500nm | -0.2250 | -5.500 to 5.050 | ns | 0.9991 |
| DMSO vs. new H-151 1uM | 0.6788 | -4.596 to 5.954 | ns | 0.9784 |
| 4Gy | | | | |
| DMSO vs. new H-151 250nm | -0.3726 | -5.648 to 4.902 | ns | 0.9962 |
| DMSO vs. new H-151 500nm | -0.1475 | -5.422 to 5.127 | ns | 0.9997 |
| DMSO vs. new H-151 1uM | 0.01350 | -5.261 to 5.288 | ns | >0.9999 |
| 8Gy | | | | |
| DMSO vs. new H-151 250nm | -0.04609 | -5.321 to 5.229 | ns | >0.9999 |
| DMSO vs. new H-151 500nm | 0.007596 | -5.267 to 5.283 | ns | >0.9999 |
| DMSO vs. new H-151 1uM | -0.02876 | -5.304 to 5.246 | ns | >0.9999 |

Supplementary Table 20. Primer sequences (Integrated DNA Technologies) used for evaluating the expression levels of SMARCA1 and SMARCD3, used for generating data shown in Figures 18, 19. (RT-PCR for SMARCA1/D3).

| | |
|----------------|------------------------|
| SMARCA1 | |
| Forward | GGTCCACCTTATACCACTGATG |
| Reverse | CCAAAATATCCAGCAAGCGAG |
| | |
| SMARCD3 | |
| Forward | TGTGGCAGTATGTGAAGACC |
| Reverse | TCTCAGAAAACCTTCAGCCGG |

Supplementary Table 21. One-way ANOVA analysis results for SMARCA1 data represented in Figure 18 (RT-PCR for SMARCA1).

| Tukey's multiple comparisons test | Mean Diff. | 95.00% CI of diff. | Summary | Adjusted P Value |
|--|-------------------|---------------------------|----------------|-------------------------|
| 0Gy_DMSO vs. 4Gy_DMSO | -4.521 | -8.155 to -0.8867 | ** | 0.0091 |
| 0Gy_DMSO vs. 4Gy_TLR3i_10uM | -0.6239 | -4.023 to 2.776 | ns | 0.9833 |
| 0Gy_DMSO vs. 4Gy_TLR4i_10uM | -1.591 | -4.738 to 1.557 | ns | 0.5916 |
| 0Gy_DMSO vs. 4Gy_CQ_10uM | -0.4456 | -4.896 to 4.005 | ns | 0.9984 |
| 4Gy_DMSO vs. 4Gy_TLR3i_10uM | 3.897 | 0.4976 to 7.296 | * | 0.0184 |
| 4Gy_DMSO vs. 4Gy_TLR4i_10uM | 2.930 | -0.2169 to 6.077 | ns | 0.0775 |
| 4Gy_DMSO vs. 4Gy_CQ_10uM | 4.075 | -0.3756 to 8.526 | ns | 0.0853 |
| 4Gy_TLR3i_10uM vs. 4Gy_TLR4i_10uM | -0.9667 | -3.840 to 1.906 | ns | 0.8638 |
| 4Gy_TLR3i_10uM vs. 4Gy_CQ_10uM | 0.1782 | -4.083 to 4.440 | ns | >0.9999 |
| 4Gy_TLR4i_10uM vs. 4Gy_CQ_10uM | 1.145 | -2.918 to 5.208 | ns | 0.9232 |

Supplementary Table 22. One-way ANOVA analysis results for SMARCD3 data represented in Figure 18 (RT-PCR for SMARCD3).

| Tukey's multiple comparisons test | Mean Diff. | 95.00% CI of diff. | Summary | Adjusted P Value |
|--|-------------------|---------------------------|----------------|-------------------------|
| 0Gy_DMSO vs. 4Gy_DMSO | -6.116 | -10.60 to -1.634 | ** | 0.0036 |
| 0Gy_DMSO vs. 4Gy_TLR3i_10uM | -0.5618 | -4.755 to 3.631 | ns | 0.9949 |
| 0Gy_DMSO vs. 4Gy_TLR4i_10uM | -1.861 | -5.743 to 2.021 | ns | 0.6382 |
| 0Gy_DMSO vs. 4Gy_CQ_10uM | 0.01055 | -5.479 to 5.501 | ns | >0.9999 |
| 4Gy_DMSO vs. 4Gy_TLR3i_10uM | 5.555 | 1.362 to 9.748 | ** | 0.0049 |
| 4Gy_DMSO vs. 4Gy_TLR4i_10uM | 4.255 | 0.3734 to 8.137 | * | 0.0262 |
| 4Gy_DMSO vs. 4Gy_CQ_10uM | 6.127 | 0.6371 to 11.62 | * | 0.0228 |
| 4Gy_TLR3i_10uM vs. 4Gy_TLR4i_10uM | -1.299 | -4.843 to 2.245 | ns | 0.8235 |
| 4Gy_TLR3i_10uM vs. 4Gy_CQ_10uM | 0.5724 | -4.684 to 5.829 | ns | 0.9977 |
| 4Gy_TLR4i_10uM vs. 4Gy_CQ_10uM | 1.872 | -3.140 to 6.883 | ns | 0.8136 |

Supplementary Table 23. One-way ANOVA analysis results for SMARCA1 data represented in Figure 19 (RT-PCR for SMARCA1 with 4Gy TLR9i).

| Tukey's multiple comparisons test | Mean Diff. | 95.00% CI of diff. | Summary | Adjusted P Value |
|--|-------------------|---------------------------|----------------|-------------------------|
| 0Gy_HycloneWater vs. 4Gy_HycloneWater | -1.410 | -3.016 to 0.1971 | ns | 0.1084 |
| 0Gy_HycloneWater vs. 4Gy_TLR9i_2.5uM | -0.2598 | -1.867 to 1.347 | ns | 0.9899 |
| 0Gy_HycloneWater vs. 4Gy_TLR9i_5uM | -0.7601 | -2.367 to 0.8466 | ns | 0.6551 |
| 0Gy_HycloneWater vs. 4Gy_TLR9i_7.5uM | 0.003661 | -2.269 to 2.276 | ns | >0.9999 |
| 4Gy_HycloneWater vs. 4Gy_TLR9i_2.5uM | 1.150 | -0.4569 to 2.757 | ns | 0.2603 |
| 4Gy_HycloneWater vs. 4Gy_TLR9i_5uM | 0.6495 | -0.9572 to 2.256 | ns | 0.7713 |
| 4Gy_HycloneWater vs. 4Gy_TLR9i_7.5uM | 1.413 | -0.8590 to 3.686 | ns | 0.3952 |
| 4Gy_TLR9i_2.5uM vs. 4Gy_TLR9i_5uM | -0.5003 | -2.107 to 1.106 | ns | 0.8961 |
| 4Gy_TLR9i_2.5uM vs. 4Gy_TLR9i_7.5uM | 0.2635 | -2.009 to 2.536 | ns | 0.9972 |
| 4Gy_TLR9i_5uM vs. 4Gy_TLR9i_7.5uM | 0.7638 | -1.508 to 3.036 | ns | 0.8676 |

Supplementary Table 24. One-way ANOVA analysis results for SMARCD3 data represented in Figure 19 (RT-PCR for SMARCD3 with 4Gy TLR9i).

| Tukey's multiple comparisons test | Mean Diff. | 95.00% CI of diff. | Summary | Adjusted P Value |
|---------------------------------------|------------|--------------------|---------|------------------|
| 0Gy_HycloneWater vs. 4Gy_HycloneWater | -0.4325 | -0.9671 to 0.1021 | ns | 0.1605 |
| 0Gy_HycloneWater vs. 4Gy_TLR9i_2.5uM | -0.3698 | -0.9044 to 0.1649 | ns | 0.2916 |
| 0Gy_HycloneWater vs. 4Gy_TLR9i_5uM | -0.7069 | -1.242 to -0.1723 | ** | 0.0048 |
| 0Gy_HycloneWater vs. 4Gy_TLR9i_7.5uM | -0.3131 | -1.069 to 0.4430 | ns | 0.7556 |
| 4Gy_HycloneWater vs. 4Gy_TLR9i_2.5uM | 0.06271 | -0.4719 to 0.5973 | ns | 0.9971 |
| 4Gy_HycloneWater vs. 4Gy_TLR9i_5uM | -0.2745 | -0.8091 to 0.2602 | ns | 0.5831 |
| 4Gy_HycloneWater vs. 4Gy_TLR9i_7.5uM | 0.1194 | -0.6367 to 0.8755 | ns | 0.9908 |
| 4Gy_TLR9i_2.5uM vs. 4Gy_TLR9i_5uM | -0.3372 | -0.8718 to 0.1974 | ns | 0.3813 |
| 4Gy_TLR9i_2.5uM vs. 4Gy_TLR9i_7.5uM | 0.05667 | -0.6994 to 0.8127 | ns | 0.9995 |
| 4Gy_TLR9i_5uM vs. 4Gy_TLR9i_7.5uM | 0.3939 | -0.3622 to 1.150 | ns | 0.5695 |

References:

- Agustinus, A. S., Al-Rawi, D., Dameracharla, B., Raviram, R., Jones, B., Stransky, S., . . . Bakhoun, S. F. (2023). Epigenetic dysregulation from chromosomal transit in micronuclei. *Nature*, *619*(7968), 176-183. doi:10.1038/s41586-023-06084-7
- Al-Bari, M. A. A. (2017). Targeting endosomal acidification by chloroquine analogs as a promising strategy for the treatment of emerging viral diseases. *Pharmacol Res Perspect*, *5*(1), e00293. doi:10.1002/prp2.293
- Alvarado, A. G., Thiagarajan, P. S., Mulkearns-Hubert, E. E., Silver, D. J., Hale, J. S., Alban, T. J., . . . Lathia, J. D. (2017). Glioblastoma Cancer Stem Cells Evade Innate Immune Suppression of Self-Renewal through Reduced TLR4 Expression. *Cell Stem Cell*, *20*(4), 450-461 e454. doi:10.1016/j.stem.2016.12.001
- Amarante-Mendes, G. P., Adjemian, S., Branco, L. M., Zanetti, L. C., Weinlich, R., & Bortoluci, K. R. (2018). Pattern Recognition Receptors and the Host Cell Death Molecular Machinery. *Front Immunol*, *9*, 2379. doi:10.3389/fimmu.2018.02379
- Baatout Sarah, D. M., Vlastimil Válek. (2023). *Radiobiology Textbook*: Springer International Publishing .
- Batchelor, T. Initial treatment and prognosis of IDH-wildtype glioblastoma in adults. Retrieved from https://www.uptodate.com/contents/initial-treatment-and-prognosis-of-idh-wildtype-glioblastoma-in-adults?search=glioblastoma%20multiform%20adult&source=search_result&selectedTitle=1~80&usage_type=default&display_rank=1#H13374802
- Berger, G., Knelson, E. H., Jimenez-Macias, J. L., Nowicki, M. O., Han, S., Panagioti, E., . . . Lawler, S. E. (2022). STING activation promotes robust immune response and NK cell-mediated tumor regression in glioblastoma models. *Proc Natl Acad Sci U S A*, *119*(28), e2111003119. doi:10.1073/pnas.2111003119
- Bhat, K., Duhachek-Muggy, S., Ramanathan, R., Saki, M., Alli, C., Medina, P., . . . Schaeue, D. (2019). 1-[(4-Nitrophenyl) sulfonyl]-4-phenylpiperazine increases the number of Peyer's patch-associated regenerating crypts in the small intestines after radiation injury. *Radiotherapy and Oncology*, *132*, 8-15.
- Bhat, K., Medina, P., He, L., Zhang, L., Saki, M., Ioannidis, A., . . . Pajonk, F. (2020). 1-[(4-Nitrophenyl)sulfonyl]-4-phenylpiperazine treatment after brain irradiation preserves cognitive function in mice. *Neuro Oncol*, *22*(10), 1484-1494. doi:10.1093/neuonc/noaa095
- Bhat, K., Saki, M., Cheng, F., He, L., Zhang, L., Ioannidis, A., . . . Pajonk, F. (2021). Dopamine Receptor Antagonists, Radiation, and Cholesterol Biosynthesis in Mouse Models of Glioblastoma. *J Natl Cancer Inst*, *113*(8), 1094-1104. doi:10.1093/jnci/djab018
- Bhat, K., Saki, M., Vlashi, E., Cheng, F., Duhachek-Muggy, S., Alli, C., . . . Pajonk, F. (2020). The dopamine receptor antagonist trifluoperazine prevents phenotype conversion and improves survival in mouse models of glioblastoma. *Proc Natl Acad Sci U S A*, *117*(20), 11085-11096. doi:10.1073/pnas.1920154117

- Briard, B., Place, D. E., & Kanneganti, T. D. (2020). DNA Sensing in the Innate Immune Response. *Physiology (Bethesda)*, 35(2), 112-124. doi:10.1152/physiol.00022.2019
- Cao, X. (2016). Self-regulation and cross-regulation of pattern-recognition receptor signalling in health and disease. *Nat Rev Immunol*, 16(1), 35-50. doi:10.1038/nri.2015.8
- Caragher, S. P., Shireman, J. M., Huang, M., Miska, J., Atashi, F., Baisiwala, S., . . . Ahmed, A. U. (2019). Activation of Dopamine Receptor 2 Prompts Transcriptomic and Metabolic Plasticity in Glioblastoma. *J Neurosci*, 39(11), 1982-1993. doi:10.1523/JNEUROSCI.1589-18.2018
- Chanda, P. K., Meng, S., Lee, J., Leung, H. E., Chen, K., & Cooke, J. P. (2019). Nuclear S-Nitrosylation Defines an Optimal Zone for Inducing Pluripotency. *Circulation*, 140(13), 1081-1099. doi:10.1161/CIRCULATIONAHA.119.042371
- Chapman, J. D., Reuvers, A. P., Borsa, J., & Greenstock, C. L. (1973). Chemical radioprotection and radiosensitization of mammalian cells growing in vitro. *Radiat Res*, 56(2), 291-306. Retrieved from <https://www.ncbi.nlm.nih.gov/pubmed/4749593>
- Chen, C., & Xu, P. (2023). Cellular functions of cGAS-STING signaling. *Trends Cell Biol*, 33(8), 630-648. doi:10.1016/j.tcb.2022.11.001
- Chen, G. Y., & Nunez, G. (2010). Sterile inflammation: sensing and reacting to damage. *Nat Rev Immunol*, 10(12), 826-837. doi:10.1038/nri2873
- Chen, X., Cheng, F., Liu, Y., Zhang, L., Song, L., Cai, X., . . . Zhu, H. (2019). Toll-like receptor 2 and Toll-like receptor 4 exhibit distinct regulation of cancer cell stemness mediated by cell death-induced high-mobility group box 1. *EBioMedicine*, 40, 135-150. doi:10.1016/j.ebiom.2018.12.016
- Cheray, M., Begaud, G., Deluche, E., Nivet, A., Battu, S., Lalloue, F., . . . Bessette, B. (2017). Cancer Stem-Like Cells in Glioblastoma. In S. De Vleeschouwer (Ed.), *Glioblastoma*. Brisbane (AU).
- Cooke, J. P. (2019). Inflammation and Its Role in Regeneration and Repair. *Circ Res*, 124(8), 1166-1168. doi:10.1161/CIRCRESAHA.118.314669
- Cooke, J. P., & Lai, L. (2023). Transflammation in tissue regeneration and response to injury: How cell-autonomous inflammatory signaling mediates cell plasticity. *Adv Drug Deliv Rev*, 203, 115118. doi:10.1016/j.addr.2023.115118
- Cowan, C. A., Atienza, J., Melton, D. A., & Eggan, K. (2005). Nuclear reprogramming of somatic cells after fusion with human embryonic stem cells. *Science*, 309(5739), 1369-1373. doi:10.1126/science.1116447
- Cui, S., Yu, Q., Chu, L., Cui, Y., Ding, M., Wang, Q., . . . Wang, C. (2020). Nuclear cGAS Functions Non-canonically to Enhance Antiviral Immunity via Recruiting Methyltransferase Prmt5. *Cell Rep*, 33(10), 108490. doi:10.1016/j.celrep.2020.108490

- Davis, R. L., Weintraub, H., & Lassar, A. B. (1987). Expression of a single transfected cDNA converts fibroblasts to myoblasts. *Cell*, 51(6), 987-1000. doi:10.1016/0092-8674(87)90585-x
- Dewar, J. M., & Walter, J. C. (2017). Mechanisms of DNA replication termination. *Nat Rev Mol Cell Biol*, 18(8), 507-516. doi:10.1038/nrm.2017.42
- Dietrich, J. (2024). Clinical presentation, diagnosis, and initial surgical management of high-grade gliomas. Retrieved from <https://www.uptodate.com/contents/clinical-presentation-diagnosis-and-initial-surgical-management-of-high-grade-gliomas>.
- Dou, Z., Ghosh, K., Vizioli, M. G., Zhu, J., Sen, P., Wangensteen, K. J., . . . Berger, S. L. (2017). Cytoplasmic chromatin triggers inflammation in senescence and cancer. *Nature*, 550(7676), 402-406. doi:10.1038/nature24050
- Duhachek-Muggy, S., Bhat, K., Medina, P., Cheng, F., He, L., Alli, C., . . . Pajonk, F. (2020). Radiation mitigation of the intestinal acute radiation injury in mice by 1-[(4-nitrophenyl)sulfonyl]-4-phenylpiperazine. *Stem Cells Transl Med*, 9(1), 106-119. doi:10.1002/sctm.19-0136
- Dunphy, G., Flannery, S. M., Almine, J. F., Connolly, D. J., Paulus, C., Jonsson, K. L., . . . Unterholzner, L. (2018). Non-canonical Activation of the DNA Sensing Adaptor STING by ATM and IFI16 Mediates NF-kappaB Signaling after Nuclear DNA Damage. *Mol Cell*, 71(5), 745-760 e745. doi:10.1016/j.molcel.2018.07.034
- El-Zayat, S. R., Sibaii, H., & Mannaa, F. A. (2019). Toll-like receptors activation, signaling, and targeting: an overview. *Bulletin of the National Research Centre*, 43(1), 187. doi:10.1186/s42269-019-0227-2
- EPA. Radiation Terms and Units. Retrieved from <https://www.epa.gov/radiation/radiation-terms-and-units#:~:text=A%20material's%20radioactivity%20is%20measured,radiation%20released%20by%20the%20material>.
- Evans, M. J., & Kaufman, M. H. (1981). Establishment in culture of pluripotential cells from mouse embryos. *Nature*, 292(5819), 154-156. doi:10.1038/292154a0
- Feldman, N., Rotter-Maskowitz, A., & Okun, E. (2015). DAMPs as mediators of sterile inflammation in aging-related pathologies. *Ageing Res Rev*, 24(Pt A), 29-39. doi:10.1016/j.arr.2015.01.003
- Fenech, M. (2007). Cytokinesis-block micronucleus cytome assay. *Nat Protoc*, 2(5), 1084-1104. doi:10.1038/nprot.2007.77
- Fernandes, C., Costa, A., Osorio, L., Lago, R. C., Linhares, P., Carvalho, B., & Caeiro, C. (2017). Current Standards of Care in Glioblastoma Therapy. In S. De Vleeschouwer (Ed.), *Glioblastoma*. Brisbane (AU).
- Ferrandez, E., Gutierrez, O., Segundo, D. S., & Fernandez-Luna, J. L. (2018). NFkappaB activation in differentiating glioblastoma stem-like cells is promoted by hyaluronic acid signaling through TLR4. *Sci Rep*, 8(1), 6341. doi:10.1038/s41598-018-24444-6

- Figueroa, M. Principles of epigenetics. Retrieved from https://www.uptodate.com/contents/principles-of-epigenetics?search=glioblastoma&source=search_result&selectedTitle=45~80&usage_type=default&display_rank=45#H396132
- Fulda, S., Gorman, A. M., Hori, O., & Samali, A. (2010). Cellular stress responses: cell survival and cell death. *Int J Cell Biol*, 2010, 214074. doi:10.1155/2010/214074
- Gaidt, M. M., Ebert, T. S., Chauhan, D., Ramshorn, K., Pinci, F., Zuber, S., . . . Hornung, V. (2017). The DNA Inflammasome in Human Myeloid Cells Is Initiated by a STING-Cell Death Program Upstream of NLRP3. *Cell*, 171(5), 1110-1124 e1118. doi:10.1016/j.cell.2017.09.039
- Ganguly, D., Sims, M., Cai, C., Fan, M., & Pfeffer, L. M. (2018). Chromatin Remodeling Factor BRG1 Regulates Stemness and Chemosensitivity of Glioma Initiating Cells. *Stem Cells*, 36(12), 1804-1815. doi:10.1002/stem.2909
- Gao, W., Xiong, Y., Li, Q., & Yang, H. (2017). Inhibition of Toll-Like Receptor Signaling as a Promising Therapy for Inflammatory Diseases: A Journey from Molecular to Nano Therapeutics. *Front Physiol*, 8, 508. doi:10.3389/fphys.2017.00508
- Ge, S. X., Son, E. W., & Yao, R. (2018). iDEP: an integrated web application for differential expression and pathway analysis of RNA-Seq data. *BMC Bioinformatics*, 19(1), 534. doi:10.1186/s12859-018-2486-6
- Gies, V., Bekaddour, N., Dieudonne, Y., Guffroy, A., Frenger, Q., Gros, F., . . . Korganow, A. S. (2020). Beyond Anti-viral Effects of Chloroquine/Hydroxychloroquine. *Front Immunol*, 11, 1409. doi:10.3389/fimmu.2020.01409
- Gong, T., Liu, L., Jiang, W., & Zhou, R. (2020). DAMP-sensing receptors in sterile inflammation and inflammatory diseases. *Nat Rev Immunol*, 20(2), 95-112. doi:10.1038/s41577-019-0215-7
- Gonugunta, V. K., Sakai, T., Pokatayev, V., Yang, K., Wu, J., Dobbs, N., & Yan, N. (2017). Trafficking-Mediated STING Degradation Requires Sorting to Acidified Endolysosomes and Can Be Targeted to Enhance Anti-tumor Response. *Cell Rep*, 21(11), 3234-3242. doi:10.1016/j.celrep.2017.11.061
- Guey, B., Wischniewski, M., Decout, A., Makasheva, K., Kaynak, M., Sakar, M. S., . . . Ablasser, A. (2020). BAF restricts cGAS on nuclear DNA to prevent innate immune activation. *Science*, 369(6505), 823-828. doi:10.1126/science.aaw6421
- Gui, X., Yang, H., Li, T., Tan, X., Shi, P., Li, M., . . . Chen, Z. J. (2019). Autophagy induction via STING trafficking is a primordial function of the cGAS pathway. *Nature*, 567(7747), 262-266. doi:10.1038/s41586-019-1006-9
- Gurdon, J. B. (1962). The developmental capacity of nuclei taken from intestinal epithelium cells of feeding tadpoles. *J Embryol Exp Morphol*, 10, 622-640. Retrieved from <https://www.ncbi.nlm.nih.gov/pubmed/13951335>

- Gurdon, J. B., Elsdale, T. R., & Fischberg, M. (1958). Sexually mature individuals of *Xenopus laevis* from the transplantation of single somatic nuclei. *Nature*, *182*(4627), 64-65. doi:10.1038/182064a0
- Hanahan, D. (2022). Hallmarks of Cancer: New Dimensions. *Cancer Discov*, *12*(1), 31-46. doi:10.1158/2159-8290.CD-21-1059
- Hanahan, D., & Weinberg, R. A. (2011). Hallmarks of cancer: the next generation. *Cell*, *144*(5), 646-674. doi:10.1016/j.cell.2011.02.013
- Hansen, T. O., Rehfeld, J. F., & Nielsen, F. C. (2000). Cyclic AMP-induced neuronal differentiation via activation of p38 mitogen-activated protein kinase. *J Neurochem*, *75*(5), 1870-1877. doi:10.1046/j.1471-4159.2000.0751870.x
- Harding, S. M., Benci, J. L., Irianto, J., Discher, D. E., Minn, A. J., & Greenberg, R. A. (2017). Mitotic progression following DNA damage enables pattern recognition within micronuclei. *Nature*, *548*(7668), 466-470. doi:10.1038/nature23470
- He, L., Azizad, D., Bhat, K., Ioannidis, A., Hoffman, C. J., Arambula, E., . . . Pajonk, F. (2024). Radiation-Induced Cellular Plasticity: A Strategy for Combatting Glioblastoma. *bioRxiv*, 2024.2005.2013.593985. doi:10.1101/2024.05.13.593985
- He, L., Bhat, K., Duhacheck-Muggy, S., Ioannidis, A., Zhang, L., Nguyen, N. T., . . . Pajonk, F. (2021). Tumor necrosis factor receptor signaling modulates carcinogenesis in a mouse model of breast cancer. *Neoplasia*, *23*(2), 197-209. doi:10.1016/j.neo.2020.12.007
- He, L., Bhat, K., Ioannidis, A., & Pajonk, F. (2023). Effects of Dopamine Receptor Antagonists and Radiation on Mouse Neural Stem/Progenitor Cells. *bioRxiv*. doi:10.1101/2023.01.18.524632
- He, L., Bhat, K., Ioannidis, A., Zhang, L., Nguyen, N. T., Allen, J. E., . . . Pajonk, F. (2021). Effects of the DRD2/3 antagonist ONC201 and radiation in glioblastoma. *Radiother Oncol*, *161*, 140-147. doi:10.1016/j.radonc.2021.05.027
- He, L., Ioannidis, A., Arambula, E., Hoffman, C. J., Joshi, P., Kathiravan, A., . . . Pajonk, F. (2023). Activation of the mevalonate pathway in response to anti-cancer treatments drives glioblastoma recurrences through activation of Rac-1. *bioRxiv*. doi:10.1101/2023.07.23.550205
- He, L., Liu, H., & Tang, L. (2012). SWI/SNF chromatin remodeling complex: a new cofactor in reprogramming. *Stem Cell Rev Rep*, *8*(1), 128-136. doi:10.1007/s12015-011-9285-z
- Hernandez, C., Huebener, P., & Schwabe, R. F. (2016). Damage-associated molecular patterns in cancer: a double-edged sword. *Oncogene*, *35*(46), 5931-5941. doi:10.1038/onc.2016.104
- Herrmann, A., Cherryholmes, G., Schroeder, A., Phallen, J., Alizadeh, D., Xin, H., . . . Yu, H. (2014). TLR9 is critical for glioma stem cell maintenance and targeting. *Cancer Res*, *74*(18), 5218-5228. doi:10.1158/0008-5472.CAN-14-1151

- Hiramatsu, H., Kobayashi, K., Kobayashi, K., Haraguchi, T., Ino, Y., Todo, T., & Iba, H. (2017). The role of the SWI/SNF chromatin remodeling complex in maintaining the stemness of glioma initiating cells. *Sci Rep*, 7(1), 889. doi:10.1038/s41598-017-00982-3
- Holm, C. K., Rahbek, S. H., Gad, H. H., Bak, R. O., Jakobsen, M. R., Jiang, Z., . . . Paludan, S. R. (2016). Influenza A virus targets a cGAS-independent STING pathway that controls enveloped RNA viruses. *Nat Commun*, 7, 10680. doi:10.1038/ncomms10680
- Hong, C., Schubert, M., Tijhuis, A. E., Requesens, M., Roorda, M., van den Brink, A., . . . Foijer, F. (2022). cGAS-STING drives the IL-6-dependent survival of chromosomally unstable cancers. *Nature*, 607(7918), 366-373. doi:10.1038/s41586-022-04847-2
- Hong, Z., Mei, J., Guo, H., Zhu, J., & Wang, C. (2022). Intervention of cGAS–STING signaling in sterile inflammatory diseases. *J Mol Cell Biol*, 14(2). doi:10.1093/jmcb/mjac005
- Hopfner, K. P., & Hornung, V. (2020). Molecular mechanisms and cellular functions of cGAS-STING signalling. *Nat Rev Mol Cell Biol*, 21(9), 501-521. doi:10.1038/s41580-020-0244-x
- Hu, B., Jin, C., Li, H. B., Tong, J., Ouyang, X., Cetinbas, N. M., . . . Flavell, R. A. (2016). The DNA-sensing AIM2 inflammasome controls radiation-induced cell death and tissue injury. *Science*, 354(6313), 765-768. doi:10.1126/science.aaf7532
- Hu, J., Shi, B., Liu, X., Jiang, M., Yuan, C., Jiang, B., . . . Wang, G. (2018). The activation of Toll-like receptor 4 reverses tumor differentiation in human glioma U251 cells via Notch pathway. *Int Immunopharmacol*, 64, 33-41. doi:10.1016/j.intimp.2018.08.019
- Hu, Y., & Smyth, G. K. (2009). ELDA: extreme limiting dilution analysis for comparing depleted and enriched populations in stem cell and other assays. *J Immunol Methods*, 347(1-2), 70-78. doi:10.1016/j.jim.2009.06.008
- Jang, S., Cho, H. H., Cho, Y. B., Park, J. S., & Jeong, H. S. (2010). Functional neural differentiation of human adipose tissue-derived stem cells using bFGF and forskolin. *BMC Cell Biol*, 11, 25. doi:10.1186/1471-2121-11-25
- Jellinger, K. (1977). Human central nervous system lesions following radiation therapy. *Zentralbl Neurochir*, 38(2), 199-200. Retrieved from <https://www.ncbi.nlm.nih.gov/pubmed/607710>
- Jesenko, T., Bosnjak, M., Markelc, B., Sersa, G., Znidar, K., Heller, L., & Cemazar, M. (2020). Radiation Induced Upregulation of DNA Sensing Pathways is Cell-Type Dependent and Can Mediate the Off-Target Effects. *Cancers (Basel)*, 12(11). doi:10.3390/cancers12113365
- Jessen, K. R., Mirsky, R., & Arthur-Farraj, P. (2015). The Role of Cell Plasticity in Tissue Repair: Adaptive Cellular Reprogramming. *Dev Cell*, 34(6), 613-620. doi:10.1016/j.devcel.2015.09.005
- Jia, D., Yang, W., Li, L., Liu, H., Tan, Y., Ooi, S., . . . Wang, L. (2015). beta-Catenin and NF-kappaB co-activation triggered by TLR3 stimulation facilitates stem cell-like phenotypes in breast cancer. *Cell Death Differ*, 22(2), 298-310. doi:10.1038/cdd.2014.145

- Jiang, J., Chan, Y. S., Loh, Y. H., Cai, J., Tong, G. Q., Lim, C. A., . . . Ng, H. H. (2008). A core Klf circuitry regulates self-renewal of embryonic stem cells. *Nat Cell Biol*, *10*(3), 353-360. doi:10.1038/ncb1698
- Jiang, Q., Huang, X., Hu, X., Shan, Z., Wu, Y., Wu, G., & Lei, L. (2020). Histone demethylase KDM6A promotes somatic cell reprogramming by epigenetically regulating the PTEN and IL-6 signal pathways. *Stem Cells*, *38*(8), 960-972. doi:10.1002/stem.3188
- Jiralerspong, S., & Goodwin, P. J. (2016). Obesity and Breast Cancer Prognosis: Evidence, Challenges, and Opportunities. *J Clin Oncol*, *34*(35), 4203-4216. doi:10.1200/JCO.2016.68.4480
- Kadoch, C., & Crabtree, G. R. (2015). Mammalian SWI/SNF chromatin remodeling complexes and cancer: Mechanistic insights gained from human genomics. *Sci Adv*, *1*(5), e1500447. doi:10.1126/sciadv.1500447
- Kashani, B., Zandi, Z., Pourbagheri-Sigaroodi, A., Bashash, D., & Ghaffari, S. H. (2021). The role of toll-like receptor 4 (TLR4) in cancer progression: A possible therapeutic target? *J Cell Physiol*, *236*(6), 4121-4137. doi:10.1002/jcp.30166
- Kato, H., Sato, S., Yoneyama, M., Yamamoto, M., Uematsu, S., Matsui, K., . . . Akira, S. (2005). Cell type-specific involvement of RIG-I in antiviral response. *Immunity*, *23*(1), 19-28. doi:10.1016/j.immuni.2005.04.010
- Kawai, T., & Akira, S. (2005). Toll-like receptor downstream signaling. *Arthritis Res Ther*, *7*(1), 12-19. doi:10.1186/ar1469
- Kawai, T., Takahashi, K., Sato, S., Coban, C., Kumar, H., Kato, H., . . . Akira, S. (2005). IPS-1, an adaptor triggering RIG-I- and Mda5-mediated type I interferon induction. *Nat Immunol*, *6*(10), 981-988. doi:10.1038/ni1243
- Kim, W. Y., & Snider, W. D. (2011). Functions of GSK-3 Signaling in Development of the Nervous System. *Front Mol Neurosci*, *4*, 44. doi:10.3389/fnmol.2011.00044
- Konno, H., Yamauchi, S., Berglund, A., Putney, R. M., Mule, J. J., & Barber, G. N. (2018). Suppression of STING signaling through epigenetic silencing and missense mutation impedes DNA damage mediated cytokine production. *Oncogene*, *37*(15), 2037-2051. doi:10.1038/s41388-017-0120-0
- Kooistra, S. M., & Helin, K. (2012). Molecular mechanisms and potential functions of histone demethylases. *Nature reviews Molecular cell biology*, *13*(5), 297-311.
- Krombach, J., Hennel, R., Brix, N., Orth, M., Schoetz, U., Ernst, A., . . . Lauber, K. (2019). Priming anti-tumor immunity by radiotherapy: Dying tumor cell-derived DAMPs trigger endothelial cell activation and recruitment of myeloid cells. *Oncoimmunology*, *8*(1), e1523097. doi:10.1080/2162402X.2018.1523097
- Krupina, K., Goginashvili, A., & Cleveland, D. W. (2021). Causes and consequences of micronuclei. *Curr Opin Cell Biol*, *70*, 91-99. doi:10.1016/j.ceb.2021.01.004

- Kumar, V., Bauer, C., & Stewart, J. H. t. (2023). Cancer cell-specific cGAS/STING Signaling pathway in the era of advancing cancer cell biology. *Eur J Cell Biol*, *102*(3), 151338. doi:10.1016/j.ejcb.2023.151338
- Lagadec, C., Vlashi, E., Della Donna, L., Dekmezian, C., & Pajonk, F. (2012). Radiation-induced reprogramming of breast cancer cells. *Stem Cells*, *30*(5), 833-844. doi:10.1002/stem.1058
- Lai, A. Y., & Wade, P. A. (2011). Cancer biology and NuRD: a multifaceted chromatin remodelling complex. *Nat Rev Cancer*, *11*(8), 588-596. doi:10.1038/nrc3091
- Laks, D. R., Crisman, T. J., Shih, M. Y., Mottahedeh, J., Gao, F., Sperry, J., . . . Kornblum, H. I. (2016). Large-scale assessment of the gliomasphere model system. *Neuro Oncol*, *18*(10), 1367-1378. doi:10.1093/neuonc/now045
- Laks, D. R., Visnyei, K., & Kornblum, H. I. (2010). Brain tumor stem cells as therapeutic targets in models of glioma. *Yonsei Med J*, *51*(5), 633-640. doi:10.3349/ymj.2010.51.5.633
- Lannoy, V., Cote-Biron, A., Asselin, C., & Rivard, N. (2023). TIRAP, TRAM, and Toll-Like Receptors: The Untold Story. *Mediators Inflamm*, *2023*, 2899271. doi:10.1155/2023/2899271
- Larjavaara, S., Mantyla, R., Salminen, T., Haapasalo, H., Raitanen, J., Jaaskelainen, J., & Auvinen, A. (2007). Incidence of gliomas by anatomic location. *Neuro Oncol*, *9*(3), 319-325. doi:10.1215/15228517-2007-016
- Lee, J., Sayed, N., Hunter, A., Au, K. F., Wong, W. H., Mocarski, E. S., . . . Cooke, J. P. (2012). Activation of innate immunity is required for efficient nuclear reprogramming. *Cell*, *151*(3), 547-558. doi:10.1016/j.cell.2012.09.034
- Li, Q., & Verma, I. M. (2002). NF-kappaB regulation in the immune system. *Nat Rev Immunol*, *2*(10), 725-734. doi:10.1038/nri910
- Li, S., Wang, C., Chen, J., Lan, Y., Zhang, W., Kang, Z., . . . Li, W. (2023). Signaling pathways in brain tumors and therapeutic interventions. *Signal Transduct Target Ther*, *8*(1), 8. doi:10.1038/s41392-022-01260-z
- Li, Y., Wang, D., Ge, H., Gungor, C., Gong, X., & Chen, Y. (2022). Cytoskeletal and Cytoskeleton-Associated Proteins: Key Regulators of Cancer Stem Cell Properties. *Pharmaceuticals (Basel)*, *15*(11). doi:10.3390/ph15111369
- Li, Y., Wang, W., Wang, F., Wu, Q., Li, W., Zhong, X., . . . Zhou, Y. (2017). Paired related homeobox 1 transactivates dopamine D2 receptor to maintain propagation and tumorigenicity of glioma-initiating cells. *J Mol Cell Biol*, *9*(4), 302-314. doi:10.1093/jmcb/mjx017
- Liberti, M. V., & Locasale, J. W. (2016). The Warburg Effect: How Does it Benefit Cancer Cells? *Trends Biochem Sci*, *41*(3), 211-218. doi:10.1016/j.tibs.2015.12.001
- Liu, H., Zhang, H., Wu, X., Ma, D., Wu, J., Wang, L., . . . Ge, B. (2018). Nuclear cGAS suppresses DNA repair and promotes tumorigenesis. *Nature*, *563*(7729), 131-136. doi:10.1038/s41586-018-0629-6

- Liu, W. T., Jing, Y. Y., Yu, G. F., Han, Z. P., Yu, D. D., Fan, Q. M., . . . Wei, L. X. (2015). Toll like receptor 4 facilitates invasion and migration as a cancer stem cell marker in hepatocellular carcinoma. *Cancer Lett*, 358(2), 136-143. doi:10.1016/j.canlet.2014.12.019
- Louis, D., Schiff, D., Batchelor, T. Classification and pathologic diagnosis of gliomas, glioneuronal tumors, and neuronal tumors. Retrieved from https://www.uptodate.com/contents/classification-and-pathologic-diagnosis-of-gliomas-glioneuronal-tumors-and-neuronal-tumors?search=glioma&source=search_result&selectedTitle=1~150&usage_type=default&display_rank=1#H11
- Louis, D. N., Perry, A., Wesseling, P., Brat, D. J., Cree, I. A., Figarella-Branger, D., . . . Ellison, D. W. (2021). The 2021 WHO Classification of Tumors of the Central Nervous System: a summary. *Neuro Oncol*, 23(8), 1231-1251. doi:10.1093/neuonc/noab106
- Louis, D. N., Schiff, D., & Batchelor, T. (2024). Classification and pathologic diagnosis of gliomas, glioneuronal tumors, and neuronal tumors. Retrieved from https://www.uptodate.com/contents/classification-and-pathologic-diagnosis-of-gliomas-glioneuronal-tumors-and-neuronal-tumors?search=diffuse%20glioma&source=search_result&selectedTitle=1%7E150&usage_type=default&display_rank=1.
- Low, J. T., Chandramohan, V., Bowie, M. L., Brown, M. C., Waitkus, M. S., Briley, A., . . . Ashley, D. M. (2022). Epigenetic STING silencing is developmentally conserved in gliomas and can be rescued by methyltransferase inhibition. *Cancer Cell*, 40(5), 439-440. doi:10.1016/j.ccell.2022.04.009
- Martin, G. R. (1981). Isolation of a pluripotent cell line from early mouse embryos cultured in medium conditioned by teratocarcinoma stem cells. *Proc Natl Acad Sci U S A*, 78(12), 7634-7638. doi:10.1073/pnas.78.12.7634
- Mavragani, I. V., Laskaratou, D. A., Frey, B., Candeias, S. M., Gaipf, U. S., Lumniczky, K., & Georgakilas, A. G. (2016). Key mechanisms involved in ionizing radiation-induced systemic effects. A current review. *Toxicol Res (Camb)*, 5(1), 12-33. doi:10.1039/c5tx00222b
- Mayo_Clinic. How your brain works. Retrieved from <https://www.mayoclinic.org/brain/sls-20077047?s=3>
- Mayo_Clinic. Radiation therapy. Retrieved from <https://www.mayoclinic.org/tests-procedures/radiation-therapy/about/pac-20385162#:~:text=In%20fact%2C%20more%20than%20half,t%20cancerous%2C%20called%20benign%20tumors>
- McKelvey, K. J., Hudson, A. L., Back, M., Eade, T., & Diakos, C. I. (2018). Radiation, inflammation and the immune response in cancer. *Mamm Genome*, 29(11-12), 843-865. doi:10.1007/s00335-018-9777-0
- McKinnon, C., Nandhabalan, M., Murray, S. A., & Plaha, P. (2021). Glioblastoma: clinical presentation, diagnosis, and management. *BMJ*, 374, n1560. doi:10.1136/bmj.n1560

- Meng, S., Chanda, P., & Cooke, J. P. (2016). Role of innate immune signaling in nuclear reprogramming. *Regenerative Medicine-from Protocol to Patient: 1. Biology of Tissue Regeneration*, 291-305.
- Meng, S., Chanda, P., Thandavarayan, R. A., & Cooke, J. P. (2017). Transflammation: Innate immune signaling in nuclear reprogramming. *Adv Drug Deliv Rev*, 120, 133-141. doi:10.1016/j.addr.2017.09.010
- Moreira, D., Zhang, Q., Hossain, D. M., Nechaev, S., Li, H., Kowolik, C. M., . . . Kortylewski, M. (2015). TLR9 signaling through NF-kappaB/RELA and STAT3 promotes tumor-propagating potential of prostate cancer cells. *Oncotarget*, 6(19), 17302-17313. doi:10.18632/oncotarget.4029
- Morgan, A., LeGresley, S., & Fischer, C. (2020). Remodeler Catalyzed Nucleosome Repositioning: Influence of Structure and Stability. *Int J Mol Sci*, 22(1). doi:10.3390/ijms22010076
- Muraguchi, A., Miyazaki, K., Kehrl, J. H., & Fauci, A. S. (1984). Inhibition of human B cell activation by diterpine forskolin: interference with B cell growth factor-induced G1 to S transition of the B cell cycle. *J Immunol*, 133(3), 1283-1287. Retrieved from <https://www.ncbi.nlm.nih.gov/pubmed/6086754>
- Muthukrishnan, S. D., Kawaguchi, R., Nair, P., Prasad, R., Qin, Y., Johnson, M., . . . Kornblum, H. I. (2022). P300 promotes tumor recurrence by regulating radiation-induced conversion of glioma stem cells to vascular-like cells. *Nat Commun*, 13(1), 6202. doi:10.1038/s41467-022-33943-0
- Nakagawa, M., Koyanagi, M., Tanabe, K., Takahashi, K., Ichisaka, T., Aoi, T., . . . Yamanaka, S. (2008). Generation of induced pluripotent stem cells without Myc from mouse and human fibroblasts. *Nat Biotechnol*, 26(1), 101-106. doi:10.1038/nbt1374
- Nakagawa, M., Takizawa, N., Narita, M., Ichisaka, T., & Yamanaka, S. (2010). Promotion of direct reprogramming by transformation-deficient Myc. *Proc Natl Acad Sci U S A*, 107(32), 14152-14157. doi:10.1073/pnas.1009374107
- Navickas, S. M., Giles, K. A., Brettingham-Moore, K. H., & Taberlay, P. C. (2023). The role of chromatin remodeler SMARCA4/BRG1 in brain cancers: a potential therapeutic target. *Oncogene*, 42(31), 2363-2373. doi:10.1038/s41388-023-02773-9
- NCI. Radiation Therapy to Treat Cancer. Retrieved from www.cancer.gov/about-cancer/treatment/types/radiation-therapy#:~:text=during%20radiation%20therapy-,How%20radiation%20therapy%20works%20against%20cancer,and%20removed%20by%20the%20body
- Neftel, C., Laffy, J., Filbin, M. G., Hara, T., Shore, M. E., Rahme, G. J., . . . Suva, M. L. (2019). An Integrative Model of Cellular States, Plasticity, and Genetics for Glioblastoma. *Cell*, 178(4), 835-849 e821. doi:10.1016/j.cell.2019.06.024

- Ostrom, Q. T., Bauchet, L., Davis, F. G., Deltour, I., Fisher, J. L., Langer, C. E., . . . Barnholtz-Sloan, J. S. (2014). The epidemiology of glioma in adults: a "state of the science" review. *Neuro Oncol*, *16*(7), 896-913. doi:10.1093/neuonc/nou087
- Ostrom, Q. T., Gittleman, H., Truitt, G., Boscia, A., Kruchko, C., & Barnholtz-Sloan, J. S. (2018). CBTRUS Statistical Report: Primary Brain and Other Central Nervous System Tumors Diagnosed in the United States in 2011-2015. *Neuro Oncol*, *20*(suppl_4), iv1-iv86. doi:10.1093/neuonc/noy131
- Ostrom, Q. T., Price, M., Neff, C., Cioffi, G., Waite, K. A., Kruchko, C., & Barnholtz-Sloan, J. S. (2023). CBTRUS Statistical Report: Primary Brain and Other Central Nervous System Tumors Diagnosed in the United States in 2016-2020. *Neuro Oncol*, *25*(12 Suppl 2), iv1-iv99. doi:10.1093/neuonc/noad149
- Paksa, A., & Rajagopal, J. (2017). The epigenetic basis of cellular plasticity. *Curr Opin Cell Biol*, *49*, 116-122. doi:10.1016/j.ceb.2018.01.003
- Pan, J., Fei, C. J., Hu, Y., Wu, X. Y., Nie, L., & Chen, J. (2023). Current understanding of the cGAS-STING signaling pathway: Structure, regulatory mechanisms, and related diseases. *Zool Res*, *44*(1), 183-218. doi:10.24272/j.issn.2095-8137.2022.464
- Pastrana, E., Silva-Vargas, V., & Doetsch, F. (2011). Eyes wide open: a critical review of sphere-formation as an assay for stem cells. *Cell Stem Cell*, *8*(5), 486-498. doi:10.1016/j.stem.2011.04.007
- Patel, A. P., Tirosh, I., Trombetta, J. J., Shalek, A. K., Gillespie, S. M., Wakimoto, H., . . . Bernstein, B. E. (2014). Single-cell RNA-seq highlights intratumoral heterogeneity in primary glioblastoma. *Science*, *344*(6190), 1396-1401. doi:10.1126/science.1254257
- Phillips, T., & Shaw, K. (2008). Chromatin remodeling in eukaryotes. *Nature Education*, *1*(1), 209.
- Rehwinkel, J., & Gack, M. U. (2020). RIG-I-like receptors: their regulation and roles in RNA sensing. *Nat Rev Immunol*, *20*(9), 537-551. doi:10.1038/s41577-020-0288-3
- Reyes, A. A., Marcum, R. D., & He, Y. (2021). Structure and Function of Chromatin Remodelers. *J Mol Biol*, *433*(14), 166929. doi:10.1016/j.jmb.2021.166929
- Roberts, C. W., & Orkin, S. H. (2004). The SWI/SNF complex--chromatin and cancer. *Nat Rev Cancer*, *4*(2), 133-142. doi:10.1038/nrc1273
- Roh, J. S., & Sohn, D. H. (2018). Damage-Associated Molecular Patterns in Inflammatory Diseases. *Immune Netw*, *18*(4), e27. doi:10.4110/in.2018.18.e27
- Rosin, D. L., & Okusa, M. D. (2011). Dangers within: DAMP responses to damage and cell death in kidney disease. *J Am Soc Nephrol*, *22*(3), 416-425. doi:10.1681/ASN.2010040430
- Rubartelli, A., & Lotze, M. T. (2007). Inside, outside, upside down: damage-associated molecular-pattern molecules (DAMPs) and redox. *Trends Immunol*, *28*(10), 429-436. doi:10.1016/j.it.2007.08.004

- Sameer, A. S., & Nissar, S. (2021). Toll-Like Receptors (TLRs): Structure, Functions, Signaling, and Role of Their Polymorphisms in Colorectal Cancer Susceptibility. *Biomed Res Int*, 2021, 1157023. doi:10.1155/2021/1157023
- Sayed, N., Ospino, F., Himmati, F., Lee, J., Chanda, P., Mocarski, E. S., & Cooke, J. P. (2017). Retinoic Acid Inducible Gene 1 Protein (RIG1)-Like Receptor Pathway Is Required for Efficient Nuclear Reprogramming. *Stem Cells*, 35(5), 1197-1207. doi:10.1002/stem.2607
- Sayed, N., Wong, W. T., Ospino, F., Meng, S., Lee, J., Jha, A., . . . Cooke, J. P. (2015). Transdifferentiation of human fibroblasts to endothelial cells: role of innate immunity. *Circulation*, 131(3), 300-309. doi:10.1161/CIRCULATIONAHA.113.007394
- Seamon, K. B., & Daly, J. W. (1986). Forskolin: its biological and chemical properties. *Adv Cyclic Nucleotide Protein Phosphorylation Res*, 20, 1-150. Retrieved from <https://www.ncbi.nlm.nih.gov/pubmed/3028083>
- Shaker, B., Lee, J., Lee, Y., Yu, M. S., Lee, H. M., Lee, E., . . . Na, D. (2023). A machine learning-based quantitative model (LogBB_Pred) to predict the blood-brain barrier permeability (logBB value) of drug compounds. *Bioinformatics*, 39(10). doi:10.1093/bioinformatics/btad577
- Song, J. X., Villagomes, D., Zhao, H., & Zhu, M. (2022). cGAS in nucleus: The link between immune response and DNA damage repair. *Front Immunol*, 13, 1076784. doi:10.3389/fimmu.2022.1076784
- Tada, M., Takahama, Y., Abe, K., Nakatsuji, N., & Tada, T. (2001). Nuclear reprogramming of somatic cells by in vitro hybridization with ES cells. *Curr Biol*, 11(19), 1553-1558. doi:10.1016/s0960-9822(01)00459-6
- Takahashi, K., Tanabe, K., Ohnuki, M., Narita, M., Ichisaka, T., Tomoda, K., & Yamanaka, S. (2007). Induction of pluripotent stem cells from adult human fibroblasts by defined factors. *Cell*, 131(5), 861-872. doi:10.1016/j.cell.2007.11.019
- Takahashi, K., & Yamanaka, S. (2006). Induction of pluripotent stem cells from mouse embryonic and adult fibroblast cultures by defined factors. *Cell*, 126(4), 663-676. doi:10.1016/j.cell.2006.07.024
- Takahashi, K., & Yamanaka, S. (2016). A decade of transcription factor-mediated reprogramming to pluripotency. *Nat Rev Mol Cell Biol*, 17(3), 183-193. doi:10.1038/nrm.2016.8
- Takeda, K., Kaisho, T., & Akira, S. (2003). Toll-like receptors. *Annu Rev Immunol*, 21, 335-376. doi:10.1146/annurev.immunol.21.120601.141126
- Takeuchi, O., & Akira, S. (2010). Pattern recognition receptors and inflammation. *Cell*, 140(6), 805-820. doi:10.1016/j.cell.2010.01.022
- Tan, R. S., Ho, B., Leung, B. P., & Ding, J. L. (2014). TLR cross-talk confers specificity to innate immunity. *Int Rev Immunol*, 33(6), 443-453. doi:10.3109/08830185.2014.921164

- Tang, L., Nogales, E., & Ciferri, C. (2010). Structure and function of SWI/SNF chromatin remodeling complexes and mechanistic implications for transcription. *Prog Biophys Mol Biol*, *102*(2-3), 122-128. doi:10.1016/j.pbiomolbio.2010.05.001
- Tejero, R., Huang, Y., Katsyv, I., Kluge, M., Lin, J. Y., Tome-Garcia, J., . . . Friedel, R. H. (2019). Gene signatures of quiescent glioblastoma cells reveal mesenchymal shift and interactions with niche microenvironment. *EBioMedicine*, *42*, 252-269. doi:10.1016/j.ebiom.2019.03.064
- Tian, J., Avalos, A. M., Mao, S. Y., Chen, B., Senthil, K., Wu, H., . . . Coyle, A. J. (2007). Toll-like receptor 9-dependent activation by DNA-containing immune complexes is mediated by HMGB1 and RAGE. *Nat Immunol*, *8*(5), 487-496. doi:10.1038/ni1457
- Travis, L. B., Hill, D., Dores, G. M., Gospodarowicz, M., van Leeuwen, F. E., Holowaty, E., . . . Gail, M. H. (2005). Cumulative absolute breast cancer risk for young women treated for Hodgkin lymphoma. *J Natl Cancer Inst*, *97*(19), 1428-1437. doi:10.1093/jnci/dji290
- Tsompana, M., & Buck, M. J. (2014). Chromatin accessibility: a window into the genome. *Epigenetics Chromatin*, *7*(1), 33. doi:10.1186/1756-8935-7-33
- Vashi, N., & Bakhoun, S. F. (2021). The Evolution of STING Signaling and Its Involvement in Cancer. *Trends Biochem Sci*, *46*(6), 446-460. doi:10.1016/j.tibs.2020.12.010
- Venereau, E., Ceriotti, C., & Bianchi, M. E. (2015). DAMPs from Cell Death to New Life. *Front Immunol*, *6*, 422. doi:10.3389/fimmu.2015.00422
- Verhaak, R. G., Hoadley, K. A., Purdom, E., Wang, V., Qi, Y., Wilkerson, M. D., . . . Cancer Genome Atlas Research, N. (2010). Integrated genomic analysis identifies clinically relevant subtypes of glioblastoma characterized by abnormalities in PDGFRA, IDH1, EGFR, and NF1. *Cancer Cell*, *17*(1), 98-110. doi:10.1016/j.ccr.2009.12.020
- Vlashi, E., Kim, K., Lagadec, C., Donna, L. D., McDonald, J. T., Eghbali, M., . . . Pajonk, F. (2009). In vivo imaging, tracking, and targeting of cancer stem cells. *J Natl Cancer Inst*, *101*(5), 350-359. doi:10.1093/jnci/djn509
- Volkman, H. E., Cambier, S., Gray, E. E., & Stetson, D. B. (2019). Tight nuclear tethering of cGAS is essential for preventing autoreactivity. *Elife*, *8*. doi:10.7554/eLife.47491
- Wang, C. H., Wang, P. J., Hsieh, Y. C., Lo, S., Lee, Y. C., Chen, Y. C., . . . Yuan, S. S. (2018). Resistin facilitates breast cancer progression via TLR4-mediated induction of mesenchymal phenotypes and stemness properties. *Oncogene*, *37*(5), 589-600. doi:10.1038/onc.2017.357
- Wang, F., Zhang, P., Yang, L., Yu, X., Ye, X., Yang, J., . . . Bian, X. W. (2015). Activation of toll-like receptor 2 promotes invasion by upregulating MMPs in glioma stem cells. *Am J Transl Res*, *7*(3), 607-615. Retrieved from <https://www.ncbi.nlm.nih.gov/pubmed/26045899>
<https://www.ncbi.nlm.nih.gov/pmc/articles/PMC4448199/pdf/ajtr0007-0607.pdf>
- Wang, H., Yang, Y., Liu, J., & Qian, L. (2021). Direct cell reprogramming: approaches, mechanisms and progress. *Nat Rev Mol Cell Biol*, *22*(6), 410-424. doi:10.1038/s41580-021-00335-z

- Wang, Q., Hu, B., Hu, X., Kim, H., Squatrito, M., Scarpace, L., . . . Verhaak, R. G. W. (2017). Tumor Evolution of Glioma-Intrinsic Gene Expression Subtypes Associates with Immunological Changes in the Microenvironment. *Cancer Cell*, 32(1), 42-56 e46. doi:10.1016/j.ccell.2017.06.003
- Wang, S., Xia, P., Ye, B., Huang, G., Liu, J., & Fan, Z. (2013). Transient activation of autophagy via Sox2-mediated suppression of mTOR is an important early step in reprogramming to pluripotency. *Cell Stem Cell*, 13(5), 617-625. doi:10.1016/j.stem.2013.10.005
- Wang, Y., Xu, H., Liu, T., Huang, M., Butter, P. P., Li, C., . . . Fan, Y. (2018). Temporal DNA-PK activation drives genomic instability and therapy resistance in glioma stem cells. *JCI Insight*, 3(3). doi:10.1172/jci.insight.98096
- Weinhold, B. (2006). Epigenetics: the science of change. *Environ Health Perspect*, 114(3), A160-167. doi:10.1289/ehp.114-a160
- Wu, Y., Song, K., Hao, W., Li, J., Wang, L., & Li, S. (2022). Nuclear soluble cGAS senses double-stranded DNA virus infection. *Commun Biol*, 5(1), 433. doi:10.1038/s42003-022-03400-1
- Xie, J., Sheng, M., Rong, S., Zhou, D., Wang, C., Wu, W., . . . Shi, Y. (2023). STING activation in TET2-mutated hematopoietic stem/progenitor cells contributes to the increased self-renewal and neoplastic transformation. *Leukemia*, 37(12), 2457-2467. doi:10.1038/s41375-023-02055-z
- Yamaga, S., Aziz, M., Murao, A., Brenner, M., & Wang, P. (2024). DAMPs and radiation injury. *Front Immunol*, 15, 1353990. doi:10.3389/fimmu.2024.1353990
- Yang, W. C., Patel, K. G., Lee, J., Ghebremariam, Y. T., Wong, H. E., Cooke, J. P., & Swartz, J. R. (2009). Cell-free production of transducible transcription factors for nuclear reprogramming. *Biotechnol Bioeng*, 104(6), 1047-1058. doi:10.1002/bit.22517
- Yasuda, H., Leelahavanichkul, A., Tsunoda, S., Dear, J. W., Takahashi, Y., Ito, S., . . . Star, R. A. (2008). Chloroquine and inhibition of Toll-like receptor 9 protect from sepsis-induced acute kidney injury. *Am J Physiol Renal Physiol*, 294(5), F1050-1058. doi:10.1152/ajprenal.00461.2007
- Yeh, D. W., Huang, L. R., Chen, Y. W., Huang, C. F., & Chuang, T. H. (2016). Interplay between Inflammation and Stemness in Cancer Cells: The Role of Toll-Like Receptor Signaling. *J Immunol Res*, 2016, 4368101. doi:10.1155/2016/4368101
- Zang, J., Zheng, M. H., Cao, X. L., Zhang, Y. Z., Zhang, Y. F., Gao, X. Y., . . . Liang, L. (2020). Adenovirus infection promotes the formation of glioma stem cells from glioblastoma cells through the TLR9/NEAT1/STAT3 pathway. *Cell Commun Signal*, 18(1), 135. doi:10.1186/s12964-020-00598-7
- Zeuner, M. T., Kruger, C. L., Volk, K., Bieback, K., Cottrell, G. S., Heilemann, M., & Widera, D. (2016). Biased signalling is an essential feature of TLR4 in glioma cells. *Biochim Biophys Acta*, 1863(12), 3084-3095. doi:10.1016/j.bbamcr.2016.09.016

- Zhang, L., Bochkur Dratver, M., Yazal, T., Dong, K., Nguyen, A., Yu, G., . . . Vlashi, E. (2019). Mebendazole Potentiates Radiation Therapy in Triple-Negative Breast Cancer. *Int J Radiat Oncol Biol Phys*, 103(1), 195-207. doi:10.1016/j.ijrobp.2018.08.046
- Zhang, Q., & Cao, X. (2019). Epigenetic regulation of the innate immune response to infection. *Nat Rev Immunol*, 19(7), 417-432. doi:10.1038/s41577-019-0151-6
- Zheng, H., Wu, L., Xiao, Q., Meng, X., Hafiz, A., Yan, Q., . . . Cao, J. (2023). Epigenetically suppressed tumor cell intrinsic STING promotes tumor immune escape. *Biomed Pharmacother*, 157, 114033. doi:10.1016/j.biopha.2022.114033
- Zhou, G., Meng, S., Li, Y., Ghebre, Y. T., & Cooke, J. P. (2016). Optimal ROS Signaling Is Critical for Nuclear Reprogramming. *Cell Rep*, 15(5), 919-925. doi:10.1016/j.celrep.2016.03.084